

# The Physics of Herwig 7

J. Bellm<sup>1</sup>, G. Bewick<sup>2</sup>, S. Ferrario Ravasio<sup>3</sup>, S. Gieseke<sup>4</sup>, D. Grellscheid<sup>5</sup>, S. Kiebacher<sup>4</sup>,  
 P. Kirchgaeßer<sup>4</sup>, F. Loshaj<sup>4</sup>, M.R. Masouminia<sup>2</sup>, G. Nail<sup>6</sup>, A. Papaefstathiou<sup>7</sup>, S. Plätzer<sup>8</sup>,  
 M. Rauch<sup>4</sup>, P. Reimitz<sup>9</sup>, C. Reuschle<sup>1</sup>, P. Richardson<sup>2</sup>, D. Samitz<sup>10</sup>, P. Sarmah<sup>11</sup>, P. Schichtel<sup>2</sup>,  
 M.H. Seymour<sup>12</sup>, A. Siódmodk<sup>11,13</sup>, D. Stafford<sup>14</sup>, C.B. Strange<sup>4</sup>, S. Sule<sup>12</sup>, S. Webster<sup>2</sup>,  
 J. Whitehead<sup>11</sup>

<sup>1</sup>Department of Astronomy and Theoretical Physics, Lund University

<sup>2</sup>Institute for Particle Physics Phenomenology, Department of Physics, University of Durham

<sup>3</sup>Dipartimento di Fisica, Universitá di Torino, and INFN, Sezione di Torino

<sup>4</sup>Institute for Theoretical Physics, Karlsruhe Institute of Technology

<sup>5</sup>Department of Informatics, University of Bergen

<sup>6</sup>Higgs Centre for Theoretical Physics, University of Edinburgh

<sup>7</sup>Department of Physics, Kennesaw State University

<sup>8</sup>Theoretical Physics, NAWI Graz, University of Graz

<sup>9</sup>Instituto de Física, Universidade de São Paulo

<sup>10</sup>Department of Physics and Astronomy, University of Victoria

<sup>11</sup>Jagiellonian University, Kraków

<sup>12</sup>Particle Physics Group, Department of Physics and Astronomy, University of Manchester

<sup>13</sup>Theoretical Physics Department, CERN

<sup>14</sup>DESY, Hamburg

December 19, 2025

**Abstract** We present the physics foundations and recent developments of Herwig 7, the modern C++ successor of the original Fortran-based HERWIG and the Herwig++ 2.x series. Herwig 7 provides a flexible and systematically improvable framework for the simulation of high-energy lepton-lepton, lepton-hadron, and hadron-hadron collisions, with particular emphasis on QCD and electroweak (EW) effects. Hard scattering processes are generated within the automated *Matchbox* framework, which integrates external amplitude providers, supports tree-level, next-to-leading-order (NLO), and loop-induced matrix elements, and implements subtraction schemes, multi-channel phase-space sampling, dynamic scale choices, and both POWHEG- and MC@NLO-type matching algorithms. Consistent multijet merging at LO and NLO is provided, enabling precise predictions across a wide range of Standard Model processes. Parton radiation is simulated using two complementary showers: an angular-ordered shower incorporating QCD coherence and the heavy-quark dead-cone effect, and a dipole shower optimised for NLO matching and multijet merging. Higher-order corrections are included through matrix-element corrections and dedicated reweighting techniques, while QED and EW radiation are treated using a Yennie–Frautschi–Suura formalism and EW showering algorithms. The modelling of non-perturbative physics employs an advanced cluster hadronization framework with improved cluster formation, fission and decay, as well as colour reconnection models, heavy-quark effects, and interfaces to alternative hadronization schemes. The simulation of the underlying event is achieved with an extended eikonal multiple-partonic-scattering model, incorporating both semi-hard and soft components together with diffractive interactions, thereby enabling realistic descriptions of minimum-bias and underlying-event data. Herwig 7 thus represents a versatile event generator, providing a coherent, modular, and extensible platform for Standard Model and beyond-the-Standard-Model collider phenomenology at current and future facilities.

---

## Contents

1	Preface	3
2	Introduction	4
3	Hard processes	6
3.1	Overview	6
3.2	Leading-Order computations	7
3.3	Next-to-Leading Order computations	11
3.4	Cuts and jet definitions	17
3.5	Scale choices	18
3.6	Cross-section integrators and event sampling	19
3.7	Amplitude providers	22
3.8	Internal cross-checks	23
3.9	Built-in matrix elements	25
3.10	Les Houches interface	27
3.11	‘Blob’ Matrix Elements	28
3.12	Processes with incoming photons	28
3.13	Code structure	29
4	Parton showers	32
4.1	Overview	32
4.2	Angular-Ordered parton shower	35
4.3	Dipole shower	57
4.4	Perturbative decays and spin correlations	74
4.5	Intrinsic transverse momentum	76
4.6	Forced splitting	77
4.7	YFS-based QED radiation	77
4.8	Shower variations and reweighting	78
4.9	Code structure	83
5	Matching and merging	88
5.1	Overview	88
5.2	Handling of matching subtractions	88
5.3	KrkNLO	93
5.4	Multijet merging	94
5.5	Matrix element corrections	97
5.6	Matching and merging with <code>MadGraph5_aMC@NLO</code> LHE files	99
5.7	Code structure	99
6	Physics Beyond the Standard Model	102
6.1	Hard process	102
6.2	Decays	102
6.3	Off-shell effects	103
6.4	Model descriptions	104
6.5	Code structure	109
7	Hadronization	117
7.1	Cluster formation	118
7.2	Colour reconnection	118
7.3	Cluster fission	123
7.4	Cluster decays	125
7.5	HQET and spin-hadronization	128
7.6	Hadronization in BSM models	132
7.7	Interface to string hadronization model	134
7.8	Event-by-event hadronization corrections	134
7.9	Code structure	134
8	Underlying Event and beam remnants	137
8.1	Semi-hard partonic scatters	137
8.2	Soft partonic scatters	139
8.3	Soft particle production model	142
8.4	Diffraction	144
8.5	Connection to different simulation phases	144
8.6	Older soft models	145
8.7	Code structure	145
9	Hadronic decays	148
9.1	Particle properties	148
9.2	Line shapes	150
9.3	Tau decays	151
9.4	Strong and electromagnetic hadron decays	154
9.5	Weak hadronic decays	163
9.6	EvtGen interface	169
9.7	Code structure	169
10	Summary	171
Appendix A	Tuning of model parameters	173
Appendix B	Solution of the Sudakov equation	178
Appendix C	Treatment of the running coupling	180
Appendix D	Massless dipoles	183

## 1 Preface

The Monte Carlo event generator Herwig 7 is the result of the collective effort of a large number of people who have contributed to the project over the years. The development began in 2001 as a complete rewrite of the original Fortran code Herwig, which was then available as Herwig 6.5 [1–5]. The author list of this article comprises all contributors who have made significant contributions to the development of Herwig 7 since the publication of the last write-up for the Herwig++ 2 series [6]. Over the years, many authors have joined the collaboration and later moved on, after making valuable contributions to the code. We would like to express our gratitude for their efforts by acknowledging their contributions to the various releases. These are, in alphabetical order: Ken Arnold (2.6), Manuel Bähr (M, 2.1, 2.2, 2.3), Luca d'Errico (2.6), Nadine Fischer (7.0), Martyn Gigg (M, 2.1, 2.2, 2.3), Keith Hamilton (M, 2.0, 2.1, 2.2, 2.3, 2.5, 2.6), Marco Harrendorf (7.0), Seyi Latunde-Dada (M, 2.1, 2.2), Radek Podskubka (7.1), Daniel Rauch (7.0), Alberto Ribon (1.0, 2.0  $\beta$ , 2.0), Christian Röhr (2.5, 2.6, 2.7), Pavel Růžička (2.5), Alex Schofield (2.6), Thomas Schuh (2.7), Alexander Sherstnev (M, 2.1, 2.2), Phil Stephens (1.0, 2.0  $\beta$ , 2.0), Martin Stoll (2.6), Louise Suter (2.5), Jon Tully (M, 2.3), Alexandra Wilcock (2.7, 7.0), David Winn (2.5, 2.6), Benedikt Zimmermann (2.7). In parentheses we list their contributions to the previous release notes for the respective Herwig++ versions 1.0 [7], 2.0  $\beta$  [8], 2.0 [9], 2.1 [10], 2.2 [11], 2.3 [12], 2.5 [13], 2.6 [14], 2.7 [15], 7.0 [16], 7.1 [17], 7.2 [18], and 7.3 [19], as well as authorship of the previous write-up (M) [6]. At this point the name change from Herwig++ 2.x to Herwig 7 should be explained. As of version 7, we consider the program the true successor of the previous Fortran series, as all parts of the simulation are at least on an equal, and in many cases even superior, level of sophistication and detail.

A very special thank you goes to Bryan Webber, one of the principal authors of the original Herwig program and founders of the Herwig++ project (M, 1.0, 2.0  $\beta$ , 2.0, 2.1, 2.2), whose guidance and enthusiasm have made him a constant source of inspiration and a true *spiritus rector* for our collaboration. His continuous engagement and generous advice, from the early days of the project to the present, have been invaluable. We would also like to acknowledge Pino Marchesini, whose pioneering contributions laid essential foundations for our work. Our gratitude extends to Leif Lönnblad for his close collaboration and steadfast support of the ThePEG framework, which underpins much of our development. Finally, we thank Torbjörn Sjöstrand and Frank Krauss for many stimulating discussions, which have greatly enriched this project.

## 2 Introduction

Event generators are indispensable tools for high energy physics. General-purpose event generators describe high energy reactions across vastly different energy scales, multiplicity regimes, and at all levels of detail thereby enabling direct comparison to measurements carried out at colliders. Within the LHC era, there are three multi-purpose event generators, which have extensively been improved as compared to their older versions. The PYTHIA event generator is now available as PYTHIA 8 [20, 21], SHERPA [22, 23] has been developed as an independent project, and the THEPEG framework [24] for multi-purpose event generators has emerged from the PYTHIA 7 development. In the present document we describe the HERWIG 7 event generator, based on THEPEG, which has originated from the HERWIG++ development and continues in the spirit of the old HERWIG 6 program.

Multi-purpose event generators like HERWIG describe high energy particle collisions in several stages, expecting factorization due to the disparate energy and length scales:

1. *Elementary hard subprocess.* The incoming particles interact to produce the primary outgoing states. In lepton collisions these are the fundamental incoming leptons; in hadron collisions the incoming partons are extracted from the hadrons. The hard interaction is generally calculated at LO or NLO in perturbation theory. The energy scale of the hard scattering, together with its flow of colour, electric and weak charge, sets the initial conditions for subsequent QCD and EW parton showers.
2. *Initial- and final-state parton showers.* Coloured particles are perturbatively evolved from the hard scale down to an infrared cutoff. QCD coherence can be implemented through angular ordering, and dipole showers provide an alternative to describe QCD parton showers in the large- $N_c$  limit. Corrections beyond the large- $N_c$  limit, and the quest for logarithmic accuracy pose additional constraints.
3. *Decay of heavy objects.* Massive particles such as the top quark, EW bosons, Higgs bosons, and many BSM states decay on timescales comparable to parton showering. Radiation in both production and decay needs to be simulated consistently, ideally with full spin correlations preserved between stages.
4. *Multiple scattering.* At high energies, multiple partonic interactions within a single hadron-hadron collision are significant. Eikonal multiple interaction models are central to the HERWIG program, and can be extended to include diffractive contributions.
5. *Hadronization.* After perturbative evolution, coloured partons are projected into hadrons. This can be done using the string model, or through projections on colour-singlet clusters [2], which decay into hadrons and resonances. Colour reconnection plays an important role in dense environments with many coloured particles.
6. *Hadron decays.* Hadronic decays are typically modelled with matrix-element techniques, including off-shell effects and spin correlations, fully consistent with those in perturbative production and decay.

Herwig is a general-purpose event generator for the simulation of high-energy lepton-lepton, lepton-hadron and hadron-hadron collisions, built around the above paradigm. Particular emphasis is put on the accurate simulation of QCD radiation. It builds upon the heritage of the HERWIG Fortran program [1–5], while providing a much more flexible modular structure for future development. In comparison to the final Fortran version, HERWIG 7 already incorporates a number of substantially more advanced features. It provides a full simulation of high-energy collisions with the following special components:

- **Initial- and final-state QCD parton showers:** Herwig provides two complementary shower algorithms. The traditional angular-ordered shower incorporates the coherence of soft-gluon emission through angular ordering, correctly reproducing the logarithmic structure of QCD radiation [25]. A dipole-based shower [26, 27] is also available, designed for improved treatment of colour coherence and for systematic NLO matching and multijet merging. Developments of logarithmic accuracy and initial-state radiation in the angular-ordered shower are discussed in [28, 29], the accuracy in the presence of massive quarks has been addressed in [30], while studies of quark/gluon jet properties are presented in [31]. Mass effects in both showers are extensively discussed in [32], and spin correlations in shower branchings are detailed in [33]. Parton-shower uncertainties, along with their evaluation by reweighting, are analysed in [32, 34, 35]. All Herwig showers dynamically reproduce heavy quark contributions and hence the *dead-cone effect* [36] by using quasi-collinear splitting functions. The sensitivity to the parton shower cutoff and the logarithmic accuracy for heavy quark contributions have been studied in detail in [37].
- **Electroweak showers:** The simulation of the emission of quasi-collinear  $W$  and  $Z$  bosons has been developed to provide a consistent description of mixed QCD-EW radiation in high-energy collisions. The implementation of the EW parton shower in Herwig is described in [38]. Electroweak corrections within hard processes have also been considered in [39].
- **Matching and merging to higher-order calculations:** NLO QCD calculations are facilitated by the MATCHBOX framework [27]. MATCHBOX automates NLO fixed-order and matched calculations, to either of the two Herwig

shower algorithms, with both the MC@NLO and POWHEG matching methods. Interfaces to external matrix-element libraries allow a wide variety of processes to be calculated. Systematic NLO multi-jet merging [40, 41] is also implemented in MATCHBOX, for the dipole shower. An alternative matching method, the KrkNLO method, is described in [42, 43].

- **Colour matrix element corrections** provide full-colour real emission corrections to QCD radiation in the dipole shower. Their implementation is discussed in detail in [44, 45]
- **Hadronization and non-perturbative dynamics:** Jet hadronization is modelled using the cluster approach originally proposed in [2]. The model has been substantially extended in Herwig 7 to describe baryon production [46], enhanced strangeness production [47], and colour reconnection effects based on soft-gluon evolution [48]. The interplay of the perturbative cutoff with hadronization is analysed in [37], where first steps towards a new hadronization model are proposed. Spin effects in the hadronization of heavy hadrons have been described in [49]. Colour-sextet diquarks are incorporated as discussed in [50].
- **Decays of partons and hadrons:** A comprehensive framework is provided for the decays of hadrons and heavy particles. The treatment of multiple soft QED radiation is based on the Yennie–Frautschi–Suura (YFS) formalism [51]. Radiation in top-quark decays is described in [52], while general spin correlations in hadronic decays are implemented following [53]. The simulation of hard radiation in BSM decays is given in [54],  $\tau$ -lepton decays are detailed in [55], and a general framework for many-body BSM decays is provided in [56].
- **BSM physics:** Beyond-the-Standard-Model scenarios are supported through flexible interfaces to new models encoded via Feynman rules. Specific studies include parton-shower simulations of  $R$ -parity-violating supersymmetry, as well as collider phenomenology of split supersymmetry [57].
- **Underlying event and soft physics:** The description of the underlying event relies on an eikonal multiple parton-interaction model [58], rooted in the earlier JIMMY approach [59] and supplemented by non-perturbative extensions [60]. Subsequent developments include colour-reconnection models [61] and a dedicated treatment of soft and diffractive scattering based on the cluster model [62].

Some of these features were already present in the first release of Herwig++ [7]. However, there have been extensive improvements to both the physics content and the internal structure of the simulation since that first release, and Herwig 7 has added and consolidated many features on top of the first generations of Herwig++, ultimately replacing both the HERWIG 6 and Herwig++ developments. Given the significant differences between the current version of the program, 7.3, and that described in [7], we present here a comprehensive description of all features of the code. Updates to this manual will cover the novel features developed for the 7.4 series and beyond.

The program and additional documentation are available from

<https://herwig.hepforge.org>

Herwig is distributed under the GNU General Public License (GPL), version 3. This ensures that the source code remains available to users, who may use and modify it under the conditions of the licence. As Herwig is developed within an academic research collaboration and represents the result of many years of work, it is accompanied by guidelines<sup>1</sup> agreed within the MCnet collaboration. These set out expectations of responsible use, in particular the citation of relevant physics publications. The designated reference for each Herwig release (this manual for versions 7.0 onwards) should always be cited, along with the original literature on which a given study relies. To facilitate this, Herwig automatically produces a `LATEX` file listing the appropriate primary citations for the modules used in any given run. The authors are happy to assist users in determining the correct citations for their studies.

The structure of this manual closely follows the general workflow of an event generator. In Sec. 3 we discuss calculations of the hard process, including the interfaces to external matrix element libraries which can provide input for matrix elements. Sec. 4 focuses on the two available parton showers, the angular ordered shower and the dipole shower. Sec. 5 presents how parton showers and hard matrix elements at leading and next-to-leading order can be consistently combined with each other using matching and merging algorithms. Sec. 6 is devoted to the simulation of physics beyond the standard model, while Sec. 7 discusses hadronization and colour reconnection. Sec. 8 describes how HERWIG models multiple parton interactions and the beam remnants. Finally, hadronic decays are covered in Sec. 9, before we briefly summarize what has been presented in this manual, and give pointers to further resources. Each section discusses the physics assumptions and models, as well as the user flags and some of the code structure. We devote appendices to tuning, and some of the core algorithms used.

<sup>1</sup>These guidelines are contained in the `GUIDELINES` file distributed with the release and are also available from [http://www.montecarlonet.org/publications\\_guidelines](http://www.montecarlonet.org/publications_guidelines).

## 3 Hard processes

### 3.1 Overview

#### 3.1.1 Philosophy

The improved physics implementation of the hard process, specifically the approaches that include higher-order corrections and the production of additional jets, require a very detailed control over the hard process input, typically beyond the level that can be achieved by using event files. Within Herwig 7 the philosophy for generating the hard process has hence been one of automation, making use of external libraries to calculate scattering amplitudes, while all of the other methods required to assemble full NLO QCD matched and/or merged cross sections are provided within the program itself.

The core module responsible for the set up of hard cross sections along with the subtractions required for matching, and the further handling of contributions to form a multijet-merged simulation, is called Matchbox. Matchbox contains modules for process bookkeeping, diagram generation and mapping, the creation of subtraction terms, phase-space sampling, scale choices, generation cuts and parton shower matching to both available shower modules. Amplitudes for a small number of processes are available through in-house calculations shipped with a Herwig release, while Matchbox in general requires external amplitude libraries to work in a truly automated fashion.

In previous Herwig releases, hard processes have been implemented in a small library of built-in matrix elements for Herwig++, some of them at NLO. These can be used for the simulation of dedicated processes and are documented in the section on [Section 3.9](#).

#### 3.1.2 General components and workflow

The Matchbox module is centred around a Factory object responsible for assembling hard process cross sections using external input at the level of amplitudes, where interfaces are inherited from the MatchboxAmplitude base class. Details of the code are documented in [Section 3.13](#).

Once a process at a certain coupling order has been requested, Matchbox determines the possibly contributing partonic subprocesses based on typical restrictions such as charge conservation (these restrictions can be lifted if required for physics simulation beyond the Standard Model), scans the repository for MatchboxAmplitude objects which claim to be capable of calculating the desired process either at tree level, loop level or both and will then determine Feynman diagram topologies; a similar treatment is applied to the real emission process. The diagram information is used to determine both the subtraction terms required to render the individual cross section contributions finite, as well as to set up a multi-channel phase-space generator to perform efficient sampling of events, see [Section 3.2.6](#).

Since each amplitude can represent more than one process through the use of crossing, amplitudes are hooked into the actual (subtracted) matrix element objects which represent a contribution to the total cross section. If a matching to a parton shower is requested, Matchbox will also supplement the subtraction terms by the matching subtractions and rearrange the cross section into Born/virtual, integrated subtraction, and real/shower subtracted contributions. Details of the matching algorithm are discussed in [Section 5.1](#).

Additional components are used to perform the jet finding and cuts on various objects in the final state of the hard process; also a number of (dynamical) scale choices is provided within the module. The merging of cross sections for the production of different jet multiplicities is described in [Section 5.4](#).

Matchbox has been used and is used to perform fixed-order calculations for state-of-the-art processes. One of the earliest examples where it has been used for challenging processes is the full EW Higgs boson plus three jet production at Next-to-Leading Order (NLO) QCD [63, 64], from which example results are shown in [Fig. 3.1](#).

#### 3.1.3 Input file steering

In preparation for the Herwig 7 release the input files were simplified in order to reflect the more generic handling of the hard process. Several sequences of logically interrelated commands have been grouped into small building block input files called snippets and should serve as the main source of steering the hard process generation and the selection of matching paradigm and hard process accuracy within Herwig. A small number of changes to the example input files are required to set up a hard process, notably the

- incoming and outgoing particles of the hard process, also referring to groups of particles such as jets,
- desired coupling orders,
- scale choice and generation cuts, and the

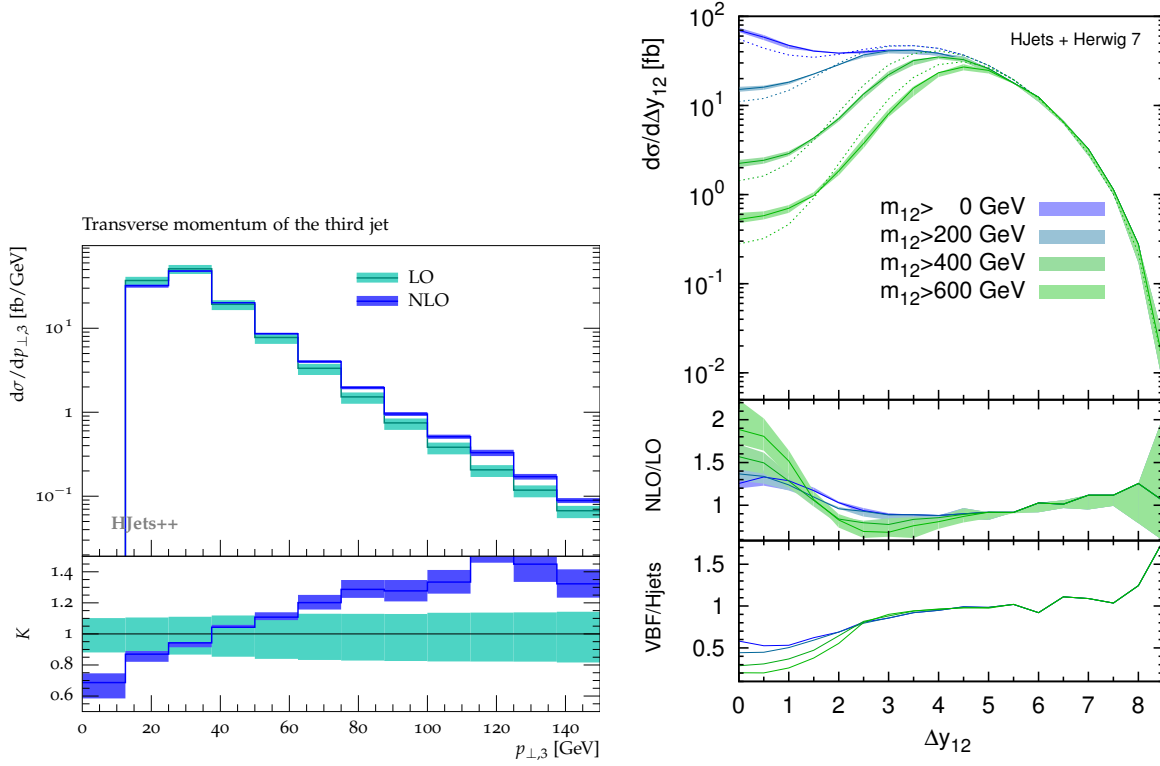


Fig. 3.1: Sample results from fixed-order calculations of VBF processes obtained with Matchbox. The left panel shows the spectrum of the third jet in Higgs-plus-three-jet events at NLO QCD using the full EW process. The right panel shows a comparison of the rapidity difference of the tagged jets, comparing the VBF approximation to the full calculations in events with one Higgs and three jets.

- matching algorithm and hard process accuracy.

As such, a typical Matchbox-based collider simulation is set up with an input file enabling the Matchbox module and making adjustments for a particular collider type before setting the couplings and defining the process of interest. More details of these input files are covered in the [herwig-tutorials](#). Tree-level and loop-induced leading-order cross-sections are both supported, and phase-space generation can be adapted to the latter, see [Section 3.2.6](#).

## 3.2 Leading-Order computations

The starting point for all cross-section calculations are cross-sections at the Leading Order (LO), mostly mediated through tree-level scattering amplitudes.<sup>2</sup> In this section we outline the basic definitions and set some notation, before presenting the algorithmic techniques used for the generation of leading-order cross-sections. Advanced topics relevant for NLO computations, as well as matching and merging are covered in [Section 3.3](#) as well as [Section 5.1](#) respectively.

### 3.2.1 LO cross-section

The LO cross-section,  $\sigma^{\text{LO}}[u]$ , is given by integrals over longitudinal momentum fractions,  $x_a, x_b$ , of two (incoming) initial state partons, and the Lorentz invariant phase-space,  $\phi_n$ , of  $n$  (outgoing) final-state partons. In a notation in anticipation of [Section 3.3](#), we write the total LO cross-section for the scattering of two incoming hadrons,  $A, B$ , as

$$\begin{aligned} \sigma^{\text{LO}}[u] &= \int df d\sigma^B(\phi_n) u(\phi_n) \\ &= \sum_{a,b} \sum_{\{n|ab\}} \int df_{ab}(x_a, x_b) d\sigma^B_{ab}(\phi_{n|ab}|p_a(x_a), p_b(x_b)) u(\phi_{n|ab}|p_a(x_a), p_b(x_b)) , \end{aligned}$$

<sup>2</sup>If matrix elements for loop-induced processes are provided, these can be used in leading-order computations too. The details for the kinematic mapping in the phase-space generation differ slightly in this case, as described in [Section 3.2.6](#).

where we sum over all possible partonic configurations, also referred to as the hard processes or subprocesses,  $a, b \rightarrow f_n = \{n|ab\}$ , that can occur in the hadronic scattering. The longitudinal momentum fractions define the partonic initial state momenta,  $p_a, p_b$ , in terms of the incoming hadron momenta,  $P_A, P_B$ , through  $p_a = p_a(x_a) = x_a P_A$  and  $p_b = p_b(x_b) = x_b P_B$  respectively. Momentum conservation in the partonic centre-of-mass frame,  $p_a(x_a) + p_b(x_b) = Q = p_1 + \dots + p_n$ , with a total momentum  $Q$ , tells us that the (Lorentz invariant) partonic final-state phase-space depends implicitly on the longitudinal momentum fractions, i.e.  $\phi_n = \{\phi_{n|ab}|p_a(x_a), p_b(x_b)\} = \{\phi_{n|ab}|x_a P_A, x_b P_B\}$ . More details on phase-space generation, and the mapping of  $\phi_n$  to a unit hypercube, will be covered in [Section 3.2.6](#).

The differential cross-section for the subprocess  $a, b \rightarrow f_n = \{n|ab\}$  is given by the Born matrix element (or amplitude) squared, weighted by the parton distribution functions for the incoming partons and the flux factor (plus additional factors for the unit conversion),

$$\frac{d f_{ab} d\sigma_{ab}^B}{d\phi_{n|ab} dx_a dx_b} = \frac{\hbar^2 c^2}{\mathcal{F}(p_a(x_a)p_b(x_b))} f_{a/A}(x_a, \mu_F) f_{b/B}(x_b, \mu_F) \times \\ \times \mathcal{B}_{n|ab}(\phi_{n|ab}|p_a(x_a), p_b(x_b)) \theta_c(\phi_{n|ab}|p_a(x_a), p_b(x_b)) ,$$

and where the Born matrix element squared is essentially evaluated as the square of a vector in spin and colour space<sup>3</sup>  $\langle \mathcal{M}^{(0)} | \mathcal{M}^{(0)} \rangle$ ,

$$\mathcal{B}_{n|ab}(\phi_{n|ab}|p_a(x_a), p_b(x_b)) \\ = N_{n|ab} \left\langle \mathcal{M}_{n|ab}^{(0)}(\phi_{n|ab}|p_a(x_a), p_b(x_b)) \left| \mathcal{M}_{n|ab}^{(0)}(\phi_{n|ab}|p_a(x_a), p_b(x_b)) \right. \right\rangle ,$$

with the additional weight  $N_{n|ab} = 1/(S_{n|ab} n_s(a, b) n_c(a, b))$  containing symmetry factors for identical final-state partons and averaging factors for initial state spin and colour degrees of freedom. The default convention for amplitudes within the Matchbox framework is that all physical processes are calculated by crossing an amplitude with all legs outgoing to the reaction under consideration, though this can be overwritten within the amplitude interfaces to be described in [Section 3.7](#). The amplitude interfaces also provide the possibility to return results for squared matrix elements directly. The choice of a basis for colour space and the evaluation of the matrix element squared will be discussed in detail in [Section 3.2.5](#). The spin degrees of freedom are currently summed over, though some amplitude providers can provide spin density matrices.

The flux factor is  $\mathcal{F}(p_a p_b) = 4 p_a p_b = 2 x_a x_b S$  and  $S$  denotes the hadronic centre-of-mass energy. The definition of the total cross-section requires a choice for renormalization and factorization scales  $\vec{\mu} = (\mu_R, \mu_F, \mu^{\text{QED}})$ , to be discussed in detail in [Section 3.5](#), and a set of acceptance criteria, or phase-space cuts  $\theta_c(\phi_n)$  applied to the kinematic configuration (on the Monte Carlo generation level), which will be covered in [Section 3.4](#). The cross-section  $\sigma^{\text{LO}}[u]$  is a functional of the infrared-safe observable  $u(\phi_n)$ , also defined over the phase-space configuration  $\phi_n$ . In order for it to be calculated correctly, the phase-space cuts  $\theta_c(\phi_n)$  must not be stronger than those implied by  $u(\phi_n)$  (that is, there must be no region of  $\phi_n$  in which  $\theta_c$  is zero but  $u$  is non-zero). Events are distributed according to the differential cross-section, normalized to the total cross-section.

### 3.2.2 Process setup

Subprocesses are typically specified by groups of allowed incoming partons, and desired outgoing partons, as well as a coupling power which here refers to the cross-section at the lowest order in perturbation theory. At the moment only powers of the strong and electromagnetic coupling are considered, with the assumption that Yukawa interactions are mediated by an electromagnetic coupling. For loop-induced processes, the proper powers of couplings required to make the loop graphs need to be chosen.

Groups of particles can also be provided as the initial- and final-states of a process, e.g. to supply a list of jet constituents, charged leptons, or the like. For all possible combinations the MatchboxFactory class then determines if the subprocess satisfies charge conservation, colour conservation, conservation of lepton and quark number, and possibly the compatibility with flavour-diagonal interactions if desired. These restrictions help reducing the complexity of further bookkeeping tasks but can be relaxed individually.

Once a set of subprocesses compatible with the restrictions is identified, the list of available MatchboxAmplitude objects is considered to provide the actual matrix element calculations and further steps required for the assembly of a complete cross-section. Notably, MatchboxAmplitude objects will be queried if they are able to provide matrix elements for the

<sup>3</sup>Here we assume the leading-order (or Born) cross-section for  $n$  final-state partons to be defined through tree-level matrix elements  $\mathcal{M}_n^{(0)}$ . This is different for loop-induced processes, for which the lowest order matrix elements contain loops. If the corresponding matrix elements are provided, these can be used in leading-order computations too. The details for the kinematic mapping in the phase-space generation differ slightly in this case, as described in [Section 3.2.6](#).

process considered and will then be used to build full matrix element objects, as well as instances of the XComb objects responsible for caching information associated with a given phase-space point. In the case that several amplitude objects claim responsibility for a given subprocess, the user can choose to prioritize some implementations amongst others.

A typical matrix element implementation will then invoke a Tree2toNGenerator to determine the diagrams contributing to the process, given the coupling powers considered as well as a set of vertices to be considered. The diagrams are determined by a clustering procedure on the basis of the list of vertices, however their use is only in aiding some phase-space generator implementations, to determine a set of subtraction terms contributing to a given process at NLO, and to provide (unphysical) information when assigning mother-daughter relations to the partons contributing to a hard subprocess. For an overview of the core components and code structure see [Section 3.13](#).

### 3.2.3 Low-level amplitude interfaces

While Matchbox fully supports interfaces at the level of matrix elements squared, the default choice is to work at the level of colour and helicity dependent amplitudes. Once a colour basis has been fixed and the contributing colour structures have been enumerated, a matrix element implementation needs to be able to supply the amplitude multiplying a given colour structure, for a fixed set of spins of the external legs.  $2s + 1$  combinations are considered for a spin  $s$  particle, however after a number of evaluations of the matrix element only those combinations are kept for which the implementation has not returned a zero amplitude, i.e. we assume that such combinations vanish for all phase-space points. A similar treatment is foreseen for colour structures where up to now we rely on the colour basis object (see [Section 3.2.5](#)) supplied with the matrix element implementation to be aware of the colour structures actually contributing to a given process.

The amplitude values obtained at a given phase-space point are cached together in a MatchboxXComb object, and the colour basis object will then be responsible for evaluating squared matrix elements, and subsequently colour and spin correlated matrix elements required in NLO calculations, see [Section 3.3](#). Using the spin dependent amplitudes, spin density matrices can also be evaluated and be supplied to the spin correlation algorithms in our decay and parton shower modules. Full flexibility is provided as far as the inclusion of fixed reference or running couplings, averaging factors, and other conventions relevant to virtual corrections are concerned.

### 3.2.4 BLHA-type interfaces

BLHA-type interfaces are an interface level for evaluating cross-sections at the level of amplitudes squared, in the spirit of directly implementing interfaces of the Binôth Les Houches Accord (BLHA) [\[65\]](#). This is the preferred mechanism to obtain one-loop virtual corrections for NLO calculations, and we hence typically refer to amplitude interfaces using this paradigm as ‘One-Loop Providers (OLPs)’. OLP interfaces do inherit from the base MatchboxAmplitude object but are limited to the case of matrix elements squared, interferences of one-loop with tree level amplitudes, and the direct evaluation of colour and spin correlated amplitudes. They can hence fully be used for fixed-order computations, however if a physically sensible assignment of colour flows to the hard process for subsequent showering is desired, amplitude information is required. If not available, colour flows will be randomly assigned without any specific weighting.

### 3.2.5 Handling of colour bases

For a fixed colour basis a general (QCD) amplitude  $|\mathcal{M}\rangle$  can be decomposed in terms of a finite set (dimension  $d_c$ ) of colour structures  $|\alpha\rangle$  as

$$|\mathcal{M}\rangle = \sum_{\alpha=1}^{d_c} \mathcal{M}_\alpha |\alpha\rangle .$$

Examples for such bases are the so-called trace basis or colour flow basis, both available in the Matchbox module. Suppressing spin indices for readability, we consider colour amplitudes to fill a complex vector  $\mathcal{M}_\alpha$  and information on the colour basis is handled through linear algebra in this complex vector space.

In general colour bases are not orthogonal, thus calculating a squared matrix element or similarly for NLO calculations a Born/one-loop interference requires knowledge of a scalar product matrix  $S_{\alpha\beta} = \langle\alpha|\beta\rangle$ , in terms of which a colour-summed, squared matrix element is calculated as  $|\mathcal{M}|^2 = \mathcal{M}_\alpha^* S_{\alpha\beta} \mathcal{M}_\beta$ .

Similarly, colour-correlated matrix elements – needed for NLO corrections – can be expressed as

$$\langle\mathcal{M}|\mathbf{T}_i \cdot \mathbf{T}_j|\mathcal{M}\rangle = \mathcal{M}_\alpha^* T_{i,\alpha\gamma}^\dagger S'_{\gamma\delta} T_{j,\delta\beta} \mathcal{M}_\beta ,$$

where  $S'$  is the scalar product matrix for a final state with an additional parton and the  $T_{i,\alpha\gamma}$  are appropriate representations of the colour charge operators, see e.g. [27]. Once  $T_{i,\alpha\gamma}^* S'_{\gamma\delta} T_{j,\delta\beta}$  is determined, the problem reduces to linear algebra, which we perform with the boost library [66].

While setting up a process calculation, the amplitudes used initialize the colour basis object, which calculates the scalar product matrices and colour charge representations required. The results are then stored in an external file for further reference. Currently, some built-in colour bases for low multiplicities are available, and we also release a copy of the ColorFull package [67], as well as some components of the CVolver library [68, 69] with appropriate interfaces to Matchbox amplitudes.

In order to generate colour flow information for the hard process, the ColourBasis objects provide information on colour connections and the respective partial subamplitudes to evaluate the weights by which a certain colour flow is selected. In all cases we use, a single colour flow can be assigned from a given colour structure and we choose those with weights

$$w_\alpha = \frac{|\mathcal{M}_\alpha|^2}{\sum_\beta |\mathcal{M}_\beta|^2}.$$

### 3.2.6 Phase-space generation

The Lorentz invariant phase-space for  $n$  outgoing particles with momenta  $p_i$  and masses  $m_i$ , and of total momentum  $Q$  is given by

$$d\phi_n(p_1, m_1, \dots, p_n, m_n | Q) = (2\pi)^4 \delta \left( \sum_{i=1}^n p_i - Q \right) \prod_{i=1}^n \frac{d^4 p_i}{(2\pi)^3} \delta(p_i^2 - m_i^2) \theta(p_i^0)$$

A phase-space generator maps random numbers to physical momenta,

$$\phi_n = \{p_1, \dots, p_n\} = \Phi_n(\vec{r})$$

where the mapping from random numbers  $\vec{r}$  to the actual momenta is in general not unique, and more random numbers might be required then there are actual degrees of freedom. An importance sampling phase-space generator determines a mapping in such a way that the resulting Jacobian factor broadly resembles the inverse of the behaviour of the cross-section to integrate in order to ensure a fast convergence of the Monte Carlo integration.

Phase-space generators within the Matchbox module inherit from a general interface, and are also responsible for assigning a tree-structure to a hard process that represents the diagram that most probably contributes the bulk of the cross-section at this point. This is, by default, done based on the propagator and coupling structure of the topologies encountered, evaluated with the momenta which have just been generated. Indeed, if  $D_i = p_i^2 - M_i^2 + iM_i\Gamma_i$  is the propagator for the  $i$ -th internal line, and  $g_k$  is the (canonical) coupling of vertex  $k$ , we associate a weight

$$w_{(E, V)} = \prod_{\text{lines } i \in E} \prod_{\text{vertices } k \in V} \frac{|g_k|^2}{(|D_i|^2)^\xi} f(|p_i^2|)$$

where  $\xi$  and  $f$  are additional quantities depending on the particle species propagating along the given line, and a topology is selected with a probability proportional to this weight.

The phase-space generators can, if desired, generate the incoming legs' momentum fraction either directly or indirectly through generating the other momenta, though the default way of operation is that the incoming momenta have been fixed by the responsible PartonExtractor instance and the phase-space generators solely need to determine a set of final-state momenta.

#### 3.2.6.1 The TreePhasespace generator

The TreePhasespace generator uses the diagram information supplied previously to determine several different mappings according to decomposing the phase-space measure as

$$d\phi_n = \frac{1}{\sum_{(E', V')} w_{(E', V')}} \sum_{(E, V)} w_{(E, V)} d\phi_n|_{\phi_n = \Phi_{E, V}(\vec{r})}$$

The tree mappings are organized as  $1 \rightarrow 2$  splittings of either incoming to incoming and outgoing ('spacelike') or outgoing to two outgoing ('timelike') particles and are iteratively used to build up the tree diagram identified by  $V, E$ .

The factorization underlying timelike splittings is the standard phase-space factorization for decays,

$$\begin{aligned} d\phi_n(p_1, m_1, \dots, p_i, m_i, \dots, p_j, m_j, \dots, p_n, m_n | Q) = \\ dm_{ij}^2 \theta(m_{ij} - m_i - m_j) \times \\ d\phi_{n-1}(p_1, m_1, \dots, p_{ij}, m_{ij}, \dots, p_n, m_n | Q) d\phi_2(p_i, p_j | p_{ij}) \end{aligned}$$

For spacelike splittings the situation is more complicated. Here we use a composition similar to the one above, however we consider scattering of a possibly off-shell and on-shell leg, and use a light-cone type decomposition for the outgoing momentum considered. This way, rungs on a  $t$ -channel ladder are subsequently removed until a core two to two scattering can be generated. As the procedure has a preferred direction, we randomly select one of the incoming legs to start the algorithm. Once all space-like splittings have been performed, the time-like ones are initiated using the standard decay factorization.

In both cases the virtualities of the intermediate line  $ij$  or  $ia$  are determined in a way to cancel the behaviour of the propagator factor  $D_{ij}$  or  $D_{ia}$  such that the Jacobian is adapting to the structure of the weight for this topology, with the expectation that the normalization of the topology weights will resemble the leading behaviour of the (tree level) cross-section. The procedure of successive splitting proceeds until a 2-to-2 (sub-)diagram is encountered for which the final momenta are then determined to cancel either the  $s$ - or  $t$ -channel we are left with. Since we do introduce a preferred direction by applying splittings from one incoming leg towards the other one, the choice of direction the algorithm proceeds in is randomized.

### 3.2.6.2 Phase-space generation for loop-induced processes

For setting up more suitable kinematic mappings in the case of loop induced processes we introduce fictitious particles, and the corresponding vertices and couplings, to emulate the kinematics transmitted through loops. The TreePhasespace generator will find associated fictitious diagrammatic information in that case, and assemble the corresponding weights in the kinematic mappings. Currently implemented are versions of such fictitious particles corresponding to colour and charge flowing through loops ( $ccLP-$  and  $ccLP+$ ), only colour ( $cLP$ ), or none of the above ( $nLP$ ), more specifically the ones necessary for loop-induced  $W^+W^-$  production at the LHC, which means only colour octets and integer charges. For example for the loop-induced process  $gg \rightarrow W^+W^-$ , we need such configurations as the vertices  $(g, g, nLP)$ , with coupling  $\alpha_s^2 \alpha_e^0$ , and  $(nLP, W^+, W^-)$ , with coupling  $\alpha_s^0 \alpha_e^2$ , with an intermediate  $nLP$  particle in an  $s$ -channel configuration, or as the vertices  $(ccLP-, g, W^+)$ , with coupling  $\alpha_s^1 \alpha_e^1$ , and  $(ccLP+, g, W^-)$ , with coupling  $\alpha_s^1 \alpha_e^1$ , with an intermediate  $ccLP$  particle in a  $t$ -channel configuration.

### 3.2.6.3 The RAMBO generator

The RAMBO phase-space generator performs flat phase-space sampling as detailed in [70, 71]; it is used for cross checks and phenomenological studies and not recommended as a production algorithm.

### 3.2.6.4 The FlatInvertible generator

The FlatInvertible phase-space generator performs flat phase-space sampling as detailed in [71]; this is the only phase-space generator that provides a unique and invertible mapping from  $3n - 4$  random numbers to  $3n - 4$  physical degrees of freedom in the phase-space point. It is used for pre-sampling matrix element correction factors and not recommended as a production algorithm.

### 3.2.6.5 Two-to-one processes

The phase-space generators described above do not apply for two-to-one processes and are overwritten in the Matchbox framework, by a routine that generates a rapidity for the final-state system, and determines the incoming momentum fractions from this rapidity and the system's mass.

## 3.3 Next-to-Leading Order computations

### 3.3.1 NLO cross-section

For NLO computations, we follow the paradigm of NLO subtraction and matching, further described in Section 5.1, as outlined in [16, 27] and further in [32], and as detailed in [72, 73]. Within the subtraction paradigm the NLO cross-section, e.g. for a process with  $n$  final-state partons at the Born level, is written as

$$\sigma^{\text{NLO}}[u] = \sigma^{\text{LO}}[u] + \sigma^{\text{R}-\text{A}}[u] + \sigma^{\text{V+A+C}}[u],$$

where  $\sigma^{\text{LO}}$  denotes the LO or Born cross section,  $\sigma^{\text{R}-\text{A}}$  the NLO subtracted real-emission cross-section, and  $\sigma^{\text{V+A+C}}$  the combination of NLO virtual cross-section, analytically integrated subtraction terms and collinear counterterms (PDF

counterterms) for initial state partons. The LO or Born cross-section was already discussed in Section 3.2.1. Below we will briefly outline how these cross-sections are calculated, focusing on the real-subtracted cross-section which is the most relevant for matching to parton showers.

### 3.3.1.1 NLO subtracted real-emission cross-section

The NLO subtracted real-emission cross-section is written as

$$\begin{aligned} \sigma^{R-A}[u] &= \int df \left[ d\sigma^R(\phi_{n+1}) u(\phi_{n+1}) - \sum_i d\sigma_{(i)}^A(\phi_{n+1}) u(\tilde{\phi}_{n|(i)}(\phi_{n+1})) \right] \\ &= \sum_{a,b} \sum_{\{n+1|ab\}} \int df_{ab}(x_a, x_b) \left[ d\sigma_{ab}^R(\phi_{n+1|ab}|p_a(x_a), p_b(x_b)) u(\phi_{n+1|ab}|p_a(x_a), p_b(x_b)) \right. \\ &\quad \left. - \sum_i d\sigma_{(i)}^A(\phi_{n+1|ab}|p_a(x_a), p_b(x_b)) u(\tilde{\phi}_{n|(i)}(\phi_{n+1|ab}|p_a(x_a), p_b(x_b))) \right], \end{aligned}$$

where

$$\begin{aligned} \frac{df_{ab} d\sigma_{ab}^R}{d\phi_{n+1|ab} dx_a dx_b} &= \frac{\hbar^2 c^2}{\mathcal{F}(p_a(x_a)p_b(x_b))} f_{a/A}(x_a, \mu_F) f_{b/B}(x_b, \mu_F) \times \\ &\quad \times \mathcal{R}_{n+1|ab}(\phi_{n+1|ab} | p_a(x_a), p_b(x_b)) \theta_c(\phi_{n+1|ab}|p_a(x_a), p_b(x_b)), \end{aligned}$$

with

$$\begin{aligned} \mathcal{R}_{n+1|ab}(\phi_{n+1|ab} | p_a(x_a), p_b(x_b)) \\ = N_{n+1|ab} \left\langle \mathcal{M}_{n+1|ab}^{(0)}(\phi_{n+1|ab} | p_a(x_a), p_b(x_b)) \mid \mathcal{M}_{n+1|ab}^{(0)}(\phi_{n+1|ab} | p_a(x_a), p_b(x_b)) \right\rangle, \end{aligned}$$

and where

$$\begin{aligned} \frac{df_{ab} d\sigma_{(i)}^A}{d\phi_{n+1|ab} dx_a dx_b} &= \frac{\hbar^2 c^2}{\mathcal{F}(p_a(x_a)p_b(x_b))} f_{a/A}(x_a, \mu_F) f_{b/B}(x_b, \mu_F) \times \\ &\quad \times \mathcal{A}_{(i)}(\phi_{n+1|ab}|p_a(x_a), p_b(x_b)) \theta_c(\tilde{\phi}_{n|(i)}(\phi_{n+1|ab}|p_a(x_a), p_b(x_b))), \end{aligned}$$

with

$$\mathcal{A}_{(i)}(\phi_{n+1|ab}|p_a(x_a), p_b(x_b)) = N_{n+1|ab} n_c(a, b) \mathcal{D}_{(i)}(\phi_{n+1|ab}|p_a(x_a), p_b(x_b)).$$

$\{\phi_{n+1|ab}|p_a, p_b\}$  denotes the phase-space of the hard process  $a, b \rightarrow f_{n+1} = \{n+1|ab\}$ . The corresponding differential phase-space is  $d\phi_{n+1|ab} = d\phi_{n+1|ab}(\phi_{n+1|ab}|p_a, p_b)$ . Here we have again  $p_a = p_a(x_a) = x_a P_A$ ,  $p_b = p_b(x_b) = x_b P_B$ , and  $\mathcal{F}(p_a p_b) = 4 p_a p_b = 2 x_a x_b S$ .  $N_{n+1|ab} = \frac{1}{S_{n+1|ab} n_s(a, b) n_c(a, b)}$  accounts for symmetry factors for identical final-state partons, as well as for the averaging over spin and colour degrees of freedom of the initial state partons, which are denoted by  $n_s(a, b)$  and  $n_c(a, b)$  respectively.

The sum over  $i$  is taken over all possible dipole configurations, where the  $\mathcal{D}_{(i)} \in \{\mathcal{D}_{ij,k}, \mathcal{D}_{ij}^a, \mathcal{D}_k^{ai}, \mathcal{D}^{ai,b}\}$  denote the dipole subtraction terms, as defined in [72, 73]. The dipole subtraction terms depend on spin- and colour-correlated Born matrix elements, further discussed in Section 3.3.5. The  $\tilde{\phi}_{n|(i)}(\phi_{n+1|ab}|p_a, p_b)$  denote the corresponding so-called reduced tilde kinematic mappings, and for later reference we further define the inverse tilde kinematic mappings  $\tilde{\phi}_{n+1|(i)}$ , such that

$$\tilde{\phi}_{n+1|(i)}(\tilde{\phi}_{n|(i)}(\phi_{n+1|ab}|p_a, p_b), R_{(i)}(\phi_{n+1|ab}|p_a, p_b)) = \{\phi_{n+1|ab}|p_a, p_b\},$$

or in short

$$\tilde{\phi}_{n+1|(i)}(\tilde{\phi}_{n|(i)}(\phi_{n+1}), R_{(i)}(\phi_{n+1})) = \phi_{n+1},$$

and where  $R_{(i)}$  denotes the set of additional emission variables – an emission scale, a momentum fraction and an azimuthal variable – corresponding to the dipole configuration  $i$ .

### 3.3.1.2 NLO virtual cross-section and integrated subtraction terms

The combination of NLO virtual cross-section, analytically integrated subtraction terms and collinear counterterms (PDF counterterms) for initial state partons, is cast in terms of the insertion operators **I**, **P** and **K**, such that

$$\sigma^{V+A+C}[u] = \sigma^{V+I}[u] + \sigma^{P+K}[u],$$

The explicit poles in dimensional regularisation cancel between the (UV renormalised) NLO virtual cross-section, the integrated subtraction terms and the PDF counterterms, such that  $\sigma^{V+A+C}$  can be integrated numerically in four dimensions. The **I** operator contains all the explicit poles in dimensional regularisation, from the integrated subtraction terms and the PDF counterterms, that are necessary to cancel the IR poles in the NLO virtual cross-section. The **P** and **K** operators contain finite remainders, which are left after the factorisation of initial state collinear singularities into the PDFs. The **V** + **I** contributions have identical kinematics to the leading order contribution, while the **P** + **K** contribution contains an additional convolution over an incoming momentum fraction, as will be discussed in more detail below.

By default, all contributions that are considered to be virtual corrections are evaluated together with the leading order contribution. For efficiency reasons, however, the contributions from the virtual corrections together with the **I** operator, i.e.  $\sigma^{V+I}$ , and the contributions from the **P** and **K** operators, i.e.  $\sigma^{P+K}$ , can be treated as independent contributions to the same subprocess and will in this case be integrated separately. The partons which are summed in the insertion operator contributions are all inferred from the content of the particle groups defining the proton and jet content, including the possibility of massive jet constituents.

Several internal cross-checks can be performed for the cancellation of  $\epsilon$  terms, and the independence of phase-space restrictions on the subtraction terms and other finite-term ambiguities, see Section 3.8

### 3.3.1.3 The **V**+**I** contribution

The **V**+**I** contribution is written as

$$\begin{aligned} \sigma^{V+I}[u] &= \int df \left[ d\sigma^V(\phi_n) + d\sigma^B(\phi_n) \otimes \mathbf{I}(\epsilon) \right] u(\phi_n) \\ &= \sum_{a,b} \sum_{\{n|ab\}} \int df_{ab}(x_a, x_b) \left[ d\sigma_{ab}^V(\phi_{n|ab}|p_a(x_a), p_b(x_b)) \right. \\ &\quad \left. + d\sigma_{ab}^B(\phi_{n|ab}|p_a(x_a), p_b(x_b)) \otimes \mathbf{I}(\epsilon) \right] u(\phi_{n|ab}|p_a(x_a)p_b(x_b)), \end{aligned}$$

where

$$\begin{aligned} \frac{df_{ab} d\sigma_{ab}^V}{d\phi_{n|ab} dx_a dx_b} &= \frac{\hbar^2 c^2}{\mathcal{F}((p_a(x_a)p_b(x_b)))} f_{a/A}(x_a, \mu_F) f_{b/B}(x_b, \mu_F) \times \\ &\quad \times \mathcal{V}_{n|ab}(\phi_{n|ab}|p_a(x_a), p_b(x_b)) \theta_c(\phi_{n|ab}|p_a(x_a), p_b(x_b)), \end{aligned}$$

with

$$\begin{aligned} \mathcal{V}_{n|ab}(\phi_{n|ab}|p_a(x_a), p_b(x_b)) \\ = N_{n|ab} 2\text{Re} \left\langle \mathcal{M}_{n|ab}^{(0)}(\phi_{n|ab}|p_a(x_a), p_b(x_b)) \mid \mathcal{M}_{n|ab}^{(1)}(\phi_{n|ab}|p_a(x_a), p_b(x_b)) \right\rangle, \end{aligned}$$

and where

$$\begin{aligned} \frac{df_{ab} (d\sigma_{ab}^B \otimes \mathbf{I})}{d\phi_{n|ab} dx_a dx_b} &= \frac{\hbar^2 c^2}{\mathcal{F}(p_a(x_a)p_b(x_b))} f_{a/A}(x_a, \mu_F) f_{b/B}(x_b, \mu_F) \times \\ &\quad \times (\mathcal{B}_{n|ab}(\phi_{n|ab}|p_a(x_a), p_b(x_b)) \otimes \mathbf{I}(\epsilon)) \theta_c(\phi_{n|ab}|p_a(x_a), p_b(x_b)), \end{aligned}$$

with

$$\begin{aligned} \mathcal{B}_{n|ab}(\phi_{n|ab}|p_a(x_a), p_b(x_b)) \otimes \mathbf{I}(\epsilon) \\ = N_{n|ab} n_c(a, b) \left\langle \mathcal{M}_{n|ab}^{(0)}(\phi_{n|ab}|p_a(x_a), p_b(x_b)) \mid \mathbf{I}(\epsilon) \mid \mathcal{M}_{n|ab}^{(0)}((\phi_{n|ab}|p_a(x_a), p_b(x_b))) \right\rangle, \end{aligned}$$

containing the colour-correlated Born matrix elements, with the colour correlations induced by the **I** operator, as defined in [72, 73].

The **V**+**I** contribution contains  $d\sigma_{ab}^V(\phi_{n|ab}|x_a P_A, x_b P_B)$  and  $\mathbf{I}(\epsilon) \otimes d\sigma_{ab}^B(\phi_{n|ab}|x_a P_A, x_b P_B)$ , both evaluated at the same partonic phase-space point  $\{\phi_{n|ab}|x_a P_A, x_b P_B\}$  with which also the LO contribution as well as scales, cuts and observables are calculated. While the (UV-renormalized) virtual one-loop matrix elements  $|\mathcal{M}_n^{(1)}(\phi_n)\rangle$  with  $n$  final-state partons, contained in  $d\sigma_{ab}^V(\phi_{n|ab}|x_a P_A, x_b P_B)$ , are received from the one-loop amplitude providers, see Section 3.7,  $\mathbf{I}(\epsilon) \otimes d\sigma_{ab}^B(\phi_{n|ab}|x_a P_A, x_b P_B)$  is implemented as described in [72, 73].

### 3.3.1.4 The P+K contribution

The implementation of the P+K contribution is a bit more involved. The **P** and **K** operators contain finite remainders, which are left after the factorization of initial state collinear singularities into the PDFs. This involves an integration over an additional initial state momentum fraction  $z$  and, in line with the definitions in [72] and the main text of [73], a continuous reevaluation of the underlying Born matrix elements, in the convolution of the initial state dependent **P** and **K** operators, at the corresponding underlying Born phase-space points  $\{\phi_{n|a'b}|zx_a P_A, x_b P_B\}$  and  $\{\phi_{n|ab'}|x_a P_A, zx_b P_B\}$ .

Continuously reevaluating matrix elements, even Born matrix elements, can be computationally expensive, and is thus not ideal for an implementation in Monte Carlo event generators. A change of variables  $x_a \rightarrow \frac{x_a}{z}$  or  $x_b \rightarrow \frac{x_b}{z}$ , together with a rearrangement of integrations and summations, can be performed, such that the corresponding correlations are shifted from the underlying Born matrix elements to correspondingly redefined PDFs. In this parameterization the P+K contribution is written as

$$\begin{aligned} & \sigma^{P+K}[u] \\ &= \sum_{a',b} \sum_{\{n|a'b\}} \int df_{a'b}(\frac{x_a}{z}, x_b) \otimes \left[ (\mathbf{P}(z, x_a P_A, \mu_F) + \mathbf{K}(z))_{a'} \otimes d\sigma_{a'b}^B(\phi_{n|a'b}|x_a P_A, x_b P_B) \right] \times \\ & \quad \times u(\phi_{n|a'b}|x_a P_A, x_b P_B) \\ &+ \sum_{a,b'} \sum_{\{n|ab'\}} \int df_{ab'}(x_a, \frac{x_b}{z}) \otimes \left[ (\mathbf{P}(z, x_b P_B, \mu_F) + \mathbf{K}(z))_{b'} \otimes d\sigma_{ab'}^B(\phi_{n|ab'}|x_a P_A, x_b P_B) \right] \times \\ & \quad \times u(\phi_{n|ab'}|x_a P_A, x_b P_B) , \end{aligned}$$

where the differential P+K contribution for the first incoming parton is written as

$$\begin{aligned} & \frac{df_{a'b} \otimes ((\mathbf{P} + \mathbf{K})_{a'} \otimes d\sigma_{a'b}^B)}{d\phi_{n|a'b} dz dx_a dx_b} \\ &= \frac{\hbar^2 c^2}{\mathcal{F}(x_a P_A x_b P_B)} f_{b/B}(x_b, \mu_F) N_{n|a'b} n_c(a', b) \times \\ & \quad \times \langle \mathcal{M}_{n|a'b}^{(0)} \left| \sum_a \theta(z - x_a) f_{a/A}(\frac{x_a}{z}, \mu_F) \frac{1}{z} (\mathbf{P}_{aa'}(z, x_a P_A, \mu_F) + \mathbf{K}_{aa'}(z)) \right| \mathcal{M}_{n|a'b}^{(0)} \rangle \times \\ & \quad \times \theta_c(\phi_{n|a'b}|x_a P_A, x_b P_B) , \end{aligned}$$

with  $\mathcal{M}_{n|a'b}^{(0)} = \mathcal{M}_{n|a'b}^{(0)}(\phi_{n|a'b}|x_a P_A, x_b P_B)$ , and similarly for the second incoming parton.

The advantage of the above parameterization is that the matrix elements of the hard underlying Born process are evaluated at the phase-space points  $\{\phi_{n|a'b}|x_a P_A, x_b P_B\}$  and  $\{\phi_{n|ab'}|x_a P_A, x_b P_B\}$ , which are kept fixed during  $z$ -integration and match the  $x$ -dependencies of those in the LO and V+I contributions, at the expense of evaluating the PDFs at the correspondingly reparameterized  $x$ -values  $\frac{x_a}{z}$  or  $\frac{x_b}{z}$ .

This can also be imagined as follows: If a splitting occurs with a momentum fraction  $z$  transferred to the child parton  $a'$  of the splitting, which participates in the hard underlying Born process, in order to keep  $p_{a'}$  fixed the parent parton  $a$  is extracted from the proton  $A$  with a correspondingly higher momentum.

This reparameterization has further consequences, due to different quantities being fixed during  $z$ -integration. Before the reparameterization:  $p_a = x_a P_A$  is kept fixed, whereas  $p_{a'} = z p_a = z x_a P_A$  is not. After the reparameterization:  $p_{a'} = x_a P_A$  is kept fixed, whereas  $p_a = \frac{x_a}{z} P_A$  is not. The prescription to match the integrated endpoint contributions is not readily applicable after reparameterization and finite terms have to be rearranged. As a consequence, compared to [72] and the main text of [73], the **P** and **K** operators need to be modified. This has no effect in the massless case and in general also not for the **P** operator, but only for the **K** operator in the massive case, for which it is necessary to make use of the formulation in Appendix B of [73].

Matchbox sums over all required contributions of all those initial state partons  $a$  or  $b$  that might, upon splitting, give rise to the partons  $a'$  or  $b'$  participating in the hard underlying Born process. It generates a list of hard underlying Born processes and for each the action of  $(\mathbf{P} + \mathbf{K})$  is evaluated. The folding with the rescaled PDFs is thereby included in the definition of the various terms contributing to  $(\mathbf{P} + \mathbf{K})$ . The sums over the correlated products of rescaled PDFs times  $(\mathbf{P} + \mathbf{K})$  are implemented in `Dipole*PKOperator::sumParton(id)`, inheriting from `MatchboxInsertionOperator`, where  $id = a$  or  $b$ . For further details see Section 3.13.

### 3.3.2 Process setup and analyses

After a leading order process has been determined for the setup of an NLO computation the amplitude instances claiming responsibility for the leading order process are also queried for virtual corrections. A number of conventions need to be communicated by the interface chosen, which we discuss in detail below.

For the real emission contribution, the leading order process is considered with an additional outgoing jet, at an increased order in the strong coupling, and the partons entered in the jet particle group determine what real emission processes are considered. The lookup of these processes is subject to the same constraints as have already been applied by searching for contributing leading order processes. An enhanced bookkeeping that allows for mixed expansions and QED corrections is currently under development.

While the Born and virtual contributions can be analysed just as plain leading order phase-space points, care needs to be taken for the subtracted real emission contribution. In an unmatched calculation (which is determined by the MatchboxFactory object through the absence of a ShowerApproximation object), real emission phase-space points are generated, and the contributing ‘tilde’ kinematics are determined, together with the weights governed by the individual subtraction terms. We then form a so-called event group, consisting of a ‘head’ subprocess, along with a set of dependent phase-space points reflecting the subtraction contributions. Such a composite needs to be analysed in a correlated way, i.e. the individual subprocesses in the group can in general not be viewed as independent events. If the results of the calculation are to be written to HepMC events, Herwig indeed writes out a sequence of independent events, however the fact that they are correlated is signaled through an identical event number for all of them.

A set of built-in analyses is available for fixed order calculations, as well, which directly takes into account the correlations between real emission and subtraction term contributions. These analyses also apply a fuzzy bin definition in order to aid the convergence of distributions and reduce the impact of mis-binning effects in a way consistent with recovering the underlying integrable divergence in the limit of zero smearing. A similar approach is applied to generation cuts on the hard process where we choose a linear smearing, corresponding to replacing the event contribution by a box approximation to a  $\delta$ -function.

### 3.3.3 One-loop amplitude interfaces

Interfaces to one-loop amplitudes, or interferences of tree-level and one-loop amplitudes, are implemented much along the lines of the tree level amplitude providers; in contrast to the tree-level contributions to a NLO QCD cross section, one-loop providers can also only exclusively provide input at the cross-section level.

In any case, a convention needs to be adopted to define the finite part by fixing what quantities are expanded in the dimensional regularization parameter  $\varepsilon$  prior to removing the poles of the virtual contribution. We support one scheme where everything but a global prefactor of  $(4\pi)^\varepsilon/\Gamma(1-\varepsilon)$  is expanded, one where the amplitudes are cast in a form similar to the one reported in [74], and one where they are cast into the form of the insertion operators presented in [72,73].

Further to this information, the interfaces of the one-loop providers need to communicate about the precise type of regularization (conventional dimensional regularization or dimensional reduction), and their normalization scheme ( $\overline{\text{MS}}$  or  $\overline{\text{DR}}$ ). The insertion operators will be adjusted accordingly. The philosophy of the virtual corrections used inside Matchbox is that the t’Hooft mass parameter and the actual renormalization scale are kept different, and the value of the former will also be reported by the one loop interface. This allows for strong cross checks as the t’Hooft mass  $\mu$  needs to exactly cancel between the integrated subtraction terms and the one-loop amplitudes, while the renormalization scale dependence will only cancel out to  $\mathcal{O}(\alpha_s^2)$ . In view of mixed expansions, however, we also allow the amplitude providers, and the one-loop providers in particular, to use their own running coupling in case of which the insertion operators will not contain the logarithms relating the t’Hooft mass and renormalization scale as dictated by the one-loop UV counter term.

### 3.3.4 Generation of subtraction terms

At the core of the framework for an NLO calculation in the subtraction formalism is the identification of the subtraction terms that contribute to a given process, along with the projection of the phase-space point to an underlying Born process.

Within the Matchbox module, we perform the setup of the subtraction terms on a diagrammatic basis as follows: For each contributing real emission diagram, two external legs are clustered together, i.e. the vertex connecting exactly these two external legs is removed from the diagram. The resulting partonic subprocess is checked against the list of Born processes contributing to the computation at leading order. If no such process has been found, the clustering is not considered, while if there is a process the diagram obtained after clustering is compared against the list of diagrams contributing to the Born process. This allows dipoles to be ruled out that, e.g., are not compatible with an approximation leaving out a specific set of diagrams, as is the case in VBF processes.

While the clustering determines how the momenta of an emission and emitter are combined into the underlying Born phase-space point, the assignment of all other momenta is not unique and we therefore compare the diagrams on the basis of their topology to finally obtain a dictionary of how the other momenta need to be assigned to the hard process. Once such a diagrammatic comparison and mapping has been successfully obtained, a list of `SubtractionDipole` objects is checked for a contributing subtraction term (indeed, these objects are queried at several stages of the dipole identification process to rule out non-contributing clusterings and spectator assignments as early as possible).

All of the `SubtractionDipole` objects are then considered as functions of the real emission phase-space point, and the subtraction cross sections generically take the form described in [Section 3.3.1.1](#).

### 3.3.5 Spin- and colour-correlated Born matrix elements

The subtraction dipoles  $\mathcal{D}_{(i)} \in \{\mathcal{D}_{ij,k}, \mathcal{D}_{ij}^a, \mathcal{D}_k^{ai}, \mathcal{D}^{ai,b}\}$ , as defined in [Section 3.3.1](#) and in detail in [\[72, 73\]](#), require colour-correlated and in the case of external state gluons at Born level also spin-correlated Born-type matrix elements.

For example, in the case of gluons splitting into gluons or quarks we have

$$\mathcal{D}_{\tilde{g},k} \propto \left| \mathcal{M}_{a,b \rightarrow f_n}^{\tilde{g},k} \right|^2$$

where

$$\left| \mathcal{M}_{a,b \rightarrow f_n}^{\tilde{g},k} \right|^2 = - \left\langle \mathcal{M}_{a,b \rightarrow f_n}^{\mu} \left| \mathcal{C}_{\mu\nu} \frac{\mathbf{T}_{\tilde{g}} \cdot \mathbf{T}_k}{C_A} \right| \mathcal{M}_{a,b \rightarrow f_n}^{\nu} \right\rangle$$

is a spin- and colour-correlated matrix element in the standard notation using an open Lorentz index to denote the gluon's polarization degree of freedom. While an implementation at this level is possible by representing the amplitude as an explicit, complex four-vector and the spin correlation tensor as a four-by-four matrix, the information content is significantly less in this case. In fact, by inserting a polarization sum for the contractions of the amplitude and conjugate amplitude with the spin correlation tensor, we find that, for

$$\mathcal{C}_{\mu\nu} = \mathcal{A} \eta_{\mu\nu} + \mathcal{B} n_{\mu} n_{\nu}$$

the correlated matrix element can as well be expressed as

$$\begin{aligned} \left| \mathcal{M}_{a,b \rightarrow f_n}^{\tilde{g},k} \right|^2 &= - \left( \mathcal{A} - \mathcal{B} |\epsilon_+ \cdot n|^2 \right) \left\langle \mathcal{M}_{a,b \rightarrow f_n} \left| \frac{\mathbf{T}_{\tilde{g}} \cdot \mathbf{T}_k}{C_A} \right| \mathcal{M}_{a,b \rightarrow f_n} \right\rangle \\ &\quad + 2\text{Re} \left( \mathcal{B} (n \cdot \epsilon_+)^2 \left\langle \mathcal{M}_{a,b \rightarrow f_n}^{(+)} \left| \frac{\mathbf{T}_{\tilde{g}} \cdot \mathbf{T}_k}{C_A} \right| \mathcal{M}_{a,b \rightarrow f_n}^{(-)} \right\rangle \right) \end{aligned}$$

where instead of an open Lorentz index the spin information is now encoded in a colour-correlated matrix element interfering a positive and negative helicity amplitude for the gluon in question. In the case of gluon emission from a quark only colour correlations exist, for which we have

$$\left| \mathcal{M}_{a,b \rightarrow f_n}^{\tilde{q},k} \right|^2 = - \left\langle \mathcal{M}_{a,b \rightarrow f_n} \left| \frac{\mathbf{T}_{\tilde{q}} \cdot \mathbf{T}_k}{C_F} \right| \mathcal{M}_{a,b \rightarrow f_n} \right\rangle$$

The correlated matrix elements can be determined at various levels of interfaces, either directly for the BLHA-type handling, or as a net result from the colour basis data and the colour and helicity subamplitudes. Our treatment of the spin correlation has also served as the reasoning behind extensions of the BLHA standard [\[65\]](#) and proof of concept of an implementation thereof, see [\[75\]](#). The spin and colour-correlated matrix elements in each of the cases are stored in caches associated with the phase-space point considered, and downstream use of these does not require knowledge of the level of interface they have been obtained with. Note, however, that in the case of an amplitude level interface an agreement and possibly a method to return, a polarization vector for the splitting gluon is required to use a consistent phase definition.

## 3.4 Cuts and jet definitions

At the level of the hard process of interest, acceptance cuts might need to be imposed for a finite answer; they may also just be imposed to increase the efficiency of the event generation. The cuts discussed in this section only define such constraints at the level of the hard process and caution should always be taken that these are compatible with the desired analysis criteria within some safety margin to account for the dynamics of the subsequent physics happening within parton showering and the phenomenological models.

Within the process of implementing NLO QCD contributions in Herwig, the framework for cuts needed to be revisited considerably as most of the cuts had parton level origin and were hence problematic or impossible to be used in the context of an NLO calculation. They are still provided in a legacy manner and we document them towards the end of this section. The new cut implementations have seen a twofold improvement:

- It is now possible that a jet clustering can take place prior to the actual evaluation of a final state definition. This jet clustering is steered through a `Matcher` object, which contains the information on the jet constituents. Definitions involving, e.g. a democratic clustering algorithm for photons are hence straightforward to implement.
- Cuts on the hard process, in general, are not anymore implemented as sharp theta-function constraints on the partonic cross section but can actually reflect a definition involving some smearing function. This is highly important in the context of convergence of NLO calculation, where such flexibility allows for a (one-sided) bin smearing in the definition of the cross section. Currently a linear smearing is provided, consistent with approximating the delta function to represent a single event by a box approximation.

### 3.4.1 Jet finding

ThePEG provides a general interface to jet finding algorithms through the `JetFinder` class. This class, if present, will be considered to act on the final state presented to the `Cut` objects to perform jet clustering prior to the actual cut evaluation. Currently `fastjet` [76] is used as the only working implementation behind this interface, with nearly all options available to the jet finding algorithm. Jet finders make use of `Matcher` objects, which classify which of the final state particles of the hard process should be considered for jet clustering, and can also be synchronized with `ParticleGroups` set up for the `MatchboxFactory` object. The `FastJetFinder` class instantiates the more general `JetFinder` interface for using the `fastjet` package and currently supports the `Kt`, `CA` and `AntiKt` algorithms, as well as their spherical counterparts to be used in the context of electron-positron collisions. All algorithms can be operated with two different recombination schemes.

After jets have been formed by the clustering algorithm, a definite jet final state needs to be required. These constraints are collected in a `JetCuts` object, which assembles single or pairwise constraints on the jet final state, subject to an ordering of jets. Ordering of jets can be applied through the `JetCuts:Ordering` interface and can be either set to ordering in transverse momentum or in rapidity. Individual phase-space requirements on the final state jets are encoded in `JetRegion`, `JetPairRegion` and `MultiJetRegion` objects, see Section 3.4.2 for more details. A `JetCuts` object then assembles an entire jet final state definition composed of a `Matcher` object set through `JetCuts:UnresolvedMatcher`, an ordering choice, and several jet regions, jet veto regions, jet pair regions as well as multi-jet regions.

On top of this a simple jet multiplicity cut, possibly used together with an exclusive resolution for the jet finder object is provided for typical jet definitions in  $e^+e^-$  collisions using the `NJetsCut` class.

### 3.4.2 Jet and jet pair regions

Each `JetRegion` object represents a slice in phase-space composed out of an interval in transverse momentum  $[p_{\perp,\min}, p_{\perp,\max}]$  and a set of (mutually disjoint) rapidity intervals  $([y_{1,-}, y_{1,+}], \dots, [y_{n,-}, y_{n,+}])$  in which a jet is accepted (no restrictions are applied in azimuthal angle in the transverse plane). Each jet region can accept (or match) any, or only certain entries in the ordered list of reconstructed jets, however only one jet per region is allowed. Multi-jet final states can then be composed through combining several `JetRegion` objects into a `JetCuts` object. Each jet region might also serve as a jet veto region in case of which no jets are allowed in certain phase-space slices, i.e. events for which such a region matches will not be accepted.

`JetPairRegion` objects can be composed out of two `JetRegion` objects and will impose additional constraints on the pair of matched jets, such as distances in rapidity, azimuth, lego-plot separation or invariant mass of the pair. Finally, `MultiJetRegion` objects contain an arbitrary number of `JetRegion` objects onto which, once matched, pairwise constraints on typical inter-jet separations can be applied.

### 3.4.3 Default cuts

A number of cuts are available by default, specifically to be used within NLO calculations and the Matchbox framework. Apart from jet cuts the cuts in Herwig are defined either on individual, pair or multi particle level (ThePEG’s OneCut, TwoCut or MultiCut). Here the property of the objects affected by the cuts are defined via matchers. Internally the cut object will then check for this property and apply the restrictions on the phase-space point. For numerical stability the cuts in Herwig can be and are by default defined with a fuzzy cut instead of sharp cuts, i.e. we replace

$$\theta(x - x_c) \rightarrow \theta_\lambda(x - x_c)$$

where  $\theta_\lambda(x - x_c)$  is a turn-on function, in practice chosen to rise linearly from zero to one along an interval of width  $\lambda$ , centred around  $x_c$  in units of the cut quantity considered. This width can be changed in the FuzzyTheta object.

Several cut classes, which can be supplemented by Matcher objects to identify the final state particles to which they will be applied, are provided as a default. To be precise, Herwig provides the following classes:

- IdentifiedParticleCut, which cuts on individual particle properties like transverse momentum or rapidity;
- InvariantMassCut, which checks for pairwise invariant masses;
- MatchboxDeltaRCut which checks for pairwise lego plot separation;
- MissingPtCut, cutting on the sum of invisible momenta such as neutrinos; and
- FrixionePhotonSeparationCut, providing photon isolation according to [77].
- JetCuts are instances of JetRegion objects outlined in Section 3.4.2, they default to accept jets with  $|y_j| < 5$  and  $p_{\perp,j} > 20\text{GeV}$ .

Further details on using cut objects can be found in the [tutorials](#). This library of typically used cuts however is nowhere comprehensive. Custom constraints on the final state at the hard process level can be implemented rather easily by inheriting from ThePEG’s OneCut, TwoCut or MultiCut base classes or the JetRegion or JetPairRegion classes. Even a jet clustering algorithm not provided by our fastjet interface can be used within Herwig through a class deriving from ThePEG’s JetFinder class. Any such implementation does not require change or other interaction with an existing Herwig installation but can be compiled into a shared library readily available for a custom run.

## 3.5 Scale choices

Matchbox provides full flexibility regarding (dynamic) scale choices for the hard process, and all dynamical scales inherit from the MatchboxScaleChoice class. In particular, the QCD renormalization and factorization scales  $\mu_R$  and  $\mu_F$ , as well as the QED renormalization scale  $\mu_{R,QED}$  can be implemented depending on the phase-space point considered. By default, if only an implementation of  $\mu_R$  is provided, we put  $\mu_F = \mu_R$ , and  $\mu_{R,QED} = M_Z$ . In order to guarantee a consistent subtraction calculation of the NLO QCD cross sections, dynamic scales need to obey infrared safety in the sense that their functional form depending on the real emission phase-space point approaches the functional form defined on the Born phase-space point in any of the unresolved limits:

$$\mu_R(\phi_{n+1}|ab) \rightarrow \mu_R(\tilde{\phi}_{n|(i)}(\phi_{n|ab}))$$

if the unresolved limit is associated to the dipole configuration  $(i)$ . Any scale based on jets or jet-like objects fulfills this property. Notice that this also applies to a dynamic QED scale even in absence of NLO EW corrections.

In the case of NLO plus parton shower matched calculations, the hard veto scale of the parton shower evolution can also be determined in the scale setting object. This scale determines the maximally allowed hardness of emissions generated in the parton shower, which is needed to avoid a double counting of hard emissions in particular when the hard process already involves additional jets. Note that a simple prescription of taking the minimum transverse momentum at the hard process to set the limit on parton shower emissions is not applicable in the NLO matched context anymore. More details about this can be found in the section on matching parton showers to NLO QCD corrections. By default, the hard shower scale, which we refer to as  $\mu_Q$ , is set equal to the implementation of the QCD factorization scale choice, though a scale based on the average transverse momentum of the hard objects is available in several scale setting implementations and might become the default in a future version.

The tutorials provide instructions on how custom scale choices can be implemented by inheriting from the MatchboxScaleChoice base class, while a range of implementations are available by default, among them

- Fixed Scale:

$$\mu = \mu_{\text{fixed}}$$

The base class ‘‘MatchboxScaleChoice’’ implements a fixed scale choice that can be modified by the interface ‘‘FixedScale’’. This choice is for testing. Actual physics simulations should make use of a variable scale choice.

- MatchboxHtScale:

$$\mu = \sum_i p_T^i + M_T^{\text{non-jets}}$$

This scale choice sums the scalar transverse momenta of the jets above a given scale, defined by the interface ‘‘JetPtCut’’. Furthermore, if the interface ‘‘IncludeMT’’ is set to ‘‘Yes’’, the  $M_T$  of the vector resulting when adding all non jet particles is added to the scale.

- MatchboxParticlePtScale:

$$\mu = \sum_i p_T^i \delta_{\text{flav}(i)\text{flav}(X)}$$

This scale needs a ‘‘Matcher’’  $X$ , see ‘‘Matchers’’, and then sums the scalar transverse momenta of all objects that match the definition of  $X$ .

as well as a range of scales more suited to top quark production, and processes involving multiple gauge bosons.

## 3.6 Cross-section integrators and event sampling

### 3.6.1 Overview

When calculating integrated cross sections, the basic problem is the calculation of a many-dimensional integral  $\sigma = \int d^d x f(\vec{x})$ , where  $f(\vec{x})$  contains the matrix element, the phase-space and any cuts, the latter parameterized as, possibly smeared, step functions. Typically, the parameterization of the phase-space is written such that it takes a vector of  $d$  real numbers  $\vec{x}$  ranging between 0 and 1. Then the integration is performed over the  $d$ -dimensional unit hypercube  $[0, 1]^d$ .

For a finite number of sampled points  $n$ , the integral can be approximated by its discrete sum,  $\sigma_n = \frac{1}{n} \sum_{i=1}^n f(\vec{x}_i)$ . In the limit of  $n \rightarrow \infty$ , the law of large numbers ensures that the discrete sum converges to the value of the integral. The corresponding error can be approximated by an estimate for the variance, so that we obtain  $\Delta\sigma_n = \frac{1}{\sqrt{n(n-1)}} \sqrt{\sum_i (f(\vec{x}_i) - \sigma_n)^2}$ .

The contribution of each individual point to the sum can differ vastly. From the estimate of the integration error we see that for a given number of points this becomes smaller when the contribution of the points is more uniform. In the ideal case each point would give the same contribution, and a single point would hence be sufficient to exactly determine the integral. As a step towards this goal, two important techniques exist:

- Stratified sampling divides the integration region into subparts, performs a Monte Carlo integration in each part, and then sums the results;
- Importance sampling introduces a weight function  $p(x)$  into the integral,  $\sigma = \int d^d x p(\vec{x}) \frac{f(\vec{x})}{p(\vec{x})}$ , which is positive-valued and integrates to unity on the hypercube; then the integral can be computed by sampling according to  $d^d P(\vec{x}) = p(\vec{x}) d^d x$ . Typically this requires the inverse function of the integral of  $p(\vec{x})$  to be available, either numerically or analytically. If the weight function approximates the true integrand reasonably well, the integration error is significantly reduced.

Both techniques are also helpful when generating unweighted events, as the generated events should ideally already have comparable weights.

The *GeneralSampler* class manages the cross section integration and is responsible for selecting among the different subprocesses contributing to the cross section. Each subprocess is integrated using a *BinSampler*, which is a base class to the different adaptive methods we offer (flat integration is of course available as a cross check). The *GeneralSampler* class also controls the final unweighting step. The main switches used to control the sampling independent of the adaptive algorithm chosen are:

- *MaxEnhancement*

The actual maximum weight used for unweighting should be chosen slightly higher than the largest weight found during the integration step, so there is an additional safety margin for larger events appearing in the run phase. This option specifies the factor by which the weight is increased.

- *MinSelection*

Individual subprocesses are usually sampled according to their relative weights. This option sets a minimal probability for how often a subprocess must be chosen nevertheless.

- *AlmostUnweighted*

When using unweighted events and an individual event has a weight larger than the guessed maximum weight, the event is still written out with a unit weight. Hence, this introduces a difference on the cross section. If this option is switched on, these events are output with the correct weight, which is larger than one.

- *ParallelIntegration*

Setting this option allows the integration to be performed in parallel using multiple jobs. The number of jobs can be controlled with the following two options:

- *IntegratePerJob*

This sets the number of subprocesses per integration job. The number of jobs necessary is then calculated from the total number of subprocesses.

- *IntegrationJobs*

This sets the number of integration jobs. The subprocesses are then distributed equally between the different jobs.

The typical setup, which we follow in Herwig, is that for all samplers at first a certain number of points with the starting setup, a flat distribution on the hypercube of random numbers, is performed. Then these results are used for the optimization procedure of the sampler, i.e. splitting the integration space for stratified sampling and calculating the appropriate weight function for importance sampling. Then a new iteration is started, where again we collect points and afterwards use the total results to improve the sampling. This iterative procedure will then usually be performed a few times until the integration space splitting or weight function is sufficiently well adapted.

The following options are common to all adaptive algorithms inheriting from the *BinSampler* class and control the behaviour of the integration routine, as defined in the *BinSampler* class which gives the common framework.

- *InitialPoints*

This sets the number of points used in the first iteration of the adaption.

- *NIterations*

The number of iterations is controlled with this setting. Note that if results from a previous integration run exist already, only a single iteration is performed, independently of the setting of this variable, as we assume that the previous integration has already given a reasonably well converging adaptation and only additional improvements are necessary. If build parameters like masses or phase-space cuts have been altered and a new integration starting from scratch becomes necessary, the old integration results in *Herwig-scratch/* must be deleted manually. Herwig will also issue a warning reminding you about this if previous integration data is found.

- *EnhancementFactor*

Calculating the first iterations with fewer points and then subsequently increasing the points with the following iterations can be helpful to lower the time needed for integration, as the coarse adaptation during the first few iterations can be done with fewer points and the refinement later on is performed with higher statistics. This parameter is the factor by which the number of points increases from iteration to iteration.

For some samplers (specifically the *CellGridSampler* and the *FlatSampler*), besides the normal behaviour of the algorithm, a ‘remapping’ can be applied to individual random number dimensions, in which case projections of the integrand are recorded along these axes and an importance sampling deduced from the histogram. This particularly improves the sampling of those dimensions that correspond to the incoming parton’s luminosity, though other options can be chosen, see the [tutorials](#) for more details.

By default, two different samplers are available in Herwig, which are described below. Additionally, for simple checks and debugging, an identity mapping, meaning that the input random number vector is returned as output unmodified, is implemented as *FlatSampler*.

### 3.6.2 CellGridSampler

The *CellGridSampler* is based on the *ExSample* library [78]. The integration hypercube is represented by a tree of so-called cells, where the top cell represents the full unit hypercube. This one and each intermediate cell contains two

children cells, which are derived from the parent cell by splitting it along one of the integration dimensions. The measure to evaluate possible splits of a dimension  $k$  is called the gain, and is defined as

$$\text{gain}_k(r_k) = \frac{\left| \int_{\vec{r}_{-}}^{\vec{r}_{+,k}} d\vec{r} f(\vec{r}) - \int_{\vec{r}_{-,k}}^{\vec{r}_{+}} d\vec{r} f(\vec{r}) \right|}{\int_{\vec{r}_{-}}^{\vec{r}_{+}} d\vec{r} f(\vec{r})},$$

where  $\vec{r}_{\pm}$  is the upper or lower bound of the cell, respectively, and  $\vec{r}_{\pm,k}$  denotes  $r_k$  for the random number in dimension  $k$  and again the upper or lower bound for all other dimensions. This means that the two integrals in the numerator denote the two half cells which have been split at  $r_k$  for dimension  $k$  and span the whole cell space for the other dimensions, whereas the denominator is simply the integral over the whole cell, i.e. the gain is the normalized difference between the lower left and upper right half of the cell. A cell split happens along the dimension where the gain is largest. In the current version of the *CellGridSampler*, for performance reasons only splits along the middle of the cell, i.e.  $r_k = \frac{r_{+,k} - r_{-,k}}{2}$  are considered. After a cell has been split, the new child cell which does not contain the largest weight is immediately sampled again, so that we get a good estimate of the maximum weight also for this half.

The usual splitting algorithm described so far can give non-satisfactory results. One example would be an integrand which is symmetric in one dimension, but strongly peaked at  $\frac{1}{2}$ . Then, the splitting algorithm would see a gain of 0 and thus never consider this dimension for splitting, while in practice for example an initial split into three equally sized pieces would have been highly beneficial. Usually, these symmetries are relevant only at the level of the full unit hypercube, though particular integrands, possibly defined as step-wise functions, might exhibit this behaviour also for sub-cells. Therefore, it is possible to generate some forced splittings of the cells already before any sampling has taken place. This then further refines the set of cells with which the algorithm starts. The main parameters to be considered for this algorithm are

- *ExplorationPoints*

To get an initial estimate of the size of the contributions, each cell needs to be sampled with a certain number of points, before possible splits can be evaluated. *ExplorationPoints* defines how many points are used for this.

- *Epsilon*

This variable uses the ratio of the average integration point weight over the maximum weight. If this ratio exceeds the parameter *Epsilon*, i.e. the distribution of weights is sufficiently flat, no more splits of this cell take place.

- *Gain*

Correspondingly, this variable defines the minimum value the gain must reach before splitting the cell is considered.

- *MinimumSelection*

This variable enforces a minimum selection probability for each cell that the algorithm guarantees, even if the integral value of the cell would yield only a smaller probability.

### 3.6.3 MonacoSampler

The *MonacoSampler* is an implementation of the importance sampling method *Vegas* [79, 80]. It is derived from the VBFNLO implementation of the same name.

The basic idea is a combination of importance sampling and stratified sampling. Each integration dimension is split into a number of bins, where the bin boundaries are chosen such that the integral over each bin has the same value. Over the full unit hypercube, this leads to a  $d$ -dimensional grid of smaller hyperrectangles. The random points are then distributed such that each hyperrectangle receives the same number of random points and the distribution is uniformly inside each hyperrectangle, and the weight function factorizes over the different dimensions,  $p(\vec{r}) = \prod_{i=1}^d p_i(r_i)$ . To calculate the bin boundaries, the integrand is first sampled with *InitialPoints* points using equally spaced bins and hence uniformly distributed random points over the whole hypercube. This information is then used to generate the new bin boundaries. A damping factor protects against over-optimization, which could destabilize the grid optimization and lead to strong fluctuations in the grid adaptation.

In the Herwig implementation, in addition to the general parameters discussed beforehand, two parameters specific to this algorithm can be set:

- *GridDivisions*

This specifies how many bins are used for each integration dimension.

- *Alpha*

The damping behaviour is controlled with this parameter. Instead of the actual relative contribution  $c_i$  of each bin, the modified expression

$$\left( \frac{c_i}{(1-c_i) \ln(c_i)} \right)^\alpha$$

is used to calculate the new bins. Typical values of the exponent are between 0.2 and 2, where larger values result in less damping. When setting *Alpha* to zero, no grid adaptation occurs and the algorithm reduces to the *FlatBinSampler*.

### 3.7 Amplitude providers

The Matchbox module can use several libraries to calculate scattering amplitudes and/or amplitudes squared to build up cross sections. The interfaces are set up within a broad range, from run-time interfaces providing low level amplitude information, up to programs which generate code at the squared amplitude level in correspondence to the BLHA2 interface standard [65, 81], which is then loaded as a dynamical library by the Matchbox framework. In this section we summarize the available libraries.

While some libraries provide the entire list of quantities required to set up NLO calculations, some of them are only capable of calculating cross section level quantities and thus need to be combined with a native amplitude provider in a hybrid setup to obtain meaningful selection of colour flows or the filling of spin density matrices for the hard process.

#### 3.7.1 MatchboxCurrents

Several matrix elements in Matchbox are based on a library of leptonic and hadronic currents [82] which have been set up using spinor helicity techniques and caching of sub-amplitudes, together with a small collection of colour structures for low jet multiplicities. These amplitude building blocks are also used for the amplitudes available in the *HJets* library. Herwig interfaces to MatchboxCurrents at the amplitude level, and all quantities relevant to NLO predictions for the processes provided can be obtained from the single library.

The MatchboxCurrents library is directly shipped with the Herwig release and can be used to generate any process involving a lepton pair, and two or three partons at leading and next-to-leading order. This includes  $e^+e^- \rightarrow 2, 3$  jets, DIS  $0+1$  and  $1+1$  jet production, as well as Drell-Yan and  $V +$  jet processes, all at NLO QCD with the real emission additional jet production also available to leading order multi-jet merging.

#### 3.7.2 GoSam

GoSam [83–85] provides functionality to generate code for scattering amplitudes at the tree and one-loop level, and interfaces to Herwig via the BLHA2 interface standard at the level of the squared amplitudes. Process code is generated as requested and the corresponding libraries compiled and linked dynamically at run time. Spin- and colour-correlated Born matrix elements can be provided by GoSam, as described in [65, 75] (see Section 3.3.5 for more details), as well as squared one-loop amplitudes for loop induced processes at the leading order.

Per default Herwig’s GoSam interface assumes GoSam’s Standard Model implementation, with a diagonal CKM matrix, but it is possible to switch to a Higgs effective model as well. All Standard Model parameters as well as the EW scheme are automatically communicated from Herwig to GoSam, and the complex-mass scheme can be used. Per BLHA the light lepton masses are set to zero by default though (GoSam then assumes its own hard-coded default for the tau mass). The interface assumes GoSam’s matrix elements to be provided in conventional dimensional regularization, but they may be provided in dimensional reduction if required. Further, settings related to the one-loop reduction in GoSam might be accessed through the interface as well, such as the one-loop reduction algorithm that is used in GoSam or the target accuracy of the one-loop matrix elements.

GoSam uses a setup file, in which model assumptions, diagram filters, one-loop reduction settings, etc. are specified beyond its hard-coded defaults. Herwig provides a template GoSam setup file, which is used per default, modified according to the settings that are chosen through Herwig’s GoSam interface. However, a custom GoSam setup file may also be provided, e.g. to implement custom diagram filters or to specify physics models beyond what can be specified through the interface (as for instance used in [86] for anomalous  $ggW^+W^-$  couplings, originating from dimension-8 operators).

More details on the various interface options can be found in the [tutorials](#). More information on GoSam specific settings can be found in the GoSam manual.

#### 3.7.3 HJets

HJets [63] builds on the MatchboxCurrents library, the ColorFull package [67], and the methods developed in [87] to provide a library which can calculate EW (VBF) Higgs production in association with two or three jets, including all contributing diagrams (VBF-type and VH-type) at the orders  $\mathcal{O}(\alpha^3 \alpha_s)$  and  $\mathcal{O}(\alpha^3 \alpha_s^2)$  relevant to NLO QCD corrections. Herwig interfaces to HJets at the amplitude level.

### 3.7.4 NJet

NJet [88] is a library dedicated to QCD jet production at hadron colliders, and provides tree and one-loop amplitudes for up to  $pp \rightarrow 4$  jet production. NJet is interfaced to Herwig at the level of squared amplitudes, and purely as a dynamic library such that no code generation is happening while the processes are set up.

### 3.7.5 MadGraph5\_aMC@NLO

MadGraph5\_aMC@NLO [89] provides functionality to generate code for scattering amplitudes at the tree and one-loop level, and interfaces to Herwig at the amplitude level as well as on the level of the squared amplitude. Process code is generated as requested and the corresponding libraries compiled and linked dynamically at run time. At the amplitude level, partial subamplitudes, in either the trace or the color flow basis, can be provided (see Section 3.2.5 for more information), particularly also in the large- $N$  limit, for use within the parton showers. At the level of the squared amplitude, spin- and colour-correlated Born matrix elements can be provided (see Section 3.3.5 for more information).

Per default Herwig’s MadGraph interface assumes MadGraph’s Standard Model implementation, but it is possible to switch to a Higgs effective model as well. All Standard Model parameters are automatically communicated from Herwig to MadGraph, and the complex-mass scheme can be used.

More details on the various interface options can be found in the [tutorials](#).

### 3.7.6 OpenLoops

OpenLoops [90] implements the Open Loops algorithm for the fast numerical evaluation of scattering amplitudes at the tree and one-loop level [91], and interfaces to Herwig via the BLHA2 interface standard at the level of the squared amplitudes, and purely as a dynamic library such that no code generation is happening while the processes are set up. OpenLoops also provides spin- and colour-correlated Born matrix elements (see Section 3.3.5 for more information).

By default, Herwig’s OpenLoops interface assumes OpenLoops’ Standard Model implementation, but it is possible to switch to a Higgs effective model as well. All Standard Model parameters are automatically communicated from Herwig to OpenLoops, and the complex-mass scheme can be used. For the one-loop reduction OpenLoops uses the Collier library [92] per default.

More details on the various interface options can be found in the [tutorials](#).

### 3.7.7 VBFNLO

VBFNLO [93–96] is a flexible parton-level Monte Carlo program for processes with EW bosons. It provides amplitudes at the tree and one-loop level, and interfaces to Herwig via the BLHA2 interface standard at the level of the squared amplitudes. VBFNLO also provides spin- and colour-correlated Born matrix elements (see Section 3.3.5 for more information). These and the standard Born matrix elements can in particularly also be provided in the large- $N$  limit, for use within the parton showers.

All Standard Model parameters are automatically communicated from Herwig to VBFNLO. In addition anomalous couplings of the EW bosons, originating from dimension-6 and possibly dimension-8 operators, can be enabled.

In order to improve the convergence of the Monte Carlo integration, Herwig’s VBFNLO interface has the possibility to use the VBFNLO internal phase-space generator, which is particularly tailored to the processes available through VBFNLO and which for more complex final states, as the gains can be highly significant, is in general recommended.

Further, there is the possibility to sample the helicities of the leptons and photons in the final state randomly instead of summing them; the computation time spent per phase-space point will be reduced at the expense of a larger variation, but overall a slightly improved integration accuracy is expected.

More details on the various interface options can be found in the [tutorials](#). More information on VBFNLO specific settings can be found in the VBFNLO manual [94].

## 3.8 Internal cross-checks

For calculations beyond LO, the different pieces of virtual corrections and real emissions are individually divergent. Only when looking at their sum, and well-defined, infrared-safe observables, the KLN theorem [97, 98] guarantees that the sum of all contributions is finite. Subtraction schemes like Catani–Seymour [72] or FKS [99] make use of that by constructing approximations to the real-emission process from the corresponding Born plus a term describing the extra

emission, such that it equals the full matrix element in the soft or collinear divergent region, and the difference of the two can be integrated numerically in four dimensions. Integrating analytically over the extra-emission term in  $d = 4 - 2\epsilon$  dimensions generates poles in  $1/\epsilon^2$  and  $1/\epsilon$ , which then exactly cancel the corresponding poles of the virtual amplitude.

Herwig generates the Catani–Seymour dipoles themselves, using the Born, colour-correlated and spin-colour-correlated Born processes from the matrix-element provider as an input. Therefore, comparing these expressions numerically to the real-emission process in the singular limits and the  $\epsilon$  poles of the Born-virtual interference, respectively, provides a powerful check of the consistency of the calculation.

### 3.8.1 Singularity cancellation

For the real-emission part, we can check that the approximation from the dipole subtraction term approaches the real-emission matrix element when coloured final-state particles become soft or a pair of them becomes collinear. This check can be switched on by setting *SubtractionData* to a string and creating a directory with the name of this string in the run directory. The exact type of output can be controlled by two variables. In all cases a histogram for each singular limit is generated. The x-axis value contains the energy of the gluon in the soft limit, and the virtuality  $q = \sqrt{2p_i \cdot p_j}$  of the two collinear particles  $i$  and  $j$  in the collinear limit. The corresponding y value is defined by the setting of

*SubtractionPlotType*:

- *LinRatio* The result is the ratio of all dipole contributions over the real-emission matrix element,  $\left| \frac{\sum \mathcal{D}}{|\mathcal{M}_{\text{real-emission}}|^2} \right|$ , i.e. should go to one in the soft or collinear limit. The scaling of the y axis is linear.
- *LogRelDiff* The result is the sum of dipole and real-emission matrix element normalized over the real-emission matrix element,  $\left| \frac{\sum \mathcal{D} + |\mathcal{M}_{\text{real-emission}}|^2}{|\mathcal{M}_{\text{real-emission}}|^2} \right|$ , i.e. should go to zero in the soft or collinear limit. The scaling of the y axis is logarithmic.

*SubtractionScatterPlot*

Setting this to *Yes* instead of the default *No* additionally generates the data file for a scatter plot from the same data points as used for the histograms.

### 3.8.2 Pole cancellation

For the virtual corrections we can verify explicitly that the poles of the Born-virtual interference are cancelled by the corresponding contributions from the dipole subtraction terms, namely the *I*-operator. To activate this check one should set *PoleData* to a string and create a directory of the same name in the run directory, where the histogram output will then be written. For each subprocess two histogram files are produced: *epsilonSquarePoles*, containing the contributions proportional to  $1/\epsilon^2$ , and *epsilonPoles*, containing those proportional to  $1/\epsilon$ . The entries are binned according to

$$\log_{10} \left( 1 - \left| \frac{|\mathcal{M}_{\text{Dipole}}|^2}{2 \operatorname{Re}(\mathcal{M}_{\text{Born}}^* \mathcal{M}_{\text{Virtual}})} \right| \right),$$

with the ordinate giving the number of sampled phase-space points. The distribution should be sharply peaked near  $-16$ , reflecting the fact that the cancellation holds up to the level of double-precision numerical accuracy (i.e. relative differences of order  $10^{-16}$ ).

### 3.8.3 Independence of finite terms

In Ref. [100, 101], a modification of the Catani–Seymour dipole subtraction terms has been introduced, which restricts the contribution of the dipoles to a region around the singular poles. This is realized by multiplying the dipole expressions with an additional step function  $\Theta(\alpha - y_{ij,k})$ , where  $y_{ij,k}$  is the dimensionless variable of the Catani–Seymour algorithm that is used to calculate the momenta of spectator and emitter in the tilde kinematic, and  $\alpha$  is a dimensionless parameter,  $\alpha \in (0, 1]$ . Setting  $\alpha$  to 1 restores the original Catani–Seymour version, while using smaller values subsequently restricts the dipole phase-space closer to the pole. In Herwig, this parameter can be set via *AlphaParameter*. The integrated dipoles, which enter in the calculation of the virtual corrections, then receive corresponding terms also depending on  $\alpha$  such that in the full NLO cross section everything drops out again.

The use of this parameter is two-fold. Restricting the contribution of the dipoles to a smaller region than the full real-emission phase-space means that they do not need to be calculated there. This will therefore reduce the computation time spent on the phase-space point. In practice, the gain turns out to be rather low only. Additionally, varying the parameter allows one to check that the total contribution of the dipoles on the cross section drops out, as the cross section should be independent of the value of  $\alpha$ . In particular, this also checks that the values of the coupling constants and the cuts are the same for the virtual corrections and the real-emission contributions.

## 3.9 Built-in matrix elements

In Herwig 7 the library of matrix elements for QCD and EW processes is similar to that available in its FORTRAN predecessor [4, 5]. While the library of Standard Model processes provides a core of important processes with which to test the program it is our intention that, in general, users should study most processes of interest via the Matchbox module, or external programs using the Les Houches Accord.

Nevertheless, there are still some cases for which it is useful to have Herwig handle all stages of the event generation process. This is particularly true for processes in which spin correlations between the production and decay stages are significant, *e.g.* those involving top quarks or tau leptons. Such correlation effects are hard to treat correctly if different programs handle different steps of the simulation process.

In order to facilitate the process of adding new matrix elements, where needed, and to enable us to generate the spin correlation effects [53, 102, 103], we have based all matrix element calculations on the helicity libraries of ThePEG. As well as providing a native library of Standard Model processes and an interface to parton-level generators, Herwig also includes matrix elements for hard  $2 \rightarrow 2$  collisions and  $1 \rightarrow 2$  and  $1 \rightarrow 3$  decays, arising in various models of new physics (see Section 6).

We also include a number of next-to-leading-order (NLO) matrix elements in the POsitive Weight Hardest Emission Generator (POWHEG) scheme of Refs. [104, 105].

### 3.9.1 Leading-order matrix elements

For  $e^+e^-$  colliders only a small number of processes are included natively:

- Quark-antiquark production, via interfering photon and  $Z^0$  bosons, is implemented in the `MEee2gZ2qq` class. No approximation is made regarding the masses of the particles. This process is essential for us to validate the program using QCD analyses of LEP data.
- Dilepton pair production, via interfering photon and  $Z^0$  bosons, is implemented in the `MEee2gZ2ll` class. No approximation is made regarding the masses of the particles<sup>1</sup>. This process is used to check the implementation of spin correlations in  $\tau$  decays.
- The Bjorken process,  $Z^0h^0$  production, which is implemented in the `MEee2ZH` class. This process is included as it is very similar to the production of  $Z^0h^0$  and  $W^\pm h^0$  in hadron-hadron collisions and uses the same base class for most of the calculation.
- The vector-boson fusion (VBF) processes,  $e^+e^- \rightarrow e^+e^-h^0$  and  $e^+e^- \rightarrow \nu_e\bar{\nu}_e h^0$ , are implemented in the `MEee2HiggsVBF` class.
- The production of a pair of EW gauge bosons,  $W^+W^-$  and  $Z^0Z^0$ , is simulated using the `MEee2VV` class. The decays of the gauge bosons are not included in the matrix element but the spin correlations for the decays are correctly described (Section 4.4).
- The resonant production of the Higgs boson followed by its decay to Standard Model particles is simulated using the `MEee2Higgs2SM` class. This process has a minuscule production rate and is only included to allow the easy simulation of gluon jets and the decay  $h^0 \rightarrow \tau^+\tau^-$ .
- The resonant production of vector mesons is simulated using the `MEee2VectorMeson` class. This process is included to allow the simulation of the production of charmonium and bottomonium resonances, primarily the  $\Upsilon(4S)$ , to test the hadron decay model.

For deep inelastic scattering (DIS) only two processes are included. Neutral and charged current processes are implemented in the `MENeutralCurrentDIS` and `MEChargedCurrentDIS` classes, respectively. In neutral current processes both the incoming and outgoing partons are considered to be massless, whereas in the charged current process the masses of the outgoing partons are included. For neutral current scattering both photon and  $Z^0$  boson exchange are included.

A much wider range of matrix elements is included for the simulation of events in hadron colliders:

- Difermion production via *s*-channel EW gauge bosons. The matrix elements for the production of fermion-antifermion pairs through  $W^\pm$  bosons, or interfering photons and  $Z^0$  bosons, are implemented in the `MEqq2W2ff` and `MEqq2gZ2ff` classes respectively. Only *s*-channel EW gauge boson diagrams are included for the hadronic modes.
- The production of a  $Z^0$  or  $W^\pm$  boson in association with a hard jet is simulated using the `MEPP2ZJet` or `MEPP2WJet` class respectively. The decay products of the bosons are included in the  $2 \rightarrow 3$  matrix element and the option of including the photon for  $Z^0$  production is supported.

<sup>1</sup> *t*-channel photon and  $Z^0$  boson exchange are not included.

- The production of a pair of EW gauge bosons,  $W^+W^-$ ,  $W^\pm Z^0$  and  $Z^0Z^0$  is implemented in the [MEPP2VV](#) class. The decays of the gauge bosons are not included in the matrix element, although the spin correlations for the decay products are correctly treated using the algorithm described in [Section 4.4](#).
- The production of a single top quark is implemented in the [MEPP2SingleTop](#) class. This process proceeds via either  $t$ -channel  $W^\pm$  exchange,  $s$ -channel  $W^\pm$  exchange, or in association with a  $W^\pm$  boson.
- The production of an EW gauge boson,  $W^\pm$  or  $Z^0$ , in association with a hard photon is simulated using the [MEPP2VGamma](#) class. As with EW gauge boson pair production the decays of the gauge bosons are not included in the matrix element, although the spin correlations for the decay products are correctly treated as described in [Section 4.4](#).
- The  $2 \rightarrow 2$  QCD scattering processes are implemented in the [MEQCD2to2](#) class. Currently all the particles are treated as massless in these processes.
- The matrix element for the production of a heavy quark-antiquark pair (top, bottom or charm quark pairs), is coded in the [MEPP2QQ](#) class. No approximations are made regarding the masses of the outgoing  $q\bar{q}$  pair.
- The [MEPP2GammaGamma](#) class implements the matrix element for the production of prompt photon pairs. In addition to the tree-level  $q\bar{q} \rightarrow \gamma\gamma$  process the loop-mediated  $gg \rightarrow \gamma\gamma$  process is included.
- Direct photon production in association with a jet is simulated using the [MEPP2GammaJet](#) class. As with the QCD  $2 \rightarrow 2$  process all of the particles are treated as massless in these processes.
- The production of an  $s$ -channel Higgs boson via both  $gg \rightarrow h^0$  and  $q\bar{q} \rightarrow h^0$  is simulated using the [MEPP2Higgs](#) class.
- The production of a Higgs boson in association with the  $Z^0$  or  $W^\pm$  bosons is simulated using the [MEPP2ZH](#) or [MEPP2WH](#) class respectively.
- The production of the Higgs boson in association with a hard jet is simulated using the [MEPP2HiggsJet](#) class.
- The production of the Higgs boson via the vector-boson fusion process is implemented in the [MEPP2HiggsVBF](#) class.
- The production of the Higgs boson in association with either a heavy quark-antiquark pair, either top or bottom, is implemented in the [MEPP2QQHiggs](#) class.

In addition we have a matrix element class, [MEQCD2to2Fast](#), that uses hard-coded formulae for the QCD  $2 \rightarrow 2$  scattering matrix elements rather than the helicity libraries of ThePEG. This class is significantly faster than the default [MEQCD2to2](#) class, although it does not implement spin correlations. It is intended to be used in the generation of the multiple parton-parton scatterings for the underlying event where the spin correlations are not important but due to the number of additional scatterings that must be generated the speed of the calculation can significantly affect the run time of the event generator. There are also the:

- [MEMinBias](#) class which is only used to simulate soft scattering processes as part of the underlying event model;
- [MEDiffractive](#) class which is only used to simulate diffractive processes.

There are a small range of matrix elements for processes initiated by a real photon. The [MEGammaGamma2ff](#) class implements the matrix elements for the production of a fermion-antifermion pair in photon–photon collisions,  $\gamma\gamma \rightarrow f\bar{f}$ . The [MEGammaGamma2WW](#) simulates the production of a  $W^+W^-$  pair in photon–photon collisions. The [MEGammaP2Jets](#) simulates jet production in photon–hadron collisions via the subprocesses  $q\gamma \rightarrow qg$ ,  $\bar{q}\gamma \rightarrow qg$  and  $g\gamma \rightarrow q\bar{q}$ .

### 3.9.2 Next-to-leading-order matrix elements

A small number of hard-coded processes [106–110] in the POWHEG scheme are implemented in Herwig together with a full implementation of the truncated shower. These processes are implemented in the following way:

- the matrix elements are calculated with NLO accuracy and a Born configuration supplied in the same way as for the leading-order matrix elements;
- the matrix element class generates a real emission configuration according to the POWHEG Sudakov form-factor;
- the event is then showered, including the truncated shower.

Currently the following processes are implemented:

- $e^+e^- \rightarrow q\bar{q}$  via photon and  $Z^0$  boson exchange is simulated using the [MEee2gZ2qqPowheg](#) class and includes both the QCD and FSR QED corrections.

- $e^+e^- \rightarrow l^+l^-$  via photon and  $Z^0$  boson exchange is simulated using the `MEee2gZ2llPowheg` class and includes FSR QED corrections.
- neutral- and charged-current DIS [110] are implemented in the `MENeutralCurrentDIS` and `MEChargedCurrentDIS` classes, respectively which also implement the leading-order processes;
- the Drell Yan production [106] of neutral vector bosons  $\gamma/Z^0$  is simulated using the `MEqq2gZ2ffPowheg` class;
- the Drell Yan production [106] of charged vector bosons, *i.e.*  $W^\pm$ , is implemented in the `MEqq2W2ffPowheg` class;
- the production of the Higgs boson via the gluon-gluon fusion process [109] is simulated using the `MEPP2HiggsPowheg` class;
- the production of the Higgs boson in association with the  $W^\pm$  boson [106] is implemented in the `MEPP2WHPowheg` class;
- the production of the Higgs boson in association with the  $Z^0$  boson [106] is simulated using the `MEPP2ZHPowheg` class;
- the production of pairs of EW gauge bosons  $W^+W^-$ ,  $W^\pm Z^0$  and  $Z^0 Z^0$  [107] is simulated using the `MEPP2VVPowheg` class;
- the production of the Higgs boson via the vector boson fusion process [110] is implemented in the `MEPP2HiggsVBFpowheg` class.
- the production of photon pairs [108] is implemented in the `MEPP2GammaGammaPowheg` class.

More details of the simulation of QCD radiation can be found in Ref. [106].

## 3.10 Les Houches interface

The `LesHouchesEventHandler` class inherits from the `EventHandler` class of ThePEG. The class has a list of `LesHouchesReader` objects that are normally connected to files with event data produced by an external matrix element generator program, although it could in principle include a direct run-time link to the matrix element generator or read events ‘on the fly’ from the output of a matrix element generator connected to a pipe.

When an event is requested by `LesHouchesEventHandler`, one of the readers is chosen according to the cross section of the process for which events are supplied by that reader. An event is read in and subsequently handled in the same way as for an internally generated process.

There are a number of matrix element generators available that can generate parton-level events using either the original Les Houches Accord [111] or the subsequent extension [112], which specified a file format for the transfer of the information between the matrix element generator and a general-purpose event generator, such as Herwig, rather than the original FORTRAN COMMON block.

In addition to the internal mechanism for the generation of hard processes, ThePEG provides a general `LesHouchesEventHandler` class, which generates the hard process using the Les Houches Accord. In principle a run-time interface could be used to directly transfer the information between the matrix element generator and Herwig, however we expect that the majority of such interfaces will be via data files containing the event information using the format specified in Ref. [112].

We also support option of reading the particle data for BSM models from the event file, as described in [113], and controlled by the `QNumbers` switch. We also support the reading of the event file as a SUSY Les Houches Accord (SLHA) [114, 115] file for internal supersymmetric models, see Section 6.4.2 for more details.

It is important that the settings for the parton shower are consistent with the matching scheme used by the external package generating the events. In all cases where NLO matching is included we advise that all the kinematics generation cuts are applied in program which generates the hard process. The two major packages supplying external events are:

### POWHEG BOX [116]

In the case of hard configurations generated using the POWHEG approach the parton shower should not generate any radiation with transverse momentum harder than the hardest emission supplied by the external program, *i.e.* the settings `MaxPtIsMuF=Yes` and `RestrictPhasespace=Yes` should be used.

### mg5\_aMC@NLO [89]

For hard configurations generated using the `mg5_aMC@NLO` program the settings of the parton shower must be consistent with those used to calculate the subtraction terms in the MC@NLO approach. This means that

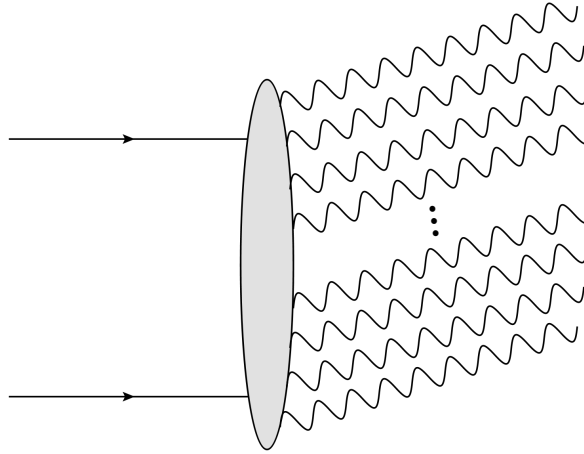


Fig. 3.2: A schematic diagram of a  $2 \rightarrow n$  processes that can be simulated via the “blob” matrix elements.

only the angular-ordered parton shower can be used and the settings no longer correspond to our current defaults. The options `PartnerMethod=Random`, `ScaleChoice=Partner`, `InitialInitialBoostOption=LongTransBoost`, `ReconstructionOption=General`, `FinalStateReconOption=Default`, `InitialStateReconOption=Rapidity`, must be used.

### 3.11 ‘Blob’ Matrix Elements

The default method for constructing the diagrams contributing to a given hard process is through the `Tree2toNGenerator` class, which only allows  $1 \rightarrow 2$  interactions. However, for several models containing new types of interactions, such as those involving two incoming particles and  $n$  outgoing,  $2 \rightarrow n$ , where  $n \gg 2$ , this procedure is not ideal. This is in particular the case for processes for which only the  $2 \rightarrow n$  matrix element is known, such as sphaleron [117] or instanton-like processes, shown schematically in Fig. 3.2. The `BlobME` class provides the necessary functionality, replacing the `Tree2toNGenerator` class, where the two incoming and  $n$  outgoing particles are now specified by the `processes` class function, which is of the type `multimap<tcPDPair, tcPDVector>`. The matrix element squared then needs to be specified through the `me2` function. If the matrix element requires a variable number of final-state particles  $n$ , that number can be accessed via the `mePartonData` function.

### 3.12 Processes with incoming photons

It is possible to have hard scattering processes with incoming photons in hadron-hadron collisions, for example in the higher-order QED corrections to the Drell-Yan production of  $W^\pm$  or  $Z^0$  bosons. Some of these are available through the built-in matrix elements, but photon induced processes can also be generated within the Matchbox framework. While these can now be directly showered by the in the angular-ordered parton shower we also provide `IncomingPhotonEvolver` class which can be used as one of the `PreCascadeHandlers` in these processes to perform the backward evolution of the photon to a quark or antiquark which can then be evolved by the parton shower.

This performs one backward branching evolving in transverse momentum from a starting scale  $p_{T\text{start}}$  given by the  $p_T$  of the softest particle in the event, or a minimum scale `minpT` if the scale is below the minimum allowed value. This is performed using a Sudakov form factor,

$$\Delta(p_T) = \exp \left\{ - \int_{p_T^2}^{p_{T\text{start}}^2} \frac{dp_T'^2}{p_T'^2} \frac{\alpha}{2\pi} \int_x^1 dz P(z) \sum_i e_i^2 \frac{\frac{x}{z} f_i(\frac{x}{z}, p_T')}{x f_\gamma(x, p_T')} \right\},$$

where  $p_T$  is the transverse momentum of the branching,  $\alpha$  is the fine structure constant,  $x$  is the momentum fraction of the photon,  $e_i$  is the electric charge of the particle produced in the backward evolution and the sum over  $i$  runs over all the quarks and antiquarks. The splitting function is

$$P(z) = \frac{1 + (1 - z)^2}{z},$$

where  $z$  is the fraction of the momentum of incoming parton produced in the backward evolution given to the photon. The  $p_T$  and momentum fraction of the branching are generated in the same way as those in the parton shower, as described in Section 4.2. The momenta of the particles, including the new branching are then reconstructed as described in Section 4.2.5.

## 3.13 Code structure

In ThePEG the generation of the hard process is the responsibility of the `EventHandler`. The base `EventHandler` class only provides the abstract interfaces for the generation of the hard process with the actual generation of the kinematics being the responsibility of inheriting classes. There are two such classes provided in ThePEG: the `StandardEventHandler`, which implements the internal mechanism of ThePEG for the generation of the hard process; and the `LesHouchesEventHandler`, which allows events to be read from data files.

The `StandardEventHandler` provides the high-level interface of both built-in Herwig 7 matrix elements as described in Section 3.9, as well as matrix elements provided by the Matchbox module. The handling of event files is covered in Section 3.10.

The `StandardEventHandler` uses a `SubProcessHandler` to generate the kinematics of the particles involved in the hard process. In turn the `SubProcessHandler` makes use of a number of `MEBase` and `MEGroup` objects to calculate the matrix element and generate the kinematics for specific processes. A bigger network of classes exists in the case of Matchbox generated processes which we mainly cover in this appendix, though the generic interfaces for these matrix elements also resemble the high-level structures imposed by ThePEG. In particular, they need to

- define the particles that interact in a given process, by specifying a number of `DiagramBase` objects; one `DiagramBase` is specified per flavour combination, and
- return the differential partonic cross-section

$$\frac{d\sigma}{dr_1 \dots dr_n},$$

when supplied with the partonic centre-of-mass energy of the collision and  $n$  random numbers between 0 and 1, and to

- create a `HardVertex` object describing the interaction that occurred, including the spin-unaveraged matrix element (where available) to allow spin correlation effects to be generated.

One `MEBase` object is generally used to describe one physical process, possibly with different partonic flavours, though the Matchbox framework chooses to represent individual subprocesses by individual `MEBase` objects. The selection of flavours within each subprocess is carried out internally by the `EventHandler`, through the `SamplerBase` object in charge, cf Section 3.6. The resulting cross-sections can be output with varying levels of detail, controlled by the `StatLevel` switch; by default they are only broken down by `MEBase` objects.

### 3.13.1 Cross-section assembly within Matchbox

Within the Matchbox framework a central object of the class `MatchboxFactory` is administrating the assembly of all cross-sections, both at leading and next-to-leading order and possibly matched to the showers or used within a multijet merging approach. This class is deriving from a standard ThePEG `SubProcessHandler` and will, for a given process and desired cross-section order, generate `MEBase` and `MEGroup` objects to represent various contributions to the cross sections. While these classes form the high-level interface to the hard process handling of ThePEG, Matchbox's internal class structure is in close correspondence to the physical quantities required for a cross-section calculation, accompanied by book-keeping algorithms and data-base functionality required for the handling of different contributions. This core layer, which facilitates the calculation of the hard cross-sections, is interfaced to amplitudes for specific processes, or external libraries delivering a number of different subprocesses; several other interfaces are provided for the choice of scales in the hard process, the input of matching subtractions, or a hook for multijet merging. The backbone structure of the Matchbox module is shown in Fig. 3.3. In the following we list the different classes with a short description of their main functionality, and grouped with respect to the different layers.

The `MatchboxFactory` and the deriving `MergingFactory` classes inherit from ThePEG's subprocess handler and are the main classes to identify the required contributions to a given process of interest. They will determine leading order, virtual as well as subtraction terms required and create and configure `MatchboxMEBase` and `SubtractedME` objects to calculate the actual cross-section contributions. Once ready, these will be inserted into the `ME` vector of the `SubProcessHandler` which does not require access by a user in this case anymore.

#### 3.13.1.1 Core cross-section contributions

All of the cross-sections which are calculated by Matchbox are handled by ThePEG through the standard mechanism sketched above; on top of these, some extensions to NLO have been introduced specifically to represent groups of events, typically a real emission contribution with accompanying subtraction terms. Since much more detailed communication in

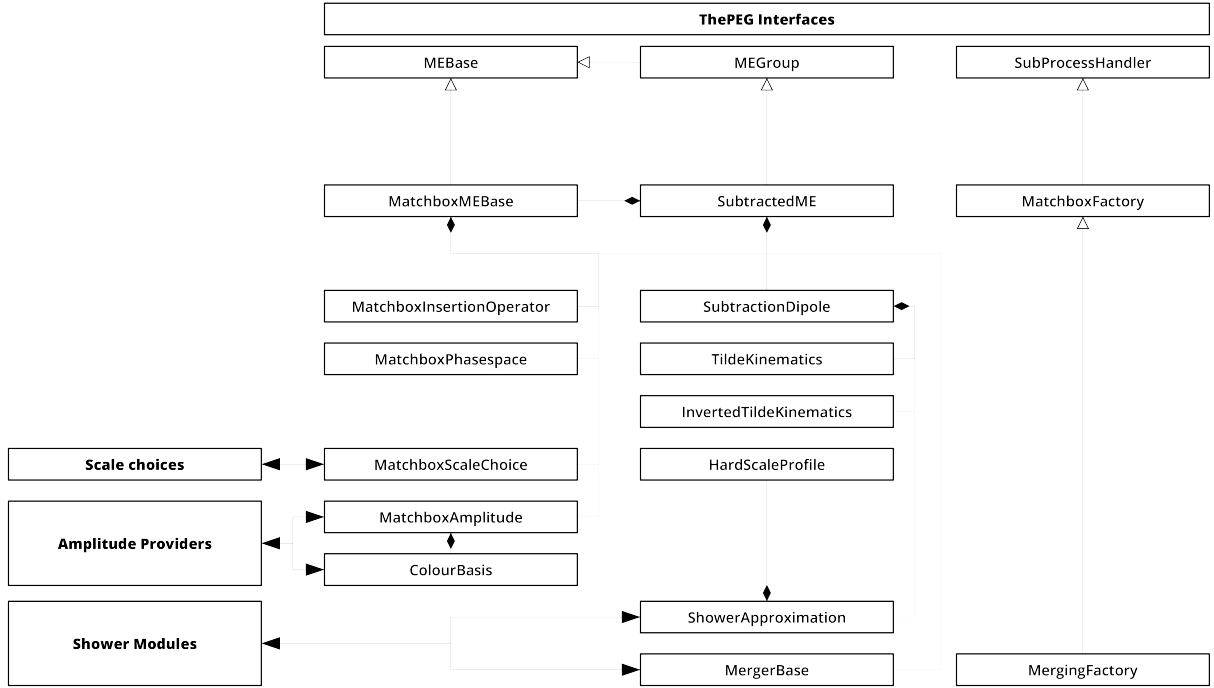


Fig. 3.3: An overview of the classes in Matchbox and their interaction.

between different matrix element classes is required by Matchbox matrix elements to use colour and spin correlated matrix elements. ThePEG’s XComb objects have been extended to contain more per-phase-space information, in particular the caching of colour and helicity amplitudes, as well as resulting correlated matrix elements. The inner core of the Matchbox framework closely follows the layout of its original development as discussed in [27, 118].

Cross-section contributions to an observable at one fixed phase-space point, i.e. all contributions which are of leading order, virtual or integrated subtraction term type are handled by a MatchboxMEBase object which uses a MatchboxAmplitude object to calculate matrix elements for a particular subprocess. MatchboxMEBase will also incorporate insertion operators deriving from the MatchboxInsertionOperator class to be combined with virtual contributions provided by the amplitude object. The diagrams contributing to a given hard process are generated by the Tree2toNGenerator class starting from a given coupling order and a set of vertex objects to be considered. A physical phase-space point is generated through a MatchboxPhaseSpace object, which is also responsible to select a diagram topology regarded as the most significant contribution to the cross-section at the selected phase-space point. This information is used to subsequently set up mother/daughter relations in the event record. The ColourBasis object contains information about the colour basis which has been used to express the amplitudes and is responsible of selecting a colour flow to be assigned to the event at the hard process level. The choice of renormalization and factorization scales, as well as the hard shower scale are contained in classes deriving from MatchboxScaleChoice. In order to optimize memory consumption to store information shared among several objects, such as diagrams contributing to a given subprocess or the tree structures describing hierachic phase-space generation within a multi-channel approach, the ProcessData object holds such data in a quasi-static way.

NLO cross-sections within Matchbox are strictly calculated in the subtraction paradigm for which we assume that an organization of the subtraction terms in one or the other incarnation of a dipole-type kernel is in place. While the default subtraction method is dipole subtraction along the lines of [72, 73] other approaches of this kind are present. The subtraction terms all derive from the SubtractionDipole class, which are accompanied by respective kinematic mappings deriving from the TildeKinematics class, and possibly their inverse in InvertedTildeKinematics to be used for a different kind of phase-space sampling or the generation of matrix element corrections. The subtraction term classes register with the DipoleRepository class to be available to the dipole finding algorithm, which is mainly contained in the MatchboxMEBase class and works using the diagram information supplied for the real emission and leading order processes in order to determine the dipole mappings. An object of class SubtractedME, inheriting from ThePEG’s MEGroup and operating on an StdXCombGroup to represent the collection of correlated phase-space points, then holds the various subtraction terms along with the real emission matrix element considered. SubtractedME is also capable of projecting a contribution calculated from a real emission phase-space point down to an underlying Born phase-space point derived from one of the subtraction terms. This mechanism is heavily used within matching to a parton shower or the multijet merging algorithm. SubtractionDipole objects also contain a reference to a shower kernel to be used in setting up the subtraction required in NLO plus parton shower matching. All shower subtractions follow the matching paradigm

outlined at the beginning of this chapter and their implementation inherits from the `ShowerApproximation` class. The `MatchboxMEBase` class is also using objects of the `MergerBase` class for hooks into the multijet merging algorithm.

### 3.13.1.2 Other helper classes and algorithms

A number of additional helper algorithms have been incorporated into the Matchbox framework; this specifically includes a versatile set of template-based sampling of one-dimensional densities, spinor helicity support, caching of intermediate amplitudes, determination of diagrams to only name a few. Most of these can also be used standalone outside of the Herwig framework and support is available from the authors on request.

### 3.13.2 Code structure of Herwig 7 built-in matrix elements

For the built-in matrix elements which are supplied with Herwig 7, typically  $2 \rightarrow 2$  scattering processes, the generation of the kinematics, including off-shell effects if required, and other technical steps is handled by the `HwMEBase` class which in turn inherits from the `MEBase` class of ThePEG. The actual calculation of the matrix elements is implemented using the `Helicity` classes of ThePEG.<sup>1</sup> This allows us to include spin correlations between the production, decay and parton showering of the particles, as described in Section 4.4. The helicity amplitudes for the production process are stored in the `ProductionMatrixElement` which is used by the `HardVertex` class to calculate the  $\rho$  and  $D$  matrices required to generate the spin correlations.

The main switch for the generation of the hard process is the `MatrixElements` interface, which allows the `MEBase` objects to be specified and hence determines which hard scattering processes are generated. In addition, each class inheriting from `MEBase` in Herwig 7 has a number of switches that control the incoming, outgoing and intermediate particles in a specific process. These are controlled by Interfaces in the specific matrix element classes. A number of different partonic subprocesses can be handled at the same time by simply specifying several `MEBase` objects.

---

<sup>1</sup> The only exception is the `MEQCD2to2Fast` class, which is ‘hand-written’ for speed.

## 4 Parton showers

### 4.1 Overview

#### 4.1.1 Philosophy

A major success of the original HERWIG program was its treatment of soft gluon interference effects, in particular the phenomenon of *colour coherence*, via the angular ordering of emissions in the parton shower [1, 119–127]. This emphasis on the accurate treatment of perturbative QCD radiation continues in Herwig 7 with two parton-shower algorithms:

- the default angular-ordered algorithm [25] which generalizes that used in the original HERWIG program [1–3]; and
- the alternative dipole-type algorithm [26, 27] which was added in a later version of the Herwig++ program.

Both shower modules are intended to provide the same level of physics predictions in order to be able to assess uncertainties, in so far as is possible, by cross comparisons when first-principle theoretical prescriptions are not available. Using the approach described in Ref. [34] a number of studies have been performed for specific processes [32, 128]. A number of efficient techniques are provided to evaluate parton-shower variations [35].

In this section, following a brief review of the core concepts common to both parton-shower algorithms, we describe the two parton-shower algorithms in detail. This is followed by a discussion of issues which are common to the two different algorithms. The section then concludes with details of the C++ code structure.

#### 4.1.2 Basics

Both parton-shower algorithms in Herwig, and in general all modern parton-shower simulations [129], have their outset from the basic properties of QCD radiation.

All parton showers start from the approximation that in the (*quasi-)*collinear<sup>1</sup> limit [130], in which the transverse momentum of the branching and the masses of the particles are small compared to the other scales. In this limit the matrix element for a process with an additional parton,  $\mathcal{M}_{n+1}$ , is approximately

$$|\mathcal{M}_{n+1}|^2 = \frac{8\pi\alpha_s}{q_{ij}^2 w^2 - m_{ij}^2} P_{\tilde{ij} \rightarrow ij}(z, q_{ij}^2) |\mathcal{M}_n|^2, \quad (4.1)$$

where  $\alpha_s$  is the strong coupling constant,  $q_{ij}^2$  is the virtuality of the branching parton  $\tilde{ij}$ ,<sup>2</sup>  $m_{ij}^2$  is the physical mass of the branching particle,  $z$  is the fraction of the momentum of  $\tilde{ij}$  carried by the parton  $i$ ,  $P_{\tilde{ij} \rightarrow ij}(z, q_{ij}^2)$  is the quasi-collinear splitting function and  $\mathcal{M}_n$  is the matrix element for the process without the additional collinear parton. As the phase-space also factorizes in this limit, we can write the probability of the  $\tilde{ij}$  branching to produce partons  $i$  and  $j$  in the *quasi-collinear limit* as

$$d\mathcal{P}_{\tilde{ij} \rightarrow ij} = \frac{\alpha_s}{2\pi} \frac{dq^2}{q^2 - m_{ij}^2} dz P_{\tilde{ij} \rightarrow ij}(z, q^2). \quad (4.2)$$

The splitting functions with soft singularities, i.e. where the emitted particle  $j$  is a gluon<sup>3</sup>, all behave as

$$\lim_{z \rightarrow 1} P_{\tilde{ij} \rightarrow ij} = \frac{2C_{\tilde{ij}}}{1-z} \left( 1 - \frac{m_i^2}{z(1-z)(q^2 - m_{ij}^2)} \right), \quad (4.3)$$

in the soft  $z \rightarrow 1$  limit, where  $C_{\tilde{ij}}$  equals  $C_F$  for  $P_{q \rightarrow qg}$  and  $P_{\tilde{q} \rightarrow \tilde{q}g}$ ,  $\frac{1}{2}C_A$ <sup>4</sup> for  $P_{g \rightarrow gg}$ , and  $C_A$  for  $P_{\tilde{g} \rightarrow \tilde{g}g}$ .

Similarly, if we consider the emission of a soft gluon, the amplitude for the process including an extra soft gluon with momentum  $q_j$  is

$$\mathcal{M}_{n+1} = g_s \mathcal{M}_n \mathbf{J}(q_j),$$

<sup>1</sup> While older parton-shower programs generally just used the collinear limit, *i.e.* assuming all the partons are massless, most modern programs including both shower algorithms in Herwig use the quasi-collinear limit to improve the treatment of radiation from massive particles.

<sup>2</sup> We reserve the tilde notation  $\tilde{ij}$  exclusively to denote the parent parton, which decays into daughters  $i$  and  $j$ .

<sup>3</sup> *i.e.*  $P_{q \rightarrow qg}$ ,  $P_{\tilde{q} \rightarrow \tilde{q}g}$ ,  $P_{g \rightarrow gg}$ , and  $P_{\tilde{g} \rightarrow \tilde{g}g}$ .

<sup>4</sup> Note that for  $g \rightarrow gg$ , there is also a soft singularity at  $z \rightarrow 0$  with the same strength, so that the *total* emission strength for soft gluons from particles of all types in a given representation is the same:  $C_F$  in the fundamental representation and  $C_A$  in the adjoint.

where  $\mathbf{J}(q_j)$  is the non-Abelian semi-classical ‘eikonal’ current for the emission of the soft gluon from the hard partons. In general the eikonal current is

$$\mathbf{J}(q_j) = \varepsilon_\mu^* \sum_{\text{external partons}} C_\alpha^b P_\alpha^{ab} \left( \frac{p_{\text{parton}}}{p_{\text{parton}} \cdot q_j} \right)^\mu,$$

for the emission of a soft gluon with momentum  $q_j$  and polarization vector  $\varepsilon$ . The colour structure of the leading-order process without the soft gluon is given by  $C_\alpha^b$ , while  $P_\alpha^{ab}$  is the colour matrix for the emission of a gluon with colour  $a$ . If we consider the simplest case of two partons,  $i, k$ , with four-momenta  $q_i, q_k$  respectively, which form a colour-singlet system, in the soft limit

$$|\mathcal{M}_{n+1}|^2 = -4\pi\alpha_s C_{\tilde{i}\tilde{j}} \left( \frac{q_k}{q_k \cdot q_j} - \frac{q_i}{q_i \cdot q_j} \right)^2 |\mathcal{M}_n|^2. \quad (4.4)$$

In order to correctly treat both the soft and collinear limits for gluon emission, and describe multiple emissions we need to define an appropriate emission probability

$$d\mathcal{P}_{\text{branching}} = d\kappa \frac{\alpha_s}{2\pi} \mathcal{K}_{\text{branching}}(\kappa),$$

with an evolution variable  $\kappa$  and kernel  $\mathcal{K}_{\text{branching}}(\kappa)$ .

In Herwig the two parton-shower algorithms make different choices :

- the angular-ordered parton shower uses an evolution variable which reduces to the angle of emission in the collinear limit, together with the quasi-collinear branching probability, Eq. (4.2), and a disjoint phase-space for emission from different partons which correctly treats both soft and collinear emission as discussed in Section 4.2;
- the dipole shower uses the transverse momentum for the evolution variable together with a dipole phase-space including both an emitter and a spectator which correctly treats both soft and collinear emission using a kernel which reduces to Eqs. (4.2) and (4.4) in the appropriate limits.

In general, the emission probability for the radiation of gluons is infinite in the soft and collinear limits. Physically these divergences would be cancelled by virtual corrections, which we do not explicitly calculate but rather include through unitarity. We therefore impose a physical cutoff and call radiation above this limit resolvable. The cutoff ensures that the contribution from resolvable radiation is finite. Equally the uncalculated virtual corrections ensure that the contribution of the virtual and unresolvable emission below the cutoff is also finite. Imposing unitarity

$$\mathcal{P}(\text{resolved}) + \mathcal{P}(\text{unresolved}) = 1$$

gives the probability of no branching in an infinitesimal increment of the evolution variable  $d\kappa$  as

$$1 - \sum_{\text{branchings}} d\mathcal{P}_{\text{branching}},$$

where the sum runs over all possible branchings of the emitting particles  $\tilde{i}\tilde{j}$  in the angular-ordered shower, and all possible branchings and spectators in the dipole shower. The probability that a parton does not branch between two scales is given by the product of the probabilities that it did not branch in any of the small increments  $d\kappa$  between the two scales. Hence, in the limit  $d\kappa \rightarrow 0$  the probability of no branching exponentiates, giving the *Sudakov form factor*

$$\Delta(\kappa, \kappa_h) = \prod_{\text{branchings}} \Delta_{\text{branching}}(\kappa, \kappa_h), \quad (4.5)$$

which is the probability of evolving between the scale  $\kappa_h$  and  $\kappa$  without resolvable emission. The Sudakov form factor for an individual branching is given by

$$\Delta_{\text{branching}}(\kappa, \kappa_h) = \exp \left( - \int d\mathcal{P}_{\text{branching}} \right) = \exp \left( - \int_\kappa^{\kappa_h} d\kappa' \frac{\alpha_s}{2\pi} \mathcal{K}_{\text{branching}}(\kappa') \right). \quad (4.6)$$

The formalism discussed above allows us, if given a starting scale  $\kappa_h$ , to evolve a parton down in scale and generate the next branching of this particle at a lower scale. The no-emission probability encoded in the Sudakov form factor is used to generate the evolution variable and any other variables, *e.g.* the momentum fraction  $z$ , for this branching. This procedure

can then be iterated to generate subsequent branchings of the particles produced until no further emission occurs above the cutoff. The procedures used solve

$$\Delta(\kappa, \kappa_h) = \mathcal{R}, \quad (4.7)$$

where  $\mathcal{R}$  is a random number uniformly distributed between 0 and 1 and generate the variables describing the emission are discussed in [Appendix B](#).

The treatment of the strong coupling constant, and its argument, are described in detail in [Appendix C](#).

#### 4.1.3 Structure of the evolution and showering of scattering processes

Both parton shower algorithms can be used to shower both  $2 \rightarrow n$  scattering processes and  $1 \rightarrow n$  decay processes, where  $n$  is the number of outgoing particles. In the case of electron-positron collisions this is simply the hard subprocess and any decay processes, however in a hadron-hadron collision, secondary collisions, or multiple parton interactions, also require showering in addition to the primary hard subprocess. The details of the simulation of the multiple and soft scattering processes are discussed in [Section 8](#). In this section we will explicitly discuss the showering of the hard subprocess and decay processes, however the procedure also applies to secondary processes.

In the first stage of these processes, the particles from the hard scattering processes are separated into the core hard scattering processes and the subsequent decays of any unstable particles.<sup>5</sup> By default both parton shower algorithms work in the narrow width approximation, therefore the hard process and any decay processes (i.e. an unstable particle and its decay products) are showered separately.

The hard process sets the initial conditions for the parton-shower evolution. There are two initial conditions the first, and most important, is the large- $N_C$  colour structure of the hard process, which determines:

- the direction of the colour partner and hence the maximum evolution scale in the angular-ordered parton shower;
- which dipoles are present in the dipole shower.

In addition to the constraints given by the colour structure, we impose that the maximum transverse momentum for the radiation in the parton shower is below a veto scale determined from the factorization scale for the hard process. This scale is interpreted differently in the two parton-shower modules:

- in the angular-ordered parton shower any emissions with transverse momenta relative to the jet axis above this scale are vetoed, as the shower emissions are not ordered in transverse momentum;
- in the dipole shower, which is ordered in transverse momentum, the scale simply sets the maximum emission scale in the parton shower.

These scales and their variations, in order to assess uncertainties, are discussed in more detail in [Section 4.8.1](#).

The two parton showers also differ in their treatment of mass effects. The dipole shower requires a fixed flavour number scheme so that the masses are consistently defined in both the hard process and subsequent parton showering, for example if working in a five-flavour scheme then the bottom mass will consistently be set to zero. The angular-ordered parton shower uses a more pragmatic approach where the masses of the partons in the hard process can be zero but they are put on mass-shell in the parton shower in order to ensure the correct radiation at small scales.

#### 4.1.4 Outline

We will now discuss the two parton shower algorithms in detail, this is followed by a discussion of issues which are common to the two different parton-shower algorithms:

- perturbative decays and spin correlations;
- variations of the shower scales;
- forced splitting and the handling of multiple partonic scattering processes;
- the simulation of QED radiation in the YFS formalism [131].

<sup>5</sup> This behaviour is controlled using the `SplitHardProcess` switch which by default separates the hard and decay processes. This is necessary in order to correctly shower any almost on-shell intermediates and preserve their masses when the decays of the particles have been generated as part of the hard scattering processes. It is not usually required in processes where Herwig 7 generates the hard processes as we handle the decays as part of the showering process but can be required for external events supplied in the Les Houches Event format.

## 4.2 Angular-Ordered parton shower

The default parton shower algorithm is the *coherent branching algorithm* [25], which extends the formalism originally developed for the HERWIG program [1–3]. The new algorithm:

- retains angular ordering as a central feature;
- uses a covariant formulation of the showering algorithm, which is invariant under boosts along the jet axis;
- improves the treatment of heavy quark fragmentation through the use of mass-dependent splitting functions [130] and kinematics, providing a complete description of the so-called *dead-cone* region;
- includes azimuthal correlations between the hard scattering process, perturbative decays and all shower emissions using the approach of Refs. [33, 53, 102, 103];
- includes interleaved QCD, QED and EW radiations, with the option of choosing/omitting interactions.
- supports multiple choices for the control of the evolution scale  $\tilde{q}$ , i.e. the transverse momentum-preserving [7, 25], virtuality-preserving [31] and dot-product-preserving [28, 29] schemes.

In this section we give a full description of the angular-ordered parton shower model. We begin by introducing the fundamental kinematics and dynamics underlying the shower algorithm. This is followed by descriptions of the initial conditions and the Monte Carlo algorithms used to generate the showers.

### 4.2.1 Shower kinematics

Each of the colour, weak or electromagnetically charged leg of the hard sub-process is considered to be a *shower progenitor*. We associate a set of basis vectors to each progenitor, in terms of which we can express the momentum ( $q_i$ ) of each particle in the resulting shower as

$$q_i = \alpha_i p + \beta_i n + q_{\perp i}, \quad (4.8)$$

that is the well-known *Sudakov basis*. The vector  $p$  is equal to the momentum of the shower progenitor generated by the prior simulation of the hard scattering process, *i.e.*  $p^2 = m^2$ , where  $m$  is the on-shell mass of the progenitor. The *reference vector*  $n$  is a light-like vector that satisfies  $n \cdot p > m^2$ . In practice  $n$  is chosen anticolinear to  $p$  in the frame where the shower is generated, maximizing  $n \cdot p$ . Since we almost always generate the shower in the rest frame of the progenitor and an object with which it shares a colour line<sup>1</sup>,  $n$  is therefore collinear with this *evolution partner* object. The  $q_{\perp i}$  vector gives the remaining components of the momentum, transverse to  $p$  and  $n$ .

Our basis vectors satisfy the following relations:

$$\begin{aligned} q_{\perp i} \cdot p &= 0, & p^2 &= m^2, & q_{\perp i}^2 &= -\mathbf{q}_{\perp i}^2, \\ q_{\perp i} \cdot n &= 0, & n^2 &= 0, & n \cdot p &> m^2. \end{aligned} \quad (4.9)$$

where  $\mathbf{q}_{\perp i}$  is the spatial component of  $q_{\perp i}$  in the frame where the shower is generated ( $\mathbf{q}_{\perp i}^2 \geq 0$ ). Given these definitions, calculating  $q_i^2$ , one finds that  $\beta_i$  may be conveniently expressed in terms of the mass and transverse momentum of particle  $i$  as

$$\beta_i = \frac{q_i^2 - \alpha_i^2 m^2 - q_{\perp i}^2}{2\alpha_i n \cdot p}. \quad (4.10)$$

The shower algorithm does not generate the momenta or Sudakov parameters directly. In practice what is generated first is a set, each element of which consists of three *shower variables*, which fully parameterize each parton branching. One of these variables parameterizes the scale of each branching, the so-called *evolution scale*, which we shall discuss in more detail below. Typically this evolution scale starts at a high value, characteristic of the process that produces the progenitors, and continually reduces as the shower develops, via the radiation of particles. When the evolution scale has reduced to the point where there is insufficient phase-space to produce any more branchings, the resulting partons are considered to be on-shell, and the reconstruction of the momenta from the shower variables may begin in full.

<sup>1</sup> In the case that the particle is both colour and electromagnetically charged we use the colour partner for the evolution, however if the particle is only electromagnetically charged we pick a partner from the other charged particles using the product of the charges of the particles as required for coherence of the QED radiation.

The first shower variable is the *light-cone momentum fraction*  $z$ . Given a branching,  $\tilde{i}\tilde{j} \rightarrow i + j$ , this parameterizes how the momentum component of the parent parton,  $\tilde{i}\tilde{j}$ , in the direction of the shower progenitor, is divided between its two daughter partons,  $i$  and  $j$ . We define  $z$  as

$$z = \frac{\alpha_i}{\alpha_{\tilde{i}\tilde{j}}} = \frac{n \cdot q_i}{n \cdot q_{\tilde{i}\tilde{j}}}. \quad (4.11)$$

For particles in the final state we use a forward evolution algorithm where the parton shower consists of a sequence of branchings  $\tilde{i}\tilde{j} \rightarrow i + j$ , ordered in the evolution scale. For incoming particles we use a backward evolution algorithm where we start at the large evolution scale of the scattering process and evolve the incoming particles backwards toward the incoming hadron to give the mother  $\tilde{i}\tilde{j}$  and the sister parton  $j$ , again with a decreasing evolution scale. We use the definition of  $z$  in Eq. (4.11) both for forward and backward parton shower algorithms.

The second variable used to parameterize a branching is the azimuthal angle,  $\phi$ , of the relative transverse momentum of each branching  $p_\perp$ , measured with respect to the  $p$  direction. The relative transverse momentum  $p_\perp$  is *defined* to be

$$p_\perp = q_{\perp i} - z q_{\perp \tilde{i}\tilde{j}}. \quad (4.12)$$

As with the definition of  $z$ , this definition of the relative transverse momentum is the same for both forward and backward parton-shower evolution algorithms.

The last, and most important, of the shower variables defining a branching is the evolution scale. Parton shower algorithms may be formulated as an evolution in the virtualities of the branching partons, or as an evolution in the transverse momentum of the branching products. However, a careful treatment of colour coherence effects [1, 119–127] reveals that branchings involving soft gluons should be ordered in the angle between the branching products.

The key finding of these studies is that, when soft gluon emissions are considered, branchings that are not angular-ordered do not give any leading-logarithmic contributions. This is a dynamical effect whereby radiation from the emitting partons, with smaller angular separations, interferes destructively in these non-ordered regions. Some intuitive understanding of the effect may be gained by considering that a soft gluon, emitted at a large angle from a jet-like configuration of partons, does not have sufficient transverse resolving power to probe the internal jet structure. As a result, it is only sensitive to the *coherent sum* of the collinear singular contributions associated with the constituents, resulting in a contribution equivalent to that from the original progenitor parton. Destructive interference in the non-ordered region effectively decreases the available phase-space for each branching, from the virtuality-ordered region to the angular-ordered region.

It may be shown that the contributions that angular ordering misses are purely soft and suppressed by at least one power of  $N_C^2$ , where  $N_C = 3$ , the number of colours in QCD. Formally then, omitting such contributions amounts to neglecting terms of next-to-leading-log accuracy that are *also* strongly colour suppressed. We stress however, that whereas angular ordering leads to an *omission* of these suppressed higher order terms, other forms of ordering must prove that they do not overestimate leading-log contributions.

For the forward evolution of partons with time-like virtualities, the variable used to achieve such ordering,  $\tilde{q}^2$ , is defined according to

$$z(1-z)\tilde{q}^2 = -m_{\tilde{i}\tilde{j}}^2 + \frac{m_i^2}{z} + \frac{m_j^2}{1-z} - \frac{p_\perp^2}{z(1-z)}, \quad (4.13)$$

where  $m_i$  is the on-shell mass of particle  $i$  etc. This definition is arrived at by generalizing the FORTRAN HERWIG angular-evolution variable,  $\tilde{q}^2 = q_i^2/(z(1-z))$ , to include the effects of the mass of the emitting parton. This may be seen by writing  $q_{\tilde{i}\tilde{j}} = q_i + q_j$ , and calculating  $q_{\tilde{i}\tilde{j}}^2(z, p_\perp^2, q_i^2, q_j^2)$ , which shows

$$\tilde{q}^2 = \frac{q_{\tilde{i}\tilde{j}}^2 - m_{\tilde{i}\tilde{j}}^2}{z(1-z)} \bigg|_{q_i^2 = m_i^2, q_j^2 = m_j^2}. \quad (4.14)$$

For showers involving the evolution of partons with space-like virtualities, the evolution variable is instead defined by

$$(1-z)\tilde{q}^2 = -z m_{\tilde{i}\tilde{j}}^2 + m_i^2 + \frac{z m_j^2}{1-z} - \frac{p_\perp^2}{1-z}. \quad (4.15)$$

Once again this definition of the evolution variable is a generalization of the analogous FORTRAN HERWIG angular-evolution variable used for initial-state radiation:  $\tilde{q}^2 = -q_i^2/(1-z)$ . Using momentum conservation,  $q_{\tilde{i}\tilde{j}} = q_i + q_j$ ,

we may calculate  $q_i^2(z, p_\perp^2, q_{ij}^2, q_j^2)$ , giving

$$\tilde{q}^2 = \frac{m_i^2 - q_i^2}{1 - z} \Big|_{q_{ij}^2 = m_{ij}^2, q_j^2 = m_j^2}. \quad (4.16)$$

To see how these variables relate to the angle between the branching products, consider that the parton shower is generated in the frame where the light-like basis vector  $n$  is anticollinear to the progenitor. For forward evolving partons with small time-like virtualities, expanding  $z$  and  $q_{ij}^2$  in component form,

$$\tilde{q}^2 = \frac{2E_{ij}^2 (1 - \cos \theta_{ij}) (1 + \cos \theta_{ij})^2}{(1 + \cos \theta_i) (1 + \cos \theta_j)}, \quad (4.17)$$

where  $\theta_i$  and  $\theta_j$  are the angles between the daughter particles  $i, j$  and the progenitor,  $\theta_{ij}$  is the angle between the parent and the progenitor, and  $\theta_{ij}$  is the angle between the two daughters, and  $E_{ij}$  is the energy of the parent. This expression for the time-like evolution variable in terms of angles is more complicated than the analogous FORTTRAN HERWIG formula:  $\tilde{q}^2 = 2E_{ij}^2 (1 - \cos \theta_{ij})$ . This is because in FORTTRAN HERWIG  $z$  was defined to be the energy fraction  $E_i/E_{ij}$ , instead of the light-cone momentum fraction as given in Eq. (4.11). Nevertheless, for small angles we find that the Herwig 7 and FORTTRAN HERWIG evolution variables are both given by

$$\tilde{q} = E_{ij} \theta_{ij} (1 - \mathcal{O}(\theta_x^2)). \quad (4.18)$$

When a branching occurs, the daughter partons  $i$  and  $j$ , with momentum fractions  $z$  and  $1 - z$ , have their starting evolution scales set to  $z\tilde{q}$  and  $(1 - z)\tilde{q}$  respectively, where  $z\tilde{q} \approx E_i \theta_{ij}$  and  $(1 - z)\tilde{q} \approx E_j \theta_{ij}$ . In this way the maximum opening angle of any subsequent branching is  $\theta_{ij}$ , thereby implementing angular ordering.

For initial-state showers the same QCD coherence argument applies, so in evolving backwards, away from the hard process, the angle between the mother of the branching and its final-state daughter parton must decrease. Writing the space-like evolution variable (Eq. (4.15)) in terms of angles, neglecting parton virtualities, one finds the same form as for the time-like variable in Eq. (4.18). This means that once a branching has occurred in the course of the backward evolution, the mother of the branching evolves backwards from scale  $\tilde{q}$ , and the daughter evolves forwards from scale  $(1 - z)\tilde{q}$ , as in the time-like case.

Even at leading-logarithmic accuracy there are correlations between subsequent emissions in the parton-shower which affect the azimuthal angles of the partons. There can also be correlations between emissions from different progenitors which depend on the nature of the hard scattering process. As in FORTTRAN HERWIG, Herwig 7 includes these correlations using a generalisation [33, 53] of the spin correlation algorithm [102, 103] used in FORTTRAN HERWIG. This approach allows the emissions to be generated as a Markov chain while including the correlations using the spin density formalism. The approach is described in detail in Section 4.4 for the simulation of perturbative decays. In addition to the collinear spin correlations, the correlations for soft emission which are present in the full eikonal factor are also included multiplicatively.

When the evolution in terms of the shower variables has run its course, *i.e.* there is no more phase-space available for further emissions, the external particles are taken as being on-shell and the reconstruction in terms of the physical momenta can start.

In performing this reconstruction we must make a number of formally subleading choices which can however significantly affect the results. In particular in the case of subsequent emission from the daughter partons  $i$  and/or  $j$  we must decide which properties of the originally generated kinematics to preserve once the masses of  $i$  and/or  $j$  in Eqns. (4.13)(4.15) are no longer the infrared cut-off masses but the virtualities generated by any subsequent emissions. The choice of which kinematic quantities to preserve affects how we proceed with reconstruction of the momenta.

First, all of the  $\alpha$  coefficients in the Sudakov decomposition of each momentum are calculated. This is done by first setting  $\alpha$  equal to one for final-state progenitors and to the associated PDF light-cone momentum fraction  $x$ , generated in the preceding simulation of the hard process, for initial-state progenitors. Using the relation defining  $z$ , Eq. (4.11), together with the momentum conservation relation  $\alpha_{ij} = \alpha_i + \alpha_j$ , one can iteratively calculate all  $\alpha$  values, starting from the hard process and working outward to the external legs.

To proceed with the reconstruction, we need to decide which quantity is preserved after multiple emissions. We now illustrate the alternative options supported by Herwig.

1. The simplest choice we can then make for the reconstruction is to preserve the transverse momentum  $p_T$ . Therefore, we always calculate the transverse momenta of the branchings using Eqns. (4.13)(4.15) using the cutoff values of the masses. This was the originally implemented option. However, when generating final-state radiation the virtuality of the emitting parton is increased and too much radiation can be generated into the non-angular-ordered region after multiple emissions, motivating implementation of other options [28, 29].
2. Alternatively, we can choose to preserve the virtuality of the branching parton. The transverse momentum of the branching is then computed using the virtual masses the daughter partons develop due to subsequent emissions. This means that if the daughter partons develop large virtual masses the transverse momentum of the branching is reduced. This can lead to situations where there is no solution of Eq. (4.13) and the emission would have to be vetoed which inhibits further soft emission and significantly changes the evolution leading to incorrect evolution of observables. Thus, instead of vetoing the event, we set  $p_T = 0$  and allow the virtuality to increase. Although this alternative reconstruction retains in general better agreement with the data in the hard region of the spectrum, it has been shown that this can formally violate the logarithmic accuracy of the parton shower [28].
3. The last option that has been introduced, which is the current default, preserves the dot product of the emitted partons [28, 29]. The ordering variable can be rewritten as

$$\tilde{q}^2 = \frac{2q_i \cdot q_j + m_j^2 + m_i^2 - m_{ij}^2}{z(1-z)}, \quad (4.19)$$

and it is easy to check that if just one emissions take place, Eq. (4.19) and (4.14) are identical. With this definition the transverse momentum is thus given by

$$p_T^2 = z^2(1-z)^2\tilde{q}^2 - q_i^2(1-z)^2 - q_j^2z^2 + z(1-z)[m_{ij}^2 - m_i^2 - m_j^2]. \quad (4.20)$$

This can still lead to a negative  $p_T^2$  if one of the particle is massive, but the fraction of events where this happens is significantly smaller than the one obtained preserving the virtuality. In particular, if an emission is soft, the variation it introduces in the transverse momentum of the previous emission is small, while this happens to be the case in the virtuality-preserving scheme only if the emission is softer than the previous one. The default behaviour is thus to preserve the dot product and in cases in which a solution with negative transverse momentum is encountered,  $p_T$  is set to 0 and the dot product increases.

In all the approaches the magnitude of the relative transverse momentum  $|\mathbf{p}_\perp| = \sqrt{-p_\perp^2}$  is calculated in terms of the evolution variables  $z$  and  $\tilde{q}^2$  once the evolution of the daughter partons has terminated.

For final-state showers the  $q_\perp$  components of each momentum may then be calculated simultaneously. Final-state showering cannot change the direction of the progenitor since the transverse momentum must be conserved at each branching, hence the  $q_\perp$  component of the progenitor is zero.

The  $q_\perp$  components of the branching products are iteratively computed by adding the relative transverse momentum,

$$p_\perp = (|\mathbf{p}_\perp| \cos \phi, |\mathbf{p}_\perp| \sin \phi, 0; 0), \quad (4.21)$$

to  $z$  times the transverse momentum of the mother,  $q_{\perp ij}$ , to give  $q_{\perp i}$  according to Eq. (4.12);  $q_{\perp j} = q_{\perp ij} - q_{\perp i}$  immediately follows by momentum conservation.

The only remaining Sudakov parameters to be determined are the  $\beta$  values. These can be obtained once the evolution in terms of the shower variables is complete, by using the fact that the external partons are on-shell, in order to compute their  $\beta$  coefficients from Eq. (4.10). The coefficients of their parent momenta may then be computed using momentum conservation:  $\beta_{ij} = \beta_i + \beta_j$ . The latter step may be iterated until the progenitor is reached, yielding all  $\beta$  coefficients.

The reconstruction of the initial-state parton showers is slightly different but it follows essentially the same reasoning. Our aim here has been to simply sketch how the reconstruction occurs. More detailed presentations of these procedures will be given later in Section 4.2.4, Section 4.2.5 and Section 4.2.7.

## 4.2.2 Shower dynamics

With the kinematics defined, we now consider the dynamics governing the parton branchings. Each parton branching is approximated by the *quasi-collinear limit* [130], in which the transverse momentum squared,  $\mathbf{p}_\perp^2$ , and the mass squared of the particles involved are small (compared to  $p \cdot n$ ) but  $\mathbf{p}_\perp^2/m^2$  is not necessarily small. In this limit the probability of the branching  $\tilde{i}\tilde{j} \rightarrow i + j$  and with our choice of evolution variables Eq. (4.2) can be written as

$$d\mathcal{P}_{\tilde{i}\tilde{j} \rightarrow ij} = \frac{\alpha_s}{2\pi} \frac{d\tilde{q}^2}{\tilde{q}^2} dz P_{\tilde{i}\tilde{j} \rightarrow ij}(z, \tilde{q}), \quad (4.22)$$

where  $P_{\tilde{i}j \rightarrow ij}(z, \tilde{q})$  are the quasi-collinear splitting functions derived in [130]. In terms of our light-cone momentum fraction and (time-like) evolution variable the quasi-collinear splitting functions are<sup>2</sup>

$$\begin{aligned} P_{q \rightarrow qg} &= \frac{C_F}{1-z} \left[ 1 + z^2 - \frac{2m_q^2}{z\tilde{q}^2} \right], \\ P_{g \rightarrow gg} &= C_A \left[ \frac{z}{1-z} + \frac{1-z}{z} + z(1-z) \right], \\ P_{g \rightarrow q\bar{q}} &= T_R \left[ 1 - 2z(1-z) + \frac{2m_q^2}{z(1-z)\tilde{q}^2} \right], \\ P_{\tilde{g} \rightarrow \tilde{g}g} &= \frac{C_A}{1-z} \left[ 1 + z^2 - \frac{2m_{\tilde{g}}^2}{z\tilde{q}^2} \right], \\ P_{\tilde{q} \rightarrow \tilde{q}g} &= \frac{2C_F}{1-z} \left[ z - \frac{m_{\tilde{q}}^2}{z\tilde{q}^2} \right], \end{aligned} \quad (4.23)$$

for QCD and singular SUSY QCD branchings<sup>3</sup>. These splitting functions give a correct physical description of the dead-cone region  $\mathbf{p}_\perp \lesssim m$ , where the collinear singular limit of the matrix element is screened by the mass  $m$  of the emitting parton.

The soft limit of the splitting functions is also important. As described in Section 4.1.2, in the soft limits the probability for emission of a soft gluon is universal, Eq. (4.3). Using the definitions of our shower variables, Eq. (4.11), and making the soft emission approximations  $q_{ij} \approx q_i \approx p$ ,  $q_i^2 \approx m_i^2 = m_{ij}^2$  in Eqs. (4.3), (4.1) we find [52]

$$\lim_{z \rightarrow 1} \frac{8\pi\alpha_s}{q_{ij}^2 - m_{ij}^2} P_{\tilde{i}j \rightarrow ij} = -4\pi\alpha_s C_{\tilde{i}j} \left( \frac{n}{n \cdot q_j} - \frac{p}{p \cdot q_j} \right)^2. \quad (4.24)$$

Recalling that we choose our Sudakov basis vector  $n$  to point in the direction of the colour partner of the gluon emitter ( $\tilde{i}j/i$ ), Eq. (4.24) is then just the usual soft eikonal dipole function, Eq. (4.4), describing soft gluon radiation by a colour dipole [132], at least for the majority of cases where the colour partner is massless or nearly massless. In practice, the majority of processes we intend to simulate involve massless or light partons, or partons that are light enough that  $n$  reproduces the colour partner momentum to high accuracy<sup>4</sup>.

For the case that the underlying process with matrix element  $\mathcal{M}_n$  is comprised of a single colour dipole (as is the case for a number of important processes), the parton shower approximation to the matrix element  $\mathcal{M}_{n+1}$ , Eq. (4.1), then becomes exact in the soft limit as well as, and independently of, the collinear limit. This leads to a better description of soft wide angle radiation, at least for the first emission, which is of course the widest angle emission in the angular-ordered parton shower. Should the underlying hard process consist of a quark anti-quark pair, this exponentiation of the full eikonal current, Eq. (4.24), hidden in the splitting functions, combined with a careful treatment of the running coupling (Appendix C), will resum all leading and next-to-leading logarithmic corrections [105, 133–135]. In the event that there is more than one colour dipole in the underlying process, the situation is more complicated due to the ambiguity in choosing the colour partner of the gluon, and the presence of non-planar colour topologies.

With this choice of emission kernel and evolution variable the no-emission probability for a given type of radiation, Eq. (4.6), is

$$\Delta_{\tilde{i}j \rightarrow ij}(\tilde{q}, \tilde{q}_h) = \exp \left\{ - \int_{\tilde{q}}^{\tilde{q}_h} \frac{d\tilde{q}'^2}{\tilde{q}'^2} \int dz \frac{\alpha_s(z, \tilde{q}')}{2\pi} P_{\tilde{i}j \rightarrow ij}(z, \tilde{q}') \Theta(\mathbf{p}_\perp^2 > 0) \right\}. \quad (4.25)$$

In practice we use the transverse momentum of the branching as the scale, *i.e.* we use

$$\alpha_s(z^2(1-z)^2\tilde{q}^2), \quad (4.26)$$

<sup>2</sup> The  $P_{g \rightarrow gg}$  splitting presented here is for final-state branching where the outgoing gluons are not identified and therefore it lacks a factor of two due to the identical particle symmetry factor. For initial-state branching one of the gluons is identified as being space-like and one as time-like and therefore an additional factor of 2 is required.

<sup>3</sup> The splitting functions for photon emission from fermions and scalars can be obtained by replacing the colour charge  $C_F$  with the square of the charge of the radiating particle in the  $P_{q \rightarrow qg}$  and  $P_{\tilde{q} \rightarrow \tilde{q}g}$  splitting functions. Similarly the splitting function for  $\gamma \rightarrow f\bar{f}$  can be obtained from that for  $P_{g \rightarrow q\bar{q}}$  by replacing the colour factor  $T_R$  with the square of the charge of fermion. The splitting functions for EW emissions are, however, more involved and require treatment beyond simple charge substitutions. These are discussed in detail in Section 4.2.8.1.

<sup>4</sup> Even when the colour partner has a large mass, as in  $e^+e^- \rightarrow t\bar{t}$ , the fact that each shower evolves into the forward hemisphere, in the opposite direction to the colour partner, means that the difference between Eq. (4.24) and the exact dipole function is rather small in practice.

as argument of the strong coupling (Appendix C).

We currently support two different choices for the cutoff, controlled by the `CutOffOption` switch:

- Our default option (`CutOffOption=pT`) is to impose a cutoff on the transverse momentum of the branching, ensuring that  $p_\perp > p_\perp^{\min}$  as this gives a more physical behaviour and better agreement with experimental data, see Ref. [31] and Appendix A for more details. In this case the  $p_\perp^{\min}$  (`pTmin`) is one of the main parameters which is tuned to data.
- Alternatively the default behaviour in earlier versions was to impose a physical cutoff on the gluon and light quark virtualities, (`CutOffOption=default`). The allowed phase-space for each branching is obtained by requiring that the relative transverse momentum is real, or  $\mathbf{p}_\perp^2 > 0$ . For a general time-like branching  $\tilde{i}\tilde{j} \rightarrow i + j$  this gives

$$z^2 (1-z)^2 \tilde{q}^2 - (1-z) m_i^2 - z m_j^2 + z (1-z) m_{ij}^2 > 0, \quad (4.27)$$

from Eq. (4.13).

In practice rather than using the physical masses for the light quarks and gluon we impose a cutoff to ensure that the emission probability is finite. We use a cutoff,  $Q_g$ , for the gluon mass, and we take the masses of the other partons to be  $\mu = \max(m, Q_g)$ , *i.e.*  $Q_g$  is the lowest mass allowed for any particle.

The cutoff parameter,  $Q_g$ , is the minimum virtuality of the gluon. However, if we consider the phase-space that is available to the parton shower we would expect a natural threshold of order  $m + Q_g$  for gluon emission from a quark of mass  $m$ . In practice for the radiation of a gluon from a quark, Eq. (4.13) gives a threshold that behaves as  $Q_{\text{thr}} \simeq 1.15(m_q + 2Q_g)$ . This means that the phase-space limit is well above our expectation, particularly for heavy quarks.

There is no reason why  $Q_g$  should be the same for all quark flavours. Therefore, we have chosen to parameterize the threshold for different flavours as

$$Q_g = \max \left( \frac{\delta - am_q}{b}, c \right),$$

where  $a$  (`aParameter=0.3`) and  $b$  (`bParameter=2.3`) are parameters chosen to give a threshold  $Q_{\text{thr}} = \beta m_q + \delta$ , with  $\beta = 0.85$ , in order to slightly reduce the threshold distance for heavier quarks. As a result, the threshold for radiation from heavy quarks is closer to its physical limit. The parameter  $\delta$  is tuned to data and, only relevant for partons heavier than the bottom quark, the parameter  $c$  (`cParameter=0.3`) is chosen to prevent the cutoff becoming too small.

We can combine the calculation of the limits on  $z$  in both approaches using

$$z^2 (1-z)^2 \tilde{q}^2 - (1-z) m_i^2 - z m_j^2 + z (1-z) m_{ij}^2 > p_\perp^{\min 2}, \quad (4.28)$$

There are two important special cases.

1.  $q \rightarrow qg$ , the radiation of a gluon from a quark, or indeed any massive particle, with mass  $\mu = m_{ij}$ . In this case Eq. (4.28) simplifies to

$$z^2 (1-z)^2 \tilde{q}^2 > p_\perp^{\min 2} + (1-z)^2 \mu^2 + z Q_g^2,$$

which gives a complicated boundary in the  $(\tilde{q}, z)$  plane. However as

$$(1-z)^2 \mu^2 + z Q_g^2 > (1-z)^2 (p_\perp^{\min 2} + \mu^2), z^2 (p_\perp^{\min 2} + Q_g^2)$$

the phase-space lies inside the region

$$\frac{\sqrt{\mu^2 + p_\perp^{\min 2}}}{\tilde{q}} < z < 1 - \frac{\sqrt{Q_g^2 + p_\perp^{\min 2}}}{\tilde{q}} \quad (4.29)$$

and approaches these limits for large values of  $\tilde{q}$ . In this case the relative transverse momentum of the branching can be determined from the evolution scale as

$$\mathbf{p}_\perp = \sqrt{(1-z)^2 (z^2 \tilde{q}^2 - \mu^2) - z Q_g^2}. \quad (4.30)$$

2.  $g \rightarrow gg$  and  $g \rightarrow q\bar{q}$ , or the branching of a gluon into any pair of particles with the same mass. In this case the limits on  $z$  are

$$z_- < z < z_+, z_{\pm} = \frac{1}{2} \left( 1 \pm \sqrt{1 - \frac{4\sqrt{\mu^2 + p_{\perp}^{\min 2}}}{\tilde{q}}} \right) \text{ and } \tilde{q} > 4\sqrt{\mu^2 + p_{\perp}^{\min 2}},$$

where  $\mu = m_i = m_j$ . Therefore analogously to Eq. (4.29) the phase-space lies within the range

$$\frac{\sqrt{\mu^2 + p_{\perp}^{\min 2}}}{\tilde{q}} < z < 1 - \frac{\sqrt{\mu^2 + p_{\perp}^{\min 2}}}{\tilde{q}} \quad (4.31)$$

In this case the relative transverse momentum of the branching can be determined from the evolution scale as

$$\mathbf{p}_{\perp} = \sqrt{z^2 (1-z)^2 \tilde{q}^2 - \mu^2}. \quad (4.32)$$

These two special cases are sufficient for all the branchings currently included in the simulation, although the general case of three unequal masses for the particles in the branching is supported.

The formalism discussed above allows us, if given a starting scale  $\tilde{q}_h$ , to evolve a parton down in scale and generate the next branching of this particle at a lower scale. The no-emission probability encoded in the Sudakov form factor is used to generate  $(\tilde{q}, z)$  for this branching. This procedure can then be iterated to generate subsequent branchings of the particles produced until no further emission occurs above the cutoff.

### 4.2.3 Initial conditions

Before simulating radiation from a hard process, we must first determine the initial conditions, *i.e.*, the scale  $\tilde{q}_h$  from which the evolution begins. The initial conditions for QCD radiation in the parton shower are set by the colour flow in the hard process [3]. For each particle involved, a colour partner is assigned. In the case of particles in the fundamental representation of the SU(3) gauge group, this partner is uniquely defined, at least in processes that conserve baryon number. For gluons, a uniform random choice is made between the two possible partners. In baryon number violating processes, the colour partner is selected uniformly at random from all potential options [136, 137]. In the angular-ordered parton shower, the direction of the chosen colour partner determines the maximum angle for QCD radiation from the particle.

If a particle carries both colour and EW charge, the colour partner is used to determine the direction of radiation in the parton shower. This ensures that QCD radiation dominates the coherence structure. If the particle carries only EW charges, an appropriate partner is selected from among the other charged particles in the event, depending on the type of radiation. For QED radiation, a partner is chosen based on the product of the electric charges of the particle and its partner, to preserve the correct coherence pattern. For weak radiation, the selection depends on the relevant SU(2) interactions, and takes into account weak isospin and particle identity.

Following the choice of the *evolution partner*, the maximum scale for radiation from the particle must be calculated, as must the choice of the  $p$  and  $n$  reference vectors defined in Eq. (4.8). We always take the choice of  $p$  along the direction of the radiating particle but the choice of  $n$  is related to the direction of the evolution partner.

#### 4.2.3.1 Final-final evolution

Consider the evolution of a final-state particle,  $b$ , with a final-state evolution partner,  $c$ . In their centre-of-mass frame, the momenta are

$$p_b = \frac{1}{2} Q(\mathbf{0}, \lambda; 1 + b - c), \\ p_c = \frac{1}{2} Q(\mathbf{0}, -\lambda; 1 - b + c),$$

where  $Q^2 = (p_b + p_c)^2$ ,  $b = m_b^2/Q^2$ ,  $c = m_c^2/Q^2$ , and

$$\lambda = \lambda(1, b, c) = \sqrt{1 + b^2 + c^2 - 2b - 2c - 2bc},$$

is the Källén function.

As described in Section 4.2.1, the  $p$  basis vector (Eq. (4.8)) corresponds to the progenitor momentum generated in the hard process. The light-like basis vector  $n$  is aligned with the partner's momentum in the rest frame of the pair. For radiation from  $b$ , we define

$$n = \frac{1}{2}Q(\mathbf{0}, -\lambda; \lambda). \quad (4.33)$$

To simulate parton showering from  $c$ , the spatial components of  $n$  in Eq. (4.33) are reversed.

To ensure soft coherence, the initial evolution scales  $\tilde{q}_{h\,b}$  and  $\tilde{q}_{h\,c}$  are constrained via

$$(\tilde{\kappa}_b - b)(\tilde{\kappa}_c - c) = \frac{1}{4}(1 - b - c + \lambda)^2,$$

where  $\tilde{\kappa}_b = \tilde{q}_{h\,b}^2/Q^2$  and  $\tilde{\kappa}_c = \tilde{q}_{h\,c}^2/Q^2$  [25]. In Herwig 7, the choice of initial conditions is implemented via the `PartnerFinder` class. The method `calculateFinalFinalScales` assigns evolution scales to each particle based on an internal key. Available strategies include:

- *Symmetric*: assigns equal phase-space coverage,

$$\begin{aligned} \tilde{\kappa}_b &= \frac{1}{2}(1 + b - c + \lambda), \\ \tilde{\kappa}_c &= \frac{1}{2}(1 - b + c + \lambda). \end{aligned}$$

- *Maximal*: maximises the radiation scale for one leg,

$$\tilde{\kappa}_b = 4(1 - 2\sqrt{b} - b + c),$$

with the converse applied to  $\tilde{\kappa}_c$ .

- *Randomised*: chooses between these configurations probabilistically per event.

In Ref. [28] it has been observed that the phase space for the production of  $n$  additional partons from a 2-body final state, that forms a colour singlet, requires an additional Jacobian factor

$$J = \frac{\lambda(b', c')}{\lambda(b, c)},$$

where  $b' = q_b^2/Q^2$  and  $c' = q_c^2/Q^2$  are calculated with the two final-jet momenta. To take into account this factor, at the end of the shower evolution we accept the event with a probability given by  $J$ . This prevents an overpopulation of the non-angular-ordered region after multiple emissions. Currently, this behaviour is only available when the initial state is colourless and we have only two shower progenitors, which thus form a colour singlet. In decay topologies, an internal flag `isDecayCase` enables an alternate strategy for assigning evolution scales, accounting for the different phase-space structure in decaying systems. This ensures appropriate soft coverage and coherence in configurations such as heavy-particle decays.

#### 4.2.3.2 Initial-initial evolution

Again we opt to work in the rest frame of the evolution partners, so that the momenta of the particles are:

$$\begin{aligned} p_b &= \frac{1}{2}Q(\mathbf{0}, 1; 1); \\ p_c &= \frac{1}{2}Q(\mathbf{0}, -1; 1); \end{aligned}$$

where  $Q$  is the partonic centre-of-mass energy of the collision.

In this case, as we assume that the incoming particles are massless, we can simply take the  $p$  reference vector to be the momentum of the beam particle from which the emitting parton was extracted and the  $n$  reference vector to be the momentum of the beam particle from which its colour partner was extracted. The fact that  $p$  is parallel to the momentum of the emitting parton makes it easier to reconstruct the momenta of the shower particles in terms of the fraction of the beam momentum they carry.

Defining the  $p$  and  $n$  vectors as being equal to the beam momenta rather than the actual parton momenta does not affect our earlier assertions relating to the soft limit of the splitting functions, since Eq. (4.24) is clearly invariant under overall rescalings of the dipole momenta  $n$  and  $p$ .

In this case the requirement that the soft region of phase-space is smoothly covered is simply

$$\tilde{\kappa}_b \tilde{\kappa}_c = 1. \quad (4.34)$$

Contrary to the case of the final-final evolution, there is no upper bound on the values of  $\tilde{\kappa}_b$  or  $\tilde{\kappa}_c$ , *i.e.* there is no choice that maximizes the phase-space available to one parton relative to the other (at least none that might reasonably be expected to give sensible results). Currently only the most symmetric choice, *i.e.*  $\tilde{\kappa}_b = \tilde{\kappa}_c = 1$ , is implemented.

#### 4.2.3.3 Initial-final evolution in the hard process

If we consider the initial-final-state evolution in the context of a process  $a + b \rightarrow c$ , where  $a$  is a colour-singlet system and  $b$  and  $c$  are evolution partners, *e.g.* deep inelastic scattering. As in the last two cases we work in the rest frame of the evolution partners, in this case the Breit frame, where we may write:

$$\begin{aligned} p_b &= \frac{1}{2} Q(\mathbf{0}, 1 + c; 1 + c); \\ p_c &= \frac{1}{2} Q(\mathbf{0}, -1 + c; 1 + c); \end{aligned}$$

with  $Q^2 = -p_a^2$ .

For emission from the final-state particle, the  $p$  vector is taken to be the momentum of the radiating particle and the  $n$  reference vector is set equal to the momentum of the beam particle from which the initial-state evolution partner was extracted. For emission from the initial-state particle the  $p$  vector is defined to be the momentum of the beam particle from which the radiating parton was extracted and

$$n = \frac{1}{2} Q(\mathbf{0}, -1 - c; 1 + c),$$

in the Breit frame. As discussed in Section 4.2.3.2, the normalization of  $n$  and/or  $p$ , does not affect the eikonal dipole limit of the splitting functions Eq. (4.24).

Achieving a smooth matching of the phase-space for the first emission from parton  $b$ 's shower with that of parton  $c$ 's shower, at wide angles, requires the initial evolution scales  $(\tilde{q}_{h\,b}, \tilde{q}_{h\,c})$  obey

$$\tilde{\kappa}_b (\tilde{\kappa}_c - c) = (1 + c)^2. \quad (4.35)$$

In practice, we opt to assign roughly the same phase-space volume to each shower, *i.e.* we use the most symmetric choice:  $\tilde{\kappa}_b = 1 + c$ ,  $\tilde{\kappa}_c = 1 + 2c$ . Of course, a larger or smaller combination that satisfies Eq. (4.35) is also allowed.

#### 4.2.3.4 Initial-final Evolution in decays

The Herwig 7 angular-ordered shower differs from other approaches in including initial-state radiation from a decaying particle, as well as final-state radiation from the decay products. This is required in order to ensure that the full soft region of phase-space is filled by radiation from the parton shower [25, 52].

Consider the decay  $b \rightarrow a\,c$ , where  $b$  and  $c$  are evolution partners and  $a$  is a colour-singlet system, in the rest frame of the decaying particle. In this frame, the momenta of  $b$  and its evolution partner  $c$  are:

$$\begin{aligned} p_b &= m_b(\mathbf{0}, 0; 1); \\ p_c &= \frac{1}{2} m_b(\mathbf{0}, \lambda; 1 - a + c), \end{aligned}$$

where  $c = m_c^2/m_b^2$ ,  $a = m_a^2/m_b^2$  and  $\lambda = \lambda(1, a, c)$ .

For radiation from the decaying particle,  $p$  is chosen to be the momentum of the decaying particle and

$$n = \frac{1}{2} m_b(\mathbf{0}, 1; 1),$$

in its rest frame, *i.e.*  $n$  is aligned with the evolution partner.

In the case of radiation from the final-state particle,  $p$  is set equal to its momentum as generated in the hard decay process. However, there is no obvious choice of  $n$  related to the evolution partner since we are working in its rest frame. We therefore choose  $n$  such that it is in the opposite direction to the radiating particle in this frame, *i.e.*

$$n = \frac{1}{2} (\mathbf{0}, -\lambda; \lambda).$$

A more rigorous approach to this problem was carried out in [52], using a more generalised splitting function derived assuming a massive gauge vector  $n$ . This feature is not implemented in the standard released code, since any related deficiency in the shower is completely avoided by using the associated matrix element correction (Section 5.5).

In this case, the requirement that the full soft region of phase-space is filled by radiation from the parton shower gives

$$(\tilde{\kappa}_b - 1)(\tilde{\kappa}_c - c) = \frac{1}{4}(1 - a + c + \lambda)^2. \quad (4.36)$$

While there is no limit on the value of  $\tilde{\kappa}_b$ , as with the final–final evolution, the maximum value of  $\tilde{\kappa}_c$  is

$$\tilde{\kappa}_c = 4(1 - \sqrt{a})^2 - 4c. \quad (4.37)$$

Herwig 7 currently uses a fixed, symmetric configuration of the initial evolution scales, given by

$$\begin{aligned} \tilde{\kappa}_b &= \frac{1}{2}(3 - a + c + \lambda), \\ \tilde{\kappa}_c &= \frac{1}{2}(1 - a + 3c + \lambda), \end{aligned}$$

which ensures approximately equal phase-space coverage from both the decaying particle and its colour-connected final-state partner.

#### 4.2.4 Final-state radiation

##### 4.2.4.1 Evolution

The parton-shower algorithm generates the radiation from each progenitor independently, *modulo* the prior determination of the initial evolution scale and the  $n$  and  $p$  basis vectors. Consider the evolution of a given final-state progenitor, downward from its initial evolution scale  $\tilde{q}_h$ . Given that  $\Delta(\tilde{q}, \tilde{q}_h)$  gives the *probability* that this parton evolves from scale  $\tilde{q}_h$  to  $\tilde{q}$  without any resolvable branchings, we may generate the scale of this first branching ( $\tilde{q}$ ) by solving

$$\Delta(\tilde{q}, \tilde{q}_h) = \mathcal{R}, \quad (4.38)$$

where  $\mathcal{R}$  is a random number uniformly distributed between 0 and 1.

The details of the solution of this equation, the generation of the type of branching and variables describing the evolution are described in Appendix B.

The relative transverse momentum for the branching  $p_\perp$  (Eq. (4.12)) is then calculated, using Eq. (4.30) or Eq. (4.32) depending on the type of branching. The azimuthal angle of  $p_\perp$  is generated such that the correction spin and soft correlations as described in [33, 53, 102, 103] are included.

The requirement of angular ordering, as discussed in Section 4.2.1, defines the initial scales for the daughter particles,  $\tilde{q}_{h,i}$  and  $\tilde{q}_{h,j}$ , produced in each branching,  $\tilde{q} \rightarrow i + j$ , to be

$$\tilde{q}_{h,i} = z\tilde{q}, \quad \tilde{q}_{h,j} = (1 - z)\tilde{q}, \quad (4.39)$$

where  $\tilde{q}$  and  $z$  are the evolution scale and light-cone momentum fraction of the branching. By imposing these upper bounds on the evolution scale of the emitted partons, subsequent branchings will have a nesting of the angular separation of the resulting daughters, where each one is smaller than the one preceding it.

All of the steps above, required to generate the shower variables associated with this initial branching, may then be repeated for the daughter partons, and their daughter partons, should they also branch. All showering terminates when the evolution scale ( $\tilde{q}$ ) for each final-state parton falls below its minimum value, when there is no phase-space for any more resolvable emissions. The resulting partons, at the end of each shower, are deemed to be on mass-shell, as defined in Section 7, at which point the perturbative parton-shower evolution is no longer sensible, since hadronization effects dominate at these scales. By default, the parton shower puts partons onto their *constituent* parton mass-shell, thereby including some part of the non-perturbative hadronization effects into the termination of the parton shower. As an alternative, from Herwig 7.3, it is possible to keep partons on their current mass-shells (massless for gluons) and momentum is ‘shuffled’ as the first stage of hadronization to put them onto their constituent mass-shells, as discussed in Section 7.

#### 4.2.4.2 Kinematic reconstruction

At this point we have a set of partons produced in the parton shower from each of the progenitor partons, the scales  $\tilde{q}$  at which they are produced, the momentum fractions  $z$  and azimuthal angles  $\phi$  of the branchings. Mapping these kinematic variables into physical momenta is what we call *kinematic reconstruction*. We will now describe this procedure for showers generated by final-state progenitors. First, the kinematics of the individual showers are reconstructed by putting the external masses on their mass-shell and working back through the shower, as described in Section 4.2.1.

The shower evolution causes all progenitor partons,  $J$ , produced in the hard process to gain a virtual mass, *i.e.* the progenitor partons, which initiated the jets, are no longer on mass shell,  $q_J^2 \neq m_J^2$ . We want to preserve the total energy of the system in the centre-of-mass frame of the hard collision. If the momenta of the progenitor partons before the shower evolution were  $p_J = (\mathbf{p}_J; \sqrt{\mathbf{p}_J^2 + m_J^2})$  in this frame, then

$$\sum_{J=1}^n \sqrt{\mathbf{p}_J^2 + m_J^2} = \sqrt{s},$$

while the sum of the spatial momenta is zero. As the jet parents have momenta  $q_J = (\mathbf{q}_J; \sqrt{\mathbf{q}_J^2 + q_J^2})$  after the parton showering, we need to restore momentum conservation in a way that disturbs the internal structure of the jet as little as possible. The easiest way to achieve this is by boosting each jet along its axis so that their momenta are rescaled by a common factor  $k$  determined from

$$\sum_{J=1}^n \sqrt{k^2 \mathbf{p}_J^2 + q_J^2} = \sqrt{s},$$

which can be solved analytically for two jets or numerically for higher multiplicities. For every jet a Lorentz boost is applied such that

$$q_J = \left( \mathbf{q}_J; \sqrt{\mathbf{q}_J^2 + q_J^2} \right) \xrightarrow{\text{boost}} q'_J = \left( k \mathbf{p}_J; \sqrt{k^2 \mathbf{p}_J^2 + q_J^2} \right).$$

Applying these boosts to each of the jets, in the centre-of-mass frame of the collision, ensures global energy-momentum conservation. Typically the rescaling parameters  $k$  are close to unity, hence the resulting boosts and rotations are small.

#### 4.2.5 Initial-state radiation

##### 4.2.5.1 Evolution

As stated in Section 4.2.1, in generating the initial-state radiation we use a backward evolution algorithm, starting with the space-like daughter parton that initiates the hard scattering process,  $i$ , and evolving it backward to give its space-like parent,  $ij$ , and time-like sister parton  $j$ . This evolution algorithm therefore proceeds from the high scale of the hard process to the low scale of the external hadrons. Such a procedure is significantly more efficient than the alternative forward evolution algorithm, which would start from the incoming beam partons and evolve them to the scale of the hard collision. This is because the forward evolution cannot be constrained to end on the  $x$  and  $Q^2$  values associated to the hard process, which in turn makes it impossible to perform importance sampling of any significant resonant contributions.

While forward evolution would dynamically generate the parton distribution functions (PDFs), backward evolution uses the measured PDFs to guide the evolution. As with the final-state shower, the initial conditions for the initial-state shower are determined by the evolution partners of the incoming particles (Section 4.2.3.2).

The angular-evolution variable  $\tilde{q}^2$  for space-like showers was defined in Eq. (4.15). We shall work exclusively with light initial-state partons so we take  $m_{ij} = m_i = 0$ , and  $m_j = \mu$  if  $j$  is a quark and  $m_j = Q_g$  if  $j$  is a gluon, to regulate the infrared divergent regions, hence Eq. (4.15) simplifies to

$$\tilde{q}^2 = \frac{zm_j^2 - p_\perp^2}{(1-z)^2}, \quad (4.40)$$

where  $p_\perp^2 = -\mathbf{p}_\perp^2$  (Eqs. ((4.12), (4.21))).

The requirement that  $\mathbf{p}_\perp^2 \geq 0$ , Eq. (4.40) implies an upper limit on  $z$ ,

$$z \leq z_+ = 1 + \frac{Q_g^2}{2\tilde{q}^2} - \sqrt{\left(1 + \frac{Q_g^2}{2\tilde{q}^2}\right)^2 - 1}.$$

In addition, if the light-cone momentum fraction of parton  $i$  is  $x$ , we must have  $z \geq x$  to prevent the initial-state branching simulation evolving backward into a parent with  $x > 1$ .

In this case the Sudakov form factor for backward evolution is [3, 138]

$$\Delta(x, \tilde{q}, \tilde{q}_h) = \prod_{\tilde{i}j, j} \Delta_{\tilde{i}j \rightarrow ij}(x, \tilde{q}, \tilde{q}_h),$$

where the Sudakov form factor for the backward evolution of a given parton  $i$  is

$$\Delta_{\tilde{i}j \rightarrow ij}(x, \tilde{q}, \tilde{q}_h) = \exp \left\{ - \int_{\tilde{q}}^{\tilde{q}_h} \frac{d\tilde{q}'^2}{\tilde{q}'^2} \int_x^{z+} dz \frac{\alpha_s(z, \tilde{q}')}{2\pi} P_{\tilde{i}j \rightarrow ij}(z, \tilde{q}') \frac{\frac{x}{z} f_{\tilde{i}j}(\frac{x}{z}, \tilde{q}')}{x f_i(x, \tilde{q}')} \Theta(p_\perp^2 > 0) \right\}, \quad (4.41)$$

and the product runs over all possible branchings  $\tilde{i}j \rightarrow i + j$  capable of producing a parton of type  $i$ . This is similar to the form factor used for final-state radiation, Eq. (4.25), with the addition of the PDF factor, which guides the backward evolution. The solution of Eq. (4.41) and the generation of the variables describing the emission is discussed in Section Appendix B.

When a branching is generated, the relative transverse momentum  $p_\perp$  (Eqs. (4.12), (4.21)) is calculated according to Eq. (4.40). The azimuthal angle is generated including spin and soft correlations as described in [33, 53, 102, 103]. In the case of backward evolution the angular-ordering requirement is satisfied by simply continuing the backward evolution downward in  $\tilde{q}$ , starting from the value generated in the previous generated branching.

As stated above, when the evolution scale has reduced to the point where there is no phase-space for further resolvable branchings, the backward evolution ends. The incoming particle produced in the last backward branching, assumed to be on-shell (massless), has no transverse momentum, since this is measured with respect to the beam axis<sup>6</sup>. This final parton also has a light-cone momentum fraction  $x / \prod_i z_i$ , with respect to the incoming hadron's momentum, where  $x$  is the light-cone momentum fraction generated in the initial simulation of the hard process, and the product is comprised of all  $z$  values generated in the backward evolution.

Before any momentum reconstruction can begin, we must simulate the effects of final-state showers from each time-like daughter parton  $j$ , generated from the backward evolution of each space-like parton  $i$ , in branchings  $\tilde{i}j \rightarrow i + j$ . As discussed in Section 4.2.1, for such a branching occurring at scale  $\tilde{q}$  with light-cone momentum fraction  $z$ , angular ordering is achieved by evolving  $j$  down from an initial scale  $\tilde{q}_h = (1 - z) \tilde{q}$ . This initial condition ensures that for each parton  $j$ , the angular separation of any of  $j$ 's subsequent branching products is less than the angle between  $j$  and  $j$ 's sister  $i$ .

This algorithm is all that is needed to generate the values of the scales, momentum fractions and azimuthal angles, for the evolution of both the incoming particles and the time-like particles emitted in their backward evolution. These values are sufficient for us to determine the momenta of all of the particles in the associated showers, to perform the kinematic reconstruction.

#### 4.2.5.2 Kinematic reconstruction

The kinematic reconstruction begins by finding the last initial-state particle produced in the backward evolution of each of the beam particles. This parton momentum is calculated as described in the previous section. The momentum of the final-state time-like jet that it radiates is then reconstructed in the same way as for the final-state shower. Knowing the momenta of the former light-like parent parton and the latter final-state, time-like, daughter parton, the momentum of the initial-state, space-like, daughter, follows by momentum conservation. This process is iterated for each initial-state branching, eventually giving the momentum of the space-like progenitor parton, colliding in the hard process.

The reconstructed momentum of the colliding parton incident from the  $+z$  direction is denoted  $q_\oplus$ , and that of the colliding parton incident from the  $-z$  direction is denoted  $q_\ominus$ .

The final reshuffling of the momentum then proceeds in different ways depending on whether the colour partner is an initial- or final-state parton. Final-state radiation is reconstructed first, including the global recoil from the parton shower, which rescales the jet momenta to restore overall energy-momentum conservation in the centre-of-mass frame. Initial-state radiation is then reconstructed by backward evolution, starting from the incoming partons participating in the hard process and proceeding down to the hadron scale, using the final-state kinematics as fixed input.

<sup>6</sup> Herwig 7 supports the option of including a non-perturbative intrinsic transverse momentum for the partons inside the incoming hadron, as described in Section 4.5 and Appendix A, which can give the initial incoming parton a transverse momentum.

### 4.2.5.2.1 Initial-state partner

As discussed in Section 4.2.3.2 the hadronic beam momenta,  $p_{\oplus}$  and  $p_{\ominus}$ , define the Sudakov basis for the initial-state shower algorithms, in terms of which we can write the momenta of the original colliding partons at the end of the showering phase

$$q_{\oplus} = \alpha_{\oplus} p_{\oplus} + \beta_{\oplus} p_{\ominus} + q_{\perp\oplus}.$$

Here  $q_{\oplus}$  refers to the parton momentum at the end of the backward evolution, before the final reshuffling. The Sudakov coefficients may be calculated using the fact that  $p_{\oplus}$  and  $p_{\ominus}$  are light-like and orthogonal to the  $q_{\perp}$  component:

$$\begin{aligned}\alpha_{\oplus} &= 2p_{\oplus} \cdot q_{\oplus} / s; \\ \beta_{\oplus} &= 2p_{\ominus} \cdot q_{\oplus} / s;\end{aligned}$$

where  $s = 2p_{\oplus} \cdot p_{\ominus}$  is the hadronic centre-of-mass energy squared. The  $q_{\perp}$  components follow by subtracting  $\alpha_{\oplus} p_{\oplus} + \beta_{\oplus} p_{\ominus}$  from the reconstructed momentum  $q_{\oplus}$ .

Through the emission of initial-state radiation, the colliding partons acquire both space-like virtualities and transverse momenta, of which they had neither in the initial simulation of the hard process. Consequently, whereas momentum conservation in the prior simulation of the hard process implies that the total initial- and final-state momentum were equal to  $p_{\text{cms}} = x_{\oplus} p_{\oplus} + x_{\ominus} p_{\ominus}$ , we now have a momentum imbalance between the two:  $q_{\oplus} + q_{\ominus} \neq x_{\oplus} p_{\oplus} + x_{\ominus} p_{\ominus}$ , where  $x_{\oplus} p_{\oplus} + x_{\ominus} p_{\ominus}$  now corresponds to the sum of the momenta of the final-state shower progenitors, *i.e.* the momenta after final-state shower reconstruction, including the global boost applied to restore energy-momentum conservation.

We first impose that the invariant mass of the system comprising the two colliding partons is equal to the one of the system comprising the final-state progenitors: this guarantees the existence of a Lorentz boost that we can apply to the final state to achieve full momentum conservation.

To achieve this task, we begin by rescaling the energies and longitudinal momenta of the colliding initial-state partons, in such a way that their invariant mass is left unchanged. Because of this, we can then calculate a Lorentz boost (for each colliding parton) that produces the same effect. This boost is then applied to all elements of the initial-state shower, including the final-state jets they emit. We label with  $k_{\oplus}$  and  $k_{\ominus}$  the two rescaling factors, and we introduce the *shuffled momenta*  $q'_{\oplus}$  and  $q'_{\ominus}$

$$q'_{\oplus} = \alpha_{\oplus} k_{\oplus} p_{\oplus} + \frac{\beta_{\oplus}}{k_{\oplus}} p_{\ominus} + q_{\perp\oplus}.$$

It is trivial to check that  $q'^2_{\oplus} = q^2_{\oplus}$ .

In simulating the hard process the momentum of the partonic centre-of-mass system was

$$p_{\text{cms}} = x_{\oplus} p_{\oplus} + x_{\ominus} p_{\ominus}, \quad (4.42)$$

and in terms of the shuffled momenta it is

$$q'_{\text{cms}} = \left( \alpha_{\oplus} k_{\oplus} + \frac{\beta_{\ominus}}{k_{\ominus}} \right) p_{\oplus} + \left( \alpha_{\ominus} k_{\ominus} + \frac{\beta_{\oplus}}{k_{\oplus}} \right) p_{\ominus} + q_{\perp\oplus} + q_{\perp\ominus}. \quad (4.43)$$

Imposing that the centre-of-mass energy generated in the simulation of the hard process is preserved,  $q'^2_{\text{cms}} = p_{\text{cms}}^2$  and using the Sudakov decompositions of Eqs. (4.42), (4.43)) imply that the product of the rescalings  $k_{\oplus}$  and  $k_{\ominus}$  obeys the relation

$$\alpha_{\oplus} \alpha_{\ominus} s k_{\oplus\ominus}^2 + \left( (\alpha_{\oplus} \beta_{\oplus} + \alpha_{\ominus} \beta_{\ominus} - x_{\oplus} x_{\ominus}) s + (q_{\perp\oplus} + q_{\perp\ominus})^2 \right) k_{\oplus\ominus} + \beta_{\oplus} \beta_{\ominus} s = 0, \quad (4.44)$$

where we used the short notation  $k_{\oplus\ominus} = k_{\oplus} k_{\ominus}$ . In order to fully determine the rescaling factors we need a second constraint. We provide a number of options, which are controlled by the `InitialStateReconOption` switch:

- Our default choice (`InitialStateReconOption=SofterFraction`) is to set  $k_{\oplus\ominus}$  equal to the rescaling factor of the parton that had the emission with the largest transverse momentum, and to set the other rescaling factor to 1. This choice exactly reproduces the kinematics of the Catani–Seymour dipoles [72], which makes matching to higher-order matrix elements simpler.

- The option to preserve the rapidity of the partonic centre-of-mass (`InitialStateReconOption=Rapidity`) requires that the ratio of the  $p_{\oplus}$  coefficient to the  $p_{\ominus}$  Sudakov coefficient in  $q'_{\text{cms}}$  equal that in  $p_{\text{cms}}$ . This implies a second constraint on  $k_{\oplus}$  and  $k_{\ominus}$ :

$$k_{\oplus}^2 = k_{\oplus\ominus} \cdot \frac{x_{\oplus}}{x_{\ominus}} \cdot \frac{\beta_{\oplus} + \alpha_{\ominus} k_{\oplus\ominus}}{\alpha_{\oplus} k_{\oplus\ominus} + \beta_{\ominus}} \quad (4.45)$$

This is more physically motivated than the first choice and was the default in Herwig++ and FORTRAN HERWIG.

- Another option is to preserve the longitudinal momentum of the system (`InitialStateReconOption=Longitudinal`). In this case,  $k_{\oplus}$  is the solution of:

$$\left( \alpha_{\oplus} + \frac{\beta_{\ominus}}{k_{\oplus\ominus}} \right) k_{\oplus}^2 + (x_{\oplus} - x_{\ominus}) k_{\oplus} - (\alpha_{\ominus} k_{\oplus\ominus} + \beta_{\oplus}) = 0$$

In Herwig 7, the hardest emission is defined as the one with the largest transverse momentum  $p_T$  *at the time of emission*. However, because momentum reshuffling is applied to ensure global energy and momentum conservation, the final  $q_{\perp}$  of this emission may not correspond exactly to the originally generated  $p_T$ . Among the available reshuffling strategies, the *Rapidity* option, which preserves the centre-of-mass energy and the rapidity of the hard system, best maintains the kinematics of the hardest emission. This makes it the preferred choice when a consistent definition of the hardest emission is needed, such as in matching to fixed-order calculations.

The two relations above fully determine the  $k_{\oplus}$  and  $k_{\ominus}$  rescaling factors. Having solved these equations for  $k_{\oplus}$  and  $k_{\ominus}$ , we go on to determine a longitudinal boost for each initial-state jet such that

$$q_{\oplus} \xrightarrow{\text{boost}} q'_{\oplus}. \quad (4.46)$$

This boost may then be applied to all elements of the initial-state shower, including any final-state partons or jets they emit.

Since the initial and final state now have the same invariant mass, a second boost can be defined to ensure overall momentum conservation:

$$x_{\oplus} p_{\oplus} + x_{\ominus} p_{\ominus} \xrightarrow{\text{boost}'} q'_{\text{cms}} = \left( \alpha_{\oplus} k_{\oplus} + \frac{\beta_{\ominus}}{k_{\ominus}} \right) p_{\oplus} + \left( \alpha_{\ominus} k_{\ominus} + \frac{\beta_{\oplus}}{k_{\oplus}} \right) p_{\ominus} + q_{\perp\oplus} + q_{\perp\ominus}$$

This second boost is applied to the entire final-state system, including all partons resulting from the evolution of the final-state shower progenitors, to ensure that the total momentum of the event is conserved. This procedure is sufficient for the production of colour-singlet systems, such as EW gauge bosons in the Drell-Yan process.

#### 4.2.5.2.2 Final-state partner

For systems that have an initial-state parton that is colour connected to a final-state parton the reconstruction is performed in their Breit frame in order to preserve the  $Q^2$  of the system in, for example, DIS processes.

The momenta of the initial- and final-state jets are first reconstructed as described above for initial-state jets and in Section 4.2.4.2 for final-state jets. The momenta of the jet progenitors, which are now off-shell, are then boosted to the Breit-frame of the original system before the radiation. We take  $p_b$  to be the momentum of the original (on-shell) incoming parton and  $p_c$  the one of the original (on-shell) outgoing parton. We thus define the space-like momentum  $p_a = p_c - p_b$  that in the Breit frame is simply given by

$$p_a = Q(0, 0, -1; 0).$$

We construct a set of basis vectors, similar to the Sudakov basis defined in Section 4.2.3.3 for the initial-final colour connection,

$$\begin{aligned} n_1 &= Q(0, 0, +1; 1), \\ n_2 &= Q(0, 0, -1; 1). \end{aligned}$$

In this basis the original momentum  $p_a$  is simply given by

$$p_a = \frac{1}{2}(n_1 - n_2),$$

while the momentum of the incoming jet is decomposed as

$$q_{\text{in}} = \alpha_{\text{in}} n_1 + \beta_{\text{in}} n_2 + q_{\perp},$$

where  $\alpha_{\text{in}} = \frac{n_2 \cdot q_{\text{in}}}{n_1 \cdot n_2}$ ,  $\beta_{\text{in}} = \frac{n_1 \cdot q_{\text{in}}}{n_1 \cdot n_2}$ , and  $q_{\perp} = q_{\text{in}} - \alpha_{\text{in}} n_1 - \beta_{\text{in}} n_2$ . Note that the incoming jet momentum  $q_{\text{in}}$  includes a transverse component  $q_{\perp}$  due to the emission of radiation, whereas the original momentum  $p_a$  is defined from on-shell partons and lies purely in the longitudinal direction.

In order to reconstruct the final-state momentum, we first apply a rotation to align the frame such that the momentum of the outgoing jet can be expressed as

$$q_{\text{out}} = \alpha_{\text{out}} n_1 + \beta_{\text{out}} n_2 + q_{\perp},$$

where  $q_{\perp}$  is the same transverse component as in the incoming jet. The rotation ensures that the total momentum  $p_a$  lies entirely in the longitudinal plane, i.e., it has no transverse component.

We take  $\beta_{\text{out}}$  to be approximately one in the limit where the recoil is small and  $n_1 \sim Q$ . More precisely, if  $n_1$  and  $n_2$  are defined with  $Q(0, 0, \pm 1; 1)$ , then  $\beta_{\text{out}}$  is approximately  $\frac{1}{2}$ . The correct value is determined from the requirement that the virtual mass is preserved, which yields

$$\alpha_{\text{out}} = \frac{q_{\text{out}}^2 + p_{\perp}^2}{2n_1 \cdot n_2},$$

where  $q_{\perp}^2 = -p_{\perp}^2$ .

We now rescale the momenta of the jets to implement momentum conservation. We introduce the rescaling factors  $k_{\text{in},\text{out}}$  and define the *shuffled momenta* as

$$q'_{\text{in},\text{out}} = \alpha_{\text{in},\text{out}} k_{\text{in},\text{out}} n_1 + \frac{\beta_{\text{in},\text{out}}}{k_{\text{in},\text{out}}} n_2 + q_{\perp},$$

which have the same virtual mass as the original jets. The requirement that

$$p_a = \frac{1}{2}(n_1 - n_2) \equiv q'_{\text{out}} - q'_{\text{in}} = (\alpha_{\text{in}} k_{\text{in}} - \alpha_{\text{out}} k_{\text{out}}) n_1 + \left( \frac{\beta_{\text{in}}}{k_{\text{in}}} - \frac{\beta_{\text{out}}}{k_{\text{out}}} \right) n_2,$$

leads to the equations

$$\begin{aligned} \alpha_{\text{in}} k_{\text{in}} - \alpha_{\text{out}} k_{\text{out}} &= \frac{1}{2}, \\ \frac{\beta_{\text{in}}}{k_{\text{in}}} - \frac{\beta_{\text{out}}}{k_{\text{out}}} &= -\frac{1}{2}. \end{aligned}$$

As with the initial-initial case, once the rescaling factors have been determined, the jets are transformed using a longitudinal boost such that

$$q_{\text{in},\text{out}} \xrightarrow{\text{boost}} q'_{\text{in},\text{out}}.$$

This boost is defined in the rotated Breit frame. After the boost, a reverse rotation is applied to bring the momenta back into the original frame. Any net transverse momentum carried by the incoming jet prior to reshuffling is absorbed by the final-state system via this boost–rotate–boost sequence, ensuring momentum conservation across the full event.

#### 4.2.6 Reconstruction options

The procedures described above are sufficient for simple cases such as the Drell–Yan production of vector bosons in hadron-hadron collisions or deep inelastic scattering. In general however the colour structure of the event, particularly in hadron collisions, requires a more general procedure.

We currently support a number of procedures which have developed and become more sophisticated during the evolution of the program. The options are controlled by the `ReconstructionOption` switch. In order of the sophistication and our recommendation the options are:

1. In Herwig 7 our default approach (`ReconstructionOption=Colour3`) attempts to use as much information as possible on the colour structure of the hard process when performing the reconstruction. In order to achieve this we consider all the partons in the hard process and commence the reconstruction with the parton which had the hardest, *i.e.* the highest  $p_{\perp}$ , emission in the parton shower. The system formed by this parton and its colour partner is then reconstructed, with either a full reconstruction of the jet produced by the evolution partner (`ReconstructionOption=Colour3`), the default, or optionally just using the partner to absorb the recoil leaving it on its partonic mass shell (`ReconstructionOption=Colour4`) and do not reconstruct the full jet. This procedure is then repeated for the parton with the hardest shower emission which has not been reconstructed until all the kinematics of all the jets have been reconstructed. Together with an additional option of preserving the momentum fraction of the softer incoming parton in the hard process for systems with colour connections between initial-state partons this means that for a single emission the kinematics reduce to those of the Catani–Seymour dipoles making matching in the MC@NLO approach simpler.
2. Another option using the colour structure is to first construct colour singlet systems from the jet progenitors (`ReconstructionOption=Colour`), this was the default approach in Herwig++ from version 2.3. Depending on the result different approaches are used.
  - If the incoming particles are colour neutral then any final-state colour singlet systems are reconstructed as described in Section 4.2.4.2, for example in  $e^+ e^- \rightarrow q\bar{q}$ .
  - If there is a colour-singlet system consisting of the incoming particles together with a number of final-state colour singlet systems, *e.g.* Drell–Yan vector boson production, then the kinematics are reconstructed as described above for the initial-initial system. The final-state systems are then reconstructed in their rest frames as described in Section 4.2.4.2 and boosts applied to ensure the recoil from the initial-state radiation is absorbed by the final-state systems.
  - If the system consists of colour-neutral particles and an initial-final state colour connected system, *e.g.* deep inelastic scattering, then the kinematics are reconstructed as described above for an initial-final system.
  - If the system consists of two separate initial-final state colour connected systems together with a number of colour-singlet final-state systems, for example Higgs boson production via vector boson fusion or  $q\bar{q} \rightarrow t\bar{t}$ , then the colour-singlet initial-final systems are reconstructed as described above and the final-state systems as described in Section 4.2.4.2.
  - In general in hadron-collisions the hard process cannot be decomposed into colour singlet systems and a general procedure which preserves the rapidity and mass of the hard collision is used. The initial-state jets are reconstructed as discussed above for the initial-initial connection. The final-state jets are then reconstructed in the partonic centre-of-mass frame of the original hard scattering process as described in Section 4.2.4.2. This is effectively the same as reconstructing them in the  $q'_{\text{cms}}$  rest frame, since the kinematic reconstruction for initial-initial connection preserves the invariant mass of the hard process. In the end, the jets originating from the final-state particles in the hard process are boosted back to the lab frame, where they have a total momentum  $q'_{\text{cms}}$ .

This procedure uses the underlying colour flow in the hard process to determine how global energy and momentum conservation is enforced where possible and resorts to the general approach used before Herwig++ 2.3 when this is not possible.

3. The general procedure described above is used in all cases (`ReconstructionOption=General`). This was the default in FORTRAN HERWIG and Herwig++ versions prior to 2.3.

It is still possible to use the general procedure which ignores the colour flow for all processes rather than the default option which uses the colour structure where possible.<sup>7</sup>

<sup>7</sup> When showering partonic configurations calculated in the MC@NLO scheme by MadGraph5/aMC@NLO [89] program a specific set of reconstruction options have to be selected due to the calculation of the shower subtraction terms inside the MadGraph5/aMC@NLO program. In particular `ReconstructionOption=General`, `InitialInitialBoostOption=LongTransBoost`, and `InitialStateReconOption=Longitudinal`.

### 4.2.7 Radiation in particle decays

In general, the hard processes simulated by Herwig 7 consist of  $2 \rightarrow n$  scatterings. These are generated by first using the relevant matrix elements to produce an initial configuration, and then initiating parton showers from the external legs of the matrix element. After this showering phase, the final state consists of a set of partons with effective (constituent) masses assigned during the shower.

For processes involving the production and decay of unstable particles, including decay chains, rather than attempting to calculate high-multiplicity matrix elements, the simulation is simplified by appealing to the *narrow width approximation*—that is, by treating the production and decay processes according to separate matrix elements, assuming no interference between them. Unstable coloured particles are therefore produced in hard processes or as the decays of other unstable particles, and are showered like any other final-state coloured particle. In this case, the showering process preserves the mass assigned during the production stage, rather than assigning a new constituent mass.

For very high-mass coloured particles, *e.g.* the top quark, the available phase-space for decay can be so large that the decay occurs before any hadronization can take place. Consequently, as well as undergoing time-like showers ( $q^2 > m^2$ ) during their production phase, these partons also undergo additional *space-like* showering ( $q^2 < m^2$ ) of QCD radiation prior to their decay. Additionally, due to colour conservation, the decay products themselves will also initiate time-like showers.

Since, under the narrow width approximation, the matrix element factorizes into a component for the production and another for the decay, we may regard these as two independent hard processes. This is the interpretation used in Herwig’s simulation of the associated parton showers. Within this framework, the time-like showers from coloured decay products follow an *identical* evolution to that used for final-state radiation in the production process. Only the initial conditions for the evolution differ, although these are still determined by examining the colour flow in the underlying hard decay (see Section 4.2.3.4).

In contrast, the initial-state space-like shower created by a decaying particle differs significantly from that of an incoming parton from the production process (Section 4.2.5). In particular, it involves no parton distribution functions (PDFs), since the heavy parton originates from a hard scattering, not a hadron. In hard production processes, the initial-state partons are evolved backward from the hard interaction to the incoming hadrons to efficiently sample any resonant structure in the matrix element. In decays, however, the emission of radiation that reduces the invariant mass of the decaying particle does not impact the efficiency with which any resonant structures are sampled. Therefore, it is natural to evolve the space-like shower forward from the heavy unstable particle produced in the hard process towards its eventual decay.

#### 4.2.7.1 Evolution

As in our discussion of the other showering algorithms, the description here uses the Sudakov decomposition of the momenta given in Eq. (4.8). In space-like decay showers, the decaying particle  $\tilde{ij}$  undergoes branchings  $\tilde{ij} \rightarrow i + j$ , where  $j$  is a final-state time-like parton and  $i$  is the same decaying particle with an increased space-like virtuality:  $q_i^2 < q_{ij}^2 \leq m_{ij}^2$ . In this process the original particle acquires a space-like virtuality,

$$q_i^2 = z q_{ij}^2 + \frac{p_\perp^2 - z q_j^2}{1 - z},$$

where  $z = \alpha_i / \alpha_{ij}$ ,  $\mathbf{p}_\perp^2 = -p_\perp^2 \geq 0$ , and  $p_\perp = q_{\perp i} - z q_{\perp ij}$ . Since, in the decay shower, the invariant mass of the decaying particle remains unchanged, *i.e.*,  $m_i = m_{ij}$ , the space-like evolution variable from Eq. :eq:qtilde\_spacelike simplifies to

$$\tilde{q}^2 = m_i^2 + \frac{z m_j^2 - p_\perp^2}{(1 - z)^2}. \quad (4.47)$$

Unlike in the final- and initial-state showers, the evolution variable in this forward-evolving decay shower increases toward the decay scale. Requiring the transverse momentum of the branching to be real,  $\mathbf{p}_\perp^2 \geq 0$ , imposes an upper limit,  $z_+$ , on  $z$  where

$$z_+ = 1 - \frac{m_j^2}{2(\tilde{q}^2 - m_i^2)} \left( \sqrt{1 + 4(\tilde{q}^2 - m_i^2) / m_j^2} - 1 \right).$$

For the space-like decay shower we have the further constraint that the parton showering cannot degrade the invariant mass of the decaying object below the threshold required for the decay process, which imposes a lower limit on  $z$ .

Since no PDF is involved in this forward parton-shower evolution algorithm, the Sudakov form factor has exactly the same form as that used for final-state radiation in Eqs. ((4.5), (4.25)). Consequently the forward evolution can be performed

using the veto algorithm in almost exactly the same way as was done for the final-state showers, see [Appendix B](#). The main difference is in the implementation of the angular-ordering bounds for subsequent branchings. For final-state radiation involving branchings  $ij \rightarrow i + j$ , where  $i$  has a light-cone momentum fraction  $z$ , we evolved  $i$  and  $j$  *downward* from  $\tilde{q}_{h,i} = z\tilde{q}$  and  $\tilde{q}_{h,j} = (1-z)\tilde{q}$  respectively, where  $\tilde{q}$  was the scale of the  $i\tilde{j}$  branching. Since the decay shower is really a forward-evolving initial-state shower, we evolve  $i$  *upward* from  $\tilde{q}_{h,i} = \tilde{q}$  and  $j$  *downward* from  $\tilde{q}_{h,j} = (1-z)\tilde{q}$ . This procedure is iterated until the scale  $\tilde{q}$  approaches the minimum compatible with the threshold for the underlying decay process.

#### 4.2.7.2 Kinematic reconstruction

In the approach of [\[25\]](#), for the simulation of QCD radiation in particle decays, the recoil due to the radiation emitted from the decaying particle is absorbed by its final-state colour partner. The reconstruction described in [\[52\]](#), valid for the decay of a coloured particle to a colour connected final-state particle and a colour-singlet system, was designed to preserve the mass of the colour-singlet system. In the case of top decay this amounts to preserving the mass of the W boson, and the momentum of the decaying particle. More complicated colour structures, involving more coloured particles in the final-state, *e.g.* gluino decays, require a generalization of this momentum reconstruction procedure.

Consider the decay of a coloured particle with momentum  $p$ , to  $n + 1$  particles. We denote the momentum of the colour partner of the decaying particle  $\bar{p}$ , and the momenta of the remaining primary decay products are denoted  $p_{i=1,n}$ . Prior to simulating the effects of QCD radiation,

$$p = \bar{p} + \sum_{i=1}^n p_i.$$

After simulating parton-shower radiation in the decay, the original momenta of the decay products must be shifted and rescaled to accommodate the additional *initial-state* radiation. We require the sum of the new momenta of the colour partner,  $\bar{q}$ , the other primary decay products,  $q_i$ , and the radiation emitted prior to the decay,  $q_{ISR}$ , to equal that of the decaying particle:

$$p = \bar{q} + q_{ISR} + \sum_{i=1}^n q_i.$$

To achieve this momentum balance we rescale the three-momenta of all  $p_i$  by a common factor  $k_1$ , and the three-momentum of the colour partner  $\bar{p}$  by a separate factor  $k_2$ . The component of the momentum of the emitted radiation transverse to the colour partner is absorbed by the colour partner. In the rest frame of the decaying particle these rescalings and shifts are:

$$\begin{aligned} p &= (\mathbf{0}; m); \\ q_i &= \left( k_1 \mathbf{p}_i; \sqrt{k_1^2 |\mathbf{p}_i|^2 + p_i^2} \right); \\ \bar{q} &= \left( k_2 \bar{\mathbf{p}} - \mathbf{q}_{\perp ISR}; \sqrt{k_2^2 |\bar{\mathbf{p}}|^2 + |\mathbf{q}_{\perp ISR}|^2 + \bar{p}^2} \right), \end{aligned}$$

where  $m$  is the mass of the decaying particle and  $\mathbf{q}_{\perp ISR}$  is the component of the three-momentum of the initial-state radiation perpendicular to  $\bar{p}$ .

The rescaling factors  $k_{1,2}$  allow for the conservation of energy and of momentum in the longitudinal direction. Three-momentum conservation in the longitudinal,  $\bar{\mathbf{p}}$ , direction requires that

$$k_2 \bar{\mathbf{p}} + k_1 \sum_{i=1}^n \mathbf{p}_i + \mathbf{q}_{\parallel ISR} = 0. \quad (4.48)$$

The momentum of the initial-state radiation perpendicular to the direction of the colour partner,  $\mathbf{q}_{\perp ISR}$ , can be projected out, leaving the parallel component  $\mathbf{q}_{\parallel ISR}$ , by taking the dot product with the spatial component of the  $n$  basis vector (aligned with  $\bar{p}$ ), *i.e.*

$$k_1 = k_2 + \frac{\mathbf{q}_{ISR} \cdot \mathbf{n}}{\bar{\mathbf{p}} \cdot \mathbf{n}}. \quad (4.49)$$

Finally, from the conservation of energy we have

$$\sum_{i=1}^n \sqrt{k_1^2 |\mathbf{p}_i|^2 + p_i^2} + \sqrt{k_2^2 |\bar{\mathbf{p}}|^2 + |\mathbf{q}_{\perp ISR}|^2 + \bar{p}^2} + E_{ISR} = m, \quad (4.50)$$

where  $E_{\text{ISR}}$  is the energy of the initial-state radiation. This system of equations Eqs. ( (4.48), (4.49), (4.50)) for the rescaling factors can be solved analytically for two-body decays, or numerically, using the Newton-Raphson method, for higher multiplicities.

#### 4.2.8 Shower interactions

The conventional  $QCD+QED$  schemes for generating collinear parton showers effectively describe experimental data up to current LHC energies (e.g. [139–142]). However, in higher CoM frameworks, contributions from pure EW radiations become significant. At these energies, heavy particles like EW gauge bosons, Higgs bosons, and top quarks may appear as part of jets and behave as massless partons as  $\tilde{q}$  increases beyond their masses. This expectation is supported by LHC observations of Higgs boson production via vector-boson fusion [143, 144] and recent studies [86, 145–148]. Furthermore, excluding EW emissions from high-energy processes can cause an imbalance due to large, negative virtual corrections [149]. This justifies introducing a process-independent EW parton shower to enhance the production rate of underlying events and upgrade the conventional parton shower to a  $QCD+QED+EW$  scheme, as outlined in [38]. Several theoretical studies have addressed parts of the EW parton shower [150–153], with more complete studies on EW splitting functions in [154]. Attempts to incorporate EW parton showers in event generators include [155–159], and most recently [160].

The implementation of the  $QCD+QED+EW$  AO shower includes the calculation of initial-state (IS) and final-state (FS) quasi-collinear EW splittings in their spin-unaveraged forms for both massless and massive cases, including FFV and FFS splittings:

$$q \rightarrow q' W^\pm, \quad q \rightarrow q Z^0, \quad q \rightarrow q H,$$

in addition to VVV and VVS splittings:

$$\begin{aligned} W^\pm \rightarrow W^\pm Z^0, \quad W^\pm \rightarrow W^\pm \gamma, \quad Z^0 \rightarrow W^+ W^-, \quad \gamma \rightarrow W^+ W^-, \\ W^\pm \rightarrow W^\pm H, \quad Z^0 \rightarrow Z^0 H. \end{aligned}$$

These, along with existing SVV and VFF decay modes, provide a comprehensive framework for IS and FS EW radiations in simulated events. Among these splittings, only FFV and FFS contribute to both ISR and FSR. Implementing VVV and VVS would require incorporating EW PDFs into the backward evolution of the corresponding progenitors. However, the required calculations are computationally expensive and physically insignificant for IS radiations. Additionally, the available EW PDFs are neither reliable nor accurate enough to be introduced in a general-purpose event generator [161, 162].

In the following discussions, we outline the method for deriving the explicit analytic forms of the EW splitting functions and analyse their numerical efficiency.

##### 4.2.8.1 EW splitting functions

Following Herwig 7’s convention, we define the helicity-dependent splitting function of a generic  $\tilde{i}\tilde{j} \rightarrow i+j$  splitting as

$$P_{\tilde{i}\tilde{j} \rightarrow i+j}(z, \tilde{q}) = \sum_{\lambda_i, i=0}^2 \left| H_{\tilde{i}\tilde{j} \rightarrow i+j}(z, \tilde{q}; \lambda_0, \lambda_1, \lambda_2) \right|^2, \quad (4.51)$$

with a helicity amplitude  $H_{\tilde{i}\tilde{j} \rightarrow i+j}(z, \tilde{q}; \lambda_0, \lambda_1, \lambda_2)$  defined as

$$H_{\tilde{i}\tilde{j} \rightarrow i+j}(z, \tilde{q}; \lambda_0, \lambda_1, \lambda_2) = g F_{\lambda_0, \lambda_1, \lambda_2}^{\tilde{i}\tilde{j} \rightarrow i+j}, \quad (4.52)$$

where  $\lambda_i$  are the helicity states of the progenitor ( $i = 0$ ) and the children ( $i = 1, 2$ ), and  $F_{\lambda_0, \lambda_1, \lambda_2}^{\tilde{i}\tilde{j} \rightarrow i+j}$  is the corresponding vertex function, which is determined through the Feynman rules.

One notes that most QED branchings can be derived from the equivalent QCD splittings by substituting  $\alpha_s$  with  $\alpha_{em}$  and replacing the colour factor with the charge squared of the fermion or scalar boson involved. However, this approach does not apply to EW branchings. EW branchings are more complex due to the mass of the gauge bosons and the presence of additional longitudinal polarisation states. Moreover, all particles involved in these processes have non-zero masses. In the following, we will outline these computations case-by-case, following the footsteps of Ref. [38].

#### 4.2.8.1.1 FFV splittings

In a *FFV* branching with  $V = W^\pm, Z^0$ , the transverse polarisation vectors ( $\lambda_2 = \pm 1$ ) of the vector boson are the same as for gluonic radiation from a quark splitting, i.e.,

$$\epsilon_{\lambda_2=\pm 1}^\mu(q_2) = \left[ 0; -\frac{\lambda_2}{\sqrt{2}} \left( 1 - \frac{p_\perp^2 \lambda^2 e^{i\lambda_2 \phi} \cos \phi}{2p^2 (1-z)^2} \right), -\frac{i}{\sqrt{2}} + \frac{\lambda_2 p_\perp^2 \lambda^2 e^{i\phi} \sin \phi}{2\sqrt{2}p^2 (1-z)^2}, -\frac{\lambda_2 p_\perp \lambda e^{i\lambda_2 \phi}}{\sqrt{2} (1-z) p} \right], \quad (4.53)$$

while the longitudinal polarisation vector ( $\lambda_2 = 0$ ) is

$$\begin{aligned} \epsilon_0^\mu(q_2) = & \left[ \frac{p(1-z)}{\lambda m_2} + \frac{p_\perp^2 + m_0^2(1-z)^2 - m_2^2}{4p(1-z)m_2} \lambda; \cos \phi \left( \frac{p_\perp}{m_2} - \frac{m_2 p_\perp \lambda^2}{2p^2 (1-z)^2} \right), \right. \\ & \left. - \sin \phi \left( \frac{p_\perp}{m_2} - \frac{m_2 p_\perp \lambda^2}{2p^2 (1-z)^2} \right), \frac{p(1-z)}{\lambda m_2} - \frac{p_\perp^2 - m_0^2(1-z)^2 - m_2^2}{4p(1-z)m_2} \lambda \right]. \end{aligned} \quad (4.54)$$

In these and subsequent equations,  $\lambda$  is a power-counting parameter that helps to identify the quasi-collinear limit, which is the leading term of the small- $\lambda$  limit, and  $p$  is the magnitude of the 3-momentum of the incoming parton,  $p = |\mathbf{p}_0|$ .

The spinors for the incoming and outgoing fermion are given by

$$u_{\frac{1}{2}}(p) = \begin{pmatrix} \frac{m_0}{\sqrt{2}p} \lambda \\ 0 \\ \sqrt{2p} \left( 1 + \frac{m_0^2 \lambda^2}{8p^2} \right) \\ 0 \end{pmatrix}, \quad u_{-\frac{1}{2}}(p) = \begin{pmatrix} 0 \\ \sqrt{2p} \left( 1 + \frac{m_0^2 \lambda^2}{8p^2} \right) \\ 0 \\ \frac{m_0}{\sqrt{2}p} \lambda \end{pmatrix}, \quad (4.55)$$

$$\bar{u}_{\frac{1}{2}}(q_1) = \left[ \sqrt{2zp} \left( 1 + \frac{m_0^2 \lambda^2}{8p^2} \right), \frac{e^{-i\phi} p_\perp \lambda}{\sqrt{2zp}}, \frac{m_1}{\sqrt{2zp}} \lambda, \frac{e^{-i\phi} p_\perp m_1 \lambda^2}{[2zp]^{3/2}} \right], \quad (4.56)$$

$$\bar{u}_{-\frac{1}{2}}(q_1) = \left[ -\frac{e^{i\phi} p_\perp m_1 \lambda^2}{[2zp]^{3/2}}, \frac{m_1}{\sqrt{2zp}} \lambda, -\frac{e^{i\phi} p_\perp \lambda}{\sqrt{2zp}}, \sqrt{2zp} \left( 1 + \frac{m_0^2 \lambda^2}{8zp} \right) \right]. \quad (4.57)$$

Consequently, the vertex function for a FFV branching can be written as

$$F_{\lambda_0, \lambda_1, \lambda_2}^{FFV} = \sqrt{\frac{1}{2(\tilde{q}_0^2 - m_0^2)}} \bar{u}_{\lambda_1}(q_1) (g_L P_L + g_R P_R) \gamma \cdot \epsilon_{\lambda_2} u_{\lambda_0}(q_0), \quad (4.58)$$

with separate couplings to the left- and right-handed helicities,  $g_L$  and  $g_R$ . Combining Eqs. (4.58), (4.52) and (4.51) would readily result in the spin-unaveraged splitting function for the generic FFV branching. One however, immediately realizes that due to the presence of  $p_\perp/m$  type terms in the longitudinal polarisation vector of the vector particle, the longitudinal part of the splitting function would become divergent in the infinite-momentum frame  $\tilde{q}^2 \gg m^2$  as [38]

$$P_{FFV}^L(z, \tilde{q}) \xrightarrow{p_\perp \gg m_2} \frac{1}{2} \left( g_L^2 \rho_{-1, -1} + g_R^2 \rho_{1, 1} \right) \frac{\tilde{q}^2 z^2 (1-z)}{m_2^2},$$

where  $\rho$  is the spin-density matrix of the emitter particle 0.

To address this divergent behaviour, we adopt Dawson's approach [162], where the component of the longitudinal polarisation vector proportional to its momentum is subtracted. This yields:

$$\epsilon_{0^*}^\mu(q_2) = \frac{\lambda m_2}{2p(1-z)} \left[ -1; \frac{\lambda \cos \phi p_\perp}{p(1-z)}, \frac{\lambda \sin \phi p_\perp}{p(1-z)}, 1 \right], \quad (4.59)$$

which vanishes as  $m_2 \rightarrow 0$ . Using this approach, we derive the longitudinal polarisation as:

$$\begin{aligned} P_{FFV}^L(z, \tilde{q}) &= \sum_{\lambda_0, \lambda_1 = \pm \frac{1}{2}; \lambda_2 = 0} |H_{FFV}(z, \tilde{q}; \lambda_0, \lambda_1, \lambda_2)|^2 \\ &= \left( g_L^2 \rho_{-1, -1} + g_R^2 \rho_{1, 1} \right) \frac{2m_2^2}{\tilde{q}^2 (1-z)^3}. \end{aligned} \quad (4.60)$$

Additionally, the transverse parts of the spin-averaged FFV splitting function can be calculated as

$$\begin{aligned} P_{FFV}^T(z, \tilde{q}) &= \sum_{\lambda_0, \lambda_1 = \pm \frac{1}{2}; \lambda_2 = \pm 1} |H_{FFV}(z, \tilde{q}; \lambda_0, \lambda_1, \lambda_2)|^2 \\ &= \frac{1}{1-z} \left( \frac{(g_L^2 + g_R^2)}{2} \left[ 1 + z^2 + \frac{(1-z^2)(m_0^2 - m_1^2) - (1+z^2)m_2^2}{z(1-z)^2 \tilde{q}^2} \right] \right. \\ &\quad \left. - 2g_L g_R \frac{m_0 m_1}{z \tilde{q}^2} \right) \end{aligned} \quad (4.61)$$

The total FFV splitting function can be simply written as the summation of Eq. (4.60) and (4.61), but a more useful format would be to decompose it into massless and massive parts:

$$P_{FFV}^{\text{massless}}(z, \tilde{q}) = \left( g_L^2 \rho_{-1, -1} + g_R^2 \rho_{1, 1} \right) \frac{1+z^2}{1-z}, \quad (4.62)$$

$$\begin{aligned} P_{FFV}^{\text{massive}}(z, \tilde{q}) &= \frac{1}{1-z} \left[ \left( g_L^2 \rho_{-1, -1} + g_R^2 \rho_{1, 1} \right) \left\{ \frac{m_0^2(1+z^2)}{\tilde{q}^2 z(1-z)} - \frac{m_1^2(1+z)}{z \tilde{q}^2(1-z)} - \frac{m_2^2}{z \tilde{q}^2} \right\} \right. \\ &\quad \left. + \frac{m_0^2}{\tilde{q}^2} \left( g_L^2 \rho_{1, 1} + g_R^2 \rho_{-1, -1} \right) - \frac{2m_0 m_1 g_L g_R}{z \tilde{q}^2} (\rho_{1, 1} + \rho_{-1, -1}) \right]. \end{aligned} \quad (4.63)$$

It is easy to see that in the massless limit, the EW FFV splitting function reduces to its QCD counterpart.

#### 4.2.8.1.2 FFS splittings

For the case of Higgs boson radiation from a parent quark, the spinors of the incoming and outgoing quarks are the same as in Eqs. (4.55), (4.56), and (4.57). The corresponding vertex function can be written as:

$$F_{\lambda_0, \lambda_1}^{FFS} = \sqrt{\frac{1}{2(\tilde{q}_0^2 - m_0^2)}} \bar{u}_{\lambda_1}(q_1) u_{\lambda_0}(q_0), \quad (4.64)$$

resulting in the following explicit forms:

$$\begin{aligned} F_{+,+}^{FFS} &= \frac{m_0(1+z)}{\sqrt{2z(\tilde{q}^2 - m_0^2)}}, & F_{+,-}^{FFS} &= -\frac{p_{\perp} e^{i\phi}}{\sqrt{2z(\tilde{q}^2 - m_0^2)}}, \\ F_{-,+}^{FFS} &= \frac{p_{\perp}}{\sqrt{2z(\tilde{q}^2 - m_0^2)}}, & F_{-,-}^{FFS} &= \frac{m_0(1+z)e^{-i\phi}}{\sqrt{2z(\tilde{q}^2 - m_0^2)}}. \end{aligned}$$

These can be combined to form the  $P_{FFS}$  splitting function,

$$\begin{aligned} P_{FFS}(z, \tilde{q}) &= \sum_{\lambda_0, \lambda_1 = \pm \frac{1}{2}} |H_{FFS}(z, \tilde{q}; \lambda_0, \lambda_1)|^2 \\ &= g^2 \left( \frac{m_0}{m_W} \right)^2 \left[ (1-z) + \frac{(m_0 + m_1)^2 - m_2^2}{\tilde{q}^2(1-z)z} \right], \end{aligned} \quad (4.65)$$

where  $m_i$ , for ( $i=0,1,2$ ), are the running masses of the progenitor and the children. While working within the Standard Model (SM), one can always further simplify Eq. (4.65) by setting  $m_0 = m_1$ .

#### 4.2.8.1.3 VVV splittings

In the most general case of a VVV EW splitting, both the parent and the children are considered to be massive gauge vector bosons with both transverse and longitudinal polarisation vectors. For the parent gauge boson, we can write the transverse polarisation vectors as:

$$\epsilon_{\lambda_0 = \pm 1}^{\mu}(p) = \left[ 0, -\frac{\lambda_0}{\sqrt{2}}, -\frac{i}{\sqrt{2}}, 0 \right], \quad (4.66)$$

The longitudinal polarisation vector is given by:

$$\epsilon_0^{\mu}(p) = \left[ \frac{p}{\lambda m_0}, 0, 0, \frac{\sqrt{\lambda^2 m_0^2 + p^2}}{\lambda m_0} \right], \quad (4.67)$$

To avoid the singularities that would emerge from the longitudinal polarisation vector as  $m_0 \rightarrow 0$ , we employ Dawson's approach and rewrite this vector as:

$$\epsilon_{0^*}^\mu(p) = \left[ -\frac{\lambda m_0}{p + \sqrt{\lambda^2 m_0^2 + p^2}}, 0, 0, \frac{\lambda m_0}{p + \sqrt{\lambda^2 m_0^2 + p^2}} \right], \quad (4.68)$$

Furthermore, we use the polarisation vectors from Eqs. (4.56) and (4.59) for the second child, while applying the transformation  $z \rightarrow (1 - z)$  will reproduce the polarisation vectors of the first child. Therefore, we can write

$$H_{VVV}(z, \tilde{q}; \lambda_0, \lambda_1, \lambda_2) = ig F_{\lambda_0, \lambda_1, \lambda_2}^{VVV}, \quad (4.69)$$

where  $g = e \tan \theta_W$  when  $V', V'' = W^\pm, Z^0$  and  $g = e \tan \theta_W$  when either  $V$  or  $V''$  is a photon. For these splittings, the vertex functions take on the form:

$$F_{\lambda_0, \lambda_1, \lambda_2}^{VVV} = \sqrt{\frac{1}{2(\tilde{q}_0^2 - m_0^2)}} [(q_1 \cdot \epsilon_{\lambda_2}^*)(\epsilon_{\lambda_0} \cdot \epsilon_{\lambda_1}^*) + (q_2 \cdot \epsilon_{\lambda_0}^*)(\epsilon_{\lambda_1} \cdot \epsilon_{\lambda_2}^*) - (q_2 \cdot \epsilon_{\lambda_1}^*)(\epsilon_{\lambda_0} \cdot \epsilon_{\lambda_2}^*)]. \quad (4.70)$$

In Ref. [38] this vertex function is tabulated for different transverse/longitudinal configurations while considering Dawson's approach to carry out the  $1/m_i$  terms. It is shown that the massless and massive terms can be summarised as

$$P_{VVV}^{\text{massless}}(z, \tilde{q}) = 2(\rho_{-1, -1} + \rho_{1, 1}) \frac{(1 - (1 - z)z)^2}{(1 - z)z}, \quad (4.71)$$

$$P_{VVV}^{\text{massive}}(z, \tilde{q}) = \frac{1}{(1 - z)z} \left[ (\rho_{-1, -1} + \rho_{1, 1}) \left\{ 2m_{0,t}^2 (1 - (1 - z)z)^2 - 2m_{1,t}^2 (1 - (1 - z)z)^2 \right. \right. \\ \left. \left. - 2m_{2,t}^2 (1 - (1 - z)^2 z) \right\} + 4\rho_{0,0} m_{0,t}^2 z (1 - z)^3 \right], \quad (4.72)$$

with  $m_{i,t}^2 = m_i^2 / (\tilde{q}^2 z (1 - z))$ .

#### 4.2.8.1.4 VVS splittings

Similarly, for the generic case of VVS EW branching, one can write a vertex function

$$F_{\lambda_0, \lambda_1}^{VVS} = m_0 \sqrt{\frac{1}{2(\tilde{q}_0^2 - m_0^2)}} (\epsilon_{\lambda_0} \cdot \epsilon_{\lambda_1}^*), \quad (4.73)$$

to be used in the VVS helicity amplitude

$$H_{VVS}(z, \tilde{q}; \lambda_0, \lambda_1) = g F_{\lambda_0, \lambda_1}^{VVS}, \quad (4.74)$$

where  $g = e / \sin \theta_W$  for  $W^\pm$  bosons and  $g = e / (\sin \theta_W \cos \theta_W)$  for  $Z^0$  bosons, while the dynamics of the particles will remain the same as the previous cases, i.e. Eqs. (4.66) and (4.68) for the progenitor and Eqs. (4.54) and (4.59) for the children. Accordingly, different helicity configurations of the splitting function can be individually derived [38], resulting in

$$P_{VVS}^{\text{Massless}}(z, \tilde{q}) = \frac{1 - z}{4z} [z^2(\rho_{-1, -1} + \rho_{1, 1}) + 2\rho_{0,0}], \quad (4.75)$$

$$P_{VVS}^{\text{Massive}}(z, \tilde{q}) = -\frac{m_{H,t}^2}{4z} [z^2(\rho_{-1, -1} + \rho_{1, 1}) + 2\rho_{0,0}] - \frac{m_{0,t}^2}{4z^2} \left[ (2z^2 - 4z + 2) \rho_{0,0} \right. \\ \left. + (z^4 - 2z^3 - z^2) (\rho_{-1, -1} + \rho_{1, 1}) \right]. \quad (4.76)$$

#### 4.2.8.2 Validation of EW shower

The validation of the EW parton shower implementation has been an essential aspect of ensuring the accuracy and reliability of the simulation results, particularly due to the use of Dawson's approach in dealing with longitudinal divergences in the polarisation vectors of the involving massive vector bosons. In Ref. [38], all four pure EW splitting classes - FFV, FFH, VVV and VVS - have been subjected to rigorous performance tests. For this purpose, we initially chose a suitable fixed order (FO) process that one can meaningfully split into a smaller hard process plus a single resummed splitting (RS). The aforementioned splitting then can be replaced by a single-radiation EW shower, providing a test bed for investigating the performance of individual splitting functions and their kinematic reconstruction within our implementation. In this context, special care was paid to VVV and VVS cases, where in order to keep gauge invariance of the FO analysis intact, additional channels had to be included, some of which could not be seen as an interpretation of a RS case, i.e. where a child is not emitted directly from the target parent. In these scenarios, one can make use of the assumption that if the parent and child are connected, one expects to observe a small distance between them in the pseudorapidity-azimuthal angle plane, compared to the non-RS-related cases. Therefore, applying a  $\Delta R$  cut to ensure a smaller separation between the prospective children could suppress non-RS-related channels [38].

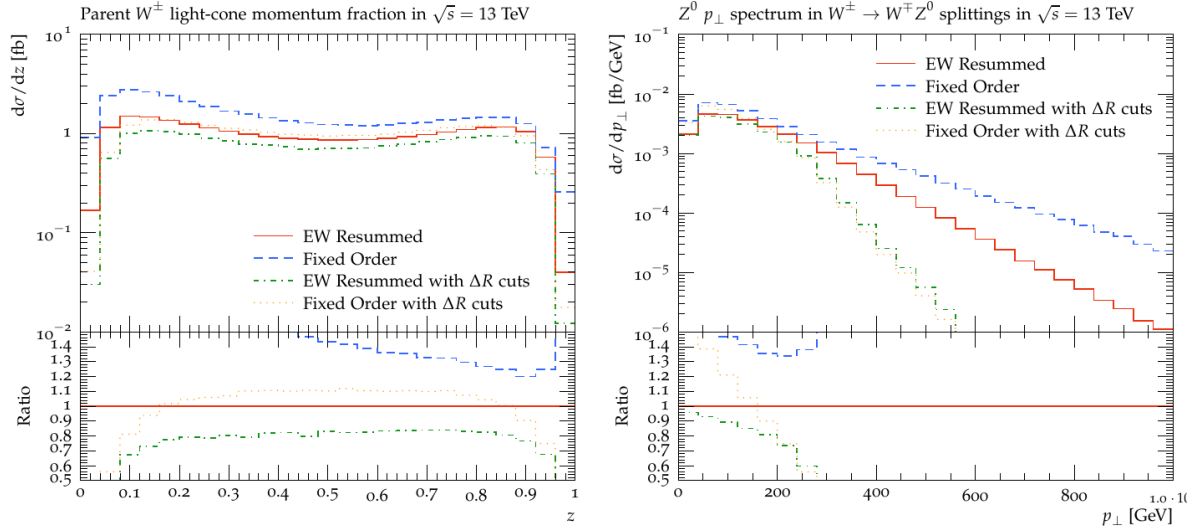


Fig. 4.1: Performance test for  $W^\pm \rightarrow W^\pm Z^0$  EW branching. In order to suppress the non-RS-related contributions, we have imposed the following cuts:  $\Delta R_{W^\pm, V} > 1$ ,  $\Delta R_{W^\pm, jet} < 1$  and  $\Delta R_{V, jet} < 1$ .

Secondly, it is essential to examine the effects of incorporating the entire tree of interleaved EW shower on the resulting predictions. To this end, in Ref. [38], we looked at the production of  $W^\pm$  bosons in the presence of a high- $p_\perp$  leading jet from the LHC's first run, as detailed in [163]. Here, the explicit production of prompt  $W^\pm$  bosons with one/two jets and inclusively was compared to a case where a pure QCD  $2 \rightarrow 2$  hard process (with no explicit  $W^\pm$  boson) is showered with the EW shower, allowing the EW boson to be sourced solely from the shower. Comparing the results showed an interesting resemblance between the explicit  $ME(pp \rightarrow W^\pm jj) \oplus QCD+QED$  shower and  $ME(pp \rightarrow jj) \oplus QCD+QED+EW$  shower. Further phenomenological studies were also conducted, explicitly targeting EW-sensitive observables in Refs. [164] and [148], both of which outlined the positive effects of incorporating EW shower in increasing the precision of the predictions.

## 4.3 Dipole shower

The dipole parton shower algorithm used in Herwig 7 [26, 165]:

- maintains exact energy-momentum conservation at each step of the evolution;
- ensures colour coherence by careful treatment of the recoils;
- uses the dipole splitting functions and kinematics of [72, 73] to make matching to next-to-leading order emissions easier;
- has a sophisticated treatment of quark mass effects [32];
- includes spin correlation effects [33].

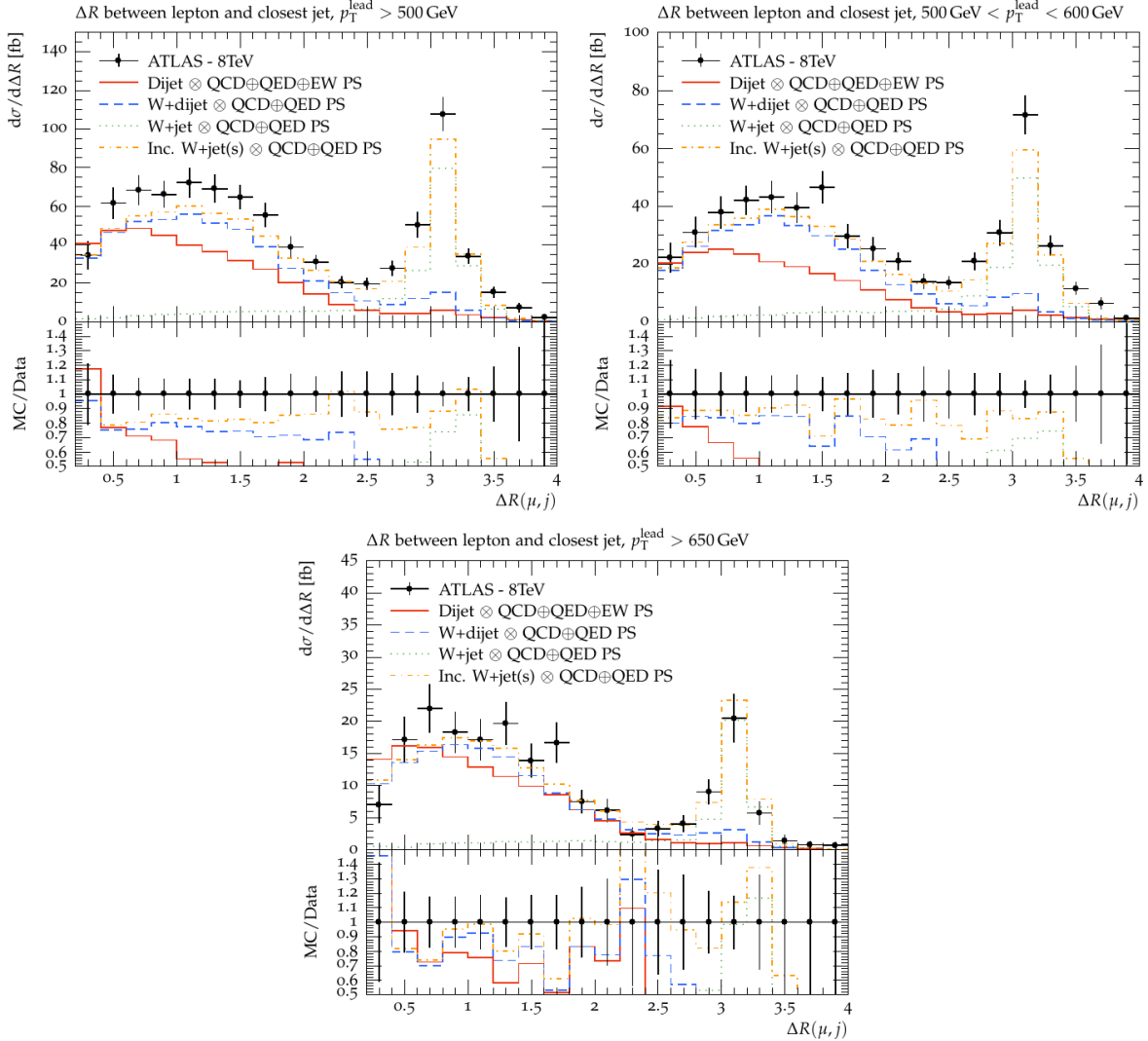


Fig. 4.2: Angular distribution of  $W^\pm$  bosons with high transverse momentum jets at  $\sqrt{s} = 8$  TeV (ATLAS data [163]).

In this section, we give a full description of the dipole shower algorithm.

### 4.3.1 Structure of the evolution

The hard process is showered first, followed by the handling of any unstable particles. Prior to showering the hard process, the initial conditions required by the shower must be constructed as described in Section 4.3.2. This procedure arranges the external incoming and outgoing coloured particles into a set of dipole chains, which are colour-singlet groups of particles arranged into sequentially linked colour dipoles. Dipole chains are the independently evolving structures in the dipole shower. Partons are emitted from a single parton in a dipole, the emitter, and another parton, the spectator, is required to absorb recoil to ensure energy-momentum conservation in each splitting. Therefore we refer to ‘splittings from dipoles’ in our discussion of the dipole shower.

It is implicit from the description above that each dipole has two possible configurations. Either the coloured parton (a parton carrying colour line, and being one member in the dipole) is the emitter and the anti-coloured parton (a parton carrying an anti-colour line, being the other member in the dipole) is the spectator, or the emitter/spectator identifications are reversed. For clarity, when we refer to a dipole we always refer to a dipole in a specific configuration of emitter and spectator, unless we specify otherwise. In the construction of the initial conditions, the emitter in each dipole is assigned a starting scale from which to begin the shower evolution. This scale, referred to as the hard scale of the emitter, is simply the maximum allowed scale for an emission from the given dipole.

With the initial conditions set, the showering of the process can proceed. The generation of splittings proceeds according to the veto algorithm, as described in Section Appendix B.

A splitting from a dipole is described by three variables. The first quantity is the scale of the splitting which, following the arguments in [26], is chosen to be the transverse momentum,  $q_\perp$ , of the emission. The transverse momentum is the ordering variable in the dipole shower, *i.e.* subsequent emissions in each dipole chain decrease in this scale, and it is generated according to the distribution defined by the Sudakov form factor as defined in Section 4.1.2. The form of the branching probabilities,  $d\mathcal{P}_{\text{branching}}$ , for splittings in the dipole shower are given, for each type of dipole, in Section 4.3.3.4. The second variable required is a splitting variable, which we label  $z$ , to parameterize the splitting. This variable is identified in 4.3.3.2 and is generated according to the distribution given by the branching probability. Finally we also require the azimuthal angle,  $\phi$ , of the plane of the splitting. The azimuthal angle is generated subject to the spin correlation algorithm.

As long as the set of dipole chains to be evolved is not empty the shower proceeds by selecting a chain to evolve, referred to as the ‘current chain’. All possible splittings from all of the dipoles in the current chain are considered to be in competition, therefore all of these possible splittings are trialled. Accordingly a value of the scale  $q_\perp$  is generated according to the Sudakov form factor for each possible splitting.

If no trial splittings are generated with  $q_\perp$  above the infrared cutoff,  $\mu_{\text{IR}}$ , the evolution of the current chain is terminated. In this case the current chain is removed from the set of chains to be evolved and the shower algorithm continues with the next chain.

If at least one trial splitting is generated with  $q_\perp > \mu_{\text{IR}}$ , the trial splitting with the largest  $q_\perp$  value is selected for execution. The splitting variable  $z$  for the chosen splitting is then generated according to the probability distribution. With  $q_\perp$  and  $z$  determined,  $\phi$  is sampled from a uniform distribution, and the momenta of the splitting products and spectator are calculated following the relevant formulation in Section 4.3.3.3.

A splitting removes dipoles that contained the emitter and produces new dipoles which contain the splitting products. The hard scale of the splitting products in the dipoles in which they are emitters is set to  $q_\perp$ . As described in detail in Section 4.3.2, if the selected splitting was a  $g \rightarrow q\bar{q}$  splitting the structure of the current dipole chain changes due to the colour structure of this splitting. In the case that the current dipole chain breaks up into two independent chains, the newly produced chain is added to the list of chains to be evolved.

Finally the hard scale of the emitter in every dipole in the current chain, and if applicable the newly created chain, is updated. Simply, for each dipole, if  $q_\perp$  is less than the current hard scale of the emitter in that dipole the hard scale of the emitter is set to  $q_\perp$ .

The evolution of the current chain now continues by returning to the first step in the showering algorithm for the current chain. The showering of the hard process terminates once all of the dipole chains have been evolved. The showered partons are now ‘reshuffled’ onto their respective constituent mass-shells, as defined in Section 7, following the procedure described in Section 4.3.5.

Following the showering of the hard process, the dipole shower handles any particles recorded as being unstable. The treatment of a two-body decay in the dipole shower is straightforward. The correct treatment of higher multiplicity decays in the dipole shower currently requires that such processes take place via a decay tree, *i.e.* a sequence of two-body decays. For example it is common to perform top quark decays as a  $1 \rightarrow 3$  process with an internal W-boson, in order to correctly include off-shell effects for the W-boson. In this case each  $1 \rightarrow 2$  decay is showered separately, starting from the particle incoming to the decay tree and working towards the end of the decay tree. To ensure the correct treatment in this situation, for any given decay tree, we include only one of the  $1 \rightarrow 2$  decay processes in the record of unstable particles at any point in the shower. The record is updated following the showering of each decay as described later in this section.

As long as the record of unstable particles is not empty an unstable particle is selected. If the selected particle does not have any associated decay products it will be decayed. We refer to the incoming decayed particle and the outgoing decay products as the ‘current decay’.

If the current decay contains coloured decay products and the decay was performed at LO then the user has the option to include an NLO-corrected first emission from the current decay prior to showering. This is done using the built-in POWHEG decay corrections available in Herwig [54]. As for the hard process, the initial conditions must be constructed for the current decay prior to showering. This procedure is described in Section 4.3.2 and again produces a set of dipole chains and sets the starting hard scale for the emitter in each dipole. The dipole chains are evolved following the same procedure described above for the hard process. Once there are no dipole chains remaining for the current decay, the partons outgoing from the decay are reshuffled as described in Section 4.3.5.

Alternatively, if there are no coloured decay products, the shower simply attempts to produce photon radiation from the current decay according to the YFS approach [51], see Section 4.7.

In contrast to the treatment of the hard process, following the treatment of a decay process there are additional considerations that must be made to ensure that any unstable decay products are treated correctly. There are three possible cases that must be considered.

- The simplest case is that the decay products in the current decay are stable, for example, the decay of a W-boson into two stable quarks. In this case no further considerations are necessary.
- The second case is that one or more of the decay products in the current decay are unstable but do not have any decay products, for example, the W-boson produced in a two-body top quark decay. In this case the unstable outgoing particles are simply added to the record of unstable particles.
- The final case is that one or more of the decay products in the current decay are unstable and already have decay products. For instance, the W-boson produced in a three-body top quark decay serves as our example. The momenta of the W-boson and its decay products were originally set in the three-body decay of the top quark, however the momentum of the W-boson can change during the treatment of the current decay, *i.e.* the top-bottom-W system. This change can occur through both the treatment of recoil in shower splittings, see Section 4.3.3.3.9, and in the reshuffling procedure. Therefore the momenta of the decay products of the W-boson are updated, through a straightforward boost, to ensure energy-momentum conservation in the W-boson decay. This procedure is implemented for decay trees of any length, such that, in general, the momenta of all outgoing particles further down the decay tree are updated, as required, following the treatment of the current decay. Any unstable decay products in the current decay process, *e.g.* the W-boson in the example above, are then added to the record of unstable particles.

The current decay is now removed from the record of unstable particles and the algorithm continues by selecting the next particle in the record.

### 4.3.2 Initial conditions

As described in Section 4.3.1, prior to performing any emissions in the dipole shower, we must compute the initial conditions required by the shower for the given process. These initial conditions are the colour structure of the process and the initial starting scales for the shower evolution.

The procedure for the construction of the required colour structure is identical for hard processes, secondary processes and decay processes. In the first step the process is assigned colour-flow information in the large- $N_C$  limit, which we use to sort the *external* coloured partons incoming to and outgoing from the process into colour singlets. To achieve this, we note that a colour singlet is ‘simply connected’, that is any parton in a colour singlet can be reached from another parton in the same singlet by following colour lines and changing from a colour line to an anti-colour line when an external gluon is encountered.

Finally, the partons in each colour singlet are sorted into a sequence in which colour-connected partons are located in neighbouring positions. In other words each of the colour singlets is sorted into a series of colour dipoles. We refer to these sorted colour singlet sequences as ‘dipole chains’. Dipole chains can be ‘circular’ or ‘non-circular’. A dipole chain is called non-circular if there exists a circular permutation of the partons in it such that the partons in the first and last positions are not colour-connected. A dipole chain is called circular if no such permutation exists. We note that the structure of a given dipole chain is changed in the case of a  $g \rightarrow q\bar{q}$  splitting in that chain during showering. If the dipole chain was circular prior to the splitting, it becomes non-circular following the splitting. If the current dipole chain was non-circular prior to the splitting then it breaks up into two independent chains.

As discussed in Section 4.3.1, a dipole consists of two partons in a given configuration in which one parton is assigned the role of ‘emitter’ and the other is assigned the role of ‘spectator’. It is the emitter in a given dipole that can split to produce a shower emission. Prior to showering, each emitter needs to be assigned an initial scale which defines the maximum allowed scale for an emission from the given dipole.

The calculation of the initial shower scale for each emitter differs for hard processes, secondary processes and decay processes. The treatment of hard processes and secondary processes roughly follow the same procedure. The maximum possible allowed scale for an emission from a given hard or secondary process is the partonic centre-of-collision energy of the process, however there are several cases when a more restrictive maximum emission scale is required. One option, which is only applicable to hard processes, is to set this maximum scale to some fixed scale or dynamical scale associated with the hard process, for example the factorisation scale calculated for the hard process. Alternatively, if this is not the required behaviour for a given or hard process or if a secondary process is being considered, a more restrictive scale can be constructed by considering the particles outgoing from the process. In this case there are two possible cases. If there are outgoing coloured particles the maximum scale is set to the minimum transverse mass of the outgoing coloured particles. If there are no coloured outgoing particles the scale is set to the invariant mass of the system of outgoing particles.

There are additional scales associated with each emitter that must also be taken into account. For a given dipole we can calculate the maximum physically allowed splitting scale for each possible splitting from the dipole. By comparing the maximum scale for each of the possible splittings we determine the maximum physically possible scale for an emission from the emitter in the given dipole.

In addition a ‘veto scale’ can be set for any given particle. If the veto scale is set for at least one parton in a given dipole chain, the smallest veto scale of all of the particles in that dipole chain is identified.

For every emitter there are now three relevant scales which we compare: the maximum allowed scale for emissions from the process, the maximum physically allowed splitting scale for the given emitter and the minimum veto scale of all the partons in the dipole chain to which the emitter belongs. For each emitter we compare these three scales and set the starting scale to the smallest of the three. This is done for the emitter in every dipole in every dipole chain, *i.e.* every parton that can produce an emission is assigned a scale.

The computation of the initial scales in a decay process is more straightforward. A decay process can be presented to the shower with or without an NLO-corrected first emission. In a LO decay process, *i.e.* without an NLO-corrected first emission, the starting scale for each emitter in the set of dipole chains is set to the mass of the decayed particle incoming to the process. Otherwise, if an NLO emission is included, the starting scale for each emitter is set to the scale of this emission. In both cases if the maximum physically allowed emission scale for a given emitter is smaller than the scale stated above, the starting scale for this emitter is instead set to this maximum scale.

### 4.3.3 Shower kinematics and splitting kernels

In this section, we present the splitting kernels and the kinematics formulation used to describe splittings in the dipole shower. The dipole shower for massless partons has previously been documented in Ref. [26]. We provide the full kinematics formulae here for completeness, incorporating changes made since the original implementation. The original treatment of massive quarks in the dipole shower described in Ref. [132], based on Ref. [165], has been replaced in Herwig 7.1 by an improved description [32] which we present here. In addition, spin correlations are now included so that the azimuthal angles are calculated as described in Ref. [33]. We note that the dipole shower currently does not support dipoles with massive incoming partons.

#### 4.3.3.1 Notation

Throughout the following sections we use a consistent notation to denote partons and their properties according to their identification as an emitter, an emission or a spectator and whether they are incoming to, or outgoing from a dipole. We use the letters  $\{a, b\}$  and  $i, j, k$  to denote partons incoming to and outgoing from a dipole respectively. The partons in a dipole prior to a splitting are indicated by a ‘tilde’ and their momenta are denoted by the letter  $p$ . The momenta of partons following a splitting are denoted by the letter  $q$ . Parton masses are denoted by the letter  $m$ . For clarity we make this notation explicit below:

- Prior to splitting:
  - Outgoing emitter -  $\tilde{i}, \tilde{j}, \tilde{p}_{ij}, m_{ij}$ ; Incoming emitter -  $\tilde{a}, \tilde{j}, \tilde{p}_{aj}, m_{aj}$ ;
  - Outgoing spectator -  $\tilde{k}, \tilde{p}_k, m_k$ ; Incoming spectator -  $\tilde{b}, \tilde{p}_b, m_b$ ;
- Following a splitting:
  - Outgoing emitter -  $i, q_i, m_i$ ; Incoming emitter -  $a, q_a, m_a$ ;
  - Outgoing spectator -  $k, q_k, m_k$ ; Incoming spectator -  $b, q_b, m_b$ ;
  - Outgoing emission -  $j, q_j, m_j$ ;

where the incoming parton following an emission refers to that incoming from the beam particle.

The reader should note that, in order to be as general as possible, we have included the masses of incoming partons in the above list. In all cases where such a parton is incoming to the hard process these masses are necessarily zero and are not included in the following. It is also important to note that the mass of the spectator is necessarily conserved in any given splitting.

Dipole configurations are written in the format  $\text{state}_{\text{emitter}} - \text{state}_{\text{spectator}}$  where  $\text{state}_{\text{parton}}$  is the state, initial or final, of that parton. There are five dipole configurations included in the dipole shower, final-final dipoles, final-initial dipoles, initial-final dipoles, initial-initial dipoles and final-initial decay-dipoles which include an incoming decayed coloured particle.

#### 4.3.3.2 Generalities

The splitting kernels [72, 73] for each dipole are parameterized in terms of two splitting variables, or just one in the case of the initial-initial dipole, and the definition of these variables depends upon the dipole. In Herwig, we generate the transverse momentum,  $p_\perp$ , and the light-cone momentum fraction,  $z$ . These variables follow the quasi-collinear Sudakov parameterization of splitting momenta, as described in Section 4.2.1, which we summarize below. In order to compute the splitting kernels for each dipole, we must write the splitting variables in terms of the generated variables. We provide the expressions required to do this in each of the following sections.

In the Sudakov parameterization we choose a light-like vector  $n$  to define the collinear direction of the splitting. In a splitting from a final-state emitter we write the momentum of the emitted parton, the ‘emission’, as

$$q_j = (1-z)\tilde{p}_{ij} + \frac{m_j^2 - (1-z)^2 m_{ij}^2 + p_\perp^2}{2\tilde{p}_{ij} \cdot n(1-z)} n - k_\perp , \quad (4.77)$$

where  $k_\perp$  is a space-like vector which satisfies  $k_\perp^2 = -p_\perp^2$  and  $k_\perp \cdot \tilde{p}_{ij} = k_\perp \cdot n = 0$ . Similarly, for a splitting from a massless incoming parton, we write:

$$q_j = (1-z)q_a + \frac{p_\perp^2}{2q_a \cdot n(1-z)} n - k_\perp . \quad (4.78)$$

Note that our assumption that  $m_{aj} = m_a = 0$  implies also that  $m_j = 0$  in all relevant cases.

#### 4.3.3.3 Dipole splitting kinematics

In each of the following sections, we first state the definition of the splitting variables in terms of the physical parton momenta following the splitting. We also state the momentum-quantity that is conserved in a splitting from the given dipole. In the original specification of the kernels, an expression of the parton momenta prior to the splitting is given, for each dipole, in terms of the momenta following the splitting. Our formulation of the parton momenta following a splitting must satisfy these expressions. We present a set of expressions for the parton momenta following a splitting in terms of either the splitting variables or the generated variables, as appropriate.

We provide expressions for the splitting variables in terms of the generated variables and expressions for the limits on both the splitting variables and the generated variables. Unless otherwise stated, the limits on the splitting variables are the integration limits given in Refs. [72, 73]. Finally, we describe the Jacobian factors required to express the one-particle phase-space, given in terms of the splitting variables in Refs. [72, 73], in terms of the generated variables in Herwig. The one-particle phase-space expressions, and hence the Jacobian terms, are required to compute the branching probabilities, given in their general form in Section 4.3.3.4.

We refer to dipoles which contain no massive partons as ‘massless dipoles’ and dipoles which contain at least one massive parton as ‘massive dipoles’.

We will present the results for the massive dipoles here, except for the case of initial-initial dipoles, where there is only a massless dipole which we therefore include, and present the result for the massless dipoles in Appendix D. In all cases, the massless dipole results can be recovered as the massless limit of the massive case. However, in Herwig, we implement them separately to avoid unnecessary computations.

##### 4.3.3.3.1 Final-final dipole kinematics

The final-final dipole splitting kernels, given in Section 4.3.3.4.1, are written in terms of the splitting variables  $z_i$  and  $y_{ij,k}$ , defined in terms of the physical momenta as

$$z_i = \frac{q_i \cdot q_k}{q_i \cdot q_k + q_j \cdot q_k} , \quad (4.79)$$

$$y_{ij,k} = \frac{q_i \cdot q_j}{q_i \cdot q_j + q_i \cdot q_k + q_j \cdot q_k} . \quad (4.80)$$

We define the conserved dipole momentum,  $Q$ , and its self-product,  $s$ , as

$$Q = \tilde{p}_{ij} + \tilde{p}_k = q_i + q_j + q_k , \quad (4.81)$$

$$s = Q^2 .$$

The final-final dipole with a massive spectator presents a particular challenge. While it is possible to construct expressions for the physical momenta following the splitting in terms of the splitting variables and the momenta prior to the splitting, the expressions become convoluted and a simpler formulation is preferable.

We present a more convenient formulation of the splitting momenta based on the standard quasi-collinear formulation, however we replace  $\tilde{p}_{ij}$  in Eq. (4.77) with an alternative choice. We continue to use  $z$  to denote the generated variable although strictly speaking its definition in terms of invariant products of momenta changes according to the replacement of  $\tilde{p}_{ij}$ .

We first introduce the light-like vectors  $n_{ij}$  and  $n_k$ ,

$$2n_{ij} \cdot n_k \equiv s_{ij,k},$$

where  $s_{ij,k}$  is an invariant quantity dependent upon the choice of  $n_{ij}$  and  $n_k$ . We define these vectors in terms of the emitter and spectator momenta as

$$\begin{aligned} n_{ij} &= \frac{s_{ij,k}^2}{s_{ij,k}^2 - m_{ij}^2 m_k^2} \left( p_{ij} - \frac{m_{ij}^2}{s_{ij,k}} p_k \right), \\ n_k &= \frac{s_{ij,k}^2}{s_{ij,k}^2 - m_{ij}^2 m_k^2} \left( p_k - \frac{m_k^2}{s_{ij,k}} p_{ij} \right), \end{aligned}$$

and solve to find an explicit expression

$$s_{ij,k} = \frac{1}{2} \left( Q^2 - m_{ij}^2 - m_k^2 + \sqrt{(Q^2 - m_{ij}^2 - m_k^2)^2 - 4m_{ij}^2 m_k^2} \right).$$

In addition, we introduce two scaling variables,  $x_{ij}$  and  $x_k$ , and introduce the scaled four-momenta

$$\begin{aligned} q_{ij} &= x_{ij} n_{ij} + \frac{m_{ij}^2}{x_{ij} s_{ij,k}} n_k, \\ q_k &= x_k n_k + \frac{m_k^2}{x_k s_{ij,k}} n_{ij}, \end{aligned} \tag{4.82}$$

where, following our notation,  $q_k$  is the momentum of the spectator following the splitting. The momenta  $q_{ij}$  and  $n_k$  are now inserted into the quasi-collinear Sudakov parameterization to obtain expressions for the parton momenta following the splitting

$$\begin{aligned} q_i &= z q_{ij} + \frac{m_i^2 - z^2 m_{ij}^2 - k_\perp^2}{2q_{ij} \cdot n_k z} n_k + k_\perp, \\ q_j &= (1-z) q_{ij} + \frac{m_j^2 - (1-z)^2 m_{ij}^2 - k_\perp^2}{2q_{ij} \cdot n_k (1-z)} n_k - k_\perp. \end{aligned} \tag{4.83}$$

In order to implement this formulation we require explicit expressions for the scaling variables  $x_{ij}$  and  $x_k$ . For convenience we first introduce the scaled propagator invariant

$$w = \frac{1}{x_{ij} z (1-z) s_{ij,k}} \left[ p_\perp^2 + z m_j^2 + (1-z) m_i^2 - z(1-z) m_{ij}^2 \right] = \frac{(q_i + q_j)^2 - m_{ij}^2}{2q_{ij} \cdot n_k},$$

and define the variables

$$\lambda_k = 1 + \frac{m_k^2}{s_{ij,k}}, \quad \lambda_{ij} = 1 + \frac{m_{ij}^2}{s_{ij,k}}.$$

From the momentum-conservation requirement in Eq. (4.81)

$$x_{ij} = 1 - \frac{m_k^2}{s_{ij,k}} \frac{(1-x_k)}{x_k}, \tag{4.84}$$

$$x_k = \frac{1}{2\lambda_k} \left[ \left( \lambda_k + \frac{m_k^2}{s_{ij,k}} \lambda_{ij} - x_{ij} w \right) \pm \sqrt{\left( \lambda_k + \frac{m_k^2}{s_{ij,k}} \lambda_{ij} - x_{ij} w \right)^2 - 4\lambda_k \lambda_{ij} \frac{m_k^2}{s_{ij,k}}} \right]. \tag{4.85}$$

With these, the outgoing momenta following a splitting can be computed, given the two generated variables  $z$  and  $p_\perp^2$ .

Following directly from its definition in Eq. (4.80),  $y_{ij,k}$  can be written in terms of  $z$  and  $p_\perp$

$$\begin{aligned} y_{ij,k} &= \frac{1}{\bar{s}} \left[ x_{ij} s_{ij,k} w + m_{ij}^2 - m_i^2 - m_j^2 \right], \\ &= \frac{1}{\bar{s}z(1-z)} \left[ p_\perp^2 + (1-z)^2 m_i^2 + z^2 m_j^2 \right], \end{aligned} \tag{4.86}$$

where  $\bar{s} = s - m_i^2 - m_j^2 - m_k^2$ . Given this expression for  $y_{ij,k}$  we obtain an expression for  $z_i$  by solving

$$z_i = \frac{1}{(1 - y_{ij,k})\bar{s}} 2q_i \cdot q_k ,$$

to give

$$z_i = \frac{1}{(1 - y_{ij,k})\bar{s}} \left[ x_{ij} x_k s_{ij,k} z + \frac{m_k^2}{x_{ij} x_k s_{ij,k} z} (p_\perp^2 + m_i^2) \right] ,$$

The phase-space limits on the splitting variables are

$$y_- = \frac{2m_i m_j}{s - m_i^2 - m_j^2 - m_k^2} , \quad (4.87)$$

$$y_+ = 1 - \frac{2m_k(\sqrt{s} - m_k)}{s - m_i^2 - m_j^2 - m_k^2} , \quad (4.88)$$

$$z_{i,\pm}(y_{ij,k}) = \frac{2m_i^2 + (s - m_i^2 - m_j^2 - m_k^2) y_{ij,k}}{2 [m_i^2 + m_j^2 + (s - m_i^2 - m_j^2 - m_k^2) y_{ij,k}]} \times (1 \pm v_{ij,i} v_{ij,k}) , \quad (4.89)$$

where the relative velocities  $v_{ij,k}$  and  $v_{ij,i}$  are

$$v_{ij,k} = \frac{\sqrt{[2m_k^2 + (s - m_i^2 - m_j^2 - m_k^2)(1 - y_{ij,k})]^2 - 4m_k^2}}{(s - m_i^2 - m_j^2 - m_k^2)(1 - y_{ij,k})} , \quad (4.90)$$

$$v_{ij,i} = \frac{\sqrt{(s - m_i^2 - m_j^2 - m_k^2)^2 y_{ij,k}^2 - 4m_i^2 m_j^2}}{(s - m_i^2 - m_j^2 - m_k^2) y_{ij,k} + 2m_i^2} . \quad (4.91)$$

Working in a frame where  $\vec{Q} = 0$ , the kinematic upper limit on the transverse momentum,  $p_{\perp,\max}$ , is simply the magnitude of the emission 3-momentum in the limit that the spectator following the splitting has zero momentum. The momentum conservation requirement in Eq. (4.81) can then be rearranged to give

$$p_{\perp,\max}^2 = \frac{\lambda(m_i^2, m_j^2, (\sqrt{s} - m_k)^2)}{4(\sqrt{s} - m_k)^2} ,$$

and the limits on  $z$  follow from  $y_{ij,k} < y_+$ , giving

$$z_\pm = \frac{1}{2(\sqrt{s} - m_k)^2} \left[ m_i^2 - m_j^2 + (\sqrt{s} - m_k)^2 \pm \sqrt{\lambda(m_i^2, m_j^2, (\sqrt{s} - m_k)^2)} \sqrt{1 - \frac{p_\perp^2}{p_{\perp,\max}^2}} \right] .$$

In the case of a massive dipole we require

$$\begin{aligned} \tilde{p}_k &= \frac{\sqrt{\lambda(s, m_{ij}^2, m_k^2)}}{\sqrt{\lambda(s, (q_i + q_j)^2, m_k^2)}} \left( q_k - \frac{Q \cdot q_k}{s} Q \right) + \frac{s + m_k^2 - m_{ij}^2}{2s} Q , \\ \tilde{p}_{ij} &= Q - \tilde{p}_k . \end{aligned} \quad (4.92)$$

In the massless case it is simple to show explicitly that the corresponding requirements in Eq. (D.1) are satisfied by the expressions in Eq. (D.2). It would be an involved and complex procedure to show explicitly that the expressions in Eq. (4.83) and Eq. (4.82) satisfy this requirement. It is, however, straightforward to show that momentum conservation requires that the four-momenta of the partons following a splitting are parameterized by three variables. One of these variables is the azimuthal angle of the splitting which is generated as described in Ref. [33]. Therefore for a given  $z_i$  and  $y_{ij,k}$  the momenta are fully constrained. As a cross-check, we have also verified numerically that the requirement in Eq. (4.92) is satisfied by the expressions in Eq. (4.83) and Eq. (4.82).

### 4.3.3.3.2 Single-particle phase-space

The single-particle phase-space can be expressed in terms of  $z_i$  and  $y_{ij,k}$

$$dq_j = \frac{1}{16\pi^2} \frac{\bar{s}^2}{\sqrt{\lambda(s, m_{ij}^2, m_k^2)}} (1 - y_{ij,k}) dy_{ij,k} dz_i \frac{d\phi}{2\pi}.$$

In order to write this in terms of our generated variables, we need the Jacobian  $J_{p_\perp^2, z \rightarrow z_i, y_{ij,k}}$ , such that,

$$dy_{ij,k} dz_i = \left( J_{p_\perp^2, z \rightarrow z_i, y_{ij,k}} \right) p_\perp^2 \frac{dp_\perp^2}{p_\perp^2} dz.$$

This is in general given by

$$J_{p_\perp^2, z \rightarrow z_i, y_{ij,k}} = \left| \frac{\partial z_i}{\partial p_\perp^2} \frac{\partial y_{ij,k}}{\partial z} - \frac{\partial z_i}{\partial z} \frac{\partial y_{ij,k}}{\partial p_\perp^2} \right|,$$

which can be written as

$$\frac{dy_{ij,k}}{y_{ij,k}} dz_i = \left[ \frac{p_\perp^2}{p_\perp^2 + (1-z)^2 m_i^2 + z^2 m_j^2} \right] \left[ 1 - 2 \frac{1}{\bar{s}(1-y_{ij,k})} \frac{m_k^2 Q^2}{x_{ij} x_k s_{ij,k}} \right] \frac{dp_\perp^2}{p_\perp^2} dz.$$

### 4.3.3.3.3 Final-initial dipole kinematics

The final-initial dipole splitting kernels, given in Section 4.3.3.4.2, are written in terms of the splitting variables  $z_i$  and  $x_{ij,b}$ , defined in terms of the physical momenta as

$$z_i = \frac{q_i \cdot q_b}{q_i \cdot q_b + q_j \cdot q_b}, \quad (4.93)$$

$$x_{ij,b} = \frac{q_i \cdot q_b + q_j \cdot q_b - q_i \cdot q_j + \frac{1}{2} (m_{ij}^2 - m_i^2 - m_j^2)}{q_i \cdot q_b + q_j \cdot q_b}. \quad (4.94)$$

In addition, we define the conserved momentum transfer

$$Q = \tilde{p}_{ij} - \tilde{p}_b = q_i + q_j - q_b,$$

and the invariant

$$s_{ij,b} = 2\tilde{p}_{ij} \cdot \tilde{p}_b.$$

In both the massless and massive case, we require that the dipole momenta can be written in terms of the momenta following the splitting

$$\tilde{p}_b = x_{ij,b} q_b, \quad (4.95)$$

$$\tilde{p}_{ij} = q_i + q_j - (1 - x_{ij,b}) q_b. \quad (4.96)$$

The incoming spectator is necessarily massless, therefore it is most straightforward to write the new particle momenta in the quasi-collinear Sudakov parameterization, using the generated variables. It is straightforward in both cases to rewrite the results in terms of the splitting variables, as we have done for the other dipole configurations.

Using the quasi-collinear Sudakov parameterization, the physical momenta following the splitting are

$$\begin{aligned} q_i &= z\tilde{p}_{ij} + \frac{m_i^2 - z^2 m_{ij}^2 + p_\perp^2}{s_{ij,b} z} \tilde{p}_b + k_\perp, \\ q_j &= (1-z)\tilde{p}_{ij} + \frac{m_j^2 - (1-z)^2 m_{ij}^2 + p_\perp^2}{s_{ij,b} (1-z)} \tilde{p}_b - k_\perp, \\ q_b &= \frac{1}{x_{ij,b}} \tilde{p}_b. \end{aligned}$$

As the spectator is massless we have  $z_i = z$ , and we can write  $x_{ij,b}$  in terms of the generated variables as,

$$x_{ij,b} = \left[ 1 + \frac{p_\perp^2 + (1-z)m_i^2 + zm_j^2 - z(1-z)m_{ij}^2}{s_{ij,b}z(1-z)} \right]^{-1}.$$

We can derive a lower limit on the spectator momentum fraction  $x_{ij,b}$ . We first denote the momentum of the incoming proton as  $P$  and the proton momentum-fraction carried by the spectator prior to the splitting as  $x_s$ . We can write

$$q_b = \frac{1}{x_{ij,b}} \tilde{p}_b = \frac{1}{x_{ij,b}} (x_s P) < P,$$

we therefore have the requirement

$$x_{ij,b} > x_s. \quad (4.97)$$

The phase-space limits on the splitting variables  $z_i$  and  $x_{ij,b}$  are

$$z_{i,\pm}(x_{ij,b}) = \frac{s_{ij,b}/x_{ij,b} - s_{ij,b} + m_{ij}^2 + m_i^2 - m_j^2 \pm \sqrt{(s_{ij,b}/x_{ij,b} - s_{ij,b} + m_{ij}^2 - m_i^2 - m_j^2)^2 - 4m_i^2m_j^2}}{2(s_{ij,b}/x_{ij,b} - s_{ij,b} + m_{ij}^2)},$$

$$x_- = x_s,$$

$$x_+ = \frac{s_{ij,b}}{s_{ij,b} - m_{ij}^2 + (m_i + m_j)^2},$$

where  $x_-$  is simply the limit in (4.97). Following from the inequality in Eq. (4.97) we obtain the following limits on  $z$  and  $p_\perp$

$$p_{\perp,\max}^2 = \frac{s'_{ij,b}}{4} \lambda \left( 1, \frac{m_i^2}{s'_{ij,b}}, \frac{m_j^2}{s'_{ij,b}} \right),$$

$$z_\pm = \frac{1}{2} \left[ 1 + \frac{m_i^2 - m_j^2}{s'_{ij,b}} \pm \sqrt{\lambda \left( 1, \frac{m_i^2}{s'_{ij,b}}, \frac{m_j^2}{s'_{ij,b}} \right)} \sqrt{1 - \frac{p_\perp^2}{p_{\perp,\max}^2}} \right],$$

where  $\lambda$  is the standard Källén function and for convenience we have defined the modified invariant

$$s'_{ij,b} = s_{ij,b} \left( \frac{1 - x_s}{x_s} \right) + m_{ij}^2.$$

#### 4.3.3.3.4 Single-particle phase-space

The single-particle phase-space can be expressed in terms of  $z_i$  and  $x_{ij,b}$

$$dq_j = \frac{1}{16\pi^2} 2\tilde{p}_{ij} \cdot q_b dz_i dx_{ij,b} \frac{d\phi}{2\pi}.$$

Recalling that  $z_i = z$ , the Jacobian for expressing this phase-space in terms of the generated variables,  $J_{p_\perp^2 \rightarrow x_{ij,b}}$ , is simply

$$J_{p_\perp^2 \rightarrow x_{ij,b}} = \left| \frac{\partial x_{ij,b}}{\partial p_\perp^2} \right|,$$

such that

$$dx_{ij,b} dz = \left( J_{p_\perp^2 \rightarrow x_{ij,b}} \right) p_\perp^2 \frac{dp_\perp^2}{p_\perp^2} dz.$$

Noting that  $z_i = z$ , we can express the phase-space integration in terms of the generated variables using the replacement

$$\frac{1}{x_{ij,b}(1-x_{ij,b})} dz_i dx_{ij,b} = \left[ \frac{p_\perp^2}{p_\perp^2 + (1-z)m_i^2 + zm_j^2 - z(1-z)m_{ij}^2} \right] \frac{dp_\perp^2}{p_\perp^2} dz.$$

### 4.3.3.5 Initial-final dipole kinematics

The initial-final dipole splitting kernels, given in Section 4.3.3.4.3, are written in terms of the splitting variables  $u_j$  and  $x_{jk,a}$ , defined in terms of the physical momenta

$$x_{jk,a} = \frac{q_a \cdot q_j + q_a \cdot q_k - q_j \cdot q_k}{(q_j + q_k) \cdot q_a} ,$$

$$u_j = \frac{q_a \cdot q_j}{(q_j + q_k) \cdot q_a} .$$

We also define the conserved momentum transfer

$$Q = \tilde{p}_k - \tilde{p}_{aj} = q_j + q_k - q_a ,$$

and the invariant

$$s_{aj,k} = 2\tilde{p}_{aj} \cdot \tilde{p}_k .$$

In both cases, *i.e.* either a massless or massive spectator, our expressions for the momenta following the splitting must satisfy

$$\begin{aligned} \tilde{p}_{aj} &= x_{jk,a} q_a , \\ \tilde{p}_k &= q_j + q_k - (1 - x_{jk,a}) q_a . \end{aligned} \tag{4.98}$$

It follows from this requirement that, in contrast to the case of a final-state splitting, the longitudinal recoil is absorbed by the incoming emitter and the outgoing spectator acquires a transverse momentum. Following the condition in (4.98), the physical momenta after the splitting can be expressed in terms of the splitting variables as

$$\begin{aligned} q_a &= \frac{1}{x_{jk,a}} \tilde{p}_{aj} , \\ q_j &= \left[ \left( \frac{1 - x_{jk,a}}{x_{jk,a}} \right) (1 - u_j) - u_j \frac{2m_k^2}{s_{aj,k}} \right] \tilde{p}_{aj} + u_j \tilde{p}_k - k_\perp , \\ q_k &= \left[ \left( \frac{1 - x_{jk,a}}{x_{jk,a}} \right) u_j + u_j \frac{2m_k^2}{s_{aj,k}} \right] \tilde{p}_{aj} + (1 - u_j) \tilde{p}_k + k_\perp . \end{aligned}$$

We set  $n = \tilde{p}_k - (m_k^2/s_{aj,k})\tilde{p}_{aj}$  in Eq. (4.78) and equate this to  $q_j$  above to obtain expressions for the splitting variables in terms of  $z$  and  $p_\perp^2$ ,

$$x_{jk,a} = \frac{s_{aj,k}}{2r(s_{aj,k} - m_k^2)} (1 - z + r) \times \left[ 1 - \sqrt{1 - \frac{4r(s_{aj,k} - m_k^2)}{s_{aj,k}} \frac{z(1 - z)}{(1 - z + r)^2}} \right] , \tag{4.99}$$

$$u_j = x_{jk,a} \left( \frac{r}{1 - z} \right) . \tag{4.100}$$

Following an analogous argument to that in Section 4.3.3.3, we obtain the limit on  $x_{jk,a}$ ,

$$x_{jk,a} > x_e , \tag{4.101}$$

where  $x_e$  is the proton momentum-fraction carried by the emitter prior to the splitting.

The phase-space limits on the splitting variables  $u_j$  and  $x_{jk,a}$  are

$$\begin{aligned} u_- &= 0 , & u_+ &= \frac{1 - x_{jk,a}}{1 - x_{jk,a}(1 - m_k^2/s_{aj,k})} , \\ x_- &= x_e , & x_+ &= 1 . \end{aligned}$$

The limits on the generated variables  $z$  and  $p_\perp$  follow from the inequality in (4.101) and are

$$\begin{aligned} p_{\perp,\max}^2 &= \frac{s'_{aj,k}^2}{4} \left[ \frac{1}{m_k^2 + s'_{aj,k}} \right] , \\ z_\pm &= \frac{1}{2} \left[ (1 + x_e) \pm (1 - x_e) \sqrt{1 - \frac{p_\perp^2}{p_{\perp,\max}^2}} \right] , \end{aligned}$$

where for convenience we have defined the rescaled invariant

$$s'_{aj,k} = s_{aj,k} \left( \frac{1 - x_e}{x_e} \right) .$$

#### 4.3.3.6 Single-particle phase-space

The single-particle phase-space can be expressed in terms of  $u_j$  and  $x_{jk,a}$  as

$$dq_j = \frac{1}{16\pi^2} 2\tilde{p}_k \cdot q_a dx_{jk,a} du_j \frac{d\phi}{2\pi} .$$

In order to write this in terms of our generated variables, we need the Jacobian  $J_{p_\perp^2, z \rightarrow u_j, x_{jk,a}}$ , such that

$$dx_{jk,a} du_j = \left( J_{p_\perp^2, z \rightarrow u_j, x_{jk,a}} \right) p_\perp^2 \frac{dp_\perp^2}{p_\perp^2} dz .$$

It is easier to rearrange the explicit equations for  $x_{jk,a}(z, p_\perp)$  and  $u_j(z, p_\perp)$  to obtain equations  $z(x_{jk,a}, u_j)$  and  $p_\perp(x_{jk,a}, u_j)$  and instead compute  $J_{u_j, x_{jk,a} \rightarrow p_\perp^2, z}$ . This is simply the reciprocal of the required Jacobian  $J_{p_\perp^2, z \rightarrow u_j, x_{jk,a}}$  and is given by

$$J_{u_j, x_{jk,a} \rightarrow p_\perp^2, z} = \left| \frac{\partial z}{\partial u_j} \frac{\partial p_\perp^2}{\partial x_{jk,a}} - \frac{\partial z}{\partial x_{jk,a}} \frac{\partial p_\perp^2}{\partial u_j} \right| .$$

We can therefore express the phase-space integration in terms of the generated variables using the replacement

$$\frac{1}{u_j} \frac{1}{x_{jk,a}} du_j dx_{jk,a} = \left[ u_j + x_{jk,a} - 2u_j x_{jk,a} \left( 1 - \frac{m_k^2}{s_{aj,k}} \right) \right]^{-1} \frac{dp_\perp^2}{p_\perp^2} dz .$$

#### 4.3.3.7 Initial-initial dipole kinematics

In the case of initial-initial dipoles we only consider the case where all partons in the dipole, before and after the splitting, are massless.

The initial-initial dipole splitting kernels, given in Section 4.3.3.4.4, are written in terms of the splitting variable  $x_{j,ab}$ , defined in terms of the physical momenta

$$x_{j,ab} = \frac{q_a \cdot q_b - q_j \cdot q_a - q_j \cdot q_b}{q_a \cdot q_b} .$$

In order to express the kinematics and the single-particle phase-space we require an additional splitting variable

$$v_j = \frac{q_a \cdot q_j}{q_a \cdot q_b} .$$

It is convenient in the case of the initial-initial dipole to leave the momentum of the incoming spectator unchanged following the splitting, *i.e.*  $\tilde{p}_b = q_b$ . Furthermore, as in the case of the initial-final dipole, the momentum of the incoming emitter changes only by a simple rescaling, that is it absorbs only longitudinal recoil. The remaining recoil from the splitting is absorbed by all of the final-state particles, including non-coloured particles, in the process prior to the splitting.

As this splitting involves all of the particles in the event we do not explicitly consider a conserved dipole momentum or dipole momentum transfer  $Q$  as we have for the other dipoles. Instead we consider the momentum conservation requirements of the process before and after the splitting, these are

$$\begin{aligned} \tilde{p}_{aj} + q_b &= \sum_n \tilde{k}_n , \\ q_a + q_b &= \sum_n k_n + q_j , \end{aligned} \tag{4.102}$$

respectively. We use  $\{\tilde{k}_n\}$  and  $\{k_m\}$  to denote the momenta of all of the final-state particles, except the emission from the splitting, before and after the splitting respectively. For convenience we also define the invariant

$$s_{aj,b} = 2\tilde{p}_{aj} \cdot q_b .$$

The momenta prior to the splitting must satisfy

$$\begin{aligned}\tilde{p}_{aj} &= x_{j,ab} q_a, \\ \tilde{k}_m &= \Lambda(q_a + q_b - q_j, \tilde{p}_{aj} + q_b) k_m,\end{aligned}$$

where the Lorentz transformation  $\Lambda$  satisfying the momentum conservation requirements in (4.102) is

$$\Lambda^\mu{}_\nu \left( K, \tilde{K} \right) = g^\mu{}_\nu - \frac{2 \left( K + \tilde{K} \right)^\mu \left( K + \tilde{K} \right)_\nu}{\left( K + \tilde{K} \right)^2} + \frac{2 \tilde{K}^\mu K_\nu}{K^2}.$$

With these requirements the physical momenta following the splitting are

$$\begin{aligned}q_a &= \frac{1}{x_{j,ab}} \tilde{p}_{aj}, \\ q_j &= \frac{1 - x_{j,ab} - v_j}{x_{j,ab}} \tilde{p}_{aj} + v_j q_b + k_\perp, \\ k_m &= \Lambda(\tilde{p}_{aj} + q_b, q_a + q_b - q_j) \tilde{k}_m,\end{aligned}$$

and the splitting variables  $x_{j,ab}$  and  $v_j$  are written in terms of the generated variables

$$\begin{aligned}x_{j,ab} &= \frac{z(1-z)}{(1-z+r)}, \\ v_j &= x_{j,ab} \frac{r}{1-z},\end{aligned}$$

where we have defined  $r = \frac{p_\perp^2}{s_{aj,b}}$ .

Following an analogous argument to that in Section 4.3.3.3.3, we obtain the limit on  $x_{j,ab}$ ,

$$x_{j,ab} > x_e, \quad (4.103)$$

where  $x_e$  is the proton momentum-fraction carried by the emitter prior to the splitting. The limits on the splitting variable  $x_{j,ab}$  are

$$\begin{aligned}x_- &= x_e, & x_+ &= 1, \\ v_- &= 0, & v_+ &= 1 - x.\end{aligned}$$

The limits on the generated variables are

$$p_{\perp,\max}^2 = s_{aj,b} \frac{(1-x_e)^2}{4x_e}, \quad (4.104)$$

$$z_\pm = \frac{1}{2} \left[ (1+x_e) \pm (1-x_e) \sqrt{1 - \frac{p_\perp^2}{p_{\perp,\max}^2}} \right]. \quad (4.105)$$

#### 4.3.3.8 Single-particle phase-space

The single-particle phase-space can be expressed in terms of  $v_j$  and  $x_{j,ab}$

$$dq_j = \frac{1}{16\pi^2} 2q_a \cdot q_b dx_{j,ab} dv_j \frac{d\phi}{2\pi}.$$

In order to write this in terms of our generated variables, we need the Jacobian  $J_{p_\perp^2, z \rightarrow v_j, x_{j,ab}}$ , such that

$$dx_{j,ab} dv_j = \left( J_{p_\perp^2, z \rightarrow v_j, x_{j,ab}} \right) p_\perp^2 \frac{dp_\perp^2}{p_\perp^2} dz.$$

This is given by

$$J_{p_\perp^2, z \rightarrow v_j, x_{j,ab}} = \left| \frac{\partial v_j}{\partial p_\perp^2} \frac{\partial x_{j,ab}}{\partial z} - \frac{\partial v_j}{\partial z} \frac{\partial x_{j,ab}}{\partial p_\perp^2} \right|,$$

so that

$$\frac{1}{x_{j,ab}} \frac{1}{v_j} dx_{j,ab} dv_j = \frac{1}{z} \frac{dp_\perp^2}{p_\perp^2} dz.$$

### 4.3.3.9 Decay dipoles

The final distinct type of dipole which must be considered is that consisting of an incoming decayed particle and an outgoing colour-connected partner. The outgoing partner is a parton produced either in the decay of the incoming particle or the subsequent showering of the decay system prior to the current splitting. In principle, such a dipole can be considered with the emitter identified as either the incoming or outgoing parton, however, we currently only include the latter case in Herwig 7. Following our terminology for the other dipoles, we only include final-initial decay dipoles and do not consider initial-final decay dipoles. This is discussed in Section 4.3.3.4.5.

As it is the colour partner of the emitter, we refer to the incoming particle as the spectator, however we wish to preserve the 4-momentum of the incoming particle as its momentum has been set, before its decay, in the showering of the production process. This is in line with the principle of the narrow-width approximation. Therefore, in contrast with the majority of the other dipoles discussed in the previous sections, the spectator does not absorb any recoil from the splitting. Instead we choose to absorb the recoil by sharing it amongst all of the particles outgoing from the decay and any previous emissions from the showering of the decay system, excluding the emitter and the emitted parton from the current splitting. We refer to this set of particles as the ‘recoil system’. This is similar to the approach used in the case of the initial-initial dipole in Section 4.3.3.7.

We will now show that the kinematics for a splitting from a decay dipole are identical to those for a splitting from a massive final-final dipole. Following the notation outlined in Section 4.3.3.1, we denote the momenta of the incoming decayed particle and the outgoing emitter prior to the splitting as  $\tilde{p}_b$  and  $\tilde{p}_{ij}$  respectively. The momentum of the recoil system is denoted by  $\tilde{p}_k$ . Following the splitting the momentum of the incoming particle is unchanged,  $q_b = \tilde{p}_b$ , the momenta of the new outgoing emitter and emission are denoted by  $q_i$  and  $q_j$  respectively and the momentum of the recoil system is denoted by  $q_k$ . It follows from our definition of the recoil system that the incoming particle momentum  $q_b$  is in fact the conserved dipole momentum

$$\begin{aligned} Q = q_b &= \tilde{p}_{ij} + \tilde{p}_k \\ &= q_i + q_j + q_k. \end{aligned} \tag{4.106}$$

Comparing (4.106) and (4.81) it is clear that the required kinematics are simply those for a splitting from a massive final-final dipole in Section 4.3.3.1.

### 4.3.3.4 Splitting kernels

The splitting kernels for light and massive dipoles were originally given in Ref. [72] and Ref. [73] respectively, we give them in the following sections in order to provide a complete reference. For further details we refer the reader to the original publications. For simplicity we here only report on the spin averaged splitting kernels. Furthermore we choose to neglect those multiplicative factors that are not relevant to the implementation of these kernels in a parton shower.

For each dipole we present the kernels for both the massless and massive cases. While the massless case can always be obtained from the massive result, as with the splitting kinematics we choose to implement the two cases separately in Herwig in order to avoid unnecessary computations in the case of splittings from massless dipoles. Unless otherwise stated, all of the notation used in the expressions of the splitting kernels is defined in 4.3.3.1 and the relevant kinematics sections.

The colour factors,  $C_F$  and  $C_A$  follow their standard definitions in terms of the number of colours,  $N_C$ ,

$$\begin{aligned} C_F &= \frac{N_C^2 - 1}{2N_C}, \\ C_A &= N_C. \end{aligned}$$

We highlight to the reader that the dipole shower currently obeys the strict large- $N_C$  limit. We also use the factor  $T_R = 1/2$ . The strong coupling, denoted by  $\alpha_S$ , is described in detail in Section Appendix C.3.

Splittings from decay dipoles were not included in the original publication of the splitting kernels. We present them in Section 4.3.3.4.5 for the first time and provide a detailed discussion.

#### 4.3.3.4.1 Final-final dipole kernels

We denote the kernel for the splitting  $\{\tilde{i}, \tilde{j}, \tilde{k}\} \rightarrow \{i, j, k\}$  as  $\langle V_{X_i Y_j, k}(z_i, y_{ij, k}) \rangle$  where  $X$  and  $Y$  denote the type of parton

$$\langle V_{q_i g_j, k}(z_i, y_{ij, k}) \rangle = 8\pi\alpha_S C_F \left\{ \frac{2}{1 - z_i(1 - y_{ij, k})} - \frac{\tilde{v}_{ij, k}}{v_{ij, k}} \left[ 1 + z_i + \frac{2\mu_i^2}{\bar{s}y_{ij, k}} \right] \right\},$$

$$\langle V_{q_i \bar{q}_j, k} (z_i, y_{ij,k}) \rangle = 8\pi\alpha_S T_R \frac{1}{v_{ij,k}} \left\{ 1 - 2 \left[ z_i(1-z_i) - (1-\kappa)z_{i,+}z_{i,-} - \frac{\kappa\mu_i^2}{2\mu_i^2 + (1-2\mu_i^2 - \mu_k^2)y_{ij,k}} \right] \right\},$$

$$\langle V_{g_i g_j, k} (z_i, y_{ij,k}) \rangle = 16\pi\alpha_S C_A \left[ \frac{1}{1-z_i(1-y_{ij,k})} + \frac{1}{1-(1-z_i)(1-y_{ij,k})} - \frac{z_i(1-z_i) - (1-\kappa)z_{i,+}z_{i,-} - 2}{v_{ij,k}} \right],$$

where the relative velocity term  $\tilde{v}_{ij,k}$ , *i.e.* the velocity between  $\tilde{p}_{ij}$  and  $\tilde{p}_k$ , is written as

$$\tilde{v}_{ij,k} = \frac{\sqrt{\lambda(s, m_{ij}^2, m_k^2)}}{s - m_{ij}^2 - m_k^2}.$$

The corresponding massless results are given in [Appendix D.4](#). The branching probability for a splitting from a final-final dipole is written in its general form

$$d\mathcal{P}_{\text{branching}} = \frac{1}{(q_i + q_j)^2 - m_{ij}^2} \langle V_{X_i Y_j, k} (z_i, y_{ij,k}) \rangle dq_j.$$

#### 4.3.3.4.2 Final-initial dipole kernels

We denote the kernel for the splitting  $\{\tilde{i}, \tilde{j}\} \rightarrow \{i, j, b\}$  as  $\langle V_{X_i Y_j}^b (z_i, x_{ij,b}) \rangle$  where  $X$  and  $Y$  denote the parton types

$$\langle V_{q_i g_j}^b (z_i, x_{ij,b}) \rangle = 8\pi\alpha_S C_F \left\{ \frac{2}{1-z_i + (1-x_{ij,b})} - (1+z_i) - \mu_i^2 \frac{2x_{ij,b}}{\bar{s}(1-x_{ij,b})} \right\},$$

$$\langle V_{q_i \bar{q}_j}^b (z_i, x_{ij,b}) \rangle = 8\pi\alpha_S T_R [1 - 2(z_{i,+} - z_i)(z_i - z_{i,-})].$$

The corresponding massless results are given in [Appendix D.5](#). The branching probability for a splitting from a final-initial dipole is written in its general form

$$d\mathcal{P}_{\text{branching}} = \frac{1}{(q_i + q_j)^2 - m_{ij}^2} \frac{1}{x_{ij,b}} \frac{f_b(x_s/x_{ij,b})}{f_b(x_s)} \langle V_{X_i Y_j}^b (z_i, x_{ij,b}) \rangle dq_j,$$

here, in general,  $f_l(x)$  is the parton density function of parton  $l$ .

#### 4.3.3.4.3 Initial-final dipole kernels

We denote the kernel for the splitting  $\{\tilde{a}, \tilde{j}\} \rightarrow \{a, j, k\}$  as  $\langle V_k^{X_a Y_j} (u_j, x_{jk,a}) \rangle$  where  $X$  and  $Y$  denote the type of parton

$$\langle V_k^{q_a g_j} (u_j, x_{jk,a}) \rangle = 8\pi\alpha_S C_F \left[ \frac{2}{1-x_{jk,a} + u_j} - (1+x_{jk,a}) \right],$$

$$\langle V_k^{g_a q_j} (u_j, x_{jk,a}) \rangle = 8\pi\alpha_S T_R [1 - 2x_{jk,a}(1-x_{jk,a})],$$

$$\langle V_k^{q_a q_j} (u_j, x_{jk,a}) \rangle = 8\pi\alpha_S C_F \left[ x_{jk,a} + \frac{2(1-x_{jk,a})}{x_{jk,a}} - 2\mu_k^2 \frac{u_j}{1-u_j} \right],$$

$$\langle V_k^{g_a g_j} (u_j, x_{jk,a}) \rangle = 16\pi\alpha_S C_A \left[ \frac{1}{1-x_{jk,a} + u_j} + \frac{1-x_{jk,a}}{x_{jk,a}} - 1 + x_{jk,a}(1-x_{jk,a}) - \mu_k^2 \frac{u_j}{1-u_j} \right].$$

The corresponding massless results are given in [Appendix D.6](#). The branching probability for a splitting from an initial-final dipole is written in its general form

$$d\mathcal{P}_{\text{branching}} = \frac{1}{2q_j \cdot q_a} \frac{1}{x_{jk,a}} \frac{f_a(x_e/x_{jk,a})}{f_{\tilde{a}j}(x_e)} \langle V_k^{X_a Y_j} (u_j, x_{jk,a}) \rangle dq_j.$$

#### 4.3.3.4.4 Initial-initial dipole kernels

We denote the kernel for the splitting  $\{\tilde{a}, \tilde{j}, \tilde{b}\} \rightarrow \{a, j, b\}$  as  $\langle V^{X_a Y_j, b} (x_{j,ab}) \rangle$  where  $X$  and  $Y$  denote the type of parton

$$\begin{aligned}\langle V^{q_a g_j, b} (x_{j,ab}) \rangle &= 8\pi\alpha_S C_F \left[ \frac{1 + x_{j,ab}^2}{1 - x_{j,ab}} \right], \\ \langle V^{g_a q_j, b} (x_{j,ab}) \rangle &= 8\pi\alpha_S T_R [1 - 2x_{j,ab}(1 - x_{j,ab})], \\ \langle V^{q_a q_j, b} (x_{j,ab}) \rangle &= 8\pi\alpha_S C_F \left[ \frac{1}{x_{j,ab}} + \frac{(1 - x_{j,ab})^2}{x_{j,ab}} \right], \\ \langle V^{g_a g_j, b} (x_{j,ab}) \rangle &= 16\pi\alpha_S C_A \left[ \frac{x_{j,ab}}{1 - x_{j,ab}} + \frac{1 - x_{j,ab}}{x_{j,ab}} + x_{j,ab}(1 - x_{j,ab}) \right].\end{aligned}$$

The branching probability for a splitting from an initial-initial dipole is written in its general form

$$d\mathcal{P}_{\text{branching}} = \frac{1}{2q_j \cdot q_a} \frac{1}{x_{j,ab}} \frac{f_a(x_e/x_{j,ab})}{f_{\tilde{a}\tilde{j}}(x_e)} \langle V^{X_a Y_j, b} (x_{j,ab}) \rangle dq_j,$$

where there is no parton distribution function term for the spectator because the momentum of the spectator parton is unchanged by the splitting.

#### 4.3.3.4.5 Decay dipoles

We stated in Section 4.3.3.3.9 that we do not include splittings from initial-final decay dipoles. This is because the kernel for this splitting contains a large negative term proportional to the mass-squared of the decaying particle. The kernel is therefore negative in a very large proportion of trialled splittings. In the case of a negative kernel that trial splitting is entirely discarded and does not contribute to the overall probability distribution implicitly used to generate the emission. The splitting kernel for the final-initial decay dipole does not suffer from this issue. We therefore only explicitly consider final-initial decay dipoles, however in order to correctly reproduce the probability distribution for each splitting we must include the splitting kernel expression for the initial-final decay dipole in that used to generate splittings from final-initial decay dipoles. The sum of the two contributions is positive in most trial splittings and therefore correctly produces the required distribution of emissions.

We refer the reader to [32] for a more detailed discussion of the treatment of emissions from decay dipoles and the choices made. We also highlight that, as always with splitting kernels, we can within reason keep, discard and add finite terms to the kernels.

As discussed in Section 4.3.3.3.9 the kinematics in the case of decay dipoles are identical to the final-final dipole splitting kinematics. The notation therefore follows that in Section 4.3.3.3.1, with the addition of the mass of the incoming decayed particle, denoted as  $m_b$ . Similarly the Jacobian factors and branching probabilities follow the same formulation as for

the final-final dipole we therefore do not repeat them for the decay dipole. The kernels are

$$\begin{aligned}
\langle V_{q_i g_j, k}^b(z_i, y_{ij, k}) \rangle = & \\
8\pi\alpha_S C_F \left\{ \frac{2(2m_i^2 + 2y_{ij, k}\bar{s} + \bar{s})}{(1+y_{ij, k})\bar{s} - z_i(1-y_{ij, k})\bar{s}} - \frac{\tilde{v}_{ij, k}}{v_{ij, k}} \left( (1+z_i) + \frac{2m_i^2}{y\bar{s}} \right) \right. & \\
\left. + \frac{y_{ij, k}}{1-z_i(1-y_{ij, k})} \left[ \frac{2(2m_i^2 + 2y_{ij, k}\bar{s} + \bar{s})}{(1+y_{ij, k})\bar{s} - z_i(1-y_{ij, k})\bar{s}} - \frac{\tilde{v}_{ij, k}}{v_{ij, k}} \left( 2 + \frac{2m_b^2}{(1-z_i(1-y_{ij, k}))\bar{s}} \right) \right] \right\}, & \\
\langle V_{g_i g_j, k}^b(z_i, y_{ij, k}) \rangle = & \\
16\pi\alpha_S C_A \left\{ \frac{1+2y_{ij, k}}{(1+y_{ij, k}) - z_i(1-y_{ij, k})} + \frac{1+2y_{ij, k}}{(1+y_{ij, k}) - (1-z_i)(1-y_{ij, k})} \right. & \\
\left. + \frac{1}{v_{ij, k}} [z_i(1-z_i) - (1-\kappa)z_{i,+}z_{i,-} - 2] \right\} & \\
+ 8\pi\alpha_S C_F \left\{ \frac{y_{ij, k}}{1-z_i(1-y_{ij, k})} \left[ \frac{2(1+2y_{ij, k})}{(1+y_{ij, k}) - z_i(1-y_{ij, k})} - \frac{\tilde{v}_{ij, k}}{v_{ij, k}} \left( 2 + \frac{2m_b^2}{(1-z_i(1-y_{ij, k}))\bar{s}} \right) \right] \right. & \\
\left. + \frac{y_{ij, k}}{1-(1-z_i)(1-y_{ij, k})} \left[ \frac{2(1+2y_{ij, k})}{(1+y_{ij, k}) - (1-z_i)(1-y_{ij, k})} - \frac{\tilde{v}_{ij, k}}{v_{ij, k}} \left( 2 + \frac{2m_b^2}{(1-(1-z_i)(1-y_{ij, k}))\bar{s}} \right) \right] \right\}, & \\
\langle V_{q_i \bar{q}_j, k}^b(z_i, y_{ij, k}) \rangle = & \\
8\pi\alpha_S T_R \left\{ 1 - 2 \left( z_i(1-z_i) - (1-\kappa)z_{i,+}z_{i,-} - \frac{\kappa m_i^2}{2m_i^2 + \bar{s}y_{ij, k}} \right) \right\}. &
\end{aligned}$$

#### 4.3.4 Colour Matrix Element Corrections

Within the dipole shower algorithm the method of improving the radiation pattern by subleading- $N_C$  corrections is available following the work outlined in [44, 45]. The colour matrix element corrections successively adjust the distribution of gluon emissions by a correction factor

$$w_{ij}^{\text{CMEC}} = -\frac{\text{Tr}[\mathbf{T}_i \cdot \mathbf{T}_j \mathbf{M}_n]}{\mathbf{T}_i^2 \text{Tr}[\mathbf{M}_n]}$$

to each dipole splitting kernel with emitter  $i$  and spectator  $j$ , in terms of the colour space density operator for  $n$  additional partons,  $\mathbf{M}_n$ . The initial condition for this object is  $\mathbf{M}_0 = |\mathcal{M}\rangle\langle\mathcal{M}|$  in terms of the hard scattering amplitude  $|\mathcal{M}\rangle$ , and it is successively updated using

$$\mathbf{M}_{n+1} = \sum_{i,j} W_{ij} \mathbf{T}_i \mathbf{M}_n \mathbf{T}_j^\dagger.$$

The colour matrix element corrections heavily rely on the Matchbox infrastructure and use the interface to the ColorFull package [67]. They can be enabled using the *Matchbox/CMEC.in* snippet, and employ the reweighting facilities Section 4.8.3 of the dipole shower to apply the correction factors.

#### 4.3.5 Constituent reshuffling

The Herwig cluster hadronization model expects partons with momenta on their constituent mass shell at the end of the perturbative shower evolution. Unlike the angular ordered shower which ensures energy-momentum conservation only at the end of the showering process, the dipole shower preserves four momentum at each shower emission. It also strictly keeps partons on their perturbative mass-shell. A transition to their constituent mass shell is therefore required and applied at the end of the dipole shower evolution. As with similar problems elsewhere in the simulation the method of choice was outlined in the context of the RAMBO phase space generator [70]. This method, transforming pole to constituent mass shells, boosts the system of final partons into their centre-of-mass system, and then scales the three momenta by a factor  $\xi$  solving

$$\sum_i \sqrt{\mathbf{p}_i^2 + m_i^2} = \sum_i \sqrt{\xi^2 \mathbf{p}_i^2 + M_i^2},$$

where  $m_i$  are the pole masses, and  $M_i$  are the constituent masses. In the highly unlikely case of an event extremely close to threshold, where there is no solution of this equation, the showering is restarted from the hard process. The total momenta of partons originating from a decay system is preserved independently. The `ConstituentReshuffler` class of the dipole shower performs the transformation above and allows for a different approach if desired. If the treatment of the constituent reshuffling within the hadronization framework, possibly including a dynamic gluon mass, no reshuffling at this level is needed.

#### 4.4 Perturbative decays and spin correlations

When calculating the matrix element for a given hard process or decay one must take into account the effect of spin correlations, as they will affect the distributions of particles in the final state. In particular these correlations are important in the production and decay of the top quark, for the production of tau leptons in Higgs decays and in models of BSM physics. They can also effect the azimuthal angles for emissions in the parton shower. In Herwig the decays of the fundamental particles and the unstable hadrons are calculated in the same way in order that correlation effects for particles such as the tau lepton, which is produced perturbatively but decays non-perturbatively, are correctly treated. The angular-ordered and dipole parton showers now include spin correlations requiring that these particles are decayed during the parton-shower stage of the event.

The spin correlation algorithm of Refs. [33, 53, 102, 103] is used to implement the correct spin correlations between the production and decay of particles, and any emissions generated by the parton shower. This algorithm is explained in general in Ref. [33, 53, 102, 103], here we will explain it using the example of the process  $e^+e^- \rightarrow t\bar{t}$  where the top quark subsequently decays, via a  $W^+$  boson, to a  $b$  quark and a pair of light fermions.

Initially, the outgoing momenta of the  $t\bar{t}$  pair are generated according to the usual cross-section integral

$$\frac{(2\pi)^4}{2s} \int \frac{d^3 p_t}{(2\pi)^3 2E_t} \frac{d^3 p_{\bar{t}}}{(2\pi)^3 2E_{\bar{t}}} \mathcal{M}_{\lambda_t \lambda_{\bar{t}}}^{e^+ e^- \rightarrow t\bar{t}} \mathcal{M}_{\lambda_t \lambda_{\bar{t}}}^{*e^+ e^- \rightarrow t\bar{t}}, \quad (4.107)$$

where  $\mathcal{M}_{\lambda_t \lambda_{\bar{t}}}^{e^+ e^- \rightarrow t\bar{t}}$  is the matrix element for the initial hard process and  $\lambda_{t,\bar{t}}$  are the helicities of the  $t$  and  $\bar{t}$  respectively. One of the outgoing particles is then picked at random, say the top quark, and a spin density matrix calculated

$$\rho_{\lambda_t \lambda_{t'}}^t = \frac{1}{N} \mathcal{M}_{\lambda_t \lambda_{\bar{t}}}^{e^+ e^- \rightarrow t\bar{t}} \mathcal{M}_{\lambda_t \lambda_{\bar{t}}}^{*e^+ e^- \rightarrow t\bar{t}}, \quad (4.108)$$

with  $N$  defined such that  $\text{Tr } \rho = 1$ .

The top quark is decayed and the momenta of the decay products distributed according to

$$\frac{(2\pi)^4}{2m_t} \int \frac{d^3 p_b}{(2\pi)^3 2E_b} \frac{d^3 p_{W^+}}{(2\pi)^3 2E_{W^+}} \rho_{\lambda_t \lambda_{t'}}^t \mathcal{M}_{\lambda_t \lambda_{W^+}}^{t \rightarrow b W^+} \mathcal{M}_{\lambda_{t'} \lambda_{W^+}}^{*t \rightarrow b W^+},$$

where the inclusion of the spin density matrix ensures the correct correlation between the top quark decay products and the beam.

A spin density matrix is calculated for the  $W^+$  only, because the  $b$  is stable

$$\rho_{\lambda_{W^+} \lambda_{W^+}}^{W^+} = \frac{1}{N} \rho_{\lambda_t \lambda_{t'}}^t \mathcal{M}_{\lambda_t \lambda_{W^+}}^{t \rightarrow b W^+} \mathcal{M}_{\lambda_{t'} \lambda_{W^+}}^{*t \rightarrow b W^+},$$

and the  $W^+$  decayed in the same manner as the top quark. Here the inclusion of the spin density matrix ensures the correct correlations between the  $W^+$  decay products, the beam and the bottom quark.

The decay products of the  $W^+$  are stable fermions so the decay chain terminates here and a decay matrix for the  $W^+$

$$D_{\lambda_{W^+} \lambda_{W^+}}^{W^+} = \frac{1}{N} \mathcal{M}_{\lambda_t \lambda_{W^+}}^{t \rightarrow b W^+} \mathcal{M}_{\lambda_{t'} \lambda_{W^+}}^{*t \rightarrow b W^+},$$

is calculated. Moving back up the chain a decay matrix for the top quark is calculated using the decay matrix of the  $W^+$

$$D_{\lambda_t \lambda_{t'}}^t = \frac{1}{N} \mathcal{M}_{\lambda_t \lambda_{W^+}}^{t \rightarrow b W^+} \mathcal{M}_{\lambda_{t'} \lambda_{W^+}}^{*t \rightarrow b W^+} D_{\lambda_{W^+} \lambda_{W^+}}^{W^+}.$$

Since the top quark came from the hard scattering process we must now deal with the  $\bar{t}$  in a similar manner but instead of using  $\delta_{\lambda_t \lambda_{t'}}$  when calculating the initial spin density matrix, the decay matrix of the top quark is used and the  $\bar{t}$  decay

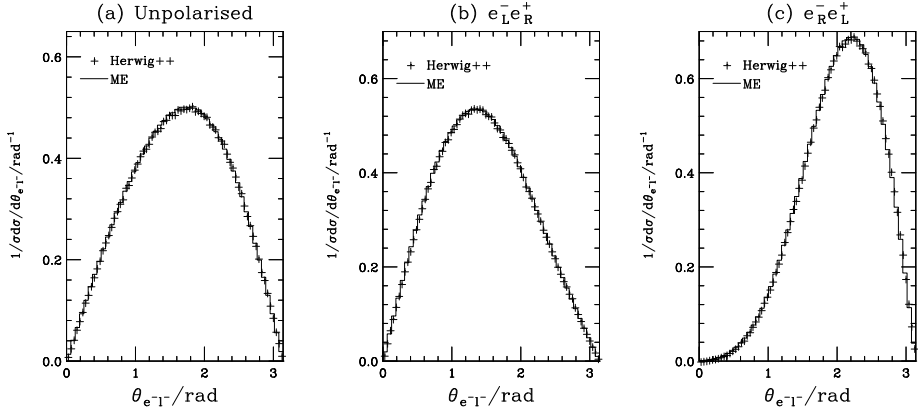


Fig. 4.3: Angle between the beam and the outgoing lepton in  $e^+e^- \rightarrow t\bar{t} \rightarrow b\bar{b}l^+\nu_ll^-\bar{\nu}_l$  in the lab frame for a centre-of-mass energy of 500 GeV with (a) unpolarized incoming beams, (b) negatively polarized electrons and positively polarized positrons and (c) positively polarized electrons and negatively polarized electrons. The data points show the results of the simulation as production and decay including spin correlations, while the histograms use the full matrix element for  $e^+e^- \rightarrow t\bar{t} \rightarrow b\bar{b}l^+\nu_ll^-\bar{\nu}_l$ . Reproduced from [56].

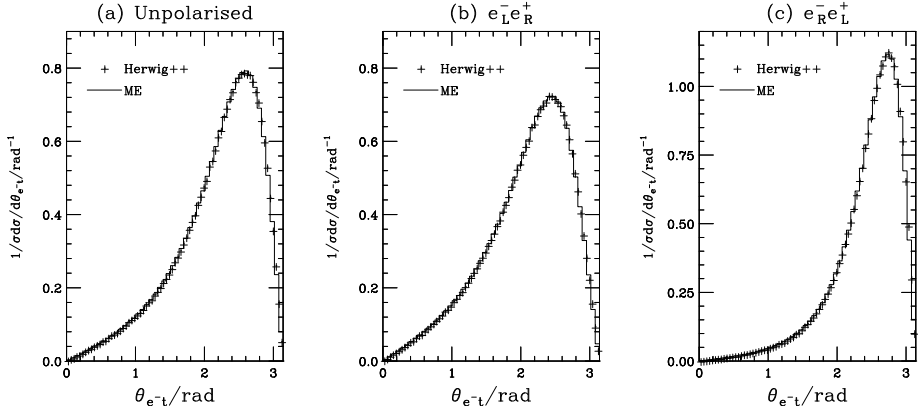


Fig. 4.4: Angle between the lepton and the top quark in  $e^+e^- \rightarrow t\bar{t} \rightarrow b\bar{b}l^+\nu_ll^-\bar{\nu}_l$  in the lab frame for a centre-of-mass energy of 500 GeV with (a) unpolarized incoming beams, (b) negatively polarized electrons and positively polarized positrons and (c) positively polarized electrons and negatively polarized electrons. The data points show the results of the simulation as production and decay including spin correlations, while the histograms use the full matrix element for  $e^+e^- \rightarrow t\bar{t} \rightarrow b\bar{b}l^+\nu_ll^-\bar{\nu}_l$ . Reproduced from [56].

is generated accordingly. The density matrices pass information from one decay chain to the associated chain thereby preserving the correct correlations.

The production and decay of the top quark, using the spin correlation algorithm, is demonstrated in Fig. 4.3, Fig. 4.4 and Fig. 4.5. The hard scattering process and subsequent decays were generated using the general matrix elements described in Section 6 rather than the default ones. The results from the full matrix element calculation are also included to show that the algorithm has been correctly implemented. The separate plots illustrate the different stages of the algorithm at work. Fig. 4.3 gives the angle between the beam and the outgoing lepton. The results from the simulation agree well with the full matrix element calculation, which demonstrates the consistency of the algorithm for the decay of the  $\bar{t}$ .

Fig. 4.4 gives the angle between the top quark and the produced lepton. This shows the same agreement as the previous figure and demonstrates the correct implementation of the spin density matrix for the  $\bar{t}$  decay. Finally, Fig. 4.5 gives the results for the angle between the final-state lepton/anti-lepton pair showing the correct implementation of the decay matrix that encodes the information about the  $\bar{t}$  decay. Distributions for various processes within the Minimal Supersymmetric Standard Model and for tau production in Higgs boson decay are shown in Refs. [55, 56].

The same algorithm is used regardless of how the particles are produced, in order to consistently implement the spin correlations in all stages of the event generation process.

The important perturbative decays in the Standard Model are implemented in dedicated `Decayer` classes used in Herwig to perform the decays of the fundamental Standard Model particles. The decays of fundamental particles in new physics models are performed using `Decayer` classes based on the spin structures, as described in Section 6.2.

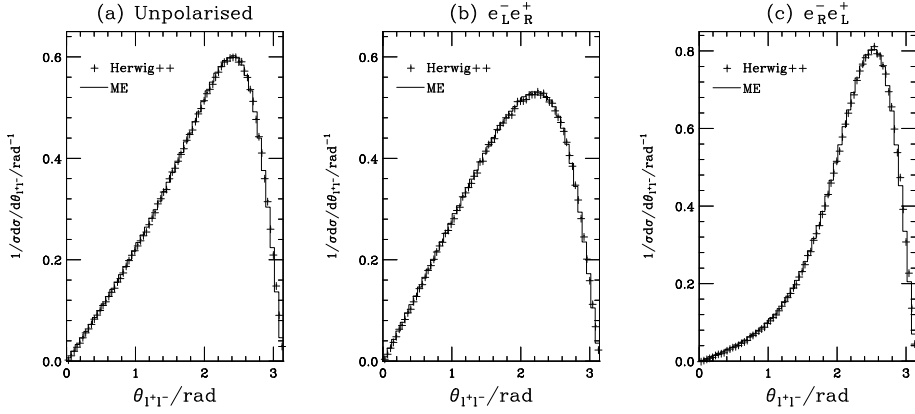


Fig. 4.5: Angle between the outgoing lepton and anti-lepton in  $e^+e^- \rightarrow t\bar{t} \rightarrow b\bar{b}l^+\nu_ll^-\bar{\nu}_l$  in the lab frame for a centre-of-mass energy of 500 GeV with (a) unpolarized incoming beams, (b) negatively polarized electrons and positively polarized positrons and (c) positively polarized electrons and negatively polarized electrons. The data points show the results of the simulation as production and decay including spin correlations, while the histograms use the full matrix element for  $e^+e^- \rightarrow t\bar{t} \rightarrow b\bar{b}l^+\nu_ll^-\bar{\nu}_l$ . Reproduced from [56].

## 4.5 Intrinsic transverse momentum

The formalism of collinear factorisation assumes that incoming partons within colliding hadrons are exactly collinear to their parent beam. As a high-energy approximation, this is extremely successful, but enforcing exact collinearity is incompatible with the uncertainty principle. Simple arguments predict intrinsic transverse momentum of a few hundred MeV. Within Herwig this is modelled as a tunable distribution with simple ansätze, whose precise form depends on the shower used.

### 4.5.1 Angular-Ordered shower

In the angular-ordered parton shower an intrinsic transverse momentum is added to the initial-state parton that results from the backward evolution in the initial-state parton shower, *i.e.* the parton extracted directly from the incoming hadron. This is then included in the standard kinematic reconstruction described in Section 4.2.5.2.

We model this using a non-perturbative distribution. Either a Gaussian

$$d^2 p_\perp \frac{(1-\beta)}{\pi p_\perp^G} \exp \left[ -\frac{p_\perp^2}{p_\perp^G} \right],$$

an inverse quadratic

$$d^2 p_\perp \frac{\beta}{\pi \ln \left( 1 + \frac{p_{T_{\max}}^2}{\Gamma^2} \right)} \frac{1}{\Gamma^2 + p_\perp^2},$$

or a combination of both distributions can be used. The fraction of the inverse quadratic distribution is  $\beta$  (`IntrinsicPtBeta`),  $p_\perp$  is the generated intrinsic transverse momentum,  $p_\perp^G$  is the root-mean squared of the Gaussian distribution (`IntrinsicPtGaussian`), and  $\Gamma$  controls the shape of the inverse quadratic distribution (`IntrinsicPtGamma`).

By default  $\beta = 0$ , such that a Gaussian distribution is used.

### 4.5.2 Dipole shower

Just as for the reshuffling to constituent masses, within the dipole shower there is no means of adding intrinsic transverse momentum simply on top of the evolution, and the respective transformation is generated for the initial-state partons at the end of the evolution.

For each of the incoming partons a  $p_\perp$  ‘kick’ with magnitude generated according to the distribution

$$\frac{dP}{dp_\perp^2} = \frac{1}{2p_{\perp,S}^2} \exp \left( -\frac{p_\perp^2}{2p_{\perp,S}^2} \right)$$

and a flat distribution in azimuth is selected. The labels  $S = F, A$  here refer to whether the incoming parton is valence or sea, respectively. The motivation behind this distinction originates in the phenomenological assumption that gluons experience a larger transverse spread than (valence) quarks essentially by a factor of  $\sqrt{C_A/C_F}$  though detailed studies have never been undertaken within this implementation and the values are set to be equal by default.

The `DipoleShowerHandler` class delegates this task to an `IntrinsicPtGenerator` class, which implements the procedure outlined above with two `interfaces` for the mean values  $p_{\perp,F}$  (`ValenceIntrinsicPtScale`) and  $p_{\perp,A}$  (`SeaIntrinsicPtScale`), respectively.

## 4.6 Forced splitting

After the perturbative shower evolution has terminated, the cluster hadronization model may necessitate some additional *forced splitting* of the initial-state parton that results, *i.e.* the parton that extracted from the hadron which is produced by the backward evolution in the initial-state parton shower. In hadronic collisions we require the external initial-state partons, which give rise to the first hard interaction, to be valence quarks (antiquarks), *i.e.* colour triplet (antitriplet) states. This allows us to treat each proton (antiproton) remnant as a diquark (antidiquark) which will be in a colour antitriplet/triplet state, in order to keep the incoming hadron colour neutral. Modelling the dissociation in this way allows for a simple, minimal, hadronization of the remnant in the cluster hadronization model.

Usually, the perturbative evolution, which is guided by the PDFs, will terminate on a valence quark, since the evolution works towards large  $x$  and small  $Q^2$ . In the cases where this has not happened, we force the resulting initial-state parton to undergo one or two additional splittings. The generation of these additional forced splittings is largely based on the same principles as that of the perturbative splittings.

In the perturbative evolution the scale of the PDFs is frozen at a value  $Q_s$  for values  $Q < Q_s$ . The default value of  $Q_s$  is chosen to be small, close to the non-perturbative region but still above typical values for the parton shower cutoff (`PDFFreezingScale=2.5 GeV`). This freezing scale leaves a little phase-space for the (non-perturbative) forced splittings. The forced splittings are generated in much the same vein as the perturbative splittings. The evolution starts at  $Q_s$  and the next branching scale is distributed according to  $dQ/Q$ , with a lower limit determined by the available phase-space. The  $z$  values are determined from the splitting functions in the same way as in the perturbative evolution. The splittings are reweighted by ratios of PDFs as in the perturbative evolution. There is only one slight difference, the evolution of the PDFs themselves with  $Q$  is frozen below  $Q_s$ . Nevertheless, this reweighting gives the right flavour content of the initial hadron. For example in the case of a proton we produce twice as many  $u$  quarks as  $d$  quarks. To force the evolution to end up on a valence quark, we only allow one or two flavours in the evolution:

1. if the initial parton is a sea quark ( $q$ ) or antiquark ( $\bar{q}$ ), it is forced to evolve into a gluon, emitting a  $\bar{q}$  or  $q$ , respectively.
2. if the initial parton is a gluon, from either the perturbative evolution or the forced splitting of a seaquark, it is forced to evolve into a valence quark, emitting the matching antiquark.

In the initial-state showering of additional hard scatters we force the backward evolution of the colliding partons to terminate on a gluon. We therefore only need the first kind of forced splitting in this case. This gluon is assumed to be relatively soft and branches from the remnant diquark. Again, this allows us to uniquely match up the final-state partons to the cluster hadronization model. The emitted partons from these forced splittings, as well as the remnant diquarks, will show up in the event record as decay products of a fictitious remnant particle, in order to distinguish them from those which originate from the perturbative evolution. Additional details about the colour structure and the event record can be found in [58].

## 4.7 YFS-based QED radiation

While the angular-ordered parton shower includes QED radiation we also have the option of simulating QED radiation using the approach of Ref. [52]. This included for both particle decays and unstable  $s$ -channel resonances produced in the hard process. This approach is based on the Yennie–Frautschi–Suura (YFS) formalism [131], which takes into account large double- and single- soft photon logarithms to all orders. In addition, the leading collinear logarithms are included to  $\mathcal{O}(\alpha)$  by using the dipole splitting functions. By default the production of QED radiation is switched off for both decays and hard processes. It may be included by using the `QEDRadiationHandler` in the `EventHandler` as one of the `PostSubProcessHandlers` for the hard process or using the `PhotonGenerator` interface of the relevant `Decayer` inheriting from the `DecayIntegrator` class for the decays.

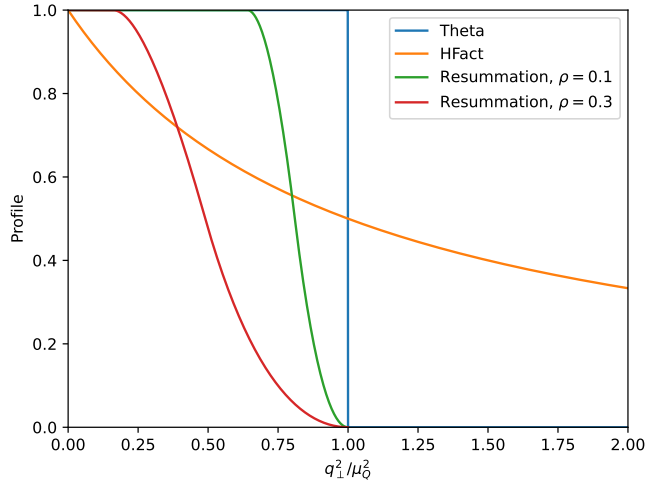


Fig. 4.6: Comparison of the different profile scales.

## 4.8 Shower variations and reweighting

For a general parton shower algorithm there are a number of components that dictate its behaviour. The primary components of a particular algorithm are its splitting kernels, evolution variable and phase-space constraints. Beyond this is the dependence on the unphysical scales introduced by the truncation of the expansion series. The variation of these scales in the parton shower serves to quantify missing higher-logarithmic contributions. The typical recipe to assess these perturbative uncertainties is to vary the chosen scales by factors of 1/2 and 2 around the central value as an estimate of these missing contributions.

Typically, these variations are performed via independent runs of the Monte Carlo after varying the scales detailed in Section 4.8.1. However, it is also possible to use shower reweighting, as described in Section 4.8.3, to perform these variations during a single run. The shower reweighting framework can also be employed for other applications, which are detailed in Section 4.8.4.

### 4.8.1 Shower scale variations

There are three main scales that can be varied within a parton shower algorithm. The first two are the familiar renormalization and factorization scales, which, respectively, set the argument  $\alpha_S$  and the PDFs in the shower. The other scale is the hard-veto scale, which is the characteristic scale that bounds the hardness of emissions. Each of these scales can be varied independently of the others.

For both parton shower algorithms the values of the rescaling factors are controlled by the `RenormalizationScaleFactor`, `FactorizationScaleFactor` and `HardScaleFactor` interfaces of the `ShowerHandler` class. In addition for processes simulated using the POWHEG scheme using Matchbox with the angular-ordered parton shower the `HardScaleFactor` also needs to be set in the matching.

Additionally, one can also vary the infrared cutoff of the parton shower as an indication of regions expected to be sensitive to the interplay between the parton shower and hadronization.

### 4.8.2 Profile scale choices

Within the parton shower, we include the freedom to weight emissions with an arbitrary function  $\kappa$ , the *profile scale choice*. This function modifies the Sudakov form factor such that

$$-\ln \Delta_{K_\perp^2}(p_\perp^2 | \mu_Q^2) = \int_{p_\perp^2}^{R_\perp^2} \frac{dq_\perp^2}{q_\perp^2} \kappa(\mu_Q^2, q_\perp^2) \int dz P_{K_\perp^2}(q_\perp^2, z),$$

where  $R_\perp$  is the scale at which all of the phase-space is available to emissions, and  $K_\perp$  gives the boundary condition for  $z$ .

In order for the shower to retain the desired resummation properties the profile scales must satisfy:

- $\kappa(\mu_Q^2, p_\perp^2) \rightarrow 1$  as  $p_\perp^2 \ll \mu_Q^2$ ;
- $\kappa(\mu_Q^2, p_\perp^2) \rightarrow 0$  as  $p_\perp^2 \sim R_\perp^2 \gg \mu_Q^2$ .

These conditions ensure that the small and large  $p_\perp$  limits are retained.

Beyond these constraints we also require that  $K_\perp^2 \sim \mu_Q^2$ , such that the correct logarithmic resummation is obtained, and that  $\kappa(\mu_Q^2, p_\perp^2)$  is slowly varying when  $p_\perp$  is far from  $\mu_Q$  such that terms involving the derivative of the profile scale are subleading.

In Herwig a number of choices are implemented:

- the `Theta` profile scale implements a hard cutoff at the veto scale, and has the functional form

$$\kappa(\mu_Q^2, q_\perp^2) = \theta(\mu_Q^2 - q_\perp^2);$$

- the `Resummation` profile is similar to the `Theta` profile, but smoothly approaches the cutoff via quadratic interpolation

$$\kappa(\mu_Q^2, q_\perp^2) = \begin{cases} 1 & q_\perp/\mu_Q \leq 1 - 2\rho, \\ 1 - \frac{(1-2\rho-q_\perp/\mu_Q)^2}{2\rho^2} & q_\perp/\mu_Q \in (1-2\rho, 1-\rho], \\ \frac{(1-q_\perp/\mu_Q)^2}{2\rho^2} & q_\perp/\mu_Q \in (1-\rho, 1], \\ 0 & q_\perp/\mu_Q > 1, \end{cases}$$

instead of a hard cutoff, where the  $\rho$  parameter controls the region over which the profile changes. For  $\rho = 0$  the `Resummation` and `Theta` profiles are equivalent;

- rather than the cutoff type behaviour of the previous two profiles, the `HFact` profile dampens emissions around the veto scale, and allows emissions above the veto scale. In this profile, the veto scale is the scale at which  $\kappa = 1/2$ . The `HFact` profile is described by the equation

$$\kappa(\mu_Q^2, q_\perp^2) = \left(1 + q_\perp^2/\mu_Q^2\right)^{-1}.$$

- the final profile scale choice corresponds to the `Power` shower, *i.e.* it imposes no constraints on emissions aside from those inherent to the shower algorithm

$$\kappa(\mu_Q^2, q_\perp^2) = 1,$$

it is equivalent to having no profile scale and is therefore used by setting the `HardScaleProfile` to `NULL`.

A comparison of the different profile scale choices is shown in Fig. 4.6 and their impact on some observables can be found in a phenomenological study [34].

In addition both the `HFact` and `Power` choices require that restrictions on the phase-space for emission in the parton shower are switched off, *i.e.* `RestrictPhasespace=Off`.

### 4.8.3 Parton shower variations reweighting

The method typically used to evaluate uncertainties arising from scale choices in the parton shower is to perform a full Monte Carlo simulation of the process in question for each set of scales of interest. Clearly this method becomes very computationally intensive if there are multiple scale variations to be evaluated, as is often the case in a phenomenological study. Alternatively, the same scale variations can be evaluated by performing a single run using a central set of scales and applying a reweighting factor, calculated for each set of scale variations, to the central result. Using this method, the hard process evaluation and hadronization steps are performed only once which can lead to a significant reduction in runtime compared to performing many separate runs.

In Herwig 7, we have implemented reweighting for variations of the renormalization and factorization scales used in the shower. We evolve a reweighting factor for each set of scales on a splitting-by-splitting basis such that when it is applied to the result from the central run, we produce the distribution expected from showering using the scales of interest. In Section 4.8.3.1 we first review the standard Sudakov veto algorithm used in parton showers and then present the modified veto algorithm for performing shower reweighting. Additionally, in 4.8.3.2, we discuss the key points relevant to the implementation of this algorithm in Herwig 7. More details of our approach can be found in Ref. [35].

#### 4.8.3.1 The weighted Sudakov veto algorithm

Parton shower evolution is performed using the Sudakov veto algorithm, see [Section Appendix B](#) for more details and references. We start showering from a given starting scale  $Q$  and need to generate the scale of the next emission  $q$  and the  $d$  additional associated splitting variables  $x$ . These are generated according to the distribution

$$\begin{aligned} dS_P(\mu, x_\mu | q, x | Q) = dq d^d x & \left[ \Delta_P(\mu | Q) \delta(q - \mu) \delta(x - x_\mu) \right. \\ & \left. + P(q, x) \theta(Q - q) \theta(q - \mu) \Delta_P(q | Q) \right], \end{aligned} \quad (4.109)$$

where  $x_\mu$  is a parameter point associated to the infra-red cutoff scale  $\mu$ , the splitting kernel is  $P(q, x)$  and the Sudakov form factor is

$$\Delta_P(q | Q) = \exp \left( - \int_q^Q dk \int d^d z P(k, z) \right). \quad (4.110)$$

The distribution  $S_P$  is normalized to unity.

In we consider an overestimate of the kernel,  $R(q, x)$ , such that

$$R(q, x) \geq P(q, x) \quad \forall q, x. \quad (4.111)$$

The overestimate is chosen to be integrable and invertible so that  $q, x$  can easily be generated according to the overestimated distribution

$$\begin{aligned} dS_R(\mu, x_\mu | q, x | Q) = dq d^d x & \left[ \Delta_R(\mu | Q) \delta(q - \mu) \delta(x - x_\mu) \right. \\ & \left. + R(q, x) \theta(Q - q) \theta(q - \mu) \Delta_R(q | Q) \right], \end{aligned} \quad (4.112)$$

with a Sudakov form factor

$$\Delta_R(q | Q) = \exp \left( - \int_q^Q dk \int d^d z R(k, z) \right).$$

Starting at a scale  $k = Q$ , the standard Sudakov veto algorithm proceeds as follows:

1. a trial splitting scale and variables,  $q, x$ , are generated according to  $S_R(\mu, x_\mu | q, x | k)$ ;
2. if the scale  $q = \mu$  then there is no emission and the cut-off scale,  $\mu$ , and associated parameter point  $x_\mu$  are returned;
3. The trial scale and splitting variables are accepted with probability

$$\frac{P(q, x)}{R(q, x)}, \quad (4.113)$$

otherwise the process is repeated with  $k = q$ .

This algorithm reproduces the distribution in [Eq. \(4.109\)](#), see [Refs. \[129, 166\]](#).

The standard veto algorithm presented above can be generalised, see [Refs. \[35, 166–169\]](#) to include weights and to relax the requirements so that  $P$  is not required to be positive and removing the restriction on  $R$ , [Eq. \(4.111\)](#). We note that  $S_P$  is still normalized to unity. To achieve this generalization we introduce an acceptance probability  $\epsilon(q, x | k, y)$  such that

$$0 \leq \epsilon(q, x | k, y) < 1.$$

We start with a weight  $w = 1$ , which will be evolved on a splitting-by-splitting basis. Again we start at a scale  $k = Q$  and the modified veto algorithm proceeds as follows:

1. A trial splitting scale and variables,  $q, x$ , are generated according to  $S_R(\mu, x_\mu | q, x | k)$ ;
2. If the scale  $q = \mu$  then there is no emission and the cut-off scale,  $\mu$ , and associated parameter point  $x_\mu$  are returned with weight  $w$ ;

3. The trial splitting variables  $q, x$  are accepted with probability  $\epsilon(q, x|k, y)$  and the returned weight is

$$w \times \frac{1}{\epsilon(q, x|k, y)} \times \frac{P(q, x)}{R(q, x)}; \quad (4.114)$$

4. otherwise the weight becomes

$$w \times \frac{1}{1 - \epsilon(q, x|k, y)} \times \left(1 - \frac{P(q, x)}{R(q, x)}\right), \quad (4.115)$$

and the algorithm continues with  $k = q$ .

The proof that this algorithm produces the correct probability distribution is given in Ref. [35].

#### 4.8.3.2 Application of the modified veto algorithm

The primary motivation for the development of the weighted veto algorithm presented above is to enable more efficient evaluation of shower uncertainties due to scale choices. Using the modified veto algorithm we can perform a shower splitting using a ‘default’ splitting kernel and at the same time calculate the weights for one or several different splitting kernels. In order to evaluate scale variations, we choose our ‘default’ kernel,  $P_0(q, x)$ , to be a given splitting kernel evaluated at some chosen ‘central’ renormalization and factorisation scales,  $\mu_{R,0}$  and  $\mu_{F,0}$ . We generate splitting variables for the shower with this central scale choice, therefore the overestimate,  $R(q, x)$ , is necessarily calculated with these scales. We then choose the acceptance probability to be

$$\epsilon(q, x|k, y) = \frac{P_0(q, x)}{R(q, x)}. \quad (4.116)$$

With this choice the central, unweighted, result is identical to the result obtained using the standard veto algorithm for the default kernel. If we denote the kernel using a different set of scales,  $\mu_{R,i}$  and  $\mu_{F,i}$ , as  $P_i(q, x)$ , we can then evaluate the weight for this variation by substituting  $P(q, x) \rightarrow P_i(q, x)$  in Eqs. (4.114) and (4.115).

There are several additional potential uses of the weighted Sudakov veto algorithm which we will not discuss in detail here. One example is its application to the generation of shower emissions using more complicated, potentially negative, splitting kernels.

There are two considerations that a user should be aware of when using the reweighting approach to evaluate shower uncertainties.

The first consideration is that it should take less time to calculate the results of a given set of scale variations using shower reweighting than by performing a separate event generator run for each scale choice. In cases where the other stages of event generation take significantly more time to run than the shower generation, reweighting should give a sizeable time saving. However, if the process of interest is simple and the hard process simulation is quick, the two approaches can be comparable.

When evaluating uncertainties in the dipole shower, it is virtually always quicker to use reweighting than to perform separate runs, regardless of the complexity of the process. When using the angular-ordered shower, however, it can be the case that for very simple hard processes the time consumed using the reweighting method is comparable to that used by generating separate runs. This is due to differences in the sampling methods used in the two showers.

The dipole shower uses an adaptive-sampling method in which only one acceptance probability is calculated for each trial splitting. The angular-ordered parton shower uses a method in which the computation of the acceptance probability, Eq. (4.116) is split into several parts, as described in [Appendix B](#). As an example, for space-like evolution the splitting kernel is

$$P(q, z) = \frac{1}{q} \frac{\alpha_s(z(1-z)\tilde{q})}{2\pi} P_{\tilde{i}j \rightarrow ij}(z, \tilde{q}) \frac{\frac{x}{z} f(x/z, \tilde{q})}{x f(x, \tilde{q})},$$

where  $\tilde{q}$  is the angular-ordered evolution variable,  $x$  is the momentum fraction of the branching parton and  $P_{\tilde{i}j \rightarrow ij}(z, \tilde{Q})$  is the splitting function given in Eq. (4.23). A simple overestimate can be written as

$$R(q, z) = \frac{1}{q} \frac{\alpha_s^{\text{over}}}{2\pi} P_{\tilde{i}j \rightarrow ij}^{\text{over}}(z) \text{PDF}^{\text{over}}(z),$$

where  $\alpha_S^{\text{over}}$ ,  $P_{ij \rightarrow ij}^{\text{over}}(z)$  and  $\text{PDF}^{\text{over}}(z)$  are the overestimates of  $\alpha_s(z(1-z)q)$ ,  $P_{ij \rightarrow ij}(z, q)$  and  $\frac{\frac{x}{z}f(x/z, q)}{xf(x, q)}$ , respectively. The veto is applied separately for the three weights

$$w_1 = \frac{\alpha_s(z(1-z)q)}{\alpha_S^{\text{over}}}, \quad w_2 = \frac{P_{ij \rightarrow ij}(z, q)}{P_{ij \rightarrow ij}^{\text{over}}(z)}, \quad w_3 = \frac{\frac{\frac{x}{z}f(x/z, q)}{xf(x, q)}}{\text{PDF}^{\text{over}}(z)}.$$

The evaluation of  $w_3$  is the most time-consuming piece of the calculation. In the standard algorithm, the calculation is organised such that  $w_3$  is only evaluated if the emission is accepted following the tests on  $w_1$  and  $w_2$ . The reweighting method however requires that the complete weights are calculated for the central run and all of the variation runs for each trial emission. This is because the weights are evolved according to Eqs. (4.114) and (4.115) for accepted and vetoed emissions respectively. If the time taken to evaluate these weights is significant compared to the rest of the evolution it is possible that, for the given process, the reweighting method could be slower than performing separate runs.

In practice when all parts of the simulation, e.g. hadronization and decays, are included, reweighting is faster than performing separate runs even for the majority of simple processes. Furthermore, performance will improve rapidly with increasing complexity of the hard process.

The second point to consider is that if the variation of the weights about 1 is large for one or more of the scale variations, then a large number of reweighted events will be required in order for the reweighted result to converge, within an acceptable error, on that obtained by directly simulating the events. Furthermore, there may be regions of phase-space which would be populated with the varied scales but which are not filled for the central value, and hence have infinite weight.

A very efficient sequence of the veto algorithm at the central scale is one where the overestimate is very similar to the kernel, i.e.  $\epsilon(q, x|k, y) \sim 1$ . It follows from Eq. (4.115) that a very efficient central evolution is likely to significantly broaden the weight distributions of the reweighted results. There is therefore a trade-off between achieving an efficient algorithm for the central scale choice, which reduces run time, and producing a narrow weight distribution for the reweighted runs, which reduces the number of events required.

We can make the veto algorithm for the central run less efficient by introducing a ‘detuning’ parameter  $\lambda > 1$  which multiplies the overestimate in the denominator of the acceptance probability, Eq. (4.116). The only requirement on the overestimate used to compute the acceptance probability is that it is greater than the splitting kernel in the numerator at all points in phase-space. Therefore we can increase the denominator in Eq. (4.116), to reduce the efficiency of the algorithm without affecting its validity.

Using the reweighting method, multiple scale variations can be specified and evaluated in a single run. The `AddVariation` interface of the `ShowerHandler` class can be used to add variation. Each variation requires a name, `NameOfVariation`, and a specification of the scale factors to apply to the central renormalization and factorisation scales,  $\mu_R$  and  $\mu_F$  respectively. Finally we can choose to apply the scale variation in the showering of the hard process only, the showering of secondary interactions only or in both by specifying `Hard`, `Secondary` or `All` respectively. The detuning parameter discussed above can be set using the `Detuning` interface of the `SplittingGenerator` class for the angular-ordered parton shower and the `Detuning` interface of the `DipoleShowerHandler` class for the dipole shower.

#### 4.8.4 Parton shower reweighting

##### 4.8.4.1 Angular-Ordered shower

There are two mechanisms provided in the angular-ordered parton shower to allow either individual emissions, or the whole parton shower to be vetoed so that different matching techniques to be implemented, or the event generation optimised by requiring the shower to have specific features, for example the presence of a  $b\bar{b}$  pair. Both types of veto can be implemented by inheriting from the relevant base class and then implementing the veto requirement.

- **Shower Veto** Classes inheriting from the `ShowerVeto` class only have access to the parton initiating the parton shower, the parton currently undergoing showering and the kinematics of the trial emission. The inheriting classes have the option of vetoing the individual emission, the full parton shower, or the whole event.
- **Full Shower Veto** Classes inheriting from the `FullShowerVeto` class have access to the full event and therefore can apply a veto to the whole showering process, an example can be found in the `Contrib/ShowerVeto` which veto parton showers which have not produced a  $b\bar{b}$  pair so that  $b\bar{b}$  final states can be efficiently simulated.

In Ref. [170], the implementations of both the Shower Veto and the Full Shower Veto classes are used to consistently match Les Houches events for the process of  $t\bar{t}$  production that already contain radiative corrections in the top decay, as generated by the POWHEG BOX RES framework [171].

#### 4.8.4.2 Dipole shower

There are two mechanisms provided in the Dipole Shower that allow for the reweighting of either a single splitting or the whole parton shower cascade. Both mechanisms are available to classes inheriting from the `DipoleEventReweight`.

- **Splitting Reweighting** is accomplished by the `weight` member function of the inheriting classes. This has access to the implementation of the strong couplings used in the parton shower and the kinematics of both the hard process and the splitting (i.e. the weight can be a function of the splitting’s kinematics). The weight can be applied to all or only to selected branching’s of the Parton Shower.
- **Cascade Reweighting** is accomplished by the `weightCascade` member function. As in the case of the Splitting Reweighting, this weight can be a function of the splitting kinematics. However, this weight is applied to a cascade only once, even in the case of no-emissions.

For example, the `KrkNLO` and `Colour Matrix Element Corrections` methods utilise both of these reweighting mechanisms, the former method is described below.

## 4.9 Code structure

The Herwig shower module has one main `ShowerHandler` class which inherits from the `CascadeHandler` class of ThePEG and implements the core functionality which is independent of the nature of the shower. It has responsibility for the overall administration of showering and the multiple interactions, including:

- Identifying the partons which should be showered;
- Using the inheriting classes to generate the radiation from the primary hard process;
- Performing the decays of any particles whose lifetime is less than the hadronization time-scale, or identify any cases where external programs have supplied partonic configurations which include particle decays, and then using the inheriting classes to perform the parton shower;
- Generating any additional scattering processes using a class inheriting from the `UEBase` class as described in Section 8, and using the inheriting classes to perform the parton shower;
- Performing the forced splitting and handling of the beam remnants using the `HwRemDecayer` class.

The `ShowerHandler` class also provides `switches` to either enable or disable radiation, in the initial or final state, for different interactions:

- `DoISR` switch on (Yes) and off (No) initial-state radiation.
- `DoFSR` switch on (Yes) and off (No) final-state radiation.
- `SplitHardProcess` whether or not to try and split the hard process into production and decay processes.
- `RestrictPhasespace` switch on (Yes) or off (No) phase-space restrictions
- `MaxPtIsMuF` Whether or not to use the factorization scale for the hard process as the maximum transverse momentum for emission in the parton shower.

In addition the scales used in the parton shower can be varied using the interfaces described in Section 4.8.

There are two inheriting classes which implement the details of the angular-ordered and dipole shower using a number of helper classes. Both use the `ShowerTriesVeto` to signal that complete showering of a given event failed a predefined number of times. This is handled together with the generation of multiple interactions.

We will only describe the structure of the code, *i.e.* how the various classes work together to generate the parton shower evolution. Detailed documentation of all the classes can be found in Doxygen.

### 4.9.1 Angular-Ordered shower

The angular-ordered shower consists of a large number of classes and is designed to implement the improved angular-ordered shower based on [25] and described above. The main class implementing the angular-ordered parton shower is the `QTildeShowerHandler`, which inherits from the `ShowerHandler`. This class performs the showering of primary and secondary hard scattering processes, and the generation of any radiation produced in the decay of unstable fundamental particles. The `QTildeShowerHandler` uses a number of helper classes to implement various parts of the algorithm together with some data storage classes, which hold information needed to generate the parton shower. This proceeds as follows:

- The particles supplied by the `ShowerHandler` are converted from `Particle` objects, which store particle information in ThePEG, to `ShowerParticle` objects, which inherit from `Particle` and include the storage of the additional information, such as the evolution scales and colour partners, needed to generate the parton shower. Each particle in a hard process, be that the primary scattering process or the subsequent decay of a fundamental particle, is assigned to a `ShowerProgenitor` object containing references to the particle together with additional information required for particles that initiate a parton shower. For each hard process a `ShowerTree` object is created containing the objects for all the particles in the hard process and the information required to shower that process.
- The `PartnerFinder` is then used to find the evolution partners and initial scale for the parton shower from each particle, as described in Section 4.2.3.
- For hard processes if the matrix element used to generate the process inherits from the `HwMEBase` class and implements either hard matrix element corrections, or real emission in the POWHEG scheme, this is generated. Similarly for decay processes if the `Decayer` class inherits from the `DecayIntegrator` and implements either type of correction this is generated. This is described in more detail in sub:Matrix-element-corrections.
- The intrinsic  $p_{\perp}$  of incoming partons in hadronic collisions is also generated at this stage.
- Given the initial scale, the evolution of the particles proceeds as described in Section 4.2.4– Section 4.2.7, using the `SplittingGenerator` class to generate the types and scales of the branchings. In turn the `SplittingGenerator` uses the `SudakovFormFactor` to generate the possible evolution scales for each allowed type of branching and then selects the branching with the highest scale, as described in Section 4.2.4.
- The new `ShowerParticle` <[https://herwig.hepforge.org/doxygen/classHerwig\\_1\\_1ShowerParticle.html](https://herwig.hepforge.org/doxygen/classHerwig_1_1ShowerParticle.html)>``_s` produced in the branching are then evolved until no further branching is possible. When all the particles have been evolved the `KinematicsReconstructor` reconstructs the momentum of all the particles in the shower ( Section 4.2.4– Section 4.2.7).
- Finally, once the parton shower has been generated the `QTildeShowerHandler` inserts them into the `Event` object.

The `QTildeShowerHandler` class is primarily administrative, the actual physics is implemented in the various helper classes. In turn many of the helper classes used by the main classes implementing the shower have their own helper classes for various parts of the simulation.

The `SplittingGenerator` class holds lists of available branchings. They are used to generate the shower variables associated with each branching using objects. The `SplittingGenerator` and `SudakovFormFactor` classes use the following helper classes:

- The `SplittingFunction` class is the base class for defining splitting functions used in the shower evolution. This includes the calculation of the splitting function together with the overestimate, integral and inverse integral of it required to implement the veto algorithm as described in Section 4.2.4 and Section 4.2.5. The splitting functions implemented in Herwig are listed in Section 4.2.2.
- The `ShowerAlpha` class is the base class implementing the running couplings used in the shower evolution.

The `QTildeShowerHandler` uses the `ShowerVeto` class to provide a general interface to veto emission attempts by the shower. The veto may be applied to either a single emission (resetting the evolution scale for the particle to the attempted branching scale), an attempt to shower a given event, or the overall event generation.

Two exception classes are used inside the angular-ordered parton shower module, mainly to communicate exceptional events or configurations, rather than signalling a serious error during event generation. In particular we use `VetoShower` to communicate vetoing of a complete shower attempt and `KinematicsReconstructionVeto` is used to signal an exceptional configuration that cannot be handled by the `KinematicsReconstructor`, resulting in restarting the shower from the original event (similar to a exception).

#### 4.9.1.1 Shower options and interface

After Herwig-7.3.0 the default choice for parton shower for all input files is the AO *QCD+QED+EW* shower with the *dot-product* preserving recoil scheme. If not enabled by default or if a change in the shower setting is needed, the `ShowerHandler` interface can be explicitly configured with:

```
cd /Herwig/Shower
set ShowerHandler:Interactions ALL
```

The `ALL` option corresponds to the *QCD+QED+EW* shower scheme. Other available options include `QEDQCD`, `QCD`, `QED`, and `EWOnly`. Note that the  $\gamma \rightarrow W^+W^-$  EW branching is part of the QED parton shower and can be accessed using either the `ALL` or `QED` options.

Also, the recoil schemes for both final-state and initial-state radiation are introduced: transverse-momentum preserving, virtuality-preserving, and dot-product preserving scheme. The evolution scheme can be altered using the commands:

```
cd /Herwig/Shower
set ShowerHandler:EvolutionScheme DotProduct
```

which is the default, while the other schemes can be chosen via the Q2 or pT switches.

### 4.9.2 Dipole shower

The primary class which steers the dipole shower is the `DipoleShowerHandler`, which inherits from the `ShowerHandler` class. The `DipoleShowerHandler` controls the showering of primary and secondary hard scatterings, and the showering of the decays of any unstable fundamental particles. The decay processes are showered in the `DipoleShowerHandler`, directly after the showering of a primary hard scattering. The `DipoleShowerHandler` uses several helper classes and data storage classes to perform and record the showering procedure.

The dipole shower proceeds as follows:

- The `DipoleEventRecord` contains the data storage objects for the showering of an event and is responsible for updating these objects throughout the showering procedure. In the first step of showering a hard scattering, the `DipoleEventRecord` takes the particles provided by the `ShowerHandler` and stores them as required by the dipole shower. The `DipoleEventRecord` sorts the incoming and outgoing particles for the given process into `DipoleChains`, in which neighbouring pairs of partons form `Dipole` objects as described in [Section 4.3.2](#). In the case of a decay process, if the `Decayer` class inherits from the `DecayIntegrator` and implements the QCD real emission in the POWHEG scheme, this first emission is generated and the `DipoleEventRecord` is updated accordingly.
- The `DipoleShowerHandler` assigns an initial scale to each parton in each dipole, as described in detail in [Section 4.3.2](#). The `DipoleEvolutionOrdering` class is used to return the maximum physically allowed splitting scale for each dipole.
- The `DipoleSplittingGenerator` class interfaces to the ExSample library [78] and directs the sampling of the branching probability and Sudakov form factor for a given splitting. The `DipoleIndex` class identifies a *type* of dipole based on the properties of the emitter and spectator partons. The dipole shower algorithm proceeds as described in [Section 4.3.1](#), whereby all possible splittings from each dipole under consideration are tried. For each dipole the `DipoleIndex` is constructed and, if the `DipoleIndex` has not previously been encountered, a `DipoleSplittingGenerator` object is constructed, and stored, for each possible splitting.
- The `DipoleSplittingInfo` class is a data-storage class used to store the information required to generate a splitting from a particular dipole. `DipoleSplittingInfo` objects are created and used as required throughout the showering procedure.
- For each trial splitting the `DipoleEvolutionOrdering` class uses output from the `DipoleSplittingGenerator` object to return the splitting scale for that splitting. The `DipoleShowerHandler` selects the trial splitting with the highest splitting scale. The chosen splitting is performed by the `Dipole` object which uses the `DipolePartonSplitter` class to update the parent-child relationships of the partons involved. The showering of a process finishes once all of the `DipoleChains` have been evolved.
- The generation of the intrinsic  $p_{\perp}$  of incoming partons in hadronic collisions is performed by the `IntrinsicPtGenerator`, according to the procedure described in [Section 4.5.2](#).
- Following the showering of a hard scattering or decay process, the `ConstituentReshuffler` class is used to put the outgoing partons on their constituent mass shell according to the procedure described in [Section 4.3.5](#).
- Finally the `DipoleEventRecord` updates the `Event` object to include the completed shower.

In the above we have stated that `DipoleSplittingGenerator` objects are stored. The numerical sampling of a multi-dimensional distribution is computationally expensive, whereas the memory requirements of storing these distributions are, in the case at hand, very small. `DipoleSplittingGenerator` objects are therefore created and stored once and are used throughout each generator run. Furthermore the ExSample library implements an adaptive sampling method, which necessarily requires the storage and reuse of the distributions to provide a benefit over non-adaptive sampling.

The `ConstituentReshuffler`, `IntrinsicPtGenerator` and `DipoleEvolutionOrdering` objects used in the shower are all set via interfaces to the `DipoleShowerHandler`. Currently only a single default implementation is available for each of these classes, however this structure enables future development and investigation. The `DipoleEvolutionOrdering` class is a pure abstract class and in practice the inheriting `DipoleChainOrdering` class, which implements the default  $p_{\perp}$ -ordered scheme, is used.

There are two other important classes that are necessary for the implementation of the dipole shower which, for clarity, we have avoided referring to explicitly in the description above:

- The `DipoleSplittingKernel` class is the base class for defining splitting kernels used within the dipole shower. There is an inheriting class corresponding to each possible splitting in the dipole shower, each of which includes the calculation of the appropriate splitting function, see [Section 4.3.3.4](#). Each `DipoleSplittingGenerator` object contains a `DipoleSplittingKernel` object, which it uses to construct the branching probability for the given splitting.
- The `DipoleSplittingKinematics` class is the base class for implementing the kinematical prescription for a splitting from a dipole. There is an inheriting class for each type of dipole discussed in [Section 4.3.3.3](#), each of which includes the computation of the momenta of the new partons following a given splitting and the calculation of several important scales. Additionally, the `DipoleSplittingKinematics` class computes the Jacobians required by the `DipoleSplittingGenerator` to construct the branching probabilities.

### 4.9.3 Decays

The code structure for particle decays in Herwig is described in more detail in [Section 9](#) for the hadronic decays. All of the `Decayer` classes for fundamental particles inherit from the `DecayIntegrator` class in order to use the multi-channel phase-space integration it provides.

There are a small number of decays of fundamental Standard Model particles currently implemented. These are implemented as `Decayer` classes for top quark,  $W^\pm$  and  $Z^0$ , and Higgs boson decays. The following classes are available:

- the `SMTopDecayer` implements the three-body decay of the top quark to the bottom quark and a Standard Model fermion-antifermion pair, via an intermediate  $W^+$  boson. This class implements the soft and hard matrix-element corrections to top decay for use with the angular-order parton shower [\[52\]](#). In addition the `SMTopDecayer` class also implements the hardest emission in the POWHEG scheme for use with either parton shower module [\[54\]](#).
- the `SMWDecayer` class implements the decay of the  $W^\pm$  boson to a Standard Model fermion-antifermion pair including the soft and hard matrix-element corrections for use with the angular-ordered parton shower. The `SMWDecayer` class also implements the hardest emission in the POWHEG scheme for use with either parton shower module.
- the `SMZDecayer` class implements the decay of the  $Z^0$  bosons to a Standard Model fermion-antifermion pair including the soft and hard matrix-element corrections for use with the angular-ordered parton shower. The `SMZDecayer` class also implements the hardest emission in the POWHEG scheme for use with either parton shower module.
- the `SMHiggsFermionsDecayer` class implements the decay of the Higgs boson to a Standard Model fermion-antifermion pair, *i.e.*  $h^0 \rightarrow f\bar{f}$ . The `SMHiggsFermionsDecayer` class implements the hardest emission and next-to-leading order rate in the POWHEG scheme for use with either parton shower module [\[172\]](#).
- the `SMHiggsWWDecayer` implements the decay of the Higgs boson to  $W^\pm$  or  $Z^0$  bosons, *i.e.*  $h^0 \rightarrow W^+W^-$ ,  $Z^0Z^0$ , including the decay of the gauge bosons.
- the `SMHiggsGGHiggsPPDecayer` implements the decay of the Higgs boson to a pair of either gluons or photons.

In many cases off-shell effects for the EW gauge bosons are included by generating the gauge bosons as intermediate particles, for example in top quark and Higgs boson decays. In general, external top quarks and  $W^\pm$  and  $Z^0$  bosons are produced off mass-shell using the approach described in Ref. [\[173\]](#). Given the observed mass of the Standard Model Higgs boson, the mass of the Higgs boson is now generated with a simple Breit-Wigner lineshape. Rather than the more sophisticated approach described in Ref. [\[174\]](#), which was used in versions of Herwig before the discovery of the Higgs boson.

The `SMHiggsMassGenerator` implements the generation of the mass of off-shell Higgs bosons using the running width implemented in the `SMHiggsWidthGenerator` class. These classes inherit from the `GenericMassGenerator` and `GenericWidthGenerator` classes of Herwig in order to have access to the full infrastructure for the simulation of off-shell particles described in [Section 9](#).

### 4.9.4 YFS-based QED radiation

The structure of the code for the simulation of QED radiation in particle decays is designed to be general, so that other approaches can be implemented. The generation of the radiation is handled by a class inheriting from the abstract `DecayRadiationGenerator` class. Currently only the YFS approach, as described in Ref. [\[52\]](#), is implemented in the `SOPHTY` class, which uses the helper `FFDipole` and `IFDipole` classes for radiation from final-final and initial-final

dipoles, respectively. In addition the `QEDRadiationHandler` is included to allow the `DecayRadiationGenerator` to be used to generate radiation in the decay of particles generated as *s*-channel resonances in the hard process.

## 5 Matching and merging

### 5.1 Overview

Higher-order, in our case next-to-leading-order QCD, corrections cannot be combined naively with parton showers, as the parton shower itself provides approximate higher-order corrections. The inclusion of both the exact and the approximate higher-order corrections amounts to a double counting which needs to be removed, for example by subtracting the approximate calculation from the fixed-order calculation at a given order. This can then be combined with subsequent showering in order to obtain a physical, improved description of the process, retaining NLO formal accuracy. For such an NLO ‘matched’ calculation, the main challenge is to set up the subtracted cross-section incorporating the ‘matching subtractions’, which remove double-counted contributions to  $\mathcal{O}(\alpha_s)$ .

A similar problem arises when one tries to combine several jet multiplicities into one inclusive event sample, such that well-separated hard jets are described by the fixed-order QCD cross section. The transition point to a lower multiplicity in this case should reflect the Sudakov suppression associated with this limit. These merging approaches can exploit both leading-order as well as next-to-leading order QCD cross sections for jet production, and are algorithmically more involved than the NLO matching, and allow for more ambiguities. At the next-to-leading order recent work has particularly focused on the inclusive cross sections obtained from integrating merged samples over additional activity.

Both approaches notably require detailed knowledge of, and interaction with, the subsequent showering, and variations in the parton shower need to be taken into account in setting up the hard, subtracted cross sections for matched and merged predictions. Specifically, the merging algorithms further require detailed control over different contributions of NLO cross sections entering the entire simulation, an option which is available using the Matchbox module.

In this section we will cover the matching and merging algorithms available in Herwig 7, and explain in detail how subtracted cross sections are calculated to be consistently combined with subsequent showering. NLO QCD matching, covered in Section 5.2, is available for both the angular-ordered shower and the dipole shower, while multijet merging, using both LO and NLO QCD multijet cross sections, can currently only be combined with the dipole shower and is described in Section 5.4. The matching and merging modules are closely integrated with the Matchbox module and to some extend with the dipole shower, as far as the merging is concerned, and will be described in Section 5.7.

### 5.2 Handling of matching subtractions

#### 5.2.1 General structure

The NLO matching paradigm in Matchbox [27] is driven by solving a matching condition where the combination of NLO cross section and parton-shower evolution reproduces the NLO cross section exactly, plus higher-order terms, and unavoidably terms suppressed by the parton shower infrared cutoff. In the following sections we will elaborate on the available matching algorithms and their implementation, and on uncertainties from scale variations in matched predictions. We will also address details connected to shower and hard process scale choices, and how they impact the matching uncertainties.

Before we go on to explain how the shower subtractions are exactly combined with the NLO real-emission subtraction terms of a NLO cross section in the subtraction paradigm, however, we quickly repeat the basic ingredients of the latter itself. We write the partonic cross section for the hard process at leading order as

$$\sigma^{\text{LO}}[u] = \int d\sigma^B(\phi_n) df u(\phi_n) ,$$

where  $df$  denotes the parton distribution functions, and  $d\sigma^B(\phi_n)$  and  $u(\phi_n)$  represent the Born cross section and a generic observable as a function of the Born phase-space  $\phi_n = \{p_a, p_b \rightarrow p_1, \dots, p_n\}$ . For more details see Section 3.2.1.

For the NLO calculation, carried out in the subtraction method as detailed in Section 3.3.1, the cross section reads

$$\sigma^{\text{NLO}}[u] = \sigma^{\text{LO}}[u] + \sigma^{V+A+C}[u] + \sigma^{R-A}[u] , \quad (5.1)$$

combined from the leading-order cross section  $\sigma_{\text{LO}}$ , as well as the finite combination  $\sigma^{V+A+C}$  of virtual corrections, analytically integrated subtraction terms, as well as collinear counterterms, all defined over the Born phase-space point  $\phi_n$  and handled accordingly. For further details see Section 3.3.1.2.

The matching of parton showers to NLO calculations generically proceed through subtracting a fixed-order expansion of the parton shower from the hard process calculation. As our parton shower algorithms, including those supplemented by

a matrix element correction, are based on unitarity, virtual contributions from the parton shower appear in a similar form as the subtraction terms in the NLO calculation, and real emission contributions from the parton shower can accordingly be viewed on the same level as the real emission in the fixed-order calculation. Owing to this we focus in particular on the NLO subtracted real-emission cross section, including an additional jet,

$$\sigma^{R-A}[u] = \int \left[ d\sigma^R(\phi_{n+1}) u(\phi_{n+1}) - \sum_i d\sigma_{(i)}^A(\phi_{n+1}) u(\tilde{\phi}_{n|(i)}(\phi_{n+1})) \right] df ,$$

where the subtraction terms  $d\sigma_{(i)}^A(\phi_{n+1})$  and the real-emission contributions  $d\sigma^R(\phi_{n+1})$  are functions of the real-emission phase-space point  $\phi_{n+1}$ ; each of the dipole configurations  $(i)$  is associated with a particular kinematic mapping  $\tilde{\phi}_{n|(i)}(\phi_{n+1})$  onto the corresponding underlying tilde Born phase-space point. These mappings admit phase-space convolutions which can be cast into phase-space factorizations upon introducing suitably adapted parton distribution functions,

$$d\phi_{n+1} df|_{\phi_{n+1}=\tilde{\phi}_{n+1|(i)}(\phi_n, r)} = \mathcal{J}_{(i)}(\phi_n, r) d\phi_n df_{(i)} dr ,$$

Here  $\tilde{\phi}_{n+1|(i)}(\phi_n, r)$  is the inverse mapping to  $\tilde{\phi}_{n|(i)}(\phi_{n+1})$ , and  $r$  denotes the set of additional emission variables – typically chosen to be scale of the emission, a momentum fraction, and an azimuthal variable. In terms of the corresponding real emission variables  $R_{(i)}(\phi_{n+1})$  we have

$$\tilde{\phi}_{n+1|(i)}(\tilde{\phi}_{n|(i)}(\phi_{n+1}), R_{(i)}(\phi_{n+1})) = \phi_{n+1} .$$

For more details see Section 3.3.1.1. As further described in Section 3.3, Matchbox uses diagrammatic information to deduce which subtraction terms need to be included, and automatically sets up the NLO calculation in the form described above.

## 5.2.2 Matching subtractions

The parton-shower action can formally be described in terms of a parton-shower operator as

$$\sigma[u] \rightarrow \sigma[\text{PS}_{\mu_{\text{IR}}}[u]] ,$$

with the parton-shower operator itself being defined by

$$\begin{aligned} \text{PS}_{\mu_{\text{IR}}}[u](\phi_n) &= \Delta(\phi_n, \mu_{\text{IR}}) u(\phi_n) \\ &+ \sum_i dP_{(i)}(\phi_n, r) \kappa(Q_{(i)}(\phi_n), p_{\perp}(r)) \theta(q(r) - \mu_{\text{IR}}) \\ &\times \Delta(\phi_n, q(r)) \text{PS}_{\mu_{\text{IR}}}[u](\tilde{\phi}_{n+1|(i)}(\phi_n, r)) , \end{aligned} \quad (5.2)$$

or up to the first emission by

$$\begin{aligned} \text{PS}_{\mu_{\text{IR}}}[u](\phi_n) &= \prod_i \Delta_{(i)}(\phi_n, \mu_{\text{IR}}) u(\phi_n) \\ &+ \sum_i dP_{(i)}(\phi_n, r) \kappa(Q_{(i)}(\phi_n), p_{\perp}(r)) \theta(q(r) - \mu_{\text{IR}}) \\ &\times \prod_j \Delta_{(j)}(\phi_n, \mu_{\text{IR}}) u(\tilde{\phi}_{n+1|(i)}(\phi_n, r)) . \end{aligned} \quad (5.3)$$

Here  $q(r)$  is the evolution variable, limited from above by a hard scale  $Q_{(i)}(\phi_n)$  – given a splitting configuration  $(i)$  – and from below by the infrared cutoff  $\mu_{\text{IR}}$ , and  $r$  denotes the set of associated emission or splitting variables. The splitting probability density then involves the no-emission probability in terms of the Sudakov form factor

$$-\ln \Delta_{(i)}(\phi_n, \mu_{\text{IR}}) = \int dP_{(i)}(\phi_n, r) \kappa(Q_{(i)}(\phi_n), p_{\perp}(r)) \theta(q(r) - \mu_{\text{IR}}) . \quad (5.4)$$

Note that the constraint on the hard scale is in general not a sharp cutoff, but might be imposed in different ways, as indicated by the profile scale choice  $\kappa(Q_{(i)}(\phi_n), p_{\perp}(r))$  above, further discussed below and in Section 4.8.1. Further note that we choose the same kinematic mapping as for the dipole subtraction terms. In fact, the kinematic reconstruction, as well as the kinematics used in the dipole shower and the Powheg correction discussed further below, are for one emission equal to the dipole subtraction kinematics, and we do not consider any additional Jacobian factors because of

it. We stress, however, that the Matchbox module does allow to include such additional Jacobian factors, and that this is not a conceptual limitation. Notice that we have not specified what shower we consider here – the structure outlined can cover both the angular ordered, as well as the dipole shower; they might also include matrix element corrections, which we view in the same way.

At this point we can expand the shower action to first order in  $\alpha_s$  and then subtract this from the NLO cross section. In order to facilitate the subtraction we recast both the integrand of the Sudakov exponent as well as the emission rate times Born cross section into a cross section level form using the inverse of the kinematic mapping,

$$d\sigma_{(i)}^{\text{PS}}(\phi_{n+1}) df \equiv \left[ d\sigma^B df_{(i)} dP_{(i)}(\phi_n, r) \kappa(Q_{(i)}(\phi_n), p_\perp(r)) \right]_{\phi_n = \tilde{\phi}_{n|(i)}(\phi_{n+1}), r = R_{(i)}(\phi_{n+1})}, \quad (5.5)$$

where we have not yet discussed the infrared cutoff for reasons which will become clear below. Eventually the NLO matching subtraction term to start with is

$$\sigma^{R-A,\text{PS}}[u] = \sum_i \int d\sigma_{(i)}^{\text{PS}}(\phi_{n+1}) df \theta(q_{(i)}(\phi_{n+1}) - \mu_{\text{IR}}) (u(\phi_{n+1}) - u(\tilde{\phi}_{n|(i)}(\phi_{n+1}))),$$

with the shorthand  $q_{(i)}(\phi_{n+1}) = q(R_{(i)}(\phi_{n+1}))$ . From this the matching-subtracted NLO cross section is

$$\sigma^{\text{NLO,matched}}[u] = \sigma^{\text{NLO}}[u] - \sigma^{R-A,\text{PS}}[u],$$

such that  $\sigma^{\text{NLO,matched}}[\text{PS}_{\mu_{\text{IR}}}[u]] = \sigma^{\text{NLO}}[u] + \text{h.o.}$  Combining with the dipole subtraction terms, which enumerate the possible shower branchings assuming that the showers we consider here do require the introduction of a spectator or colour partner, we can write

$$\sigma^{\text{NLO,matched}}[u] = \sigma^S[u] + \sigma^H[u],$$

with

$$\begin{aligned} \sigma^S[u] &= \sigma^{\text{LO}}[u] + \sigma^{V+A+C}[u] \\ &+ \sum_i \int (d\sigma_{(i)}^{\text{PS}}(\phi_{n+1}) \theta(q_{(i)}(\phi_{n+1}) - \mu_{\text{IR}}) - d\sigma_{(i)}^A(\phi_{n+1})) df u(\tilde{\phi}_{n|(i)}(\phi_{n+1})), \end{aligned}$$

which constitutes Born-type configurations, referred to as  $S$  events, as well as

$$\sigma^H[u] = \int (d\sigma^R(\phi_{n+1}) - \sum_i d\sigma_{(i)}^{\text{PS}}(\phi_{n+1}) \theta(q_{(i)}(\phi_{n+1}) - \mu_{\text{IR}})) df u(\phi_{n+1}),$$

to provide real-emission type configurations, referred to as  $H$  events. Note that these contributions are not yet finite owing to the presence of the parton shower infrared cutoff. Even if the parton-shower approximated cross section would be able to reproduce the full singularity structure of the real emission, uncancelled divergences will remain unless the parton shower cutoff is eliminated from the matching subtraction. In order to achieve this we introduce an additional auxiliary cross section,

$$\sigma^X[u] = \sum_i \int d\sigma_{(i)}^X(\phi_{n+1}) df \theta(\mu_{\text{IR}} - q_{(i)}(\phi_{n+1})) (u(\tilde{\phi}_{n|(i)}(\phi_{n+1})) - u(\phi_{n+1})),$$

which is added to the matched cross section and yields modified versions of  $\sigma^S$  and  $\sigma^H$ , which can be employed to generate events. In practice, we use the dipole subtraction terms themselves to facilitate this, i.e.  $d\sigma^X = d\sigma^A$ . Note that, for infrared-safe observables  $u$ ,  $\sigma^X$  only adds power corrections below the infrared cutoff. Technically, the combination of the auxiliary cross section, the shower kernels and the NLO subtraction terms are combined into one modified subtraction. The matching modules, in particular the ShowerApproximation class instances, hold pointers to the respective shower objects such that they will consistently adjust changes to the showers in evaluating the matching subtractions.

### 5.2.3 Showers without matrix element correction – subtractive matching

Both the angular-ordered and the dipole showers fit into the framework outlined above, which constitutes the subtractive, or MC@NLO-type, matching in Herwig 7, and the sole task is to determine the shower matching subtraction  $d\sigma^{R-A,PS}$ , which we have implemented in a process-independent way in Matchbox. These subtractions are very similar to the dipole subtraction terms, but averaged over azimuthal angle and for colour correlators evaluated in the large- $N_c$  limit. With the recent development of spin-correlation algorithms in both shower modules [33], spin correlations can be restored in these subtractions, and full colour correlations can be justified when using colour matrix-element corrections [44,45], at least for the dipole shower algorithm. For more details on the two showers see Section 4.2 and Section 4.3. It is important to stress that at this point no additional Jacobian factors accounting for different kinematic mappings than the dipole mapping is needed, since there are choices to distribute recoil in the angular ordered shower in a way fully compatible with the Catani–Seymour mapping for a single emission. In fact, we find that for initial-final colour connections there is no alternative due to the constraints imposed, while for final state connections the reshuffling procedure turns out to reproduce the subtraction term mapping even in the fully massive case, and an additional choice for the initial-initial reconstruction has been introduced to reproduce the dipole mapping. Note, however, that this is not a general limitation and all of the structures are in place to account for a broader variety of kinematic mappings and the associated Jacobian factors. Extensions of the matching objects to accommodate different mappings are possible.

### 5.2.4 Matching with matrix element corrections – multiplicative matching

In the previous section we have discussed the subtractive, or MC@NLO-type matching in Herwig 7. Another choice is the multiplicative, or Powheg-type matching for which we employ a hardest emission generator, which performs a shower emission using a modified splitting function, or matrix-element correction determined from the real-emission and Born matrix elements as

$$P_{(i)}(\phi_n, r) \rightarrow \frac{w_{(i)}(\tilde{\phi}_{n+1|(i)}(\phi_n, r))}{\sum_j w_{(j)}(\tilde{\phi}_{n+1|(j)}(\phi_n, r))} \frac{|\mathcal{R}(\tilde{\phi}_{n+1|(i)}(\phi_n, r))|^2}{|\mathcal{B}(\phi_n)|^2},$$

for which the full divergent behaviour is reproduced by construction. A truncated, vetoed shower needs to be included if the hardest emission generated this way is not the first one to occur. For the  $w^{(i)}$  in practice we use dipole-type partitioned Eikonal factors, and the ExSample library [78] to generate emissions according to the Sudakov form factor obtained from the above matrix-element correction. Notice that the matrix element correction simply constitutes another kind of shower, which we handle on equal footing to the other matching subtractions. In particular the remarks regarding scale choices and phase-space restrictions apply equally well to all cases. Matrix element corrections using built-in matrix elements are discussed in detail in Section 5.5.

### 5.2.5 Advanced choices

The infrastructure employed by Matchbox to facilitate the matching subtractions and the generation of the hard emission are also available to other combinations such as pure matrix element corrections for which real emission corrections to the shower are included; virtual corrections are then typically deduced only by employing unitarity. This provides an alternative to study matrix element corrections in a different context and to investigate options such as the scale choices and profiles discussed below in the context of a leading-order merging type procedure. It can simply be achieved by turning off the virtual corrections when using the multiplicative matching paradigm; one then obtains a simulation with leading-order cross section in which the parton shower has been supplemented by a matrix element correction according to the Powheg method.

### 5.2.6 Scales in matching

#### 5.2.6.1 Hard process and veto scales

The two shower modules in Herwig imply an upper limit, the hard veto scale  $Q_\perp$ , which limits the transverse momentum that is available to an emission by the shower. For the  $p_\perp$ -ordered dipole shower this hard veto scale is identical to the starting scale of the dipole shower, while for the angular-ordered shower it is implemented as a veto on the reconstructed transverse momentum. For more details on the two shower modules see Section 4.3 and Section 4.2.

The hard veto scale is not generally fixed but should be of the order of the hard scale that is set by the hard process. The default choice for the hard veto scale is to be equal to the hard process scale,  $Q_\perp = \mu_H$ , which in turn is typically set to the factorization and renormalization scale,  $\mu_H = \mu_R = \mu_F$ . However, all these scales may also be chosen independently in Herwig 7, and in general, depending on the choice for  $\mu_H$ , different choices for  $Q_\perp$  can have differing and significant effects on predicted observables.

For NLO matched predictions, the S and H events (see previous section) separately undergo showering. The S events constitute Born-type events and are treated as such. For H events, however, several complications may arise. The subtracted real-emission cross section could possibly still contain power corrections in the regions where the real emission is soft or collinear. However, there is no strict requirement of exact cancellation between the real-emission matrix element and the subtraction term in any region of phase-space away from these limits. Correspondingly, we can expect to obtain a number of H events with a soft or collinear emission. For such H events it does, however not seem reasonable to choose the hard veto scale to be of the order of the small transverse momentum of the real emission.

We want to set the hard veto scale  $Q_\perp$  to a fairly general choice of scale for the final states that may arise from the hard process. For relatively hard real emissions this scale will probably be of the order of the transverse momentum of that emission. On the other hand this is to be avoided for very soft emissions where we would probably associate the general hard scale of the hard process, as e.g. given by an invariant of the hard final scale. There are choices for  $\mu_H$  that, despite being reminiscent of the scale of the real emission, are relatively large over a wide range of real emission scales. If  $\mu_H$  is large enough, the maximum scale for the first emission will be the maximum scale that is allowed for the given splitting kinematics. In this case, while  $\mu_H$  may be directly affected by the scale of the real emission, the scale of the real emission will have only a small impact on the subsequent showering. In such cases one should consider using an alternative choice for  $Q_\perp$ . There are various scale choices implemented in Herwig 7, that can be used directly, further details on these choices can be found in [Section 3.5](#).

### 5.2.6.2 Profile scale functions

The hard veto scale from the parton shower,  $Q_\perp$  should be large enough to account for the hardness of the process and should not be too small for real emissions in order to remain in the perturbative domain. The balance of these had been discussed above, however,  $Q_\perp$  is too large we find another effect, the summation of an unphysical tower of logarithms in the Sudakov exponent. Here, we think that as this stems entirely from hard emissions, these logarithms should be controlled by fixed-order computations and not the parton shower.

In order to avoid these contributions we introduce a profile scale function  $\kappa(Q^{(i)}(\phi_n), p_\perp(r))$  (cf Eqs. (5.2) to (5.5)). This function, also described in [Section 4.8](#), facilitates an upper limit for the scale of hard parton shower emissions. This upper limit is controlled by the profile scale function in that it interpolates between regions of phase space where too hard emissions are completely vetoed and where they are taken into account completely with a smooth transition between the regions, i.e. for any emission it is some function of the phase-space  $Q_{(i)}(\phi_n) = Q_\perp$ .

The same function will be needed to modify the kernels in the matching subtraction, and in turn regulates how much of the real emission contributions we include as a new, hard process, and how much we let the shower populate regions of hard emission. Note that to first order in the strong coupling, by definition, different profile scales do not generate a difference. However beyond this there will be visible differences, and in particular the transition region between the shower and hard jet phase-space will be affected. In [\[34\]](#) several possible parametrizations of the profile scale choices were investigated for leading-order plus parton-shower predictions. There it was pointed out that the choice of the profile scale, i.e. how to approach the boundary of hard emissions, is non-trivial and highly relevant in the context of NLO plus parton-shower matching.

The choice function that determines the profile scale for any emission is constrained by consistency conditions on central predictions and uncertainties. On the one hand they should not modify the input distributions of the hard process and in addition, uncertainties are expected to become large only in unreliable regions or regions where hadronization effects are dominant. Furthermore, stable results are expected in the Sudakov region. It was found in [\[34\]](#) that the hfact profile does not admit results compatible with these criteria. Instead, using the resummation profile it was found that the angular-ordered and dipole showers are compatible with each other, both in central predictions and uncertainties (despite their very different nature). Further studies, comparing the resummation and hfact profiles in next-to-leading-order plus parton-shower predictions were performed in [\[32\]](#).

In Herwig 7, we set the upper limit on the transverse momentum available to the shower to the hard process scale,  $Q_\perp = \mu_H$ , by default. This in turn is normally set to the factorization and renormalization scale,  $\mu_H = \mu_R = \mu_F$ , however, the hard process, factorization and renormalization scales may also be chosen independently in Herwig 7 as discussed above.

### 5.2.6.3 Scale uncertainties

It is sometimes useful to be able to quantify uncertainties for event generator predictions. To this end variations of the scales involved as well as different central choices and distributions of the scales may be pursued. In order to understand matched predictions it is useful to discriminate the effects of scale uncertainties in different parts of the simulation. This will give a complete picture to understanding similarly systematic uncertainty estimates in more sophisticated setups, like multi-jet merging.

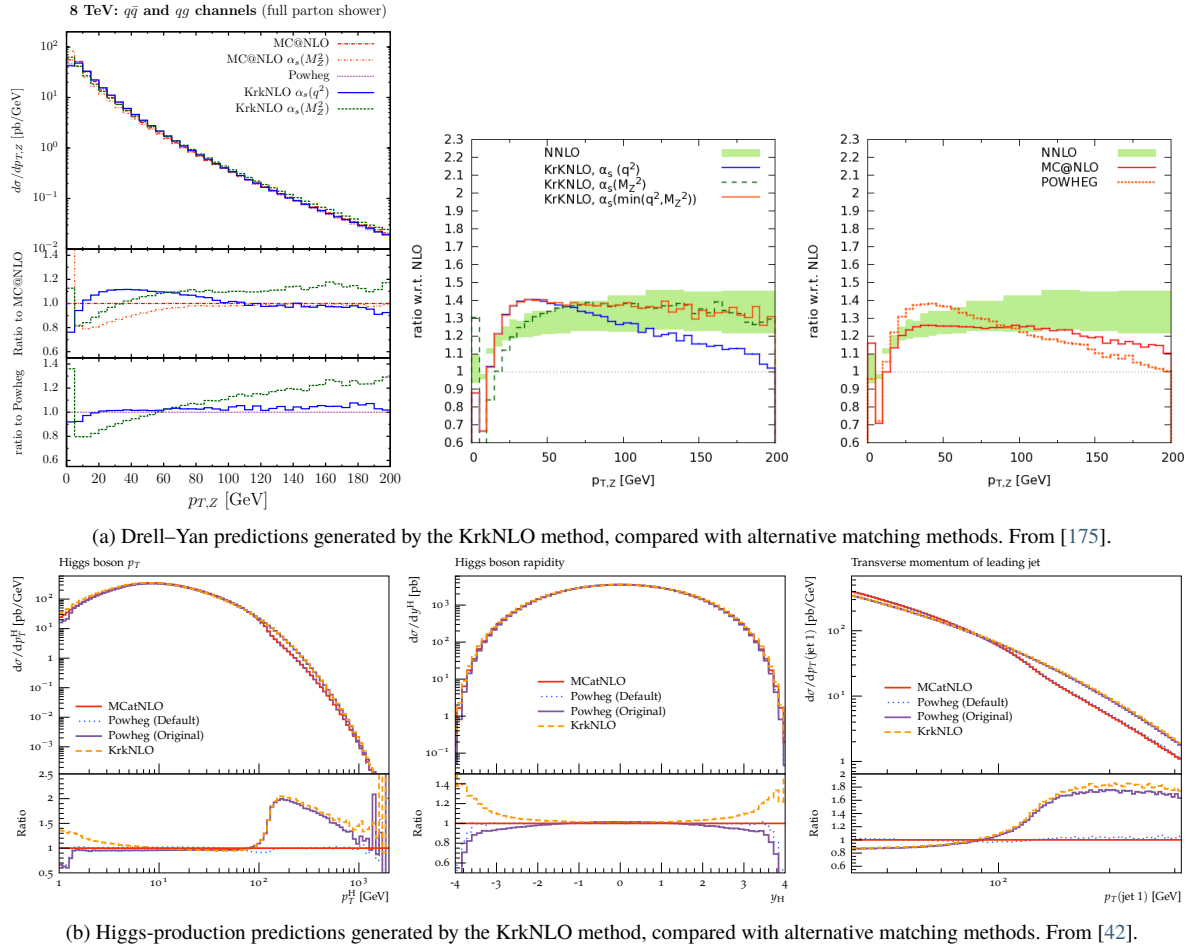


Fig. 5.1: Examples of the KrkNLO method for the processes available in Herwig 7.3.

In regards to scale variations, variations of the scales involved in the hard production process as well as the scales involved in the subsequent parton showering may be pursued. Following the approach in [34] and [32], variations of three scales may be considered:

- the hard process scale  $\mu_H$ , which we typically set to the factorization and renormalization scale in the hard process, i.e.  $\mu_H = \mu_R = \mu_F$ ;
- the parton shower hard scale, or hard veto scale,  $Q_\perp$ ;
- the arguments of  $\alpha_s$  and the PDFs in the parton shower, which we collectively denote as shower scale  $\mu_S$ <sup>1</sup>.

For a full set of scale variations, consisting of 27 different combinations for three scales, one central and one up and down for each, we typically apply multiplicative factors of 0.5, 1 and 2 to each of the corresponding central scales. For more details see also Section 4.8.

In addition to scale variations, one should further consider the impact of different choices for the hard veto scale, depending on the choice of the hard process scale, and the impact of choosing different profile scale functions on top of that, as also described in [34] and [32].

### 5.3 KrkNLO

The KrkNLO method for parton shower matching [42, 43, 175–177] is able to provide NLO matching for colour-singlet processes. In contrast with MC@NLO and Powheg, the KrkNLO method achieves NLO accuracy using a special-purpose factorisation scheme for the parton distribution functions (PDFs), the ‘Krk’ scheme [176] (formerly called the ‘MC’

<sup>1</sup> We are concerned only with variations of the arguments of  $\alpha_s$  and the PDFs in the parton showers. Therefore, even though they can differ, we use the common terminology ‘shower scale’ for these scales. In the angular-ordered shower the argument of the strong coupling is related to the transverse momentum of the emitted parton and differs for initial- and final-state evolution, while the argument of the PDFs is simply the ordering variable for initial-state evolution [25]. In the dipole shower the transverse momentum of the emitted parton is used for both scales.

scheme) instead of the  $\overline{\text{MS}}$  scheme. This is defined to absorb into the PDFs collinear convolution terms, similar in form to  $\sigma^C[u]$ , which cancel those arising from the NLO expansion of the dipole shower Sudakov factor, allowing NLO accuracy to be achieved through a simple multiplicative reweight alone.

Concretely, the method can be expressed as

$$\begin{aligned} \sigma^{\text{KrkNLO}}[u] = & \int d\sigma^B(\phi_n) \left( 1 + \frac{\alpha_s(\mu_R)}{2\pi} \mathcal{B}_n(\phi_n)^{-1} \left( \mathcal{V}_n(\phi_n) + \mathcal{I}(\phi_n) + \Delta_0^{\text{Krk}} \right) \right) \left[ \Delta(\phi_n, \mu_{\text{IR}}) u(\phi_n) \right. \\ & + \sum_i dP_{(i)}(\phi_n, r) \theta(Q_{\max}^{(i)}(\phi_n) - p_\perp(r)) \theta(p_\perp(r) - \mu_{\text{IR}}) \Delta(\phi_n, p_\perp(r)) \\ & \times \left. \frac{\mathcal{R}_{n+1}(\phi_{n+1|(i)}(\phi_n, r))}{\sum_j \mathcal{B}_n(\tilde{\phi}_{n|(j)}(\tilde{\phi}_{n+1|(i)})) P_j(\tilde{\phi}_{n+1|(i)})} \text{PS}_{\mu_{\text{IR}}}[u](\tilde{\phi}_{n+1|(i)}(\phi_n, r)) \right], \end{aligned}$$

where  $\mathcal{I}$  denotes the integrated dipole contributions detailed in Section 3.3.1.3,  $\Delta_0^{\text{Krk}}$  denotes a virtual-like correction arising from the factorisation scheme transition, and  $Q_{\max}^{(i)}$  is the maximum kinematically-permitted scale for an emission from splitting  $(i)$ . For more details please consult [43].

This gives NLO accuracy only when convolved with parton distributions in the Krk factorisation scheme, due to the otherwise-uncancelled  $\mathcal{O}(\alpha_s)$  collinear contributions from the phase-space integral within the Sudakov factor in the first line.

Two versions of the Krk factorisation scheme exist: KrkDY, in which only the quark and antiquark PDFs are transformed (the gluon PDF remains identical to the input  $\overline{\text{MS}}$  scheme gluon PDF), and the full Krk scheme which additionally transforms the gluon PDF. Further details about the properties of the Krk factorisation scheme may be found in [178].

In Herwig, the KrkNLO method is implemented on top of the Dipole Shower using the `DipoleEventReweight`- and `Cascade`- reweight functions. The former is used to apply a matrix-element-correction after the first shower-generated emission, which corrects the weight implied by the Born matrix-element and dipole shower splitting-function to the weight implied by the real-emission matrix element (the third line above). The latter is used to apply a virtual-type correction to the entire shower cascade, which (in particular) corrects the weight of the no-emission events from the weight implied by the Born matrix element to that implied by the Born and virtual matrix elements and the compensatory terms required by the factorisation scheme transformation (the first line above).

In Herwig 7.3.0, only the Drell-Yan and Higgs production (via gluon-fusion) processes are currently supported.<sup>2</sup> Process selection within KrkNLO is controlled by the `Mode` switch of the `KrkNloEventReweight` class:

- **Drell-Yan** [175] The process  $pp \rightarrow Z \rightarrow e^+e^-$  is supported, and can be used with both versions of the PDF factorisation scheme: KrkDY and Krk. The real weight is calculated in an approximation which factorises production from decay, neglecting spin-correlations between the initial- and final-states. This mode is selected by choosing `p p -> e+ e-` as your process in Herwig, and setting `Mode=Z`.
- **Higgs production via Gluon Fusion** [42, 176] The process  $gg \rightarrow H$  is supported and can be used only with the Krk scheme PDFs. The calculation is performed in the large top-mass limit. This mode is selected by choosing `p p -> H` as your process in Herwig, and setting `Mode=H`, as well as `read Matchbox/HiggsEffective.in`. Note that the  $qq$ -initiated tree-level diagram must be generated separately and added manually.

Please note that the KrkNLO method requires the use of the factorisation scale  $\mu_F = \sqrt{\hat{s}_{12}}$ . The renormalisation scale choice used for the real emission is by default the emission scale of the dipole shower, but can be changed to the virtuality of the vector boson or the physical mass of the boson. The renormalisation scale choice used for the virtual (and factorisation scheme) corrections is by default the virtuality of the boson, but can be changed to its physical mass.

A selection of PDF sets, transformed from the  $\overline{\text{MS}}$  to the Krk scheme, are available in LHAPDF6 format from [krknlo.hepforge.org](http://krknlo.hepforge.org). For others, or to request a specific set, please contact the authors.

## 5.4 Multijet merging

The (N)LO merging in Herwig is thoroughly described in [40, 41]. Here we highlight the main features and some aspects of the algorithms. While in the case of next-to-leading order matching there is essentially no ambiguity, once a parton shower to match to has been identified, the multi-jet merging requires an additional resolution criterion to separate regions of hard jet production from regions of jet evolution performed by the parton shower. For one additional emission, one

<sup>2</sup> Additional processes will be supported from Herwig 7.4; see [43, 177].

can view this procedure as a different choice of hard profile scale to be used within the parton shower, but for higher multiplicities this intuitive picture is no longer applicable.

To ensure consistency between the hard multi-jet (matrix-element) regime and the parton-shower-emission regime, the higher jet-multiplicities must explicitly be weighted by Sudakov factors, which account for the exclusiveness of the jet configuration in the hard, matrix-element, region. As described in detail in [40, 41], at leading-order, such a combination does not leave a spurious logarithmic dependence on the resolution criterion, provided that several key criteria are met. At next-to-leading order, however, a naive generalization leads to sub-leading logarithmic contributions which eventually spoil the NLO accuracy of the inclusive cross sections with fewer jets, due to the parton shower itself not containing NLO corrections in a flexible and differential way [40] (some NLO corrections are accounted for inclusively through the CMW scheme).

These spurious contributions can be removed by explicitly subtracting them. The subtraction can be calculated by enforcing that the inclusive cross section is reproduced exactly at its input value. Alternatively, in [41] we have proposed a different scheme, which classifies configurations with additional jets depending on whether we assume that they will lead to a logarithmic enhancement (if they could have been generated by a strongly-ordered parton shower evolution), or should rather be considered an additional, finite correction to the process of interest. In the former case, they will be removed by subtraction; in the latter case they will be explicitly presented to the shower as an additional hard process. This criterion, in particular, allows us also to consider processes with jets at the level of the hard process, and so does not limit the applicability of the merging for hadron-colliders to the case of colour-singlet production.

The hard, matrix element (ME) region is defined by requiring all clusterings which correspond to QCD vertices and a branching in the dipole shower algorithm to yield a transverse momentum larger than the merging scale  $\rho$ , such that in the ordering inherent to the shower evolution they will be produced at scales larger than  $\rho$ . The parton shower (PS) region is complementary to the ME region, and will be populated by parton shower emissions subject to a veto in the ME region. Since we are interested in combining different jet multiplicities, each hard matrix element configuration needs to be interpreted as if it had been produced by the parton shower, and a history is extracted up to the point where we could not have obtained the configuration by an ordered parton shower evolution. This configuration is classified as a core hard process to start the evolution from, and the entire process of clustering into a parton shower history is described in Section 5.4.2.

A complication arises at NLO: while the subtracted virtual corrections are straightforwardly interpreted as a Born-type configuration at a fixed jet multiplicity, the real configurations could now be attributed to either an additional jet, or an unresolved correction to the jet multiplicity associated with the Born process. In the ME region, the real emission is indeed accounted for as an additional jet, while we do perform a ‘standard’ NLO matching in the PS region, by subtracting the parton shower action expanded to the relevant order in the strong coupling. Attaching vetoed parton shower evolution to the configurations thus obtained completes our multijet merging algorithm. We note that momentum conservation with a recoil scheme on an emission-by-emission basis is needed to properly define the phase-space boundaries between the ME and PS regions, and to decide on what should be interpreted as the hard process, and how possible jet selections would act on the hard process definition. Thus unfortunately the multijet merging is only possible with the dipole shower, which conserves momentum on a per-emission basis.

### 5.4.1 General formalism

In order to decide whether a single emission from the parton shower should be kept as a parton shower emission or would fall into the ME phase-space region we use a transparent (vetoed) parton shower, as outlined in [41]

$$\mathcal{PS}_\mu[u(\phi_n, Q)] = \widetilde{\mathcal{PSV}}_\mu[\widetilde{\mathcal{PS}}_\rho[u(\phi_n, Q)]]$$

This shower is aware of the possibility that the emission scale  $q_i$  for a given emission might be chosen different if that emission would have been made from another leg and hence may still fall into the ME region even though it wouldn’t for this particular splitting. This allows us to ensure that parton shower emissions truly populate the parton shower phase-space below the merging scale.  $\widetilde{\mathcal{PS}}_\rho$  only emits in the ME region while  $\widetilde{\mathcal{PSV}}_\mu$  only emits into the PS region. With this definition we can replace emissions in the ME region from  $\widetilde{\mathcal{PS}}_\rho$  by emissions from the full matrix elements in order to achieve a merging algorithm. We thereby ensure that the emission phase-space is completely covered by all emissions and all regions are only accessible by a single type of emission.

The unitarized merging is based on the following expression,

$$d\sigma_n u(\phi_n, q_n) \frac{\partial w_H^n}{\partial \alpha_s} \Big| - \int_\rho^{q_n} dq \sum_\alpha \frac{w_{C,\alpha}}{\sum_\beta w_{C,\beta}} u(\phi_n^\alpha, q_n^\alpha) d\sigma_{n+1} + d\sigma_{n+1} u(\phi_{n+1}, q_{n+1})$$

Here, the first term contains the Born and virtual part of the cross section with a merging weight expanded to NLO in  $\alpha_s$ . The last term contains the contribution of the usual real correction matrix element. The second term subtracts the contributions from possible hard parton shower emissions above the merging scale  $\rho$ . Here, the history weights  $w_H^k$  play a key role and are explained in the following section.

### 5.4.2 History extraction and weights

To construct the shower history of the process with  $n$  additional legs, a tree of cluster nodes is constructed. The nodes are determined by the possible dipoles in the CS subtraction procedure. Each node is able to find the next steps in the reduced multiplicities recursively. With this tree at hand, each node can be asked to find the next set of ordered histories. The extraction requires to find no ordering scale below the merging scale and at least one scale in the “ $n - 2$ ” stage that is larger than the “ $n - 1$ ” evolution scale. If the process with “ $n - 2$ ” legs is part of the multiplicity defining the underlying process, we require that the scale – calculated from the ScaleChoice object – is bigger than the evolution scale.

Once all the possible next-ordered nodes are extracted the algorithm decides probabilistically which node to choose. The probability can be chosen by the user as described in [Section 5.4.5](#).

With the full history at hand, the weights are calculated for each of the shower history steps  $k$  as,

$$w_H^k = \frac{f_k(\eta_k, q^k)}{f_k(\eta_k, \mu_F)} \prod_{i=0}^{k-1} \frac{\alpha_s(q^i)}{\alpha_s(\mu_R)} \frac{f_i(\eta_i, q^i)}{f_i(\eta_i, q^{i+1})} w_N(q^i | q^{i+1}, \phi_i) \quad (5.6)$$

$$w_N(q_a | q_b) = \Pi^{(1,2)}(q_a | q_b) \prod_f \Delta^f(q_a | q_b)$$

### 5.4.3 History expansion

For the fixed order accuracy it is crucial to expand the impact of the shower/resummation to the same accuracy as it is added with the improved full calculation. Compared to the matching, where the expansion of the shower leads to the shower approximation only, the handling in the NLO merging includes more parts. To claim NLO the fixed order accuracy one has to expand not only the same multiplicity and the following as in NLO matching but also the full history of states that contributed to the process in question. In [Section 5.4.2](#) the algorithm to extract the history is described. For each step in this evolution history the weights in Eq. (5.6) need to be expanded to their respective  $\alpha_s$ -expansion. Codewise similar functions are used to calculate the expansions and the actual weights and only minor modifications are needed. To preserve the accuracy of the shower but also the fixed order expansion care needs to be taken that the virtual and real corrections are reweighted similar as the expansion weights, however, there are still ambiguities of how to define the  $\alpha_s$ -expansion (e.g. multiplicative or additive). As every weight is a product of a PDF-weight ( $f$ ), an  $\alpha_s$ -weight ( $\alpha$ ) and a Sudakov-weight ( $\Delta$ ) we can formally subtract the NLO contributions *e.g.* at the level of each factor or globally. Variations should only affect terms of order  $\alpha_s^2$ . To be able to perform such a variation several schemes ( $s$ ) are defined:

- No subtraction of  $\alpha_s$  terms ( $s = 0$ ). This is formally incorrect and is kept for comparison only.
- The  $\alpha_s$ -terms from each weight are subtracted straight away ( $s = 1$ ). This choice seems least ambiguous.
- The  $\Delta$ -weight is kept fixed in the subtraction ( $s = 2$ ).
- All weights are kept fixed in the subtraction ( $s = 3$ ).
- The  $\alpha$ -weight is kept fixed in the subtraction ( $s = 3$ ).

Further details and a comparison of these schemes can be found in [\[41\]](#). While formally all schemes (except  $s = 0$ !) are at the same level of accuracy there are notably numerical differences which should be considered an estimate for this source of uncertainty.

The parameter that controls those expansions is `ShowerExpansionWeights` that belongs to the `Merger` and can be set to the schemes  $s$  as described above.

### 5.4.4 MC-scheme treatment

The so-called MC-scheme [\[133\]](#) that is commonly used in parton showers is used to capture effects of higher-order corrections for final state gluon emissions. Those scheme-dependent corrections, however, are also included if NLO corrections are calculated for the additional emissions. In particular, the modification that is proposed in [\[133\]](#) to make the transition from  $\overline{\text{MS}}$  to MC will have an impact. Including the actual NLO correction and in addition taking into account the main effects of the approximated correction can, therefore, lead to double counting. To circumvent the issue the NLO-merging treats the transition from  $\overline{\text{MS}}$  to MC as an  $\alpha_s$  effect that is taken care of in the  $\alpha_s$ -expansion of the history weight.

### 5.4.5 Merging user choices

As described in Section 5.4.2 a choice has to be made in the extraction of the shower history. To allow variations the weights to choose the history can be modified with the switch,

- `chooseHistory`: The weight to choose the history are calculated from the 0: dipole XS (default): 1: dipole/born: 2: flat: 3:  $1/p_{t,\text{dip}}$
- `MergingScale`: The merging scale is the key scale that is used to define the matrix element region. The scale can be modified with the interface, e.g. ‘set Merger:MergingScale 20\*GeV’.
- `MergingScaleSmearing`: In general the merging scale is an unphysical parameter and the effects of the scale are mild. To minimize further dependencies it is possible to smear the scale. For this, the parameter belonging to the interface Merger: MergingScaleSmearing can be used. E.g. a value of 0.1 would mean a 10% variation.
- `CMWScheme`: As described in Section 5.4.4 the scheme we use to describe the strong coupling is of importance to be consistent with the NLO merging. The merging and the dipoles can be used with three schemes. For comparison, the MC-scheme can be switched off, but the Linear,

$$\alpha_s^{\text{MC}}(q) = \alpha_s^{\overline{\text{MS}}}(q) \left( 1 + K_g \frac{\alpha_s^{\overline{\text{MS}}}(q)}{2\pi} \right) \text{ with } K_g = C_A \left( \frac{67}{18} - \frac{\pi^2}{6} \right) - \frac{5}{9} N_f .$$

or Factor,

$$\alpha_s^{\text{MC}}(q) = \alpha_s^{\overline{\text{MS}}}(kq) \text{ with } k = \exp \left( -\frac{67 - 3\pi^2 - \frac{10}{3}N_f}{33 - 2N_f} \right)$$

schemes are preferred. To steer the behavior the input files `Merging/FactorCMWScheme.in` or `Merging/LinearCMWScheme.in` should be read.

- `ShowerExpansionWeights`: see Section 5.4.3.

### 5.4.6 MergingFactory

As in the case of the matching of NLO calculations to the showers in Herwig, the merging procedure is set up in a SubprocessHandler, here called `MergingFactory`. The syntax to initiate a process is kept close to that used for matching. Compared to the matching an additional square-bracket is included in the process definition, to indicate additional jet multiplicities, e.g. “`p p -> l+ l- [j j]`” would generate the Drell–Yan process with two additional, merged, Born-like processes ( $Z + j$ ,  $Z + 2j$ ) at LO.

These additional merged processes can also be calculated at NLO, using the parameter `NLOProcesses` within the `MergingFactory`. `NLOProcesses` is an integer corresponding to the number of merged processes to be calculated at NLO. The counting starts with the underlying process (i.e., excluding the square-brackets), such that a `NLOProcesses` value of 1 includes only NLO corrections to the underlying Born-like process (“`p p -> l+ l-`” in the example above). Example results from just such a calculation, with `NLOProcesses` set to 2, are shown in Fig. 5.2 and Fig. 5.3, compared to NLO matched results from Matchbox, and CMS data from [179, 180].

As the number of generated subprocesses can be large, it is possible to split up the integration- and run-steps into chunks of subsets. If the `MergingFactory:Chunk` parameter is set to an integer larger than zero, the integration- and run-steps are split into smaller pieces. Each input-file with an integer parameter `MergingFactory:ChunkPart` with values in  $[0, \text{Chunk}]$  contains a subset of processes. The result of each of the subsets needs to be merged by the user at a later stage. Further, the uniqueness and completeness of the sets must be ensured by the user.

## 5.5 Matrix element corrections

For a few processes, we provide a simpler matrix element improvement to the angular-ordered parton shower, which we call matrix element corrections. These can be thought of as a simple form of matching, in that next-order real emission matrix elements are used in phase-space regions that cannot be generated by the parton shower (‘hard’ corrections) and are used to reweight the parton shower distributions via the Sudakov veto algorithm in the region that they do cover (‘soft corrections’). However, no virtual corrections are included, so the normalization is still to the leading order cross section.

These corrections are available for all processes involving a pair of colour-connected partons, i.e.  $e^+e^- \rightarrow q\bar{q}$  and related processes like EW vector boson decay; deep inelastic scattering; Drell–Yan processes; and top quark decay.

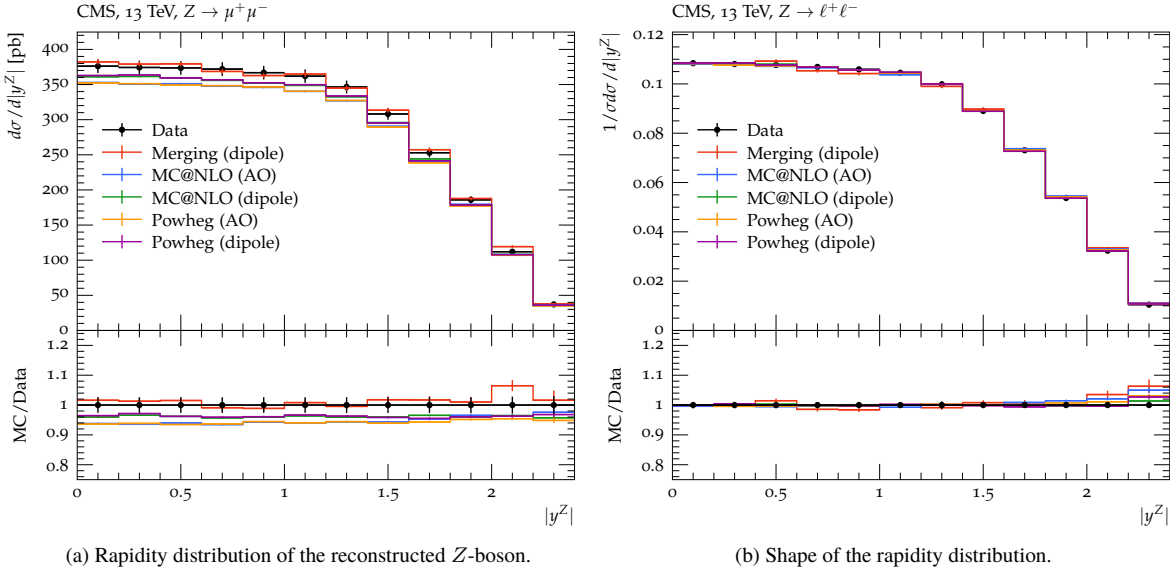


Fig. 5.2: Matching and merging with Matchbox for the Drell–Yan process at the LHC ([179]; CMS\_2019\_I1753680).

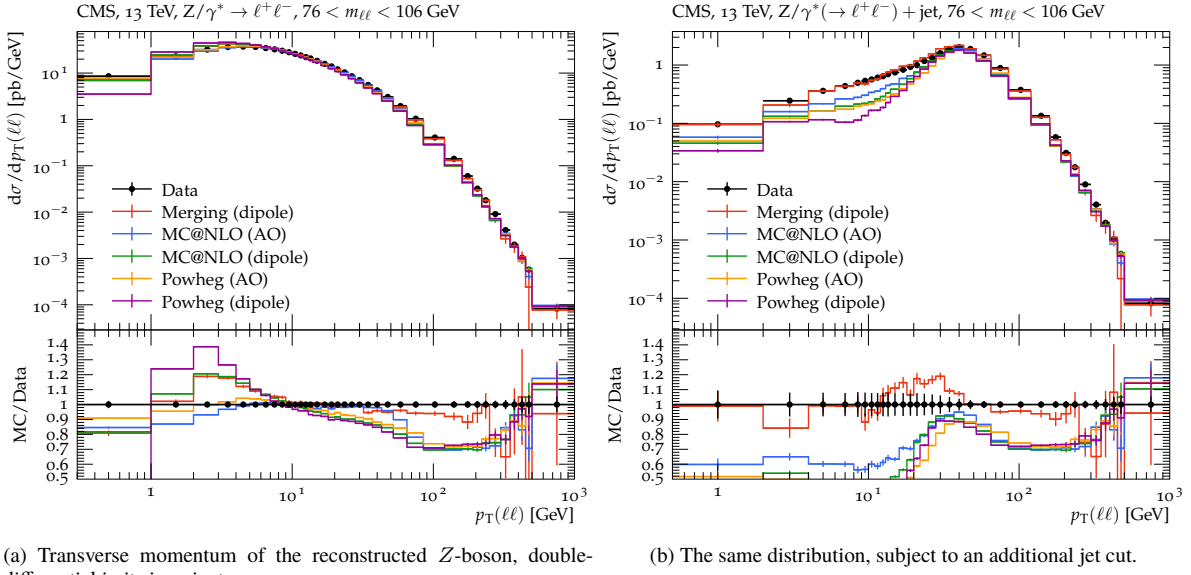


Fig. 5.3: Matching and merging with Matchbox, applied to the Drell–Yan process at the LHC ([180]; CMS\_2022\_I2079374). Even with the additional jet cut, the merged prediction retains NLO accuracy for the transverse-momentum distribution. This could also be obtained from an NLO-matched  $Z + j$  prediction.

In this section, we briefly recap the main features of these hard and soft matrix element corrections. More details can be obtained from Ref. [181].

### 5.5.1 Hard matrix element corrections

Since angular-ordered parton showers only generate radiation within some angularly-defined subset of phase-space, it is common that the first emission cannot cover the whole of phase-space, as is the case for the  $\tilde{q}$ -shower implemented in Herwig 7. Soft emission from the individual emitters is possible at all angles, and their emission regions just ‘touch’ each other, meaning that soft emission is counted once and only once. Collinear emission from each parton populates the full available hard collinear phase-space. However, hard emission cannot be emitted at all angles, and there is a region of phase-space that the shower misses, which we call the dead region.

Since the dead region does not include any soft or collinear emission, the integral of the real-emission matrix element over it is finite. Moreover, it is typically small. Thus it is consistent to ignore any resummation / form factor effects and to simply generate phase-space points across this region weighted by the tree-level matrix element. These are then

used as the starting point for a subsequent parton shower. Since the partons in these configurations are always hard and well-separated there is no merging ambiguity or double-counting with this subsequent emission.

### 5.5.2 Soft matrix element corrections

The parton shower approximation is, by construction, accurate in the soft and collinear limits, and is not guaranteed to remain accurate away from those limits. The idea of the soft matrix element correction is to use the next-order real emission matrix element as a multiplicative reweighting of the emission distribution, similar to elements of the Powheg and KrkNLO methods. The additional element is that it is applied to *every emission that is the hardest* (highest transverse momentum) *so far*. Thus, not only is the hardest emission in the event corrected by the hard matrix element as in those approaches, but when there are multiple widely-separated emissions, they are all emitted independently according to the real emission matrix element.

The veto algorithm used by the shower is then simply augmented by an additional veto with probability given by the ratio of the matrix element distribution over the analytically-calculated parton shower distribution. In cases that this ratio can be greater than unity, a simple extension of the algorithm multiplies the shower emission probability by the smallest integer that bounds the ratio (in practice, 2 is always sufficient) and then the veto brings this down to the correct value.

## 5.6 Matching and merging with `MadGraph5_aMC@NLO` LHE files

The `FxFx` merging module provides support for the NLO multi-jet merging method of [182], via Les Houches-accord event files generated by `MadGraph5_aMC@NLO` [183]. The framework also provides an interface for merging of tree-level events generated either by `MadGraph5_aMC@NLO` or `AlpGen` [158] via the MLM technique. The relevant input files for the `FxFx` merging and tree-level merging are now `LHE-FxFx.in` and `LHE-MGMerging.in` respectively. We emphasize that it is essential to include the MC@NLO matching settings for `MadGraph5_aMC@NLO` when performing the `FxFx` merging, as given in `LHE-MCatNLO.in`. These settings should not be included when merging tree-level events. The tree-level merging functionality via `MadGraph5_aMC@NLO` events uses the event tags in the appropriately-generated LHE files and requires the option `MergeMode` to be set to `TreeMG5`, as is done by default in `LHE-MGMerging.in`. To enable merging with events generated via `AlpGen`, `MergeMode` should be switched to `Tree`.

The `FxFx` functionality was tested thoroughly for  $W +$  jets and  $Z +$  jets events in [184], where it was compared against LHC data at 7 and 8 TeV. Here, we present results at 13 TeV, matched and merged at NLO including 0, 1, 2, 3 jet multiplicities at matrix-element level, with the rapidity distribution of the reconstructed  $Z$ -boson shown in Fig. 5.4, compared to CMS data. The transverse momentum of the reconstructed  $Z$ -boson is shown in Fig. 5.5. A merging scale of 30 GeV was employed, along with hard process scale variations by a factor of 2 up or down.

We note that no tuning was performed using events generated via this interface.

## 5.7 Code structure

The key task of the matching-specific code within Matchbox is to construct explicitly the parton-shower approximation to the real-emission matrix-element in a manner consistent with that constructed implicitly by the active `ShowerHandler` object, which generates the first-emission of the parton-shower algorithm (and then the others) as described in Section 4.9.

This shower-approximation contribution is then combined consistently with the other contributions to the matched cross-section in the `SubtractionDipole` object as described in Section 3.13.

### 5.7.1 Shower approximation

The `ShowerApproximation` class is a base class storing information required by both the angular-ordered and the dipole-shower matching, including pointers to the real and Born `XComb` objects, the `SubtractionDipole` object responsible for the same emission as is under consideration, and the `TildeKinematics` and `InvertedTildeKinematics` objects governing the phase-space mappings between the Born and real phase-space configurations.

It also contains methods which may be overridden by shower-specific implementations in the `DipoleMatching` and `QTildeMatching` subclasses, as described below.

Methods which are common to all concrete implementations (aside from ‘getters’ and ‘setters’) are primarily concerned with identifying the scales and PDF weights associated with the respective Born and real phase-space configurations.

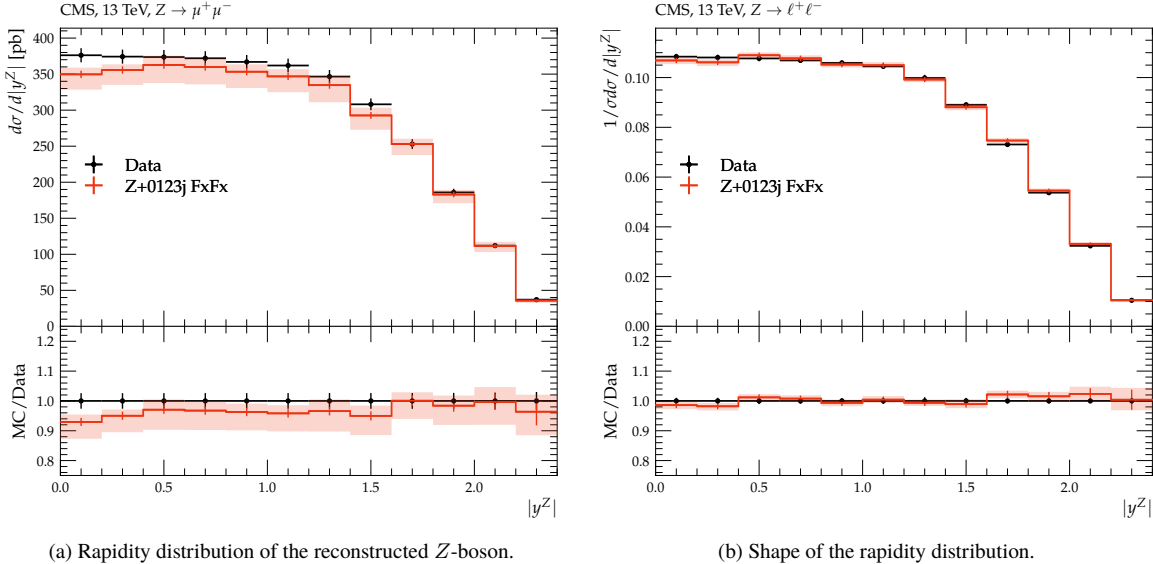


Fig. 5.4: Matching and merging of `MadGraph5_aMC@NLO` LHE files, for the Drell–Yan process at the LHC ([179]; CMS\_2019\_I1753680). A merging scale of 30 GeV was employed, and the bands represent hard process scale variations by a factor of 2 up or down.

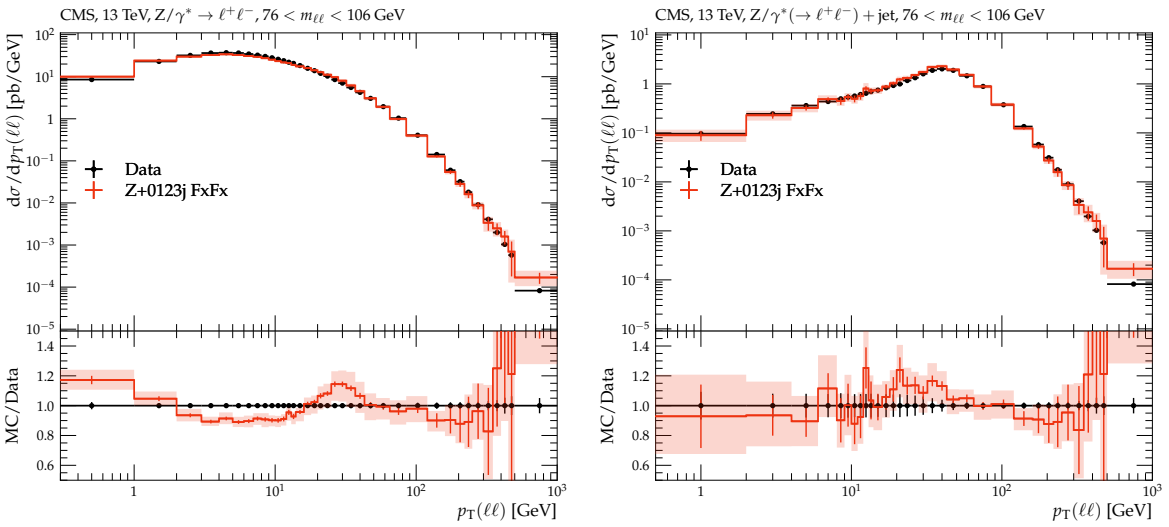


Fig. 5.5: Matching and merging of `MadGraph5_aMC@NLO` LHE files, applied to the Drell–Yan process at the LHC ([180]; CMS\_2022\_I2079374). A merging scale of 30 GeV was employed, and the bands represent hard process scale variations by a factor of 2 up or down.

### 5.7.2 Subtractive matching

As described in Section 5.2.3, Matchbox allows ‘subtractive’, MC@NLO-type matching to both the angular-ordered and dipole showers. These are handled by the `QTildeMatching` and `DipoleMatching` subclasses of the `ShowerApproximation` base class respectively.

In both cases, for each relevant splitting identified by the `MatchboxFactory`, `QTildeMatching` or `DipoleMatching` checks if the specified real phase-space point is within the phase-space region that could be generated via that splitting from the underlying Born configuration, including whether it is above the cut-off scale and below the starting ‘hard’ scale.

If so, it calculates the product of the relevant splitting function with the underlying Born matrix-element, dresses it with the appropriate Born PDF and coupling factors, and prepares it as a contribution to the matched cross-section to be included alongside the others in `SubtractionDipole`.

### 5.7.2.1 Matching to the angular-ordered shower

The `QTildeMatching` class governs subtractive matching to the angular-ordered shower. Concretely, it contains an implementation of the splitting functions associated with each splitting and uses these to construct the shower-approximation.

The shower IR-cutoff is propagated from the `QTildeShower` and applied consistently to the shower approximation, subject to a technical cut-off specified by `SafeCut`.

### 5.7.2.2 Matching to the dipole shower

The `DipoleMatching` class governs subtractive matching to the Herwig dipole shower. In this case, the implementation uses the `SubtractionDipole` objects to calculate the dipole functions.

The shower-approximation IR cutoff is set separately from that used within the dipole shower itself, again subject to the `SafeCut` technical cut-off.

## 5.7.3 Multiplicative matching

As described in [Section 5.2.4](#), Matchbox allows multiplicative matching in which the emission is sampled according to the ratio of real-emission to Born matrix-elements. In practice, this is implemented as a special case of the `ShowerApproximation` class in `MEMatching`, which uses the information provided by the `MatchboxFactory` to assemble the possible splittings together with the corresponding real and Born matrix-elements.

### 5.7.3.1 Shower approximation kernels

The `ShowerApproximationKernel` class implements a splitting generator for sampling from a splitting kernel. For the sampling itself, it uses an instance of the `ExSample` adaptive sampler [78] to construct an adaptive overestimate function for each possible splitting. Since the effective ‘splitting functions’ in the matrix-element corrections case also depend on the Born phase-space, through the Born matrix-element in the denominator of the ratio, the sampler also adapts to the random numbers used to generate the Born phase-space, to help improve the sampling efficiency.

### 5.7.3.2 Shower approximation generator

The `ShowerApproximationGenerator` class implements a single step of the parton shower, by performing a competition between the `ShowerApproximationKernel` splittings identified by the `MatchboxFactory` as being possible from the underlying Born phase-space configuration. These are stored in the `KernelMap` for each Born partonic configuration.

The real-emission matrix-element is partitioned among splitting channels according to dipole-type eikonal factors computed in the `channelWeight` method of the `ShowerApproximation` base class.

Once the competition has been performed and the winning splitting with the highest-scale emission identified, the event record is updated to correspond to the chosen real-emission subprocess.

### 5.7.3.3 Merging

The `MergingFactory` organizes the matrix elements for all involved subprocesses at different orders and provides events with the individual weights. All calculations are carried out by the `Merger`. Here the merging histories are determined and assigned weights as described above. Both classes inherit from `MergerBase` that provides some common interfaces.

## 6 Physics Beyond the Standard Model

No one knows what kind of new physics, if any, will be encountered in the LHC era and a wide variety of new physics models must be studied. This motivated the design of the Herwig program, with the inclusion of a general framework for the implementation of new physics models. Using this framework, new models can be realized quickly and efficiently. This method is described in full in Refs. [56, 173] and will be reviewed and updated here.

In describing the features needed to simulate Beyond the Standard Model (BSM) processes, we need only to concern ourselves with the hard collisions, either producing known particles through modified couplings or the exchange of new particles, or producing new particles in the final state, and with decays of the new particles. All other steps of event generation are handled in the same way as for Standard Model processes.<sup>1</sup> Both of these steps involve calculating an amplitude, which in turn relies on knowledge of the Feynman rules within the model being used. In Herwig, the Feynman rules are implemented as a series of Vertex classes that inherit from the generic classes of ThePEG. These Vertex classes are based on the HELAS formalism [185], with each class able to evaluate the vertex as a complex number or, given different information, an off-shell wavefunction that can be used as input for another calculation. Each Feynman diagram contributing to a given process is evaluated in terms of these vertex building blocks and the sum of the resulting contributions is squared to give the matrix element.

While a number of models are available internally in Herwig, we also provide an interface that can convert models in the UFO format [186] into a library usable by Herwig. We therefore do not expect any further models to be directly implemented in Herwig.

In this section we start by briefly describing the generation of the hard processes and decays in models of new physics. This is followed by a description of the models currently implemented in Herwig, including the Standard Model, the interface to UFO models, and finally the structure of the code.

### 6.1 Hard process

Section 3.9 gave details on the default matrix elements available for generating Standard Model processes in Herwig. These classes are based on specific particle interactions whereas the classes used for BSM models are determined by the external spin structure of a  $2 \rightarrow 2$  scattering process. To generate a specific process the user specifies the desired states that are to participate in the hard interaction, using configuration files, and the code then generates the relevant diagrams and a `MatrixElement` object for each process.<sup>2</sup> In addition to the general  $2 \rightarrow 2$  scattering processes a small number of higher-multiplicity processes are available for neutral scalar bosons, including associated production with either a  $W^\pm$  or  $Z^0$  boson or heavy quark-antiquark pair, and for the vector-boson fusion process.

### 6.2 Decays

In order to decay the BSM states, the possible decay modes must first be known. If a supersymmetric model is required a spectrum generator can be used to produce not only the required spectrum, in accordance with the SUSY Les Houches Accord [114], but also a decay table. Herwig is designed to be able to read this information and set up the appropriate decay modes for later use. Other models do not have such programs and therefore the list of possible two- and three-body decays is generated automatically, together with the option of using hadronic-currents for decays where the mass splitting is small and four-body decays of scalars to fermions.

When generating the possible decays automatically we also need to be able to calculate the partial width of a given mode so that the branching fraction and total width can be calculated. For a general two-body decay, the matrix element only depends on the mass-square values of each particle so the phase-space factor can be integrated separately and the partial width is given by

$$\Gamma(a \rightarrow b, c) = \frac{|\bar{\mathcal{M}}|^2 p_{cm}}{8\pi m_a^2},$$

where  $|\bar{\mathcal{M}}|^2$  is the matrix element squared summed over final-state colours and spins and averaged over initial-state colours and spins and  $p_{cm}$  is the centre-of-mass momentum

$$p_{cm} = \frac{1}{2m_a} \left[ \left( m_a^2 - (m_b + m_c)^2 \right) \left( m_a^2 - (m_b - m_c)^2 \right) \right]^{1/2}.$$

<sup>1</sup> Other features do emerge in certain models, for example the hadronization of new long-lived coloured particles, which is not yet fully implemented in Herwig, but for the majority of new physics models under active study this is the case.

<sup>2</sup> It is only necessary to specify a single outgoing particle as the code will produce all processes with this particle in the final state.

A three-body decay has a partial width given by

$$\Gamma(a \rightarrow b, c, d) = \frac{1}{(2\pi)^3} \frac{1}{32m_a^3} \int_{(m_b+m_c)^2}^{(m_a-m_d)^2} dm_{bc}^2 \int_{(m_{cd}^2)_{\min}}^{(m_{cd}^2)_{\max}} dm_{cd}^2 |\mathcal{M}|^2, \quad (6.1)$$

with

$$(m_{cd}^2)_{\max} = (E_c^* + E_d^*)^2 - \left( \sqrt{E_c^{*2} - m_c^2} - \sqrt{E_d^{*2} - m_d^2} \right)^2, \quad (6.2)$$

$$(m_{cd}^2)_{\min} = (E_c^* + E_d^*)^2 - \left( \sqrt{E_c^{*2} - m_c^2} + \sqrt{E_d^{*2} - m_d^2} \right)^2, \quad (6.3)$$

where  $E_c^* = (m_{bc}^2 - m_b^2 + m_c^2)/2m_{bc}$  and  $E_d^* = (m_a^2 - m_{bc}^2 - m_d^2)/2m_{bc}$  are the energies of  $c$  and  $d$  respectively, in the  $(bc)$  rest frame. In general, the phase-space integration can no longer be performed analytically, because the matrix element is a complicated function of the invariant mass combinations  $m_{bc}$  and  $m_{cd}$ , therefore it must be performed numerically. Given the low number of dimensions of the phase-space integrals in Eq. (6.1), they are performed using standard techniques rather than by the Monte Carlo method. The total width of the parent is simply the sum of the partial widths.

To compute the momenta of the decay products, we need to be able to calculate the matrix element for a selected decay mode. When each mode is created, it is assigned a `Decayer` object that is capable of calculating the value of  $|\mathcal{M}|^2$  for that process. This is done in a similar manner to the hard matrix element calculations, *i.e.* using the helicity libraries of ThePEG.

In decays involving coloured particles that have more than one possible colour flow, the colour is treated in exactly the same way as described in Section 6.1 for hard processes.

In addition for two-body decays we include the real emission correction in the POWHEG matching scheme [54].

### 6.3 Off-shell effects

The production and decay processes described above have their external particles on mass shell throughout. This assumes that the narrow width approximation, defined by the following assumptions:

1. the resonance has a small width  $\Gamma$  compared with its pole mass  $M$ ,  $\Gamma \ll M$ ;
2. we are far from threshold,  $\sqrt{s} - M \gg \Gamma$ , where  $\sqrt{s}$  denotes the centre-of-mass energy;
3. the propagator is separable;
4. the mass of the parent is much greater than the mass of the decay products;
5. there are no significant non-resonant contributions;

is a valid approximation. In general, given that we do not have a specific mass spectrum, this is not a good enough approximation. In particular, if processes occur at or close to threshold, there can be large corrections that we need to take into account.

To improve our simulation we provide an option to include the weight factor

$$\frac{1}{\pi} \int_{m_{\min}^2}^{m_{\max}^2} dm^2 \frac{m\Gamma(m)}{(m^2 - M^2)^2 + m^2\Gamma^2(m)}, \quad (6.4)$$

throughout the production and decay stages, where  $\Gamma(m)$  is the running width of the particle to be considered off shell,  $M$  is the pole mass and  $m_{\min, \max}$  are defined such that the maximum deviation from the pole mass is a constant times the on-shell width. A derivation of this factor can be found in the appendix of Ref. [173].

This procedure could, if naively applied, lead to violations of gauge invariance in production processes. Instead, the distribution (6.4) is used for each particle in the kinematics, but the masses of particle-(anti)particle pairs are projected onto a common value for use in the matrix element evaluation, as discussed and validated in Ref. [173].

## 6.4 Model descriptions

This section gives a description of the models that are included in Herwig. In general within Herwig, the implementation of a physics model consists of a main class, which inherits from the `StandardModel` class and implements the calculation of any parameters required by the model or, for a SUSY model, reads them from an input SUSY Les Houches Accord (SLHA) [114, 115] file. In addition, there are various classes that inherit from the general Vertex classes of ThePEG, which implement the Feynman rules of the model. There may also be some classes implementing other features of the model, for example the running couplings in the specific model.

### 6.4.1 Standard Model

The implementation of the Standard Model in Herwig inherits from the `StandardModelBase` class of ThePEG. ThePEG includes classes to implement the running strong and electromagnetic couplings, together with the CKM matrix.

In Herwig we include our own implementations of the running electromagnetic coupling, in the `AlphaEM` class, and the running strong coupling in the `O2AlphaS` class. However, by default we use the implementations of the running couplings from ThePEG and the Herwig implementations are only provided to allow us to make exact comparisons with the FORTRAN HERWIG program.

In order to perform helicity amplitude calculations we need access to the full CKM matrix. However, the `CKMBase` class of ThePEG only provides the squares of its components. The `StandardCKM` class therefore provides access to the matrix elements as well and is used in all our helicity amplitude calculations.

Also included is a structure for the implementation of running mass calculations. The `RunningMassBase` class provides a base class and the two-loop QCD running mass is implemented in the `RunningMass` class.

The Standard Model input parameters in Herwig do not form a minimal set, because it is possible to independently set the value of the weak mixing angle, the  $W^\pm$  masses and the  $Z^0$  boson mass, without satisfying the tree-level relationship between them. A number of formally consistent schemes are however also supported using the `EW/Scheme` switch. The EW parameters we use are:

- the value of the electromagnetic coupling at zero momentum transfer, `EW/AlphaEM`;
- the value of  $\sin^2 \theta_W$ , `EW/Sin2Theta`;
- the masses of the  $W^\pm$ ,  $M_W = 80.403 \text{ GeV}$ , and  $Z^0$ ,  $M_Z = 91.1876 \text{ GeV}$ , bosons, which are taken from their `ParticleData` objects;
- the mixing angles,  $\theta_{12}$ ,  $\theta_{13}$ , and  $\theta_{23}$ , and phase,  $\delta$ , of the CKM matrix.

In addition, many of the Standard Model couplings to the  $Z^0$  boson can be changed to simulate non-Standard Model effects if desired.

### 6.4.2 Supersymmetric Models

#### 6.4.2.1 Minimal Supersymmetric Standard Model

The Minimal Supersymmetric Standard Model (MSSM) is the most studied supersymmetric model and as such it should be included in any generator attempting to simulate BSM physics. As its name suggests, it contains the smallest number of additional fields required for the theory to be consistent. The additional particle content over that of the Standard Model is listed in Table 6.1.

Table 6.1: The additional particle content of the MSSM contained in Herwig. The particle's PDG codes are the standard ones given by the Particle Data Group [187].

Spin	Particles
0	$\tilde{d}_L, \tilde{u}_L, \tilde{s}_L, \tilde{c}_L, \tilde{b}_1, \tilde{t}_1$
	$\tilde{e}_L, \tilde{\nu}_{eL}, \tilde{\mu}_L, \tilde{\nu}_{\mu L}, \tilde{\tau}_1, \tilde{\nu}_{\tau L}$
	$\tilde{d}_R, \tilde{u}_R, \tilde{s}_R, \tilde{c}_R, \tilde{b}_2, \tilde{t}_2$
	$\tilde{e}_R, \tilde{\mu}_R, \tilde{\tau}_2$
	$H^0, A^0, H^+$
1/2	$\tilde{g}, \tilde{\chi}_1^0, \tilde{\chi}_2^0, \tilde{\chi}_3^0, \tilde{\chi}_4^0, \tilde{\chi}_1^+, \tilde{\chi}_2^+$

The additional particles must have masses and couplings to be of any use in an event simulation. For supersymmetric models various programs are available that, given some set of input parameters, produce a spectrum containing all of the

other parameters necessary to be able to calculate physical quantities within the model. As stated in the previous section the output from such a generator must comply with the SLHA [114, 115] for it to be used with Herwig.

While reading the information from an SLHA file is straightforward, there is a minor complication when dealing with particle masses that have a mixing matrix associated with them. For example, consider the neutralinos, which are an admixture of the bino  $\tilde{b}$ , third wino  $\tilde{w}_3$  and 2 higgsinos  $\tilde{h}_1$  and  $\tilde{h}_2$ . The physical eigenstates  $\tilde{\chi}_i^0$  are given by

$$\tilde{\chi}_i^0 = N_{ij} \tilde{\psi}_j^0, \quad (6.5)$$

where  $N_{ij}$  is the neutralino mixing matrix in the  $\tilde{\psi}^0 = (-i\tilde{b}, -i\tilde{w}, \tilde{h}_1, \tilde{h}_2)^T$  basis. The diagonalized mass term for the gauginos is then  $N^* \mathcal{M}_{\tilde{\psi}^0} N^\dagger$ , which in general can produce complex mass values. To keep the mass values real the phase is instead absorbed into the definition of the corresponding field thereby yielding a strictly real mass and mixing matrix. There is however a price to be paid for this — while the masses are kept real they can become negative. For an event generator, a negative mass for a physical particle does not make sense so we instead choose a complex-valued mixing matrix along with real and non-negative masses. If a negative mass is encountered while reading an SLHA file, the physical mass is taken as the absolute value and the appropriate row of the mixing matrix is multiplied by a factor of  $i$ . This approach is used in order to facilitate the implementation of extended supersymmetric models in the future.

#### 6.4.2.2 Next-to-Minimal Supersymmetric Standard Model

The next-to-minimal Supersymmetric Standard Model (NMSSM) includes an additional Higgs singlet and therefore leads to an additional scalar Higgs boson, an additional pseudoscalar Higgs boson and an additional neutralino state. Many of the Feynman rules are the same as those of the MSSM and hence Vertex classes can be adapted by just adding the additional states in the mixing matrices. As with the MSSM the parameters of the model are usually generated using external programs according to the second version of the SLHA [115].

#### 6.4.2.3 R-parity Violating Supersymmetric Models

The R-parity violating supersymmetric model includes additional terms in the superpotential

$$\begin{aligned} \mathbf{W}_{R_p} = & \kappa_i \varepsilon^{ab} L_a^i H_b^2 + \frac{1}{2} \lambda_{ijk} \varepsilon^{ab} L_a^i L_b^j \overline{E}^k \\ & + \lambda'_{ijk} \varepsilon^{ab} L_a^i Q_b^j \overline{D}^k + \frac{1}{2} \lambda''_{ijk} \varepsilon^{\alpha\beta\gamma} \overline{U}_\alpha^i \overline{D}_\beta^j \overline{D}_\gamma^k, \end{aligned} \quad (6.6)$$

where  $L_i$ ,  $E_i$ ,  $Q_i$ ,  $U_i$ ,  $D_i$  are respectively the lepton doublet, lepton singlet, quark doublet, up and down quark singlet  $SU(2)$  superfields for the  $i$  th generation. The couplings  $\lambda_{i,j,k}$ ,  $\lambda'_{i,j,k}$  and  $\lambda''_{i,j,k}$  couple the different generations and  $H^2$  is the hypercharge  $Y = 1$  Higgs boson supermultiplet. The indices  $a, b$  are  $SU(2)$  indices and  $\alpha, \beta, \gamma$  are  $SU(3)$  indices.

The first three terms in Eq. (6.6) violate the conservation of lepton number. The first bilinear term is the most complicated of these to handle as it involves mixing between the neutralinos and Standard Model neutrinos, and charginos and Standard Model charged leptons. The final term in the superpotential also proves complicated as it involves the violation of baryon number and the antisymmetric tensor in the colours of the interacting quarks. The simulation of these models is described in Ref. [136]. The model allows the inclusion of either all the terms, or just the trilinear couplings.

### 6.4.3 Extra-Dimensional Models

#### 6.4.3.1 Randall-Sundrum Model

The first models proposed with extra dimensions were of the Randall-Sundrum (RS) [188] type where a tensor particle, namely the graviton, is included and is allowed to propagate in the extra dimensions. All other matter, however, is restricted to our usual 4D brane and as a result all of the SM couplings are left unchanged. The only extra couplings required are those of the graviton to ordinary matter, which depend on a single parameter  $\Lambda_\pi$ .

Two parameters can be controlled in the Randall-Sundrum model; the cutoff  $\Lambda_\pi$  and the mass of the graviton. The default mass of the graviton is 500 GeV, which can be changed via the `NominalMass` interface of its `ParticleData` object. The cutoff is set via the `Lambdapi` interface of the `RSModel` object and has a default value of 10 TeV.

#### 6.4.3.2 Minimal Universal Extra Dimensions Model

We also include a model based on the idea of universal extra dimensions where all fields are allowed to propagate in the bulk. Following similar lines to supersymmetry, the model included in Herwig is of a minimal type and has a single compact extra dimension of radius  $R$  [189].

Compactifying the extra dimension and allowing all fields to propagate in it leads to a rich new structure within the theory. Analogous to the particle-in-a-box scenario, one obtains an infinite number of excitations of the fields all characterized by a quantity called the Kaluza-Klein (KK) number. This is most easily demonstrated by showing how a scalar field  $\Phi$  would be decomposed after compactification

$$\Phi(x^\mu, y) = \frac{1}{\sqrt{\pi R}} \left[ \Phi_0(x^\mu) + \sqrt{2} \sum_{n=1}^{\infty} \Phi_n(x^\mu) \cos\left(\frac{ny}{R}\right) \right],$$

where  $x^\mu$  are the 4D coordinates,  $y$  is the position in the 5th dimension and  $n$  is the KK-number of the mode with  $n = 0$  identified as the SM mode. In general, in some compactification schemes, it is possible to have KK-number-violating interactions but in the Minimal Universal Extra Dimensions (MUED) framework in Herwig we include only those interactions that conserve KK-parity  $P = (-1)^n$  and also limit ourselves to  $n = 1$ .

Table 6.2 shows the MUED particle content contained in Herwig along with the particle ID codes used, which have not been standardized by the Particle Data Group [187]. Unlike the MSSM, there are no external programs available that calculate the mass spectrum, so this is performed internally by the `UEDBase` class, which implements the UED model. At tree level, the mass of any level- $n$  particle is simply given by  $(m_0^2 + (n/R)^2)^{1/2}$ , where  $m_0$  is the mass of the SM particle, and  $1/R$  is generally much larger than the SM mass so the spectrum is highly degenerate and no decays can occur. This situation changes once radiative corrections are taken into account and a spectrum that can be phenomenologically similar to the MSSM arises. The full set of radiative corrections, as derived in Ref. [190], is incorporated in the `UEDBase` class to give a realistic spectrum.

Table 6.2: The MUED particle spectrum contained in Herwig along with their ID codes.  $\bullet$  denotes a doublet under  $SU(2)$  and  $\circ$  a singlet. As with the standard PDG codes an antiparticle is given by the negative of the number in the table.

Spin	Particle	ID code	Spin	Particle	ID code
0	$h_1^0$	5100025	1	$g_1^*$	5100021
	$A_1^0$	5100036		$\gamma_1^*$	5100022
	$H_1^+$	5100037		$Z_1^0$ *	5100023
				$W_1^+$ *	5100024
1/2	$d_1^\bullet$	5100001	1/2	$d_1^\circ$	6100001
	$u_1^\bullet$	5100002		$u_1^\circ$	6100002
	$s_1^\bullet$	5100003		$s_1^\circ$	6100003
	$c_1^\bullet$	5100004		$c_1^\circ$	6100004
	$b_1^\bullet$	5100005		$b_1^\circ$	6100005
	$t_1^\bullet$	5100006		$t_1^\circ$	6100006
	$e_1^-$ $\bullet$	5100011		$e_1^-$ $\circ$	6100011
	$\nu_{e1}^\bullet$	5100012			
	$\mu_1^-$ $\bullet$	5100013		$\mu_1^-$ $\circ$	6100013
	$\nu_{\mu1}^\bullet$	5100014			
	$\tau_1^-$ $\bullet$	5100015		$\tau_1^-$ $\circ$	6100015
	$\nu_{\tau1}^\bullet$	5100016			

There are three parameters that can be set to control the UED model: the inverse of the radius of compactification  $R^{-1}$ ; the cutoff scale  $\Lambda$ ; and the mass of the Higgs boson at the boundary of the compactified dimension  $\bar{m}_h$ . These are controlled through the interfaces:

- `InverseRadius` the value of  $R^{-1}$ , the default value is 500 GeV;
- `LambdaR` the dimensionless number  $\Lambda R$ , the default value is 20;
- `HiggsBoundaryMass` the value of the Higgs mass at the boundary, the default value is 0 GeV.

### 6.4.3.3 ADD Model

In the ADD Model [191–197], gravity propagates in  $\delta$  extra spatial dimensions, which have a flat metric. The large size of these extra dimensions leads to a tower of Kaluza-Klein excitations of the graviton, which can either contribute as virtual particles to Standard Model processes, or be produced leading to missing energy signatures. This model is implemented using the conventions of Ref. [198].

Three parameters can be controlled in the ADD model:

- the number of extra dimensions  $\delta$ , which is controlled by the `Delta` interface of the `ADDModel`;
- the  $d$ -dimensional Planck mass  $M_D$ , which can be set using the `DdPlanckMass` interface of the `ADDModel`;
- the scale for virtual processes  $\Lambda_T$ , which is controlled by the `LambdaT` interface of the `ADDModel`.

### 6.4.4 Little Higgs Models

The main ideas behind Little Higgs models are [199]:

- the Higgs fields are the Goldstone bosons associated with global symmetry breaking at a higher scale;
- the Higgs bosons become pseudo-Goldstone bosons and acquire a mass via symmetry breaking at the EW scale;
- the masses of the Higgs bosons are protected by the approximate global symmetry, which ensures the Higgs bosons remain light.

We currently include two models, the Littlest Higgs Model, which contains only new gauge bosons and a top quark partner, and the Little Higgs Model with T-parity, which includes partners for all the Standard Model particles.

#### 6.4.4.1 Littlest Higgs Model

The Littlest Higgs Model is implemented using the Feynman rules described in Ref. [199]. The additional particles are the additional heavy gauge boson states  $A_H, Z_H, W_H^\pm$ , for each of the Standard Model EW bosons, the additional partner of the top quark  $T$ , and additional scalars  $\phi^0, \phi^P, \phi^\pm$  and  $\phi^{\pm\pm}$ .

The main parameters of the model are:

- $\cot \theta$  the value of the mixing between the  $W$  bosons, specified using the `CotTheta` interface;
- $\tan \theta'$  the value of the mixing between the  $B$  bosons, set using the `TanThetaPrime` interface;
- $f$  the symmetry breaking scale is set using `f`;
- $\frac{\lambda_1}{\lambda_2}$  the ratio of the two quark couplings is set using `LambdaRatio`;
- $v'/v$  the ratio of the vacuum expectation values is set using `VEVRatio`;
- $m_H$  the mass of the Higgs boson is set using `mH`.

#### 6.4.4.2 Little Higgs Model with T-parity

In order to evade the constraints from EW precision data, the original Little Higgs models required fine-tuning. One solution to this problem is to add a discrete symmetry (analogous to R-parity of SUSY) called T-parity. This removes most of the constraints from EW precision data, gives a dark matter candidate, and leads to a spectrum of mirror fermion partners of the Standard Model particles. This model is implemented based on Ref. [200] using the Feynman rules from [200–202]. In addition to the particle content of the Little Higgs model, there are T-parity odd partners of the Standard Model fermions and of the additional top quark partner.

The main parameters of the model are:

- $f$  the symmetry breaking scale for the non-linear  $\sigma$ -model is set using `f`;
- $\sin \alpha$  the mixing in the top quark sector is set using `SinAlpha`;
- $\kappa_q$  the parameter controlling the masses of the T-odd quarks is set using `KappaQuark`;
- $\kappa_\ell$  the parameter controlling the masses of the T-odd leptons is set using `KappaLepton`;
- $m_H$  the mass of the Higgs boson is set using `HiggsMass`;

## 6.4.5 Other Models

### 6.4.5.1 Leptoquarks

Fermion masses may arise from the mixing of elementary fermions with composite, fermionic resonances of a strong sector [203] responsible for the breaking of the  $SU(2)_L \times U(1)_Y$  EW symmetry of the SM. It follows that this strongly-coupled sector must also be charged under colour  $SU(3)$  and must contain, at the very least, colour-triplet fermionic resonances that can mix with the elementary colour triplets to make the observed quarks. It is reasonable to expect that such a strongly-coupled sector will contain other coloured resonances. These may be bosonic and, depending on their charges, may couple to a quark and a lepton. These leptoquark resonances may be light if they arise as pseudo-Nambu Goldstone bosons and make an ideal target for LHC searches. They will decay exclusively to third-generation fermions due to suppression of the couplings to light fermions.

The present implementation includes non-derivatively coupled leptoquarks, which couple to Standard Model fermions as in Eq. (2.4) of Ref. [204] and single-derivatively coupled leptoquarks such as those in Eq. (2.5) of Ref. [204]. In the case of the derivatively coupled leptoquarks, the simplification that the primed lepton and primed quark couplings are equal has been made.

### 6.4.5.2 Sextet

The colour sextet diquark is, in group theory language, a rank 2 symmetric tensor formed from the direct product of two fundamental representations  $3 \otimes 3 = 6 \oplus \bar{3}$ . As such it is the lowest colour representation that has not been observed and is therefore worthy of study at the LHC. The Lagrangian, from Refs. [205–209], is

$$\mathcal{L} = (g_{1L}\bar{q}_L^c i\tau_2 q_L + g_{1R}\bar{u}_R^c d_R) \Phi_{1,1/3} + g'_{1R}\bar{d}_R^c d_R \Phi_{1,-2/3} + g''_{1R}\bar{u}_R^c u_R \Phi_{1,4/3} + g_{3L}\bar{q}_L^c i\tau_2 \tau q_L \cdot \Phi_{3,1/3} + g_2\bar{q}_L^c \gamma_\mu d_R V_{2,-1/6}^\mu + g'_2\bar{q}_L^c \gamma_\mu u_R V_{2,5/6}^\mu + h.c.,$$

where  $q_L$  is the left-handed quark doublet,  $u_R$  and  $d_R$  are the right-handed quark singlet fields, and  $q^c \equiv C\bar{q}^T$  is the charge conjugate quark field. The colour and generation indices are omitted to give a more compact notation and the subscripts on the scalar,  $\Phi$ , and vector,  $V^\mu$ , fields denote the SM EW gauge quantum numbers:  $(SU(2)_L, U(1)_Y)$ . The Lagrangian is assumed to be flavour diagonal to avoid any flavour-changing currents arising from the new interactions. The main parameters are the couplings of the model, which can be set using the interfaces of the `SextetModel` class, and the masses of the sextet diquarks, which can be set via their `ParticleData` objects.

The simulation of the sextet colour structure in both hard production processes, decays and the parton shower are described in Ref. [50] together with the phenomenology of the model.

### 6.4.5.3 Transplanckian

This model describes the  $2 \rightarrow 2$  scattering of partons at high energy, in the transplanckian regime, using the eikonal approximation, as investigated in [210]. The approximation is valid in the high-energy, low-angle scattering regime, where the centre-of-mass scattering angle of the incoming parton  $\hat{\theta} \rightarrow 0$  or, in terms of Mandelstam variables,  $-\hat{t}/\hat{s} \rightarrow 0$ . The matrix elements for the scattering are proportional to the functions  $F_n$  that appear in [210], which we have calculated numerically and tabulated. The implementation allows variation of the Planck scale (`PlanckMass`) as well as the number of extra dimensions (`NumberExtraDimensions`), up to a maximum of 6.

### 6.4.5.4 TTbAsymm

The addition of this model was motivated by the initially anomalously large, mass-dependent forward-backward asymmetry in  $t\bar{t}$  production, observed at the Tevatron CDF experiment, *e.g.* [211]. The discrepancy has since been reduced through the inclusion of higher-order corrections in the SM calculation [212–214]. Such asymmetries may invoke new interactions in the top sector. In this implementation, we have included four types of new interaction that have been shown to reproduce the measured asymmetry (see, *e.g.* [215]):

- a flavour-changing  $W'$  (prime) vector boson that couples top quarks to down quarks

$$\mathcal{L} \supset \bar{t}\gamma^\mu(g_L P_L + g_R P_R)d W'_\mu + h.c.,$$

where  $g_{L,R}$  are the left- and right-handed couplings, *i.e.* those corresponding to the left- and right-handed projection operators  $P_{L,R}$ , respectively;

- an Abelian  $Z'$ -prime vector boson that couples top quarks to up quarks

$$\mathcal{L} \supset g_{Z'}^{(R,L)}\bar{u}\gamma^\mu P_{R,L}t Z'_\mu + h_{Z',i}^{(R,L)}\bar{u}_i\gamma^\mu P_{R,L}u_i Z'_\mu + h.c.,$$

where  $g_{Z'}^{(R,L)}$  are the right- and left-handed flavour-changing couplings respectively, and  $h_{i}^{(R,L)}$  are flavour-conserving couplings for the  $i^{\text{th}}$  generation;

- an axial heavy gluon that couples to  $\bar{q}q$  and  $\bar{t}t$

$$\mathcal{L} \supset g_s \left[ \bar{q} T^A \gamma^\mu (g_L^q P_L + g_R^q P_R) q + \bar{t} T^A \gamma^\mu (g_L^t P_L + g_R^t P_R) t \right] G_\mu^{'A} ,$$

where  $g_s$  is the QCD strong coupling,  $T^A$  ( $A \in \{1, 8\}$ ) are the  $SU(3)$  generator matrices in the adjoint representation,  $g_{L,R}^q$  are the left- and right-handed couplings to  $q\bar{q}$  (excluding the top quark), and  $g_{L,R}^t$  is the left- and right-handed coupling to  $t\bar{t}$ ;

- a model that includes an additional, non-Abelian,  $SU(2)_X$  gauge interaction, for further details see Ref. [216].

The “active” model can be chosen through the `modelselect` interface of the `TTbAModel`<sup>3</sup>.

#### 6.4.5.5 Zprime

This simple model describes a heavy vector boson ( $Z$ -prime), which is neutral under  $U(1)_{\text{e.m.}}$ . The interactions are flavour-conserving and the corresponding Lagrangian has the form

$$\mathcal{L} \supset g_{q_i}^{(R,L)} \bar{q}_i \gamma^\mu P_{R,L} q_i Z'_\mu + g_{\ell_i}^{(R,L)} \bar{\ell}_i \gamma^\mu P_{R,L} \ell_i Z'_\mu + \text{h.c.} ,$$

where  $g_{q_i}^{(R,L)}$  and  $g_{\ell_i}^{(R,L)}$  are the right- and left-handed couplings to the quarks and leptons of the  $i^{\text{th}}$  generation respectively. The couplings can be modified, see `ZprimeModel` for more details.

#### 6.4.6 UFO

There are a number of programs available (*e.g.* LanHEP [217, 218], FeynRules [219, 220] and Sarah [221, 222]) that can output the Feynman rules for a new physics model in the Universal FeynRules Output (UFO) [186] format. To enable these Feynman rules to be used with Herwig 7 we provide a program, `ufo2herwig`, that can convert the UFO format into a set of C++ classes that can be compiled into a model library. As UFO is a python format, it was convenient to write the conversion program in python as well. The model library produced by this conversion can be used in the same way as the internal models described above.

If possible we map the Lorentz structures of these vertices to the generic perturbative forms implemented in ThePEG, so that we only have to implement the couplings in the specific model. However, there are a number of models where the Lorentz structure does not have the perturbative form. Starting from version 7.2 the `ufo2herwig` converter will now generate all the code required to implement arbitrary Lorentz structures, including for spin- $\frac{3}{2}$  and spin-2 particles, making use of the `sympy` package [223]. Most colour structures are also supported, at least for phenomenologically relevant interactions. Some four-point vertices still cannot be handled, however these are rarely phenomenologically relevant, *i.e.* they involve at least three new particles.

## 6.5 Code structure

The `ModelGenerator` class is responsible for setting up the new `MatrixElement` objects, which inherit from the `GeneralHardME` class, and `DecayMode` objects for a new physics model. Helper classes aid in the creation of these objects, they are:

### 6.5.1 HardProcessConstructor

The `ModelGenerator` uses one or more classes inheriting from the `HardProcessConstructor` base class to create the diagrams for the requested processes and construct the appropriate matrix elements. The inheriting classes are:

`TwoToTwoProcessConstructor`

The `TwoToTwoProcessConstructor` is responsible for constructing the diagrams for  $2 \rightarrow 2$  scattering processes and creating an object inheriting from the `GeneralHardME` class based on the spin structure of the process. The full range of supported spin structures is given in Table 6.3.

`ResonantProcessConstructor`

The `ResonantProcessConstructor` is of a similar design to the `HardProcessConstructor` but it only constructs the diagrams for a process with a given  $s$ -channel resonance.

<sup>3</sup> Note that if the axial gluon model is selected, the line in the corresponding input file that excludes the “Ag” particle should be commented out.

### HiggsVBFProcessConstructor

The `HiggsVBFProcessConstructor` class constructs the diagrams for the production of a neutral (colour and electrically) scalar boson via the vector boson fusion (VBF) process and creates an object of the `GeneralfftoffH` class to calculate matrix elements for the process.

### HiggsVectorBosonProcessConstructor

The `HiggsVectorBosonProcessConstructor` class constructs the diagrams for the production of a neutral (colour and electrically) scalar boson in association with a Standard Model EW vector boson ( $W^\pm, Z^0$ ) including the decay products of the vector boson. An object of the `GeneralfftoVH` class is created to calculate matrix elements for the process.

### QQHiggsProcessConstructor

The `QQHiggsProcessConstructor` class constructs the diagrams for the production of a neutral (colour and electrically) scalar boson in association with a heavy quark-antiquark pair and constructs an object of the `GeneralQQHiggs` class to calculate matrix elements for the process.

## 6.5.2 DecayConstructor

The `DecayConstructor` stores a collection of objects that inherit from the `NBodyDecayConstructorBase` class. Each of these is responsible for constructing the decay modes for the  $n$ -body decays. Currently the following classes are implemented:

`TwoBodyDecayConstructor`,

for two-body decays;

`ThreeBodyDecayConstructor`,

for three-body decays;

`FourBodyDecayConstructor`,

for four-body decays;

`WeakCurrentDecayConstructor`,

for weak decays using the weak currents from Section 9.3.1 for decays where two particles are almost mass degenerate.

While all the important type of two- and three-body decays are currently implemented only the most phenomenologically relevant four body decay, of a scalar boson to four fermions, is implemented. This decay mode can be important for Higgs bosons decays via off-shell gauge bosons and the lightest stau in R-parity violating SUSY models.

In addition, the `ModelGenerator` class is responsible for setting up objects of `BSMWidthGenerator` and `GenericMassGenerator` type so that off-shell effects can be simulated. To achieve this either, `ParticleData` objects are added to the `Offshell` interface so that the selected particles are treated as off shell, or the `WhichOffshell` interface is set to `All` so that all BSM particles are treated as off shell.

The matrix element classes all inherit from the `GeneralHardME` class and implement the matrix element for a particular spin configuration. The classes inheriting from the `GeneralHardME` class and the spin structures they implement are given in Table 6.3.

The on-shell decayer classes inherit from the `GeneralTwoBodyDecayer`, `GeneralThreeBodyDecayer` or `GeneralFourBodyDecayer` class and each is responsible for calculating the value of the matrix element for that particular set of spins. A `VectorCurrentDecayer` class also exists for decay modes created with the `WeakCurrentDecayConstructor` class. The `Decayer` classes implemented in Herwig and the types of decay they implement are given in Table 6.4.

Table 6.3: The general hard process matrix elements, based on spin structures, implemented in Herwig.

Class Name	Hard Process
<code>MEff2ff</code>	Fermion fermion to fermion fermion.
<code>MEff2ss</code>	Fermion fermion to scalar scalar.
<code>MEff2sv</code>	Fermion fermion to scalar vector.
<code>MEff2tv</code>	Fermion fermion to tensor vector.
<code>MEff2vs</code>	Fermion fermion to vector scalar.
<code>MEff2vv</code>	Fermion fermion to vector vector.
<code>MEfv2fs</code>	Fermion vector to fermion scalar.
<code>MEfv2tf</code>	Fermion vector to tensor fermion.
<code>MEfv2vf</code>	Fermion vector to vector fermion.
<code>MEvv2ff</code>	Vector vector to fermion fermion.
<code>MEvv2ss</code>	Vector vector to scalar scalar.
<code>MEvv2tv</code>	Vector vector to tensor vector.
<code>MEvv2vv</code>	Vector vector to vector vector.
<code>MEvv2vs</code>	Vector vector to vector scalar.

Table 6.4: The general decays based on spin structures implemented in Herwig.

Class Name	Decay
<code>FFSDecayer</code>	Fermion to fermion scalar decay.
<code>FFVDecayer</code>	Fermion to fermion vector decay.
<code>FRVDecayer</code>	Fermion to spin- $\frac{3}{2}$ fermion vector decay.
<code>FRSDecayer</code>	Fermion to spin- $\frac{3}{2}$ fermion scalar decay.
<code>SFFDecayer</code>	Scalar to fermion fermion decay.
<code>SRFDecayer</code>	Scalar to spin- $\frac{3}{2}$ fermion fermion decay.
<code>SSSDecayer</code>	Scalar to two scalar decay.
<code>SSVDecayer</code>	Scalar to scalar vector decay.
<code>SVVDecayer</code>	Scalar to two vector decay.
<code>StoFFFFDecayer</code>	Scalar to four fermion decay.
<code>VFFDecayer</code>	Vector to two fermion decay.
<code>VSSDecayer</code>	Vector to two scalar decay.
<code>VVSDecayer</code>	Vector to vector scalar decay.
<code>VVVDecayer</code>	Vector to two vector decay.
<code>TFFDecayer</code>	Tensor to two fermion decay.
<code>TSSDecayer</code>	Tensor to two scalar decay.
<code>TVVDecayer</code>	Tensor to two vector decay.
<code>FtoFFFDecayer</code>	Fermion to three fermion decay.
<code>FtoFVVDecayer</code>	Fermion to fermion and two vector decay.
<code>StoSFFDecayer</code>	Scalar to scalar and two fermion decay.
<code>StoFFVDecayer</code>	Scalar to two fermion and vector decay.
<code>VtoFFVDecayer</code>	Vector to two fermion and vector decay.
<code>FFVCurrentDecayer</code>	Fermion to fermion vector decay with the vector off-shell and decaying via a weak current from Section 9.3.1.

The specification of the particles involved in the hard process is achieved through the `Incoming` and `Outgoing` interfaces of the `HardProcessConstructor`. Both interfaces are lists of `ParticleData` objects. The switch `IncludeEW` can be set to `No` to include only the strong coupling diagrams.

In order to pass spin correlations through the decay stage, `DecayIntegrator` objects must be created. This is achieved by populating a list held in the `ModelGenerator` class, which can be accessed through the `DecayParticles` interface. The particles in this list will have spin correlation information passed along when their decays are generated. If a decay table is read in for a SUSY model then the `CreateDecayModes` interface should be set to `No` so that only the decay modes

listed in the externally generated decay table are created<sup>4</sup>. For all other models the possible decay modes are also created from the particles in the `DecayParticles` list.

In addition, we provide a number of classes to allow the loop-mediated but phenomenologically important couplings of the Higgs bosons in a model to photon or gluon pairs to be automatically generated from the vertices of the model. The `VVSLoopVertex` class implements the loop calculations while the `GenericHPPVertex` and `GenericHGGVertex` classes implement the couplings to photon and gluon pairs, respectively.

In addition to the code that handles the calculation of the matrix elements for the decays and scattering cross sections each model requires a number of classes to implement the model.

The Standard Model is implemented in the `StandardModel` class, which inherits from the `StandardModelBase` class of ThePEG and implements access to the helicity Vertex classes and some additional couplings, such as the running mass, used by Herwig. The Vertex classes that implement the Standard Model interactions are given in Table 6.5.

Table 6.5: Herwig Vertex classes for the Standard Model.

Class	Interaction
<code>SMFFGVertex</code>	Interaction of the gluon with the SM fermions
<code>SMFFPVertex</code>	Interaction of the photon with the SM fermions
<code>SMFFWVertex</code>	Interaction of the $W^\pm$ boson with the SM fermions
<code>SMFFZVertex</code>	Interaction of the $Z^0$ boson with the SM fermions
<code>SMFFHVertex</code>	Interaction of the Higgs boson with the SM fermions
<code>SMGGGVertex</code>	Triple gluon vertex
<code>SMGGGGVertex</code>	Four gluon vertex
<code>SMWWWVertex</code>	Triple EW gauge boson vertex
<code>SMWWWWVertex</code>	Four EW gauge boson vertex
<code>SMWWHVertex</code>	Interaction of the Higgs boson with the EW gauge bosons
<code>SMWWHHVertex</code>	Two Higgs bosons, two EW gauge boson vertex
<code>SMHHHVertex</code>	Triple Higgs boson couplings
<code>SMHGGVertex</code>	Higgs boson coupling to two gluons via quark loops
<code>SMHPPVertex</code>	Higgs boson coupling to two photons via fermion and boson loops

Most of the BSM models in Herwig implement a class describing the model, which inherits from the `BSMModel` class, which in turn inherits from the `StandardModel` class. This allows an instance of this class, which implements any additional particles used in the model, to be used instead of an instance of the `StandardModel` when simulating this model. The `BSMModel` class also implements the reading of particle masses and decay modes in the SLHA format so that this can be used in all BSM models.

The structure of the implementation of the SUSY model is designed to allow the implementation of extended SUSY models. The `SusyBase` class, which inherits from the `BSMModel` class, is designed to read in the SLHA files specifying the SUSY spectrum.

Table 6.6: Herwig Vertex classes for the MSSM.

<sup>4</sup> If a decay table is being used with a SUSY model then the `DecayParticles` list must still be populated so that the decays will have spin correlation information included.

Class	Interaction
SSNFSVertex	Neutralino with a SM fermion and a sfermion
SSCFSVertex	Chargino with a SM fermion and a sfermion
SSGFSVertex	Gluino with a quark and squark
SSNNZVertex	A pair of neutralinos with a $Z^0$ boson
SSCCZVertex	A pair of charginos with a $Z^0$ boson
SSCNWVertex	Chargino with a neutralino and a $W^\pm$ boson
SSGSGSGVertex	SM gluon with a pair of gluinos
SSGSSVertex	SM gluon with a pair of squarks
SSWSSVertex	SM gauge boson with a pair of sfermions
SSFFHVertex	A pair of SM fermions with a Higgs boson
SSWHHVertex	SM EW gauge boson with a pair of Higgs bosons
SSWWHVertex	A pair of gauge bosons with a Higgs boson
SSWWHHVertex	A pair of gauge bosons with a pair Higgs bosons
SSGOGOHVertex	A pair of gauginos with a Higgs boson
SSHHSFSVertex	A Higgs boson with a pair of sfermions
SSHHHVertex	Triple Higgs boson self coupling
SSHGGVertex	A Higgs boson with a pair of gluons via quark and squark loops
SSHPPVertex	A Higgs boson with a pair of photons loops diagrams
SSGGSQSQVertex	A pair of gluons with a pair of squarks
SSGVFSVertex	Gravitino with a fermion and a scalar boson
SSGVNVVertex	Gravitino with a neutralino and vector boson
SSGVNHHVertex	Gravitino with a neutralino and Higgs boson
SSGNGVertex	Gluino with a neutralino and gluon via loop diagrams
SSNNPVertex	Neutralino with a neutralino and a photon via loop diagrams
SSNCTVertex	Flavour changing neutralino, charm stop coupling

The details of the MSSM are implemented in the `MSSM` class, which inherits from the `SusyBase` class. The Vertex classes for the MSSM are given in Table 6.6. A spectrum file in SLHA format must be supplied or the MSSM model cannot be used. `MSSM` in Herwig is designed to allow extended SUSY models to be added and for example supports additional neutralino states to make the implementation of the NMSSM model easier.

The details of the NMSSM model are implemented in the `NMSSM` class, which inherits from the `MSSM` class. Some vertices are the same as those in the MSSM, or the MSSM vertices can be easily modified, for example by including the additional neutralino state, so we make use of the `MSSM` Vertex classes. The additional Vertex classes for the NMSSM are given in Table 6.7.

Table 6.7: Herwig Vertex classes for the NMSSM.

Class	Interaction
NMSSMFFHVertex	A pair of SM fermions with a Higgs boson
NMSSMWHHVertex	SM EW gauge boson with a pair of Higgs bosons
NMSSMWWHVertex	A pair of gauge bosons with a Higgs boson
NMSSMWWHHVertex	A pair of gauge bosons with a pair Higgs bosons
NMSSMGOGOHVertex	A pair of gauginos with a Higgs boson
NMSSMHSFSVertex	A Higgs boson with a pair of sfermions
NMSSMHHHVertex	Triple Higgs boson self coupling

The details of the R-parity violating SUSY model are implemented in the `RPV` class, which inherits from the `MSSM` class. Many vertices are the same as those in the MSSM and therefore we make use of the `MSSM` Vertex classes. The additional Vertex classes for the R-parity violating model are given in Table 6.8.

Table 6.8: Herwig Vertex classes for the R-parity violating SUSY model.

Class	Interaction
RPVFFZVertex	A pair of fermions with the $Z^0$ boson
RPVFFWVertex	A pair of fermions with the $W^\pm$ boson
RPVFFSVertex	A pair of fermions with a scalar fermion
RPVWSSVertex	A pair of scalar fermions with the $W^\pm$ boson
RPVWWHVertex	A pair of $W^\pm$ bosons with the Higgs bosons
RPVSSSVertex	Three scalar bosons
RPVLLEVertex	Three leptons via the R-parity violating LLE term
RPVLQDVertex	A lepton and two quarks via the R-parity violating LQD term
RPVUDDVertex	Three quarks via the R-parity violating UDD term

Table 6.9: Herwig Vertex classes for the Randall-Sundrum model.

Class	Interaction
RSModelFFGRVertex	Coupling of the graviton to SM fermions
RSModelSSGRVertex	Coupling of the graviton to a Higgs boson pair
RSModelFFGGRVertex	Coupling of the graviton to two SM fermions and a gluon
RSModelFFWGRVertex	Coupling of the graviton to two SM fermions and an EW gauge boson
RSModelVVGRVertex	Coupling of the graviton to two gauge bosons
RSModelGGGGRVertex	Coupling of the graviton to three gluons
RSModelWWWGRVertex	Coupling of the graviton to three EW gauge bosons

The `RSModel` class inherits from the `BSMModel` class and implements the calculations needed for the Randall-Sundrum model. We have only implemented the vertices that are phenomenologically relevant and therefore some four-point vertices that are not important for resonance graviton production are not included. The Vertex classes implemented for the Randall-Sundrum model are given in Table 6.9.

Table 6.10: Herwig Vertex classes for the UED model.

Class	Interaction
UEDF1F1P0Vertex	SM photon with a pair of KK-1 fermions
UEDF1F1W0Vertex	SM $W^\pm$ boson with a pair of KK-1 fermions
UEDF1F1Z0Vertex	SM $Z^0$ boson with a pair of KK-1 fermions
UEDF1F1G0Vertex	SM gluon with a pair of KK-1 fermions
UEDF1F0W1Vertex	KK-1 fermion with an EW KK-1 boson and a SM fermion
UEDF1F0G1Vertex	KK-1 fermion with a KK-1 gluon and a SM fermion
UEDF1F0H1Vertex	KK-1 fermion with a KK-1 Higgs boson and a SM fermion
UEDP0H1H1Vertex	SM photon with a pair of KK-1 charged Higgs bosons
UEDW0W1W1Vertex	A pair of KK-1 gauge bosons with a SM $W^\pm$ or $Z^0$ boson
UEDG1G1G0Vertex	A pair of KK-1 gluons with a SM gluon
UEDG0G0G1G1Vertex	A pair of SM gluons with a pair of KK-1 gluons
UEDW0A1H1Vertex	SM $W^\pm$ boson with a KK-1 charged Higgs boson and a KK-1 pseudoscalar Higgs boson
UEDZ0H1H1Vertex	SM $Z^0$ boson with a pair of KK-1 charged Higgs bosons
UEDZ0A1h1Vertex	SM $Z^0$ boson with a KK-1 pseudoscalar Higgs boson and a KK-1 scalar Higgs boson

The UED model is implemented in the `UEDBase` class, which inherits from the `BSMModel` class and implements the calculation of the parameters of the model. The Vertex classes for the UED model are given in Table 6.10.

The `ADDModel` class inherits from the `BSMModel` class and implements the calculations needed in this model. We have only implemented the vertices that are phenomenologically relevant and therefore the five-point vertices that are not

important for  $2 \rightarrow 2$  scattering processes are not included. The Vertex classes implemented for the ADD model are given in [Table 6.11](#). In addition the `GravitonMassGenerator` class is used to generate the mass of external gravitons, due to the sum over the tower of Kaluza-Klein states.

Table 6.11: Herwig Vertex classes for the ADD model.

Class	Interaction
<code>ADDModelFFGRVertex</code>	Coupling of the graviton to SM fermions
<code>ADDModelSSGRVertex</code>	Coupling of the graviton to a Higgs boson pair
<code>ADDModelFFGGRVertex</code>	Coupling of the graviton to two SM quarks and a gluon
<code>ADDModelFFWGRVertex</code>	Coupling of the graviton to two SM fermions and an EW gauge boson
<code>ADDModelVVGRVertex</code>	Coupling of the graviton to two gauge bosons
<code>ADDModelGGGGRVertex</code>	Coupling of the graviton to three gluons
<code>ADDModelWWGRVertex</code>	Coupling of the graviton to three EW gauge bosons

The `LHModel` class inherits from the `BSMModel` class and implements the calculations needed in the Little Higgs model. We have only implemented the vertices that are phenomenologically relevant, which are described in [Table 6.12](#).

Table 6.12: Herwig Vertex classes for the Little Higgs model.

Class	Interaction
<code>LHFFGVertex</code>	Interaction of the gluon with the fermions
<code>LHFFPVertex</code>	Interaction of the photon with the fermions
<code>LHFFWVertex</code>	Interaction of the $W^\pm$ boson with the fermions
<code>LHFFZVertex</code>	Interaction of the $Z^0$ boson with the fermions
<code>LHFFHVertex</code>	Interaction of the Higgs boson with the fermions
<code>LHWHHVertex</code>	Two Higgs bosons, EW gauge boson vertex
<code>LHWWWVertex</code>	Triple EW gauge boson vertex
<code>LHWWWWVertex</code>	Four EW gauge boson vertex
<code>LHWWHVertex</code>	Interaction of the Higgs boson with the EW gauge bosons
<code>LHWWHHVertex</code>	Two Higgs bosons, two EW gauge boson vertex

The `LHTPModel` class inherits from the `BSMModel` class and implements the parameters calculations needed in the Little Higgs model with T-parity conservation. We have only implemented the vertices that are phenomenologically relevant, which are described in [Table 6.13](#).

Table 6.13: Herwig Vertex classes for the Little Higgs model with T-parity conservation.

Class	Interaction
<code>LHTPFFGVertex</code>	Interaction of the gluon with the fermions
<code>LHTPFFPVertex</code>	Interaction of the photon with the fermions
<code>LHTPFFWVertex</code>	Interaction of the $W^\pm$ boson with the fermions
<code>LHTPFFZVertex</code>	Interaction of the $Z^0$ boson with the fermions
<code>LHTPFFHVertex</code>	Interaction of the Higgs boson with the fermions
<code>LHTPWHHVertex</code>	Two Higgs bosons, EW gauge boson vertex
<code>LHTPWWHVertex</code>	Interaction of the Higgs boson with the EW gauge bosons
<code>LHTPWWWVertex</code>	Triple EW gauge boson vertex
<code>LHTPHHHVertex</code>	Triple Higgs boson couplings

The `SextetModel` class inherits from the `BSMModel`. The vertices for the interactions of the sextet particles are given in [Table 6.14](#).

Table 6.14: Herwig Vertex classes for the Sextet model

Class	Interaction
SextetFFSVertex	Interaction of two fermions with a scalar Sextet
SextetFFVVertex	Interaction of two fermions with a vector Sextet
SextetGSSVertex	Interaction of the gluon with two scalar Sextets
SextetGVVVertex	Interaction of the gluon with two vector Sextets
SextetGGSSVertex	Interaction of two gluons with two scalar Sextets
SextetGGVVVertex	Interaction of two gluons with two vector Sextets

The Transplanckian scattering matrix elements are implemented in the `METRP2to2` class for  $2 \rightarrow 2$  transplanckian scattering.

The `TTbAModel` class inherits from the `BSMModel`. The vertices for the interactions of the particles are given in Table 6.15.

Table 6.15: Herwig Vertex classes for the TTbAModel.

Class	Interaction
<code>TTbAModelSU2XVertex</code>	Interaction of two fermions in the SU2X model
<code>TTbAModelZPQQVertex</code>	Interaction of two fermions with a Z prime
<code>TTbAModelAGQQVertex</code>	Interaction of the axial gluon with two quarks
<code>TTbAModelWPTDVertex</code>	Interaction of two fermions with a W prime

The `LeptoquarkModel` class inherits from the `BSMModel`. The vertices for the interactions of the leptoquarks are given in Table 6.16.

Table 6.16: Herwig Vertex classes for the LeptoQuark model.

Class	Interaction
<code>LeptoquarkModelSLQLQGGVertex</code>	Interaction of two leptoquarks and two gluons
<code>LeptoquarkModelSLQLQGVertex</code>	Interaction of two leptoquarks and one gluon
<code>LeptoquarkModelSLQFFVertex</code>	Interaction of the leptoquark, a lepton and a quark

The `ZprimeModel` class inherits from the `BSMModel`. The vertex is implemented in the `ZprimeModelZPQQVertex` class.

The full list of interfaces for all the classes is provided in the `Doxygen` documentation.

## 7 Hadronization

Hadronization occurs in the step after the conclusion of the parton shower: the resulting quarks and gluons are assembled into the observed hadrons. The cluster model [2] used in Herwig 7 is based on the principle of colour preconfinement [224], satisfied by coherent parton showers; the quarks and gluons emerging from the shower are organised in clusters, whose mass distribution is independent of both the hard process considered, and the energy scale of the hard scattering.

The cluster model is local in the colour of the partons, and asymptotically independent of both the hard process and the centre-of-mass energy of the collision [2,3]. It is motivated by consideration of the mass spectrum of hadronic resonances of a given (quark-antiquark) flavour. The lowest-lying states are very narrow, but higher resonances become increasingly broad until one can imagine, rather than individual resonances, a continuum of completely overlapping hadronic states.

The preconfined colour singlets which emerge from the parton shower are projected onto this continuum, and called clusters. In the simplest model, they decay directly to narrower-resonance lighter mesons. Because the clusters are considered to be the overlap of multiple states of different spins, the simplest model assumes that this decay is isotropic.

This simple model has been refined and extended, so that for a single event hadronization proceeds as:

1. cluster formation, from final-state quarks and gluons (Section 7.1);
2. colour reconnection, to rearrange the constituents of the primordial clusters (Section 7.2);
3. cluster fission, to split heavy clusters into lighter clusters (Section 7.3);
4. cluster decay, into observed hadrons (Section 7.4).

Each step is described in further detail in the indicated section below and represented pictorially in Fig. 7.1.

The optional inclusion of spin effects for heavy mesons and baryons is described in Section 7.5; the application of the hadronization model to models containing BSM physics is described in Section 7.6. Finally, Herwig 7.3 also supports the Lund string model via an interface to Pythia. This is described in Section 7.7.

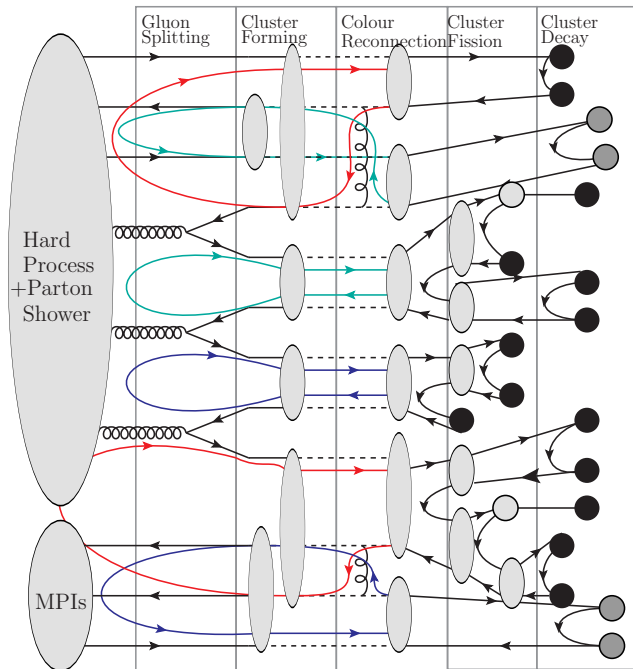


Fig. 7.1: Pictorial representation of the Herwig cluster hadronization model.

## 7.1 Cluster formation

Clusters are formed by non-perturbatively splitting the gluons in the final-state of the parton shower into quark-antiquark pairs. For this to be possible, the constituent mass of the gluons at the end of the parton shower<sup>1</sup> must be heavier than twice the constituent mass of the lightest quark.<sup>2</sup> The gluon is allowed to decay into any of the accessible light quark flavours, with a probability given by the available phase-space for the decay.<sup>3</sup>

The gluon decays isotropically and, following this, the event contains solely colour-connected<sup>4</sup> quark and anti-quark pairs or (anti-)diquark and (anti-)quark pairs. The colour singlets formed by these colour-connected parton pairs are formed into clusters, which are each assigned a momentum corresponding to the total momentum of the constituent partons.

The mass distribution of primary clusters is shown in Fig. 7.7, and confirms that the shower algorithm in Herwig 7 satisfies the preconfinement property to a good approximation at a centre-of-mass energy of 100 GeV, and is clearly invariant beyond that.

## 7.2 Colour reconnection

The cluster formation process outlined above does not allow clusters to contain partons from colour disconnected regions different stages of the event. Colour reconnection reshuffles the cluster constituents to allow partons to form a cluster regardless of their origin within the event. This is of particular relevance for the simulation of hadronic collisions with multiple partonic scatters.

The properties of a cluster depend on the invariant cluster mass  $M$ , which is given by

$$M^2 = (p_1 + p_2)^2,$$

where  $p_1$  and  $p_2$  are the four momenta of the cluster constituents, which are either  $q\bar{q}'$  mesonic clusters or  $q(q', q'')_s/\bar{q}(\bar{q}', \bar{q}'')_s$  (anti-)diquark containing clusters. The subsequent fission and decay of the clusters depend on this invariant cluster mass  $M$ , which directly influences the multiplicity of the final state particles.

However these primordial clusters have been formed using the leading colour approximation and would therefore hadronize completely independently in our cluster model. In particular two clusters with very close-by constituents in phase-space would hadronize independently even though a more reasonable colour connection could be found by rearrangement of these clusters. Restoring more meaningful colour connections to the clusters is the job of colour reconnection, for which Herwig provides several different algorithms.

Each algorithm, which can be chosen using the interface `ColourReconnector:Algorithm`, attempts to minimize a closeness measure between the cluster constituents over the permutation space of allowed rearrangements of these constituents into colour singlet clusters.

Four colour-reconnection algorithms are currently implemented in Herwig:

- (i) ‘plain’ colour reconnection (Section 7.2.1);
- (ii) ‘statistical’ colour reconnection [61] (Section 7.2.2);
- (iii) ‘baryonic’ colour reconnection [46] (Section 7.2.3);
- (iv) ‘baryonic–mesonic’ colour reconnection [226] (Section 7.2.4).

A full description of each implemented colour-reconnection model can be found in Refs. [46, 61, 226] respectively.

The first two algorithms try to identify exchanges of cluster constituents that reduce the sum of the invariant cluster masses, while baryonic colour reconnection uses the relative rapidities of the constituents to quantify their closeness and identify alternative clusterings as either baryonic or mesonic.

The default algorithm is (iii), baryonic colour reconnection. It is possible to switch between the algorithms using the `Algorithm` switch with the values `Plain`, `Statistical`, `Baryonic`, and `BaryonicMesonic`, respectively.

<sup>1</sup> In the angular-ordered parton shower the gluons are given the constituent mass as part of the kinematic reconstruction process (see Section 4.2.4.2). In the dipole shower a momentum reshuffling is performed after the parton shower (see Section 4.3.5), so that the partons are on the constituent mass shell. As part of newly developed models [225], a dynamic gluon mass generation can now be implemented using the `GluonMassGenerator` class.

<sup>2</sup> We typically set the constituent masses of the up and down quarks to be equal, although they can in principle differ.

<sup>3</sup> The option of gluon decay into diquarks, which was available in FORTRAN HERWIG, is no longer supported. Diquarks are therefore present only as remnants of incoming baryons, or from baryon number violating processes (see Section 7.6.2).

<sup>4</sup> Note that quarks and antiquark represent a start or endpoint respectively of the colour-connected pair.

In all cases, we do not allow reconnections that would connect a quark-antiquark pair that was originally in a colour octet state, *i.e.* that came from the same gluon. This is controlled by the `OctetTreatment` switch: either only quark-antiquark pairs from a non-perturbative gluon splitting are prevented from being reconnected (`OctetTreatment=Final`), or all quark-antiquarks in an octet state are prevented from being reconnected (`OctetTreatment=All`). The latter is set as the default in Herwig 7.3 to improve the simulation of gluon jets [31].

### 7.2.1 Plain colour reconnection

The closeness measure for the Plain colour reconnection algorithm is defined as

$$\lambda = \sum_{i=1}^{N_{\text{cl}}} M_i^2.$$

This involves reclustering the pairs of quarks/antiquarks to reduce their invariant mass, and hence their contribution to  $\lambda$ .

'Plain' colour reconnection proceeds by choosing a reference quark at random from all cluster constituents; the cluster containing this quark is compared to all other clusters, each of which is considered for reclustering.

For each cluster, the sum of the invariant cluster masses of the original cluster configuration,  $M_A + M_B$ , and of the masses of the possible new clusters,  $M_C + M_D$ , are calculated. The alternative cluster configuration that results in the lowest sum of cluster masses is accepted for reconnection, with probability  $p_{\text{Reco}}$ . If the reconnection is accepted, the original clusters are replaced by the new clusters. This is iterated for each cluster in the list such that each cluster on the list has had the chance to be reconnected.

This algorithm results in modified clusters with smaller invariant masses than the original configuration and systematically replaces heavier clusters with lighter ones, resulting in a shift of the invariant cluster mass.

### 7.2.2 Statistical colour reconnection

In principle, in order to minimise colour-length among all possible clusters of the final-state partons in an event, all possible permutations of cluster configurations have to be considered.

In hadronic  $pp$  collisions, such a 'brute force' approach would be computationally prohibitive *i.e.* for  $N$  clusters the time complexity would be  $\mathcal{O}(N!)$ , due to the large number of clusters originating from the hard process and multiparton interactions. To tackle this problem, a statistical model for colour reconnection was implemented in Ref. [61].

The statistical colour reconnection model samples cluster configurations to find configurations of clusters with successively lower values of  $\lambda$ . The approach is based on a simulated annealing algorithm, which selects random pairs of clusters and accepts the reconnection if the possible new cluster configuration lowers  $\lambda$ .

To allow the configuration to escape local minima of colour-length, if the reconnection would increase  $\lambda$  it is accepted with probability

$$P = \exp\left(-\frac{\lambda_2 - \lambda_1}{T}\right),$$

where  $T$  is the control parameter of the simulated annealing algorithm, analogous to temperature.

The parameter  $T$  is progressively reduced from a starting value that is chosen from the median of 10 randomly chosen values for  $|\Delta\lambda_{ij}| = |\lambda_i - \lambda_j|$  of the particular event, multiplied by a tuneable input parameter (`InitialTemperature`). It is stepped down by a factor (`AnnealingFactor`) in each step; the number of steps (`AnnealingSteps`), and the number of colour swaps tried in each step (`TriesPerStepFactor`), can be set by the user.

### 7.2.3 Baryonic colour reconnection

This algorithm is the default within Herwig 7.3. In this case, we additionally allow baryonic-type cluster configurations, containing three quarks or three antiquarks.

This allows for a different baryon production mechanism especially for multiply strange/heavy baryons as can be seen e.g. in Fig. 7.2. Furthermore, for high multiplicity events it gives a further mechanism to reduce multiplicity even stronger than regular mesonic colour reconnection as can be seen in Fig. 7.3.

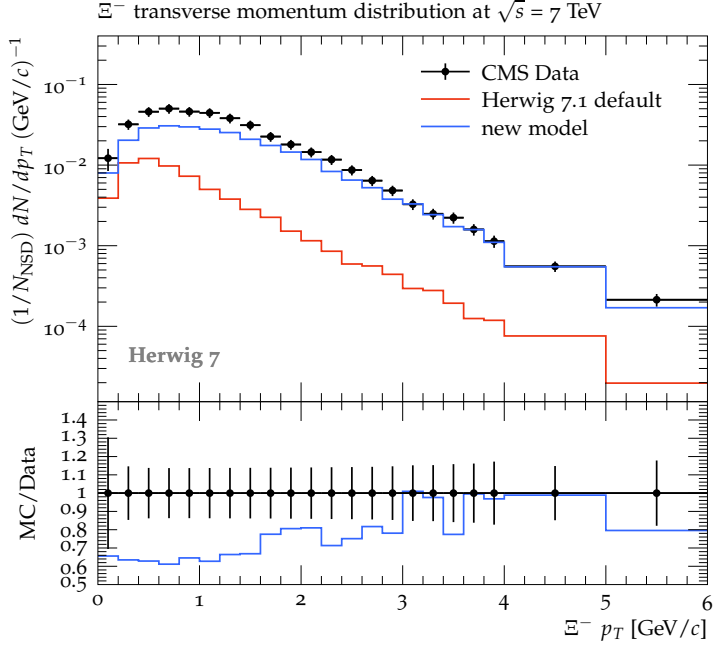


Fig. 7.2:  $p_T$  spectrum of  $\Xi^-$  baryons for minimum bias events measured by CMS [227] at  $\sqrt{s} = 7$  TeV from [48] for the old colour reconnection model and the tuned baryonic model, labelled as ‘new model’.

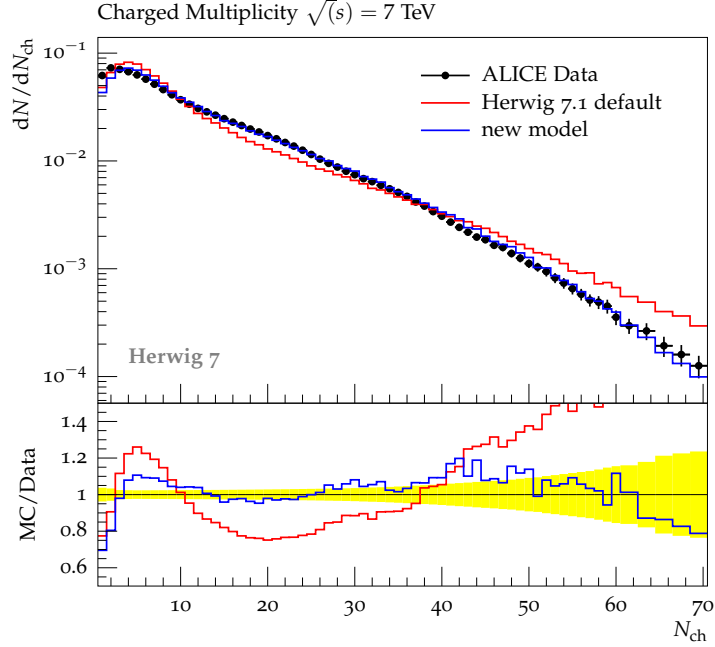


Fig. 7.3: Multiplicity distribution for minimum bias events measured by ALICE [228] at  $\sqrt{s} = 7$  TeV from [48] for the old colour reconnection model and the tuned baryonic model, labelled as ‘new model’.

Instead of finding quark combinations that directly lower the invariant cluster mass, we consider a simple geometric picture of nearest neighbours that populate approximately the same phase-space region based on their relative rapidities motivated by [48].

As with the other colour reconnection models, the starting point of the algorithm is the predefined colour configuration that emerges once the parton shower evolution has terminated, and the remaining gluons are split non-perturbatively into quark-antiquark pairs.

A cluster  $C_A$  is then picked randomly from the list of clusters and we boost into the rest frame of  $C_A$  where the direction of the antiquark in the rest frame of the cluster is defined as the positive axis.

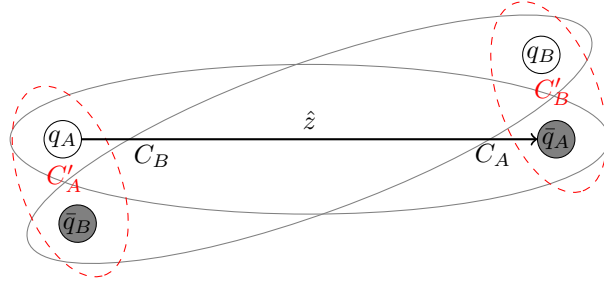


Fig. 7.4: Pictorial representation of a cluster configuration that would lead to a mesonic reconnection from  $C_A, C_B$  to  $C'_A, C'_B$ .

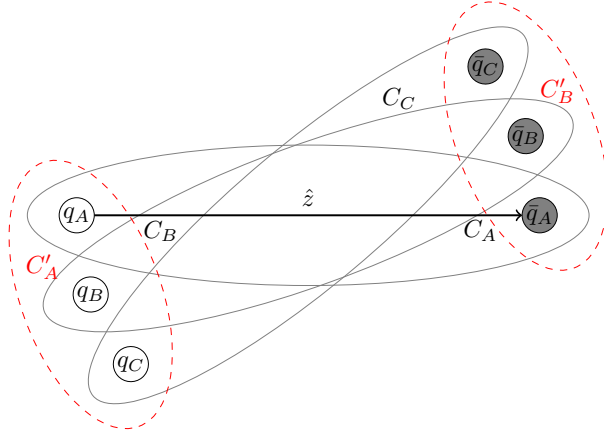


Fig. 7.5: Pictorial representation of a cluster configuration that would lead to a baryonic reconnection from  $C_A, C_B, C_C$  to  $C'_A, C'_B, C'_C$ .

In the next step we loop over all remaining clusters  $C_B$  and calculate the rapidities of the cluster constituents with respect to this axis in the rest frame of the cluster  $C_A$ . Based on the calculated rapidities, the clusters fall into one of three categories, according to the alignment of the two quark-antiquark pairs:

- Mesonic:  $y(q) > 0 > y(\bar{q})$ .
- Baryonic:  $y(\bar{q}) > 0 > y(q)$ .
- None of the above.

If the cluster falls into the last category it is not considered for reconnection. In the next step the label of the category and the sum of the absolute values  $|y(q)| + |y(\bar{q})|$  is saved for the clusters with the two largest sums. If the cluster with the largest sum is labeled *mesonic*, the reconnection is accepted with a probability given by the parameter *pReco* (*ReconnectionProbability*) as shown in Fig. 7.4. If the clusters with the two largest sums are labeled *baryonic* they are considered for baryonic reconnection with the probability *pRecoBaryonic* (*ReconnectionProbabilityBaryonic*) and the three mesonic clusters are rearranged to form two baryonic type clusters as shown in Fig. 7.5.

Once a baryonic-type cluster is formed, all participating clusters are removed from the list and not considered for further reconnections. We run this algorithm until we have every cluster  $C_A$  from the list of clusters has had the chance to be reconnected. Further details of the algorithm are described in [48].

Note that all baryonic clusters are reduced to diquark-quark at the end of the algorithm resulting in two component clusters. This reduction is done by grouping the smallest invariant mass quark pair to a diquark and rescaling the momentum to their invariant mass. Optionally one can force the mass of the reduced diquarks to be the same as the diquarks constituent mass via the interface *ClusterFinder:DiQuarkOnShell=Yes*.

#### 7.2.4 Baryonic-Mesonic colour reconnection<sup>5</sup>

<sup>5</sup> Note that in Herwig 7.3 the baryonic-mesonic colour-reconnection model is not tuned. This colour-reconnection model depends strongly on the lab frame, which means for observables which are not tied to the lab frame, results obtained using this model might not be well under control.

In this algorithm based on [226] we consider many different colour reconnection (CR) topologies of the types summarized in [Table 7.1](#) alongside with the name of the static reconnection probabilities. Note that here we have denoted mesonic clusters consisting of a quark and an antiquark with  $M, M'$  and (anti)baryonic clusters which consist of three (anti)quarks as  $B, B' (\bar{B}, \bar{B}')$ . Similarly to the baryonic colour reconnection this algorithm allows for the coalescence of three mesonic cluster to a baryonic and antibaryonic cluster. However here we allow also all possible back-reactions as displayed in table [Table 7.1](#).

In order to include all possible colour reconnection topologies we need to impose a selection algorithm, which is described in the flowchart shown in [Fig. 7.6](#). This selection algorithm draws the following possible sets of clusters from all clusters available. The possible subsets of clusters fall into one of the following categories:

- Three mesonic clusters (3M), which can reconnect to three different mesonic clusters (3M') or to a baryonic-antibaryonic cluster pair (BbarB)
- One mesonic and one (anti)-baryonic cluster (MB), which can reconnect only to a different set of one mesonic and one (anti)-baryonic cluster (M'B')
- Two (anti)-baryonic clusters (2B), which can only reconnect to two different (anti)-baryonic clusters (2B')
- One anti-baryonic and one baryonic cluster (BbarB), which can only reconnect to three mesonic clusters (3M)

With the selection algorithm described in the flowchart in [Fig. 7.6](#) we can draw randomly possible subsets of clusters of the above categories. The baryonic-mesonic colour reconnection algorithm then proceeds as follows in order to accept a new colour configuration subject to a distance measure  $\Delta R_{\text{tot}}$  defined later on:

1. Select a subset of clusters  $\mathcal{C}_{\text{ini}}$  randomly (where only the types of subsets in [Table 7.1](#) are allowed) according to the selection algorithm.
2. Minimize a measure of distance in phase-space  $\Delta R_{\text{tot}}$  in the lab frame on parton level with the constraint of having only mesonic and baryonic clusters at the end and no remaining partons. Call the configuration that minimizes this  $\mathcal{C}_{\text{proposal}}$
3. Allow the initial configuration to reconnect to the minimal CR configuration with a static probability of  $P_{\mathcal{C}_{\text{ini}} \rightarrow \mathcal{C}_{\text{proposal}}}$ , which is a tunable parameter of the model
4. Go back to 1. and repeat the process for  $f_{\text{step}} N_{\text{Clusters}}$  times, where  $N_{\text{Clusters}}$  are the initial number of clusters before CR and  $f_{\text{step}}$  is a tunable parameter.

The proposal configuration  $\mathcal{C}_{\text{proposal}}$  is determined by minimizing the distance measure  $\Delta R_{\text{tot}}$ ,

$$\Delta R_{\text{tot}}(C) = \omega_{\text{MTBF}} \sum_{\text{mesons } m} \Delta R_{q_m \bar{q}_m} + \sum_{\text{baryons } b} \sum_{i \in b} \Delta R_{i \langle b \rangle}$$

which can be seen to comprise a contribution from the mesonic clusters  $m$  in  $C$ , and a baryon-junction-inspired contribution from the baryonic clusters  $b$ . The parameter  $\omega_{\text{MTBF}}$  is tunable (`MesonToBaryonFactor`), and controls the relative distance scale between the two types of cluster. The mean rapidity and azimuth of a baryonic cluster as indicated by  $\langle b \rangle$  are defined as the arithmetic mean and circular mean (better-defined for periodic variables [229]) respectively,

$$\bar{y} = \frac{1}{3} \sum_i y_{q_i}$$

$$\bar{\phi} = \text{atan2} \left( \frac{1}{3} \sum_i \sin(\phi_{q_i}), \frac{1}{3} \sum_i \cos(\phi_{q_i}) \right)$$

and the rapidity-azimuth distance measure is defined as

$$\Delta R = \sqrt{(\Delta y)^2 + (\Delta \phi)^2}.$$

It is also possible to use a different definition of the baryonic distance measure, which instead of the above baryon junction-like measure of distance uses all permutation distances. This changes the selection criterion for baryons such that  $\Delta R_{\text{baryonic}}(C_b)$  becomes:

$$\Delta R_{\text{baryonic}}(C_b) = \Delta R_{q_1, q_2} + \Delta R_{q_2, q_3} + \Delta R_{q_1, q_3}$$

This option can be turned on by `Junction=Off`. Note that the same vetoing applies if we would propose an octet mesonic cluster as previously discussed depending on the option `OctetTreatment`.

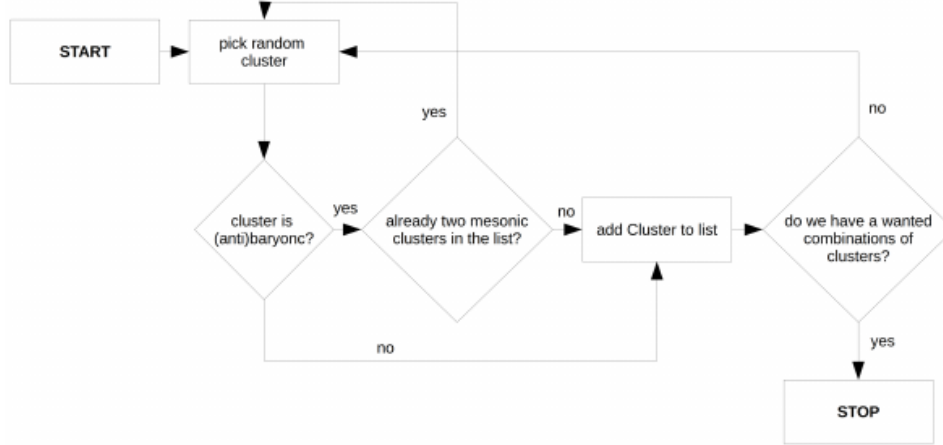


Fig. 7.6: Flowchart of selection algorithm for cluster sets of the algorithm (from [226]).

Table 7.1: In this table we summarize the different colour reconnection topologies and their corresponding static probabilities. Here we denote mesonic clusters as  $M$  and (anti)-baryonic clusters as  $B(\bar{B})$ .

Colour reconnection topology	Reconnection probability
$3M \rightarrow 3M'$	ReconnectionProbability3Mto3M
$3M \rightarrow B\bar{B}$	ReconnectionProbability3MtoBBbar
$M, B \rightarrow M', B'$	ReconnectionProbabilityMBtoMB
$M, \bar{B} \rightarrow M', \bar{B}'$	ReconnectionProbabilityMBtoMB
$\bar{B}, B \rightarrow 3M$	ReconnectionProbabilityBbarBto3M
$2B \rightarrow 2B'$	ReconnectionProbability2Bto2B
$2\bar{B} \rightarrow 2\bar{B}'$	ReconnectionProbability2Bto2B

### 7.3 Cluster fission

The cluster model is based on the observation that because the cluster mass spectrum is both universal and peaked at low masses, as shown in Fig. 7.7, the clusters can be regarded as highly excited hadron resonances and decayed, according to phase-space, into the observed hadrons. However, small fraction of clusters are too heavy for this to be a reasonable approach. These heavy clusters are therefore first split into lighter clusters before they decay.

A cluster is split into two clusters if its mass,  $M$ , is such that

$$M^{\text{Cl}_{\text{pow}}} \geq \text{Cl}_{\text{max}}^{\text{Cl}_{\text{pow}}} + (m_1 + m_2)^{\text{Cl}_{\text{pow}}}, \quad (7.1)$$

where  $\text{Cl}_{\text{max}}$  and  $\text{Cl}_{\text{pow}}$  are parameters of the model, and  $m_{1,2}$  are the masses of the constituent partons of the cluster. In practice, in order to improve the description of the production of bottom and charm hadrons, we include separate values of both  $\text{Cl}_{\text{max}}$  ( $\text{ClMaxLight}$ ,  $\text{ClMaxCharm}$  and  $\text{ClMaxBottom}$ ) and  $\text{Cl}_{\text{pow}}$  ( $\text{ClPowLight}$ ,  $\text{ClPowCharm}$  and  $\text{ClPowBottom}$ ) for clusters containing light, charm and bottom quarks, respectively. The default values of these and other important hadronization parameters are given in Table 7.5, at the end of this section.

For clusters that need to be split, a  $q\bar{q}$  pair is selected to be popped from the vacuum. Only up, down and strange quarks are chosen with probabilities given by the parameters  $\text{Pwt}_q$ ,<sup>6</sup> where  $q$  is the flavour of the quark. Once a pair is selected the cluster is decayed into two new clusters with one of the original partons in each cluster. Unless one of the partons is a remnant of the incoming beam particle the mass distribution of the new clusters is given by

$$\begin{aligned} M_1 &= m_1 + (M - m_1 - m_q) \mathcal{R}_1^{1/P}, \\ M_2 &= m_2 + (M - m_2 - m_q) \mathcal{R}_2^{1/P}, \end{aligned} \quad (7.2)$$

<sup>6</sup> We use  $\text{Pwt}_q$  to denote the probability of selecting a given quark or diquark. The same parameters are used both for cluster fission and cluster decay, with only  $\text{PwtDquark}$ ,  $\text{PwtUquark}$  and  $\text{PwtSquark}$  used for fission as well as  $\text{PwtCquark}$  and  $\text{PwtBquark}$  for decay. For diquarks in cluster decay, the product of the diquark probability  $\text{PwtDIquark}$ , the probabilities of the quarks forming the diquark, and a symmetry factor, for diquarks.

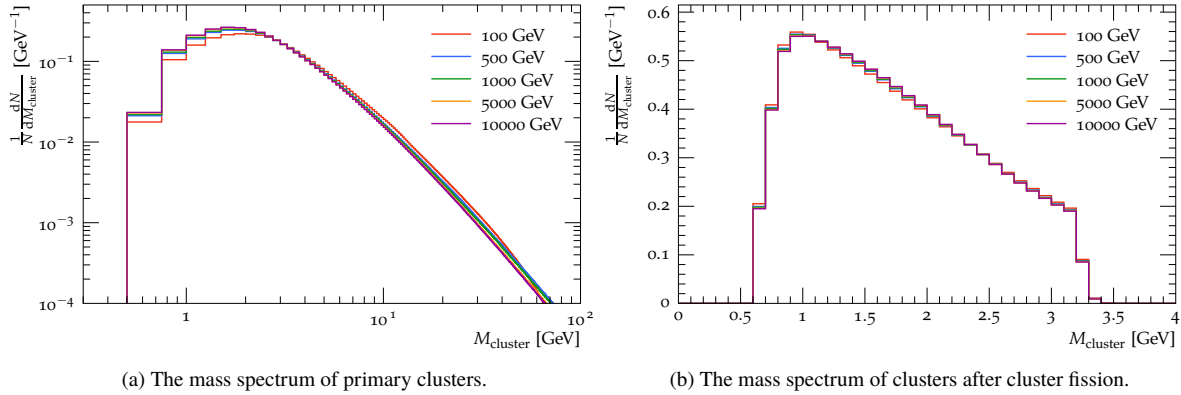


Fig. 7.7: The mass spectrum of clusters, generated using  $e^+e^- \rightarrow d\bar{d}$  collisions at the displayed centre-of-mass energies. Only clusters containing light quarks are shown.

where  $m_q$  is the mass of the parton popped from the vacuum,  $M_{1,2}$  are the masses of the clusters formed by the splitting and  $\mathcal{R}_{1,2}$  are uniformly distributed random numbers on the range  $(0, 1)$ . The distribution of the masses of the clusters is controlled by the parameter  $P$ , which is `PSplitLight`, `PSplitCharm` or `PSplitBottom` for clusters containing light, charm or bottom quarks.

In addition to selecting the mass according to Eq. (7.2), the masses of the daughter clusters are required to satisfy either a `Static`

$$M > M_1 + M_2, \quad M_1 > m_q + m_1, \quad M_2 > m_q + m_2,$$

or a `Dynamic` mass hierarchy criterion [49]:

$$M^2 > M_1^2 + M_2^2, \quad M_1^2 > m_q^2 + m_1^2 + \delta_{\text{th}}, \quad M_2^2 > m_q^2 + m_2^2 + \delta_{\text{th}}.$$

$\delta_{\text{th}}$  is the kinematic threshold shift parameter. The `Dynamic` kinematic threshold scheme also incorporates a probability distribution function,  $P_{\text{cluster}}$ , as a decision-making device:

$$P_{\text{cluster}} = \left( 1 + \left| \frac{M - \delta}{M_{\text{th}}} \right|^r \right)^{-1}, \quad P_{\text{cluster}} > \mathcal{R},$$

to either accept or reject the cluster splitting through comparison against a randomly generated number  $\mathcal{R}$  distributed uniformly on  $(0,1)$ . This function also has two new tunable parameters:  $r$  as the probability power factor and  $\delta$  as the probability shift. Here,  $M_{\text{th}}$  is the mass threshold for the cluster, defined as the sum of the masses of the constituent quarks plus the mass of the spawned di-quark. This scheme provides a smooth distribution for dynamic threshold cuts based on the cluster mass and its kinematic properties [49]. The `Dynamic` threshold option is the default choice, which can be changed via `KinematicThreshold` switch:

```
cd /Herwig/Hadronization
set ClusterFissioner:KinematicThreshold <Static/Dynamic>
```

The spectrum of the cluster masses after the cluster splitting is shown in Fig. 7.7.

For clusters that contain a remnant of the beam particle in hadronic collisions a soft distribution is used for the masses of the clusters produced in the splitting. The `RemnantOption` switch controls whether the soft distribution is used for both daughter clusters (`RemnantOption=0`) or only the daughter cluster containing the remnant (`RemnantOption=1`), the default. The mass of the soft clusters is given by

$$M_i = m_i + m_q + x,$$

where  $x$  is distributed between 0 and  $M - m_1 - m_2 - 2m_q$  according to

$$\frac{dP}{dx^2} \propto \exp(-bx),$$

where  $b = 2/\text{SoftClusterFactor}$ .

## 7.4 Cluster decays

The final step of the cluster hadronization model is the decay of the cluster into a pair of hadrons. For a cluster of a given flavour  $(q_1, \bar{q}_2)$  a quark-antiquark or antiquark-diquark pair  $(q, \bar{q})$  is extracted from the vacuum and a pair of hadrons with flavours  $(q_1, \bar{q})$  and  $(q, \bar{q}_2)$  formed. The hadrons are selected from all the possible hadrons with the appropriate flavour based on the available phase-space, spin and flavour of the hadrons. While the general approach is the same in all cluster models, several variations are implemented in Herwig 7: the original model of Ref. [2] used in FORTRAN HERWIG [4,5]; the approach of Ref. [230], which was designed to solve the problem of isospin violation in the original model if incomplete SU(2) multiplets of hadrons are included; and a new variant that addresses the issue of the low rate of baryon production in the approach of Ref. [230].

In all these approaches the weight for the production of the hadrons  $a_{(q_1, \bar{q})}$  and  $b_{(q, \bar{q}_2)}$  is

$$W(a_{(q_1, \bar{q})}, b_{(q, \bar{q}_2)}) = P_q w_a s_a w_b s_b p_{a,b}^*,$$

where  $P_q$  is the weight for the production of the given quark-antiquark or diquark-antidiquark pair,  $w_{a,b}$  are the weights for the production of individual hadrons and  $s_{a,b}$  are the suppression factors for the hadrons, which allow the production rates of individual meson multiplets, and singlet and decuplet baryons to be adjusted. The momentum of the hadrons in the rest frame of the decaying cluster,

$$p_{a,b}^* = \frac{1}{2M} \left[ \left( M^2 - (m_a + m_b)^2 \right) \left( M^2 - (m_a - m_b)^2 \right) \right]^{\frac{1}{2}},$$

measures the phase-space available for two-body decay. If the masses of the decay products are greater than the mass of the cluster then the momentum is set to zero. The weight for the individual hadron is

$$w_h = w_{\text{mix}}(2J_h + 1),$$

where  $w_{\text{mix}}$  is the weight for the mixing of the neutral light mesons<sup>7</sup> and  $J_h$  is the spin of the hadron.

The different approaches vary in how they implement the selection of the cluster decay products based on this probability.

In the approach of Ref. [2] the probability is generated in a number of pieces. First the flavour of the quark-antiquark, or diquark-antidiquark, pair popped from the vacuum is selected with probability

$$P_q = \frac{\mathbf{P}^{\text{wt}}_q}{\sum_{q'} \mathbf{P}^{\text{wt}}_{q'}}.$$

Each of the hadrons produced in the cluster decay is then selected from the available hadrons of the appropriate flavours using the weight

$$P_h = \frac{s_h w_h}{s w_{\max(q, \bar{q}')}} ,$$

where  $s w_{\max(q, \bar{q}'')}$  is the maximum value of the suppression factor times the weight for a given flavour combination.

A weight is calculated for this pair of hadrons

$$W = \frac{p_{a,b}^*}{p_{\max}^*},$$

where  $p_{a,b}^*$  is the momentum of the hadrons in the cluster rest frame and  $p_{\max}^*$  is the maximum momenta of the decay products for hadrons with the relevant flavour.<sup>8</sup> The hadrons produced are then retained according to this weight. If they are not retained, the algorithm restarts from the choice of the flavour that is popped out of the vacuum.

This procedure gives a probability of approximately

$$P(a_{(q_1, \bar{q})}, b_{(q, \bar{q}_2)} | q_1, \bar{q}_2) \propto P_q \frac{1}{N_{(q_1, \bar{q})}} \frac{1}{N_{(q, \bar{q}_2)}} \frac{s_a w_a}{s w_{\max(q_1, \bar{q})}} \frac{s_b w_b}{s w_{\max(q, \bar{q}_2)}} \frac{p_{a,b}^*}{p_{\max}^*}$$

of choosing hadrons  $a_{(q_1, \bar{q})}$  and  $b_{(q, \bar{q}_2)}$ . The number of hadrons with flavour  $(q_1, \bar{q}_2)$  is  $N_{(q_1, \bar{q}_2)}$ .

<sup>7</sup>  $w_{\text{mix}} = 1$  for all other particles.

<sup>8</sup> That is, the momentum with the lightest possible choices for  $a$  and  $b$ .

Kupčo [230] pointed out one problem with this approach: as new hadrons with a given flavour are added, the production of the existing hadrons with the same flavour is suppressed. In order to rectify this problem he proposed a new approach for choosing the decay products of the cluster. Instead of splitting the probability into separate parts, as in Ref. [2], a single weight was calculated for each combination of decay products

$$W(a_{(q_1, \bar{q})}, b_{(q, \bar{q}_2)} | q_1, \bar{q}_2) = P_q w_a w_b s_a s_b p_{a,b}^*,$$

which gives the probability of selecting the combination

$$P(a_{(q_1, \bar{q})}, b_{(q, \bar{q}_2)} | q_1, \bar{q}_2) = \frac{W(a_{(q_1, \bar{q})}, b_{(q, \bar{q}_2)} | q_1, \bar{q}_2)}{\sum_{c,d,q'} W(c_{(q_1, \bar{q}')}, d_{(q', \bar{q}_2)} | q_1, \bar{q}_2)}.$$

The addition of new hadrons now increases the probability of choosing a particular flavour, however because these new hadrons are usually heavy they will not contribute for the majority of light clusters.

The main problem with this approach is that because many more mesons are included in the simulation than baryons not enough baryons are produced. In order to address this problem in Herwig 7, if a cluster mass is sufficiently large that it can decay into the lightest baryon-antibaryon pair the parameter  $\mathbf{Pwt}_{qq}$  is used to decide whether to select a mesonic or baryonic decay of the cluster. The probabilities of selecting a mesonic decay or baryonic decay are  $\frac{1}{1+\mathbf{Pwt}_{qq}}$  and  $\frac{\mathbf{Pwt}_{qq}}{1+\mathbf{Pwt}_{qq}}$ . This modification not only increases the number of baryons produced but gives direct control over the rate of baryon production. Tetraquark states are not implemented in Herwig 7, so for the baryonic cluster that results from a hadron remnant, only ‘mesonic’ decays  $q(qq) \rightarrow q\bar{q} + q\bar{q}q$  are allowed.

Once the decay products of the cluster are selected, the cluster is decayed. In general the cluster decay products are isotropically distributed in the cluster rest frame. However, hadrons that contain a parton produced in the perturbative stage of the event retain the direction of the parton in the cluster rest frame, apart from a possible Gaussian smearing of the direction. This is controlled by the **CIDir** parameter, which by default [**CIDir=true**] retains the parton direction, and the **ClSmr** parameter, which controls the Gaussian smearing through an angle  $\theta_{\text{smear}}$  where

$$\cos \theta_{\text{smear}} = 1 + \mathbf{ClSmr} \log \mathcal{R}, \quad (7.3)$$

where  $\mathcal{R}$  is another uniformly distributed random number on the range  $(0, 1)$ . The azimuthal angle relative to the parton direction is distributed uniformly. To provide greater control the parameters **CIDir** (**CIDirLight**, **CIDirCharm** and **CIDirBottom**) and **ClSmr** (**ClSmrLight**, **ClSmrCharm** and **ClSmrBottom**) can be set independently for clusters containing light, charm and bottom quarks.

In practice there is always a small fraction of clusters that are too light to decay into two hadrons. These clusters are therefore decayed to a single hadron, with the appropriate flavours, together with a small reshuffling of energy and momentum with the neighbouring clusters to allow the hadron to be given the correct physical mass. The cluster with the smallest space-time distance that can absorb the recoil is used. In addition, for clusters containing a bottom or charm quark, in order to improve the behaviour at the threshold, the option exists of allowing clusters above the threshold mass for the production of two hadrons,  $M_{\text{threshold}}$ , to decay into a single hadron. A single hadron can be formed for masses

$$M < M_{\text{limit}} = (1 + \mathbf{SingleHadronLimit}) M_{\text{threshold}}. \quad (7.4)$$

The probability of such a single-meson cluster decay is assumed to decrease linearly for  $M_{\text{threshold}} < M < M_{\text{limit}}$ . The parameters **SingleHadronLimitCharm** and **SingleHadronLimitBottom** control the limit on the production of single clusters for charm and bottom clusters respectively. Increasing the limit has the effect of hardening the momentum spectrum of the heavy mesons. Until Herwig 7.1 the lightest hadron with the correct flavours was always chosen. However there are cases, for example:

1. ( $u\bar{b}$ ) clusters where the  $B^+$  and  $B^{*+}$  mesons both have masses which are below the threshold for the decay of the cluster to  $B\pi$ ;
2. ( $c\bar{c}$ ) clusters where there are many charmonium states with masses below the threshold for the cluster decay to open charm;

where there are many states below the threshold. If we only select the lightest state it can lead to over-production of the lightest state, and under-production of the other states which lie below the threshold. In the most extreme case for ( $c\bar{c}$ ) clusters it means that the  $J/\psi$  meson is never produced during hadronization. In Herwig 7.1 we therefore introduced a new switch **BelowThreshold** to control the treatment of clusters with masses below the two hadron threshold and by default select from all the hadrons below the threshold according to their spin weights (**BelowThreshold=All**) to pick the hadron used for single hadron decay.

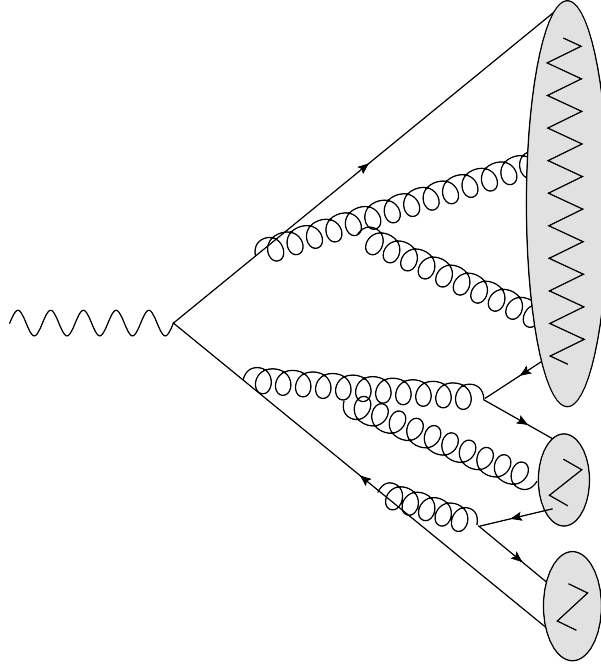


Fig. 7.8: Schematic figure of a colour singlet which can occur before the perturbative gluons from the parton shower are split non-perturbatively into  $q\bar{q}$  pairs.

#### 7.4.1 Kinematic strangeness production

In Herwig strangeness can be produced at each non-perturbative step of the hadronization stage (gluon splitting, cluster fissioning, and cluster decay). Instead of having a flat number as a weight for the probability to produce a strange and an antistrange quark, the option of kinematic strangeness production uses the available kinematic information of the relevant surrounding colour-singlet system in order to calculate the probability to produce a strange quark-antiquark pair. This procedure makes the production of strangeness more dynamic and dependent on the event topology.

At each of the hadronization stages, the flat weights are replaced by the following functional form:

$$w_s(M)^2 = \exp\left(-\frac{M_0^2}{M^2}\right), \quad (7.5)$$

where  $M_0^2$  is the characteristic mass scale for each stage and  $M^2$  is the invariant mass of the relevant colour singlet system on which the production of strangeness depends. An additional option for the mass measure is the threshold production measure  $\lambda$  which is defined by

$$\lambda = M_{cs}^2 - \left(\sum_i M_i\right)^2. \quad (7.6)$$

Here,  $M_{cs}^2$  is the total invariant mass of the the colour singlet system and  $M_i$  are the invariant masses of the endpoints for pre-clusters or the constituent partons in a normal cluster.

While at the cluster fissioning stage and at the cluster decay stage the relevant colour singlet system is a normal cluster, we introduce the concept of a pre-cluster at the stage of non-perturbative gluon splitting. Instead of immediately splitting the gluons into  $q\bar{q}$  pairs we collect the various colour singlet systems in the event and form so called *pre-clusters*. A pictorial representation of such a pre-cluster is shown in Fig. 7.8.

In order to use the kinematic strangeness production one simply has to set the interface `EnhanceSProb=Exponential` for the gluon splitting stage (`PartonSplitter`), the cluster fissioner stage (`ClusterFissioner`) and finally the cluster decay stage which is done via the hadron selector (`HadronSelector`). Additionally one can choose between two mass measures used for the exponential scaling (`MassMeasure=Mass` and `MassMeasure=Lambda`).

The option for kinematic strangeness production is explicitly recommended when trying to simulate flavour sensitive observables. A detailed description of the model can be found in [47].

### 7.4.2 Mixing weights

For neutral mesons that only contain the light (up, down and strange) quarks there is mixing. If we consider the wavefunctions of the neutral mesons, which we write for the  ${}^1S_0$  meson multiplet but the treatment applies to an arbitrary SU(3) flavour multiplet, then

$$\begin{aligned}\pi^0 &= \frac{1}{\sqrt{2}} (d\bar{d} - u\bar{u}), \\ \eta &= \psi_8 \cos \theta - \psi_1 \sin \theta, \\ \eta' &= \psi_8 \sin \theta + \psi_1 \cos \theta,\end{aligned}$$

where  $\theta$  is the nonet mixing angle and the wavefunctions for the octet and singlet components are

$$\begin{aligned}\psi_8 &= \frac{1}{\sqrt{6}} (u\bar{u} + d\bar{d} - 2s\bar{s}), \\ \psi_1 &= \frac{1}{\sqrt{3}} (u\bar{u} + d\bar{d} + s\bar{s}).\end{aligned}$$

The probabilities of finding a given quark-antiquark inside a particular neutral meson can be calculated, which gives the mixing weights for the neutral light mesons

$$\begin{aligned}w_{u\bar{u}}^{\pi^0} &= w_{d\bar{d}}^{\pi^0} = \frac{1}{2}, w_{s\bar{s}}^{\pi^0} = 0, \\ w_{u\bar{u}}^{\eta} &= w_{d\bar{d}}^{\eta} = \frac{1}{2} \cos^2(\theta + \phi), w_{s\bar{s}}^{\eta} = \sin^2(\theta + \phi), \\ w_{u\bar{u}}^{\eta'} &= w_{d\bar{d}}^{\eta'} = \frac{1}{2} \sin^2(\theta + \phi), w_{s\bar{s}}^{\eta'} = \cos^2(\theta + \phi),\end{aligned}\tag{7.7}$$

where  $\phi = \tan^{-1} \sqrt{2}$  is the ideal mixing angle.

In the approach of Ref. [2] the factor of  $\frac{1}{2}$  in the weights for the  $u\bar{u}$  and  $d\bar{d}$  components was omitted as this is approximately given by the ratio of the number of charged mesons containing up and down quarks to neutral ones, which is exactly two for ideal mixing where the  $s\bar{s}$  mesons do not mix with those containing up and down quarks.

In practice the mixing angles can be adjusted for each meson multiplet that is included in the simulation although with the exception of the lightest pseudoscalar, vector, tensor and spin-3 multiplets the assumption of ideal mixing is used.

## 7.5 HQET and spin-hadronization

Heavy quark effective theory (HQET) is a framework that systematically describes the behavior and interactions of heavy quarks within hadrons, i.e. when  $m_Q \gg \Lambda_{\text{QCD}}$ , while simultaneously assuming that the heavy quark moves at a sub-relativistic velocity. HQET leverages this mass hierarchy and velocity separation to simplify the mathematical description of heavy quark interactions within hadrons. It assumes the velocity and spin of heavy quarks can be treated as independent variables, resulting in a decoupling of the heavy quark's dynamics from the lighter degrees of freedom. This allows for a separation of scales, where interactions involving the heavy quark are analysed using a perturbative expansion, while interactions involving lighter degrees of freedom are treated non-perturbatively. This *heavy quark spin-flavour symmetry* allows for model-independent predictions of certain properties of heavy hadrons, such as their spectra and decay rates [49, 231, 232].

A hadronic state can be considered a non-recoiling source of colour when it consists of a heavy quark ( $Q$ ) and light degrees of freedom ( $q$ ) [233–237]. In this regime, since  $m_Q \gg m_q$  the heavy quark's colour magnetic moment decouples from hadronic properties, and a heavy quark *spin-flavour symmetry* emerges [231]. This symmetry can be used to produce model-independent predictions of heavy hadron spectra, weak matrix elements, and strong decay rates. An interesting consequence of this symmetry is the ability to distinguish between short- and long-distance interactions in a hadronization sequence, such as during a procedurally generated parton shower.

Generally, the strongly interacting particles produced during hard processes and subsequent parton showers in a simulated event have relatively large momenta. Therefore, the perturbative interactions during these stages occur over short time scales. Non-perturbative fragmentation processes that finalise these branches occur over longer time scales. Hadronization processes, regardless of model dependencies, are expected to occur at length scales of the order of  $\mathcal{O}(\Lambda_{\text{QCD}}^{-1})$ . This means the resulting energy redistribution is much smaller than  $m_Q$ , making it plausible to assume

that the velocity, mass, and spin of the heavy quark state (determined by short-distance physics) remain unchanged, indicating a decoupling between the dynamics of the heavy and light quark states [238–240].

This argument extends to the production of excited heavy mesons and heavy baryons in a hadronization event, where it is possible to tag the produced hadrons with the spin polarisation information of their heavy quark components [231]. This comes with a couple of caveats:

- (i) If the light-quark state's phase-space allows its angular momentum to become of the order of  $\mathcal{O}(m_Q^{-1})$ , the process can redistribute this angular momentum, meaning the outgoing heavy quark polarisation will depend on the polarisation of the light degree of freedom created in the fragmentation process.
- (ii) While conserving parity, fragmentation can produce anisotropic light degrees of freedom along its axis. The alignment of a light degree of freedom with spin  $j$  can be characterized by a model-dependent dimensionless parameter,  $\omega_j$  [231].

### 7.5.1 Kinematics of fragmentation

To properly translate the implications of HQET and the spin-flavour symmetry, one must start by projecting the kinematics and time scales of heavy quark fragmentation. Here, we closely follow [49, 231] by working in the rest frame of the heavy quark and identifying the preferred direction as the momentum of the parton shower progenitor. In this setup, the only interaction that can manipulate the spin of the heavy quark, i.e., the colour magnetic moment of the light degrees of freedom, is sufficiently suppressed by a factor of  $m_Q^{-1}$ . Collectively, the hadron can possess a total spin of  $j_{\pm} = j_q \pm 1/2$ , with  $j_q$  being the spin of the light state. We can therefore identify the  $j_{\pm}$  configurations with a spin multiplet  $(H, H^*)$ , and assume a small mass splitting  $\Delta m = m_{H^*} - m_H$ .

Due to the heavy quark constituent, the  $H$  and  $H^*$  states are considered unstable. They can decay weakly to lighter hadrons, where it is safe to assume an identical decay rate:

$$\Gamma(H \rightarrow X) = \Gamma(H^* \rightarrow X).$$

Alternatively,  $H^*$  can strongly or radiatively decay to  $H$ , with rate:

$$\gamma(H^* \rightarrow HX) \propto \Phi_{\text{phase-space}}^{H^* \rightarrow HX} \times |\mathcal{M}(H^* \rightarrow HX)|^2 \sim \mathcal{O}(m_Q^{-(2+n)}),$$

where  $n \geq 1$ , suggesting  $\Delta m \gg \gamma$ . Meanwhile, the relation between  $\Gamma$ ,  $\Delta m$ , and  $\gamma$  determines the nature of the fragmentation. Specifically, the case of  $\Gamma \gg \Delta m \gg \gamma$  allows for rapid decay of heavy hadrons while decoupling the colour magnetic moments of the heavy and light degrees of freedom. This holds true for both strong or weak decays, even for  $\Gamma \sim \Lambda_{\text{QCD}}$ , where the heavy quark can undergo partial hadronization before it decays.

The other possible cases, namely  $\Delta m \gg \Gamma \gg \gamma$  and  $\Delta m \gg \gamma \gg \Gamma$ , result in depolarisation of the heavy quark from its initial orientation. The above argument suggests that under most conditions, the angular distribution of decay products provides no information on the polarisation of the heavy quark, unless the condition  $\Gamma \gg \Delta m \gg \gamma$  is met. This is the so-called Falk–Peskin “no-win” theorem, which suggests that the polarisation of heavy quarks can remain intact only through strong, weak, or radiative decays of heavy excited mesons and heavy baryons [231].

### 7.5.2 Polarisation of excited heavy mesons

To explore the implications of HQET and spin-flavour symmetry regarding the polarisations of heavy excited mesons, we use the charm sector as an example, particularly the observed excited charmed mesons  $D_0^*$ ,  $D_1$ ,  $D_1'$ , and  $D_2^*$ . Assuming the initial  $c$  quark to be left-handed, a heavy charmed meson can be formed by combining with light degrees of freedom with  $j_q = 1/2$ . The colour magnetic interaction is decoupled, leaving the spin orientation of the light degrees independent of the charm quark and distributed uniformly, i.e.,  $j_q^{(3)} = \pm 1/2$  with equal probabilities;  $|\downarrow\rangle_c |\downarrow\rangle_q$  and  $|\downarrow\rangle_c |\uparrow\rangle_q$ . This scenario becomes more intriguing when considering the  $D_1$  and  $D_2^*$  meson states. With the assumed left-handed helicity of the charm quark, we now have light degrees of freedom with  $j_q = 3/2$ , which can manifest in any of the four possible helicity states. Parity invariance dictates that the probability of forming a specific helicity state cannot depend on the sign of its helicity,  $j_3$ , although probabilities may differ for states with distinct helicity magnitudes,  $|j_q^{(3)}|$ . Defining the parameter  $\omega_j$  ( $0 \leq \omega_j \leq 1$ ), which is the likelihood of fragmentation leading to a state with the maximum value of  $|j_q^{(3)}|$  in a system with light degrees of freedom with spin  $j_q$ , one can derive the probabilities for the emergence of different helicity states of the light degrees as

Table 7.2: Probability distribution of the helicity of the light degrees in excited heavy mesons.

$j_q^{(3)}$	-3/2	-1/2	1/2	3/2
Probability	$\frac{1}{2}\omega_{\frac{3}{2}}$	$\frac{1}{2}(1 - \omega_{\frac{3}{2}})$	$\frac{1}{2}(1 - \omega_{\frac{3}{2}})$	$\frac{1}{2}\omega_{\frac{3}{2}}$

The combination of the left-handed  $c$  spin state with a specific light degrees of freedom helicity  $j_q^{(3)}$  results in a coherent linear superposition of the charmed states with helicity  $j = j_q + j_Q$ . With this rationale one can calculate the probabilities of each helicity states getting populated as was outlined in Ref. [49].

Table 7.3: Probabilities for the population of the possible helicity states of  $D$ ,  $D^*$ ,  $D_1$ , and  $D_2^*$ . The sum of probabilities for the population of  $D$  and  $D^*$  helicity states equals 1, ensuring a proper probability distribution. The same argument is true for  $D_1$  and  $D_2^*$  states.

$j^{(3)}$	-2	-1	0	+1	+2
$D$	–	–	$\frac{1}{4}$	–	–
$D^*$	–	$\frac{1}{2}$	$\frac{1}{4}$	0	–
$D_1$	–	$\frac{1}{8}(1 - \omega_{\frac{3}{2}})$	$\frac{1}{4}(1 - \omega_{\frac{3}{2}})$	$\frac{3}{8}(1 - \omega_{\frac{3}{2}})$	–
$D_2^*$	$\frac{1}{2}\omega_{\frac{3}{2}}$	$\frac{3}{8}(1 - \omega_{\frac{3}{2}})$	$\frac{1}{4}(1 - \omega_{\frac{3}{2}})$	$\frac{1}{8}\omega_{\frac{3}{2}}$	0

To evaluate the parameter  $\omega_j$ , we consider the amplitude for the production of a pion at  $\theta, \phi$  from a  $H^* \rightarrow H\pi$  type meson decay, which is proportional to the spherical harmonics  $Y_j^\ell(\theta, \phi)$  ( $\ell$  being the angular momentum quantum number of  $H^*$ ):

$$\frac{d\Gamma(H^* \rightarrow H\pi)}{d\cos\theta} \propto \int d\phi \sum_j P_{H^*}(j) |Y_j^\ell(\theta, \phi)|^2, \quad (7.8)$$

where  $P_{H^*}(j)$  are the probabilities given in Table 6.3. Additionally,  $\theta$  and  $\phi$  are the angles of emission for the produced pion. Considering the case of  $D_2^* \rightarrow D\pi$ , Eq. (7.8) can be rewritten as [49]:

$$\frac{1}{\Gamma} \frac{d\Gamma(D_2^* \rightarrow D\pi)}{d\cos\theta} = \frac{1}{4} \left[ 1 + 3 \cos^2 \theta - 6 \omega_{\frac{3}{2}} \left( \cos^2 \theta - \frac{1}{3} \right) \right]. \quad (7.9)$$

To implement the above arguments in the context of HQET and spin-flavour symmetry principles in Herwig 7, we first generalise our calculations to an arbitrary heavy quark helicity,  $\rho_Q$ :

$$\begin{aligned} \hat{\rho}_D &= 1, \\ \hat{\rho}_{D^*} &= \text{diag} \left[ \frac{1}{2}(1 - \rho_Q), \frac{1}{2}, \frac{1}{2}(1 + \rho_Q) \right], \\ \hat{\rho}_{D_1} &= \text{diag} \left[ \frac{1}{16}[1 - \rho_Q + \omega_{\frac{3}{2}}(3 - 5\rho_Q)], \frac{1}{4}(1 - \omega_{\frac{3}{2}}), \frac{1}{16}[1 - \rho_Q + \omega_{\frac{3}{2}}(3 + 5\rho_Q)] \right], \\ \hat{\rho}_{D_2^*} &= \text{diag} \left[ \frac{1}{4}\omega_{\frac{3}{2}}(1 - \rho_Q), \frac{3}{16}(1 - \rho_Q) - \frac{1}{8}\omega_{\frac{3}{2}}(1 - \rho_Q), \frac{1}{4}(1 - \omega_{\frac{3}{2}}), \right. \\ &\quad \left. \frac{3}{16}(1 + \rho_Q) - \frac{1}{8}\omega_{\frac{3}{2}}(1 + \rho_Q), \frac{1}{4}\omega_{\frac{3}{2}}(1 + \rho_Q) \right]. \end{aligned}$$

Here,  $\hat{\rho}_H$  are the diagonal spin density matrices of the produced mesons  $H$ , with their components  $\rho_{i,i}$ , where  $i = 0, 1, 2, 3, 4$  runs from the most negative to the most positive valid helicity states. The diagonal structure of  $\hat{\rho}$  arises due to the statistical nature of hadronization, where quantum coherence between helicity states is lost. During hadronization, the strong interaction operates at non-perturbative scales, leading to the randomisation of relative phases between spin states. As a result, only diagonal elements remain, representing independent populations of helicity states. Within HQET and spin-flavour symmetry, the diagonal form of  $\hat{\rho}$  reflects parity conservation and the approximate decoupling of the heavy quark's spin from the light degrees of freedom. Off-diagonal terms, which would correspond to spin interference effects, vanish due to averaging over unobserved spin correlations in the fragmentation process. Consequently, the second index in  $\rho_{i,i}$  does not denote an intrinsic matrix structure but rather labels the helicity components, ordered from the most negative to the most positive eigenstates. To ensure numerical consistency in Herwig 7, the default parameter  $\omega_{\frac{3}{2}} = 0.20$  is introduced, governing the relative population of helicity states for mesons with light degrees of freedom in a  $j_q = 3/2$  configuration.

In Herwig 7, the above implementation is achieved through the introduction of the `SpinHadronizer` class. In particular, its `mesonSpin` function systematically handles the assignment of spin information and polarisation to generated mesons based on their spin characteristics and heavy constituent quark flavours. Starting with checks on the meson's parentage and

its constituents, `mesonSpin` employs spin information from the heavy quark to construct the spin properties of the meson, pertinent to the excited heavy mesons (in addition to their complex conjugates). The `mesonSpin` function also calculates the spin polarisation of the quark, updates the average polarisation for the specific flavour, and then assigns spin density matrix elements to the meson according to its spin value. It accommodates different spin types and meson categories, tailoring the spin behaviour and polarisation calculations to match the distinct characteristics of various excited heavy mesons.

### 7.5.3 Polarisation of heavy baryons

The ground state of a heavy baryon is formed by combining a heavy quark with a diquark system having a helicity arrangement of  $j_{qq} = 0$ . In this setup, there is no angular momentum transferred to the heavy quark, preserving the initial polarisation without dilution. This means that the polarisation of the initial heavy quarks can affect the ground state of heavy baryons. The relative probabilities of finding these states during heavy sector fragmentation are governed by two parameters,  $\omega_a$  and  $\omega_j$ . Here,  $\omega_a$  represents the relative probability of producing a  $j_{qq} = 1$  diquark compared to the ground state  $j_{qq} = 0$  configuration. In the cluster hadronization model of Herwig 7, we can set  $\omega_a = 1$ , since there is no preference between spin-0 and spin-1 diquarks [49].

Similar to excited heavy mesons, we consider the fragmentation of a left-handed polarised  $c$  quark. Then, the combination of the left-handed  $c$  spin state with a specific light degrees of freedom helicity  $j_q^{(3)}$  results in a coherent linear superposition of the charmed states with helicity  $j = j_q + j_Q$ . The probabilities of each helicity state being populated are shown in the table below [231]:

Table 7.4: Probabilities for the population of the possible helicity states of  $\Lambda_c$ ,  $\Sigma_c$ , and  $\Sigma_c^*$ .

$j^{(3)}$	-3/2	-1/2	1/2	3/2
$\Lambda_c$	--	$\frac{1}{1+\omega_a}$	0	-
$\Sigma_c$	--	$\frac{(1-\omega_1)\omega_a}{3(1+\omega_a)}$	$\frac{\omega_1\omega_a}{3(1+\omega_a)}$	-
$\Sigma_c^*$	$\frac{\omega_1\omega_a}{2(1+\omega_a)}$	$\frac{2(1-\omega_1)\omega_a}{3(1+\omega_a)}$	$\frac{\omega_1\omega_a}{6(1+\omega_a)}$	0

The parameter  $\omega_1$  can be estimated similarly to  $\omega_{\frac{3}{2}}$  by expanding and normalising the differential decay width equations for the observed decay modes  $\Sigma_c \rightarrow \Lambda_c \pi$  and  $\Sigma_c^* \rightarrow \Lambda_c \pi$ :

$$\frac{1}{\Gamma} \frac{d\Gamma(\Sigma_c \rightarrow \Lambda_c \pi)}{d \cos \theta} = \frac{1}{2},$$

$$\frac{1}{\Gamma} \frac{d\Gamma(\Sigma_c^* \rightarrow \Lambda_c \pi)}{d \cos \theta} = \frac{1}{4} \left[ 1 + 3 \cos^2 \theta - \frac{9}{2} \omega_1 \left( \cos^2 \theta - \frac{1}{3} \right) \right],$$

This results in  $\omega_1 = 2/3$ . Above arguments can be generalised for arbitrary heavy quark helicity:

$$\rho_{\Lambda_c} = \text{diag} \left[ \frac{1}{2} (1 - \rho_Q), \frac{1}{2} (1 + \rho_Q) \right],$$

$$\rho_{\Sigma_c} = \text{diag} \left[ \frac{1}{2} (1 - \rho_Q) + \omega_1 \rho_Q, \frac{1}{2} (1 + \rho_Q) - \omega_1 \rho_Q \right],$$

$$\rho_{\Sigma_c^*} = \text{diag} \left[ \frac{3}{8} \omega_1 (1 - \rho_Q), \frac{1}{2} (1 - \rho_Q) - \frac{1}{8} \omega_1 (3 - 5\rho_Q), \frac{1}{2} (1 - \rho_Q) - \frac{1}{8} \omega_1 (3 + 5\rho_Q), \right.$$

$$\left. \frac{3}{8} \omega_1 (1 + \rho_Q) \right]$$

The polarisation information of the heavy baryons is passed to the `SpinHadronizer` transitional class through the `baryonSpin` function. This function begins by checking the baryon's parentage and its constituents. It then uses the spin information from the heavy quark to determine the spin characteristics of the baryon, particularly for excited heavy baryons.

### 7.5.4 Spin-hadronization in Herwig 7

Spin handling in Herwig 7 is managed by the `SpinHadronizer` class, which assigns spin information to hadronized particles. The `mesonSpin` and `baryonSpin` functions extract spin information from the heavy quark, update the average polarisation, and assign a diagonal spin density matrix to the produced heavy hadrons.

The `SpinHadronizer` class is inserted into the hadronization sequence via:

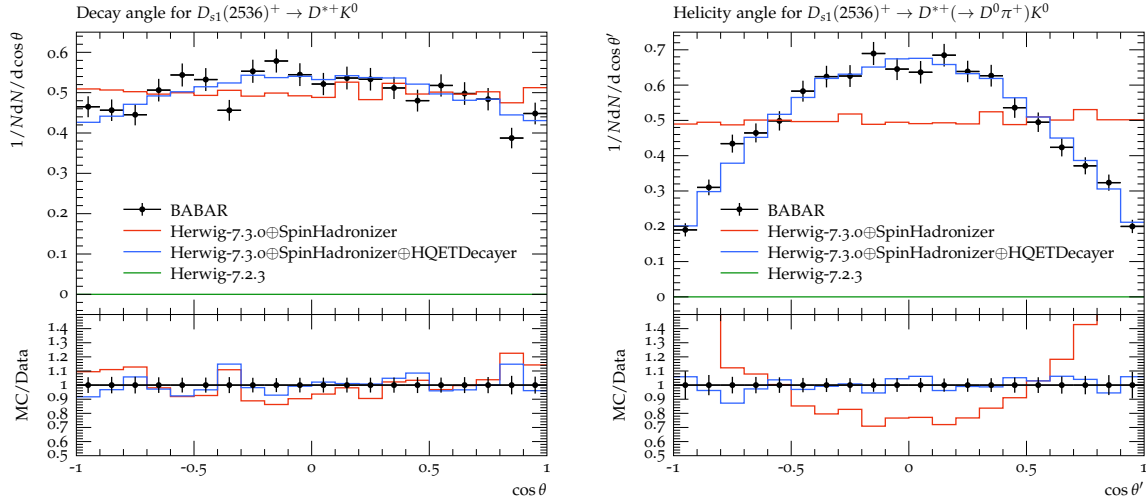


Fig. 7.9: Efficiency-corrected decay rates of the  $D_{s1}^+$  meson. The left panel shows the  $D_{s1} \rightarrow D^{*+} K^0$  decay rate as a function of the lab-frame angle  $\theta$ , while the right panel presents the same distribution in the  $D_{s1}^+$  centre-of-mass frame, denoted by  $\theta'$ . Data is sourced from [241]. The red histograms represent predictions from Herwig-7.3.0 with only SpinHadronizer enabled. The blue histograms include both SpinHadronizer and HQETDecayer, while the green histograms correspond to Herwig-7.2.3, which lacks HQET enhancements.

```
cd /Herwig/Hadronization
insert EventHandler:PostHadronizationHandlers 0 SpinHadronizer
```

ensuring that spin assignments occur after hadronization. The *src/defaults/HerwigDefaults.in* file integrates spin handling into the event generation framework by defining:

```
cd /Herwig/Hadronization
newdef EventHandler:HadronizationHandler ClusterHadHandler

insert EventHandler:PostHadronizationHandlers 0 SpinHadronizer
```

To illustrate the impact of the spin-hadronization implementation, we present efficiency-corrected decay rates of the  $D_{s1}^+$  meson, comparing different configurations of Herwig.

In the above figures, we examine how HQET and spin-flavour symmetry improve predictions of  $e^+e^-$  data for polarisation-sensitive  $D_{s1}$  meson decay measurements. The figures present normalised, efficiency-corrected rates for the  $D_{s1} \rightarrow D^{*+} K^0$  decay mode across different angular variables. The effect of SpinHadronizer and HQETDecayer in Herwig-7.3.0 is studied by enabling them separately to isolate their contributions. For comparison, we include predictions from Herwig-7.2.3, which does not incorporate HQET-based spin handling. As expected, Herwig-7.2.3 fails to predict either the existence or the angular dependence of the decay rates. In contrast, Herwig-7.3.0 correctly reproduces the mean values of the  $s$ -wave contributions when only SpinHadronizer is active, but does not fully capture the angle-dependent structure. Notably, with both SpinHadronizer and HQETDecayer enabled, Herwig-7.3.0 achieves excellent agreement with experimental data.

## 7.6 Hadronization in BSM models

In most cases the hadronization of events involving new physics, using the cluster model, proceeds in the same way as for Standard Model events. There are however some classes of new physics model that require special treatment, in particular:

**Stable strongly interacting particles**, if there are strongly interacting particles that are stable on the hadronization timescale, these particles will hadronize before they decay. If the new particles are in the fundamental representation of colour SU(3) then their hadronization proceeds in the same way as for quarks, however if they are in the octet representation the situation is more complicated [243] and is not yet implemented.

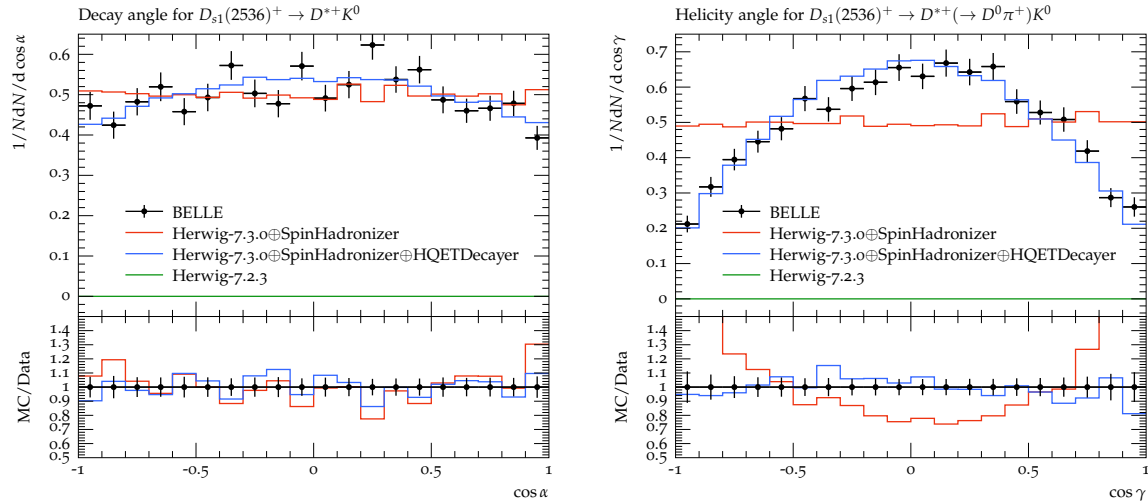


Fig. 7.10: Further efficiency-corrected decay rate analysis for the  $D_{s1}^+$  meson. The left panel shows the decay rate as a function of the lab-frame angle  $\alpha$  and the right panel displays the angular dependence of  $\gamma$ , the angle between  $\pi^+$  and  $K^0$  in the  $D^{*+}$  rest frame. Data is taken from [242], and histogram annotations follow those in Figure 1.

**Baryon number violation (BNV)**, there are models of new physics in which the conservation of baryon number is violated. This typically occurs at a vertex that has the colour tensor  $\epsilon^{ijk}$  leading to three quarks, or antiquarks, that are colour-connected to each other after the parton shower and gluon splitting.

The Herwig 7 hadronization module is designed so that both stable coloured particles and baryon number violation are correctly treated as described below.

### 7.6.1 Stable strongly interacting particles

Currently only the hadronization of objects in the fundamental representation of the SU(3) group of the strong force is supported. Provided that the relevant hadrons exist the hadronization of these particles is handled in the same way as for quarks. In an upcoming development, hadron spectra can be specified for hypothetical new interactions or for theoretical investigations. This functionality is developed in the context of studying strongly interacting dark sectors [244].

### 7.6.2 Baryon number violation

The treatment of QCD radiation and hadronization in models that violate baryon number conservation is described in Refs. [136] and [137] and was implemented in the FORTRAN HERWIG program. In events where baryon number is violated there are typically two situations that can arise.

1. The baryon-number-violating vertices are unconnected, leading to three quarks, or antiquarks, connected to each BNV vertex after the gluon splitting. These (anti)quarks must be formed into a cluster, which decays to give a (anti)baryon and a meson, giving the expected baryon number violation. In the approach of Refs. [136, 137] this is modelled by first combining two of the (anti)quarks into a (anti)diquark, which is in the (anti)-triplet representation of colour SU(3). The (anti)quark and (anti)diquark can then be formed into a colour singlet cluster, which can be handled by the hadronization module in the normal way.
2. Two baryon number-violating vertices are colour-connected to each other, leading to two quarks connected to one vertex and two antiquarks connected to the second, after gluon splitting. In this case two clusters must be formed by pairing one of the quarks with one of the antiquarks at random and then pairing up the remaining pair.

The handling of these colour flows in both the shower and hadronization is fully supported.

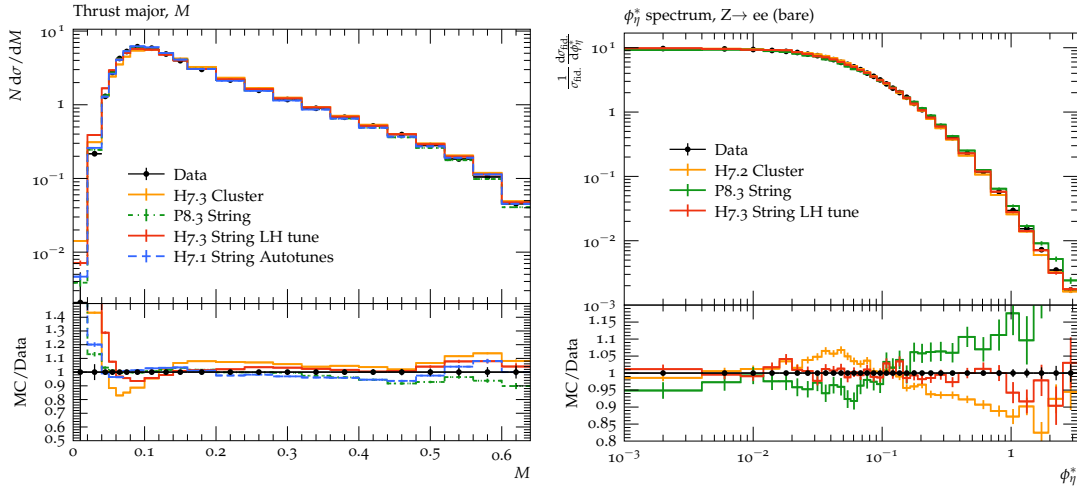


Fig. 7.11: Left panel: Thrust major observables measured by the DELPHI experiment at LEP [248]. Right panel: Normalized differential cross section of  $Z$  boson production as a function of the  $\phi_\eta^*$  parameter for  $Z \rightarrow ee$  decays [249] measured by ATLAS experiment.

## 7.7 Interface to string hadronization model

With version 7.3, Herwig includes the option to use the Lund string model for hadronization in both  $e^+e^-$  and  $pp$  collisions. The interface to the Pythia 8 string model [21] is provided through the TheP8I C++ package [245]. While the default implementation of TheP8I is sufficient for hadronization in electron–positron collisions, it has been extended to include colour reconnection, which is required for a realistic description of hadron–hadron collisions. The Lund string model, together with the angular-ordered parton shower and the colour reconnection model of [246], has been tuned to LEP and LHC data [247]. The obtained tune, referred to as the *Les Houches* tune (LH Tune), provides competitive predictions for both lepton–lepton and hadron–hadron collisions. It enables the study of uncertainties associated with non-perturbative hadronization effects by fixing all other components of the simulation in Herwig and varying only the hadronization model; see, for example, Fig. 7.11, which shows the distribution of the Thrust Major in  $e^+e^-$  collisions measured by DELPHI experiment and the  $\phi_\eta^*$  observable in  $pp$  collisions measured by ATLAS experiment, together with predictions obtained using different hadronization models (the orange line corresponds to Herwig with the cluster model and the red line to Herwig with the string model).

## 7.8 Event-by-event hadronization corrections

A new strategy has been developed to transfer the assignment of constituent masses entirely into the hadronization, which is available as an option to the hadronization. Not only does this allow to have a consistent physics interface to the string model, but it also provides the possibility to extract event-by-event hadronization corrections in a clean way, i.e. a parton level which is not ‘contaminated’ by the non-perturbative constituent mass parameters. This is achieved by reshuffling the partonic ensemble to different mass shells at the beginning of the hadronization. While this can, in principle, be done across the entire event, the more physical choice is to perform the reshuffling within colour singlet subsystems which will branch into clusters. The algorithm used is the same reshuffling algorithm as we use it elsewhere, in particular it is the one previously used in the dipole shower to assign new mass shells after showering. It can be enabled using the `Reshuffle` switch of the `ClusterHadronizationHandler` class, together with choosing the `ReshuffleMode` option to equal `ColourConnected`. At the same time, the `ShowerHandler` needs to be instructed to not put partons on their constituent mass shells using the `UseConstituentMasses` switch similarly to when the string model is in use. The intermediate partonic state is then tagged by a status code which can be chosen through the `TagIntermediates` interface of the `ShowerHandler` class.

## 7.9 Code structure

The `ClusterHadronizationHandler` inherits from the `HadronizationHandler` of ThePEG and implements the cluster hadronization model. The `ClusterHadronizationHandler` makes use of a number of helper classes to implement different parts of the model. The helper classes, in the order they are called, are:

- The `PartonSplitter` performs the non-perturbative splitting of the gluons to quark-antiquark pairs.

- The `ClusterFinder` is responsible for taking the partons after the gluon splitting and forming them into colour singlet clusters as particles.
- It is possible that rather than using the leading  $N_c$  colour structure of the event there is some rearrangement of the colour connections and this is performed by `ColourReconnector`.
- The `ClusterFissioner` class is responsible for splitting large mass clusters into lighter ones as described in Section 7.3.
- The `LightClusterDecayer` decays any clusters for which the decay to two hadrons is kinematically impossible into a single hadron with the correct flavour together with the reshuffling of momentum with neighbouring clusters, which is required to conserve energy and momentum, as described at the end of Section 7.4.
- The `ClusterDecayer` decays the remaining clusters into pairs of hadrons as described in Section 7.4.

In addition to these classes the `ClusterDecayer` makes use of a `HadronSelector` to select the hadrons produced in the cluster decay.<sup>9</sup> In order to support the different options described in Section 7.4 the base `HadronSelector` implements much of the functionality needed to select the hadrons in the cluster model but the `chooseHadronPair()` method, which is used to select the hadrons, is virtual and must be implemented in inheriting classes that implement specific variants of the cluster model. The FORTRAN HERWIG algorithm is implemented in the `Hw64Selector` class and the Kupčo and Herwig++ methods in the `HwppSelector` class. Newer versions will start to refer to `HadronSpectrum` objects, to be described in an update of this manual.

There are a number of switches and parameters that control the hadronization. Here we merely give a summary of the most important ones. All the parameters are described in full in the Doxygen documentation of the relevant classes.

The main choice is which variant of the cluster model to use. This can be controlled by using either the `Hw64Selector` for the original model of Ref. [2] or the `HwppSelector` class for the Kupčo and Herwig++ variants. The choice of whether to use the `Hw64Selector` or `HwppSelector` is controlled by setting the `HadronSelector` interface of the `ClusterDecayer` and `LightClusterDecayer` classes. In addition, for the `HwppSelector` the `Mode` switch controls whether the Kupčo (`Mode=Kupco`) or Herwig++ (`Mode=Hwpp`), the default, variant is used. The production of specific hadrons by the cluster model can be forbidden via the `Forbidden` interface of the `HadronSelector`: this option is currently only used to forbid the production of the  $\sigma$  and  $\kappa$  resonances, which are only included in the simulation to model low-mass  $s$ -wave  $\pi\pi$  and  $K\pi$  systems in certain particle decays.

In addition the mixing angles for the various multiplets can be changed in the `HadronSelector` as can the suppression weights for different SU(3) meson flavour multiplets.

If the option of using the soft underlying event model [250] is used, as described in Section 8.6, then the `UnderlyingEventHandler` interface needs to be set to the `UA5Handler`, by default this is set to the NULL pointer and the multiple scattering model of the underlying event described in Section 8 used.

The other main parameters of the cluster model, and their default values, are given in Table 7.5.

Finally the `ConstituentMass` of the gluon and, to a lesser extent the light quarks, which can be set in their `ParticleData` objects, have a major effect on the hadronization since they set the scale for the cluster mass distribution.

<sup>9</sup> The `LightClusterDecayer` also makes use of this class to select a single hadron, with a given flavour below the appropriate threshold, for cluster decay to a single hadron.

Table 7.5: Important hadronization parameters. For all parameters other than the light parton constituent masses, the limits given are enforced by the interface. For the light partons, the limits are not enforced but give a sensible range over which the parameters can be varied. For the gluon, the upper limit we give is about the largest value we would consider reasonable, although it is not a hard limit. The up and down masses must be less than half the gluon mass, otherwise the non-perturbative gluon decays are impossible. The same holds for the strange quark mass as the gluon decay into strange quarks has been found important to describe recent data on strange particle production.

Parameter	Default	Allowed	Description
	Value	Range	
<b>ColourReconnector</b>			
ReconnectionProbability	0.95	0-1	Probability for colour reconnection
ReconnectionProbabilityBaryonic	0.70	0-1	Probability for baryonic reconnection
AnnealingFactor	0.90	0-1	Parameter for statistical reconnection
AnnealingSteps	50	1-10000	Parameter for statistical reconnection
InitialTemperature	0.10	$10^{-5}$ -100	Parameter for statistical reconnection
TriesPerStepFactor	5.0	0-100	Parameter for statistical reconnection
<b>HadronSelector</b>			
PwtDquark	1.0	0-10	Weight for choosing a down quark
PwtUquark	1.0	0-10	Weight for choosing an up quark
PwtSquark	0.37	0-10	Weight for choosing a strange quark
PwtDIquark	0.33	0-10	Weight for choosing a diquark
SngWt	0.89	0-10	Weight for singlet baryons
DecWt	0.42	0-10	Weight for decuplet baryons
SingleHadronLimitBottom	0.0	0-10	Bottom cluster to 1 hadron param.
SingleHadronLimitCharm	0.0	0-10	Charm cluster to 1 hadron param.
DecayMassScale	0.0	0.1-50	Mass scale for kinematic strangeness
<b>ClusterDecayer</b>			
ClDirLight	1	0/1	Orientation of light cluster decays
ClDirBottom	1	0/1	Orientation of bottom cluster decays
ClDirCharm	1	0/1	Orientation of charm clusters
ClSmrLight	0.78	0-2	Smearing of light cluster decays
ClSmrBottom	0.08	0-2	Smearing of bottom cluster decays
ClSmrCharm	0.16	0-2	Smearing of charm cluster decays
OnShell	0	0/1	Masses of produced hadrons
<b>ClusterFissioner</b>			
ClMaxLight	3.53	0-10	Max. mass for light clusters (GeV)
ClMaxBottom	3.76	0-10	Max. mass for bottom clusters (GeV)
ClMaxCharm	3.95	0-10	Max. mass for charm clusters (GeV)
ClPowLight	1.85	0-10	Mass exponent for light clusters
ClPowBottom	0.55	0-10	Mass exponent for bottom clusters
ClPowCharm	2.56	0-10	Mass exponent for charm clusters
PSplitLight	0.91	0-10	Splitting param. for light clusters
PSplitBottom	0.63	0-10	Splitting param. for bottom clusters
PSplitCharm	0.99	0-10	splitting param. for charm clusters
RemnantOption	1	0/1	Treatment of remnant clusters
SoftClusterFactor	1	0.1-10	Remnant mass param. (GeV)
ProbablityPowerFactor	6.48	1-10	power factor in cluster splitting
ProbablityShift	-0.88	-10-10	shift in cluster splitting threshold
KineticThresholdShift	0.09	-10-10	shift in cluster splitting probability
<b>Constituent Masses</b>			
gluon	0.95	0-1	Gluon constituent mass (GeV)
up	0.325	$0-m_g/2$	Up quark constituent mass (GeV)
down	0.325	$0-m_g/2$	Down quark constituent mass (GeV)
strange	0.45	$0-m_g/2$	Strange quark constituent mass (GeV)

## 8 Underlying Event and beam remnants

The underlying event model of Herwig is based on the eikonal model discussed in [59] and described in detail in [58]. It models the underlying event activity as additional semi-hard and soft partonic scatters. In doing so, it allows the description of minimum bias events as well as the underlying event in hard scattering processes. In case of minimum bias interactions a substantial fraction of events will be diffractive, these events are modeled differently.

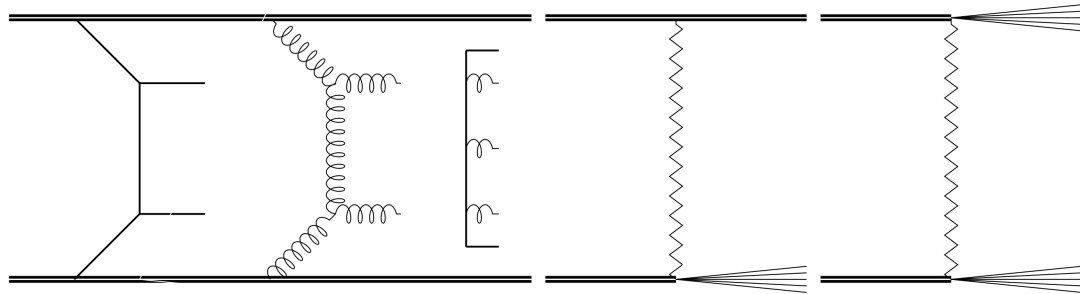


Fig. 8.1: Contributions to particle production in Herwig: dummy process to initiate a minimum bias event, semi-hard scattering, soft particle production from gluon ladder exchange (left part). Single and double diffraction (right)

In Fig. 8.1 we show the different contributions to particle production that will be described below. In Minimum-bias events the event generation is initiated with a dummy process that merely breaks up the proton by extracting two partons with zero transverse momentum (leftmost). This process will not contribute to particle production which will be performed by multiple semi-hard or soft scatters. Semi-hard scatters are described by perturbative partonic two-to-two subprocesses down to a minimum transverse momentum. Processes with very small transverse momentum are modeled as exchange of a gluon ladder. All of these processes may contribute to minimum bias events or are used to model the underlying event in a hard scattering. For minimum bias events, a fraction of events will be diffractive. These are modeled separately but still contribute to particle production in events with low multiplicities.

The perturbative part of the models provides very similar functionality to FORTRAN HERWIG + JIMMY with some minor improvements. The non-perturbative part has never been part of the JIMMY implementation. Our first implementation of soft interactions [131, 251], where these were simple models of two soft gluon production has been superseded with a model where a chain of soft gluons is produced with multiperipheral kinematics.

In this section, we briefly discuss the basics of how to calculate the multiplicities of the semi-hard scatterings, before mentioning the details of the soft additional scatters and explaining the integration into the full Monte Carlo simulation. Finally we will describe the code structure, which implements these ideas. A more detailed explanation of the semi-hard model can be found in Ref. [58]. The soft and diffractive model have been introduced in [62], where additional details can be found.

### 8.1 Semi-hard partonic scatters

The starting point is the observation that the cross section for QCD jet production may exceed the total  $pp$  or  $p\bar{p}$  cross section already at an intermediate energy range and eventually violates unitarity. For example, for QCD jet production with a minimum of 2 GeV this already happens at  $\sqrt{s} \sim 1$  TeV. This cutoff should however be large enough to ensure that we can calculate the cross section using pQCD. The reason for the rapid increase of the cross section turns out to be the strong rise of the proton structure function at small  $x$ , since the  $x$  values probed decrease with increasing centre of mass energy. This proliferation of low  $x$  partons may lead to a non-negligible probability of having more than one partonic scattering in the same hadronic collision. This is not in contradiction with the definition of the standard parton distribution function as the *inclusive* distribution of a parton in a hadron, with all other partonic interactions summed and integrated out. It does, however, signal the onset of a regime in which the simple interpretation of the pQCD calculation as describing the only partonic scattering must be unitarized by additional scatters.

In principle, predicting the rate of multi-parton scattering processes requires multi-parton distribution functions, about which we have almost no experimental information. However, the fact that the standard parton distribution functions describe the inclusive distribution gives a powerful constraint, which we can use to construct a simple model. The eikonal model used in Refs. [252–254] derives from the assumption that at fixed impact parameter,  $b$ , individual scatterings are independent and that the distribution of partons in hadrons factorizes with respect to the  $b$  and  $x$  dependence. This implies

that the average number of partonic collisions at a given  $b$  value is

$$\langle n(\mathbf{b}, s) \rangle = A(b) \sigma_{\text{hard}}^{\text{inc}}(s; p_t^{\min}), \quad (8.1)$$

where  $A(b)$  is the partonic overlap function of the colliding hadrons, with

$$\int d^2\mathbf{b} A(b) = 1,$$

and  $\sigma_{\text{hard}}^{\text{inc}}(s; p_t^{\min})$  is the inclusive cross section to produce a pair of partons with  $p_t > p_t^{\min}$ . We model the impact parameter dependence of partons in a hadron by the electromagnetic form factor, resulting in an overlap function for  $pp$  and  $p\bar{p}$  collisions of

$$A(b; \mu) = \frac{\mu^2}{96\pi} (\mu b)^3 K_3(\mu b), \quad (8.2)$$

where  $\mu$  is the inverse proton radius and  $K_3(x)$  is the modified Bessel function of the third kind. We do not fix  $\mu$  at the value determined from elastic  $ep$  scattering, but rather treat it as a free parameter, because the spatial parton distribution is assumed to be similar to the distribution of charge, but not necessarily identical.

The assumption that different scatters are uncorrelated leads to the Poissonian distribution for the number of scatters,  $n$ , at fixed impact parameter,

$$\mathcal{P}_n(b, s) = \frac{\langle n(\mathbf{b}, s) \rangle^n}{n!} e^{-\langle n(\mathbf{b}, s) \rangle}. \quad (8.3)$$

Using (8.3) the unitarized cross section can now be written as

$$\sigma_{\text{inel}}(s) = \int d^2\mathbf{b} \sum_{k=1}^{\infty} \mathcal{P}_k(b, s) = \int d^2\mathbf{b} \left[ 1 - e^{-\langle n(\mathbf{b}, s) \rangle} \right], \quad (8.4)$$

which properly takes multiple scatterings into account. The key ingredient for the Monte Carlo implementation is then the probability of having  $n$  scatterings given there is at least one, integrated over impact parameter space. This expression reads

$$P_n(s) = \frac{\int d^2\mathbf{b} \mathcal{P}_n(b, s)}{\int d^2\mathbf{b} \sum_{k=1}^{\infty} \mathcal{P}_k(b, s)}. \quad (8.5)$$

It is worth noting that this distribution, after integration over  $b$ , is much broader than Poissonian and has a long tail to high multiplicities.

Equation (8.5) is used as the basis of the multi-parton scattering generator for events in which the hard process is identical to the one used in the underlying event, *i.e.* QCD  $2 \rightarrow 2$  scattering. For scatterings of more than one type of hard process, the formulae can be easily generalised, but in fact for the realistic case in which all other cross sections are small compared to the jet cross section, they saturate at a simple form,

$$P_n(s) = \frac{n}{\sigma_{\text{hard}}^{\text{inc}}} \int d^2\mathbf{b} \mathcal{P}_n(b, s), \quad (8.6)$$

which allows for a more efficient generation of additional scatterings. It is worth noting that the fact that we have ‘triggered on’ a process with a small cross section leads to a bias in the  $b$  distribution and hence a higher multiplicity of additional scatters than in the pure QCD  $2 \rightarrow 2$  scattering case. A slight further modification to the distribution is needed when the small cross section process is a subset of the large one, for example QCD  $2 \rightarrow 2$  scattering restricted to the high  $p_t$  region.

As described so far, the  $n$  scatters are completely independent, which is expected to be a good approximation in the region in which multiple scattering dominates, *i.e.* small momentum fractions. However, some fraction of events come from higher  $x$  values and must lead to correlations between the scatters at some level. At the very least, the total momentum and flavour must be conserved: the total  $x$  value of all partons extracted from a hadron cannot exceed unity and each valence parton can only be extracted once. In Herwig these correlations are included in the simplest possible way, by vetoing any scatters that would take the total extracted energy above unity and by only evolving the first scatter back to a valence parton and all the others back to a gluon.

It has to be noted that in addition to these correlations of events from momentum constraints there will be correlations in colour space as well. At this point the assignment of colour lines to each scatter is completely ad-hoc. Cross-talk between different jets will be introduced by applying colour reconnections that colour connect nearby partons from different scatters and thereby lower the overall multiplicity and harden the transverse momenta of individual partons.

## 8.2 Soft partonic scatters

The elastic scattering amplitude,  $a(\mathbf{b}, s)$ , in impact parameter space can be expressed in terms of a real eikonal function  $\chi(\mathbf{b}, s)$ , as

$$a(\mathbf{b}, s) = \frac{1}{2i} \left[ e^{-\chi(\mathbf{b}, s)} - 1 \right]. \quad (8.7)$$

The elastic scattering amplitude,  $\mathcal{A}(s, t)$ , is the Fourier transform of  $a(\mathbf{b}, s)$  and therefore the total  $pp$  ( $p\bar{p}$ ) cross section as well as the elastic cross section can be obtained from that parameterisation as,

$$\sigma_{\text{tot}}(s) = 2 \int d^2\mathbf{b} \left[ 1 - e^{-\chi(\mathbf{b}, s)} \right], \quad \sigma_{\text{el}}(s) = \int d^2\mathbf{b} \left| 1 - e^{-\chi(\mathbf{b}, s)} \right|^2. \quad (8.8)$$

The inelastic cross section is obtained as the difference between the two cross sections,

$$\begin{aligned} \sigma_{\text{inel}} &= \sigma_{\text{tot}} - \sigma_{\text{el}} \\ &= \int d^2\mathbf{b} \left[ 1 - e^{-2\chi(\mathbf{b}, s)} \right]. \end{aligned} \quad (8.9)$$

The elastic  $t$ -slope parameter at zero momentum transfer is also calculable within this framework and yields [255]

$$b_{\text{el}} = \frac{1}{\sigma_{\text{tot}}} \int d^2\mathbf{b} b^2 \left[ 1 - e^{-\chi(\mathbf{b}, s)} \right]. \quad (8.10)$$

To reproduce the results from (8.4), we choose

$$\chi(\mathbf{b}, s) = \frac{1}{2} \langle n(\mathbf{b}, s) \rangle. \quad (8.11)$$

However we want to introduce additional scatters below the transverse momentum cut-off. Therefore, we identify this as the *hard* part of a universal eikonal function, which then has the form,

$$\chi_{\text{tot}}(\mathbf{b}, s) = \chi_{\text{QCD}}(\mathbf{b}, s) + \chi_{\text{soft}}(\mathbf{b}, s), \quad (8.12)$$

with the perturbative part

$$\chi_{\text{QCD}}(\mathbf{b}, s) = \frac{1}{2} A(\mathbf{b}; \mu) \sigma_{\text{hard}}^{\text{inc}}(s; p_t^{\text{min}}), \quad (8.13)$$

as in (8.1).

In the models of Refs. [253, 254, 256], the soft eikonal function has the form

$$\chi_{\text{soft}}(\mathbf{b}, s) = \frac{1}{2} A_{\text{soft}}(\mathbf{b}; \mu_{\text{soft}}) \sigma_{\text{soft}}^{\text{inc}}, \quad (8.14)$$

where  $\sigma_{\text{soft}}^{\text{inc}}$  is the purely non-perturbative cross section below  $p_t^{\text{min}}$ , which is a free parameter of the model. That is, we assume that soft scatters are the result of partonic interactions that are local in impact parameter. Previous Monte Carlo implementations used the simplest assumption about the partonic overlap function probed by the soft scatters,  $A_{\text{soft}}(\mathbf{b}) \equiv A(\mathbf{b})$ , i.e. an identical distribution to the one probed by semi-hard scatters. In Ref. [60] it was shown that measurements on the elastic  $t$ -slope confine the allowed parameter space of such models vastly. The remaining parameter space seems to be in contradiction with constraints obtained from measurements of the effective cross section in double parton scattering events [257, 258]. We therefore introduced the option of relaxing the condition of identical overlap distributions in Herwig. This enables the dynamical determination of the soft overlap distribution,  $A_{\text{soft}}(\mathbf{b})$ . In this case, which is the default setting, we use (8.2) but allow an independent radius parameter for the soft overlap function. The parameter  $\mu_{\text{soft}}$  is then dynamically fixed by the requirement of a correct description of the elastic  $t$ -slope from (8.10) at the current centre-of-mass energy. At the same time we fix the second free parameter in the soft sector,  $\sigma_{\text{soft}}^{\text{inc}}$ , by choosing it such that the total cross section, evaluated with the parametrisation from Ref. [259] is correctly described. At this point we also have to take into account the possibility that the inelastic cross section may contain diffractive scatters. Therefore, we fit the parameters  $\sigma_{\text{soft}}^{\text{inc}}$  and  $\mu_{\text{soft}}$  such that the inelastic cross-section will give a fraction  $1 - x_{\text{NSD}}$  of the experimental value, see Section 7.4.

We will discuss this point below. Measurements of the total cross section may deviate from the prediction in Ref. [259] and therefore the parameter can be used to set the total cross section at the current centre-of-mass energy explicitly.

With the full eikonal from (8.12), we can construct our model for additional semi-hard and soft scatters, by imposing the additional assumptions,

- The probability distributions of semi-hard and soft scatters are independent
- Soft scatters are uncorrelated and therefore obey Poissonian statistics like the semi-hard scatters

The probability  $\mathcal{P}_{h,n}(\mathbf{b}, s)$ , for having exactly  $h$  semi-hard and  $n$  soft scatters at impact parameter  $\mathbf{b}$  and centre-of-mass energy  $s$  is then given by,

$$\mathcal{P}_{h,n}(\mathbf{b}, s) = \frac{(2\chi_{\text{QCD}}(\mathbf{b}, s))^h}{h!} \frac{(2\chi_{\text{soft}}(\mathbf{b}, s))^n}{n!} e^{-2\chi_{\text{total}}(\mathbf{b}, s)}. \quad (8.15)$$

From (8.15) we can now deduce the cross section for having exactly  $h$  semi-hard and  $n$  soft scatters as,

$$\sigma_{h,n}(s) = \int d^2\mathbf{b} \mathcal{P}_{h,n}(\mathbf{b}, s). \quad (8.16)$$

The cross section for an inelastic collision (either semi-hard or soft), is obtained by summing over the appropriate multiplicities and yields

$$\begin{aligned} \sigma_{\text{inel}}(s) &= \int d^2\mathbf{b} \sum_{h+n \geq 1} \mathcal{P}_{h,n}(\mathbf{b}, s) \\ &= \int d^2\mathbf{b} \left[ 1 - e^{-\chi_{\text{total}}(\mathbf{b}, s)} \right]. \end{aligned}$$

The inelastic cross section for at least one semi-hard scattering is

$$\begin{aligned} \sigma_{\text{inel}}^{\text{semi-hard}}(s) &= \int d^2\mathbf{b} \sum_{h \geq 1, n \geq 0} \mathcal{P}_{h,n}(\mathbf{b}, s) \\ &= \int d^2\mathbf{b} \left[ 1 - e^{-\chi_{\text{QCD}}(\mathbf{b}, s)} \right]. \end{aligned}$$

With the cross sections from (8.16) and (8.17) we can construct the basis of our multiple soft and semi-hard scattering model, the probability,  $P_{h,n}$ , of having exactly  $h$  semi-hard and  $n$  soft scatters in an inelastic event ( $h + n \geq 1$ ). It is given by

$$P_{h,n}(s) = \frac{\sigma_{h,n}(s)}{\sigma_{\text{inel}}(s)} = \frac{\int d^2\mathbf{b} \mathcal{P}_{h,n}(\mathbf{b}, s)}{\int d^2\mathbf{b} \left[ 1 - e^{-\chi_{\text{total}}(\mathbf{b}, s)} \right]}, \quad h + n \geq 1, \quad (8.17)$$

which is analogous to (8.5) for the case of solely semi-hard additional scatterings. Equation defines a matrix of probabilities for individual multiplicities. This matrix is evaluated at the beginning of each run and the corresponding multiplicities are drawn for each event from this matrix according to their probability.

Equation (8.17) leads to very inefficient generation of additional scatters in cases where a rare hard scattering, with cross section  $\sigma_{\text{rare}}$ , takes place. Equation (8.6) has been deduced for this case, by exploiting the independence of different scatters. The presence of soft scatters does not alter that result as our assumption is that the soft scatters are independent from each other and from the other scatterings. Hence, the probability for  $h$  hard scatters (from which one is distinct, i.e.  $h = m + 1$ ) and  $n$  soft scatters is given by

$$\begin{aligned} P_{h=m+1,n}(s) &= \frac{\int d^2\mathbf{b} \mathcal{P}_{m,n}(\mathbf{b}, s) \frac{(A(b)\sigma_{\text{rare}})^1}{1!} e^{-A(b)\sigma_{\text{rare}}}}{\int d^2\mathbf{b} A(b)\sigma_{\text{rare}}} \\ &\approx \int d^2\mathbf{b} \mathcal{P}_{m,n}(\mathbf{b}, s) A(b) \\ &= \frac{h}{\sigma_{\text{hard}}^{\text{inc}}} \int d^2\mathbf{b} \mathcal{P}_{h,n}(\mathbf{b}, s). \end{aligned} \quad (8.18)$$

The probability for  $m$  semi-hard ( $p_t \geq p_t^{\text{min}}$ ) and  $n$  soft additional scatters is multiplied with the probability for exactly one scattering with an inclusive cross section of  $\sigma_{\text{rare}}$ . The denominator is the inclusive cross section for this distinct scattering, i.e. summed over all multiplicities for additional semi-hard and soft scatters. By approximating the exponential with unity and exploiting the normalisation of  $A(b)$  ( $\int d^2\mathbf{b} A(b) = 1$ ), we finally deduce (8.18).

Once the number of semi-hard scatters is known, they are simulated like “ordinary” hard scatters, the only exception is that we use a fast implementation of the QCD  $2 \rightarrow 2$  matrix elements as they are used in every hadronic collision. After the semi-hard scatters are sampled, the parton showering and hadronization are applied as described above. More details can be found in [58].

### 8.2.1 Transverse momentum of soft scatters

The transverse momentum of soft scatters is connected to the soft inelastic cross section described above. We take this connection quite literally for historical reasons of our implementation. We do not necessarily have to make this connection now as in the end we do not directly model the transverse momenta of soft hadrons. They only come as a result of the full soft model described below and are secondary particles only after cluster decay. We begin the discussion with the construction that the transverse momentum distribution must not exceed the lower bound of hard transverse momenta,  $p_t^{\min}$ . The functional form of it is not predetermined but a Gaussian distribution seems well-motivated by the fact that hadrons in soft hadronic interactions roughly follow a Gaussian in transverse momentum as,

$$\frac{d\sigma_{\text{soft}}^{\text{inc}}}{dp_t^2} = A e^{-\beta p_t^2},$$

to parameterise it. To fix the free parameters  $A$  and  $\beta$ , we impose the following constraints:

- The resulting soft cross section has to match the total soft cross section, which has been fixed to describe the total inelastic cross section and the slope parameter,

$$\int dp_t^2 \frac{d\sigma_{\text{soft}}^{\text{inc}}}{dp_t^2} \stackrel{!}{=} \sigma_{\text{soft}}^{\text{inc}}.$$

- The transverse momentum distribution of semi-hard and soft scatterings should be continuous at the matching scale,

$$H(s; p_t^{\min}) := \frac{d\sigma_{\text{hard}}^{\text{inc}}}{dp_t^2} \Big|_{p_t=p_t^{\min}} \stackrel{!}{=} \frac{d\sigma_{\text{soft}}^{\text{inc}}}{dp_t^2} \Big|_{p_t=p_t^{\min}},$$

where we introduced  $H$  as shorthand for the hard inclusive jet cross section at  $p_t = p_t^{\min}$ .

These conditions are fulfilled by the parameterisation,

$$\frac{d\sigma_{\text{soft}}^{\text{inc}}}{dp_t^2} = H(s; p_t^{\min}) e^{-\beta(p_t^2 - p_t^{\min 2})}, \quad (8.19)$$

where the slope,  $\beta$ , must satisfy,

$$\frac{e^{\beta p_t^{\min 2}} - 1}{\beta} = \frac{\sigma_{\text{soft}}^{\text{inc}}}{H(s; p_t^{\min})}. \quad (8.20)$$

Fig. 8.2 shows the transverse momentum spectrum for two different cut-off values. The slope,  $\beta$ , is chosen such that both curves correspond to the same integrated cross section.

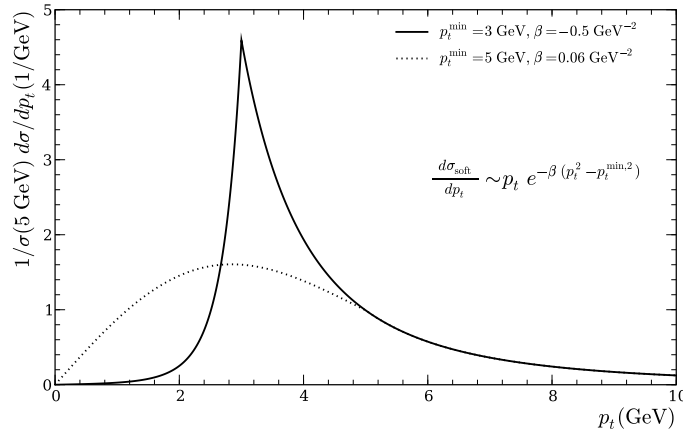


Fig. 8.2: Transverse momentum distribution of additional scatters

One peculiarity is that also negative values of  $\beta$  are possible when the soft cross section becomes small. This results in a spike-like shape in the differential partonic cross section. We make use of this distribution of transverse momenta for

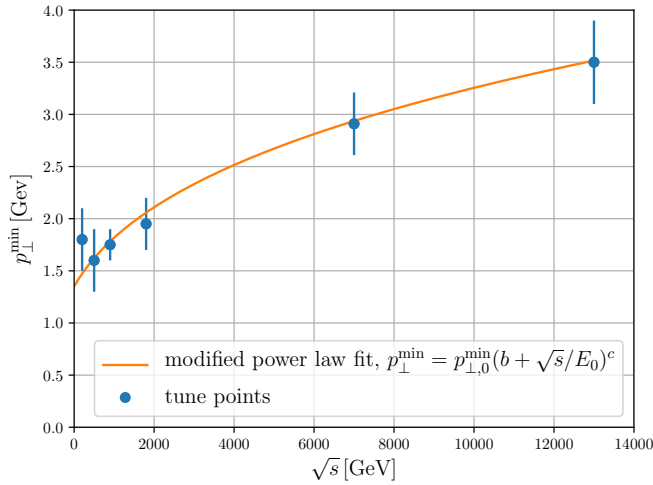


Fig. 8.3: Determination of the parameters in (8.21) from runs at various energies, cf. [260].

all soft particles generated as outlined in the next section. It was found that the parameter  $p_t^{\min}$  should not remain fixed for simulations at different centre-of-mass energies but rather evolve softly with energy,

$$p_t^{\min} = p_{t,0}^{\min} \left( \frac{b + \sqrt{s}}{E_0^2} \right)^p \quad (8.21)$$

The parameters  $p_{t,0}^{\min}$ ,  $b$  and  $p$  have been fixed from tuning the Underlying Event at different CM energy, see Fig. 8.3. Note that  $E_0$  should be kept fixed for such a set of tunes and only acts as a reference scale.

### 8.3 Soft particle production model

In this section we describe the implementation of the model for soft interactions in Herwig, *i.e.* how we set up the  $s$  soft scatters. The current model was developed in order to tackle some of the shortcomings of the old model and is described in more detail in Reference [62].

The model for additional soft interactions is based on the assumption that we expect soft particle production to be flat in rapidity and narrow in transverse momenta. It is inspired by the model for multiperipheral particle production of [261]. Multiperipheral particle production is a  $2 \rightarrow N$  process where the  $N$  resulting particles are ordered in rapidity. A process with multiperipheral particle production is shown in Fig. 8.4 where  $p_A$  and  $p_B$  are the incoming particles that interact with each other and the  $p_i$  are the outgoing particles.

The internal virtual particles are denoted by  $q_i$  and in the following we will refer to a  $2 \rightarrow N$  process with multiperipheral particle production as a particle ladder. In Herwig the final particles whose kinematics is constructed using this model will be partons. More precisely proton remnants, sea quarks and gluons. As outlined in the previous section, the soft process follows after a number of quasi hard processes where a valence quark or gluons with only longitudinal momentum are selected from the proton. The remnant takes the rest of the momentum. The total energy available to perform the multiperipheral particle production is given by the remaining energy of the proton remnants. The incoming momenta of the remnants are denoted by  $p_{r1}$  and  $p_{r2}$ . The number of the final partons in the ladder is then sampled from a Poissonian distribution with mean at

$$\langle N \rangle \approx N_{\text{ladder}} \times \ln \frac{(p_{r1} + p_{r2})^2}{m_{\text{rem}}^2} + b,$$

where  $N_{\text{ladder}}$ ,  $b$  are parameters of the model that roughly determine the number density of gluons per unit rapidity and  $m_{\text{rem}}$  is of the order of the constituent mass of the proton remnant and it is currently set to the constituent mass of the gluon.

Table 8.1: Important diffraction and underlying event models parameters.

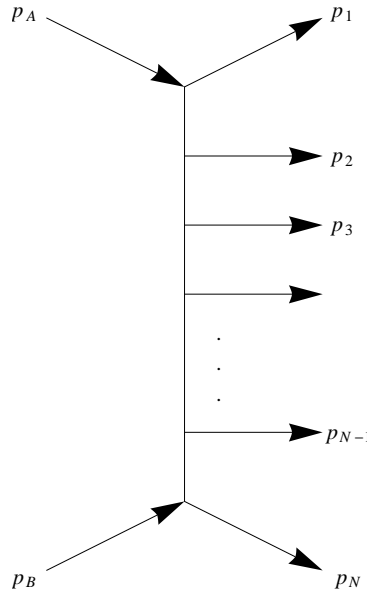


Fig. 8.4: Multiperipheral particle production.

Parameter	Allowed range	Description
<code>ladderMult</code>	0-10	The ladder multiplicity factor.
<code>DiffractiveRatio</code>	0-1	Fraction of diffractive cross section in inelastic cross section.
<code>InvRadius</code>	0.2-4.0	The inverse hadron radius squared used in the overlap function.
<code>pTmin0</code>	0-10	The $p_{T\min}$ at the reference scale for power law extrapolation of $p_{T\min}$ .
<code>Power</code>	0-10	The power for power law extrapolation of the $p_{T\min}$ cut-off.
<code>Offset</code>	500-1000	The offset used in the power law extrapolation of the $p_{T\min}$ cut-off.
<code>ReferenceScale</code>	0-2000	The reference energy for power law energy extrapolation of $p_{T\min}$ .

In Fig. 8.5 we illustrate a case with  $N = 6$  where we have the two remnants a sea quark and an antiquark and the gluons. The two sea quarks, which are generated by the soft event, are needed in order to create the correct colour connections between the partons in the ladder. The flavour and the orientation of the sea quarks is randomly chosen from up and down quarks with respective unit weights.

The kinematics of the partons in the ladder are generated with a modified Jadach algorithm [262] the partons' rapidities are distributed evenly between the rapidities of the remnants. The transverse momentum of one randomly selected parton is chosen according to Equation (8.19). The transverse momenta of the remaining partons in the ladder is then sampled from a flat probability distribution below the  $p_T$  of the first parton. Additionally all partons are flat in azimuthal angle.

Since the first quark is extracted from the proton by using a PDF we have to ensure that its rapidity is close to the second parton in the ladder, which is in our case a sea quark. This is done by choosing the proper value for  $x_{\min}$  of the PDF. This algorithm guarantees the exponential fall off of the differential cross section for large values of rapidity separation  $\Delta\eta$ . It also produces a roughly flat distribution of the clusters' rapidities and the subsequently produced final state particles.

For all of the soft scatters, the number  $s$  of which was obtained as described above from (8.17), one of these ladders is generated. As the rapidity spans are reduced ladder-by-ladder the phase space shrinks and the partons successively populate more central rapidity regions.

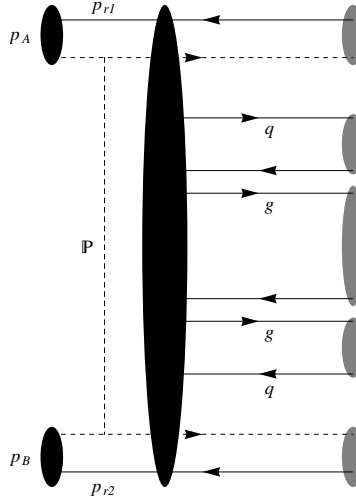


Fig. 8.5: Cluster formation in the multiperipheral final state.

## 8.4 Diffraction

A completely new feature in the current version of Herwig is the model for the simulation of diffractive events. The diffractive events are generated according to the differential cross sections for single and double diffraction which can be described by Regge theory and the generalised optical theorem [263, 264]. The process for single diffraction can be depicted by  $A + B \rightarrow X + B$  where  $A$  and  $B$  are the incoming hadrons and  $X$  is the hadronic final state in the limit  $s \gg M^2 \gg |t|$ .  $s$  is the total centre of mass energy of the incoming particles,  $M$  is the invariant mass of the dissociated hadron and  $-t$  is the momentum transfer. The same holds true for the double diffractive process  $A + B \rightarrow X_A + X_B$ . So far, we have only considered diffraction among protons. The ratio between single and double diffraction is not fixed. It is chosen roughly according to the measurements of the cross section in [265].

In order to connect the diffraction model to the other parts of the MPI model in Herwig we have to ensure that the cross sections for semi-hard and soft interactions only sum up to a certain fraction  $x_{\text{NSD}}$  of the total cross section when we fix the parameters of the soft model. The diffractive events are then generated as an independent process.

The kinematics are generated by first sampling the momentum transfer  $t$ , and the diffractive masses  $M_A, M_B$  (for single diffraction one of them is the proton mass  $m_p$ ). The scattering angle between the incoming protons and the diffractive systems is then calculated according to

$$\cos(\theta) = \frac{s(s + 2t - 2m_p^2 - M_A^2 - M_B^2)}{\lambda(s, M_A^2, M_B^2)\lambda(s, m_p^2, m_p^2)}.$$

where  $\lambda(x, y, z)$  is the Källen function.

With the invariant masses and the scattering angle the outgoing momenta can be constructed. The dissociated proton is then decayed into a quark-diquark pair which moves collinear to the direction of the dissociated proton. This final diffractive state is treated fully non-perturbatively and then handled by the hadronization model where the cluster will decay into the final state hadrons.

We point out that a fraction of the diffractive events for very low diffractive masses are modelled directly as the excitation of the proton to a  $\Delta$  baryon as a final state instead of quark-diquark pair.  $pp \rightarrow \Delta p$  for single and  $pp \rightarrow \Delta \Delta$  for double diffractive events. The  $\Delta$  is then handled by the hadronic decay handler.

## 8.5 Connection to different simulation phases

The model introduced so far is entirely formulated at the parton level. However, an event generator aims for a full description of the event at the level of hadrons. This implies that the implementation of multi-parton scattering must be properly connected to the parton shower and hadronization models, a few details of which we discuss in the following.

### 8.5.1 Parton showers and hard matrix elements

After generating the hard process and invoking parton showers on its coloured particles, the number of additional scatters is calculated according to Eq. ( (8.17)) or Eq. ( (8.18)) respectively. After the initial-state shower has terminated, the incoming partons are extracted out of the beam particles in the usual way.

The requested additional scatters are then generated using a similar but completely independent infrastructure from the one of the hard process. Dedicated hard matrix elements with hand-coded formulae summed over parton spins are used for greater speed, as mentioned in Section 3.9.1. This also has the advantage that specific cuts, different to those used for the main hard process, can be specified. E.g. the lower bound on the transverse momenta should be the very same  $p_t^{\min}$  as used in the computations for the number of scatters.

For each additional scattering, parton showers evolve the produced particles down to the hadronic scale. The backward evolution of additional scatters is forced to terminate on a gluon. After termination, these gluons are extracted out of the beam particles. If this process leads to a violation of four-momentum conservation, the scattering cannot be established. It is therefore regenerated until the desired multiplicity has been reached. If a requested scattering can never be generated without leading to violation of momentum conservation, the program eventually gives up, reducing the multiplicity of scatters.

### 8.5.2 Minimum bias process

Herwig simulates minimum bias collisions as events in which there is effectively no hard process. However, to maintain a uniform structure with the simulation of standard hard process events, we have implemented a matrix element class, that generates a ‘hard’ process with as minimal an effect as possible. It extracts only light (anti)quarks ( $d, u, \bar{d}$  or  $\bar{u}$ ) from the hadrons and allows them to ‘scatter’ through colourless exchange at zero transverse momentum, with a matrix element set to unity, so that their longitudinal momentum is determined only by their parton distribution functions. To give a predominantly valence-like distribution, a cut on their longitudinal momentum fraction  $x > 10^{-2}$  is recommended. Note that because the matrix element is set to unity, the cross section that is printed to the output file at the end of the run is meaningless.

### 8.5.3 Hadronization

The underlying event and beam remnant treatment are closely connected because the generation of additional scatters requires the extraction of several partons out of the proton. As described before, all additional partons are extracted from the incoming beam particles. This is different from the procedure that was used in FORTRAN JIMMY, where the successive partons were always extracted from the previous beam remnant, a difference in the structure of the event record that should not lead to significant differences in physical distributions.

The cluster hadronization described in the previous section can only act on (anti)quarks or (anti)diquarks. However, naively extracting several partons from a hadron will not leave a flavour configuration that is amenable to such a description in general. Therefore, the strategy we use, as already mentioned, is to terminate the backward evolution of the hard process on a valence parton of the beam hadron and additional scatterings on gluons, giving a structure that can be easily iterated for an arbitrary number of scatters. This structure is essentially the same as in FORTRAN JIMMY.

## 8.6 Older soft models

While the new multiple interaction model provides a better description of the underlying event and minimum bias data, and is recommended for all realistic physics studies, Herwig still contains the original soft model of the underlying event used before version 2.1, and also the soft model that was used with the early implementations of the MPI model in Herwig. Please refer to [6] for details.

## 8.7 Code structure

In addition to being the main class responsible for the administration of the shower, the **ShowerHandler**, described in Sect. Section 4.9, is also responsible for the generation of the additional semi-hard scattering processes. It has a reference to the **MPIHandler** in the input files, which is used to actually create the additional scattering processes. It invokes the parton shower on all the available scatters and connects them properly to the incoming beam particles. This includes potential re-extraction of the incoming parton if it is changed as a result of initial-state radiation. A number of classes are used by the **MPIHandler** to generate the additional scattering processes. Soft additional scatters are generated in the **HwRemDecayer** class.

The **MPIHandler** administers the calculation of the underlying event activity. It uses to sample the phase-space of the processes that are connected to it. Using that cross section the probabilities for the individual multiplicities of additional scatters are calculated during initialisation. The method `MPIHandler::multiplicity()` samples a number of extra scatters from that pre-tabulated probability distribution. The method `MPIHandler::generate()` creates one subprocess according to the phase-space and returns it.

The **MPISampler** performs the phase-space sampling for the additional scatterings. It inherits from **SamplerBase** and implements the Auto Compensating Divide-and-Conquer phase-space generator, **ACDCGen**.

The **HwRemDecayer** is responsible for decaying the **RemnantParticle** to something that can be processed by the cluster hadronization, *i.e.* (anti)quarks or (anti)diquarks. This includes the forced splittings to valence quarks and gluons respectively. Also the colour connections between the additional scatters and the remnants are set here. If additional soft partonic interactions, *i.e.* the non-perturbative part of the underlying event, are enabled, they are generated inside this class after the remnants have been decayed to the (anti)diquarks.

The **MPIPDF** class is used to modify the PDF's used for the initial state shower of additional scatters. All sorts of rescaling are possible but currently the mode that is used is the one where the valence part of the PDF is removed. The objects are instantiated inside and set to the default PDF's using `void ThePEG::CascadeHandler::resetPDFs(...)`

The most important interfaces to set parameters for the above mentioned classes are described here. An exhaustive description of all interfaces is provided by our Doxygen documentation. **MPIHandler** has the following important interfaces:

**SubProcessHandlers** is a vector of references to **SubProcessHandler** objects. The first element is reserved for the underlying event process. Additional references can be set to simulate additional hard processes in a single collision. See [Section 3.1](#) for details of how to use this functionality.

**Cuts** Vector of references to **Cuts** objects. The first element is used to impose the minimal transverse momentum of the additional scatters,  $p_t^{\min}$ . This is one of the two main parameters of the model. The current default, obtained from a fit to Tevatron data is 4.0 GeV. See Ref. [60] for details. Additional cuts object may be defined for additional hard processes that should be simulated in the same event.

**additionalMultiplicities** Vector of integer values to specify the multiplicity of additional hard scattering processes in a single collision. See [Section 3.1](#) for an example.

**InvRadius** sets the value of the inverse beam particle radius squared,  $\mu^2$ . The current default is 1.5 GeV<sup>2</sup>, obtained from the above mentioned fit.

#### **pTmin0, Offset, Power**

describe the energy evolution of the transverse momentum cutoff  $p_{t,0}^{\min}$ , as described in Eq. (8.21).

#### **DiffractiveRatio,**

gives the fraction of diffractive events for a given CM energy as described above as  $1 - x_{\text{NSD}}$ . Note that this parameter is generally energy dependent as the diffractive cross section will evolve with energy differently from the total cross section.

**IdenticalToUE** An integer parameter specifying which element of the list of **SubProcessHandler**'s is identical to the underlying event process. Zero means the the conventional hard subprocess is QCD jet production. -1 means that no process is identical. Any number  $> 0$  means that one of the additional hard scatterings is QCD jet production, where the exact number specifies the position in the vector. The default is -1, which is appropriate as long as no QCD jet production is simulated.

**softIn** Switch to turn the inclusion of non-perturbative scatters to the underlying event model on (Yes) or off (No). The current default is Yes.

**twoComp** Switch to toggle between an independent overlap function for soft additional scatters (Yes) and identical ones  $A_{\text{soft}}(\mathbf{b}) \equiv A(\mathbf{b})$  (No). If the two-component model is used, the parameters of the soft sector are automatically chosen to describe the total cross section as well as the elastic  $t$ -slope correctly.

**DLMode** Integer number  $\in \{1, 2, 3\}$  to choose between three different parametrizations of the total cross section as a function of the centre-of-mass energy:

1. Parametrisation of Ref. [259].
2. Parametrisation of Ref. [259] but with rescaled normalisation to match the central value of the measurement [266] by CDF. **Default**
3. Parametrization of Ref. [267].

---

**MeasuredTotalXSec** Parameter to set the total cross section (in mb) explicitly. If this parameter is used, it will overwrite the parametrisation selected with the previous switch. This is intended for first data on the total cross section and should be used instead of the parametrisation, which may deviate substantially.

In the **ShowerHandler** there is a reference to the **MPIHandler**. To switch multiple parton interactions off, this reference has to be set to NULL.

**HwRemDecayer** has just one important interface:

**ladderMult**, the number of gluons per rapidity in the soft particle production model.

## 9 Hadronic decays

Herwig uses a sophisticated model of hadronic decays, as described in Ref. [55]. The simulation of decays in Herwig is designed to have the following properties:

- a unified treatment of the decays of both fundamental particles and the unstable hadrons, this is of particular importance for particles like the  $\tau$  lepton, which, while a fundamental particle, is more akin to the unstable hadrons in the way it decays;
- up-to-date particle properties, *i.e.* masses, widths, lifetimes, decay modes and branching ratios together with a new database to store these properties to make updating the properties easier and the choices made in deriving them clearer;
- full treatment of spin correlation effects using the algorithm of Refs. [53, 102, 103] for the decay of all unstable particles, it is important that the same algorithm is used consistently in all stages of the program so that correlations between the different stages can be correctly included;
- a sophisticated treatment of off-shell effects for both unstable hadrons and fundamental particles;
- a large range of matrix elements for hadron and tau decays including both general matrix elements based on the spin structures of the decays and specific matrix elements for important decay modes;
- the accurate simulation of QED radiation in the particle decays using the Yennie–Frautschi–Suura (YFS) formalism [51].
- an interface to EvtGen [268] for the decay of bottom and charm mesons.

In this section we describe the simulation of hadron and tau lepton decays in Herwig. We start by discussing the physical properties of the hadrons used in the simulation and how they are determined. In ThePEG framework these physical properties are stored using the `ParticleData` class, which has one instance for each particle used in the simulation. In turn the properties of a given decay mode are stored using the `DecayMode` class, which contains both the particles involved in the decay and a reference to a `Decayer` object that can be used to generate the kinematics of the decay products. The `DecayHandler` class uses these `DecayMode` objects to select a decay of a given particle, according to the probabilities given by the branching ratios for the different decay modes, and then generates the kinematics using the relevant `Decayer` specified by the `DecayMode`.

Following a brief discussion of the treatment of off-shell effects we therefore discuss the different `Decayer` classes available in Herwig for the decay of tau leptons, strong and electromagnetic hadron decays and then weak hadron decays. This is followed by a discussion of the code structure.

### 9.1 Particle properties

The information in the Particle Data Group's (PDG) compilation [269] of experimental data is sufficient in many cases to determine the properties of the hadrons used in Herwig. However, there are some particles for which the data are incomplete or too inaccurate to be used. Equally, there are a number of particles that are necessary for the simulation but have not been observed, particularly excited bottom and charm hadrons, which should perhaps be regarded as part of the hadronization model affecting the momentum spectrum of lighter states, rather than as physical states. A large number of choices therefore have to be made in constructing the particle data tables used in the event generator, based on the data in Ref. [269].

In the past the data were stored as either a text file or the contents of a FORTRAN COMMON block. However, due to the relatively large amount of data that needs to be stored we decided to adopt a database approach based on the MySQL database system. The event generation still uses text files to read in the particle properties but these files are now automatically generated from the database. This provides us with a range of benefits: the data can be edited using a web interface; additional information describing how the particle properties were determined is stored in the database both improving the long-term maintenance and allowing the user to understand the uncertainties and assumptions involved.

An example of the output from the database for the properties of the  $\omega$  meson is shown in Fig. 9.1. This includes the basic properties of the particle together with an explanation of how they were derived. In addition there is a star rating between one and five, which gives an indication of how reliable the properties of the particle and the modelling of individual decay modes are.

In general we used the following philosophy to determine the particle properties used in Herwig:

$\omega$ * * * * *					
Branching Ratio	Rating	On/Off	Outgoing Particles	Description	Decayer
0.897507	*****	on	$\pi^+, \pi^-, \pi^0$	The decay of the $\omega$ to three pions. The branching ratio is taken from [1] with a small, order $10^{-4}$ addition to ensure the modes sum to one.	OmegaDalitz
0.085624	*****	on	$\pi^0, \gamma$	The decay of the $\omega$ to a pion and photon. The branching ratio is taken from [1].	VectorVP
0.015300	*****	on	$\pi^+, \pi^-$	The isospin violating decay of the $\omega$ to two pions with branching ratio taken from [1].	Vector2Meson
0.000770	***	on	$\pi^0, e^-, e^+$	The decay of the $\omega$ to a pion and an electron-positron pair with branching ratio from [1].	VectorVPff
0.000450	***	on	$\eta, \gamma$	The decay of $\omega$ to $\eta$ and a pion with branching ratio taken from [1].	VectorVP
0.000134	***	on	$\pi^0, \mu^-, \mu^+$	The decay of the $\omega$ to a pion and an $\mu^+ \mu^-$ pair with branching ratio is taken from [1].	VectorVPff
0.000074	***	on	$e^-, e^+$	The decay of the $\omega$ to an electron-positron pair. The branching ratio is obtained by averaged the electron and muon channel from [1] including a kinematic factor from the decayer.	Vector2Leptons
0.000074	***	on	$\mu^-, \mu^+$	The decay of the $\omega$ to an electron-positron pair. The branching ratio is obtained by averaged the electron and muon channel from [1] including a kinematic factor from the decayer.	Vector2Leptons
0.000067	***	on	$\pi^0, \pi^0, \gamma$	The decay of $\omega$ to two pions and a photon, with branching ratio taken from [1].	DecayME0

## References

[1] PARTICLE DATA GROUP collaboration, *Review of Particle Physics, PTEP* **2022** (2022) 083C01.

Fig. 9.1: An example of the particle properties in Herwig, in this case for the  $\omega$  meson. The properties of the particle, including the mass, width, decay modes and branching ratios, are given together with comments on how properties were determined. In the full web version, links are included to the descriptions of the objects responsible for generating the kinematics for the various decay modes.

- The properties of the light mesons in the lowest lying multiplets were taken from Ref. [269]. In some cases we used either lepton universality or the phase-space factors from our Decayers to average the branching ratios for poorly measured modes.
- Where possible, the properties of the excited light mesons were taken from Ref. [269] together with some additional interpretation of the data. The mesons needed to fill the  $1^1S_0$ ,  $1^3S_1$ ,  $1^1P_1$ ,  $1^3P_0$ ,  $1^3P_1$ ,  $1^3P_2$ ,  $1^1D_2$ ,  $1^3D_1$ ,  $1^3D_3$ ,  $2^1S_0$ ,  $1^1S_0$  and  $2^3S_1$  SU(3) multiplets are included together with the  $K$  mesons from the  $1^3D_2$  multiplet.
- We use the EvtGen package [268] for the decays of the  $D_{u,d,s}$  mesons and  $B_{u,d,s}$  mesons.
- The mass and lifetime of the  $B_c$  meson is taken from Ref. [269]. The branching ratios were taken from the theoretical calculations of Ref. [270] together with some partonic modes to ensure that the branching ratios sum to one.
- The properties and decay modes of the charmonium resonances were taken from Ref. [269] where possible, together with the use of partonic decays, to  $ggg$ ,  $gg$  or  $q\bar{q}$ , to model the unobserved inclusive modes. For some of the particles,

in particular the  $h_c$  and  $\eta_c(2S)$ , the results of Ref. [271] were used and the  $\eta_c(2S)$  branching ratios were taken from the theoretical calculation of Ref. [272].

- The properties and decay modes of the bottomonium resonances were taken from Ref. [269] where possible. In addition we have added a large number of states that are expected to have small widths, *i.e.* the mass is expected to be below the  $B\bar{B}$  threshold, using the theoretical calculations of Refs. [273–277] for many of the properties.
- The properties of the excited  $D$  and  $D_s$  mesons were taken from Ref. [269]. For many of the mesons we were forced to assume that the observed modes saturated the total width in order to obtain the branching ratios using the results in Ref. [269].
- The properties of the excited  $B_{u,d,s}$  mesons are uncertain. The  $B_{u,d,s}^*$ , together with one  $B_{1uds}$  state and the  $B_{2uds}$ , have been observed and there is evidence in Ref. [269] for further excited states, however it was unclear which states have been observed. We therefore take the properties of the remaining unobserved states from Ref. [278].
- The mass of the  $B_c(2S)^+$  is taken from [269], while the masses of the unobserved excited  $B_c$  mesons are taken from the lattice results in Ref. [279], which agree with potential model calculations. The widths and branching ratios were taken from the theoretical calculation of Ref. [280].
- The properties of the light baryons were taken from Ref. [269] where possible. In general, we have included all the light baryons from the first  $(56, 0_0^+)$  octet and decuplet multiplets. We include the light baryons from the next  $\frac{1}{2}^+$   $(56, 0_2^+)$ ,  $\frac{1}{2}^-$   $(70, 1_1^-)$ , and  $\frac{3}{2}^-$   $(70, 1_1^-)$  multiplets, although in some cases we have used higher  $\Xi$  resonances whose properties are better determined, rather than those given in Ref. [281]. In addition, the singlet  $\Lambda(1405)$  and  $\Lambda(1520)$  are also included. By default the  $\frac{3}{2}^-$   $(70, 1_1^-)$  multiplet and  $\Lambda(1520)$  are not produced in the hadronization stage in order to improve the agreement with LEP data.
- The properties of the weakly decaying charm baryons were taken from [281] together with a number of decay modes with theoretically-calculated branching ratios from [282] and partonic decay modes in order to saturate the total width.
- The experimental data on the weakly decaying bottom baryons is limited. Where possible, this data, taken from Ref. [269], was used together with a number of theoretical calculations [283–288] for the branching ratios to exclusive modes. The masses were calculated using the equivalent splitting in the charm system and the  $\Lambda_b$  mass where they have not been measured. In addition to the exclusive modes a number of partonic modes are included to model the unobserved exclusive decays.
- The properties of the strongly and radiatively decaying charm baryons, *i.e.*  $\Sigma_c$ ,  $\Xi'_c$ , and excited  $\Lambda_c$  and  $\Xi_c$ , are taken from Ref. [281] together with some results from Ref. [289] for branching ratios and widths where the experimental data is insufficient.
- The baryons containing a single charm or bottom quark from the multiplets containing the  $\Lambda(1405)$  and  $\Lambda(1520)$  have been observed and are included with the properties taken from Ref. [269] where possible and Ref. [289] for some widths.
- We include the baryons containing two heavy quarks, either  $cc$ ,  $bb$  or  $bc$ , required to complete the lightest two hadronic multiplets. We possible the properties are taken from Ref. [269], otherwise we take the masses from Ref. [290] and lifetimes from [291]. We use partonic decays to model the decay of the ground states and given the small mass splittings radiative decays for the excited states. Baryons containing more than one heavy quark cannot be produced in the cluster hadronization model, however these states are included to support future studies of these states.
- No tetraquark or pentaquarks, are currently included in the particle properties.

## 9.2 Line shapes

In general, if we wish to include the off-shell effects for an outgoing external particle in a hard production or decay process we need to include the following factor in the calculation of the matrix element

$$W_{\text{off}} = \frac{1}{\pi} \int dm^2 \frac{m\Gamma(m)}{(M^2 - m^2)^2 + m^2\Gamma^2(m)}, \quad (9.1)$$

where  $M$  is the physical mass of the particle,  $m$  is the off-shell mass and  $\Gamma(m)$  is the running width evaluated at scale  $m$ . In practice other effects can be included to improve this simple formula, for example we include the Flatté lineshape [292] for the  $a_0(980)$  and  $f_0(980)$  mesons. In Herwig, we calculate the running width of the particle based on its decay modes. The `Decayer` responsible for each decay mode specifies the form of the running partial width,  $\Gamma_i(m)$ , for the decay mode either in a closed analytic form for two-body decays or as a `WidthCalculatorBase` object, which is capable of calculating

the partial width numerically and is used to construct an interpolation table. The running width for a given particle is then the sum of the partial widths

$$\Gamma(m) = \sum_i \Gamma_i(m).$$

This both gives a sophisticated model of the running width based on the decay modes and allows us to use the partial widths to normalize the weights for the phase-space integration of the decays to improve efficiency close to the kinematic threshold for the decay.

In some cases, where the partial width varies significantly over the mass range allowed in the simulation, we can choose to use a variable branching ratio

$$\text{BR}_i(m) = \frac{\Gamma_i(m)}{\Gamma(m)},$$

both to prevent the production of kinematically unavailable modes and to improve the physics of the simulation. The classic examples are the decays of the  $f_0$  and  $a_0$  scalar mesons, which lie close to the  $K\bar{K}$  threshold. This means that, depending on their mass, they decay to either  $\pi\pi$  or  $\eta\pi$  respectively below the threshold or with a significant  $K\bar{K}$  branching fraction above the  $K\bar{K}$  threshold.

The weight in Eq. (9.1) is automatically included for all the Decayers inheriting from the `DecayIntegrator` class, which is the case for vast majority of the Herwig Decayers. The `GenericWidthGenerator` calculates the running widths using information from the Herwig Decayers inheriting from the `DecayIntegrator` class. For decayers inheriting from the `Baryon1MesonDecayerBase` class the running width is calculated using the `BaryonWidthGenerator` class. The `GenericMassGenerator` class is responsible for calculating the weight in Eq. (9.1) or generating a mass according to this distribution.

### 9.3 Tau decays

The simulation of  $\tau$  lepton decays in Herwig is described in detail in Ref. [55], together with a detailed comparison between the results of Herwig and TAUOLA [293, 294]. Here we simply describe the basic formalism for the decays of the tau and the different models available for the different decays, together with the structure of the code.

The matrix element for the decay of the  $\tau$  lepton can be written as

$$\mathcal{M} = \frac{G_F}{\sqrt{2}} L_\mu J^\mu, \quad L_\mu = \bar{u}(p_{\nu_\tau}) \gamma_\mu (1 - \gamma_5) u(p_\tau), \quad (9.2)$$

where  $p_\tau$  is the momentum of the  $\tau$  and  $p_{\nu_\tau}$  is the momentum of the neutrino produced in the decay. The information on the decay products of the virtual  $W$  boson is contained in the hadronic current,  $J^\mu$ . This factorization allows us to implement the leptonic current  $L_\mu$  for the decaying tau and the hadronic current separately and then combine them to calculate the  $\tau$  decay matrix element.

In Herwig, this factorization is used to define a `TauDecayer` class, which implements the calculation of the leptonic current for the  $\tau$  decay and uses a class inheriting from the `WeakCurrent` class to calculate the hadronic current for a given decay mode. This factorization allows us to reuse the hadronic currents in other applications, for example in weak meson decay using the naïve factorization approximation or in the decay of the lightest chargino to the lightest neutralino in Anomaly Mediated SUSY Breaking (AMSB) models where there is a small mass difference between the neutralino and chargino. We also make use of these currents, with an appropriate isospin rotation, to allow the calculation of the cross sections for exclusive hadronic final states in low energy  $e^+e^-$  collisions [295].

#### 9.3.1 Hadronic currents

We have implemented a number of hadronic currents, which are mainly used for the simulation of  $\tau$  decays or the exclusive cross sections for the production of hadrons in low-energy  $e^+e^-$  collisions. These are all based on the `WeakCurrent` class. In many cases the same currents can be used to describe both  $e^+e^- \rightarrow$  hadrons and hadronic decays. In  $e^+e^- \rightarrow$  hadrons however there can be additional isospin zero contributions. Also due to the requirement that the final state has the quantum numbers of the photon the three pion final-state is described by different currents in  $\tau$  decays and  $e^+e^-$  annihilation. In this section we list the available hadronic currents together with a brief description. A more detailed description can be found in either Refs. [55, 295] or the Doxygen documentation.

There is one current available to describe the leptonic decays of the  $\tau$  lepton.

- **LeptonNeutrinoCurrent** The current for weak decay to a lepton and the associated anti-neutrino is given by

$$J^\mu = \bar{u}(p_\ell)\gamma^\mu(1 - \gamma_5)v(p_{\bar{\nu}}),$$

where  $p_{\bar{\nu}}$  is the momentum of the anti-neutrino and  $p_\ell$  is the momentum of the charged lepton.

We provide two currents to describe the production of any spin-zero or -one mesons.

- **ScalarMesonCurrent** The simplest hadronic current is that for the production of a pseudoscalar meson, *e.g.* the current for the production of  $\pi^\pm$  in the decay of the tau. The hadronic current can be written as

$$J^\mu = f_P p_P^\mu,$$

where  $p_P^\mu$  is the momentum of the pseudoscalar meson and  $f_P$  is the pseudoscalar meson decay constant.

- **VectorMesonCurrent** The current for the production of a vector meson is given by

$$J^\mu = \sqrt{2}g_V \epsilon_V^{*\mu},$$

where  $\epsilon_V^{*\mu}$  is the polarisation vector for the outgoing meson and  $g_V$  is the decay constant of the vector meson.

We also have one base class designed to allow the easy implementation of three meson currents.

- **ThreeMesonCurrentBase** In order to simplify the implementation of a number of standard currents for the production of three pseudoscalar mesons we define the current in terms of several form factors. The current is defined to be [293]

$$J^\mu = \left( g^{\mu\nu} - \frac{q^\mu q^\nu}{q^2} \right) [F_1(p_2 - p_3)^\mu + F_2(p_3 - p_1)^\mu + F_3(p_1 - p_2)^\mu] + q^\mu F_4 + iF_5 \epsilon^{\mu\alpha\beta\gamma} p_1^\alpha p_2^\beta p_3^\gamma,$$

where  $p_{1,2,3}$  are the momenta of the mesons in the order given below and  $F_{1\rightarrow 5}$  are the form factors. We use this approach for a number of three-meson modes that occur in  $\tau$  decays:  $\pi^-\pi^-\pi^+$ ;  $\pi^0\pi^0\pi^-$ ;  $K^-\pi^-K^+$ ;  $K^0\pi^-\bar{K}^0$ ;  $K^-\pi^0K^0$ ;  $\pi^0\pi^0K^-$ ;  $K^-\pi^-\pi^+$ ;  $\pi^-\bar{K}^0\pi^0$ ;  $\pi^-\pi^0\eta$ ;  $K_S^0\pi^-K_S^0$ ;  $K_L^0\pi^-K_L^0$ ;  $K_S^0\pi^-K_L^0$ . The current is implemented in terms of these form factors in a base class so that any model for these currents can be implemented by inheriting from this class and specifying the form factors.

There are a number of currents available which can be used to describe either  $\tau$  decays or the isospin rotated state in  $e^+e^-$  collisions.

- **TwoPionRhoCurrent** The weak current for production of either two pions or two kaons via the  $\rho$  resonances has the form

$$J^\mu = (p_1 - p_2)_\nu \left( g^{\mu\nu} - \frac{q^\mu q^\nu}{q^2} \right) \frac{1}{\sum_k \alpha_k} \sum_k \alpha_k \text{BW}_k(q^2),$$

where  $p_{1,2}$  are the momenta of the outgoing mesons,  $q = p_1 + p_2$ ,  $\text{BW}_k(q^2)$  is the Breit-Wigner distribution for the intermediate vector meson  $k$  and  $\alpha_k$  is the weight for the resonance, which can be complex. The Breit-Wigner terms are summed over the  $\rho$  resonances that can contribute to a given decay mode.

The models of either Kühn and Santamaria [296], which uses a Breit-Wigner distribution with a  $p$ -wave running width, or Gounaris and Sakurai [297] are supported for the shape of the Breit-Wigner distribution.

- **TwoPionCzyzCurrent** We also supply the alternative model of Ref. [298] to describe the production of two pions via the  $\rho$  resonance, and its excited states. The parameters of this model are fitted to  $e^+e^-$  annihilation data.
- **TwoKaonCzyzCurrent** We also supply the alternative model of Ref. [298], with the parameters from the fit of Ref. [295] to  $e^+e^-$  annihilation data, for the current for the production of two kaons.
- **PionPhotonCurrent** We use the model of Ref. [299], via intermediate  $\rho$ ,  $\omega$ ,  $\phi$  and  $\omega'$  final states, to describe the current for the production of  $\pi\gamma$  final states.
- **OmegaPionSNDCurrent** The implementation of the model of Ref. [300] to describe the production of  $\omega\pi$  final states. This model is provided to make comparisons and we use models including the decay of the  $\omega$  meson by default.
- **PhiPiCurrent** We use the simple model of Refs. [295, 301] to describe the production of  $\phi\pi$  final states.

- **TwoPionPhotonCurrent** The branching ratio for the decay  $\tau^- \rightarrow \omega\pi^-\nu_\tau$  is 1.95% [269]. The majority of this decay is modelled as an intermediate state in the four-pion current described below. However there is an 8.35% [269] branching ratio of the  $\omega$  into  $\pi^0\gamma$ , which must also be modelled. We do this using a current for  $\pi^-\pi^0\gamma$  via an intermediate  $\omega$ . The hadronic current for this mode, together with the masses, widths and other parameters, are taken from Ref. [293].
- **TwoPionPhotonSNDCurrent** The implementation of the model of Ref. [300] to describe the production of two pions and a photon via the decay of the  $\omega$  meson.
- **FourPionCzyzCurrent** We use the model of [302] to describe the cross section for four pion production in electron-positron annihilation.
- **FourPionNovosibirskCurrent** We use the model of Ref. [303]<sup>1</sup> to model the decay of the  $\tau$  to four pions. The model is based on a fit to  $e^+e^-$  data from Novosibirsk.
- **EtaPiPiCurrent** We use the fit of Ref. [295] using the model of Ref. [304] which uses the  $\rho$  and its excited states to describe the production of  $\eta\pi\pi$  final states.
- **EtaPiPiDefaultCurrent** Before version 7.3 of Herwig our default model of the current for  $\eta\pi\pi$  final state was that of Ref. [305], however from version 7.3 we use the more recent fit described above.
- **EtaPrimePiPiCurrent** We use the fit of Ref. [295] using the model of Ref. [304] which uses the  $\rho$  and its excited states to describe the production of  $\eta'\pi\pi$  final states.

We also have a number of currents which can only be used to describe hadronic  $\tau$  decays. These currents usually either include a large pseudovector component which is not present in  $e^+e^-$  annihilations, or have final states which are forbidden in  $e^+e^-$  annihilations.

- **KPiKStarCurrent** The weak current for production of a kaon and a pion uses the same form as the **TwoPionRhoCurrent** described above.
- **KPiCurrent** Unlike the  $\pi^+\pi^0$  decay of the tau the  $K\pi$  decay mode can occur via either intermediate scalar or vector mesons. We therefore include a model for the current for the  $K\pi$  decay mode including the contribution of both vector and scalar resonances based on the model of Ref. [306]. The current is given by

$$J^\mu = c_V(p_1 - p_2)_\nu \frac{1}{\sum_k \alpha_k} \sum_k \alpha_k \text{BW}_k(q^2) \left( g^{\nu\mu} - \frac{q^\nu q^\mu}{M_k^2} \right) + c_S q^\mu \frac{1}{\sum_k \beta_k} \sum_k \beta_k \text{BW}_k(q^2),$$

where  $p_{1,2}$  are the momenta of the outgoing mesons,  $q = p_1 + p_2$ ,  $\text{BW}_k(q^2)$  is the Breit-Wigner distribution for the intermediate resonance  $k$  and  $\alpha_k$  is its weight. The sum over the resonances is over the vector  $K^*$  states in the first, vector, part of the current and the excited scalar  $K^*$  resonances in the second, scalar, part of the current. By default the vector part of the current includes the  $K^*(892)$  and  $K^*(1410)$  states and the scalar part of the current includes the  $K_0^*(1430)$  together with the option of including the  $\kappa(800)$  to model any low-mass enhancement in the mass of the  $K\pi$  system, although additional resonances can be included if necessary.

- **ThreePionDefaultCurrent** This is the implementation of the model of Refs. [293, 296, 305], which uses the form of Ref. [296] for the  $a_1$  width, for the current for the production of three pions in  $\tau$  lepton decays. The form factors for the different modes are given in Refs. [293, 305].
- **ThreePionCLEOCCurrent** This is the implementation of the model of Ref. [307] for the weak current for three pions. This model includes  $\rho$  mesons in both the  $s$ - and  $p$ -wave, the scalar  $\sigma$  resonance, the tensor  $f_2$  resonance and scalar  $f_0(1370)$ . The form factors for the  $\pi^0\pi^0\pi^-$  mode are given in Ref. [307] and the others can be obtained by isospin rotation.
- **OneKaonTwoPionMesonDefaultCurrent** This current implements the  $K\pi\pi$  currents using the model of Refs. [293, 296, 305], which uses the form of Ref. [296] for the  $a_1$  width. The form factors for the different modes are given in Refs. [293, 305].
- **OneKaonTwoPionMesonCurrent** This current implements the  $K\pi\pi$  currents using the model of Ref. [308]. Like the model of Ref. [305] this model is designed to reproduce the correct chiral limit for tau decays to three mesons. However, this model makes a different choice of the resonances to use away from this limit for the decays involving at least one kaon and in the treatment of the  $K_1$  resonances. The form factors for the different modes are given in Ref. [308].
- **TwoKaonOnePionMesonDefaultCurrent** This current implements the  $KK\pi$  currents using the model of Refs. [293, 296, 305] described above.

<sup>1</sup> It should be noted that there were a number of mistakes in this paper, which were corrected in Ref. [294].

- **TwoKaonOnePionMesonCurrent** This current implements the  $KK\pi$  currents using the model of Ref. [308] described above.
- **FivePionCurrent** We use the model of Ref. [309], which includes  $\rho\omega$  and  $\rho\sigma$  intermediate states, via the  $a_1$  meson, to model the five-pion decay modes of the  $\tau$ .

In addition we have a number of currents which are primarily used to describe low energy  $e^+e^-$  annihilation into hadrons. These primarily have isospin zero, or contain isospin zero and one components but not the pseudovector contributions required to describe  $\tau$  lepton decay.

- **EtaOmegaCurrent** We use the model of Ref. [310] which proceeds via excited  $\omega$  states to describe the production of  $\eta\omega$  final states.
- **EtaPhiCurrent** We use the model of Ref. [311] which uses the  $\phi(1680)$  intermediate state to describe the production of  $\eta\phi$  final states.
- **EtaPhotonCurrent** This is the implementation of the model of [312] for the production of  $\eta\gamma$  final state via intermediate  $\rho, \omega, \phi$  and  $\omega'$  states.
- **ThreePionCzyzCurrent** We use the model of Ref. [313] to describe the isospin zero current for the production of three pions, via  $\omega$  and  $\phi$  resonances, and their excited states.
- **KKPiCurrent** This is a simple model for the production of  $KK\pi$  final state in  $e^+e^-$  collisions via  $\rho$  and  $\phi$  resonances (and the relevant excited states) to an intermediate  $K^*K$  intermediate state, see Ref. [295] for more details.
- **OmegaPiPiCurrent** This is the implementation of the simple model described in Ref. [295] for the production of the  $\omega\pi\pi$  final states.

Finally we also provide a wrapper class **WeakBaryonCurrent** which allows the baryon form factors described in Section 9.5.1 to be used as a weak current in order to describe the low energy production of baryon-antibaryon pairs in  $e^+e^-$  collisions.

## 9.4 Strong and electromagnetic hadron decays

The vast majority of the strong and electromagnetic decays in Herwig are simulated using a few simple models based on the spin structure of the decay. These simple models are supplemented with a small number of specialized models, usually from experimental fits, for specific decay modes. In this section we describe the different models we use for these decays for the scalar, vector and tensor mesons. All of these are implemented in **Decayer** classes that inherit from the **DecayIntegrator** class of Herwig.

For a number of the decays of bottomonium and charmonium resonances we use inclusive electromagnetic and strong decays to  $q\bar{q}$ ,  $gg$ ,  $ggg$  and  $gg\gamma$ , which are described in a separate section.

A number of decays are still performed using a phase-space distribution generated using the **Hw64Decayer**, which implements the same models as were available in the FORTRAN HERWIG program. In addition we use the MAMBO algorithm, [314], implemented in the **MamboDecayer** class, to generate the momenta of the decay products according to a phase-space distribution for a number of high-multiplicity modes.

In the matrix elements for all the decays given below 0 refers to the decaying particle, and then 1... to the outgoing particles in the order specified by the name of the **Decayer**. The 4-momentum of any particle is given by  $p_i^\mu$ , its mass by  $m_i$ , the polarization vector of spin-1 particles by  $\epsilon_i^\mu$ , the polarization tensor of spin-2 particles by  $\epsilon_i^{\mu\nu}$  and the rank-3 polarization tensor for spin-3 particles by  $\epsilon_i^{\mu\nu\rho}$ , where the index  $i$  gives the particle. The 4-dimension Levi-Civita tensor is given by  $\epsilon^{\alpha\beta\gamma\delta}$  and  $g$  is the coupling for a specific decay channel.

### 9.4.1 Scalar mesons

While the majority of the scalar meson decays are performed using general **Decayers** based on the spin structures, there are a number of models implemented for the rare radiative decays of the light pseudoscalar mesons, three-body decays of the  $\eta$  and  $\eta'$ , and the decay  $\pi^0 \rightarrow e^+e^-e^+e^-$ .

- **EtaPiGammaGammaDecayer** We use the Vector-Meson Dominance (VMD)-based model of Ref. [315] for the decays  $\eta, \eta' \rightarrow \pi^0\gamma\gamma$ . In practice we use a running width for the  $\rho$  to include the  $\eta'$  decay as well as the  $\eta$  decay and take the parameters from Ref. [315].
- **EtaPiPiGammaDecayer** We use either a VMD type model or a model using either the theoretical or experimental form of the Omnes function<sup>2</sup> taken from Refs. [315, 316] for the decay of the  $\eta$  or  $\eta'$  to  $\pi^+\pi^-\gamma$ .

<sup>2</sup> Our default choice is to use the experimental form of the Omnes function.

- **EtaPiPiDecayer** The decay of a pseudoscalar meson, for example the  $\eta$  or  $\eta'$ , to two charged and one neutral or three neutral pions, or of the  $\eta'$  to two pions and the  $\eta$ , is performed using a parameterization of the matrix element squared taken from Ref. [317]. The experimental results of Refs. [318] and [319] are used for the  $\eta \rightarrow \pi^+ \pi^- \pi^0$  and  $\eta \rightarrow \pi^0 \pi^0 \pi^0$  decays respectively. The theoretical values from Ref. [317] are used for the other decays.
- **EtaPiFermionsDecayer** We use the model described above in the **EtaPiPiGammaDecayer** together with the electromagnetic branching of the photon to describe the decay of the  $\eta$  or  $\eta'$  to  $\pi^+ \pi^- \ell^+ \ell^-$ .
- **PScalar4FermionsDecayer** As the  $\pi^0$  is so copiously produced it is one of the small number of particles for which we include branching ratios below the level of  $10^{-4}$ . The matrix element for the sub-leading decay  $\pi^0 \rightarrow e^+ e^- e^+ e^-$  is taken to be the combination of the standard matrix element for  $\pi^0 \rightarrow \gamma\gamma$  and the branching of the photons into  $e^+ e^-$ .
- **PScalarPScalarVectorDecayer** This matrix element is used to simulate the decay of the 2S pseudoscalar mesons to a vector meson and a 1S pseudoscalar meson. It is also used for the decay of some scalar mesons to vector mesons and another scalar meson, which has the same spin structure. The matrix element has the form

$$\mathcal{M} = g\epsilon_2^\mu(p_0 + p_1)_\mu.$$

- **PScalarVectorFermionsDecayer** There are a number of decays of a pseudoscalar meson to either a vector meson or the photon and a lepton-antilepton pair. The classic example is the Dalitz decay of the neutral pion,  $\pi^0 \rightarrow \gamma e^+ e^-$ . We take the propagator of the off-shell photon to be  $\frac{1}{m_{f\bar{f}}^2}$ , where  $m_{f\bar{f}}$  is the mass of the fermion-antifermion pair. The option of including a vector meson dominance form factor is included.
- **PScalarVectorVectorDecayer** In practice the vast majority of the decays of pseudoscalar mesons to two spin-1 particles are of the form  $P \rightarrow \gamma\gamma$  for which, because the photon is stable, it is not as important to have a good description of the matrix element. There are however some decays, *e.g.*  $\eta' \rightarrow \omega\gamma$ , for which this matrix element is needed.

The matrix element is taken to be

$$\mathcal{M} = g\epsilon^{\mu\nu\alpha\beta}p_{1\mu}\epsilon_{1\nu}p_{2\alpha}\epsilon_{2\beta}.$$

- **PseudoScalar2FermionsDecayer** This is a simple model for the decay of a pseudoscalar meson to a fermion-antifermion pair. It is used to simulate the strong decays of the  $\eta_c$  meson into baryon-antibaryon pairs.
- **ScalarMesonTensorScalarDecayer** There are a limited number of decays of a (pseudo)scalar meson to a tensor meson and another (pseudo)scalar meson. The matrix element takes the form

$$\mathcal{M} = g\epsilon^{\alpha\beta}p_{0\alpha}p_{2\beta}.$$

- **ScalarScalarScalarDecayer** The decay of a scalar meson to two scalar mesons has no spin structure and we assume that the matrix element is simply constant, *i.e.*

$$\mathcal{M} = g.$$

We still include a matrix element for this decay in order to simulate both the off-shell effects in the decay and to give the correct partial width to be used in the running width calculation for the incoming particle.

- **ScalarVectorVectorDecayer** A number of the scalar mesons decay to two vector mesons. The matrix element is taken to have the form

$$\mathcal{M} = g [p_1 \cdot p_2 \epsilon_1 \cdot \epsilon_2 - p_1 \cdot \epsilon_2 p_2 \cdot \epsilon_1].$$

- **Scalar2FermionsDecayer** We implement the decay of a scalar meson to a fermion-antifermion pair in order to simulate the decay of scalar quarkonium state to baryon-antibaryon pairs.

We also make use of the **ScalarTo3ScalarDalitz** class which is primarily intended to implement three-body weak decays, see Section 9.5.2.2 for more details, to simulate a number of three-body decays of the  $\eta_c$  meson. Models for the following decays are currently implemented:

- $\eta_c \rightarrow K^+ K^- \eta$  using the model of Ref. [320], available as **EtacKpKmEtaBABAR**;
- $\eta_c \rightarrow K^+ K^- \eta'$  using the model of Ref. [321], available as **EtacKpKmEtaPBABAR**;

- $\eta_c \rightarrow K_{S,K}^0 K_{S,K}^0 \eta$  using the model of Ref. [320], available as `EtacKS0KS0EtaBABAR` and `EtacKL0KL0EtaBABAR`;
- $\eta_c \rightarrow K_{S,K}^0 K_{S,K}^0 \eta'$  using the model of Ref. [321], available as `EtacKL0KL0EtaPBABAR` and `EtacKS0KS0EtaPBABAR`;
- $\eta_c \rightarrow \pi^+ \pi^- \eta$  using the model of Ref. [321], available as `EtacPipPimEtaBABAR`;
- $\eta_c \rightarrow \pi^+ \pi^- \eta'$  using the model of Ref. [321], available as `EtacPipPimEtaPBABAR`;
- $\eta_c \rightarrow \pi^0 \pi^0 \eta$  using the model of Ref. [321], available as `EtacPi0Pi0EtaBABAR`;
- $\eta_c \rightarrow \pi^0 \pi^0 \eta'$  using the model of Ref. [321], available as `EtacPi0Pi0EtaPBABAR`;
- $\eta_c \rightarrow K_{S,K}^0 K_{S,K}^0 \pi^0$  using the model of Ref. [322], available as `EtacKL0KL0Pi0BABAR` and `EtacKS0KS0Pi0BABAR`;
- $\eta_c \rightarrow K^+ K^- \pi^0$  using the model of Ref. [322], available as `EtacKpKmPi0BABAR`;
- $\eta_c \rightarrow K_{S,L}^0 K^\pm \pi^\mp$  using the model of Ref. [322], available as `EtacKS0KpPimBABAR` and `EtacKL0KpPimBABAR`.

#### 9.4.2 Vector mesons

With the exception of the three-pion decay modes of the  $\omega$ ,  $\phi$  and  $a_1$  mesons, some four-pion decays, and the decays of onium resonances to two-pion and a lighter onium state, we use general Decayers based on the spin structure for all the strong and electromagnetic vector and pseudovector meson decays.

- `a1SimpleDecayer` This class implements the model of Kühn and Santamaria [296] for the decay of the  $a_1$  meson to three pions and only includes the lightest two  $\rho$  meson multiplets in the modelling of the decay.
- `a1ThreePionCLEODecayer` This class implements the model of CLEO [307] for  $a_1$  decay to three pions, which is a fit to CLEO data on  $\tau^- \rightarrow \pi^0 \pi^0 \pi^- \nu_\tau$ . The model includes the coupling of the  $a_1$  to the  $\rho$ ,  $\rho(1450)$ ,  $f_0(1370)$ ,  $f_2(1270)$  and  $\sigma$  mesons.
- `a1ThreePionDecayer` This class implements a model of  $a_1$  decay to three pions based on the modelling of the  $a_1$  used in the  $4\pi$  currents for tau decays presented in Ref. [303] and includes the  $\rho$  and  $\sigma$  resonances.
- `f1FourPiDecayer` The decay of the  $f_1$  meson to four pions is complicated as many of the intermediate states are either close to or below the production threshold. We include this model of the decay via the  $a_1$  and  $\rho$  mesons to investigate these effects.
- `f1RhoPiPiDecayer` This is an alternative model for the simulation of the decay of the  $f_1$  meson to four pions via the  $a_1$  meson where the decay of the  $\rho$  meson is not included.
- `OniumToOniumPiPiDecayer` The decay of onium resonances to lighter states and a pion pair,  $\mathcal{O}' \rightarrow \mathcal{O} \pi \pi$ , uses the matrix element [323]

$$\mathcal{M} = \epsilon_1 \cdot \epsilon_0 \left[ \mathcal{A} \left( q^2 - 2m_\pi^2 \right) + \mathcal{B} E_1 E_2 \right] + \mathcal{C} \left( (\epsilon_1 \cdot q_1)(\epsilon_0 \cdot q_2) + (\epsilon_1 \cdot q_2)(\epsilon_0 \cdot q_1) \right),$$

where  $\mathcal{A}$ ,  $\mathcal{B}$  and  $\mathcal{C}$  are complex couplings,  $m_\pi$  is the pion mass,  $E_{1,2}$  are the pion energies,  $q_{1,2}$  are the pion momenta and  $q$  is the momentum of the  $\pi\pi$  system.

The results of BES [324] are used for  $\psi' \rightarrow J/\psi$  and CLEO [325] for  $\Upsilon(3S)$  and  $\Upsilon(2S)$  decays. The remaining parameters are chosen to approximately reproduce the distributions from BaBar [326] and CLEO [327] for  $\Upsilon(4S)$  and  $\psi(3770)$  decays, respectively.

- `VectorMeson2FermionDecayer` Most of the decays of the vector mesons to a fermion-antifermion pair are the decays of the light vector mesons to electron and muon pairs, and of the bottomonium and charmonium resonances to all the charged leptons.

The matrix element is taken to have the form

$$\mathcal{M} = g \epsilon_{0\mu} \bar{u}(p_f) \gamma^\mu v(p_{\bar{f}}),$$

where  $p_f$  is the four-momentum of the outgoing fermion and  $p_{\bar{f}}$  is the four-momentum of the outgoing antifermion.

- `VectorMeson2MesonDecayer` The matrix element for the decay of a vector meson to two scalar mesons\_(or other decays with the same parity) is given by

$$\mathcal{M} = g \epsilon_0 \cdot (p_1 - p_2).$$

- **VectorMesonPScalarFermionsDecayer** The decay of a vector meson to a pseudoscalar meson and a fermion-antifermion pair is simulated using a matrix element based on that for the  $V \rightarrow VP$  vertex combined with the branching of the vector, which is in reality always a photon, into a fermion-antifermion pair.
- **VectorMesonTensorVectorDecayer** The matrix element for the decay of a vector meson to a tensor and vector meson is given by

$$\mathcal{M} = g\epsilon_0^{\beta_1\beta_2}\epsilon_1^\alpha\epsilon_2^\gamma \left( g_{\beta_1\alpha} + \frac{p_0\beta_1 p_1\alpha}{p_0 \cdot p_1 - m_0 m_1} \right) \left( g_{\beta_2\gamma} + \frac{p_2\beta_2 p_1\gamma}{p_0 \cdot p_1 - m_1 m_2} \right).$$

- **VectorMesonVectorPScalarDecayer** The decay of a vector meson to another spin-1 particle and a pseudoscalar meson is common in both the radiative decay of the 1S vector mesons and the decay of higher vector multiplets to the 1S vector mesons. The matrix element for the decay is

$$\mathcal{M} = g\epsilon^{\mu\nu\alpha\beta}\epsilon_{0\mu}p_{0\nu}p_{1\alpha}\epsilon_{1\beta}.$$

- **VectorMesonVectorScalarDecayer** We include a number of decays of the vector mesons to a scalar meson and either the photon or another vector meson. In practice the vast majority of these decays are radiative decays involving scalar mesons. The remaining decays use the  $\sigma$  meson as a model for four-pion decays of the excited  $\rho$  multiplets.

The matrix element for the decay is

$$\mathcal{M} = g\epsilon_0\mu [p_1 \cdot p_0\epsilon_1^\mu - p_1^\mu\epsilon_1 \cdot p_0].$$

- **VectorMesonVectorVectorDecayer** There are a small number of decays of excited  $\rho$  multiplets to  $\rho$  mesons included in the simulation. We model these decays using the matrix element

$$\mathcal{M} = \frac{g}{m_0^2}(p_{0\nu}\epsilon_0^\alpha - p_{0\alpha}\epsilon_0^\nu) \left[ (p_{1\nu}\epsilon_1^\beta - p_1^\beta\epsilon_{1\nu})(p_{2\alpha}\epsilon_{2\beta} - p_{2\beta}\epsilon_{2\alpha}) - (\nu \leftrightarrow \alpha) \right].$$

- **VectorMeson2SpinHalfBaryonsDecayer** In recent years the BES collaboration have measured the properties of a large number spin- $\frac{1}{2}$  baryon-antibaryon decay modes of the  $J/\psi$  ( $p\bar{p}$  [328],  $n\bar{n}$  [328],  $\Lambda^0\bar{\Lambda}^0$  [329–332],  $\Sigma^0\bar{\Sigma}^0$  [331],  $\Xi^0\bar{\Xi}^0$  [333, 334],  $\Xi^-\bar{\Xi}^+$  [335, 336],  $\Sigma^+\bar{\Sigma}^-$  [337]) and  $\psi(2S)$  ( $p\bar{p}$  [338],  $n\bar{n}$  [338],  $\Lambda^0\bar{\Lambda}^0$  [331],  $\Sigma^0\bar{\Sigma}^0$  [331],  $\Xi^0\bar{\Xi}^0$  [333, 339],  $\Xi^-\bar{\Xi}^+$  [329, 335],  $\Sigma^+\bar{\Sigma}^+$  [337],  $\Sigma^-\bar{\Sigma}^+$  [340]) states and also the decay  $\psi(3770) \rightarrow \Lambda^0\bar{\Lambda}^0$  [341]. We implement these decays using the most recent measurements of the asymmetry and phase.
- **VectorMeson2SpinThreeHalfBaryonsDecayer** In recent years the BES collaboration have also measured the properties of a number spin- $\frac{3}{2}$  baryon-antibaryon decay modes of the  $J/\psi$  ( $\Sigma^{*0}\bar{\Sigma}^{*0}$  [333],  $\Sigma^{*\mp}\bar{\Sigma}^{*\pm}$  [335]) and  $\psi(2S)$  ( $\Sigma^{*0}\bar{\Sigma}^{*0}$  [333],  $\Sigma^{*\mp}\bar{\Sigma}^{*\pm}$  [335],  $\Xi^{*0}\bar{\Xi}^{*0}$  [342],  $\Xi^{*-}\bar{\Xi}^{*+}$  [343]) states. We implement these decays using the most recent measurements of the asymmetry and phase.
- **VectorTo3PseudoScalarDalitz** We use the same approach as described in Section 9.5.2.2 for scalar Dalitz decays to simulate the decays of vector mesons to three pseudoscalar mesons. The **VectorTo3PseudoScalarDalitz** implements the decays but a range of intermediate states and Lorentz structures for the matrix element can be specified in order to describe a range of decays. Currently we supply three models:

1. **OmegaDalitz** for the decay  $\omega \rightarrow \pi^+\pi^-\pi^0$ ;
2. **PhiDalitz** for the decay  $\phi \rightarrow \pi^+\pi^-\pi^0$ ;
3. **JpsiPipPimPi0BABAR** for the decay  $J/\psi \rightarrow \pi^+\pi^-\pi^0$ .

For the  $\omega$  and  $\phi$  we assumed the decay is dominated by the production of the lowest lying  $\rho$  multiplet. Our default model for the matrix element for this decay is

$$\mathcal{M} = g\epsilon^{\mu\alpha\beta\nu}\epsilon_{\mu\nu}p_{1\alpha}p_{2\beta}p_{3\nu} \left[ d + \sum_i f_i [\text{BW}_i(s_{12}) + \text{BW}_i(s_{13}) + \text{BW}_i(s_{23})] \right],$$

where  $s_{ij} = (p_i + p_j)^2$ ,  $d$  is a complex coupling for the direct interaction,  $f_i$  is the coupling of the  $i$ th  $\rho$  multiplet and  $\text{BW}_i(s)$  is a Breit-Wigner distribution with a  $p$ -wave running width. This is an extension of the model used by KLOE [344] to include higher  $\rho$  multiplets.

For the decay of the  $J/\psi$  we use the model of BABAR from Ref. [345].

### 9.4.3 Tensor mesons

Only a relatively small number of tensor meson states are included in the simulation, compared to the vector and scalar mesons. All their decays are simulated using a small number of matrix elements based on the spin structure of the decays. Many of the multi-body decays of the tensor mesons are simulated using these two-body matrix elements with off-shell vector and scalar mesons.

- **PseudoTensorMesonTensorVectorDecayer** The decay of a pseudotensor meson to a tensor and vector meson is described using the matrix element

$$\mathcal{M} = g\epsilon_0^{\alpha_1\alpha_2}\epsilon_1^{\beta_1\beta_2}\epsilon_{\alpha_1\beta_1\gamma_1p_2}\epsilon_{2\gamma_1}\left(g_{\alpha_2\beta_2} + \frac{p_{1\alpha_2}p_{0\beta_2}}{p_0 \cdot p_1 - m_0 m_1}\right).$$

- **PseudoTensorMesonVectorVectorDecayer** The matrix element for a pseudotensor meson decaying to two vector meson is taken to be

$$\mathcal{M} = g\epsilon_0^{\alpha_1\alpha_2}\epsilon_1^{\beta}\epsilon_2^{\gamma}\epsilon^{\mu\alpha_1\beta'\gamma'}(p_1 - p_2)_{\alpha_2}G_{\beta\beta'}G_{\gamma\gamma'},$$

where

$$G_{\mu\nu} = g_{\mu\nu} + \frac{1}{X} \left( -p_1 \cdot p_2 (p_{2\mu}p_{1\nu}p_{1\mu}p_{2\nu}) + m_2^2 p_{1\mu}p_{1\nu} + m_1^2 p_{2\mu}p_{2\nu} \right),$$

where  $X = (p_1 \cdot p_2)^2 - m_1^2 m_2^2$ .

- **TensorMeson2PScalarDecayer** The matrix element for the decay of a tensor meson to two pseudoscalar (or scalar) mesons is

$$\mathcal{M} = g\epsilon_0^{\mu\nu}p_{1\mu}p_{2\nu}.$$

- **TensorMesonVectorPScalarDecayer** There are a number of decays of tensor mesons to a spin-1 particle, either a vector meson or the photon, and a pseudoscalar meson, examples include  $a_2 \rightarrow \rho\pi$  and  $a_2 \rightarrow \pi\gamma$ . The matrix element is taken to be

$$\mathcal{M} = g\epsilon_0^{\mu\nu}p_{2\mu}\epsilon_{\nu\alpha\beta\gamma}p_1^\alpha\epsilon_1^\beta p_2^\gamma.$$

- **TensorMesonSpin3VectorDecayer** We take the matrix element for the decay of a spin-2 meson to a spin-3 meson and a vector meson to be

$$\mathcal{M} = g\epsilon_1^{\alpha_1\alpha_2\alpha_3}\epsilon_0^{\beta_1\beta_2}\epsilon_2^{\gamma} \left( g_{\alpha_1\beta_1} - \frac{p_{1\alpha_1}p_{0\beta_1}}{p_0 \cdot p_1 - m_0 m_1} \right) \left( g_{\alpha_2\beta_2} - \frac{p_{1\alpha_2}p_{0\beta_2}}{p_0 \cdot p_1 - m_0 m_1} \right) \left( g_{\alpha_3\gamma} - \frac{p_{2\alpha_3}p_{1\gamma}}{p_0 \cdot p_1 - m_0 m_1} \right).$$

- **TensorMesonTensorPScalarDecayer** The matrix element for the decay of a spin-2 meson to a spin-2 meson and a pseudoscalar meson is taken to be

$$\mathcal{M} = g\epsilon_0^{\alpha_1\alpha_2}\epsilon_1^{\beta_1\beta_2} \left( g_{\alpha_1\beta_1} + \frac{p_{1\alpha_1}p_{0\beta_1}}{p_0 \cdot p_1 - m_0 m_1} \right) \epsilon_{\mu\nu\alpha_2\beta_2}p_{1\mu}p_{2\nu}.$$

- **TensorMesonTensorScalarDecayer** The matrix element for the decay of a spin-2 meson to a spin-2 meson and a scalar meson is taken to be

$$\mathcal{M} = g\epsilon_0^{\alpha_1\alpha_2}\epsilon_1^{\beta_1\beta_2} \left( g_{\alpha_1\beta_1} + \frac{p_{1\alpha_1}p_{0\beta_1}}{p_0 \cdot p_1 - m_0 m_1} \right) \left( g_{\alpha_2\beta_2} + \frac{p_{1\alpha_2}p_{0\beta_2}}{p_0 \cdot p_1 - m_0 m_1} \right).$$

- **TensorMesonVectorScalarDecayer** We take the matrix element for the decay of a tensor meson to a vector and pseudoscalar meson to be

$$\mathcal{M} = g\epsilon_0^{\alpha_1\alpha_2}\epsilon_1^{\beta} \left( g_{\alpha_1\beta} + \frac{p_{1\alpha_1}p_{0\beta}}{p_0 \cdot p_1 - m_0 m_1} \right) (p_1 - p_2)_{\alpha_2}.$$

- **TensorMesonVectorVectorDecayer** We have based our matrix element for the decay of a tensor meson to two vector mesons on the perturbative graviton decay matrix element [346] in such a way that it vanishes if the polarisations of the outgoing vectors are replaced with their momenta. The matrix element is

$$\mathcal{M} = g \left[ \epsilon_{0\mu\nu} \{ (\epsilon_{1\alpha} p_1^\mu - \epsilon_1^\mu p_{1\alpha}) (\epsilon_2^\alpha p_2^\nu - \epsilon_2^\nu p_{2\alpha}) + (\mu \leftrightarrow \nu) \} \right. \\ \left. - \frac{1}{2} \epsilon_\mu^\mu (\epsilon_{1\alpha} p_{1\beta} - \epsilon_{1\beta} p_{1\alpha}) (\epsilon_2^\alpha p_2^\beta - \epsilon_2^\beta p_2^\alpha) \right].$$

In practice this matrix element is mainly used with off-shell vector mesons to model three- and four-body decays of the tensor mesons.

#### 9.4.4 Spin-Three mesons

Starting with version 7.3 we also include a small number of matrix elements for the decay of spin-3 mesons based on the spin structures of the decays.

- **Spin3Meson2PScalarDecayer** The matrix element for the decay of a spin-3 meson to two (pseudo)scalar mesons is taken to be

$$\mathcal{M} = g \epsilon_0^{\mu\nu\rho} (p_1 - p_2)_\mu (p_1 - p_2)_\nu (p_1 - p_2)_\rho.$$

- **Spin3MesonTensorPScalarDecayer** The matrix element for the decay of a spin-3 meson to spin-2 meson and a pseudoscalar is taken to be

$$\mathcal{M} = g \epsilon_0^{\alpha_1\alpha_2\alpha_3} \epsilon_1^{\beta_1\beta_2} \epsilon_{\mu\nu\alpha_1\beta_1} \left( g_{\alpha_2\beta_2} - \frac{p_{1\alpha_2} p_{0\beta_2}}{p_0 \cdot p_1 - m_0 m_1} \right) p_0^\mu p_1^\nu (p_1 - p_2)_{\alpha_3}.$$

- **Spin3MesonTensorVectorDecayer** The matrix element for the decay of a spin-3 meson to spin-2 meson and a vector meson is taken to be

$$\mathcal{M} = g \epsilon_0^{\alpha_1\alpha_2\alpha_3} \epsilon_1^{\beta_1\beta_2} \epsilon_2^\gamma \left( g_{\alpha_1\beta_1} - \frac{p_{1\alpha_1} p_{0\beta_1}}{p_0 \cdot p_1 - m_0 m_1} \right) \left( g_{\alpha_2\beta_2} - \frac{p_{1\alpha_2} p_{0\beta_2}}{p_0 \cdot p_1 - m_0 m_1} \right) \\ \left( g_{\alpha_3\gamma} - \frac{p_{2\alpha_3} p_{0\gamma}}{p_0 \cdot p_2 - m_0 m_2} \right).$$

- **Spin3MesonVectorPScalarDecayer** The matrix element for the decay of a spin-3 meson to vector meson and a pseudoscalar meson is taken to be

$$\mathcal{M} = g \epsilon_0^{\mu\nu\rho} \epsilon_1^\beta \epsilon_{\alpha\gamma\mu\beta} (p_1 - p_2)_\nu (p_1 - p_2)_\rho p_0^\alpha p_1^\beta.$$

- **Spin3MesonVectorScalarDecayer** The matrix element for the decay of a spin-3 meson to vector meson and a scalar meson is taken to be

$$\mathcal{M} = g \epsilon_0^{\mu\nu\rho} \epsilon_1^\beta \left( g_{\mu\beta} - \frac{p_{1\mu} p_{0\beta}}{p_0 \cdot p_1 - m_0 m_1} \right) (p_1 - p_2)_\nu (p_1 - p_2)_\rho.$$

#### 9.4.5 Excited heavy mesons

In Ref. [49], a systematic approach to transmitting the spin information of heavy hadron constituents was detailed, aiming to simulate the polarisation states of excited heavy mesons and heavy baryons within Herwig 7 using the principles of HQET and spin-flavour symmetry. HQET has been already utilised for the strong and radiative decays of heavy baryons, as evidenced by works in references [289, 347] and its incorporation into Herwig++ [6, 16]. However, there remains a pressing need to model the decays of excited heavy mesons to better align predictions with the experimental observations. Here we focus on the interactions specific to charm mesons, though the derived results are similarly applicable to bottom mesons. Initially, we consider the *s*- and *p*-wave mesons and identify three meson multiplets under heavy quark symmetry, as presented in [232]:

- The ground state ( $J^P = 0^-, 1^-$  doublet) includes  $D$  and  $D^*$  mesons, characterised by  $l = 0$  for the light degrees of freedom.
- The  $J^P = 1^+, 2^+$  doublet consists of  $D_1$  and  $D_2^*$ , distinguished by  $l = 1$  and  $j = \frac{3}{2}$  for the light degrees of freedom.

- The  $J^P = 0^+, 1^+$  doublet includes  $D_0^*$  and  $D_1'$ , defined by  $l = 1$  and  $j = \frac{1}{2}$  for the light degrees of freedom.

Additionally, there is potential for mixing between  $D_1$  and  $D_1'$ , arising from sub-leading corrections within the heavy quark limit.

To determine the relevant matrix elements for these decays, we follow the methodology and notation detailed in Refs. [232, 348], aiming to balance a coherent representation of experimental data with theoretical accuracy. We prioritise the leading terms within the heavy quark limit for the interactions, while also accommodating the mixing between the  $D_1$  and  $D_1'$  mesons,  $\theta_q$ . This yields the following expressions for the decay matrix elements:

$$\begin{aligned}\mathcal{M}(D^* \rightarrow D\pi) &= -\frac{2g}{f_\pi} (m_D m_{D^*})^{1/2} p_0 \cdot \epsilon_0, \\ \mathcal{M}(D_2^* \rightarrow D\pi) &= -\frac{2h}{f_\pi \Lambda} (m_{D_2} m_D^*)^{1/2} \epsilon_0^{\mu\nu} p_{0,\mu} p_{0,\nu}, \\ \mathcal{M}(D_2^* \rightarrow D^* \pi) &= -i \frac{2h}{f_\pi \Lambda} \left( \frac{m_{D^*}}{m_{D_2}} \right)^{1/2} \epsilon^{\alpha\beta\mu\nu} \epsilon_{\alpha\gamma}^0 p_0^\gamma p_{0,\mu} p_{1\nu} \epsilon_{1\beta}, \\ \mathcal{M}(D_1 \rightarrow D^* \pi) &= \frac{h}{f_\pi \Lambda} \left( \frac{2}{3} m_{D_1} m_D \right)^{1/2} \left[ \epsilon_0 \cdot \epsilon_1 \left( p_0^2 - \left( \frac{p_0 \cdot p_1}{m_0} \right)^2 \right) - 3 \epsilon_0 \cdot p_0 \epsilon_1 \cdot p_0 \right], \\ \mathcal{M}(D_0^* \rightarrow D\pi) &= \frac{f''}{f_\pi} (m_{D_0^*} m_D)^{1/2} p_0 \cdot \left( \frac{p_1}{m_{D_0^*}} + \frac{p_2}{m_D} \right), \\ \mathcal{M}(D_1' \rightarrow D^* \pi) &= -\frac{f''}{f_\pi} (m_{D_1'} m_D)^{1/2} \left[ -p_0 \cdot \left( \frac{p_1}{m_{D_0^*}} + \frac{p_2}{m_D} \right) \epsilon_0 \cdot \epsilon_1 \right. \\ &\quad \left. + \frac{1}{m_{D_1'}} \epsilon_1 \cdot p_1 \epsilon_0 \cdot p_0 + \frac{1}{m_D} \epsilon_0 \cdot p_2 \epsilon_1 \cdot p_0 \right].\end{aligned}$$

Here,  $p_i$  and  $\epsilon_i$  are the momenta and polarisation vectors of the hadrons, with  $i = 0$  indicating the parent hadron and  $i = 1, 2$  the heavy and light child hadrons, respectively.  $m_H$  is the mass of hadron  $H$ , and  $g, h, \Lambda, f_\pi$ , and  $f''$  are decay parameters. We also introduce  $\theta_q$  as the mixing angles between the  $(D_1, D_1')$  and  $(D_{s1}, D'_{s1})$  mesons.

Having the matrix elements of the decays, we can calculate the partial widths using the Fermi golden rule for two-body decays:

$$\Gamma(H^* \rightarrow H\pi) = \frac{\Theta(H^* \rightarrow H\pi)}{2m_{H^*}} |\mathcal{M}(H^* \rightarrow H\pi)|^2,$$

with  $\Theta$  being the two-body phase-space factor. To ensure consistency between the theoretical calculations and our implementation in Herwig 7, we retain some sub-leading terms when considering the heavy quark limit. Explicitly, we use the following prescription for our calculations:

$$\Gamma(H^* \rightarrow H\pi) = \frac{1}{8\pi m_{H^*}^2} |\mathcal{M}(H^* \rightarrow H\pi)|^2 p_{\text{CM}},$$

where  $p_{\text{CM}}$  denotes the momentum of the parent hadron in the kinematic centre-of-mass frame of the two-body decay. The resulting partial widths are outlined below:

$$\begin{aligned}\Gamma(D^* \rightarrow D\pi) &= \frac{g^2}{6\pi f_\pi^2} \frac{m_D}{m_{D^*}} p_{\text{CM}}^3, \\ \Gamma(D_2^* \rightarrow D^* \pi) &= \frac{h^2}{15\pi f_\pi^2 \Lambda^2} \frac{m_{D^*}}{m_{D_2^*}} p_{\text{CM}}^5, \\ \Gamma(D_2^* \rightarrow D\pi) &= \frac{h^2}{10\pi f_\pi^2 \Lambda^2} \frac{m_D}{m_{D_2^*}} p_{\text{CM}}^5, \\ \Gamma(D_1 \rightarrow D^* \pi) &= \frac{h^2}{144\pi f_\pi^2 \Lambda^2} \frac{[-2m_{D_1}^2(m_{D^*}^2 - 5m_\pi^2) + (m_\pi^2 - m_{D^*}^2)^2 + 25m_{D_1}^4]}{m_{D^*} m_{D_1}^3} p_{\text{CM}}^5, \\ \Gamma(D_0^* \rightarrow D\pi) &= \frac{f''^2}{32\pi f_\pi^2} \frac{(m_{D_0^*} - m_D)^2}{m_D m_{D_0^*}^3} \left[ (m_{D_0^*} + m_D)^2 - m_\pi^2 \right]^2 p_{\text{CM}}, \\ \Gamma(D_1' \rightarrow D^* \pi) &= \frac{f''^2}{32\pi f_\pi^2} \frac{(m_{D_1'} - m_{D^*})^2}{m_{D^*} m_{D_1'}^3} \left[ (m_{D_1'} + m_{D^*})^2 - m_\pi^2 \right]^2 p_{\text{CM}}.\end{aligned}$$

To extract the numerical values of the decay parameters, we utilise the latest observed masses and decay widths of the charmed mesons from BaBar [241, 349] and LHCb [350] collaborations. The complete list of utilised masses and widths for the  $(0^-, 1^-)$ ,  $(1^+, 2^+)$ ,  $(0^+, 1^+)$  multiplets is given in Table 6 of Ref. [49], resulting in the best fits:

Table 9.1: Fitted values of the decay parameters using the charm mesons masses and decay widths from [241, 349, 350].

Parameter	Fitted Value
$f''$	-0.465 pm 0.017
$f_\pi$	0.130 pm 0.001 [GeV]
$h$	0.824 pm 0.007
$\Lambda$	1.000 pm 0.000 [GeV]
$g$	0.565 pm 0.006
$\theta_{u,d}$	0.000 pm 0.100
$\theta_s$	-0.047 pm 0.002

Besides the strong isospin-conserving decays, certain excited mesons also undergo electromagnetic decays, as well as strong isospin-violating ones. These latter decays are particularly prominent in cases where the strong isospin-conserving decays are either kinematically inhibited or strongly suppressed due to lack of sufficient rest energy, threshold effects, angular momentum conservation, particular selection rules in the given event handler, hierarchy of coupling constants, or presence of other dominant channels. These are predominantly observed in the following cases:

- $D^*$  mesons: Strong isospin-conserving decays are kinematically limited, making radiative modes crucial,
- $B^*$  mesons: Strong isospin-conserving decays cannot occur due to kinematic constraints. Thus, only the radiative mode emerges as a possibility,
- $D_s^+$ ,  $D_{s0}^+$ , and  $D_{s1}^+$ (2460) mesons: Both radiative and isospin-violating decay modes hold significance since the strong isospin-conserving  $DK$  modes are kinematically proscribed,
- $B_s^{*0}$  meson: Only the radiative mode is feasible from a kinematic perspective.

Again, our focus can be on the  $D^*$  system, as it represents the most intricate scenario, exhibiting a plethora of excited mesons below the strong decay threshold. However, our arguments can be effortlessly extended to other cases. The amplitude for the radiative decay of the  $D^*$  mesons, as detailed in [351], is given by:

$$\mathcal{M}(D^* \rightarrow D\gamma) = A \left[ 64\pi \frac{m_D}{m_{D^*}} \right]^{1/2} \epsilon^{\alpha\beta\mu\nu} \epsilon_{\gamma\alpha} p_{\gamma\beta} \epsilon_{D^*\mu} p_{D^*\nu}.$$

Here, the coupling  $A$  is expressed as:

$$A = \frac{e_Q}{4m_Q} \alpha(m_Q)^{1/2} + \frac{c_H}{\Lambda} e_q \alpha(\Lambda)^{1/2},$$

with  $e_Q$  and  $e_q$  being the electric charges of the heavy and light quarks, respectively, and  $m_Q$  being the mass of the heavy quark.  $\alpha$  is the electromagnetic coupling constant, while  $c_H = -1.058$  is the electromagnetic coefficient for heavy meson decays. The scale  $\Lambda$  is the same as in the case of strong decays. Consequently, the partial width becomes [352, 353]:

$$\Gamma(D^* \rightarrow D\gamma) = \frac{2m_D |A|^2}{3m_{D^*}} \left( \frac{m_{D^*}^2 - m_D^2}{m_{D^*}} \right)^3.$$

To implement the strong and radiative decays of excited heavy mesons in Herwig 7, we introduced two specialised classes: `HQETStrongDecayer` and `HQETRadiativeDecayer`. The decay parameters highlighted in this section are defined as user-adjustable variables. This design provides flexibility, facilitating potential tuning and refinement based on future insights or requirements. In the subsequent section, we will evaluate the robustness of our implementation by comparing it against the available experimental data.

#### 9.4.6 Baryon Decays

The strong and electromagnetic decays of the baryons are modelled in Herwig using models based on either heavy quark effective theory, for the baryons containing a bottom or charm quark, or SU(3) symmetry for the light baryons.

All the strong decays, and many of the weak hadronic decays, involve the decay of a spin- $\frac{1}{2}$  or  $\frac{3}{2}$  baryon to either a pseudoscalar meson or a vector particle and another spin- $\frac{1}{2}$  or  $\frac{3}{2}$  baryon. Lorentz invariance restricts the possible form of the matrix elements. We use the following matrix elements, which are implemented in the `Baryon1MesonDecayerBase` class from which the `Decayers` inherit.

$$\begin{aligned}
 \mathcal{M} &= \bar{u}(p_1)(A + B\gamma_5)u(p_0) & \frac{1}{2} &\rightarrow \frac{1}{2} + 0; \\
 \mathcal{M} &= \bar{u}(p_1)\epsilon^{*\beta} [\gamma_\beta(A_1 + B_1\gamma_5) + p_{0\beta}(A_2 + B_2\gamma_5)] u(p_0) & \frac{1}{2} &\rightarrow \frac{1}{2} + 1; \\
 \mathcal{M} &= \bar{u}^\alpha(p_1)p_{0\alpha} [A + B\gamma_5] u(p_0) & \frac{1}{2} &\rightarrow \frac{3}{2} + 0; \\
 \mathcal{M} &= \bar{u}^\alpha(p_1)\epsilon^{*\beta} [g_{\alpha\beta}(A_1 + B_1\gamma_5) + p_{0\alpha}(A_2 + B_2\gamma_5) + p_{0\alpha}p_{0\beta}(A_3 + B_3\gamma_5)] u(p_0) & \frac{1}{2} &\rightarrow \frac{3}{2} + 1;
 \end{aligned}$$

for spin- $\frac{1}{2}$  decays and:

$$\begin{aligned}
 \mathcal{M} &= \bar{u}(p_1)p_{1\alpha} [A + B\gamma_5] u^\alpha(p_0) & \frac{3}{2} &\rightarrow \frac{1}{2} + 0; \\
 \mathcal{M} &= \bar{u}(p_1)\epsilon^{*\beta} [g_{\alpha\beta}(A_1 + B_1\gamma_5) + p_{1\alpha}(A_2 + B_2\gamma_5) + p_{1\alpha}p_{0\beta}(A_3 + B_3\gamma_5)] u^\alpha(p_0) & \frac{3}{2} &\rightarrow \frac{1}{2} + 1; \\
 \mathcal{M} &= \bar{u}^\alpha(p_1) [(A_1 + B_1\gamma_5)g_{\alpha\beta} + p_{0\alpha}p_{1\beta}(A_2 + B_2\gamma_5)] u^\beta(p_0) & \frac{3}{2} &\rightarrow \frac{3}{2} + 0;
 \end{aligned}$$

for spin- $\frac{3}{2}$  decays. In general  $u(p_0)$  is the spinor of a decaying spin- $\frac{1}{2}$  baryon,  $u^\beta(p_0)$  is the spinor of a decaying spin- $\frac{3}{2}$  baryon,  $\bar{u}(p_1)$  is the spinor for an outgoing spin- $\frac{1}{2}$  baryon and  $\bar{u}^\beta(p_1)$  is the spinor for an outgoing spin- $\frac{3}{2}$  baryon. The momentum of the decaying baryon is  $p_0$ , of the outgoing baryon is  $p_1$  and of the outgoing meson is  $p_2$ . All the matrix elements are parameterized in terms of a number of coefficients  $A$  and  $B$ , which can in principle depend on the momentum transferred in the decay.

- [RadiativeDoublyHeavyBaryonDecayer](#) Decay of the excited doubly heavy baryons via photon emission to the weakly decaying states.
- [RadiativeHeavyBaryonDecayer](#) There are a number of radiative decays of heavy baryons included in the simulation. Apart from some transitions of charm baryons, *e.g.*  $\Xi_c' \rightarrow \Xi_c\gamma$ , these transitions have not been observed and are included based on model calculations based on heavy quark effective theory [289].
- [RadiativeHyperonDecayer](#) The radiative decays of hyperons are simulated using the model of Ref. [354].
- [StrongHeavyBaryonDecayer](#) The [StrongHeavyBaryonDecayer](#) class implements the strong decays of bottom and charm baryons using the results of Ref. [289].
- [SU3BaryonDecupletOctetPhotonDecayer](#) The decay of a decuplet baryon to an octet baryon and a photon is assumed to occur via the SU(3) conserving term in the chiral Lagrangian.
- [SU3BaryonDecupletOctetScalarDecayer](#) This Decayer is based on SU(3) symmetry for the decay of a decuplet baryon to an octet baryon and a scalar meson.
- [SU3BaryonOctetDecupletScalarDecayer](#) This performs the decay of excited octet baryons to decuplet baryons and a scalar meson using a Lagrangian based on SU(3) symmetry.
- [SU3BaryonOctetOctetPhotonDecayer](#) This models the radiative decay of excited octet baryons using a Lagrangian based on SU(3) symmetry.
- [SU3BaryonOctetOctetScalarDecayer](#) This simulates the strong decay of excited octet baryons using a Lagrangian based on SU(3) symmetry.
- [SU3BaryonSingletOctetPhotonDecayer](#) This models the radiative decay of singlet baryons using a Lagrangian based on SU(3) symmetry.
- [SU3BaryonSingletOctetScalarDecayer](#) This simulates the strong decay of singlet baryons using a Lagrangian based on SU(3) symmetry.

#### 9.4.7 Inclusive strong and electromagnetic decays

For a number of bottomonium and charmonium resonances we make use of partonic decays of the mesons to model the unobserved inclusive modes needed to saturate the branching ratios. These decays are modelled using the `QuarkoniumDecayer` class, which implements the decay of the onium resonances to  $q\bar{q}$  and  $gg$  according to a phase-space distribution, and the decay to  $ggg$  and  $gg\gamma$  according to the Ore-Powell matrix element [355]. This class inherits from the `PartonicDecayerBase`, which uses the cluster model to hadronize the resulting partonic final state with a veto to ensure that there is no double counting with the exclusive modes.

## 9.5 Weak hadronic decays

There are five classes of weak mesonic decays currently included in the simulation:

1. weak exclusive semi-leptonic decays of bottom and charm mesons;
2. weak exclusive hadronic decays of bottom and charm mesons;
3. weak inclusive decays;
4. weak leptonic decay of pseudoscalar mesons;
5. weak inclusive  $b \rightarrow s\gamma$  mediated decays.

The different approaches we adopt for each of these decays are described below.

### 9.5.1 Exclusive semi-leptonic decays

The matrix element for exclusive semi-leptonic decays of heavy mesons,  $X \rightarrow Y\ell\nu$ , can be written as

$$\mathcal{M} = \frac{G_F}{\sqrt{2}} \langle X | (V - A)_\mu | Y \rangle \bar{u}(p_\nu) \gamma^\mu (1 - \gamma_5) u(p_\ell),$$

where  $p_\ell$  is the momentum of the outgoing charged lepton,  $p_\nu$  is the momentum of the neutrino and  $G_F$  is the Fermi constant. The hadronic current  $\langle X | (V - A)_\mu | Y \rangle$  can be written as a general Lorentz structure, for a particular type of decay, with a number of unknown form factors.

We have implemented a number of form-factor models based on experimental fits, QCD sum rule calculations and quark models. The form factors for the weak decay of pseudoscalar mesons are implemented using the general Lorentz-invariant form. In each case the momentum of the decaying particle,  $X$ , is  $p_X$  while the momentum of the decay product,  $Y$ , is  $p_Y$ . In general the form factors are functions of the momentum transfer  $q^2$  where  $q = p_X - p_Y$ . The masses of the decaying particle and hadronic decay product are  $m_X$  and  $m_Y$  respectively.

The scalar-scalar transition matrix element is defined by

$$\langle Y(p_Y) | (V - A)_\mu | X(p_X) \rangle = (p_X + p_Y)_\mu f_+(q^2) + \left\{ \frac{m_X^2 - m_Y^2}{q^2} \right\} q_\mu \left[ f_0(q^2) - f_+(q^2) \right],$$

where  $f_+(q^2)$  and  $f_0(q^2)$  are the form factors for the transition. In general the terms proportional to  $q_\mu$  give rise to contributions proportional to the lepton mass for semi-leptonic decays and therefore only contribute to the production of tau leptons.

The scalar-vector transition matrix element is defined to be

$$\begin{aligned} \langle Y(p_Y) | (V - A)_\mu | X(p_X) \rangle = & -i\epsilon_\mu^*(m_X + m_Y) A_1(q^2) + i(p_X + p_Y)_\mu \epsilon^* \cdot q \frac{A_2(q^2)}{m_X + m_Y} \\ & + iq_\mu \epsilon^* \cdot q \frac{2m_Y}{q^2} (A_3(q^2) - A_0(q^2)) + \epsilon_{\mu\nu\rho\sigma} \epsilon^{*\nu} p_X^\rho p_Y^\sigma \frac{2V(q^2)}{m_X + m_Y}, \end{aligned}$$

where the form factor  $A_3(q^2)$  can be defined in terms of  $A_1$  and  $A_2$  using

$$A_3(q^2) = \frac{m_X + m_Y}{2m_Y} A_1(q^2) - \frac{m_X - m_Y}{2m_Y} A_2(q^2)$$

and  $A_0(0) = A_3(0)$ . The independent form factors are  $A_0(q^2)$ ,  $A_1(q^2)$ ,  $A_2(q^2)$  and  $V(q^2)$ .

The transition matrix element for the scalar-tensor transition is

$$\begin{aligned} \langle Y(p_Y) | (V - A)_\mu | X(p_X) \rangle &= i h(q^2) \epsilon_{\mu\nu\lambda\rho} \epsilon^{*\nu\alpha} p_{Y\alpha} (p_X + p_Y)^\lambda (p_X - p_Y)^\rho - k(q^2) \epsilon_{\mu\nu}^* p_Y^\nu \\ &\quad - b_+(q^2) \epsilon_{\alpha\beta}^* p_X^\alpha p_X^\beta (p_X + p_Y)_\mu - b_-(q^2) \epsilon_{\alpha\beta}^* p_X^\alpha p_X^\beta (p_X - p_Y)_\mu, \end{aligned}$$

where  $h(q^2)$ ,  $k(q^2)$ ,  $b_-(q^2)$  and  $b_+(q^2)$  are the Lorentz invariant form factors.

The combination of the form factors and the leptonic current is handled by the `SemiLeptonicScalarDecayer` class, which combines the form factor and the current to calculate the matrix element and uses the methods available in the `DecayIntegrator` class, from which it inherits, to generate the momenta of the decay products.

In addition to the form factors for the standard weak current we include the form factors needed for weak radiative decays where available, although these are not currently used in the simulation.

The various form factors that are implemented in Herwig are described below. They all inherit from the `ScalarFormFactor` class and implement the relevant virtual member functions for the calculation of the form factors.

- `BallZwickyScalarFormFactor` This is the implementation of the QCD sum rule calculation of the form factors of Ref. [356] for the decay of a  $B$ -meson to a light pseudoscalar meson.
- `BallZwickyVectorFormFactor` This is the implementation of the QCD sum rule calculation of the form factors of Ref. [357] for the decay of a  $B$ -meson to a light vector meson.
- `HQETFormFactor` This implements the form factors for the transitions between mesons containing bottom and charm quarks in the heavy quark limit. The parameterization of Ref. [358] for the finite-mass corrections is used together with the experimental results of Refs. [359, 360].
- `ISGWFormFactor` The ISGW form factor model [361] is one of the original quark models for the form factors and is included in the simulation mainly for comparison with the later, ISGW2 [362], update of this model. This set of form factors has the advantage that it includes form factors for most of the transitions required in the simulation. The form factors are taken from Ref. [361] together with the form factors that are suppressed by the lepton mass from Refs. [363, 364].
- `ISGW2FormFactor` The ISGW2 form factors [362] are an update of the original ISGW form factors [361]. As with the original model they are based on a quark model and supply most of the form factors we need for the simulation.
- `KiselevBcFormFactor` This is the implementation of the form factors of Ref. [365] for the weak decays of  $B_c$  mesons. This model is used as the default model for weak  $B_c$  decays as the branching ratios for the  $B_c$  meson used in the simulation are calculated using the same model.
- `MelikhovFormFactor` This is the implementation of the relativistic quark model form factors of Ref. [366] for  $B \rightarrow \pi, \rho$ .
- `MelikhovStechFormFactor` This is the implementation of the model of Ref. [367], which is an update of the model of Ref. [366] including additional form factors.
- `WSBFormFactor` This is the implementation of the form factor model of Ref. [368] for the semi-leptonic form factors. It includes form factors for a number of  $D$ ,  $B$  and  $D_s$  decays. In practice the parameters of the model were taken from Ref. [369], which includes a number of transitions that were not considered in the original paper.

This form factor model is included both to give an alternative for many modes to the ISGW models and for use in the factorization approximation for hadronic charm meson decays.

We also include exclusive semi-leptonic decays of heavy baryons in the same way. The transition matrix elements are given below for the decay  $X(p_X) \rightarrow Y(p_Y)$  with  $q_\mu = (p_X - p_Y)_\mu$ , as for the mesonic case. The transition matrix for the  $\frac{1}{2} \rightarrow \frac{1}{2}$  transition is defined as

$$\begin{aligned} \langle Y(p_Y) | (V - A)_\mu | X(p_X) \rangle &= \bar{u}(p_Y) \left[ \gamma_\mu \left( F_1^V + F_1^A \gamma_5 \right) + \frac{i}{(m_X + m_Y)} \sigma_{\mu\nu} q^\nu \left( F_2^V + F_2^A \gamma_5 \right) \right. \\ &\quad \left. + \frac{1}{(m_X + m_Y)} q_\mu \left( F_3^V + F_3^A \gamma_5 \right) \right] u(p_X), \end{aligned}$$

where we have suppressed the dependence of the form factors  $F_{1,2,3}^{V,A}$  on the momentum transfer  $q^2$ .

The transition matrix element for the  $\frac{1}{2} \rightarrow \frac{3}{2}$  transition is

$$\langle Y(p_Y) | (V - A)_\mu | X(p_X) \rangle = \bar{u}^\alpha(p_Y) \left[ g_{\alpha\mu} \left( G_1^V + G_1^A \gamma_5 \right) + \frac{1}{(m_X + m_Y)} p_{X\alpha} \gamma_\mu \left( G_2^V + G_2^A \gamma_5 \right) \right. \\ \left. + \frac{1}{(m_X + m_Y)^2} p_{X\alpha} p_{Y\mu} \left( G_3^V + G_3^A \gamma_5 \right) + \frac{1}{(m_X + m_Y)^2} p_{X\alpha} q_\mu \left( G_4^V + G_4^A \gamma_5 \right) \right] \gamma_5 u(p_X),$$

where again the dependence of the form factors  $G_{1,2,3,4}^{V,A}$  on the momentum transfer  $q^2$  has been suppressed. These definitions differ from those in the literature because we have divided some terms by the sum of the baryon masses to ensure that the form factors are all dimensionless.

We have implemented a number of different models for the baryon form factors, mainly based on quark model calculations. All the form factor classes inherit from the `BaryonFormFactor` class and implement the calculation of the form factors in the specific model. The `SemiLeptonicBaryonDecayer` class handles the combination of the form factor and the leptonic current to calculate the partial width and decay kinematics.

The models we have implemented are:

- `BaryonSimpleFormFactor` This is a simple form factor model for the semi-leptonic decay of the light baryons. The form factors are assumed to be constant and are taken from the quark model results of [370].
- `BaryonThreeQuarkModelFormFactor` This model is the implementation of the relativistic three-quark model calculation of [283] for the form factors of baryons containing a heavy quark.

As the only formulae in the paper that are in a form that can be implemented in the simulation are for the heavy-to-heavy, *i.e.* bottom to charm, decays, these are the only modes included, although the paper also includes charm decays and bottom decays to light quarks. The form factors are calculated by numerically computing the integrals from [283] to obtain the coefficients for an expansion of the form factors in  $\omega$ .

- `ChengHeavyBaryonFormFactor` This is a quark model calculation [288, 371] of form factors for bottom and charm baryons. It is used for some bottom and charm baryon semi-leptonic decays. However it is mainly intended to implement the factorization approximation results of [288] for non-leptonic decays.
- `CzyzNucleonFormFactor` This is the implementation of the model of Ref. [372] and is intended to describe the  $p\bar{p}$  and  $n\bar{n}$  cross section in low energy  $e^+e^-$  collisions.
- `KornerKurodaFormFactor` This is a simple model of the baryon form factors based on Ref. [373] which we use to simulate the production of baryon-antibaryon pairs in low-energy  $e^+e^-$  collisions.
- `LambdabExcitedLambdacSumRuleFormFactor` This is the QCD sum rule based calculation of [287] for the form factors for the decay of the  $\Lambda_b^0$  to excited  $\Lambda_c^+$  states. This is used for the semi-leptonic decay of the  $\Lambda_b^0$  to excited  $\Lambda_c^+$  states to model the part of the total semi-leptonic branching ratio of the  $\Lambda_b^0$  not accounted for by the production of the  $\Lambda_c^+$ .
- `LightBaryonQuarkModelFormFactor` This is a relativistic quark model calculation [374] of the form factors for the decay of baryons containing light quarks.
- `SingletonFormFactor` This model is a quark model calculation [375] of the form factors of spin- $\frac{1}{2}$  baryons containing a bottom or charm quark.

## 9.5.2 Exclusive hadronic decays

We include three types of simulations for exclusive weak hadronic decays:

1. using the naïve factorization approximation;
2. using isobar models for three-body Dalitz decays of bottom and charm mesons;
3. various theoretical models of weak baryon decay.

### 9.5.2.1 Naïve factorization

We include two types of simulation of exclusive weak meson decays. The first is based on the naïve factorization approximation. If we consider, for example, the decay of a charm meson, the effective Lagrangian for the interaction can be written as [369]

$$\mathcal{L}_{\text{eff}} = \frac{G_F}{\sqrt{2}} V_{ud} V_{sc} [a_1 (\bar{u} \gamma_\mu P_L d) (\bar{s} \gamma_\mu P_L c) + a_2 (\bar{s} \gamma_\mu P_L d) (\bar{u} \gamma_\mu P_L c)],$$

where  $G_F$  is the Fermi constant,  $V_{ud}$  and  $V_{sc}$  are the relevant CKM matrix elements and  $a_{1,2}$  are scale-dependent coefficients. The remainder of the expression involves the currents for the quark fields. When we consider the transition between mesonic states the matrix element can be written in terms of the form factors for the  $c \rightarrow s$  or  $c \rightarrow u$  transitions, and weak currents for  $(\bar{u}\gamma_\mu P_L d)$  or  $(\bar{s}\gamma_\mu P_L d)$ .

This allows us to simulate weak hadronic decays using the form factors we have already implemented for semi-leptonic meson decays together with the weak currents from tau decays. The combination of the form factor classes, which inherit from `ScalarFormFactor`, and weak currents, which inherit from `WeakCurrent`, is handled by the `ScalarMesonFactorizedDecayer` class for the simulation of hadronic weak meson decays in the factorization approximation. Similarly the combination of weak form factors inheriting from the `BaryonFormFactor` class and weak currents is handled by the `BaryonFactorizedDecayer` class for the simulation of hadronic weak baryon decays in the factorization approximation.

### 9.5.2.2 Isobar models for Dalitz decays

Prior to the release of Herwig 7.3 we included a small number of classes for the simulation of  $D \rightarrow K\pi\pi$  Dalitz decays based on various experimental fits. In Herwig 7.3 these simulation of these decays has been restructured so that we have a base class `DalitzBase` which handles the specification of the possible intermediate channels via Interfaces and the `ScalarTo3ScalarDalitz` which implements the Lorentz structures required to calculate the matrix element. This structure is designed so that further three body decays can use the same base classes, such as the `VectorTo3PseudoScalarDalitz` class which implements the Dalitz decays of vector mesons.

There are a large number of decay models implemented for specific decay modes.

For the  $D^+$  meson the following decays and models are available:

- $D^+ \rightarrow K^-\pi^+\pi^-$  the models of Ref. [376] as `DpKmPipPipCLEO` isobar model (Herwig default) and the model independent partial-wave analysis (MIPWA) as `DpKmPipPipCLEOMIPWA`, Ref. [377] as `DpKmPipPipE691`, Ref. [378] both the MIPWA as `DpKmPipPipE791MIPWA` and isobar model as `DpKmPipPipE791Isobar`, Ref. [379] both the isobar model as `DpKmPipPipFOCUSIsobar` and K-matrix analysis as `DpKmPipPipFOCUSKMatrix`, Ref. [380] as `DpKmPipPipFOCUSMIPWA` and Ref. [381] as `DpKmPipPipMarkIII`;
- $D^+ \rightarrow \bar{K}^0\pi^+\pi^0$  the models of Ref. [381] as `DpKbar0PipPi0MarkIII` and Ref. [382] as `DpKbar0PipPi0BES` (Herwig default);
- $D^+ \rightarrow \pi^+\pi^+\pi^-$  the model of Ref. [383] as `DpPipPipPimE791`;
- $D^+ \rightarrow K^+\bar{K}^0\pi^0$  the model of Ref. [384] as `DpKpKbar0Pi0BES`;
- $D^+ \rightarrow K^+K^-\pi^+$  the model of Ref. [385] as `DpKpKmPipCLEO`;
- $D^+ \rightarrow K^+K^+K^-$  the model of Ref. [386] as `DpKpKpKmLHCb`;
- $D^+ \rightarrow K^+\pi^+\pi^-$  the model of Ref. [387] as `DpKpPipPimFOCUS`.

For the  $D^0$  meson the following decays and models are available:

- $D^0 \rightarrow K^-\pi^+\pi^0$  the models of Ref. [388] as `D0KmPipPi0CLEO` (Herwig default), Ref. [377] as `D0KmPipPi0E691` and Ref. [381] as `D0KmPipPi0MarkIII`;
- $D^0 \rightarrow \bar{K}^0\pi^+\pi^-$  the models of Ref. [389] as `D0Kl0PipPimCLEO` and `D0Ks0PipPimCLEO`, Ref. [377] as `D0Kbar0PipPimE691`, Ref. [381] as `D0Kbar0PipPimMarkIII`, Ref. [390] as `D0Ks0PipPimCLEO2` and Ref. [391] as `D0Ks0PipPimBFactory`;
- $D^0 \rightarrow \bar{K}^0\pi^0\pi^0$  the model of Ref. [392] as `D0Ks0Pi0Pi0CLEO`;
- $D^0 \rightarrow \pi^+\pi^-\pi^0$  the models of Ref. [393] as `D0PipPimPi0CLEO`, Ref. [394] as `D0PipPimPi0BABAR` and Ref. [395] as `D0PipPimPi0BABAR2`;
- $D^0 \rightarrow K_{S,L}^0\pi^+K^-$  the models of Ref. [396] as `D0Ks0PipKmCLEO` and `D0Ks0PimKpCLEO` and Ref. [397] as `D0Ks0PipKmLHCb` and `D0Ks0PimKpLHCb`;
- $D^0 \rightarrow K^+K^-\pi^0$  the model of Ref. [398] as `D0KpKmPi0BABAR`;
- $D^0 \rightarrow K_{S,L}^0K^+K^-$  the model of Ref. [399] as `D0Ks0KpKmBABAR`;
- $D^0 \rightarrow K_{S,L}^0\pi^0\eta$  the model of Ref. [400] as `D0Ks0Pi0EtaCLEO`;
- $D^0 \rightarrow K^-\pi^+\eta$  the model of Ref. [401] as `D0KmPipEtaBELLE`.

For the  $D_s^+$  meson the following decays and models are available:

- $D_s^+ \rightarrow K^+ K^- \pi^+$  the models of Ref. [402] as `DsKpKmPipBABAR`, Ref. [403] as `DsKpKmPipCLEO` and Ref. [404] as `DsKpKmPipBES`;
- $D_s^+ \rightarrow \pi^+ \pi^- \pi^+$  the models of Ref. [405] as `DsPipPipPimE791`, Ref. [406] as `DsPipPipPimBES`, Ref. [407] as `DsPipPipPimBABAR` and Ref. [408] as `DsPipPipPimFOCUS`;
- $D_s^+ \rightarrow \pi^+ \pi^0 \pi^0$  the model of Ref. [409] as `DsPipPi0Pi0BES`;
- $D_s^+ \rightarrow K^+ \pi^+ \pi^-$  the models of Ref. [410] as `DsKpPipPimBES` and Ref. [387] as `DsKpPipPimFOCUS`;
- $D_s^+ \rightarrow K^0 \pi^+ \pi^0$  the model of Ref. [411] as `DsPipPi0K0BES`;
- $D_s^+ \rightarrow K_{S,L}^0 K_{S,L}^0 \pi^+$  the model of Ref. [412] as `DsKL0KL0PipBES` and `DsKS0KS0PipBES`;
- $D_s^+ \rightarrow K_{S,L}^0 K^+ \pi^0$  the model of Ref. [413] as `DsKS0KpPi0BES` and `DsKL0KpPi0BES`;
- $D_s^+ \rightarrow \pi^+ \pi^0 \eta$  the model of Ref. [414] as `DsPipPi0EtaBES`;
- $D_s^+ \rightarrow \pi^+ \pi^0 \eta'$  the model of Ref. [415] of `DsPipPi0EtaPBES`.

### 9.5.2.3 Weak baryonic decays

While some of the exclusive weak baryonic decays are simulated using the factorization approximation we also use a number of other models that include non-factorizable contributions. These all inherit from the `Baryon1MesonDecayerBase` class which performs the calculation of the matrix elements.

- `KornerKramerCharmDecayer` This is the implementation of the results of the spectator quark model of [282] for the non-leptonic weak decay of charm baryons, *i.e.*  $\Lambda_c^+$ ,  $\Xi_c^0$ ,  $\Xi_c^+$  and  $\Omega_c^0$ .

This model provides branching ratios and decay matrix elements for a large number of modes and is used as the default simulation for many of the hadronic decay modes of the weakly decaying charm baryons. In addition, since for many of these baryons not all the decay modes have been observed, in some cases the branching ratio calculations are used to add these modes.

- `NonLeptonicHyperonDecayer` We use the results of [416] for the matrix elements for the weak, non-leptonic, decay of a number of hyperons, *i.e.*  $\Sigma^{\pm,0}$ ,  $\Xi^{0,-}$ . The matrix element for the decay is given in terms of the invariant amplitudes

$$\mathcal{L} = \bar{u}_{B_j} \{ A + B \gamma_5 \} u_{B_i},$$

where  $B_j$  is the outgoing baryon and  $B_i$  is the incoming baryon. The default amplitudes are taken from the fit in [416].

- `NonLeptonicOmegaDecayer` We use the model of [416] for the non-leptonic weak decays of the  $\Omega^-$  to a baryon from the lightest SU(3) octet and a pseudoscalar meson. Due to problems with the size of the  $d$ -wave term in this model, and more recent measurements having given the opposite sign for the  $\alpha$  parameter, we have set this term to zero in the simulation.
- `OmegaXiStarPionDecayer` We use the model of [417] for the weak decay of the  $\Omega^-$  to the  $\Xi^*$  and a pion. This decay has a very low branching ratio and the model is mainly included to test the code involving the decay of a spin- $\frac{3}{2}$  particle to another spin- $\frac{3}{2}$  particle.

### 9.5.3 Weak inclusive decays

In addition to the exclusive weak decays of the hadrons to specific final states we include a number of models of the decay of hadrons containing a heavy, *i.e.* bottom or charm, quark, based on the partonic decay of the heavy quark. The `Herwig` cluster hadronization model is then applied to the resulting partonic final state to produce hadrons. This approach is primarily used for the bottom hadrons where there are insufficient exclusive modes to saturate the branching ratios. All of the classes implementing partonic decay models inherit from the `PartonicDecayerBase` class to use the cluster hadronization model to hadronize the partonic final state.

The `HeavyDecayer` class implements the weak decays of hadrons using either the weak  $V - A$  matrix element or flat phase-space. The `WeakPartonicDecayer` class includes additional features to simulate decays intended to increase the rate of baryon production and gluonic penguin decays and handling the polarization of decaying baryons as described in Ref. [49].

In addition, the `BtoSGammaDecayer` class for weak penguin-mediated decays, described in Section 9.5.5, and the `QuarkoniumDecayer` class for the decay of bottomonium and charmonium resonances, described in Section 9.4.7, also perform partonic decays and inherit from the `PartonicDecayerBase` class.

### 9.5.4 Leptonic decays

There are a small number of decays of pseudoscalar mesons to a charged lepton and a neutrino, *e.g.*  $\pi \rightarrow \ell\nu$  and  $D_s \rightarrow \ell\nu$ . For most of these decays the inclusion of the matrix element is superfluous as the decay products are stable. However the  $B$  and  $D_s$  mesons can decay in this way to the  $\tau$  and therefore we include the `PScalarLeptonNeutrinoDecayer` class to simulate these decays using the matrix element

$$\mathcal{M} = \frac{1}{\sqrt{2}} f_P G_F V_{CKM} m_\ell \bar{u}(p_\ell) (1 - \gamma_5) v(p_\nu),$$

where  $f_P$  is the pseudoscalar decay constant,  $G_F$  is the Fermi constant,  $V_{CKM}$  is the relevant CKM matrix element,  $m_\ell$  is the mass of the lepton,  $p_\ell$  is the momentum of the charged lepton and  $p_\nu$  is the momentum of the neutrino.

### 9.5.5 $b \rightarrow s\gamma$

There are a range of decays, both inclusive and exclusive, mediated by the  $b \rightarrow s\gamma$  transition. We currently only include modelling of the inclusive decay. These decays are simulated by using a partonic decay of the  $B$  meson to a photon and a hadronic system, composed of a quark and antiquark, which recoils against the photon. The mass spectrum of the hadronic system is calculated using a theoretical model.

The calculation of the mass spectrum is handled by a class inheriting from the `BtoSGammaHadronicMass` class. Different models of the mass spectrum can then be implemented by inheriting from this class. Currently we have only implemented two such models. The first, `BtoSGammaFlatEnergy`, is solely designed for testing and generates a mass spectrum such that the photon energy distribution is flat. The second model, `BtoSGammaKagan`, which is the default, implements the theoretical calculation of Ref. [418]. The `BtoSGammaDecayer` class then uses the calculation of the hadronic mass spectrum to simulate the partonic decay as a model of the inclusive mode. As with the Decayers described in Section 9.5.3 this inherits from the `PartonicDecayerBase` class to use the cluster model to perform the hadronization of the partonic final state.

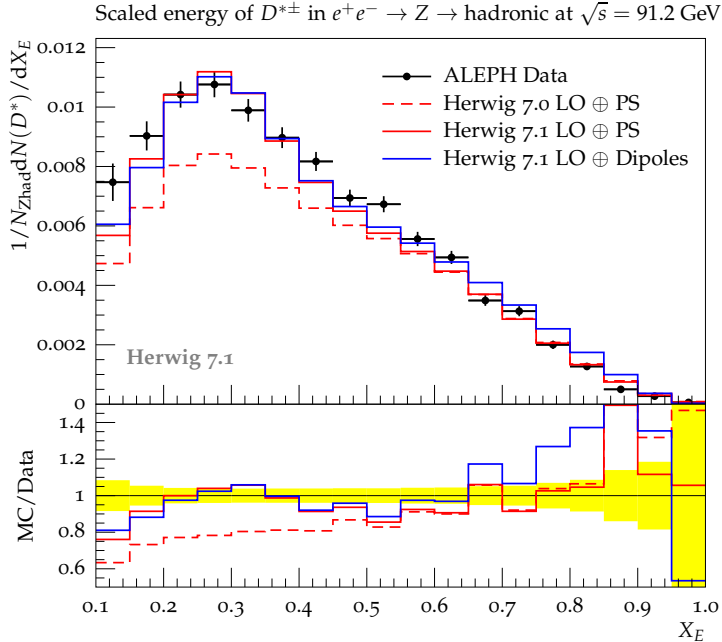


Fig. 9.2: The spectrum of  $D^*$  mesons measured by the ALEPH experiment [419] compared to Herwig. As an example, we show LO plus PS predictions, however as expected these are not significantly changed in the presence of higher order corrections. The Herwig 7.0 line corresponds to the internal decayers, while the Herwig 7.1 lines use EvtGen for bottom meson decays.

## 9.6 EvtGen interface

It has proven impossible to provide a good tune to data for the decay of bottom and charm mesons, largely due to the lack of published distributions. Given that the EvtGen package [268] has been tuned to non-public data from the B-factory experiments and internally uses similar algorithms to include spin correlations in particle decays, we include an interface to EvtGen. This communicates the spin information between the two programs, ensuring that the full correlations are generated. EvtGen is now the default for the decay of bottom and charm mesons. As there is less data for bottom and charm baryons and our modelling of baryonic form-factors is more sophisticated, the decays of heavy baryons continue to be performed by Herwig. This leads to the improvement of a number of distributions, *e.g.* the momentum distribution of  $D^*$  mesons [419], Fig. 9.2, where there is a significant contribution from  $D^*$  mesons produced in bottom meson decays.

The `EvtGenInterface` class handles the conversion between the two programs, while the `EvtGenDecayer` class is used by Herwig to perform decays using EvtGen. The `EvtGenRandom` class wraps the Herwig random number generator to ensure that the same random number stream is used by both programs.

As stated above, EvtGen is the default for the decays of bottom- and charm-mesons, while heavy-baryon decays are performed by Herwig; the interface uses `EvtGenInterface/EvtGenDecayer` and shares the random stream via `EvtGenRandom`. A frequent point of confusion concerns stability flags (*e.g.* `set pi0:Stable Stable`). With the default settings, when a  $B/D$  meson is decayed by EvtGen, the subsequent decays of its daughters are also performed by EvtGen; therefore, Herwig-level stability settings are not enforced on particles produced inside the EvtGen decay chain (so a  $\pi^0$  may still decay). If users wish EvtGen to decay only the parent heavy meson and to hand all daughters back to Herwig (so that Herwig's stability/decay settings apply), they may set:

```
set /Herwig/Decays/EvtGenDecayer:Option Parent
```

As an alternative, one can disable the use of EvtGen for heavy-meson decays entirely and revert to Herwig's internal  $B$  decays:

```
cd /Herwig/Particles
read defaults/HerwigBDecays.in
```

These options address cases such as  $\pi^0$  stability in decay chains while preserving the tuned default for heavy-meson decays when desired.

## 9.7 Code structure

The `HwDecayHandler` class, which inherits from the `DecayHandler` class of ThePEG, is responsible for handling all particle decays in Herwig. It uses the `DecaySelector` from the `ParticleData` object of the decaying particle to select a `DecayMode` object corresponding to a specific decay, according to the probabilities given by the branching ratios for the different modes. The `DecayMode` object then specifies a `Decayer` object that is responsible for generating the kinematics of the decay products for a specific decay.

All of the `Decayer` classes in Herwig inherit from the `HwDecayerBase` class, which in turn inherits from the `Decayer` class of ThePEG. In turn, with the exception of the `Hw64Decayer` and `MamboDecayer` classes, which implement general phase-space distributions for the decay products, all the `Decayer` classes in Herwig inherit from either the `DecayIntegrator` or `PartonicDecayerBase` classes.

The `DecayIntegrator` class provides a sophisticated multi-channel phase-space integrator to perform the integration over the phase-space for the decays. This means that the calculation of the matrix element and specification of the phase-space channels are all that is required to implement a new decay model. The majority of the matrix elements are calculated as helicity amplitudes, which allows the spin-propagation algorithm of Refs. [53, 102, 103, 420] to be implemented. The structure of the Herwig `Decayer` classes and the `HwDecayHandler` class is designed so that these correlations are automatically included, provided the helicity amplitudes for the matrix elements are supplied.

The `PartonicDecayerBase` class provides a structure so that the decay products of a partonic hadron decay can be hadronized using the cluster model, while at the same time ensuring that there is no overlap with the particle's exclusive decay modes. All classes implementing partonic decays in Herwig inherit from the `PartonicDecayerBase` class.

The `DalitzBase` class is designed to enable the implementation of a range of  $1 \rightarrow 3$  decay processes. The base class makes use of a number of helper classes to specify the different channels and intermediates for the decay, and how they are to be treated. The inheriting classes then calculate the matrix element for the specific type of decay. Currently there are two inheriting classes `ScalarTo3ScalarDalitz` for the decay of (pseudo)scalar mesons to three (pseudo)scalar mesons and `VectorTo3PseudoScalarDalitz` for the decay of vector mesons to three pseudoscalar mesons. The `DalitzResonance`

class specifies how the resonances in a particular channel should be handled. The `DalitzResonance` implements the standard Breit-Wigner form but can be overridden in inheriting classes. Currently we provide: `DalitzGS` implementing the form of Gounaris and Sakurai [297]; `DalitzKMatrix` allowing the use of a K-matrix inheriting from the `KMatrix` class; `DalitzLASS` for the LASS parameterization of Ref. [421] for s-wave  $K\pi$  scattering; `DalitzSigma` implementing the model of Ref. [422] for scalar resonances; `FlattéResonance` implementing the Flatté lineshape [292]; `MIPWA` to allow the implementation of MPIWA models; `PiPi2` the model of Ref. [423] for the  $I = 2$  component of  $\pi\pi$  scattering.

Certain `Decayer` classes also make use of helper classes to implement the decays. The main examples are:

- the `WeakCurrent` class provides a base class for the implementation of weak hadronic currents and is used by the `TauDecayer`, `SemiLeptonicScalarDecayer`, `SemiLeptonicBaryonDecayer`, `ScalarMesonFactorizedDecayer` and `BaryonFactorizedDecayer` classes, which implement tau decays, semi-leptonic meson and baryon decays and hadronic weak meson and baryon decays using the naïve factorization approximation, respectively;
- the `ScalarFormFactor` class provides a base class for the implementation of the scalar form factors and is used by the `SemiLeptonicScalarDecayer` and `ScalarMesonFactorizedDecayer` classes, which implement semi-leptonic meson decays and hadronic weak meson decays using the naïve factorization approximation, respectively;
- the `BaryonFormFactor` class provides a base class for the implementation of the baryon form factors and is used by the `SemiLeptonicBaryonDecayer` and `BaryonFactorizedDecayer` classes, which implement semi-leptonic baryon decays and hadronic weak baryon decays using the naïve factorization approximation, respectively;
- the `BtoSGammaHadronicMass` provides a model of the hadronic mass spectrum in inclusive  $b \rightarrow s\gamma$  decays performed by the `BtoSGammaDecayer` class.
- the `OmnesFunction` class provides as base class for the implementation of different models as of the Omnes function which are used by various decay models. There are currently two inheriting classes one implementing a version based on experimental measurements `ExperimentalOmnesFunction` and one using an analytic form `AnalyticOmnesFunction`.
- the `KMatrix` class provides a base class for the implementation of K-matrix models which are used by various decay models, primarily of three-body bottom and charm decays. Currently there are three inheriting classes `KPiIHalfFOCUSKMatrix` implementing the  $I = \frac{1}{2}$  and `KPiIThreeHalfFOCUSKMatrix` implementing the  $I = \frac{3}{2}$  model of Ref. [379] for  $K\pi$  scattering and `PiPiAnisovichKMatrix` implementing model of [424] for  $pi\pi$  scattering.

The vast majority of the decay models have a large number of parameters, all of which are accessible via the Interfaces of the classes. A more detailed description of both the physics models used in the code and their parameters can be found in the Doxygen documentation and Ref. [55].

There are a number of classes that are designed to include the off-shell weight given in Eq. ( (9.1)) in the generation of the particle decays. The `GenericWidthGenerator` class is designed to use the information on the partial widths for the different decay modes supplied by the `Decayer` classes that inherit from `DecayIntegrator`, to calculate the running width for a given particle. The `GenericMassGenerator` class then uses the running width to allow the weight given in Eq. ( (9.1)) to be included when generating the particle decays. The inheriting `ScalarMassGenerator` class implements the Flatté lineshape [292] for the  $a_0(980)$  and  $f_0(980)$  mesons.

For decays where the decay products can be off-shell, and three-body decays, integrals over either the masses of the decay products or the three-body phase-space must be performed in order to calculate the running partial widths. In order to facilitate the calculation of the partial widths a number of classes inheriting from the `WidthCalculatorBase` class are implemented to calculate the partial widths for various decays:

- the `TwoBodyAllOnCalculator` class returns the partial width for a two-body decay where both the decay products are on mass-shell;
- the `OneOffShellCalculator` class returns the partial width for a decay where one of the outgoing particles is off mass-shell;
- the `TwoOffShellCalculator` class returns the partial width for a decay where two of the outgoing particles are off mass-shell;
- the `ThreeBodyAllOnCalculator` class returns the partial width for a three-body decay where all the decay products are on mass-shell by performing the two non-trivial integrals over the phase-space variables;
- the `ThreeBodyAllOn1IntegralCalculator` class returns the partial width for a three-body decay where all the decay products are on mass-shell, by performing one integral over the phase-space variables. This requires that the second integral has already been performed analytically.

## 10 Summary

In this paper we have presented a consolidated account of the physics content, software architecture and validated performance of Herwig 7, version 7.3, the C++ successor to the Fortran-based HERWIG and the Herwig++ 2.x series. The program provides a coherent, modular framework for precision collider phenomenology in lepton-lepton, lepton-hadron and hadron-hadron environments. Hard-scattering matrix elements are automated within Matchbox, interfacing external amplitude providers at LO, NLO and for loop-induced processes, and furnishing general infrared subtraction, multi-channel phase-space sampling, dynamic scale choices and two complementary matching paradigms (POWHEG- and MC@NLO-type). Consistent multijet merging at LO and NLO is supported within the same framework, enabling inclusive-to-exclusive descriptions with controlled logarithmic structure.

Parton radiation is simulated by two shower algorithms with distinct systematics. The AO shower implements QCD coherence via angular ordering, includes heavy-quark mass effects (dead-cone suppression) and azimuthal spin correlations, and interleaves QCD, QED and EW emissions. The dipole shower is designed for local recoils, colour-coherent emissions and robust matching/merging to higher-order calculations. Perturbative accuracy is augmented by matrix-element corrections to key processes and by coordinated scale-variation and fast reweighting facilities that quantify higher-order and shower uncertainties with negligible additional event-generation cost. Multiple-soft QED effects and mixed QCD-EW radiation are handled via a Yennie–Frautschi–Suura formalism and an EW shower, providing a consistent treatment of photon and weak-boson emissions in production and decay stages.

Non-perturbative dynamics are described primarily by an advanced cluster hadronization model. Gluons are non-perturbatively split into  $q\bar{q}$  pairs, colour singlets are formed into clusters and then undergo fission and decay with spin-sensitive treatments and heavy-flavour-aware options. Several colour-reconnection schemes are available, including baryonic reconnection (default in version 7.3), which improves the description of baryon yields and high-multiplicity final states by allowing three-quark (or three-antiquark) cluster topologies. Enhanced strangeness production, consistent handling of the shower infrared cutoff, and options for alternative hadronization are provided; in particular, an interface to the Lund string model enables cross-checks against string-based fragmentation where appropriate.

The underlying event is modelled by an extended eikonal multiple-partonic-scattering framework with semi-hard and soft components and a dedicated diffraction sector, delivering realistic minimum-bias and UE phenomenology and ensuring smooth integration with colour reconnection and hadronization. A unified decay framework covers hadronic and leptonic decays, including detailed  $\tau$  decays, off-shell effects, spin correlations and hard QED/EW radiation in both SM and BSM channels. The BSM infrastructure allows import of models specified via Feynman rules (with general many-body decays and colour-sextet diquarks), while retaining consistent shower-hadronization matching and uncertainty evaluation throughout.

Herwig 7.3 thus constitutes a precision-ready event generator whose perturbative and non-perturbative components are systematically improvable and tightly integrated. In comparisons to LHC measurements across benchmark processes (vector-boson, top and multijet final states), matched/merged predictions with either shower provide competitive agreement and complementary uncertainty envelopes, reflecting the differing recoil and logarithmic-accuracy systematics of AO and dipole showers. The unified treatment of QCD, QED and EW radiation, together with modern MPI, colour reconnection and decay models, underpins reliable Standard Model predictions and broad BSM sensitivity at current and future facilities.

Technical documentation, Doxygen class references, validated examples, tutorials and FAQs are available at <https://herwig.hepforge.org>. To report issues, please contact the authors at [herwig@projects.hepforge.org](mailto:herwig@projects.hepforge.org). We rely on user feedback to refine the present release and to steer future development; we therefore encourage users to report their experience (positive or negative), provide minimal working examples illustrating issues or unexpected behaviour, and report bugs and suggest additional features or improvements. Precise, reproducible reports that isolate problems within Herwig 7 (as opposed to external tools) enable rapid diagnosis and fixes. Where appropriate, please also consult the designated references for this manual series and the primary physics papers underlying specific modules when citing Herwig in physics studies.

## Acknowledgements

This work was supported by the Science and Technology Facilities Council, formerly the Particle Physics and Astronomy Research Council, the European Union Marie Curie Training Networks MCnet (contract MRTN-CT-2006-035606), MCnetITN (contract PITN-GA-2012-315877) and MCnetITN3 (contract 722104). This work has been supported in part by the BMFTR (formerly BMBF) under grant agreements 05H21VKCCA and 05H24VKB. M.R. Masouminia is supported by the UK Science and Technology Facilities Council (grant numbers ST/T001011/1 and ST/X000745/1). A. Papaefstathiou acknowledges support by the National Science Foundation under Grant No. PHY 2210161 and the U.S. Department of Energy, Office of Science, Office of Nuclear Physics under Award Number DE-SC0025728. S. Sule would like to thank the UK Science and Technology Facilities Council (STFC) for the award of a studentship. M. H. Seymour also acknowledges STFC's support through grants ST/T001038/1 and ST/X00077X/1. The work of A. Siódtek, P. Sarmah and J. Whitehead was supported by the National Science Centre Poland grant No 2019/34/E/ST2/00457. A. Siódtek is also supported by the Priority Research Area Digiworld under the program 'Excellence Initiative – Research University' at the Jagiellonian University in Krakow and the OpenMAPP project via National Science Centre, Poland under CHISTERA programme (grant No. NCN 2022/04/Y/ST2/00186). A. Siódtek and J. Whitehead gratefully acknowledge the Polish high-performance computing infrastructure PLGrid (HPC Centre: ACK Cyfronet AGH) for providing computing facilities and support within computational grants PLG/2024/017664 and PLG/2024/017366.

Development of Herwig 7 would not have been possible without the early work of Alberto Ribon and Phil Stephens, as well as continued support provided by Leif Lönnblad and Andy Buckley. We have received technical advice and support from the HepForge project, which hosts the Herwig 7 development environment and provides a variety of related services. We acknowledge the use of computing resources provided by the Worldwide LHC Computing Grid (WLCG) and the Institute for Particle Physics Phenomenology (IPPP), Durham University, as well as at the Particle Physics Group at the University of Vienna and the HPC resources at the University of Graz. We also acknowledge the support provided by Michael Spannowsky, Jeppe Andersen and the IPPP IT management team, Adam Boulton and Paul Clark.

## Appendix A Tuning of model parameters

Herwig 7 has been tuned to a wide range of experimental data. In general we tune the majority of parameters to data from  $e^+e^-$  collisions and then those parameters which only, or predominately, affect hadronic collisions to data from hadron-hadron collisions. We have so far considered that parton shower parameters, *i.e.* the value of the strong coupling and the infrared cutoff should be considered tuning parameters. Parameters of the hadronization model are then tuned together with the parton shower parameters at LEP data, for which colour reconnection is not considered. Below we describe in detail, how different physics effects are disentangled between light and heavy quarks and other domains of the hadronization. In the future, this workflow might change also as many new observables now become available and tuning tools become more versatile. Parameters of multi-parton interactions and the colour reconnection model are then considered in comparison to hadron collider data. With the tunes we have been considering we do not consider an optimization for a specific class of processes or a specific class of observables, but we try to work as general as possible in a strive for the best overall data description of virtually all available data which we can sensibly describe.

### Appendix A.1 Tuning philosophy in detail

The original approach used to tune the angular-ordered parton shower and hadronization parameters is presented in detail in Ref. [31] and adopted in Ref. [28], where few modifications to the showering algorithm were introduced. The new strategy for tuning angular-ordered parton shower was discussed in Ref. [49].

The interested reader should consult Refs. [31], [28] and [49] for more results. The Rivet program [425, 426] was used to analyse the simulated events and compare the results with the experimental measurements. The Professor program [427] was then used to interpolate the shower response and tune the parameters by minimising the  $\chi^2$ <sup>1</sup>.

In general we use a heuristic chi-squared function

$$\chi'^2(p) = \sum_{\mathcal{O}} w_{\mathcal{O}} \sum_{b \in \mathcal{O}} \frac{(f_b(p) - \mathcal{R}_b)^2}{\Delta_b^2}$$

where  $p$  is the set of parameters being tuned,  $\mathcal{O}$  are the observables used each with weight  $w_{\mathcal{O}}$ ,  $b$  are the different bins in each observable distribution with associated experimental measurement  $\mathcal{R}_b$ , error  $\Delta_b$  and Monte Carlo prediction  $f_b(p)$ . Weighting of those observables for which a good description of the experimental result is important is used in most cases. The parameterisation of the event generator response,  $f(p)$ , is used to minimize  $\chi'^2$  and find the optimum parameter values. We take  $w_{\mathcal{O}} = 1$  in most cases except for the particle multiplicities, total charged particle multiplicities and hadron production rates where we use  $w_{\mathcal{O}} = 10$ ,  $w_{\mathcal{O}} = 50$  and  $w_{\mathcal{O}} = 100$ , respectively. This ensures that particle multiplicities influence the result of the fit and are required due to the much higher quantity of event shape and spectrum data used in the tuning. We also use  $w_{\mathcal{O}} = 10$  for data on gluon jets in order to avoid the fit being dominated by the large quantity of data sensitive to quark jets. In addition as we do not expect a Monte Carlo event generator to give a perfect description of all the data and in order to avoid the fit being dominated by a few observables with very small experimental errors we use

$$\Delta_b^{\text{eff}} = \max(0.05 \times \mathcal{R}_b, \Delta_b),$$

rather than the true experimental error,  $\Delta_b$ , in the fit.

The standard procedure which was adopted to tune the shower and hadronization parameters of the Herwig 7 parton shower and hadronization model to data is:

- first the shower and those hadronization parameters which are primarily sensitive to light quark-initiated processes are tuned to measurements of event shapes, the average charged particle multiplicity and charged particle multiplicity distribution, and identified particle spectra and rates which only involve light quark mesons and baryons;
- the hadronization parameters for bottom quarks are tuned to the bottom quark fragmentation function measured by LEP1 and SLD together with LEP1 and SLD measurements of event shapes and identified particle spectra from bottom events and measurements of the charged particle multiplicity in bottom initiated events;
- the hadronization parameters involving charm quarks are then tuned to identified particle spectra, from both the B-factories and LEP1, and LEP1 and SLD measurements of event shapes and identified particle spectra from charm events and measurements of the charged particle multiplicity in charm initiated events;
- the light quark parameters are then retuned using the new values of the bottom and charm parameters.

<sup>1</sup> While tuning the parameters sensitive to bottom quarks it proved impossible to get a reliable interpolation of the generator response with Professor and therefore a random scan of the bottom parameters was performed and the values adjusted by hand about the minimum to minimise the  $\chi'^2$ .

## Appendix A.2 Herwig 7.3 general tune

For Herwig 7.3, we utilised  $e^-e^+$  data from LEP, PETRA, SLAC, SLC, and TRISTAN, encompassing over 9,200 separate data bins [49]. The data were weighted around both light and heavy hadron production rates and multiplicities, focusing on the most dominant processes. We attempted a multi-layered, brute-force approach using the `prof2-chisq` module from Professor II [427], minimising the  $\chi^2$  as an indicator of the best tune. In this context, we analysed a total of 12 parameters, comprising 10 for cluster hadronization and 2 for the parton shower, specifically `AlphaIn` and `pTmin`. Below is a detailed breakdown of these parameters:

- `ClMaxLight`: Maximum allowable cluster mass for light quarks.
- `ClPowLight`: Power exponent for the mass of clusters with light quarks.
- `PSplitLight`: Parameter affecting the mass splitting for clusters with light quarks.
- `PwtSquark`: Probability for a  $s\bar{s}$  quark pair to be spawned during cluster splittings.
- `PwtDIquark`: Probability for quarks forming a di-quark.
- `SngWt`: Weighting factor for singlet baryons in hadronization.
- `DecWt`: Weighting factor for decuplet baryons in hadronization.
- `ProbabilityPowerFactor`: Exponential factor in the `ClusterFissioner` probability function.
- `ProbabilityShift`: Offset in the `ClusterFissioner` probability function.
- `KinematicThresholdShift`: Adjustment to the kinematic threshold in `ClusterFissioner`.
- `AlphaIn`: Initial value for the strong coupling constant at  $M_{Z^0} = 91.1876$  GeV.<sup>3</sup>
- `pTmin`: Minimum transverse momentum in the parton shower.

Following the above description and methodology, we tuned the hadronization and parton shower parameters in Herwig 7.3. The results are given in the table below [49].

Table 1.1: The values of tuned parameters in Herwig 7.3 compared to Herwig 7.2.

Tuned Parameter	Herwig-7.3.0	Herwig-7.2.0
<code>ClMaxLight</code> [GeV]	3.529	3.649
<code>ClPowLight</code>	1.849	2.780
<code>PSplitLight</code>	0.914	0.899
<code>PwtSquark</code>	0.374	0.292
<code>PwtDIquark</code>	0.331	0.298
<code>SngWt</code>	0.891	0.740
<code>DecWt</code>	0.416	0.620
<code>ProbabilityPowerFactor</code>	6.486	–
<code>ProbabilityShift</code>	-0.879	–
<code>KinematicThresholdShift</code> [GeV]	0.088	–
<code>AlphaIn</code>	0.102	0.126
<code>pTmin</code> [GeV]	0.655	0.958

Despite its computational intensity, our brute-force approach can be considered a reasonable success, achieving a substantial improvement in the overall  $\chi^2$  values. Specifically, the tuned version of Herwig 7.3 shows a  $\sim 50.75\%$  improvement in  $\chi^2$  compared to its untuned counterpart and a  $\sim 12.76\%$  improvement when compared to Herwig-7.2.3. In the following section, we will examine the effects of this new tune on the production rates of heavy mesons and baryons.

Here we discuss the tuning of the parton shower and hadronization parameters, we then go on and consider the tuning of the intrinsic  $p_\perp$  and parameters of the multiple parton and soft scattering models, together with the colour reconnection model. In this section we focus on the tuning of the angular ordered shower. While older tunings are available for the

<sup>3</sup> The reader should note that after the Herwig-7.3 release, the `AlphaIn` has been split into two separate parameters, `AlphaQCD:AlphaIn` and `AlphaQCD:AlphaIn`, that control the strong coupling constants for initial- and final-state radiations respectively. The tuned value we suggest here points to `AlphaQCD:AlphaIn`, as it is the one relevant to our  $e^+e^-$  tuning strategy.

dipole shower, including some using the autotunes framework [428], a general tune for the dipole shower will be in preparation once all next-to-leading logarithmic improvements following [429] are available.

### Appendix A.3 Angular-Ordered parton shower

In order to tune the shower and light quark hadronization parameters we used data on jet rates and event shapes for centre-of-mass energies between 14 and 44 GeV [430–432], at LEP1 and SLD [432–436] and LEP2 [432, 435, 436], particle multiplicities [433, 434] and spectra [433, 434, 437–447] at LEP 1, identified particle spectra below the  $\Upsilon(4S)$  from Babar [448], the charged particle multiplicity [449, 450] and particle spectra [449, 451, 452] in light quark events at LEP1 and SLD, the charged particle multiplicity in light quark events at LEP2 [453, 454], the charged particle multiplicity distribution at LEP 1 [455], and hadron multiplicities at the Z-pole [456]. We also implemented in Rivet and made use of the data on the properties of gluon jets [457, 458] for the first time.

### Appendix A.4 AO recoil-scheme tunes

The hadronization parameters for charm quarks were tuned using the charged particle multiplicity in charm events at SLD [450] and LEP2 [453, 454], the light hadron spectra in charm events at LEP1 and SLD [449, 451, 452], the multiplicities of charm hadrons at the Z-pole [433, 456], and charm hadron spectra below the  $\Upsilon(4S)$  [459, 460] and at LEP1 [419].

The hadronization parameters for bottom quarks were tuned using the charged particle multiplicity in bottom events at SLD [450] and LEP2 [453, 454], the light hadron spectra in bottom events at LEP1 and SLD [449, 451, 452], the multiplicities of charm and bottom hadrons at the Z-pole [433, 456], charm hadron spectra at LEP1 [419] and the bottom fragmentation function measured at LEP1 and SLD [461–463].

In order to tune the evolution of the total charged particle multiplicity in  $e^+e^-$  collisions as a function of energy the results of Refs. [433, 436, 450, 453, 454, 464–470] spanning energies from 12 to 209 GeV were used.

The following parameters were tuned:

1. the value of  $\alpha_s$  at the  $Z^0$  mass, ;
2. the cut-off scale of the transverse momentum in the parton shower;
3. the maximum mass above which clusters containing light quarks undergo cluster fission, see Eq. (7.1);
4. the exponent controlling whether clusters containing light quarks undergo fission, see Eq. (7.1);
5. the exponent controlling the masses of the daughter clusters for light quark clusters that undergo fission, see Eq. (7.2);
6. the weight for producing a strange quark-antiquark pair in the hadronization;
7. the weight for producing a diquark-antidiquark pair in the hadronization;
8. the maximum mass above which clusters containing charm quarks undergo cluster fission, see Eq. (7.1);
9. the exponent controlling whether clusters containing charm quarks undergo fission, see Eq. (7.1);
10. the exponent controlling the masses of the daughter clusters for charm quark clusters that undergo fission, see Eq. (7.2);
11. the parameter, which controls the smearing of the direction of hadrons containing perturbatively produced charm quarks, see Eq. (7.3);
12. the parameter, which controls the splitting of charm clusters to a single hadron above the threshold for producing two hadrons, see Eq. (7.4);
13. the maximum mass above which clusters containing bottom quarks undergo cluster fission, see Eq. (7.1);
14. the exponent controlling whether clusters containing bottom quarks undergo fission, see Eq. (7.1);
15. the exponent controlling the masses of the daughter clusters for bottom quark clusters that undergo fission, see Eq. (7.2);
16. the parameter, which controls the smearing of the direction of hadrons containing perturbatively produced bottom quarks, see Eq. (7.3);
17. the parameter, which controls the splitting of bottom clusters to a single hadron above the threshold for producing two hadrons, see Eq. (7.4);

For the angular-ordered parton shower tunes were performed using two choices for the reconstruction of the kinematics in the parton shower. Either the  $p_\perp$  of the emissions was calculated using the cut-off values of the masses of the daughters (called  $p_\perp$  preserving), or their virtuality (called  $q^2$  preserving), as described in Section 4.2.1.

The values of the parameters obtained from the tuning are given in Table 1.2, while the values of  $\chi^2$  are given in Table 1.3. By default we used the tune in which  $q_i \cdot q_j$  is preserved and the veto is applied.

Table 1.2: The parameters obtained for different choices of the the preserved quantity in the angular-ordered parton shower. For the dot product preserving scheme we present the results obtained both with and without the veto described in Section 4.2.3.1.

Preserved	$p_\perp$	$q^2$	$q_i \cdot q_j$ (no veto)	$q_i \cdot q_j$ (veto)
Shower and Light quark hadronization parameters				
<code>AlphaIn</code> ( $\alpha_S^{\text{CMW}}(M_Z)$ )	0.1074	0.1244	0.1136	0.1186
<code>pTmin</code>	0.900	1.136	0.924	0.958
<code>ClMaxLight</code>	4.204	3.141	3.653	3.649
<code>ClPowLight</code>	3.000	1.353	2.000	2.780
<code>PSplitLight</code>	0.914	0.831	0.935	0.899
<code>PwtSquark</code>	0.647	0.737	0.650	0.700
<code>PwtDIquark</code>	0.236	0.383	0.386	0.298
Charm quark hadronization parameters				
<code>ClMaxCharm</code>	4.204	3.564	3.796	3.950
<code>ClPowCharm</code>	3.000	2.089	2.235	2.559
<code>PSplitCharm</code>	1.060	0.928	0.990	0.994
<code>ClSmrCharm</code>	0.098	0.141	0.139	0.163
<code>SingleHadronLimitCharm</code>	0.000	0.011	0.000	0.000
Bottom quark hadronization parameters				
<code>ClMaxBottom</code>	5.757	2.900	6.000	3.757
<code>ClPowBottom</code>	0.672	0.518	0.680	0.537
<code>PSplitBottom</code>	0.557	0.365	0.550	0.625
<code>ClSmrBottom</code>	0.117	0.070	0.105	0.078
<code>SingleHadronLimitBottom</code>	0.000	0.000	0.000	0.000

Table 1.3: The values of  $\chi^2$  per degree of freedom obtained in the fit for different choices of the preserved quantity in the angular-ordered parton shower. The values are  $\chi'^2$  as described in the text for the tuning observables, normalised to the sum of the weights for the different bins. The number of degrees of freedom for each set of observables is given. The  $\chi^2$  corresponding to ATLAS jets, particle multi-plicities (mult), event shapes (event), identified-particle spectra (ident), quark jets (jet), gluon jets (gluon) and charged particle distributions (charged) are also shown.

Preserved	$p_\perp$	$q^2$	$q_i \cdot q_j$ (no veto)	$q_i \cdot q_j$ (veto)	Number of dof
$\chi^2/ndf$ considering several sets of observables					
Light jets	4.4	3.2	3.7	3.4	17746
Charm quarks	2.3	1.7	1.8	1.9	909
Bottom quarks	6.0	6.5	5.1	4.1	1745
ATLAS jets	0.16	0.41	0.19	0.54	22
$\chi^2/ndf$ considering sub-samples of the “Light jets” set					
mult	3.0	2.8	2.8	2.8	6780
event	7.0	3.5	5.2	3.9	2689
ident	10.7	10.0	9.8	10.1	953
jet	4.6	3.2	4.1	3.6	3459
gluon	1.1	1.2	1.2	1.2	1880
charged	5.4	2.5	3.7	2.9	1850

A similar philosophy was adopted to tune the parameters of the dipole shower, and the hadronization model when used in conjunction with the dipole shower. As there were no significant changes for the dipole parton shower between Herwig 7.0 and Herwig 7.1 a slightly older procedure, our default at the time Herwig 7.0 was released, which only used data from the  $Z^0$  pole and continuum near the  $\Upsilon(4S)$  resonance was used.

## Appendix A.5 Dipole shower

A simple tune of the dipole shower, only adjusting some shower cutoffs and leaving the hadronization parameters at their defaults. The values for intrinsic  $p_T$  were adjusted separately for valence and sea quarks as

$$\text{ValenceIntrinsicPtScale} = 1.26905 \text{ GeV}, \quad (\text{A.1})$$

$$\text{SeaIntrinsicPtScale} = 1.1613 \text{ GeV}. \quad (\text{A.2})$$

The infrared cutoff scales for the shower are set to  $\text{IRCutoff} = 1.014259 \text{ GeV}$  for **FFLightKinematics** and **FFMassiveKinematics**, while for all other dipoles it is set to  $1.0 \text{ GeV}$ . These values are provided as defaults for the dipole shower in the input files.

A more elaborate tune with the tool **Autotunes** [428] has been obtained and is also provided as an extra snippet with our release. Here, also hadronization parameters have been adjusted.

Table 1.4: The values of tuned parameters for the dipole shower, obtained with **Autotunes**

Tuned Parameter	Value
All input values for $\alpha_s$	0.118
<b>g:ConstituentMass</b> [GeV]	0.95
<b>b:NominalMass</b> [GeV]	4.700501
<b>b:ConstituentMass</b> [GeV]	4.084889
<b>C1SmrBottom</b>	0.085964
<b>C1SmrLight</b>	0.698877
<b>C1SmrCharm</b>	0.246296
<b>C1PowBottom</b>	0.591646
<b>C1PowLight</b>	0.99945
<b>C1PowCharm</b>	3.386187
<b>C1MaxBottom</b> [GeV]	3.771649
<b>C1MaxBottom</b> [GeV]	3.771649
<b>C1MaxCharm</b> [GeV]	4.780456
<b>C1MaxLight</b> [GeV]	3.055256
<b>PSplitLight</b>	0.7779
<b>PSplitCharm</b>	0.628766
<b>PSplitBottom</b>	0.662911
<b>SingleHadronLimitBottom</b>	0.000446
<b>SingleHadronLimitCharm</b>	0.000508
<b>SngWt</b>	0.927141
<b>DecWt</b>	0.630787

Furthermore, for all Kernels, the CMW scheme has to be switched on.

## Appendix A.6 Underlying Event, Colour Reconnection and MPI tunes

The tuning procedure of the parameters of Underlying Event (UE) and Colour Reconnection (CR) models was evolving with the evolution of the models. However, one thing has remained unchanged, this is the assumption that the tuning of Underlying Event and Colour Reconnection factorizes from the tuning of the hadronization model, i.e. it does not affect significantly the LEP observables. This assumption, for example, was explicitly checked when the first tunes of CR models were created in [61]. Therefore, the UE and CR models were always tuned only to the data from hadron-hadron collisions. More specifically, modern tunes involve the adjustment of the underlying event (UE) model parameters in HERWIG using Minimum Bias and Underlying Event data collected at the LHC and Tevatron, spanning various center-of-mass energies,  $\sqrt{s} = 0.9, 1.8, 7, 13 \text{ TeV}$ . For each energy, a separate tune was initially obtained; these are then combined to produce a single, energy-extrapolated tune. Currently, we employ the extrapolation formula given in Eq. (8.21) to perform a simultaneous fit across multiple energies, as discussed, for example, in [247, 260].

## Appendix B Solution of the Sudakov equation

There are a range of methods which can be used to solve Eq. (4.7),

$$\Delta(\kappa, \kappa_h) = \mathcal{R},$$

which is repeated here for clarity.

In the FORTRAN HERWIG program this equation was solved by a brute force numerical calculation, using an interpolation table for  $\Delta(\kappa, \kappa_h)$ . In Herwig 7 alternative approaches are used in the angular-ordered and dipole shower both based on the veto algorithm [471] which is described in detail in Ref. [129] Appendix A.3. This algorithm determines the scale of the branchings without the need for any explicit integration of the Sudakov form factor.

In the angular-ordered shower the veto algorithm is implemented using simple functional forms to overestimate the kernels while in the dipole shower the ExSample library [78] is used to adaptively compute overestimates of the splitting kernels and to sample the distribution given by the Sudakov form factor. Here we only discuss the procedure used in the angular-ordered shower in detail below.

This procedure is repeated to give a value of the evolution scale for each possible type of branching, and the branching with the largest value of evolution scale is selected, the ‘competition’ or ‘winner-takes-all’ algorithm. This correctly generates both the type of branching, the evolution scale and any auxiliary variables needed to describe the branching.

### Appendix B.1 Angular-Ordered shower

The implementation of the veto algorithm used in the angular-ordered parton shower involves generating each branching according to a crude Sudakov form factor, based on an *overestimated* branching probability (Eq. (4.22)), simple enough that Eq. (4.38) can be solved analytically. Each of these crudely determined branchings is subject to a vetoing procedure based on a series of weights relating to the true form factor. In this way the overestimated, crude emission rate and emission distribution is reduced to the exact distribution.

The first ingredient we need in order to implement the algorithm is therefore a crude approximation to the Sudakov form factor (Eq. (4.25)), for each type of branching of a parent parton  $\tilde{i}\tilde{j}$ ,  $\tilde{i}\tilde{j} \rightarrow i + j$ . We write these as

$$\Delta_{\tilde{i}\tilde{j} \rightarrow ij}^{\text{over}}(\tilde{q}, \tilde{q}_h) = \exp \left\{ - \int_{\tilde{q}}^{\tilde{q}_h} d\mathcal{P}_{\tilde{i}\tilde{j} \rightarrow ij}^{\text{over,res.}} \right\},$$

where

$$d\mathcal{P}_{\tilde{i}\tilde{j} \rightarrow ij}^{\text{over,res.}} = \frac{d\tilde{q}^2}{\tilde{q}^2} \int_{z_{-}^{\text{over}}}^{z_{+}^{\text{over}}} dz \frac{\alpha_s^{\text{over}}}{2\pi} P_{\tilde{i}\tilde{j} \rightarrow ij}^{\text{over}}(z),$$

is the overestimated probability that a resolvable branching occurs in the interval  $[\tilde{q}^2, \tilde{q}^2 + d\tilde{q}^2]$ . Overestimates of the splitting functions and the coupling constant are denoted  $P_{\tilde{i}\tilde{j} \rightarrow ij}^{\text{over}}(z) \geq P_{\tilde{i}\tilde{j} \rightarrow ij}(z, \tilde{q})$  and  $\alpha_s^{\text{over}} \geq \alpha_s(z, \tilde{q})$ , while the limits  $z_{\pm}^{\text{over}}$  also denote overestimates of the true  $z$  integration region<sup>1</sup> for all  $\tilde{q}$ . To solve Eq. (4.38) analytically we also require that  $P_{\tilde{i}\tilde{j} \rightarrow ij}^{\text{over}}(z)$  should be analytically integrable and, in order to generate  $z$  values, this integral should be an invertible function of  $z$ .

Using this simplified Sudakov form factor we may analytically solve  $\Delta_{\tilde{i}\tilde{j} \rightarrow ij}^{\text{over}}(\tilde{q}, \tilde{q}_h) = \mathcal{R}$  for  $\tilde{q}$  as

$$\tilde{q}^2 = \tilde{q}_h^2 \mathcal{R}^{\frac{1}{r}}, \quad (\text{B.1})$$

where

$$r = \frac{d\mathcal{P}_{\tilde{i}\tilde{j} \rightarrow ij}^{\text{over,res.}}}{d \ln \tilde{q}^2},$$

which can be thought of as the number of emissions per unit of the shower formation ‘time’  $\ln \tilde{q}^2$  (for the crude distribution this is a constant). It is clear from Eq. (B.1) how increasing this rate  $r$  causes the first branching to be generated ‘sooner’.

<sup>1</sup> The overestimates of these limits were given in Eqs. (4.29), (4.31).

closer to  $\tilde{q}_h$ . When a value is generated for the evolution scale of a branching, an associated  $z$  value is then generated according to

$$z = I^{-1} [I(z_-^{\text{over}}) + \mathcal{R}' (I(z_+^{\text{over}}) - I(z_-^{\text{over}}))],$$

where  $I(z)$  is the primitive integral of  $P_{\tilde{i}j \rightarrow ij}^{\text{over}}(z)$  over  $z$ ,  $I^{-1}$  is the inverse of  $I$  and  $\mathcal{R}'$  is a uniformly distributed random number in the interval  $[0, 1]$ .

We now reject these values of  $\tilde{q}$  and  $z$  if:

- the value of  $z$  lies outside the true phase-space limits, *i.e.* if  $\mathbf{p}_\perp^2 < 0$ ;
- $\frac{\alpha_s(z, \tilde{q})}{\alpha_s^{\text{over}}} < \mathcal{R}_1$ ;
- $\frac{P_{\tilde{i}j \rightarrow ij}(z, \tilde{q})}{P_{\tilde{i}j \rightarrow ij}^{\text{over}}(z)} < \mathcal{R}_2$ ,

where  $\mathcal{R}_{1,2}$  are random numbers uniformly distributed between 0 and 1.

If we reject the value of  $\tilde{q}$  we repeat the whole procedure with  $\tilde{q}_h = \tilde{q}$  until either we accept a value of  $\tilde{q}$ , or the value drops below the minimum value allowed due to the phase-space cutoffs, in which case there is no radiation from the particle. As shown in Ref. [471] this procedure, called the veto algorithm, exponentiates the rejection factors and generates the values of  $\tilde{q}$  and  $z$  according to Eq. (4.38) for one type of branching.

The backward evolution can be performed using the veto algorithm in the same way as the forward evolution. We need to solve

$$\Delta(x, \tilde{q}, \tilde{q}_h) = \mathcal{R},$$

to give the scale of the branching. We start by considering the backward evolution of  $i$  via a particular type of branching,  $\tilde{i}j \rightarrow i + j$ . We can obtain an overestimate of the integrand in the Sudakov form factor

$$\Delta_{\tilde{i}j \rightarrow ij}^{\text{over}}(x, \tilde{q}, \tilde{q}_h) = \exp \left\{ - \int_{\tilde{q}}^{\tilde{q}_h} \frac{d\tilde{q}'^2}{\tilde{q}'^2} \int_x^{z_+^{\text{over}}} dz \frac{\alpha_s^{\text{over}}}{2\pi} P_{\tilde{i}j \rightarrow ij}^{\text{over}}(z) \text{PDF}^{\text{over}}(z) \right\}, \quad (\text{B.2})$$

where  $P_{\tilde{i}j \rightarrow ij}^{\text{over}}(z)$ ,  $\alpha_s^{\text{over}}$  and the overestimate of the limits must have the same properties as for final-state branching. In addition

$$\text{PDF}^{\text{over}}(z) \geq \frac{\frac{x}{z} f_{\tilde{i}j} \left( \frac{x}{z}, \tilde{q} \right)}{x f_i(x, \tilde{q})} \forall z, \tilde{q}, x.$$

In this case the product  $P_{\tilde{i}j \rightarrow ij}^{\text{over}}(z) \text{PDF}^{\text{over}}(z)$  must be integrable and the integral invertible. If we define

$$r = \frac{\alpha_s^{\text{over}}}{2\pi} \int_x^{z_+^{\text{over}}} dz P_{\tilde{i}j \rightarrow ij}^{\text{over}}(z) \text{PDF}^{\text{over}}(z),$$

then we can solve Eq. (4.41) using this overestimated Sudakov giving

$$\tilde{q}^2 = \tilde{q}_h^2 \mathcal{R}^{\frac{1}{r}}. \quad (\text{B.3})$$

The value of  $z$  can then be generated according to

$$z = I^{-1} [I(x) + \mathcal{R}' (I(z_+^{\text{over}}) - I(x))],$$

where  $I(z) = \int dz P_{\tilde{i}j \rightarrow ij}^{\text{over}}(z) \text{PDF}^{\text{over}}(z)$ ,  $I^{-1}$  is the inverse of  $I$  and  $\mathcal{R}'$  is a random number uniformly distributed between 0 and 1.

We now reject these values of  $\tilde{q}$  and  $z$  if:

- the value of  $z$  lies outside the true phase-space limits, *i.e.* if  $\mathbf{p}_\perp^2 < 0$ ;
- $\frac{\alpha_s(z, \tilde{q})}{\alpha_s^{\text{over}}} < \mathcal{R}_1$ ;
- $\frac{P_{\tilde{i}j \rightarrow ij}(z, \tilde{q})}{P_{\tilde{i}j \rightarrow ij}^{\text{over}}(z)} < \mathcal{R}_2$ ;

$$- \frac{\frac{x}{z} f_a \left( \frac{x}{z}, \tilde{q}' \right)}{\frac{x}{z} f_b \left( x, q' \right)} < \mathcal{R}_3;$$

where  $\mathcal{R}_{1,2,3}$  are random numbers uniformly distributed between 0 and 1.

As with the final-state branching algorithm, if a set of values of  $\tilde{q}$  and  $z$ , generated according to the approximate form factor in Eq. (B.2) is rejected, a further set is then generated by repeating the process with  $\tilde{q}_h = \tilde{q}$  in Eq. (B.2). This procedure is repeated until either a generated set of branching variables passes all four vetoes, or the generated value of  $\tilde{q}$  falls below the minimum allowed value, in which case the showering of the particle in question ceases. To determine the species of partons involved, a trial value of  $\tilde{q}$  is generated for each possible type of branching and the largest selected. By applying the four vetoing criteria to each emission generated by the approximate, overestimated, Sudakov form factor, the accepted values of  $\tilde{q}$  and  $z$  are distributed according to the exact Sudakov form factor, Eq. (4.41) [471].

## Appendix C Treatment of the running coupling

The running coupling constant enters every dynamical aspect of the parton shower, so a thorough treatment of it is mandatory for all parton shower simulations. In general we work in an axial, or light-cone, gauge to derive the splitting functions.

Axial gauges have many special properties, most notable of these is that they are ghost-free. Another related interesting feature of the light-cone gauge is that, similar to QED where the Ward identities guarantee the equality of the electron field and vertex renormalization constants, in light-cone gauge QCD the Ward identities reveal that the 3-gluon vertex renormalization constant  $Z_{A^3}$ , is equal to that of the transverse components gluon field  $Z_A^{1/2}$  [472]. This simplifies the usual relation between the bare coupling  $g_S^{(0)}$  and renormalized coupling constant  $g_S$  from  $g_S^{(0)} = Z_{A^3} Z_A^{-3/2} g_S$ , to  $g_S^{(0)} = Z_A^{-1/2} g_S$ , *i.e.* in the light-cone gauge, the running of the QCD coupling constant is due to the gluon self-energy corrections alone. Thus, dimensionally regulated, one-loop calculations of the gluon self-energy in this gauge possess an ultraviolet divergence proportional to the usual QCD beta function [472, 473].

In calculating higher order corrections to the splitting functions, we must consider self-energy corrections to the emitted gluons and their associated counter-terms. The self-energy corrections are equal to zero because the gluons are on-shell and so the associated loop integrals have no scale, which means they vanish in dimensional regularization. This vanishing is due to a complete cancellation of the ultraviolet and infrared parts of the integrals. Therefore including the counter-terms cancels explicitly the ultraviolet divergent parts of the loop integrals leaving behind infrared divergent parts, which must have the same pole structure as the ultraviolet parts *i.e.* they must also be proportional to the beta function. The residual virtual infrared divergence is cancelled by the associated real emission corrections, in this case the two graphs where the emitted gluon splits either to two on-shell gluons or to a quark-antiquark pair. This cancellation of infrared poles generates an associated logarithm of the phase-space boundary divided by  $\mu$  (the renormalization scale) [120, 474] multiplied by the same coefficient as the pole (the beta function). The phase-space boundary is equal to the maximum possible virtuality of the daughter gluon, whose branchings comprise the real emission corrections. For a time-like splitting,  $\tilde{i}\tilde{j} \rightarrow i + j$  where  $\tilde{i}\tilde{j}$  is a quark,  $i$  is a daughter quark and  $j$  is the daughter gluon, to which we consider real and virtual corrections, a quick calculation in the Sudakov basis Eq. (4.8) shows that the gluon virtuality  $q_j^2$  must satisfy the relation

$$q_j^2 \leq (1 - z) q_{i\tilde{j}}^2, \quad (C.1)$$

where  $1 - z$  is the light-cone momentum carried by the emitted gluon, and  $q_{i\tilde{j}}^2$  is the virtuality of the emitting quark. The net effect of these real and virtual corrections is therefore to simply correct the leading order  $q \rightarrow qg$  splitting function by a multiplicative factor

$$1 - \beta_0 \alpha_s(\mu^2) \ln \left( (1 - z) q_{i\tilde{j}}^2 / \mu^2 \right) + \mathcal{O}(\alpha_s)$$

where the omitted  $\mathcal{O}(\alpha_s)$  terms are non-logarithmic, non-kinematic, constant terms,  $\beta_0$  is the QCD beta function, and  $\mu^2$  is the renormalization scale.

Two important points follow directly from this analysis. Firstly, for soft configurations,  $z \rightarrow 1$ , the effect of these loop contributions can produce large, numerically significant, logarithms. Secondly, plainly, by choosing the renormalization scale to be  $(1 - z) q_{i\tilde{j}}^2$ , instead of the more obvious  $q_{i\tilde{j}}^2$ , the corrections vanish, or rather, more correctly, they are absorbed in the coupling constant.

For  $g \rightarrow gg$  splittings the same arguments hold but in this case it is apparent that as well as large logarithms of  $1 - z$ , large logarithms of  $z$  are also possible from soft emission in the  $z \rightarrow 0$  region. We may simultaneously include both

types of correction by using  $z(1-z)q_{ij}^2$ , *i.e.* the transverse momentum of the branching, as the argument of the running coupling, as

$$z(1-z)q_{ij}^2 = z^2(1-z)^2\tilde{q}_{ij \rightarrow i,j}^2 = p_T^2.$$

From the point of view of the leading-log approximation, the choice of scale is technically a higher order consideration, nevertheless, these effects turn out to be highly phenomenologically significant, particularly their effect on multiplicity distributions and cluster mass spectra [224, 474].

Thus, by default, the strong coupling is evaluated at  $z^2(1-z)^2\tilde{q}^2$ . The user has the possibility to selectively change the argument from the default to  $z(1-z)\tilde{q}^2$ , that corresponds to the virtuality  $q^2$ , from certain splitting processes only using the `ScaleChoice` interface.

## Appendix C.1 The Monte Carlo scheme for $\alpha_s$

By choosing the scale of the running coupling as advocated for above we have

$$\lim_{z \rightarrow 1} \alpha_s \left( (1-z)q_{ij}^2 \right) P_{q \rightarrow qg}^{[1]}(z) = \alpha_s \frac{2C_F}{1-z} (1 - \alpha_s \beta_0 \ln(1-z)) + \mathcal{O}(\alpha_s^3), \quad (\text{C.2})$$

where we have momentarily abbreviated  $\alpha_s \left( q_{ij}^2 \right)$  by  $\alpha_s$ , and we have used a superscript [1] to denote that  $P_{q \rightarrow qg}^{[1]}$  is the *one-loop* (*i.e.* leading order)  $q \rightarrow qg$  splitting function. This is almost, but not exactly equal to the soft  $z \rightarrow 1$  singular limit of the *two-loop*  $q \rightarrow qg$  splitting function  $P_{q \rightarrow qg}^{[2]}$  with  $\alpha_s$  evaluated at  $q_{ij}^2$ ,

$$\lim_{z \rightarrow 1} \alpha_s \left( q_{ij}^2 \right) P_{q \rightarrow qg}^{[2]}(z) = \alpha_s \frac{2C_F}{1-z} \left( 1 - \alpha_s \beta_0 \ln(1-z) + \frac{\alpha_s}{2\pi} K_g \right) + \mathcal{O}(\alpha_s^3) \quad (\text{C.3})$$

where<sup>1</sup>

$$K_g = C_A \left( \frac{67}{18} - \frac{\pi^2}{6} \right) - T_R n_f \frac{10}{9}. \quad (\text{C.4})$$

On integrating over the phase-space of the two-loop splitting function the  $K_g$  term gives rise to terms proportional to  $\alpha_s^2 \ln^2 q_{ij}^2$ , *i.e.* it gives next-to-leading log soft-collinear contributions to the Sudakov exponent of the form  $\alpha_s^n \ln^n q_{ij}^2$  (as opposed to leading-log contributions that are instead proportional to  $\alpha_s^n \ln^{n+1} q_{ij}^2$ ). In a similar way to that in which the higher order  $\beta_0 \alpha_s \ln(1-z)$  term was included, we may exploit the fact that the  $z \rightarrow 1$  dependence of the  $K_g$  term in  $P_{q \rightarrow qg}^{[2]}(z)$  is equal to that of  $P_{q \rightarrow qg}^{[1]}(z)$ , to incorporate it in the running coupling as well.

This is done by replacing the usual  $\Lambda_{\overline{\text{MS}}}$  QCD scale, from which the coupling runs, to  $\Lambda_{\text{CMW}}$  [133]:

$$\Lambda_{\text{CMW}} = \Lambda_{\overline{\text{MS}}} \exp(K_g / 4\pi \beta_0),$$

where CMW denotes the so-called Catani-Marchesini-Webber (CMW) [133] or *Monte Carlo scheme*. Expanding  $\alpha_s P_{q \rightarrow qg}^{[1]}(z)$  again, as in Eq. (C.2), but with  $\alpha_s$  evaluated at  $(1-z)q_{ij}^2$  in the CMW scheme, reproduces exactly the two-loop result in Eq. (C.3). With this prescription the Sudakov form factor generally includes all leading and next-to-leading log contributions, except for those due to soft wide angle gluon emissions, however, for the case that the underlying hard process comprises of a single colour dipole, these are also included (see Section 4.2.2 and [105, 134]).

<sup>1</sup> In fact the constants  $K_g$  are given by the finite remainder of the real emission phase-space corrections due to the daughter gluon splitting discussed in Appendix C (see *e.g.* Eqs. (5.28, C.12, C.13) of [72]).

## Appendix C.2 Options for the treatment of $\alpha_s$ in the angular-ordered parton shower

Although we have made strong physical arguments restricting the argument of the coupling constant and suggesting a more physical renormalization scheme, there is still some degree of freedom in how precisely  $\alpha_s$  is calculated. In what follows below we enumerate the options associated with these in the program:

- The `InputOption` switch selects the way in which initial conditions for running the coupling constant are determined.
  - The default setting, `AlphaIn`, uses our tuned value of  $\alpha_s$  at the  $Z^0$  resonance to calculate a value of  $\Lambda_{\text{QCD}}$  from which the running coupling constant is evaluated. This input can be reset from the default value<sup>2</sup> of 0.1186 using the `AlphaIn` interface.
  - Alternatively one may select an option `LambdaQCD`, which uses the input or default value of  $\Lambda_{\text{QCD}}$  to calculate the coupling. The value may be set using the `LambdaQCD` interface.
- The `LambdaOption` flag determines whether the value of  $\Lambda_{\text{QCD}}$ , which can be calculated from  $\alpha_s(m_{Z^0})$  using the `AlphaIn` interface or inputted directly via the `LambdaQCD` interface, is already given in the CMW (Monte Carlo) scheme of Ref. [133] (option `Same`, this is the default behaviour), described in Appendix C.1, or it is in the  $\overline{\text{MS}}$  scheme and thus needs to be converted (option `Convert`).
- The `NumberOfLoops` parameter specifies the loop order of the beta function used to calculate the running of  $\alpha_s$ . The default setting uses the two-loop beta function.
- The `ThresholdOption` option selects whether to use the `Current` or `Constituent` quark masses in determining the flavour thresholds in the evolution of the coupling constant. The default is to use the  $(\overline{\text{MS}})$  current quark masses.
- The `Qmin` parameter specifies the value of  $Q_{\text{min}}$ , the scale beneath which non-perturbative effects are considered to render the usual renormalization group running with a beta function determined at some finite loop order invalid. Below this scale, which is currently tuned to 0.935 GeV, a number of parameterizations of the scaling of the coupling with energy may be selected according to the `NPAlphaS` option described below.
- The `NPAlphaS` option selects a parameterization of the scaling of the running coupling with energy in what we regard as the non-perturbative region, where the scale at which it is to be evaluated falls below the value set by `Qmin`. By setting `(NPAlphaS=Zero)` the coupling is simply taken to be zero for scales  $Q < Q_{\text{min}}$ . For the `(NPAlphaS=Const)` coupling *freezes out* at `Qmin`, *i.e.* it assumes the constant value  $\tilde{\alpha}_S = \alpha_s(Q_{\text{min}})$  for all scales below `Qmin`. This is the default parameterization. It is the same prescription used in early works on resummation by Curci and Greco [475, 476]. The options `(NPAlphaS=Linear)` and `(NPAlphaS=Quadratic)` calculate the running coupling below `Qmin` according to  $\tilde{\alpha}_S Q/Q_{\text{min}}$  and  $\tilde{\alpha}_S (Q/Q_{\text{min}})^2$  respectively. Setting `(NPAlphaS=Exx1)` assumes a quadratically decreasing running of the coupling in the non-perturbative region from the value `AlphaMaxNP` down to  $\tilde{\alpha}_S$ . Finally, `(NPAlphaS=Exx2)` sets  $\alpha_s$  equal to `AlphaMaxNP` for all input scales  $Q < Q_{\text{min}}$ , which amounts to a minor variation of the default *freeze-out* option.

## Appendix C.3 Options for the treatment of $\alpha_s$ in the dipole parton shower

The dipole parton shower, as well as the Matchbox module, in `Herwig` makes use of distinct implementations of the strong coupling constant. One and two loop running are implemented in `lo_alpha_s` and `nlo_alpha_s`, respectively.

- To set the input value and scale for the dipole shower  $\alpha_s$  classes the `input_alpha_s` and `input_scale` are to be used.
- It is possible to set the allowed number of active flavours with the `min_active_flavours` and `max_active_flavours` parameters, that effects the running as well as the threshold matching.
- The threshold matching is performed at the beginning of each run using `gsl` bisection to fix the running at the nominal quark masses.
- Both the LO and NLO implementations treat the number of active flavours as constant below a given input scale, the `freezing_scale` parameter.
- The NP behaviour in the dipole shower is screened by a so called screening scale. The `ScreeningScale` is an interface of each splitting kernel. It corresponds to the `(NPAlphaS=Const)` treatment in the angular-ordered parton shower.
- The running at LO is performed with

$$\alpha_s(q) = \frac{1}{\beta_0 L} \quad \text{with} \quad \beta_0 = \frac{33 - 2n_F}{12\pi} \quad \text{and} \quad L = \log \left( \frac{q^2}{\Lambda^2(n_F(q^2))} \right), \quad (\text{C.5})$$

<sup>2</sup> The default value is tuned to  $e^+e^-$  annihilation data as described in Appendix A and is typical of the values one gets when fitting leading order QCD predictions to data.

while the two loop running makes use of

$$\alpha_s(q) = \frac{1}{\beta_0 L} \left( 1 - \frac{\beta_1 \log(L)}{\beta_0^2 L} + LQT \right) \quad \text{with} \quad \beta_1 = \frac{153 - 19n_F}{24\pi^2},$$

where additional terms in the large  $Q$  expansion LQT

$$LQT = \frac{\beta_1^2}{\beta_0^4 L^2} \left( \left( \log(L) - \frac{1}{2} \right)^2 - \frac{5}{4} \right),$$

can be added using the `two_lageq_terms` interface. This is an approximation to the renormalization group running but the exact running can be requested and calculated with the `exact_evaluation` switch.

- The modifications needed for the Monte Carlo scheme are part of the Dipole Kernels options, called `CMWScheme`.

## Appendix D Massless dipoles

This appendix contains the results for massless dipoles which are omitted from the main text. See Section 4.3.3.3 for more details.

### Appendix D.1 Final-Final dipole kinematics

We require that the momenta prior to the splitting can be written in terms of the momenta following the splitting

$$\begin{aligned} \tilde{p}_k &= \frac{1}{1 - y_{ij,k}} q_k, \\ \tilde{p}_{ij} &= q_i + q_j - \frac{y_{ij,k}}{1 - y_{ij,k}} q_k. \end{aligned} \tag{D.1}$$

With this requirement, the physical momenta following the splitting can be written in terms of the splitting variables

$$\begin{aligned} q_i &= z_i \tilde{p}_{ij} + (1 - z_i) y_{ij,k} \tilde{p}_k + k_\perp, \\ q_j &= (1 - z_i) \tilde{p}_{ij} + z_i y_{ij,k} \tilde{p}_k - k_\perp, \\ q_k &= (1 - y_{ij,k}) \tilde{p}_k. \end{aligned} \tag{D.2}$$

As we have a massless spectator,  $z_i$  is identical to  $z$ . We can write  $y_{ij,k}$  in terms of  $z$  and  $p_\perp$

$$y_{ij,k} = \frac{p_\perp^2}{z(1-z)Q^2}.$$

and the limits on the splitting variables  $z_i$  and  $y_{ij,k}$  are simply

$$\begin{aligned} z_{i,-} &= 0, & z_{i,+} &= 1, \\ y_- &= 0, & y_+ &= 1. \end{aligned}$$

Working in a frame where  $Q = 0$ , the kinematic upper limit on the transverse momentum,  $p_{\perp,\max}$ , is simply the magnitude of the emission 3-momentum in the limit that the spectator following the splitting has zero momentum. The momentum conservation requirement in Eq. (4.81) can then be rearranged to give

$$p_{\perp,\max}^2 = \frac{s}{4}.$$

The limits on  $z$  follow from the limit  $y_{ij,k} < 1$ ,

$$z_\pm = \frac{1}{2} \left[ 1 \pm \sqrt{1 - \frac{p_\perp^2}{p_{\perp,\max}^2}} \right].$$

## Appendix D.2 Final-Initial dipole kinematics

Following the massless Sudakov parametrization, the physical momenta following the splitting are written as,

$$\begin{aligned} q_i &= z\tilde{p}_{ij} + \frac{p_{\perp}^2}{s_{ij,b}z}\tilde{p}_b + k_{\perp} , \\ q_j &= (1-z)\tilde{p}_{ij} + \frac{p_{\perp}^2}{s_{ij,b}(1-z)}\tilde{p}_b - k_{\perp} , \\ q_b &= \frac{1}{x_{ij,b}}\tilde{p}_b . \end{aligned}$$

As in the massive case we have  $z_i = z$ . We can simply insert the equations above into (4.94) to obtain an explicit expression for  $x_{ij,b}$  in terms of  $z$  and  $p_{\perp}$ ,

$$x_{ij,b} = \left[ 1 + \frac{p_{\perp}^2}{s_{ij,b}z(1-z)} \right]^{-1} .$$

The phase-space limits on the splitting variables  $z_i$  and  $x_{ij,b}$  are,

$$\begin{aligned} z_{i,-} &= 0 , & z_{i,+} &= 1 , \\ x_{-} &= x_s , & x_{+} &= 1 . \end{aligned}$$

Following from the result in (4.97) one can obtain the following limits on the generated variables,

$$\begin{aligned} p_{\perp,\max}^2 &= \frac{s_{ij,b}}{4} \left( \frac{1-x_s}{x_s} \right) , \\ z_{\pm} &= \frac{1}{2} \left[ 1 - \sqrt{1 - \frac{p_{\perp}^2}{p_{\perp,\max}^2}} \right] . \end{aligned}$$

## Appendix D.3 Initial-Final dipole kinematics

The physical momenta following the splitting can be written in terms of the splitting variables as,

$$\begin{aligned} q_a &= \frac{1}{x_{jk,a}}\tilde{p}_{aj} , \\ q_j &= \left( \frac{1-x_{jk,a}}{x_{jk,a}} \right) (1-u_j)\tilde{p}_{aj} + u_j\tilde{p}_k - k_{\perp} , \\ q_k &= \left( \frac{1-x_{jk,a}}{x_{jk,a}} \right) u_j\tilde{p}_{aj} + (1-u_j)\tilde{p}_k + k_{\perp} , \end{aligned}$$

and the splitting variables can be written in terms of the generated variables  $z$  and  $p_{\perp}$  as,

$$\begin{aligned} x_{jk,a} &= \frac{1-z+r}{2r} \left[ 1 - \sqrt{1 - \frac{4rz(1-z)}{(1-z+r)^2}} \right] , \\ u_j &= x_{jk,a} \left( \frac{r}{1-z} \right) , \end{aligned}$$

where we have defined  $r = \frac{p_{\perp}^2}{s_{aj,k}}$ .

The limits on the splitting variables  $u_j$  and  $x_{jk,a}$  are then simply,

$$\begin{aligned} u_{-} &= 0 , & u_{+} &= 1 , \\ x_{-} &= x_e , & x_{+} &= 1 . \end{aligned}$$

Following from the inequality in (4.101) we obtain the limits on the generated variables  $z$  and  $p_{\perp}$ ,

$$\begin{aligned} p_{\perp,\max}^2 &= \frac{s_{aj,k}}{4} \left( \frac{1-x_e}{x_e} \right) , \\ z_{\pm} &= \frac{1}{2} \left[ (1+x_e) \pm (1-x_e) \sqrt{1 - \frac{p_{\perp}^2}{p_{\perp,\max}^2}} \right] . \end{aligned}$$

#### Appendix D.4 Final-Final dipole kernels

$$\begin{aligned}\langle V_{q_i g_j, k} (z_i, y_{ij, k}) \rangle &= 8\pi\alpha_S C_F \left[ \frac{2}{1 - z_i(1 - y_{ij, k})} - (1 + z_i) \right] \\ \langle V_{q_i \bar{q}_j, k} (z_i, y_{ij, k}) \rangle &= 8\pi\alpha_S T_R [1 - 2z_i(1 - z_i)] \\ \langle V_{g_i g_j, k} (z_i, y_{ij, k}) \rangle &= 16\pi\alpha_S C_A \left[ \frac{1}{1 - z_i(1 - y_{ij, k})} + \frac{1}{1 - (1 - z_i)(1 - y_{ij, k})} - 2 + z_i(1 - z_i) \right]\end{aligned}$$

#### Appendix D.5 Final-Initial dipole kernels

$$\begin{aligned}\langle V_{q_i g_j}^b (z_i, x_{ij, b}) \rangle &= 8\pi\alpha_S C_F \left[ \frac{2}{1 - z_i + (1 - x_{ij, b})} - (1 + z_i) \right] \\ \langle V_{q_i \bar{q}_j}^b (z_i, x_{ij, b}) \rangle &= 8\pi\alpha_S T_R [1 - 2z_i(1 - z_i)] \\ \langle V_{g_i g_j}^b (z_i, x_{ij, b}) \rangle &= 16\pi\alpha_S C_A \left[ \frac{1}{1 - z_i + (1 - x_{ij, b})} + \frac{1}{z_i + (1 - x_{ij, b})} - 2 + z_i(1 - z_i) \right]\end{aligned}$$

#### Appendix D.6 Initial-Final dipole kernels

$$\begin{aligned}\langle V_k^{g_a g_j} (u_j, x_{jk, a}) \rangle &= 8\pi\alpha_S C_F \left[ \frac{2}{1 - x_{jk, a} + u_j} - (1 + x_{jk, a}) \right] \\ \langle V_k^{g_a \bar{q}_j} (u_j, x_{jk, a}) \rangle &= 8\pi\alpha_S T_R [1 - 2x_{jk, a}(1 - x_{jk, a})] \\ \langle V_k^{g_a q_j} (u_j, x_{jk, a}) \rangle &= 8\pi\alpha_S C_F \left[ x_{jk, a} + \frac{2(1 - x_{jk, a})}{x_{jk, a}} \right] \\ \langle V_k^{g_a g_j} (u_j, x_{jk, a}) \rangle &= 16\pi\alpha_S C_A \left[ \frac{1}{1 - x_{jk, a} + u_j} + \frac{1 - x_{jk, a}}{x_{jk, a}} - 1 + x_{jk, a}(1 - x_{jk, a}) \right]\end{aligned}$$

## References

1. G. Marchesini and B.R. Webber, *Simulation of QCD Jets including Soft Gluon Interference*, *Nucl. Phys.* **B238** (1984) 1.
2. B.R. Webber, *A QCD Model for Jet Fragmentation including Soft Gluon Interference*, *Nucl. Phys.* **B238** (1984) 492.
3. G. Marchesini and B.R. Webber, *Monte Carlo Simulation of General Hard Processes with Coherent QCD radiation*, *Nucl. Phys.* **B310** (1988) 461.
4. HERWIG collaboration, *HERWIG 6: An event generator for Hadron Emission Reactions With Interfering Gluons (including supersymmetric processes)*, *JHEP* **01** (2001) 010 [[hep-ph/0011363](#)].
5. HERWIG collaboration, *HERWIG 6.5 release note*, [hep-ph/0210213](#).
6. HERWIG collaboration, *Herwig++ Physics and Manual*, *Eur. Phys. J.* **C58** (2008) 639 [[0803.0883](#)].
7. HERWIG collaboration, *Herwig++ 1.0: An Event Generator for  $e^+e^-$  Annihilation*, *JHEP* **02** (2004) 005 [[hep-ph/0311208](#)].
8. HERWIG collaboration, *Herwig++ 2.0 $\beta$  release note*, [hep-ph/0602069](#).
9. HERWIG collaboration, *Herwig++ 2.0 Release Note*, [hep-ph/0609306](#).
10. HERWIG collaboration, *Herwig++ 2.1 Release Note*, [0711.3137](#).
11. HERWIG collaboration, *Herwig++ 2.2 Release Note*, [0804.3053](#).
12. HERWIG collaboration, *Herwig++ 2.3 Release Note*, [0812.0529](#).
13. HERWIG collaboration, *Herwig++ 2.5 Release Note*, [1102.1672](#).
14. HERWIG collaboration, *Herwig++ 2.6 Release Note*, [1205.4902](#).
15. HERWIG collaboration, *Herwig++ 2.7 Release Note*, [1310.6877](#).
16. HERWIG collaboration, *Herwig 7.0/Herwig++ 3.0 release note*, *Eur. Phys. J.* **C76** (2016) 196 [[1512.01178](#)].
17. HERWIG collaboration, *Herwig 7.1 Release Note*, [1705.06919](#).
18. HERWIG collaboration, *Herwig 7.2 release note*, *Eur. Phys. J. C* **80** (2020) 452 [[1912.06509](#)].
19. HERWIG collaboration, *Herwig 7.3 release note*, *Eur. Phys. J. C* **84** (2024) 1053 [[2312.05175](#)].
20. T. Sjöstrand, S. Mrenna and P. Skands, *A Brief Introduction to PYTHIA 8.1*, *Comput. Phys. Commun.* **178** (2008) 852 [[0710.3820](#)].
21. C. Bierlich et al., *A comprehensive guide to the physics and usage of PYTHIA 8.3*, *SciPost Phys. Codeb.* **2022** (2022) 8 [[2203.11601](#)].
22. T. Gleisberg et al., *SHERPA 1 $\alpha$ : A Proof-of-Concept Version*, *JHEP* **02** (2004) 056 [[hep-ph/0311263](#)].
23. SHERPA collaboration, *Event generation with Sherpa 3*, *JHEP* **12** (2024) 156 [[2410.22148](#)].
24. L. Lönnblad, *ThePEG, PYTHIA7, Herwig++ and ARIADNE*, *Nucl. Instrum. Meth.* **A559** (2006) 246.
25. S. Gieseke, P. Stephens and B. Webber, *New Formalism for QCD Parton Showers*, *JHEP* **12** (2003) 045 [[hep-ph/0310083](#)].
26. S. Plätzer and S. Gieseke, *Coherent Parton Showers with Local Recoils*, *JHEP* **01** (2011) 024 [[0909.5593](#)].
27. S. Plätzer and S. Gieseke, *Dipole Showers and Automated NLO Matching in Herwig++*, *Eur. Phys. J.* **C72** (2012) 2187 [[1109.6256](#)].
28. G. Bewick, S. Ferrario Ravasio, P. Richardson and M.H. Seymour, *Logarithmic accuracy of angular-ordered parton showers*, *JHEP* **04** (2020) 019 [[1904.11866](#)].
29. G. Bewick, S. Ferrario Ravasio, P. Richardson and M.H. Seymour, *Initial state radiation in the Herwig 7 angular-ordered parton shower*, *JHEP* **01** (2022) 026 [[2107.04051](#)].
30. A.H. Hoang, S. Plätzer and D. Samitz, *On the Cutoff Dependence of the Quark Mass Parameter in Angular Ordered Parton Showers*, *JHEP* **10** (2018) 200 [[1807.06617](#)].
31. D. Reichelt, P. Richardson and A. Siódtek, *Improving the Simulation of Quark and Gluon Jets with Herwig 7*, *Eur. Phys. J. C* **77** (2017) 876 [[1708.01491](#)].
32. K. Cormier, S. Plätzer, C. Reuschle, P. Richardson et al., *Parton showers and matching uncertainties in top quark pair production with Herwig 7*, *Eur. Phys. J. C* **79** (2019) 915 [[1810.06493](#)].
33. P. Richardson and S. Webster, *Spin Correlations in Parton Shower Simulations*, *Eur. Phys. J. C* **80** (2020) 83 [[1807.01955](#)].
34. J. Bellm, G. Nail, S. Plätzer, P. Schichtel et al., *Parton Shower Uncertainties with Herwig 7: Benchmarks at Leading Order*, *Eur. Phys. J. C* **76** (2016) 665 [[1605.01338](#)].
35. J. Bellm, S. Plätzer, P. Richardson, A. Siódtek et al., *Reweighting Parton Showers*, *Phys. Rev.* **D94** (2016) 034028 [[1605.08256](#)].
36. G. Marchesini and B.R. Webber, *Simulation of QCD Coherence in Heavy Quark Production and Decay*, *Nucl. Phys.* **B330** (1990) 261.
37. A.H. Hoang, O.L. Jin, S. Plätzer and D. Samitz, *Matching hadronization and perturbative evolution: the cluster model in light of infrared shower cutoff dependence*, *JHEP* **07** (2025) 005 [[2404.09856](#)].
38. M.R. Masouminia and P. Richardson, *Implementation of angularly ordered electroweak parton shower in Herwig 7*, *JHEP* **04** (2022) 112 [[2108.10817](#)].
39. S. Gieseke, T. Kasprzak and J.H. Kühn, *Vector-boson pair production and electroweak corrections in HERWIG++*, *Eur. Phys. J.* **C74** (2014) 2988 [[1401.3964](#)].
40. S. Plätzer, *Controlling inclusive cross sections in parton shower + matrix element merging*, *JHEP* **08** (2013) 114 [[1211.5467](#)].
41. J. Bellm, S. Gieseke and S. Plätzer, *Merging NLO Multi-jet Calculations with Improved Unitarization*, *Eur. Phys. J. C* **78** (2018) 244 [[1705.06700](#)].
42. S. Jadach, G. Nail, W. Placzek, S. Sapeta et al., *Monte Carlo simulations of Higgs-boson production at the LHC with the KrkNLO method*, *Eur. Phys. J.* **C77** (2017) 164 [[1607.06799](#)].
43. P. Sarmah, A. Siódtek and J. Whitehead, *KrkNLO matching for colour-singlet processes*, *JHEP* **01** (2025) 062 [[2409.16417](#)].
44. S. Plätzer and M. Sjödahl, *Subleading  $N_c$  improved Parton Showers*, *JHEP* **07** (2012) 042 [[1201.0260](#)].
45. S. Plätzer, M. Sjödahl and J. Thorén, *Color matrix element corrections for parton showers*, *JHEP* **11** (2018) 009 [[1808.00332](#)].
46. S. Gieseke, P. Kirchgässner and S. Plätzer, *Baryon production from cluster hadronisation*, *Eur. Phys. J. C* **78** (2018) 99 [[1710.10906](#)].
47. C.B. Duncan and P. Kirchgässner, *Kinematic strangeness production in cluster hadronization*, *Eur. Phys. J. C* **79** (2019) 61 [[1811.10336](#)].
48. S. Gieseke, P. Kirchgässner, S. Plätzer and A. Siódtek, *Colour Reconnection from Soft Gluon Evolution*, *JHEP* **11** (2018) 149 [[1808.06770](#)].
49. M.R. Masouminia and P. Richardson, *Hadronization and decay of excited heavy hadrons in Herwig 7*, *JHEP* **07** (2024) 278 [[2312.02757](#)].
50. P. Richardson and D. Winn, *Simulation of Sextet Diquark Production*, *Eur. Phys. J. C* **72** (2012) 1862 [[1108.6154](#)].
51. K. Hamilton and P. Richardson, *Simulation of QED radiation in particle decays using the YFS formalism*, *JHEP* **07** (2006) 010 [[hep-ph/0603034](#)].
52. K. Hamilton and P. Richardson, *A Simulation of QCD Radiation in Top Quark Decays*, *JHEP* **02** (2007) 069 [[hep-ph/0612236](#)].
53. P. Richardson, *Spin Correlations in Monte Carlo Simulations*, *JHEP* **11** (2001) 029 [[hep-ph/0110108](#)].
54. P. Richardson and A. Wilcock, *Monte Carlo Simulation of Hard Radiation in Decays in Beyond the Standard Model Physics in Herwig++*, *Eur. Phys. J. C* **74** (2014) 2713 [[1303.4563](#)].
55. D. Grellscheid and P. Richardson, *Simulation of Tau Decays in the Herwig++ Event Generator*, [arXiv:0710.1951 \[hep-ph\]](#).

56. M. Gigg and P. Richardson, *Simulation of Beyond Standard Model Physics in Herwig++*, *Eur. Phys. J.* **C51** (2007) 989 [[hep-ph/0703199](#)].
57. W. Kilian, T. Plehn, P. Richardson and E. Schmidt, *Split supersymmetry at colliders*, *eConf* **C050318** (2005) 0205 [[hep-ph/0507137](#)].
58. M. Bähr, S. Gieseke and M.H. Seymour, *Simulation of multiple partonic interactions in Herwig++*, *JHEP* **07** (2008) 076 [[0803.3633](#)].
59. J.M. Butterworth, J.R. Forshaw and M.H. Seymour, *Multi-Parton Interactions in Photoproduction at HERA*, *Z. Phys.* **C72** (1996) 637 [[hep-ph/9601371](#)].
60. M. Bähr, J.M. Butterworth and M.H. Seymour, *The Underlying Event and the Total Cross Section from Tevatron to the LHC*, *JHEP* **01** (2009) 065 [[0806.2949](#)].
61. S. Gieseke, C. Röhr and A. Siódtek, *Colour reconnections in Herwig++*, *Eur. Phys. J.* **C72** (2012) 2225 [[1206.0041](#)].
62. S. Gieseke, F. Loshaj and P. Kirchgässner, *Soft and diffractive scattering with the cluster model in Herwig*, *Eur. Phys. J.* **C77** (2017) 156 [[1612.04701](#)].
63. F. Campanario, T.M. Figy, S. Plätzer and M. Sjödahl, *Electroweak Higgs Boson Plus Three Jet Production at Next-to-Leading-Order QCD*, *Phys. Rev. Lett.* **111** (2013) 211802 [[1308.2932](#)].
64. F. Campanario, T.M. Figy, S. Plätzer, M. Rauch et al., *Stress testing the vector-boson-fusion approximation in multijet final states*, *Phys. Rev. D* **98** (2018) 033003 [[1802.09955](#)].
65. S. Alioli et al., *Update of the Binoth Les Houches Accord for a standard interface between Monte Carlo tools and one-loop programs*, *Comput. Phys. Commun.* **185** (2014) 560 [[1308.3462](#)].
66. J. Walter, M. Koch et al., *Boost: Basic Linear Algebra Library*, 2000.
67. M. Sjödahl, *ColorFull – a C++ library for calculations in SU(Nc) color space*, *Eur. Phys. J.* **C75** (2015) 236 [[1412.3967](#)].
68. S. Plätzer, *Summing Large- $N$  Towers in Colour Flow Evolution*, *Eur. Phys. J. C* **74** (2014) 2907 [[1312.2448](#)].
69. R. Ángeles Martínez, M. De Angelis, J.R. Forshaw, S. Plätzer et al., *Soft gluon evolution and non-global logarithms*, *JHEP* **05** (2018) 044 [[1802.08531](#)].
70. R. Kleiss, W.J. Stirling and S.D. Ellis, *A New Monte Carlo Treatment of Multiparticle Phase Space at High-energies*, *Comput. Phys. Commun.* **40** (1986) 359.
71. S. Plätzer, *RAMBO on diet*, [1308.2922](#).
72. S. Catani and M.H. Seymour, *A general algorithm for calculating jet cross sections in NLO QCD*, *Nucl. Phys.* **B485** (1997) 291 [[hep-ph/9605323](#)].
73. S. Catani, S. Dittmaier, M.H. Seymour and Z. Trócsányi, *The Dipole Formalism for Next-to-Leading Order QCD Calculations with Massive Partons*, *Nucl. Phys.* **B627** (2002) 189 [[hep-ph/0201036](#)].
74. Z. Bern, L.J. Dixon and D.A. Kosower, *One loop corrections to five gluon amplitudes*, *Phys. Rev. Lett.* **70** (1993) 2677 [[hep-ph/9302280](#)].
75. J.R. Andersen et al., *Les Houches 2013: Physics at TeV Colliders: Standard Model Working Group Report*, 2014 [[1405.1067](#)].
76. M. Cacciari, G.P. Salam and G. Soyez, *FastJet User Manual*, *Eur. Phys. J.* **C72** (2012) 1896 [[1111.6097](#)].
77. S. Frixione, *Isolated photons in perturbative QCD*, *Phys. Lett.* **B429** (1998) 369 [[hep-ph/9801442](#)].
78. S. Plätzer, *ExSample: A Library for Sampling Sudakov-Type Distributions*, *Eur. Phys. J.* **C72** (2012) 1929 [[1108.6182](#)].
79. G.P. Lepage, *A New Algorithm for Adaptive Multidimensional Integration*, *J. Comput. Phys.* **27** (1978) 192.
80. G.P. Lepage, *VEGAS: an Adaptive Multi-dimensional Integration Program*, Tech. Rep. CLNS-447, Cornell Univ. Lab. Nucl. Stud., Ithaca, NY (1980).
81. T. Binoth et al., *A Proposal for a Standard Interface between Monte Carlo Tools and One-Loop Programs*, *Comput. Phys. Commun.* **181** (2010) 1612 [[1001.1307](#)].
82. S. Plätzer, *SpinorHelicity*, 2010.
83. G. Cullen, N. Greiner, G. Heinrich, G. Luisone et al., *Automated One-Loop Calculations with GoSam*, *Eur. Phys. J.* **C72** (2012) 1889 [[1111.2034](#)].
84. G. Cullen et al., *GoSam-2.0: a tool for automated one-loop calculations within the Standard Model and beyond*, *Eur. Phys. J.* **C74** (2014) 3001 [[1404.7096](#)].
85. J. Braun, B. Campillo Avelaera, G. Heinrich, M. Höfer et al., *One-Loop Calculations in Effective Field Theories with GoSam-3.0*, [2507.23549](#).
86. J. Bellm, S. Gieseke, N. Greiner, G. Heinrich et al., *Anomalous coupling, top-mass and parton-shower effects in  $W^+W^-$  production*, *JHEP* **05** (2016) 106 [[1602.05141](#)].
87. K. Hagiwara and D. Zeppenfeld, *Amplitudes for Multiparton Processes Involving a Current at  $e^+e^-$ ,  $e^\pm p$ , and Hadron Colliders*, *Nucl. Phys.* **B313** (1989) 560.
88. S. Badger, B. Biedermann, P. Uwer and V. Yundin, *Numerical evaluation of virtual corrections to multi-jet production in massless QCD*, *Comput. Phys. Commun.* **184** (2013) 1981 [[1209.0100](#)].
89. J. Alwall, R. Frederix, S. Frixione, V. Hirschi et al., *The automated computation of tree-level and next-to-leading order differential cross sections, and their matching to parton shower simulations*, *JHEP* **07** (2014) 079 [[1405.0301](#)].
90. F. Buccioni, J.-N. Lang, J.M. Lindert, P. Maierhöfer et al., *OpenLoops 2*, *Eur. Phys. J. C* **79** (2019) 866 [[1907.13071](#)].
91. F. Cascioli, P. Maierhofer and S. Pozzorini, *Scattering Amplitudes with Open Loops*, *Phys. Rev. Lett.* **108** (2012) 111601 [[1111.5206](#)].
92. A. Denner, S. Dittmaier and L. Hofer, *Collier: a fortran-based Complex One-Loop Library in Extended Regularizations*, *Comput. Phys. Commun.* **212** (2017) 220 [[1604.06792](#)].
93. K. Arnold et al., *VBFNLO: A Parton level Monte Carlo for processes with electroweak bosons*, *Comput. Phys. Commun.* **180** (2009) 1661 [[0811.4559](#)].
94. J. Baglio et al., *VBFNLO: A Parton Level Monte Carlo for Processes with Electroweak Bosons – Manual for Version 2.7.0*, [1107.4038](#).
95. J. Baglio et al., *Release Note - VBFNLO 2.7.0*, [1404.3940](#).
96. J. Baglio et al., *Release note: VBFNLO 3.0*, *Eur. Phys. J. C* **84** (2024) 1003 [[2405.06990](#)].
97. T. Kinoshita, *Mass singularities of Feynman amplitudes*, *J. Math. Phys.* **3** (1962) 650.
98. T.D. Lee and M. Nauenberg, *Degenerate systems and mass singularities*, *Phys. Rev.* **133** (1964) B1549.
99. S. Frixione, Z. Kunszt and A. Signer, *Three jet cross-sections to next-to-leading order*, *Nucl. Phys.* **B467** (1996) 399 [[hep-ph/9512328](#)].
100. Z. Nagy and Z. Trócsányi, *Next-to-leading order calculation of four jet observables in electron positron annihilation*, *Phys. Rev.* **D59** (1999) 014020 [[hep-ph/9806317](#)].
101. Z. Nagy, *Next-to-leading order calculation of three jet observables in hadron hadron collision*, *Phys. Rev.* **D68** (2003) 094002 [[hep-ph/0307268](#)].
102. I.G. Knowles, *Spin Correlations in Parton-Parton Scattering*, *Nucl. Phys.* **B310** (1988) 571.
103. J.C. Collins, *Spin Correlations in Monte Carlo Event Generators*, *Nucl. Phys.* **B304** (1988) 794.
104. P. Nason, *A new method for combining NLO QCD with shower Monte Carlo algorithms*, *JHEP* **11** (2004) 040 [[hep-ph/0409146](#)].

105. S. Frixione, P. Nason and C. Oleari, *Matching NLO QCD computations with Parton Shower simulations: the POWHEG method*, *JHEP* **11** (2007) 070 [[arXiv:0709.2092 \[hep-ph\]](#)].

106. K. Hamilton, P. Richardson and J. Tully, *A Positive-Weight Next-to-Leading Order Monte Carlo Simulation of Drell-Yan Vector Boson Production*, *JHEP* **10** (2008) 015 [[0806.0290](#)].

107. K. Hamilton, *A positive-weight next-to-leading order simulation of weak boson pair production*, *JHEP* **01** (2011) 009 [[1009.5391](#)].

108. L. D'Errico and P. Richardson, *Next-to-Leading-Order Monte Carlo Simulation of Diphoton Production in Hadronic Collisions*, *JHEP* **02** (2012) 130 [[1106.3939](#)].

109. K. Hamilton, P. Richardson and J. Tully, *A Positive-Weight Next-to-Leading Order Monte Carlo Simulation for Higgs Boson Production*, *JHEP* **04** (2009) 116 [[0903.4345](#)].

110. L. D'Errico and P. Richardson, *A Positive-Weight Next-to-Leading-Order Monte Carlo Simulation of Deep Inelastic Scattering and Higgs Boson Production via Vector Boson Fusion in Herwig++*, *Eur. Phys. J.* **C72** (2012) 2042 [[1106.2983](#)].

111. E. Boos et al., *Generic User Process Interface for Event Generators*, [hep-ph/0109068](#).

112. J. Alwall et al., *A Standard Format for Les Houches Event Files*, *Comput. Phys. Commun.* **176** (2007) 300 [[hep-ph/0609017](#)].

113. J. Alwall, E. Boos, L. Dudko, M. Gigg et al., *A Les Houches Interface for BSM Generators*, Tech. Rep. **SLAC-PUB-13087**, **FERMILAB-CONF-07-621-T** (2007), DOI: [10.2172/921331](#).

114. P. Skands et al., *SUSY Les Houches accord: Interfacing SUSY spectrum calculators, decay packages, and event generators*, *JHEP* **07** (2004) 036 [[hep-ph/0311123](#)].

115. B.C. Allanach et al., *SUSY Les Houches Accord 2*, *Comput. Phys. Commun.* **180** (2009) 8 [[0801.0045](#)].

116. S. Alioli, P. Nason, C. Oleari and E. Re, *A general framework for implementing NLO calculations in shower Monte Carlo programs: the POWHEG BOX*, *JHEP* **06** (2010) 043 [[1002.2581](#)].

117. A. Papaefstathiou, S. Plätzer and K. Sakurai, *On the phenomenology of sphaleron-induced processes at the LHC and beyond*, *JHEP* **12** (2019) 017 [[1910.04761](#)].

118. S. Plätzer, *Parton Showers and Radiative Corrections in QCD*, Ph.D. thesis, KIT, Karlsruhe, Dept. Phys., 2010.

119. A. Bassutto, M. Ciafaloni, G. Marchesini and A.H. Mueller, *Jet Multiplicity and Soft Gluon Factorization*, *Nucl. Phys.* **B207** (1982) 189.

120. A. Bassutto, M. Ciafaloni and G. Marchesini, *Jet Structure and Infrared Sensitive Quantities in Perturbative QCD*, *Phys. Rept.* **100** (1983) 201.

121. S. Catani and M. Ciafaloni, *Many Gluon Correlations and the Quark Form-Factor in QCD*, *Nucl. Phys.* **B236** (1984) 61.

122. M. Ciafaloni, *Exponentiating Soft Emission in QCD*, *Phys. Lett.* **B95** (1980) 113.

123. M. Ciafaloni, *Soft Gluon Contributions to Hard Processes*, .

124. Yu. L. Dokshitzer, V.A. Khoze and S.I. Troian, *Coherence and Physics of QCD Jets*, *Adv. Ser. Direct. High Energy Phys.* **5** (1988) 241.

125. A.H. Mueller, *On the Multiplicity of Hadrons in QCD Jets*, *Phys. Lett.* **B104** (1981) 161.

126. B.I. Ermolaev and V.S. Fadin, *Log-Log Asymptotic Form of Exclusive Cross-Sections in Quantum Chromodynamics*, *JETP Lett.* **33** (1981) 269.

127. Yu. L. Dokshitzer, V.S. Fadin and V.A. Khoze, *Coherent Effects in the Perturbative QCD Parton Jets*, *Phys. Lett.* **B115** (1982) 242.

128. M. Rauch and S. Plätzer, *Parton Shower Matching Systematics in Vector-Boson-Fusion WW Production*, *Eur. Phys. J.* **C77** (2017) 293 [[1605.07851](#)].

129. A. Buckley et al., *General-purpose event generators for LHC physics*, *Phys. Rept.* **504** (2011) 145 [[1101.2599](#)].

130. S. Catani, S. Dittmaier and Z. Trócsányi, *One-Loop Singular Behaviour of QCD and SUSY QCD Amplitudes with Massive Partons*, *Phys. Lett.* **B500** (2001) 149 [[hep-ph/0011222](#)].

131. D.R. Yennie, S.C. Frautschi and H. Suura, *The Infrared Divergence Phenomena and High-energy Processes*, *Ann. Phys.* **13** (1961) 379.

132. R.K. Ellis, W.J. Stirling and B.R. Webber, *QCD and Collider Physics*, *Camb. Monogr. Part. Phys. Nucl. Phys. Cosmol.* **8** (1996) 1.

133. S. Catani, B.R. Webber and G. Marchesini, *QCD Coherent Branching and Semi-Inclusive Processes at Large x*, *Nucl. Phys.* **B349** (1991) 635.

134. R. Bonciani, S. Catani, M.L. Mangano and P. Nason, *Sudakov resummation of multiparton QCD cross sections*, *Phys. Lett.* **B575** (2003) 268 [[hep-ph/0307035](#)].

135. M. Cacciari, G. Corcella and A.D. Mitov, *Soft-Gluon Resummation for Bottom Fragmentation in Top Quark Decay*, *JHEP* **12** (2002) 015 [[hep-ph/0209204](#)].

136. H.K. Dreiner, P. Richardson and M.H. Seymour, *Parton-Shower Simulations of R-parity violating Supersymmetric Models*, *JHEP* **04** (2000) 008 [[hep-ph/9912407](#)].

137. M.J. Gibbs and B.R. Webber, *HERBVI: A Program for Simulation of Baryon and Lepton Number Violating Processes*, *Comput. Phys. Commun.* **90** (1995) 369 [[hep-ph/9504232](#)].

138. T. Sjöstrand, *A Model for Initial State Parton Showers*, *Phys. Lett.* **B157** (1985) 321.

139. ATLAS collaboration, *Measurement of the  $t\bar{t}$  production cross-section in the lepton+jets channel at  $\sqrt{s} = 13$  TeV with the ATLAS experiment*, Tech. Rep. **ATLAS-CONF-2019-044** (9, 2019).

140. ATLAS collaboration, *Observation of the associated production of a top quark and a Z boson in pp collisions at  $\sqrt{s} = 13$  TeV with the ATLAS detector*, Tech. Rep. **ATLAS-CONF-2019-043** (9, 2019).

141. ATLAS collaboration, *Search for the Higgs boson decays  $H \rightarrow ee$  and  $H \rightarrow e\mu$  in pp collisions at  $\sqrt{s} = 13$  TeV with the ATLAS detector*, *Phys. Lett. B* **801** (2020) 135148 [[1909.10235](#)].

142. ATLAS collaboration, *Measurements of inclusive and differential cross-sections of  $t\bar{t}\gamma$  production in the  $e\mu$  channel at 13 TeV with the ATLAS detector*, Tech. Rep. **ATLAS-CONF-2019-042** (9, 2019).

143. CMS collaboration, *Measurements of differential Higgs boson production cross sections in the leptonic WW decay mode at  $\sqrt{s} = 13$  TeV*, Tech. Rep. **CMS-PAS-HIG-19-002** (2019).

144. ATLAS collaboration, *Search for Higgs bosons produced via vector-boson fusion and decaying into bottom quark pairs in  $\sqrt{s} = 13$  TeV pp collisions with the ATLAS detector*, *Phys. Rev. D* **98** (2018) 052003 [[1807.08639](#)].

145. S. Dawson, A. Ismail and I. Low, *Redux on ‘When is the top quark a parton?’*, *Phys. Rev. D* **90** (2014) 014005 [[1405.6211](#)].

146. T. Han, J. Sayre and S. Westhoff, *Top-Quark Initiated Processes at High-Energy Hadron Colliders*, *JHEP* **04** (2015) 145 [[1411.2588](#)].

147. N. Darvishi, M.R. Masouminia and K. Ostrolenk,  *$k_t$  factorization versus collinear factorization in  $W^+W^-$  pair production at the LHC*, *Phys. Rev. D* **101** (2020) 014007 [[1909.13862](#)].

148. N. Darvishi and M.R. Masouminia, *Signature of the Maximally Symmetric 2HDM via  $W^\pm/Z$ -Quadruplet Productions at the LHC*, *Phys. Rev. D* **103** (2021) 095031 [[2012.14746](#)].

149. W. Beenakker and A. Werthenbach, *New insights into the perturbative structure of electroweak Sudakov logarithms*, *Phys. Lett. B* **489** (2000) 148 [[hep-ph/0005316](#)].

150. M. Ciafaloni, P. Ciafaloni and D. Comelli, *Electroweak Bloch-Nordsieck violation at the TeV scale: ‘Strong’ weak interactions?*, *Nucl. Phys. B* **589** (2000) 359 [[hep-ph/0004071](#)].

151. M. Ciafaloni, P. Ciafaloni and D. Comelli, *Electroweak double logarithms in inclusive observables for a generic initial state*, *Phys. Lett. B* **501** (2001) 216 [[hep-ph/0007096](#)].

152. P. Ciafaloni and D. Comelli, *Electroweak evolution equations*, *JHEP* **11** (2005) 022 [[hep-ph/0505047](#)].

153. U. Baur, *Weak Boson Emission in Hadron Collider Processes*, *Phys. Rev. D* **75** (2007) 013005 [[hep-ph/0611241](#)].

154. J. Chen, T. Han and B. Tweedie, *Electroweak Splitting Functions and High Energy Showering*, *JHEP* **11** (2017) 093 [[1611.00788](#)].

155. M. Chiesa, G. Montagna, L. Barzè, M. Moretti et al., *Electroweak Sudakov Corrections to New Physics Searches at the LHC*, *Phys. Rev. Lett.* **111** (2013) 121801 [[1305.6837](#)].

156. J.R. Christiansen and T. Sjöstrand, *Weak Gauge Boson Radiation in Parton Showers*, *JHEP* **04** (2014) 115 [[1401.5238](#)].

157. F. Krauss, P. Petrov, M. Schönherr and M. Spannowsky, *Measuring collinear W emissions inside jets*, *Phys. Rev. D* **89** (2014) 114006 [[1403.4788](#)].

158. M.L. Mangano, M. Moretti, F. Piccinini, R. Pittau et al., *ALPGEN, a generator for hard multiparton processes in hadronic collisions*, *JHEP* **07** (2003) 001 [[hep-ph/0206293](#)].

159. R. Kleiss and R. Verheyen, *Collinear electroweak radiation in antenna parton showers*, *Eur. Phys. J. C* **80** (2020) 980 [[2002.09248](#)].

160. H. Brooks, P. Skands and R. Verheyen, *Interleaved resonance decays and electroweak radiation in the Vincia parton shower*, *SciPost Phys.* **12** (2022) 101 [[2108.10786](#)].

161. G.L. Kane, W.W. Repko and W.B. Rolnick, *The Effective  $W^\pm, Z^0$  Approximation for High-Energy Collisions*, *Phys. Lett. B* **148** (1984) 367.

162. S. Dawson, *The Effective W Approximation*, *Nucl. Phys. B* **249** (1985) 42.

163. ATLAS collaboration, *Measurement of W boson angular distributions in events with high transverse momentum jets at  $\sqrt{s} = 8$  TeV using the ATLAS detector*, *Phys. Lett. B* **765** (2017) 132 [[1609.07045](#)].

164. N. Darvishi and M.R. Masouminia, *Electroweak radiative corrections in precision LHC measurements of  $W^\pm/Z0+jets$* , *Nucl. Phys. B* **985** (2022) 116025 [[2112.15487](#)].

165. S. Schumann and F. Krauss, *A Parton shower algorithm based on Catani-Seymour dipole factorisation*, *JHEP* **03** (2008) 038 [[0709.1027](#)].

166. S. Plätzer and M. Sjödahl, *The Sudakov Veto Algorithm Reloaded*, *Eur. Phys. J. Plus* **127** (2012) 26 [[1108.6180](#)].

167. S. Höche, S. Schumann and F. Siegert, *Hard photon production and matrix-element parton-shower merging*, *Phys. Rev. D* **81** (2010) 034026 [[0912.3501](#)].

168. L. Lönnblad, *Fooling Around with the Sudakov Veto Algorithm*, *Eur. Phys. J. C* **73** (2013) 2350 [[1211.7204](#)].

169. S. Mrenna and P. Skands, *Automated Parton-Shower Variations in Pythia 8*, *Phys. Rev. D* **94** (2016) 074005 [[1605.08352](#)].

170. S. Ferrario Ravasio, T. Ježo, P. Nason and C. Oleari, *A theoretical study of top-mass measurements at the LHC using NLO+PS generators of increasing accuracy*, *Eur. Phys. J. C* **78** (2018) 458 [[1801.03944](#)].

171. T. Ježo and P. Nason, *On the Treatment of Resonances in Next-to-Leading Order Calculations Matched to a Parton Shower*, *JHEP* **12** (2015) 065 [[1509.09071](#)].

172. P. Richardson and D. Winn, *Investigation of Monte Carlo Uncertainties on Higgs Boson searches using Jet Substructure*, *Eur. Phys. J. C* **72** (2012) 2178 [[1207.0380](#)].

173. M.A. Gigg and P. Richardson, *Simulation of Finite Width Effects in Physics Beyond the Standard Model*, [0805.3037](#).

174. M.H. Seymour, *The Higgs Boson Line Shape and Perturbative Unitarity*, *Phys. Lett. B* **354** (1995) 409 [[hep-ph/9505211](#)].

175. S. Jadach, W. Płaczek, S. Sapeta, A. Siódmodk et al., *Matching NLO QCD with parton shower in Monte Carlo scheme — the KrkNLO method*, *JHEP* **10** (2015) 052 [[1503.06849](#)].

176. S. Jadach, W. Płaczek, S. Sapeta, A. Siódmodk et al., *Parton distribution functions in Monte Carlo factorisation scheme*, *Eur. Phys. J. C* **76** (2016) 649 [[1606.00355](#)].

177. P. Sarmah, A. Siódmodk and J. Whitehead, *KrkNLO matching and phenomenology for vector boson processes*, [2511.16605](#).

178. S. Delorme, A. Kusina, A. Siódmodk and J. Whitehead, *Factorisation schemes for proton PDFs*, *Eur. Phys. J. C* **85** (2025) 505 [[2501.18289](#)].

179. CMS collaboration, *Measurements of differential Z boson production cross sections in proton-proton collisions at  $\sqrt{s} = 13$  TeV*, *JHEP* **12** (2019) 061 [[1909.04133](#)].

180. CMS collaboration, *Measurement of the mass dependence of the transverse momentum of lepton pairs in Drell-Yan production in proton-proton collisions at  $\sqrt{s} = 13$  TeV*, *Eur. Phys. J. C* **83** (2023) 628 [[2205.04897](#)].

181. M.H. Seymour, *Matrix Element Corrections to Parton Shower Algorithms*, *Comp. Phys. Commun.* **90** (1995) 95 [[hep-ph/9410414](#)].

182. R. Frederix and S. Frixione, *Merging meets matching in MC@NLO*, *JHEP* **12** (2012) 061 [[1209.6215](#)].

183. J. Alwall, M. Herquet, F. Maltoni, O. Mattelaer et al., *MadGraph 5 : Going Beyond*, *JHEP* **06** (2011) 128 [[1106.0522](#)].

184. R. Frederix, S. Frixione, A. Papageorgiou, S. Prestel et al., *A study of multi-jet production in association with an electroweak vector boson*, *JHEP* **02** (2016) 131 [[1511.00847](#)].

185. H. Murayama, I. Watanabe and K. Hagiwara, *HELAS: HELicity amplitude subroutines for Feynman diagram evaluations*, KEK-91-11.

186. C. Degrande, C. Duhr, B. Fuks, D. Grellscheid et al., *UFO - The Universal FeynRules Output*, *Comput. Phys. Commun.* **183** (2012) 1201 [[1108.2040](#)].

187. PARTICLE DATA GROUP collaboration, *Review of Particle Physics*, *Phys. Rev. D* **98** (2018) 030001.

188. L. Randall and R. Sundrum, *A Large Mass Hierarchy from a Small Extra Dimension*, *Phys. Rev. Lett.* **83** (1999) 3370 [[hep-ph/9905221](#)].

189. D. Hooper and S. Profumo, *Dark matter and Collider Phenomenology of Universal Extra Dimensions*, *Phys. Rept.* **453** (2007) 29 [[hep-ph/0701197](#)].

190. H.-C. Cheng, K.T. Matchev and M. Schmaltz, *Radiative corrections to Kaluza-Klein masses*, *Phys. Rev. D* **66** (2002) 036005 [[hep-ph/0204342](#)].

191. N. Arkani-Hamed, S. Dimopoulos and G.R. Dvali, *The hierarchy problem and new dimensions at a millimeter*, *Phys. Lett. B* **429** (1998) 263 [[hep-ph/9803315](#)].

192. N. Arkani-Hamed, S. Dimopoulos and G.R. Dvali, *Phenomenology, astrophysics and cosmology of theories with sub-millimeter dimensions and TeV scale quantum gravity*, *Phys. Rev. D* **59** (1999) 086004 [[hep-ph/9807344](#)].

193. J.D. Lykken, *Weak scale superstrings*, *Phys. Rev. D* **54** (1996) 3693 [[hep-th/9603133](#)].

194. E. Witten, *Strong Coupling Expansion Of Calabi-Yau Compactification*, *Nucl. Phys. B* **471** (1996) 135 [[hep-th/9602070](#)].

195. P. Horava and E. Witten, *Heterotic and type I string dynamics from eleven dimensions*, *Nucl. Phys. B* **460** (1996) 506 [[hep-th/9510209](#)].

196. P. Horava and E. Witten, *Eleven-Dimensional Supergravity on a Manifold with Boundary*, *Nucl. Phys. B* **475** (1996) 94 [[hep-th/9603142](#)].

197. I. Antoniadis, *A Possible new dimension at a few TeV*, *Phys. Lett. B* **246** (1990) 377.

198. G.F. Giudice, R. Rattazzi and J.D. Wells, *Quantum gravity and extra dimensions at high-energy colliders*, *Nucl. Phys. B* **544** (1999) 3 [[hep-ph/9811291](#)].

199. T. Han, H.E. Logan, B. McElrath and L.-T. Wang, *Phenomenology of the little Higgs model*, *Phys. Rev. D* **67** (2003) 095004 [[hep-ph/0301040](#)].

200. J. Hubisz and P. Meade, *Phenomenology of the littlest Higgs with T-parity*, *Phys. Rev.* **D71** (2005) 035016 [[hep-ph/0411264](#)].

201. A. Belyaev, C.-R. Chen, K. Tobe and C.P. Yuan, *Phenomenology of littlest Higgs model with  $T^-$  parity: including effects of  $T^-$  odd fermions*, *Phys. Rev.* **D74** (2006) 115020 [[hep-ph/0609179](#)].

202. J. Hubisz, S.J. Lee and G. Paz, *The Flavor of a little Higgs with T-parity*, *JHEP* **06** (2006) 041 [[hep-ph/0512169](#)].

203. D.B. Kaplan, *Flavor at SSC energies: A New mechanism for dynamically generated fermion masses*, *Nucl. Phys.* **B365** (1991) 259.

204. B. Gripaios, A. Papaefstathiou, K. Sakurai and B. Webber, *Searching for third-generation composite leptoquarks at the LHC*, *JHEP* **01** (2011) 156 [[1010.3962](#)].

205. H. Zhang, E.L. Berger, Q.-H. Cao, C.-R. Chen et al., *Color Sextet Vector Bosons and Same-Sign Top Quark Pairs at the LHC*, *Phys. Lett.* **B696** (2011) 68 [[1009.5379](#)].

206. E. Arik, O. Çakir, S.A. Çetin and S. Sultansoy, *A Search for vector diquarks at the CERN LHC*, *JHEP* **09** (2002) 024 [[hep-ph/0109011](#)].

207. O. Çakir and M. Sahin, *Resonant production of diquarks at high energy pp, ep and  $e^+e^-$  colliders*, *Phys. Rev.* **D72** (2005) 115011 [[hep-ph/0508205](#)].

208. S. Atag, O. Çakir and S. Sultansoy, *Resonance production of diquarks at the CERN LHC*, *Phys. Rev.* **D59** (1999) 015008.

209. E. Ma, M. Raidal and U. Sarkar, *Probing the exotic particle content beyond the standard model*, *Eur. Phys. J.* **C8** (1999) 301 [[hep-ph/9808484](#)].

210. G.F. Giudice, R. Rattazzi and J.D. Wells, *Transplanckian collisions at the LHC and beyond*, *Nucl. Phys.* **B630** (2002) 293 [[hep-ph/0112161](#)].

211. CDF collaboration, *Evidence for a Mass Dependent Forward-Backward Asymmetry in Top Quark Pair Production*, *Phys. Rev.* **D83** (2011) 112003 [[1101.0034](#)].

212. M. Czakon, P. Fiedler and A. Mitov, *Resolving the Tevatron Top Quark Forward-Backward Asymmetry Puzzle: Fully Differential Next-to-Next-to-Leading-Order Calculation*, *Phys. Rev. Lett.* **115** (2015) 052001 [[1411.3007](#)].

213. M. Czakon, P. Fiedler, D. Heymes and A. Mitov, *NNLO QCD predictions for fully-differential top-quark pair production at the Tevatron*, *JHEP* **05** (2016) 034 [[1601.05375](#)].

214. CDF, Do collaboration, *Combined Forward-Backward Asymmetry Measurements in Top-Antitop Quark Production at the Tevatron*, *Submitted to: Phys. Rev. Lett.* (2017) [[1709.04894](#)].

215. B. Gripaios, A. Papaefstathiou and B. Webber, *Probing the Colour Structure of the Top Quark Forward-Backward Asymmetry*, *JHEP* **11** (2013) 105 [[1309.0810](#)].

216. S. Jung, A. Pierce and J.D. Wells, *Top quark asymmetry from a non-Abelian horizontal symmetry*, *Phys. Rev.* **D83** (2011) 114039 [[1103.4835](#)].

217. A.V. Semenov, *LanHEP: A Package for automatic generation of Feynman rules in gauge models*, [hep-ph/9608488](#).

218. A. Semenov, *LanHEP - a package for automatic generation of Feynman rules from the Lagrangian. Updated version 3.1*, [1005.1909](#).

219. N.D. Christensen and C. Duhr, *FeynRules - Feynman rules made easy*, *Comput. Phys. Commun.* **180** (2009) 1614 [[0806.4194](#)].

220. A. Alloul, N.D. Christensen, C. Degrande, C. Duhr et al., *FeynRules 2.0 - A complete toolbox for tree-level phenomenology*, *Comput. Phys. Commun.* **185** (2014) 2250 [[1310.1921](#)].

221. F. Staub, *SARAH*, [0806.0538](#).

222. F. Staub, *SARAH 3.2: Dirac Gauginos, UFO output, and more*, *Comput. Phys. Commun.* **184** (2013) 1792 [[1207.0906](#)].

223. A. Meurer, C.P. Smith, M. Paprocki, O. Čertík et al., *Sympy: symbolic computing in python*, *PeerJ Computer Science* **3** (2017) e103.

224. D. Amati and G. Veneziano, *Preconfinement as a Property of Perturbative QCD*, *Phys. Lett.* **B83** (1979) 87.

225. A.H. Hoang, O.L. Jin, S. Plätzer and D. Samitz, *Matching hadronization and perturbative evolution: the cluster model in light of infrared shower cutoff dependence*, *JHEP* **07** (2025) 005 [[2404.09856](#)].

226. R. Zimmermann, *Aspects of Hadron Production in Herwig*, Master's thesis, KIT, Karlsruhe, Dept. Phys., 2021.

227. CMS collaboration, *Strange Particle Production in pp Collisions at  $\sqrt{s} = 0.9$  and 7 TeV*, *JHEP* **05** (2011) 064 [[1102.4282](#)].

228. ALICE collaboration, *Charged-particle multiplicity measurement in proton-proton collisions at  $\sqrt{s} = 7$  TeV with ALICE at LHC*, *Eur. Phys. J. C* **68** (2010) 345 [[1004.3514](#)].

229. C.M. Bishop, *Pattern Recognition and Machine Learning (Information Science and Statistics)*, Springer-Verlag, Berlin, Heidelberg (2006).

230. A. Kupčo, *Cluster Hadronization in HERWIG 5.9*, [hep-ph/9906412](#).

231. A.F. Falk and M.E. Peskin, *Production, decay, and polarization of excited heavy hadrons*, *Phys. Rev. D* **49** (1994) 3320 [[hep-ph/9308241](#)].

232. A.F. Falk and M.E. Luke, *Strong decays of excited heavy mesons in chiral perturbation theory*, *Phys. Lett. B* **292** (1992) 119 [[hep-ph/9206241](#)].

233. E.V. Shuryak, *The structure of hadrons containing a heavy quark*, *Phys. Lett. B* **93** (1980) 134.

234. W.E. Caswell and G.P. Lepage, *Effective Lagrangians for Bound State Problems in QED, QCD, and Other Field Theories*, *Phys. Lett. B* **167** (1986) 437.

235. E. Eichten, *Heavy Quarks on the Lattice*, *Nucl. Phys. B Proc. Suppl.* **4** (1988) 170.

236. G.P. Lepage and B.A. Thacker, *Effective Lagrangians for Simulating Heavy Quark Systems*, *Nucl. Phys. B Proc. Suppl.* **4** (1988) 199.

237. N. Isgur and M.B. Wise, *Weak Decays of Heavy Mesons in the Static Quark Approximation*, *Phys. Lett. B* **232** (1989) 113.

238. A.F. Falk and B. Grinstein, *Heavy meson pair production in  $e^+e^-$  annihilation from the static quark effective theory*, *Phys. Lett. B* **249** (1990) 314.

239. T. Mannel and Z. Ryzak, *Spin symmetry in  $e^+e^-$  annihilation into heavy mesons*, *Phys. Lett. B* **247** (1990) 412.

240. T.D. Cohen and J. Milana, *Heavy quark symmetry and pair production of heavy mesons: A Perturbative QCD estimate*, *Phys. Lett. B* **306** (1993) 134.

241. BABAR collaboration, *Measurement of the mass and width of the  $D_{s1}(2536)^+$  meson*, *Phys. Rev. D* **83** (2011) 072003 [[1103.2675](#)].

242. BELLE collaboration, *Observation of  $D_{s1}(2536)^+ \rightarrow D^+\pi^-K^+$  and angular decomposition of  $D_{s1}(2536)^+ \rightarrow D^*+K_S^0$* , *Phys. Rev. D* **77** (2008) 032001 [[0709.4184](#)].

243. W. Kilian, T. Plehn, P. Richardson and E. Schmidt, *Split Supersymmetry at Colliders*, *Eur. Phys. J. C* **39** (2005) 229 [[hep-ph/0408088](#)].

244. S. Kulkarni, M.R. Masouminia, S. Plätzer and D. Stafford, *Dark sector showers and hadronisation in Herwig 7*, *Eur. Phys. J. C* **84** (2024) 1210 [[2408.10044](#)].

245. L. Lönnblad et al., “TheP8I: an interface between the Pythia8 and the ThePEG toolkit.”

246. J.R. Christiansen and P.Z. Skands, *String Formation Beyond Leading Colour*, *JHEP* **08** (2015) 003 [[1505.01681](#)].

247. M. Divisova, M. Myska, P. Sarmah and A. Siódmok, *Herwig 7 with the Lund String Model: Tuning and Comparative Hadronization Studies*, [2509.02348](#).

248. DELPHI collaboration, *Tuning and test of fragmentation models based on identified particles and precision event shape data*, *Z. Phys. C* **73** (1996) 11.

249. ATLAS collaboration, *Measurement of angular correlations in Drell-Yan lepton pairs to probe  $Z/\gamma^*$  boson transverse momentum at  $\sqrt{s} = 7$  TeV with the ATLAS detector*, *Phys. Lett. B* **720** (2013) 32 [[1211.6899](#)].

250. UA5 collaboration, *The UA5 High-Energy  $\bar{p}p$  Simulation Program*, *Nucl. Phys.* **B291** (1987) 445.

251. M. Bähr, J.M. Butterworth, S. Gieseke and M.H. Seymour, *Soft interactions in Herwig++*, in *1st International Workshop on Multiple Partonic Interactions at the LHC*, pp. 239–248, 5, 2009 [[0905.4671](#)].

252. L. Durand and P. Hong, *QCD and Rising Cross Sections*, *Phys. Rev. Lett.* **58** (1987) 303.

253. L. Durand and H. Pi, *Semihard QCD and high-energy  $p\bar{p}$  and  $\bar{p}p$  scattering*, *Phys. Rev. D* **40** (1989) 1436.

254. L. Durand and H. Pi, *High-energy nucleon nucleus scattering and cosmic ray cross-sections*, *Phys. Rev. D* **38** (1988) 78.

255. M.M. Block and R.N. Cahn, *High-Energy  $p$  anti- $p$  and  $p$   $p$  Forward Elastic Scattering and Total Cross-Sections*, *Rev. Mod. Phys.* **57** (1985) 563.

256. I. Borozan and M.H. Seymour, *An eikonal model for multiparticle production in hadron hadron interactions*, *JHEP* **09** (2002) 015 [[hep-ph/0207283](#)].

257. CDF collaboration, *Measurement of double parton scattering in  $\bar{p}p$  collisions at  $\sqrt{s} = 1.8$  TeV*, *Phys. Rev. Lett.* **79** (1997) 584.

258. CDF collaboration, *Double parton scattering in  $\bar{p}p$  collisions at  $\sqrt{s} = 1.8$  TeV*, *Phys. Rev. D* **56** (1997) 3811.

259. A. Donnachie and P.V. Landshoff, *Total cross-sections*, *Phys. Lett. B* **296** (1992) 227 [[hep-ph/9209205](#)].

260. J. Bellm, S. Gieseke and P. Kirchgässner, *Improving the description of multiple interactions in Herwig*, *Eur. Phys. J. C* **80** (2020) 469 [[1911.13149](#)].

261. M. Baker and K.A. Ter-Martirosian, *Gribov's Reggeon Calculus: Its Physical Basis and Implications*, *Phys. Rept.* **28** (1976) 1.

262. S. Jadach, W. Płaczek, M. Skrzypek, B.F.L. Ward et al., *The Monte Carlo Program KoralW version 1.51 and the concurrent Monte Carlo KoralW & YFSWW3 with all background graphs and first order corrections to  $W$  pair production*, *Comput. Phys. Commun.* **140** (2001) 475 [[hep-ph/0104049](#)].

263. A.H. Mueller,  *$O(2,1)$  Analysis of Single Particle Spectra at High-energy*, *Phys. Rev. D* **2** (1970) 2963.

264. V. Barone and E. Predazzi, *High-Energy Particle Diffraction*, vol. v.565 of *Texts and Monographs in Physics*, Springer-Verlag, Berlin Heidelberg (2002).

265. ALICE collaboration, *Measurement of inelastic, single- and double-difraction cross sections in proton–proton collisions at the LHC with ALICE*, *Eur. Phys. J. C* **73** (2013) 2456 [[1208.4968](#)].

266. CDF collaboration, *Measurement of the  $\bar{p}p$  total cross-section at  $\sqrt{s} = 546$  GeV and 1800 GeV*, *Phys. Rev. D* **50** (1994) 5550.

267. A. Donnachie and P.V. Landshoff, *Does the hard Pomeron obey Regge factorisation?*, *Phys. Lett. B* **595** (2004) 393 [[hep-ph/0402081](#)].

268. D.J. Lange, *The EvtGen Particle Decay Simulation Package*, *Nucl. Instrum. Meth. A* **462** (2001) 152.

269. PARTICLE DATA GROUP collaboration, *Review of Particle Physics*, *PTEP* **2022** (2022) 083C01.

270. V.V. Kiselev, *Decays of the  $B_c$  Meson*, [hep-ph/0308214](#).

271. T. Skwarnicki, *Heavy quarkonium*, *Int. J. Mod. Phys. A* **19** (2004) 1030 [[hep-ph/0311243](#)].

272. E.J. Eichten, K. Lane and C. Quigg, *B Meson Gateways to Missing Charmonium Levels*, *Phys. Rev. Lett.* **89** (2002) 162002 [[hep-ph/0206018](#)].

273. W. Kwong and J.L. Rosner, *D Wave Quarkonium Levels of the Upsilon family*, *Phys. Rev. D* **38** (1988) 279.

274. S. Godfrey and J.L. Rosner, *Production of singlet P-wave  $c\bar{c}$  and  $b\bar{b}$  states*, *Phys. Rev. D* **66** (2002) 014012 [[hep-ph/0205255](#)].

275. E.J. Eichten and C. Quigg, *Mesons with Beauty and Charm: Spectroscopy*, *Phys. Rev. D* **49** (1994) 5845 [[hep-ph/9402210](#)].

276. D. Ebert, R.N. Faustov and V.O. Galkin, *Properties of Heavy Quarkonia and  $B_c$  mesons in the relativistic quark model*, *Phys. Rev. D* **67** (2003) 014027 [[hep-ph/0210381](#)].

277. W. Kwong, P.B. Mackenzie, R. Rosenfeld and J.L. Rosner, *Quarkonium Annihilation Rates*, *Phys. Rev. D* **37** (1988) 3210.

278. M. Di Pierro and E. Eichten, *Excited Heavy-Light systems and Hadronic Transitions*, *Phys. Rev. D* **64** (2001) 114004 [[hep-ph/0104208](#)].

279. N. Brambilla et al., *Heavy Quarkonium Physics*, [hep-ph/0412158](#).

280. S. Godfrey, *Spectroscopy of  $B_c$  mesons in the relativized quark model*, *Phys. Rev. D* **70** (2004) 054017 [[hep-ph/0406228](#)].

281. PARTICLE DATA GROUP collaboration, *Review of Particle Physics*, *J. Phys. G* **33** (2006) 1.

282. J.G. Körner and M. Kramer, *Exclusive Non-Leptonic Charm Baryon Decays*, *Z. Phys. C* **55** (1992) 659.

283. M.A. Ivanov, V.E. Lyubovitskij, J.G. Körner and P. Kroll, *Heavy Baryon Transitions in a Relativistic Three-Quark Model*, *Phys. Rev. D* **56** (1997) 348 [[hep-ph/9612463](#)].

284. A. Datta, H.J. Lipkin and P.J. O'Donnell, *Nonleptonic  $\Lambda_b$  decays to  $D_s(2317)$ ,  $D_s(2460)$  and other final states in factorization*, *Phys. Rev. D* **69** (2004) 094002 [[hep-ph/0312160](#)].

285. A.K. Leibovich, Z. Ligeti, I.W. Stewart and M.B. Wise, *Predictions for nonleptonic  $\Lambda_b$  and  $\Theta_b$  decays*, *Phys. Lett. B* **586** (2004) 337 [[hep-ph/0312319](#)].

286. M.A. Ivanov, J.G. Körner, V.E. Lyubovitskij and A.G. Rusetsky, *Exclusive nonleptonic decays of bottom and charm baryons in a relativistic three-quark model: Evaluation of nonfactorizing diagrams*, *Phys. Rev. D* **57** (1998) 5632 [[hep-ph/9709372](#)].

287. M.-Q. Huang, J.-P. Lee, C. Liu and H.S. Song, *Leading Isgur-Wise Form Factor of  $\Lambda_b$  to  $\Lambda_{c1}$  transition using QCD sum rules*, *Phys. Lett. B* **502** (2001) 133 [[hep-ph/0012114](#)].

288. H.-Y. Cheng, *Nonleptonic Weak decays of Bottom baryons*, *Phys. Rev. D* **56** (1997) 2799 [[hep-ph/9612223](#)].

289. M.A. Ivanov, J.G. Körner, V.E. Lyubovitskij and A.G. Rusetsky, *Strong and Radiative Decays of Heavy Flavored Baryons*, *Phys. Rev. D* **60** (1999) 094002 [[hep-ph/9904421](#)].

290. D. Ebert, R.N. Faustov, V.O. Galkin and A.P. Martynenko, *Semileptonic decays of doubly heavy baryons in the relativistic quark model*, *Phys. Rev. D* **70** (2004) 014018 [[hep-ph/0404280](#)].

291. A.V. Berezhnoy, A.K. Likhoded and A.V. Luchinsky, *Doubly heavy baryons at the LHC*, *Phys. Rev. D* **98** (2018) 113004 [[1809.10058](#)].

292. S.M. Flatté, *Coupled-Channel Analysis of the  $\pi\eta$  and  $K\bar{K}$  systems near  $K\bar{K}$  Threshold*, *Phys. Lett. B* **63** (1976) 224.

293. S. Jadach, Z. Wąs, R. Decker and J.H. Kühn, *The Tau decay library TAUOLA: Version 2.4*, *Comput. Phys. Commun.* **76** (1993) 361.

294. P. Golonka, B. Kercevan, T. Pierzchala, E. Richter-Wąs et al., *The Tauola photos F environment for the TAUOLA and PHOTOS packages: Release. 2.*, *Comput. Phys. Commun.* **174** (2006) 818 [[hep-ph/0312240](#)].

295. T. Plehn, P. Reimitz and P. Richardson, *Hadronic Footprint of GeV-Mass Dark Matter*, *SciPost Phys.* **8** (2020) 092 [[1911.11147](#)].

296. J.H. Kühn and A. Santamaria, *Tau decays to pions*, *Z. Phys. C* **48** (1990) 445.

297. G.J. Gounaris and J.J. Sakurai, *Finite width corrections to the vector meson dominance prediction for  $\rho \rightarrow e^+e^-$* , *Phys. Rev. Lett.* **21** (1968) 244.

298. H. Czyż, A. Grzelińska and J.H. Kühn, *Narrow resonances studies with the radiative return method*, *Phys. Rev. D* **81** (2010) 094014 [[1002.0279](#)].

299. SND collaboration, *Study of the reaction  $e^+e^- \rightarrow \pi^0\gamma$  with the SND detector at the VEPP-2M collider*, *Phys. Rev. D* **93** (2016) 092001 [[1601.08061](#)].

300. M.N. Achasov et al., *Updated measurement of the  $e^+e^- \rightarrow \omega\pi^0 \rightarrow \pi^0\pi^0\gamma$  cross section with the SND detector*, *Phys. Rev. D* **94** (2016) 112001 [[1610.00235](#)].

301. BABAR collaboration, *Measurements of  $e^+e^- \rightarrow K^+K^-\eta$ ,  $K^+K^-\pi^0$  and  $K_S^0K^\pm\pi^\mp$  cross-sections using initial state radiation events*, *Phys. Rev. D* **77** (2008) 092002 [[0710.4451](#)].

302. H. Czyż, J.H. Kühn and A. Wapienik, *Four-pion production in tau decays and  $e^+e^-$  annihilation: An Update*, *Phys. Rev. D* **77** (2008) 114005 [[0804.0359](#)].

303. A.E. Bondar et al., *Novosibirsk Hadronic currents for  $\tau \rightarrow 4\pi$  channels of tau decay library TAUOLA*, *Comput. Phys. Commun.* **146** (2002) 139 [[hep-ph/0201149](#)].

304. H. Czyż, M. Gunia and J.H. Kühn, *Simulation of electron-positron annihilation into hadrons with the event generator PHOKHARA*, *JHEP* **08** (2013) 110 [[1306.1985](#)].

305. R. Decker, E. Mirkes, R. Sauer and Z. Wąs, *Tau decays into three pseudoscalar mesons*, *Z. Phys.* **C58** (1993) 445.

306. M. Finkemeier and E. Mirkes, *The scalar contribution to  $\tau \rightarrow K\pi\nu_\tau$* , *Z. Phys.* **C72** (1996) 619 [[hep-ph/9601275](#)].

307. CLEO collaboration, *Hadronic Structure in the decay  $\tau^- \rightarrow \nu_\tau\pi^-\pi^0\pi^0$  and the sign of the tau neutrino helicity*, *Phys. Rev.* **D61** (2000) 012002 [[hep-ex/9902022](#)].

308. M. Finkemeier and E. Mirkes, *Tau decays into Kaons*, *Z. Phys.* **C69** (1996) 243 [[hep-ph/9503474](#)].

309. J.H. Kühn and Z. Wąs, *Tau decays to five mesons in TAUOLA*, *Acta Phys. Polon. B* **39** (2008) 147 [[hep-ph/0602162](#)].

310. M.N. Achasov et al., *Measurement of the  $e^+e^- \rightarrow \omega\eta$  cross section below  $\sqrt{s} = 2$  GeV*, *Phys. Rev. D* **94** (2016) 092002 [[1607.00371](#)].

311. M.N. Achasov et al., *Measurement of the  $e^+e^- \rightarrow \eta K^+K^-$  Cross Section by Means of the SND Detector*, *Phys. Atom. Nucl.* **81** (2018) 205.

312. M.N. Achasov et al., *Study of the  $e^+e^- \rightarrow \eta\gamma$  process with SND detector at the VEPP-2M  $e^+e^-$  collider*, *Phys. Rev. D* **74** (2006) 014016 [[hep-ex/0605109](#)].

313. H. Czyż, A. Grzelińska, J.H. Kühn and G. Rodrigo, *Electron-positron annihilation into three pions and the radiative return*, *Eur. Phys. J. C* **47** (2006) 617 [[hep-ph/0512180](#)].

314. R. Kleiss and W.J. Stirling, *Massive Multiplicities and Monte Carlo*, *Nucl. Phys.* **B385** (1992) 413.

315. B.R. Holstein, *Allowed eta decay modes and chiral symmetry*, *Phys. Scripta* **T99** (2002) 55 [[hep-ph/0112150](#)].

316. E.P. Venugopal and B.R. Holstein, *Chiral anomaly and  $\eta - \eta'$  mixing*, *Phys. Rev.* **D57** (1998) 4397 [[hep-ph/9710382](#)].

317. N. Beisert and B. Borasoy, *Hadronic Decays of  $\eta$  and  $\eta'$  with Coupled Channels*, *Nucl. Phys.* **A716** (2003) 186 [[hep-ph/0301058](#)].

318. M. Gormley et al., *Experimental Determination of the Dalitz-Plot distribution of the decays  $\eta \rightarrow \pi^+\pi^-\pi^0$  and  $\eta \rightarrow \pi^+\pi^-\gamma$ , and the branching ratio  $\eta \rightarrow \pi^+\pi^-\gamma/\eta \rightarrow \pi^+\pi^-\pi^0$* , *Phys. Rev.* **D2** (1970) 501.

319. CRYSTAL BALL collaboration, *Determination of the quadratic slope parameter in  $\eta \rightarrow 3\pi^0$  decay*, *Phys. Rev. Lett.* **87** (2001) 192001.

320. BABAR collaboration, *Dalitz plot analysis of  $\eta_c \rightarrow K^+K^-\eta$  and  $\eta_c \rightarrow K^+K^-\pi^0$  in two-photon interactions*, *Phys. Rev. D* **89** (2014) 112004 [[1403.7051](#)].

321. BABAR collaboration, *Light meson spectroscopy from Dalitz plot analyses of  $\eta_c$  decays to  $\eta'K^+K^-$ ,  $\eta'\pi^+\pi^-$ , and  $\eta\pi^+\pi^-$  produced in two-photon interactions*, *Phys. Rev. D* **104** (2021) 072002 [[2106.05157](#)].

322. BABAR collaboration, *Measurement of the  $I=1/2$   $K\pi$  S-wave amplitude from Dalitz plot analyses of  $\eta_c \rightarrow K\bar{K}\pi$  in two-photon interactions*, *Phys. Rev. D* **93** (2016) 012005 [[1511.02310](#)].

323. L.S. Brown and R.N. Cahn, *Chiral Symmetry and  $\psi' \rightarrow J/\psi\pi\pi$  Decay*, *Phys. Rev. Lett.* **35** (1975) 1.

324. BES collaboration,  $\psi(2s) \rightarrow \pi^+\pi^- J/\psi$  Decay Distributions, *Phys. Rev.* **D62** (2000) 032002 [[hep-ex/9909038](#)].

325. CLEO collaboration, *Study of Di-Pion Transitions Among  $\Upsilon(3s)$ ,  $\Upsilon(2s)$ , and  $\Upsilon(1s)$  States*, *Phys. Rev. D* **76** (2007) 072001 [[0706.2317](#)].

326. BABAR collaboration, *Observation of  $\Upsilon(4s)$  decays to  $\pi^+\pi^-\Upsilon(1s)$  and  $\pi^+\pi^-\Upsilon(2s)$* , *Phys. Rev. Lett.* **96** (2006) 232001 [[hep-ex/0604031](#)].

327. CLEO collaboration, *Observation of  $\psi(3770) \rightarrow \pi\pi J/\psi$  and measurement of  $\gamma(ee)(\psi(2s))$* , *Phys. Rev. Lett.* **96** (2006) 082004 [[hep-ex/0508023](#)].

328. BESIII collaboration, *Study of  $J/\psi \rightarrow p\bar{p}$  and  $J/\psi \rightarrow n\bar{n}$* , *Phys. Rev. D* **86** (2012) 032014 [[1205.1036](#)].

329. BESIII collaboration, *Observation of  $\Xi$ -hyperon transverse polarization in  $\psi(3686) \rightarrow \Xi^-\Xi^+$* , *Phys. Rev. D* **106** (2022) L091101 [[2206.10900](#)].

330. BESIII collaboration, *Polarization and Entanglement in Baryon-Antibaryon Pair Production in Electron-Positron Annihilation*, *Nature Phys.* **15** (2019) 631 [[1808.08917](#)].

331. BESIII collaboration, *Study of  $J/\psi$  and  $\psi(3686)$  decay to  $\Lambda\bar{\Lambda}$  and  $\Sigma^0\bar{\Sigma}^0$  final states*, *Phys. Rev. D* **95** (2017) 052003 [[1701.07191](#)].

332. BESIII collaboration, *Precise Measurements of Decay Parameters and CP Asymmetry with Entangled  $\Lambda - \bar{\Lambda}$  Pairs*, *Phys. Rev. Lett.* **129** (2022) 131801 [[2204.11058](#)].

333. BESIII collaboration, *Study of  $J/\psi$  and  $\psi(3686) \rightarrow \Sigma(1385)^0\bar{\Sigma}(1385)^0$  and  $\Xi^0\bar{\Xi}^0$* , *Phys. Lett. B* **770** (2017) 217 [[1612.08664](#)].

334. BESIII collaboration, *Tests of CP symmetry in entangled  $\Xi^0-\Xi^0$  pairs*, *Phys. Rev. D* **108** (2023) L031106 [[2305.09218](#)].

335. BESIII collaboration, *Study of  $J/\psi$  decays to the  $\Xi^-\bar{\Xi}^+$  and  $\Sigma(1385)^\mp\bar{\Sigma}(1385)^\pm$  final states*, *Phys. Rev. D* **93** (2016) 072003 [[1602.06754](#)].

336. BESIII collaboration, *Probing CP symmetry and weak phases with entangled double-strange baryons*, *Nature* **606** (2022) 64 [[2105.11155](#)].

337. BESIII collaboration,  *$\Sigma^+$  and  $\bar{\Sigma}^-$  polarization in the  $J/\psi$  and  $\psi(3686)$  decays*, *Phys. Rev. Lett.* **125** (2020) 052004 [[2004.07701](#)].

338. BESIII collaboration, *Observation of  $\psi(3686) \rightarrow n\bar{n}$  and improved measurement of  $\psi(3686) \rightarrow p\bar{p}$* , *Phys. Rev. D* **98** (2018) 032006 [[1803.02039](#)].

339. BESIII collaboration, *First simultaneous measurement of  $\Xi^0$  and  $\Xi^0$  asymmetry parameters in  $\psi(3686)$  decay*, *Phys. Rev. D* **108** (2023) L011101 [[2302.09767](#)].

340. BESIII collaboration, *Observation of the decay  $\psi(3686) \rightarrow \Sigma^-\bar{\Sigma}^+$  and measurement of its angular distribution*, *JHEP* **12** (2022) 016 [[2209.14564](#)].

341. BESIII collaboration, *Measurement of  $\Lambda^0$  baryon polarization in  $e^+e^- \rightarrow \Lambda\bar{\Lambda}$  at  $\sqrt{s} = 3.773$  GeV*, *Phys. Rev. D* **105** (2022) L011101 [[2111.11742](#)].

342. BESIII collaboration, *Observation of  $\psi(3686) \rightarrow \Xi(1530)^0\bar{\Xi}(1530)^0$  and  $\Xi(1530)^0\bar{\Xi}^0$* , *Phys. Rev. D* **104** (2021) 092012 [[2109.06621](#)].

343. BESIII collaboration, *Observation of  $\psi(3686) \rightarrow \Xi(1530)^-\bar{\Xi}(1530)^+$  and  $\Xi(1530)^-\bar{\Xi}^+$* , *Phys. Rev. D* **100** (2019) 051101 [[1907.13041](#)].

344. KLOE collaboration, *Study of the decay  $\phi \rightarrow \pi^+\pi^-\pi^0$  with the KLOE Detector*, *Phys. Lett.* **B561** (2003) 55 [[hep-ex/0303016](#)].

345. BABAR collaboration, *Dalitz plot analyses of  $J/\psi \rightarrow \pi^+\pi^-\pi^0$ ,  $J/\psi \rightarrow K^+K^-\pi^0$ , and  $J/\psi \rightarrow K_S^0K^\pm\pi^\mp$  produced via  $e^+e^-$  annihilation with initial-state radiation*, *Phys. Rev. D* **95** (2017) 072007 [[1702.01551](#)].

346. T. Han, J.D. Lykken and R.-J. Zhang, *On Kaluza-Klein states from Large Extra Dimensions*, *Phys. Rev.* **D59** (1999) 105006 [[hep-ph/9811350](#)].

347. M.A. Ivanov, J.G. Körner and V.E. Lyubovitskij, *One photon transitions between heavy baryons in a relativistic three quark model*, *Phys. Lett. B* **448** (1999) 143 [[hep-ph/9811370](#)].

348. A.F. Falk and T. Mehen, *Excited heavy mesons beyond leading order in the heavy quark expansion*, *Phys. Rev. D* **53** (1996) 231 [[hep-ph/9507311](#)].

349. BABAR collaboration, *Observation of new resonances decaying to  $D\pi$  and  $D^*\pi$  in inclusive  $e^+e^-$  collisions near  $\sqrt{s} = 10.58$  GeV*, *Phys. Rev. D* **82** (2010) 111101 [[1009.2076](#)].

350. LHCb collaboration, *Study of  $D_J$  meson decays to  $D^+\pi^-$ ,  $D^0\pi^+$  and  $D^{*+}\pi^-$  final states in  $pp$  collision*, *JHEP* **09** (2013) 145 [[1307.4556](#)].

351. P.L. Cho and H. Georgi, *Electromagnetic interactions in heavy hadron chiral theory*, *Phys. Lett. B* **296** (1992) 408 [[hep-ph/9209239](#)].

352. W.A. Bardeen, E.J. Eichten and C.T. Hill, *Chiral Multiplets of Heavy-Light Mesons*, *Phys. Rev. D* **68** (2003) 054024 [[hep-ph/0305049](#)].

353. P.L. Cho and M.B. Wise, *Comment on  $D_s^* \rightarrow D_s\pi^0$  decay*, *Phys. Rev. D* **49** (1994) 6228 [[hep-ph/9401301](#)].

354. B. Borasoy and B.R. Holstein, *Resonances in Radiative Hyperon Decays*, *Phys. Rev. D* **59** (1999) 054019 [[hep-ph/9902431](#)].

355. A. Ore and J.L. Powell, *Three Photon Annihilation of an Electron-Positron pair*, *Phys. Rev.* **75** (1949) 1696.

356. P. Ball and R. Zwicky, *New results on  $B \rightarrow \pi$ ,  $K$ ,  $\eta$  Decay Form Factors from Light-Cone sum rules*, *Phys. Rev. D* **71** (2005) 014015 [[hep-ph/0406232](#)].

357. P. Ball and R. Zwicky,  *$B_{d,s} \rightarrow \rho$ ,  $\omega$ ,  $K^*$ ,  $\phi$  Decay Form Factors from Light-Cone sum rules Revisited*, *Phys. Rev. D* **71** (2005) 014029 [[hep-ph/0412079](#)].

358. I. Caprini, L. Lellouch and M. Neubert, *Dispersive Bounds on the Shape of  $\bar{B} \rightarrow D^{(*)}\ell\bar{\nu}$  form factors*, *Nucl. Phys.* **B530** (1998) 153 [[hep-ph/9712417](#)].

359. BABAR collaboration, *Determination of the Form Factors for the Decay  $B^0 \rightarrow D^{*-}\ell^+\nu_\ell$  and of the CKM Matrix Element  $|V_{cb}|$* , [arXiv:0705.4008 \[hep-ex\]](#).

360. A.E. Snyder, *Review of Exclusive  $B \rightarrow D^{(*,*)}\ell\nu$  decays: Branching fractions, form-factors and  $|V(cb)|$* , [hep-ex/0703035](#).

361. N. Isgur, D. Scora, B. Grinstein and M.B. Wise, *Semileptonic  $B$  and  $D$  Decays in the Quark Model*, *Phys. Rev. D* **39** (1989) 799.

362. D. Scora and N. Isgur, *Semileptonic Meson Decays in the Quark Model: An Update*, *Phys. Rev. D* **52** (1995) 2783 [[hep-ph/9503486](#)].

363. N. Isgur and M.B. Wise, *Excited Charm Mesons in semileptonic  $\bar{B}$  decay and their contributions to a Bjorken sum rule*, *Phys. Rev. D* **43** (1991) 819.

364. D. Scora and N. Isgur, *Polarization in  $\bar{B} \rightarrow D^*e^-\bar{\nu}_e$  and  $D \rightarrow \bar{K}^*e^+\nu_e$* , *Phys. Rev. D* **40** (1989) 1491.

365. V.V. Kiselev, *Exclusive Decays and Lifetime of  $b_c$  meson in QCD sum rules*, [hep-ph/0211021](#).

366. D. Melikhov, *Semileptonic Decays  $B \rightarrow (\pi, \rho)\nu$  in Relativistic Quark Model*, *Phys. Lett. B* **380** (1996) 363 [[hep-ph/9603340](#)].

367. D. Melikhov and B. Stech, *Weak Form Factors for Heavy Meson Decays: An Update*, *Phys. Rev. D* **62** (2000) 014006 [[hep-ph/0001113](#)].

368. M. Wirbel, B. Stech and M. Bauer, *Exclusive Semileptonic Decays of Heavy Mesons*, *Z. Phys. C* **29** (1985) 637.

369. M. Bauer, B. Stech and M. Wirbel, *Exclusive Nonleptonic Decays of  $D$ ,  $D_s$ , and  $B$  Mesons*, *Z. Phys. C* **34** (1987) 103.

370. J.F. Donoghue and B.R. Holstein, *Quark Model Calculation of the Weak Electric Coupling in Semileptonic Baryon Decay*, *Phys. Rev. D* **25** (1982) 206.

371. H.-Y. Cheng and B. Tseng,  *$1/M$  Corrections to Baryonic form-factors in the quark model*, *Phys. Rev. D* **53** (1996) 1457 [[hep-ph/9502391](#)].

372. H. Czyż, J.H. Kühn and S. Tracz, *Nucleon form factors and final state radiative corrections to  $e^+e^- \rightarrow p\bar{p}\gamma$* , *Phys. Rev. D* **90** (2014) 114021 [[1407.7995](#)].

373. J.G. Körner and M. Kuroda,  *$e^+e^-$  Annihilation Into Baryon-anti-Baryon Pairs*, *Phys. Rev. D* **16** (1977) 2165.

374. F. Schlumpf, *Beta Decay of Hyperons in a Relativistic Quark Model*, *Phys. Rev. D* **51** (1995) 2262 [[hep-ph/9409272](#)].

375. R.L. Singleton, *Semileptonic Baryon Decays with a Heavy Quark*, *Phys. Rev. D* **43** (1991) 2939.

376. CLEO collaboration, *Dalitz plot analysis of the  $D^+ \rightarrow K^-\pi^+\pi^+$  decay*, *Phys. Rev. D* **78** (2008) 052001 [[0802.4214](#)].

377. E691 collaboration, *A Dalitz plot analysis of  $D \rightarrow K\pi\pi$  decays*, *Phys. Rev. D* **48** (1993) 56.

378. E791 collaboration, *Dalitz Plot Analysis of the Decay  $D^+ \rightarrow K^-\pi^+\pi^+$  and the Study of the  $K\pi$  Scalar Amplitudes*, *Phys. Rev. Lett.* **89** (2002) 121801 [[hep-ex/0204018](#)].

379. FOCUS collaboration, *Dalitz plot analysis of the  $D^+ \rightarrow K^-\pi^+\pi^+$  decay in the FOCUS experiment*, *Phys. Lett. B* **653** (2007) 1 [[0705.2248](#)].

380. FOCUS collaboration, *The  $K^-\pi^+$  S-wave from the  $D^+ \rightarrow K^-\pi^+\pi^+$  decay*, *Phys. Lett. B* **681** (2009) 14 [[0905.4846](#)].

381. MARK-III collaboration, *Resonant Substructure in  $K\pi$  pi Decays of Charmed d Mesons*, *Phys. Lett. B* **196** (1987) 107.

382. BESIII collaboration, *Amplitude Analysis of the  $D^+ \rightarrow K_S^0\pi^+\pi^0$  Dalitz Plot*, *Phys. Rev. D* **89** (2014) 052001 [[1401.3083](#)].

383. E791 collaboration, *Experimental evidence for a light and broad scalar resonance in  $D^+ \rightarrow \pi^-\pi^+\pi^+$  decay*, *Phys. Rev. Lett.* **86** (2001) 770 [[hep-ex/0007028](#)].

384. BESIII collaboration, *Study of the decay  $D^+ \rightarrow K^*(892)^+K_S^0$  in  $D^+ \rightarrow K^+K_S^0\pi^0$* , *Phys. Rev. D* **104** (2021) 012006 [[2104.09131](#)].

385. CLEO collaboration, *Search for CP Violation in the Dalitz-Plot Analysis of  $D^\pm \rightarrow K^+K^-\pi^\pm$* , *Phys. Rev. D* **78** (2008) 072003 [[0807.4545](#)].

386. LHCb collaboration, *Dalitz plot analysis of the  $D^+ \rightarrow K^-K^+K^+$  decay*, *JHEP* **04** (2019) 063 [[1902.05884](#)].

387. FOCUS collaboration, *Study of the doubly and singly Cabibbo suppressed decays  $D^+ \rightarrow K^+\pi^+\pi^-$  and  $D_s^+ \rightarrow K^+\pi^+\pi^-$* , *Phys. Lett. B* **601** (2004) 10 [[hep-ex/0407014](#)].

388. CLEO collaboration, *Dalitz analysis of the decay  $D^0 \rightarrow K^-\pi^+\pi^0$* , *Phys. Rev. D* **63** (2001) 092001 [[hep-ex/0011065](#)].

389. CLEO collaboration, *Dalitz analysis of  $D^0 \rightarrow K_S^0\pi^+\pi^-$* , *Phys. Rev. Lett.* **89** (2002) 251802 [[hep-ex/0207067](#)].

390. CLEO collaboration, *Search for CP violation in  $D^0 \rightarrow K_S^0\pi^+\pi^-$* , *Phys. Rev. D* **70** (2004) 091101 [[hep-ex/0311033](#)].

391. BABAR, BELLE collaboration, *Measurement of  $\cos 2\beta$  in  $B^0 \rightarrow D^{(*)}h^0$  with  $D \rightarrow K_S^0\pi^+\pi^-$  decays by a combined time-dependent Dalitz plot analysis of BaBar and Belle data*, *Phys. Rev. D* **98** (2018) 112012 [[1804.06153](#)].

392. CLEO collaboration, *Analysis of the Decay  $D^0 \rightarrow K_S^0\pi^0\pi^0$* , *Phys. Rev. D* **84** (2011) 092005 [[1106.3103](#)].

393. CLEO collaboration, *Searches for CP violation and  $\pi\pi$  S-wave in the Dalitz-Plot of  $D^0 \rightarrow \pi^+\pi^-\pi^0$* , *Phys. Rev. D* **72** (2005) 031102 [[hep-ex/0503052](#)].

394. BABAR collaboration, *Measurement of CP Violation Parameters with a Dalitz Plot Analysis of  $B^\pm \rightarrow D_{\pi^+\pi^-\pi^0} K^\pm$* , *Phys. Rev. Lett.* **99** (2007) 251801 [[hep-ex/0703037](#)].

395. BABAR collaboration, *Measurement of the neutral D meson mixing parameters in a time-dependent amplitude analysis of the  $D^0 \rightarrow \pi^+\pi^-\pi^0$  decay*, *Phys. Rev. D* **93** (2016) 112014 [[1604.00857](#)].

396. CLEO collaboration, *Studies of the decays  $D^0 \rightarrow K_S^0K^-\pi^+$  and  $D^0 \rightarrow K_S^0K^+\pi^-$* , *Phys. Rev. D* **85** (2012) 092016 [[1203.3804](#)].

397. LHCb collaboration, *Studies of the resonance structure in  $D^0 \rightarrow K_S^0K^\pm\pi^\mp$  decays*, *Phys. Rev. D* **93** (2016) 052018 [[1509.06628](#)].

398. BABAR collaboration, *Amplitude analysis of the decay  $D^0 \rightarrow K^-K^+\pi^0$* , *Phys. Rev. D* **76** (2007) 011102 [[0704.3593](#)].

399. BABAR collaboration, *Measurement of  $D^0$ - $\bar{D}^0$  mixing parameters using  $D^0 \rightarrow K_S^0 \pi^+ \pi^-$  and  $D^0 \rightarrow K_S^0 K^+ K^-$  decays*, *Phys. Rev. Lett.* **105** (2010) 081803 [[1004.5053](#)].

400. CLEO collaboration, *First observation and Dalitz analysis of the  $D^0 \rightarrow K_S^0 \eta \pi^0$  decay*, *Phys. Rev. Lett.* **93** (2004) 111801 [[hep-ex/0405011](#)].

401. BELLE collaboration, *Dalitz analysis of  $D^0 \rightarrow K^- \pi^+ \eta$  decays at Belle*, *Phys. Rev. D* **102** (2020) 012002 [[2003.07759](#)].

402. BABAR collaboration, *Dalitz plot analysis of  $D_s^+ \rightarrow K^+ K^- \pi^+$* , *Phys. Rev. D* **83** (2011) 052001 [[1011.4190](#)].

403. CLEO collaboration, *Dalitz Plot Analysis of  $D_s^+ \rightarrow K^+ K^- \pi^+$* , *Phys. Rev. D* **79** (2009) 072008 [[0903.1301](#)].

404. BESIII collaboration, *Amplitude analysis and branching fraction measurement of  $D_s^+ \rightarrow K^+ K^- \pi^+$* , *Phys. Rev. D* **104** (2021) 012016 [[2101.08041](#)].

405. E791 collaboration, *Study of the  $D_s^+ \rightarrow \pi^- \pi^+ \pi^+$  decay and measurement of  $f(0)$  masses and widths*, *Phys. Rev. Lett.* **86** (2001) 765 [[hep-ex/0007027](#)].

406. BESIII collaboration, *Amplitude analysis of  $D_s^+ \rightarrow \pi^+ \pi^- \pi^+$* , *Phys. Rev. D* **106** (2022) 112006 [[2108.10050](#)].

407. BABAR collaboration, *Dalitz Plot Analysis of  $D_s^+ \rightarrow \pi^+ \pi^- \pi^+$* , *Phys. Rev. D* **79** (2009) 032003 [[0808.0971](#)].

408. FOCUS collaboration, *Dalitz plot analysis of  $D_s^+$  and  $D^+$  decay to  $\pi^+ \pi^- \pi^+$  using the  $K$  matrix formalism*, *Phys. Lett. B* **585** (2004) 200 [[hep-ex/0312040](#)].

409. BESIII collaboration, *Amplitude analysis and branching fraction measurement of the decay  $D_s^+ \rightarrow \pi^+ \pi^0 \pi^0$* , *JHEP* **01** (2022) 052 [[2109.12660](#)].

410. BESIII collaboration, *Amplitude analysis and branching fraction measurement of the decay  $D_s^+ \rightarrow K^+ \pi^+ \pi^-$* , *JHEP* **08** (2022) 196 [[2205.08844](#)].

411. BESIII collaboration, *Amplitude analysis and branching-fraction measurement of  $D_s^+ \rightarrow K_S^0 \pi^+ \pi^0$* , *JHEP* **06** (2021) 181 [[2103.15098](#)].

412. BESIII collaboration, *Study of the decay  $D_s^+ \rightarrow K_S^0 K_S^0 \pi^+$  and observation an isovector partner to  $f_0(1710)$* , *Phys. Rev. D* **105** (2022) L051103 [[2110.07650](#)].

413. BESIII collaboration, *Observation of an  $a_0$ -like State with Mass of 1.817 GeV in the Study of  $D_s^+ \rightarrow K_S^0 K^+ \pi^0$  Decays*, *Phys. Rev. Lett.* **129** (2022) 182001 [[2204.09614](#)].

414. BESIII collaboration, *Amplitude analysis of  $D_s^+ \rightarrow \pi^+ \pi^0 \eta$  and first observation of the pure  $W$ -annihilation decays  $D_s^+ \rightarrow a_0(980)^+ \pi^0$  and  $D_s^+ \rightarrow a_0(980)^0 \pi^+$* , *Phys. Rev. Lett.* **123** (2019) 112001 [[1903.04118](#)].

415. BESIII collaboration, *Amplitude analysis and branching-fraction measurement of  $D_s^+ \rightarrow \pi^+ \pi^0 \eta'$* , *JHEP* **04** (2022) 058 [[2202.04232](#)].

416. B. Borasoy and B.R. Holstein, *The Role of Resonances in Non-Leptonic Hyperon Decays*, *Phys. Rev.* **D59** (1999) 094025 [[hep-ph/9902351](#)].

417. G. Duplancic, H. Pasagic and J. Trampetic, *Rare  $\Omega^- \rightarrow \Xi(1530)^0 \pi^-$  decay in the Skyrme model*, *Phys. Rev.* **D70** (2004) 077506 [[hep-ph/0405162](#)].

418. A.L. Kagan and M. Neubert, *QCD anatomy of  $B \rightarrow X_s \gamma$  Decays*, *Eur. Phys. J.* **C7** (1999) 5 [[hep-ph/9805303](#)].

419. ALEPH collaboration, *Study of Charm Production in  $Z$  decays*, *Eur. Phys. J.* **C16** (2000) 597 [[hep-ex/9909032](#)].

420. I.G. Knowles, *A Linear Algorithm for Calculating Spin Correlations in Hadronic Collisions*, *Comput. Phys. Commun.* **58** (1990) 271.

421. D. Aston et al., *A Study of  $K^- \pi^+$  Scattering in the Reaction  $K^- p \rightarrow K^- \pi^+ n$  at 11-GeV/c*, *Nucl. Phys. B* **296** (1988) 493.

422. D.V. Bugg, B.S. Zou and A.V. Sarantsev, *New results on  $\pi\pi$  phase shifts between 600-MeV and 1900-MeV*, *Nucl. Phys. B* **471** (1996) 59.

423. N.N. Achasov and G.N. Shestakov,  *$\pi\pi$  scattering  $S$  wave from the data on the reaction  $\pi^- p \rightarrow \pi^0 \pi^0 n$* , *Phys. Rev. D* **67** (2003) 114018 [[hep-ph/0302220](#)].

424. V.V. Anisovich and A.V. Sarantsev,  *$K$ -matrix analysis of the ( $IJ^{PC} = 00^{++}$ )-wave in the mass region below 1900 MeV*, *Eur. Phys. J. A* **16** (2003) 229 [[hep-ph/0204328](#)].

425. A. Buckley, J. Butterworth, L. Lönnblad, D. Grellscheid et al., *Rivet user manual*, *Comput. Phys. Commun.* **184** (2013) 2803 [[1003.0694](#)].

426. C. Bierlich et al., *Robust Independent Validation of Experiment and Theory: Rivet version 3*, *SciPost Phys.* **8** (2020) 026 [[1912.05451](#)].

427. A. Buckley, H. Hoeth, H. Lacker, H. Schulz et al., *Systematic event generator tuning for the LHC*, *Eur. Phys. J.* **C65** (2010) 331 [[0907.2973](#)].

428. J. Bellm and L. Gellerson, *High dimensional parameter tuning for event generators*, *Eur. Phys. J. C* **80** (2020) 54 [[1908.10811](#)].

429. J.R. Forshaw, J. Holguin and S. Plätzer, *Building a consistent parton shower*, *JHEP* **09** (2020) 014 [[2003.06400](#)].

430. TASSO collaboration, *Global Jet Properties at 14-GeV to 44-GeV Center-of-mass Energy in  $e^+e^-$  Annihilation*, *Z. Phys. C* **47** (1990) 187.

431. JADE collaboration, *A Study of event shapes and determinations of  $\alpha_s$  using data of  $e^+e^-$  annihilations at  $\sqrt{s} = 22$  GeV to 44 GeV*, *Eur. Phys. J. C1* (1998) 461 [[hep-ex/9708034](#)].

432. JADE collaboration, *QCD Analyses and Determinations of  $\alpha_s$  in  $e^+e^-$  annihilation at energies between 35-GeV and 189-GeV*, *Eur. Phys. J. C17* (2000) 19 [[hep-ex/0001055](#)].

433. DELPHI collaboration, *Tuning and Test of Fragmentation Models based on Identified Particles and Precision Event Shape Data*, *Z. Phys. C* **73** (1996) 11.

434. ALEPH collaboration, *Studies of Quantum Chromodynamics with the ALEPH detector*, *Phys. Rept.* **294** (1998) 1.

435. OPAL collaboration, *Measurement of event shape distributions and moments in  $e^+e^- \rightarrow$  hadrons at 91 GeV–209 GeV and a determination of  $\alpha_s$* , *Eur. Phys. J. C40* (2005) 287 [[hep-ex/0503051](#)].

436. ALEPH collaboration, *Studies of QCD at  $e^+e^-$  centre-of-mass energies between 91-GeV and 209-GeV*, *Eur. Phys. J. C35* (2004) 457.

437. OPAL collaboration, *Measurement of the Production rates of Charged Hadrons in  $e^+e^-$  annihilation at the  $Z^0$* , *Z. Phys. C* **63** (1994) 181.

438. OPAL collaboration,  *$\Delta^{++}$  production in Hadronic  $Z^0$  decays*, *Phys. Lett. B* **358** (1995) 162.

439. OPAL collaboration,  *$J/\psi$  and  $\psi'$  production in hadronic  $Z^0$  decays*, *Z. Phys. C* **70** (1996) 197.

440. DELPHI collaboration, *Strange baryon production in  $Z$  hadronic decays*, *Z. Phys. C67* (1995) 543.

441. OPAL collaboration, *Strange Baryon production in Hadronic  $Z^0$  decays*, *Z. Phys. C73* (1997) 569.

442. OPAL collaboration, *Spin Alignment of Leading  $K^{*0}(892)$  mesons in Hadronic  $Z^0$  decays*, *Phys. Lett. B* **412** (1997) 210 [[hep-ex/9708022](#)].

443. DELPHI collaboration, *Measurement of Inclusive  $\rho^0$ ,  $f^0(980)$ ,  $f_2(1270)$ ,  $K_2^{*0}(1430)$  and  $f_2'(1525)$  Production in  $Z^0$  decays*, *Phys. Lett. B* **449** (1999) 364.

444. OPAL collaboration, *Photon and Light Meson Production in Hadronic  $Z^0$  decays*, *Eur. Phys. J. C5* (1998) 411 [[hep-ex/9805011](#)].

445. OPAL collaboration, *Production of  $f_0(980)$ ,  $f_2(1270)$  and  $\phi(1020)$  in Hadronic  $Z^0$  decay*, *Eur. Phys. J. C4* (1998) 19 [[hep-ex/9802013](#)].

446. OPAL collaboration, *Multiplicities of  $\pi^0$ ,  $\eta$ ,  $K^0$  and of charged particles in Quark and Gluon Jets*, *Eur. Phys. J. C17* (2000) 373 [[hep-ex/0007017](#)].

447. ALEPH collaboration, *Inclusive production of the omega and eta mesons in Z decays, and the muonic branching ratio of the omega*, *Phys. Lett.* **B528** (2002) 19 [[hep-ex/0201012](#)].

448. BABAR collaboration, *Production of charged pions, kaons, and protons in  $e^+e^-$  annihilations into hadrons at  $\sqrt{s}=10.54$  GeV*, *Phys. Rev.* **D88** (2013) 032011 [[1306.2895](#)].

449. OPAL collaboration, *Measurements of flavor dependent fragmentation functions in  $Z^0 \rightarrow q\bar{q}$  events*, *Eur. Phys. J.* **C7** (1999) 369 [[hep-ex/9807004](#)].

450. SLD collaboration, *Measurement of the charged multiplicities in b, c and light quark events from Z0 decays*, *Phys. Lett.* **B386** (1996) 475 [[hep-ex/9608008](#)].

451. SLD collaboration, *Production of  $\pi^+$ ,  $K^+$ ,  $K^0$ ,  $K^{*0}$ ,  $\Phi$ ,  $p$  and  $\Lambda^0$  in hadronic  $Z^0$  decays*, *Phys. Rev.* **D59** (1999) 052001 [[hep-ex/9805029](#)].

452. SLD collaboration, *Production of  $\pi^+$ ,  $\pi^-$ ,  $K^+$ ,  $K^-$ ,  $p$  and anti- $p$  in light (uds), c and b jets from  $Z^0$  decays*, *Phys. Rev.* **D69** (2004) 072003 [[hep-ex/0310017](#)].

453. DELPHI collaboration, *Hadronization properties of b quarks compared to light quarks in  $e^+e^- \rightarrow q\bar{q}$  from 183-GeV to 200-GeV*, *Phys. Lett.* **B479** (2000) 118 [[hep-ex/0103022](#)].

454. OPAL collaboration, *Charged particle multiplicities in heavy and light quark initiated events above the  $Z^0$  peak*, *Phys. Lett.* **B550** (2002) 33 [[hep-ex/0211007](#)].

455. ALEPH collaboration, *Measurement of the charged particle multiplicity distribution in hadronic Z decays*, *Phys. Lett.* **B273** (1991) 181.

456. PARTICLE DATA GROUP collaboration, *Review of Particle Physics*, *Phys. Lett.* **B667** (2008) 1.

457. OPAL collaboration, *Experimental studies of unbiased gluon jets from  $e^+e^-$  annihilations using the jet boost algorithm*, *Phys. Rev.* **D69** (2004) 032002 [[hep-ex/0310048](#)].

458. OPAL collaboration, *Scaling violations of quark and gluon jet fragmentation functions in  $e^+e^-$  annihilations at  $\sqrt{s} = 91.2$  GeV and 183 GeV to 209 GeV*, *Eur. Phys. J.* **C37** (2004) 25 [[hep-ex/0404026](#)].

459. BELLE collaboration, *Charm hadrons from Fragmentation and B decays in  $e^+e^-$  annihilation at  $\sqrt{s} = 10.6$  GeV*, *Phys. Rev.* **D73** (2006) 032002 [[hep-ex/0506068](#)].

460. BABAR collaboration, *Inclusive  $\Lambda_c^+$  Production in  $e^+e^-$  Annihilations at  $\sqrt{s} = 10.54$  GeV and in  $\Upsilon(4S)$  Decays*, *Phys. Rev.* **D75** (2007) 012003 [[hep-ex/0609004](#)].

461. SLD collaboration, *Measurement of the b-quark fragmentation function in  $Z^0$  decays*, *Phys. Rev.* **D65** (2002) 092006 [[hep-ex/0202031](#)].

462. ALEPH collaboration, *Study of the fragmentation of b quarks into B mesons at the Z peak*, *Phys. Lett.* **B512** (2001) 30 [[hep-ex/0106051](#)].

463. DELPHI collaboration, *A study of the b-quark fragmentation function with the DELPHI detector at LEP I and an averaged distribution obtained at the Z Pole*, *Eur. Phys. J.* **C71** (2011) 1557 [[1102.4748](#)].

464. M. Derrick et al., *Study of Quark Fragmentation in  $e^+e^-$  Annihilation at 29-GeV: Charged Particle Multiplicity and Single Particle Rapidity Distributions*, *Phys. Rev.* **D34** (1986) 3304.

465. TPC/Two GAMMA collaboration, *Pion and kaon multiplicities in heavy quark jets from  $e^+e^-$  annihilation at 29-GeV*, *Phys. Lett.* **B184** (1987) 299.

466. PLUTO collaboration, *Multiplicity Distributions in  $e^+e^-$  Annihilations at PETRA Energies*, *Phys. Lett.* **95B** (1980) 313.

467. JADE collaboration, *Charged Particle and Neutral Kaon Production in  $e^+e^-$  Annihilation at PETRA*, *Z. Phys.* **C20** (1983) 187.

468. TASSO collaboration, *Charged Multiplicity Distributions and Correlations in  $e^+e^-$  Annihilation at PETRA Energies*, *Z. Phys.* **C45** (1989) 193.

469. AMY collaboration, *Charged hadron multiplicities in  $e^+e^-$  annihilations at  $\sqrt{s} = 50$  GeV – 61.4 GeV*, *Phys. Rev.* **D42** (1990) 737.

470. OPAL collaboration, *A Study of Charged Particle Multiplicities in Hadronic decays of the  $Z^0$* , *Z. Phys.* **C53** (1992) 539.

471. T. Sjöstrand, S. Mrenna and P. Skands, *PYTHIA 6.4 Physics and Manual*, *JHEP* **05** (2006) 026 [[hep-ph/0603175](#)].

472. A. Bassetto, G. Nardelli and R. Soldati, *Yang-Mills Theories in Algebraic Non-Covariant Gauges: Canonical Quantization and Renormalization*, *Singapore: World Scientific* (1991) 227 p.

473. M. Dalbosco, *One-Loop Gluon Self-Energy in the Light-Cone Gauge*, *Phys. Lett.* **B180** (1986) 121.

474. D. Amati, A. Bassetto, M. Ciafaloni, G. Marchesini et al., *A Treatment of Hard Processes Sensitive to the Infrared Structure of QCD*, *Nucl. Phys.* **B173** (1980) 429.

475. G. Curci and M. Greco, *Large Infrared Corrections in QCD Processes*, *Phys. Lett.* **B92** (1980) 175.

476. G. Curci and M. Greco, *Soft Corrections to the Drell-Yan Process in QCD*, *Phys. Lett.* **B102** (1981) 280.